New Approach to Connections between Members of Adjacent Box Beam Bridges

Kedar Ram Halbe

Dissertation submitted to the faculty of the Virginia Polytechnic Institute and

State University in partial fulfillment of the requirements for the degree of

DOCTOR OF PHILOSOPHY

In

CIVIL ENGINEERING

Carin L. Roberts-Wollmann, Chair

Thomas E. Cousins

Ioannis M. Koutromanos

Zachary C. Grasley

July 14, 2014

Blacksburg, Virginia

New Approach to Connections between Members of Adjacent Box Beam Bridges

Kedar Ram Halbe

ABSTRACT

The adjacent box beam bridges (ABBB) are considered as an ideal solution for short to medium span bridges and for routes with low to medium traffic volumes. The ABBB system has been utilized and is popular in several states in the United States. However, this bridge system has long term durability issues caused by shear key failure and reflective cracking in the topping. The means and methods to alleviate the problems in connections between members of the ABBB were researched and the development of new connection details was pursued.

Diagnostic tests to study the in-service behavior of ABBBs was performed. Two bridges with varying magnitude of joint deterioration were investigated. Both bridges were instrumented extensively and were subjected to known loads in the form of tandem trucks. The response of these bridges was studied and conclusions were made about the state of the bridges and the behavior after shear key failure. A finite element (FE) model of one of the tested bridges was developed to study the response of an ABBB with sound joints. The results of the finite element analysis (FEA) were compared with the results of the bridge diagnostic test. Conclusions about the FE model were made on the basis of this comparison. Another FE model, referred as the full scale bridge (FSB) was developed. The FSB model was used to simulate the behavior of an ABBB with the proposed connection details. This FSB model was subjected to design truck loads and the response was studied. The behavior of FSB model was replicated through a three beam sub-assembly that was supported on elastic supports. The stiffness of the elastic supports was calibrated such that the state of stress in the joints and the relative displacements between adjacent box beams in the sub-assemblage matched those in the FSB.

The three beam sub-assembly was constructed with the proposed connection details. Two new connection details were proposed in this research. A Kevlar and epoxy connection and a spliced connection with fiber reinforced self-consolidating concrete are proposed. A total of six specimens, with different connection details, were constructed and tested for strength and durability in the laboratory. The behavior of the proposed connections and the connection materials were studied in detail. Additional FEA was performed to study the effect of shrinkage and temperature on the proposed connection details.

DEDICATION

I dedicate this dissertation to my parents Dr. Ram and Dr. Alka Halbe, my sister Juiee Sampat and to my wife Anagha Parkar-Halbe.

ACKNOWLEDGEMENTS

Table of Contents

vi

List of Figures

xi

xiv

xvi

List of Tables

1. Introduction

1.1. General Information and Problem Statement

Adjacent box beam member bridges can be described as roadway/railway carrying structures that consist of main load carrying flexural members that are abutting one another. The salient feature of this bridge system is that the adjacent beams serve as the superstructure as well as the riding surface for vehicles albeit with a topping. The minimal gap between the beams nullifies the need for deck formwork and a topping such as asphalt or concrete can be placed directly over the beams to form the riding surface of the bridge. Typically, the flexural members consist of precast and prestressed box beams. These adjacent members are connected via a direct mechanical connection such as a shear key to facilitate load distribution between adjacent members. This mechanical contact can be achieved by placing grout in the joints between adjacent beams. Typical details of grouted joints consist of a partial depth or a full depth shear key. The application of shear key depth varies between states within USA. Transverse ties such as tensioned threaded rods or post-tensioned (PT) tendons can be used to strengthen the connections between adjacent beams. The riding surface or the deck can be composite or non-composite with the beams. For non-composite construction, bituminous materials are used to form the riding surface and for composite construction, concrete is used. The thickness of the topping varies on the basis of expected traffic on the bridge. A typical cross-section of an adjacent box beam bridge (ABBB) structure is shown in Figure 1.
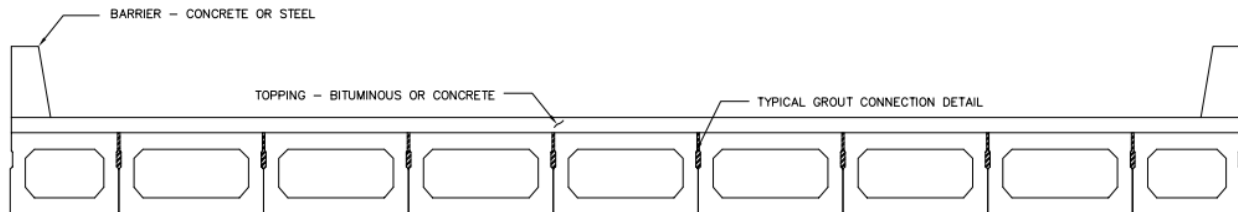
Figure 1: Typical cross-section detail of adjacent box beam bridge.

The adjacent box beam bridge (ABBB) system offers several advantages:

a) No need for deck forms. Reduces construction time.
b) Economical in terms of construction costs when compared to "I" or "bulb tee" sections for short to medium spans and low to medium volume traffic.
c) Ideal for places with low clearance tolerances due to shallow depth, which also provides an aesthetic appearance.
d) High torsional stiffness that allows for usage in curved beams.

The ABBB system has been implemented successfully in many states within USA and also in countries such as South Korea and Japan. Overall, this system has worked very well in the short term but it has proven to be problematic in the long term. The effect of the aforementioned advantages is diluted by a serious flaw that can be termed as the "Achilles heel" of the ABBB system. This is the occurrence of cracking of the shear key and reflective cracks in the riding surface of ABBB bridges. Note that "cracking of the shear key" is essentially a misnomer in the sense that the shear key does not actually crack but the shear key filler material (typically grout) debonds from the precast member causing a separation that may be termed as a crack in the shear key. This shear key failure can potentially lead to relative displacements between adjacent members and cause reflective cracking in the topping material. Typically occurring reflective cracks in ABBB with bituminous topping and ABBB with concrete topping are shown in Figure 2 and Figure 3 respectively.

Figure 2: Reflective cracks on an adjacent box beam bridge with a bituminous topping.

Figure 3: Reflective cracks on an adjacent box beam bridge with a concrete topping.

Reflective cracks in the deck may occur due to failure of the shear keys leading to relative movements between adjacent beams or due to the combination of the relative beam movements and shrinkage in the deck concrete or the connection filler material (typically grout). Moreover, the upshot of the reflective cracks is that chloride infused water penetrates into the deck and into the beams. This leads to corrosion of the reinforcement (prestressed and non-prestressed) within the beams and also of any transverse ties. The loss of transverse ties and shear key cracking is a severe condition for the bridge superstructure as it may affect the load transfer between adjacent beams. Moreover, the loss of prestressing strands and transverse ties may cause a sudden unexpected failure of the bridge superstructure. Such a superstructure failure (partial collapse) occurred in the Lake View Drive Bridge over I-70 in Pennsylvania, where a fascia beam collapsed unexpectedly under the effect of its self-weight only. The view of the fascia beam collapse is shown in Figure 4. The failure of the Lake View Drive Bridge will be covered in greater detail in the case study section of the literature review. The overall causes for shear key cracks and the reflective cracks will also be discussed in greater detail in the following chapters. Typical deterioration seen on the underside of ABBB is shown in Figure 5, Figure 6 and Figure 7.

Figure 4: Collapsed fascia beam of the Lake View Drive Bridge.
(http://www.constructionequipmentguide.com/I-70-Overpass-Collapses-in-Western-PA/6500/)

Figure 5: Cracked shear keys (with reflective cracks on topping) indicated by water leakage.

Figure 6: Concrete spalled off from beam underside including sections of prestressing strands.

Figure 7: Beam underside showing loss of prestressed strand and transverse ties.

The potential long term problems of the ABBB may seem like a "knockout blow" for the bridge system. However, the construction of these bridges is on the rise. About one-sixth of bridges being built annually on public roads are ABBB as per Russell (2009). The Federal Highway Administration (FHWA) is encouraging the use of these bridges via the Highways for LIFE (**L**onger-lasting highway infrastructure using **I**nnovations to accomplish the **F**ast construction of **E**fficient and safe highways and bridges) as per Russell (2009). With the advent of accelerated bridge construction (ABC – SHRP2 Program) the use of ABBB system is seeing a resurgence. It is to be noted that many of the newly constructed bridges happen to have the original transverse connection details (or their modified versions) and potentially face the same long term durability issues. There is certainly a need to resolve the known durability issues now that the use of ABBB is becoming widespread again.

1.2. Objectives and Scope of the Research

The objectives of this research are:

a) Determine cause(s) of shear key failure and reflective cracking in the deck.

b) Propose new connection details to improve shear key performance and bridge durability.

This document outlines the concept of each connection detail and then these details are modeled in ABAQUS and tested for repeated loads in the laboratory. The salient feature of these connections is the use of existing PCI Box Beam sections that are in widespread use in the USA. The simplest detail that is being proposed is the use of a Kevlar strip to reinforce the existing joint detail. The Kevlar strip offers the dual advantages of strengthening the joint and as a waterproof membrane even if the grouted joint fails. The other detail requires modifications to the existing beam section which essentially is the use of a blockout to form voids within top flange to make room for splice bars. These modified sections will not use grout as the connection filler material but two different mixes of Ultra High Performance Concrete (UHPC) will be investigated as an enhancement over the current connection detail. The first mix of UHPC is the prepackaged (proprietary) product sold by Lafarge called Ductal®. Ductal is a fiber reinforced, self-consolidating concrete and as such has a very good application to form the connection material for several precast concrete applications. The inherent self-consolidating properties, tensile strength and the potential for very short splices makes this product ideal for use in the new proposed connection details. The other mix, which is non-proprietary, was developed at University of Nebraska and modified at Virginia Tech. This mix consists of small aggregates, steel fibers and also offers the potential of self-consolidation. The non-proprietary mix will hence forth be referred to as Very High Performance Concrete (VHPC) for the ease of description. The salient features of these mixes will be discussed in greater detail in the following

chapters. As part of this research, tests were performed to quantify the minimum tension splice length required for Ductal®. Similar tests were performed on the VHPC but only the test results are referred in this document.

There has been a large amount of research effort guided towards solving, or at the very least, abating the issue of reflective cracking in ABBB system. Much of this effort has focused towards investigating the reasons for shear key failure, the use of different grouts, changing the shape or location of the shear key or increasing the number of transverse ties or the PT force and surface preparation techniques. However, the biggest unknown in the system is the magnitude of forces that are being transferred between adjacent box beams. Moreover, the existing practices show that there is a great variance in the magnitude of transverse PT as well as the number of PT tendons/threaded rods to use per span as per Russell (2009). To that effect an attempt is made, in this research, to quantify the forces in the transverse direction and develop a method through which forces can be calculated for the short term (traffic or other transient loads) and the long term (creep, shrinkage and temperature variations). This analysis was performed to ensure that the ABBB system will prove to be durable in the long term.

In this research the results from the field testing of bridges, finite element models and laboratory testing of sub-assemblage sections are used to derive conclusions regarding the behavior of existing bridge connections and the proposed improvements to transverse connections. Live load tests were performed on two different bridges (one with composite concrete topping and the other with non-composite bituminous topping). The field test results are used to ascertain the overall structural condition of the bridges. Although the bridges were extensively instrumented the results pertaining to relative displacements and the transverse load distribution are discussed in this report in order to keep the discussion focused on the central topic of the report. The results from the field tests are compared to 3-D finite element models with solid elements. The FEA model of the bridge was adjusted for boundary conditions (idealized supports vs. elastic springs to model elastomeric bearing pads). These models were then used to develop models of "test" bridges that were used for comparison with the specimens being tested in the lab. The response seen in the full scale "test" bridges was mimicked through a sub-assemblage model. The boundary conditions and the applied loads/displacements on this sub-assemblage setup were such that the response of the joint within the sub-assemblage was similar to that seen in the "test" bridge. The methods for attaining these results are discussed in greater detail in the following chapters.

1.3. Overview

This document is sub-divided into seven chapters. Following the introductory chapter, Chapter 2 provides a review of the literature focusing on research performed in adjacent box beam bridges, shear key materials, finite element analysis, use of innovative materials to form the transverse connections etc.

Chapter 3 covers the methodology of the research. The purpose of and the procedures used for the diagnostic tests, finite element analysis and the laboratory testing are discussed in detail.

Chapter 4 covers a part of the experimental work that was carried out in the field i.e. diagnostic tests on two bridges. The first bridge was in Almond, NY which was a two span continuous (for live loads) ABBB with a composite concrete topping. The second bridge was a simple span ABBB with a non-composite asphalt topping in Nokesville, Va. The diagnostic tests involved driving a tandem truck with known loads over the bridges to impart quasi-static and dynamic load effects. The live load tests were used to quantify the in service condition of the bridges as well as to quantify the responses at the joints of these bridges. The bridge behavior in the transverse direction is the focus of this research and results pertaining to the transverse direction are discussed here. The finite element analysis performed to simulate the diagnostic tests is also discussed in this chapter.

Chapter 5 discusses the tests performed in the laboratory to ascertain the minimum lengths of splice using UHPC and VHPC.

Chapter 6 focuses on the experimental work performed to quantify the behavior of the proposed connection details. The laboratory testing involved the application of repeated loads to the specimens to fatigue the joint and a series of static tests to measure the change in response of the specimen with increasing number of applied repeated loads. The finite element analysis of a typical ABBB bridge subjected to shrinkage and temperature gradients is also discussed in this chapter.

Chapter 7 contains the conclusions made from this research, the recommendations for ABBB system and suggestions for future work in ABBB research.

2. Literature Review

Bridges with adjacent precast box beams are a suitable system for short spans, places with low clearances and for accelerated bridge construction or replacement. This bridge system offers inherent advantages of economy, rapid construction and high torsional stiffness. However, the occurrence of reflective cracks in the deck persists to be the "Achilles heel" for this quick to implement and economical bridge system. The issue of reflective cracks in composite or non-composite decks of bridges with adjacent precast box beam bridges has been prevalent since the very first details for the bridge system were devised and implemented. Through research, experimentation and experience the connection details were updated to explore solutions to prevent or at least abate reflective cracking in bridges with adjacent precast box beams. The following paragraphs present a review of relevant research work that has been performed in investigation and abatement of reflective cracks in adjacent precast box beam bridges. The literature review is organized on the basis of the type of work involved in the research which includes materials testing, in field testing, specimen testing, analytical work and finite element modeling etc.

2.1. Typical Practices in ABBB

The typical practices used design and construction practices of ABBB are discussed.

2.1.1. AASHTO LRFD Bridge Design Specifications

The typical analysis assumptions for ABBB system are found in Chapter 4 of AASHTO (2013). ABBB system is categorized as type "f" or type "g" as defined by article 4.6.2.2.1 of AASHTO (2013). The schematic of these categories is shown in Figure 8.
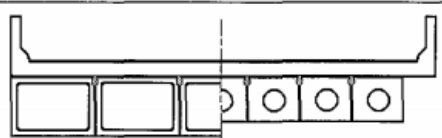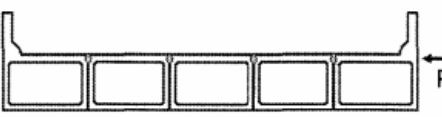
Precast Solid, Voided or Cellular Concrete Boxes with Shear Keys	Cast-in-place concrete overlay	
Precast Solid, Voided, or Cellular Concrete Box with Shear Keys and with or without Transverse Post-Tensioning	Integral concrete	

Figure 8: Superstructure category for design. AASHTO (2013).
[Reproduced as per "fair use" guidelines.]

The category type in which the actual bridge superstructure may be classified is dependent on the use of a concrete topping on the bridge superstructure. It is not clear whether the topping needs to be composite to alter the category type. Both the category types require the use of a shear key for transferring loads between beams, but the use of PT does not explicitly change the category type of the bridge superstructure. The superstructure category definition does not matter on the magnitude of the beam distribution factors (GDFs) for moments if the beams are deemed to have been connected sufficiently to act as a unit regardless of classification as "f" or "g" type. However, if the beams in the "g" type structure are not assumed to be acting as a unit then the GDFs for type "f" cannot be used. Therefore, it is indirectly indicated that the beams in the type "f" superstructure are assumed to act "as a unit". These changes in superstructure categories affect the interior beams only. The GDFs for moments are the same for exterior beams regardless of the classification. Similarly, the GDFs for shear force in interior and exterior beams are not affected by the classification.

The design assumptions for the ABBB system are found in Section 5.14.4.3 (Precast Deck Bridges) of AASHTO (2013). For shear keys intended to transfer only shear, Article 5.14.4.3.2 specifies the minimum depth of shear key (connection) shall be 7 in. And for the purpose of analysis the shear keys are to be assumed as hinges to ensure shear transfer only. In the commentary of this article, C15.4.4.3.2, it is indicated that such joints are susceptible to cracking and deterioration and in the long term the soundness of the shear key needs to be inspected. The assumption of shear transfer through hinges is analytically sound. However, in reality the depth of the key ensures that moments will be imparted on the joints causing cracking.

For shear keys intended to transfer shear as well as flexure the specifications in article 5.14.4.3.3 are applicable. As per 5.14.4.3.3a the precast components, beams in this instance, may be joined together by transverse PT, cast in place (CIP) closure joints, a structural overlay or a combination of these. The purpose of these joints is to provide a monolithic behavior. For the purposes of designing these joints the article 5.14.4.3.3d is applicable. This article specifies that the key cannot be less than 5 in. deep and a non-shrink grout is to be used that can attain a 5 ksi compressive strength within 24 hours. If transverse PT is used, the magnitude of compression across the joints should not be less than 0.25 ksi after losses. This compression is to be doubled in the last 3 ft of the member at the free end. The commentary, C15.4.4.3d, states that transverse PT is preferable in this system. The axis of the transverse PT force application has to be through the centerline of the shear key. Article 5.14.4.3.3c dictates the transvers PT requirements. Article C5.14.4.3.3c mentions that the spacing between the discrete points of PT application need not be less than the width of the beam as it is assumed that the transverse PT force spreads out in a 45 deg. or higher angle.

2.1.2. Virginia Department of Transportation Specifications

Virginia Department of Transportation (VDOT) design requirements for the ABBB system are as per VDOT (2013) and the requirements for the box beam sections and corresponding details are as per VDOT (2008).

The design requirements for prestressed concrete are specified in the Instructional and Informational memorandum version IIM-S&B-80.4 (2013) which specifies the modifications to AASHTO LRFD Bridge Design Specifications (2013). The current design requirements for VDOT are as per the current AASHTO requirements as discussed in Section 2.1.1.

The requirements for prestressed concrete box beams are found in the Manual of Structure and Bridge Division VDOT (2008). The beam sections used in ABBB system are as per the AASHO/PCI. A typical box section detail is shown in Figure 9
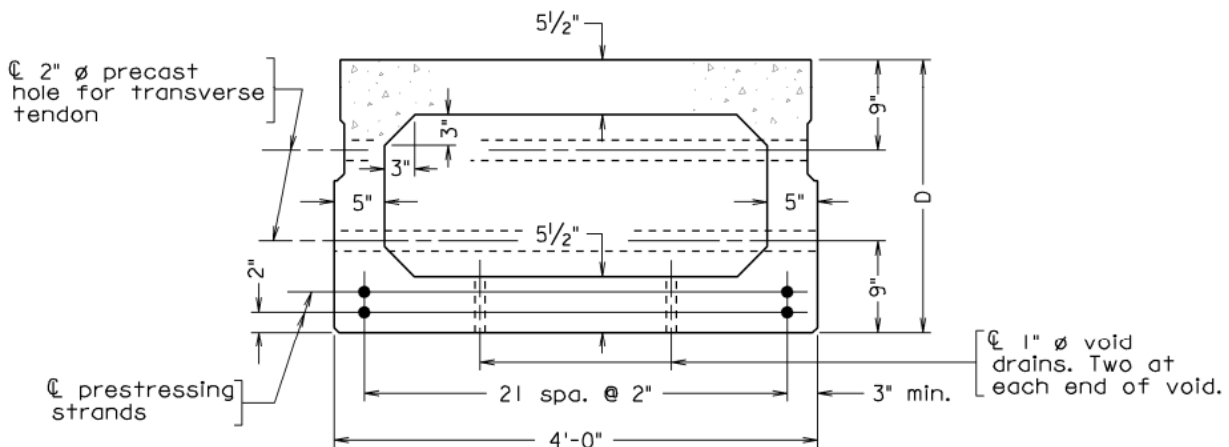
Figure 9: Typical 4 ft wide box beam section. VDOT (2008).
[Reproduced as per "fair use" guidelines.]

VDOT does not allow the use of these bridge beams on freeways and any urban or a route that may be considered as an "arterial" route. The typical usage of ABBB system and the topping detail is legislated by traffic conditions as shown in Table 1.

Table 1: Roadway functional classification for ABBB in Virginia.

Design Year ADT	ADTT	Deck/Overlay
≤ 4000	≤ 100	Asphalt Overlay
> 4000	100 < ADTT ≤ 200	Concrete deck 5 in. thick with a single layer of reinforcement.
> 4000	> 200	Concrete deck 7 in. thick with two layers of reinforcement.

VDOT specifies the use of a partial depth shear key detail as shown in Figure 10. The keys are sandblasted, cleaned and prewetted with clean water prior to grout placement. The grouting operation is performed prior to application of transverse PT force. PT force is applied to the bridge after the grout reaches a compressive strength of 4000 psi.

Figure 10: Typical shear key detail used in ABBBs in Virginia. VDOT (2008).
[Reproduced as per "fair use" guidelines.]

Transverse PT is recommended by VDOT for ABBB. Tensioned rods with threaded ends are used for bridges with width less than 20 ft. Typically these are 1¼ in. diameter galvanized steel rods conforming to ASTM A449 requirements. For bridges wider than 20 ft, the option of using aforementioned rods or ½ in. diameter coated, low relaxation Grade 270 strands are specified. The number of ties at each location is dependent on the depth of the beam sections. If the section depth is less than 33 in. then a single PT tendon is used at the beam mid-height. For beams deeper than 33 in. two ties are provided per location. These are provided near the top and the bottom of the beam. The spacing of ties per bridge span is decided as follows,

1. Bridges with ends restrained from lateral movement.
    a. One tie at midspan for spans ≤ 30 ft.
    b. Two ties, at ⅓rd points for spans ≤ 60 ft.
    c. Three ties, at ¼th points for spans > 60 ft.
2. Bridges with ends not restrained from lateral movement.
    a. Three ties, at midspan and ends for spans ≤ 30 ft.
    b. Four ties, at ⅓rd points and ends for spans ≤ 60 ft.
    c. Five ties, at ¼th points and ends for spans > 60 ft.

2.2. Known Issues and In Service Performances

El-Remaily et al. (1996) reported a survey performed by the PCI Committee on Bridges (Subcommittee on reflective cracking in ABBB). The committee sought the results of two national surveys that were conducted to identify the issues that led to longitudinal cracks in ABBB joints. The committee identified the following aspects as being important to the issue.

1. Reported leakage between joints.
2. Waterproofing membrane use over joints.
3. Limited skew for prestressed beams.
4. Shear keys grouted after PT application.
5. Problem with differential camber.
6. Uneven sealing of beam ends.
7. Material used for transverse ties.
8. Spacing of transverse ties.

The results of the first six aspects are shown in Figure 11. The above mentioned aspects were posed as questions with a "yes" or "no" answer for the occurrence of the said aspect. The results were plotted as a percentage of yes or no answers received.
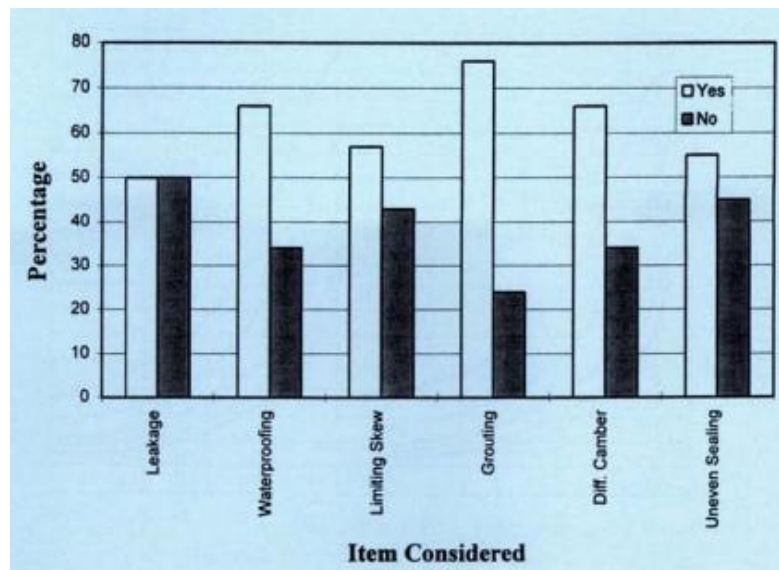
Figure 11: Summary of survey results as reported in El-Remaily et al. (1996).
[Reproduced as per "fair use" guidelines.]

The survey results showed that at least half of the bridges displayed a level of longitudinal cracking that was sufficient to cause leakage. Many states did not take advantage of imposing compression in ABBB

joints by applying PT prior to grouting the keyway. Finally, differential camber was problematic for grouting the keyway.

Russell (2009) surveyed various state DOTs and agencies to highlight the typical problems in the ABBB systems that were observed by those states/agencies. The most common issues faced by these bridge systems were the longitudinal cracks at the beam – grout interface and the corresponding water and salt leakage. The results of the survey are summarized in Figure 12.
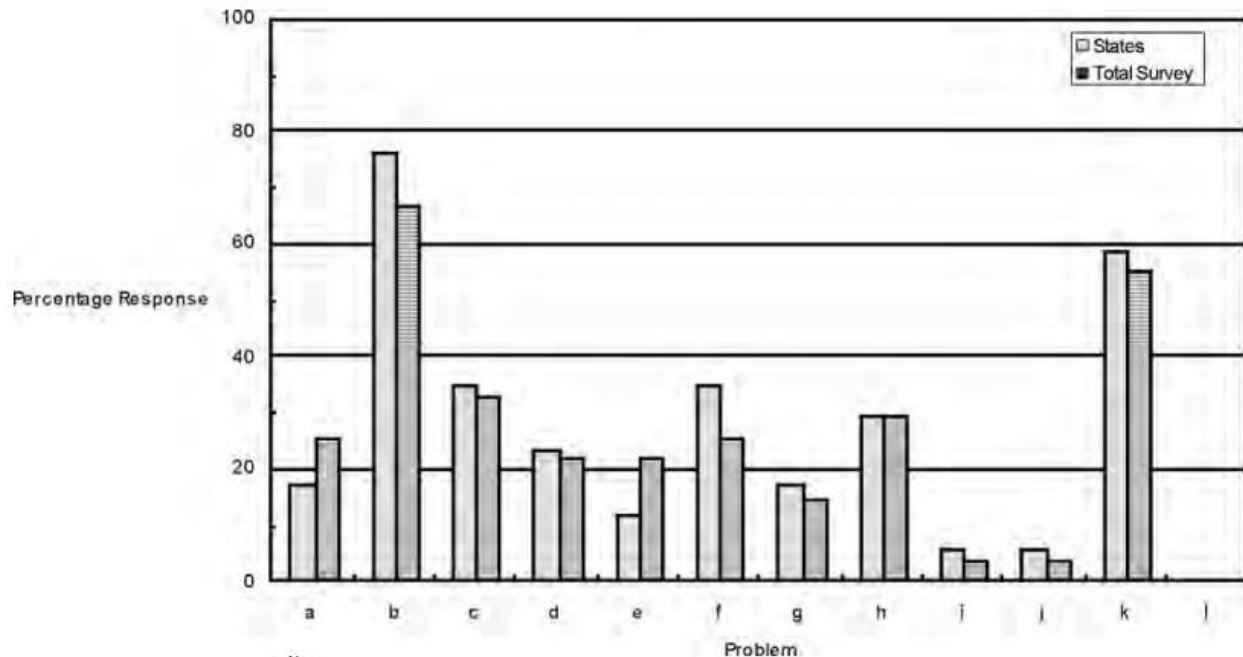
Figure 12: Summary of distresses observed in ABBB system. Russell (2009).
[Information available in public domain]

Where the x-axis of the plot corresponds to known problems and the explanation of the x-axis terms is as follows,

a. None.
b. Longitudinal cracking along grout and box beam interface.
c. Cracking within grout.
d. Spalling of the grout.
e. Spalling at the corners of the boxes.
f. Differential vertical movement between adjacent beams.
g. Corrosion of transverse ties.
h. Corrosion of longitudinal prestressing strands.
i. Freeze – thaw damage to the grout.
j. Freeze – thaw damage to the concrete adjacent to the joint.
k. Water and salt leakage through the joint.
l. Other.

2.3. Materials for Shear Keys

The materials selected for filling in the joints between beams typically were cast in place unreinforced concrete or cementitious grout. The use of epoxy as a shear key forming material has also been explored in another research.

Gulyas et al. (1995) performed laboratory tests to ascertain the effect of shrinkage and vehicular loading on the joints in ABBB. This research noted that the main focus of prevalent ABBB research (at that time) was on the post-tensioning of the transverse members to provide compression across elements and the grout used for the connection was provided the same importance. In research and practical applications the importance of surface preparation and the quality of grout was overlooked. The research involved experimental testing of keyway configurations in vertical shear, direct tension and longitudinal shear. The vertical shear specimens were used to simulate the case of vehicle induced stresses in ABBB joints. The direct tension configuration simulated a case of relative displacement between grout and beam due to shrinkage or loss of transverse prestress. The longitudinal specimen simulated the effect of differential shrinkage, creep or temperature induced movement at the grout – precast member interface. The schematic of these specimens is shown in Figure 13.

(a)

(b)

(c)
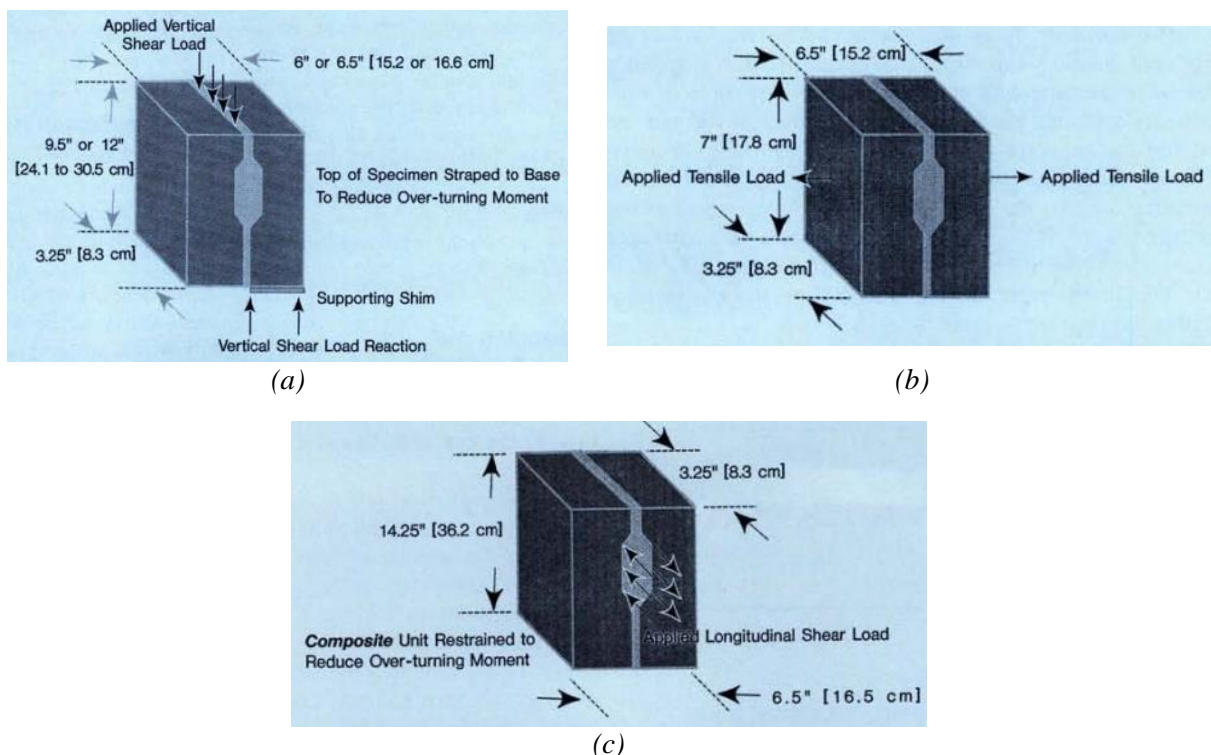
Figure 13: Schematic of test specimens (a) Vertical Shear, (b) Direct Tension and (c) Longitudinal Shear. Gulyas et al. (1995).

[Reproduced as per "fair use" guidelines.]

Two specimens were made for each test type. The vertical shear test setup was tested in two configurations with a key with 8 in. depth and a key with 12 in. depth. The longitudinal shear setup was tested with a 12 in. deep shear key while the direct tension test was performed with an 8 in. deep key. Therefore, a total of 16 specimens were tested, eight for typical non-shrink grout and eight for Magnesium Ammonium Phosphate mortar (MAP). Additionally, eight extra specimens were made to test the strength of the joint that had carbonated. MAP was used for the carbonated keyway tests. Sand blasting was used to prepare the surface. The specimens to be used as carbonated were sand blasted and then left exposed to air. The result of these tests are summarized in Table 2.

Table 2: Results of keyway tests.

Keyway Depth	Load Effect	Failure load (lb.)		
		Non-shrink grout	MAP	MAP Carbonated
12	Longitudinal Shear	2400*	14300[#]	4570[#]
12	Vertical Shear	5850*	16500[#]	8500[#]
8	Vertical Shear	7850*	20250[#]	11345[#]
8	Direct Tension	1940*	5730[#]	4145[#]

NOTES: * - indicates a bond line failure.

   # - indicates failure through base concrete.

[Reproduced as per "fair use" guidelines.]

The results show that MAP required higher loads to fail as compared to the non-shrink grout. MAP tested with a carbonated surface of the concrete element also was stronger than non-shrink grout with ideal surface preparation.

El-Esnawi (1996) conducted an experimental program on shear key forming materials and proposed new shear key configuration. The research consisted of comparison of non-shrink grout, magnesium ammonium phosphate mortar and epoxy resin mortar. The research was conducted on ABBB sub-assemblages. The sub-assemblage tests are explained in Section 2.4.1. Concrete carbonation was found to reduce the bond strength, especially when magnesium ammonium phosphate was used. Epoxy resin mortar was found to have the best bond with concrete substrate. However, the epoxy resin mortar was reported to have a significantly different co-efficient of thermal expansion than beam concrete and hence the long term use of this material required more testing as per this research.

Issa et al. (2003) evaluated the performance of four grout products as the shear key filler material. Experimental testing was performed on small scale specimens that simulated the conditions in the shear

key. A total of thirty six specimens were tested in vertical shear, direct tension and flexural capacity. The test setup for these tests was as shown in Figure 14.
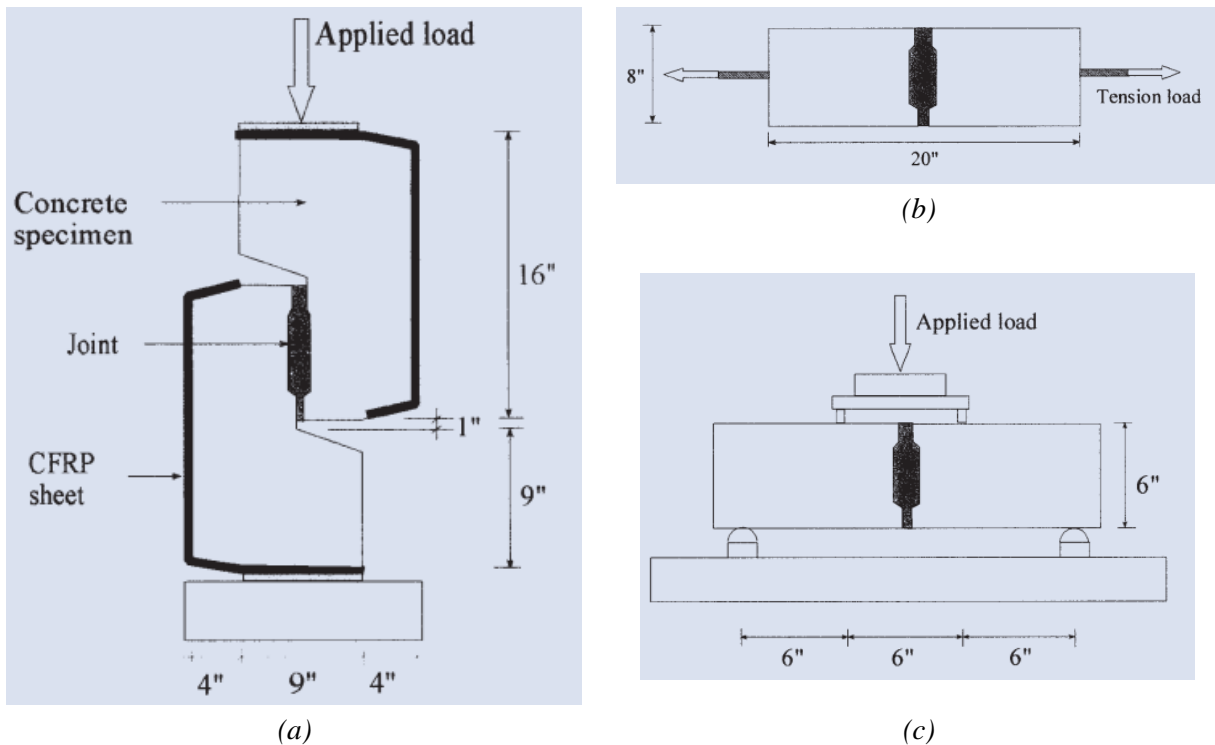
Figure 14: Test setup configurations for (a) Vertical Shear, (b) Direct Tension and (c) Flexural Tests. Issa et al. (2003).
[Reproduced as per "fair use" guidelines.]

The specimen surfaces that formed joint were sand blasted until the aggregates were visible and the surfaces were cleared of dust with air. The surfaces were tested for carbonation with a ten percent hydrochloric acid (HCl) and cleaned with HCl and water. The materials used in the testing were the Set 45, Set 45 for hot weather (HW), Set Grout and Polymer Concrete. In the direct shear tests the polymer concrete provided the highest capacity although the compressive strength of polymer concrete also was the highest. The failure mode for this test was through the base concrete for the polymer grout. Similarly, the polymer concrete provided the most resistance in the direct tension tests as wells as the flexural test. Additionally, chloride permeability tests were conducted and polymer concrete provided the highest resistance to chloride penetrations. Issa et al. recommended the use of polymer concrete in the situations where the bridge was expected to reopen in short time. However, polymer concrete was very expensive and required careful handling and mixing was required. Therefore, authors recommended the use of Set grout as the material that had acceptable strength and was easy to mix and place in the field. Note that the Set 45 and Set 45 HW were MAP mortars.

2.4. Shear Key Configurations

This section describes the research performed to investigate an improvement in the location of the shear key (along the beam depth) and alternative shear key shapes.

2.4.1. Alternative Shear Key Location

El-Esnawi (1996) proposed a mid-depth shear key as a replacement for the typical partial depth shear key at the beam top. Experiments were performed with three different filler materials as discussed in Section 2.3. The testing was performed by converting the three dimensional (3-D) bridge behavior to a two dimensional behavior (2-D). The conversion of 3-D to 2-D was achieved by constructing a 1 ft thick midspan "slice" of a typical ABBB. This sub-assemblage consisted of three beam sections. The individual beam sections were supported by neoprene pads under the webs to make the sub-assemblage behavior consistent with the full bridge behavior. The stiffness of the supports was determined from a 3D finite element analysis of ABBB and the 2D sub-assemblage specimens. The main aim of this research was to propose a new shear key design to overcome problems associated with the typical partial depth shear key detail in ABBB. The new detail called for locating the shear key at the neutral axis (mid height) of the section. The program also consisted of testing the typical shear key configuration with the proposed configuration incorporating different grout materials such as reviewed in both of the details. The specimens were loaded statically until failure and it was found that the capacity of the proposed configuration was almost thrice of that of the traditional configuration. Moreover, the fatigue life of these sections was tested and the specimens with the mid height shear key failed after 8000000 cycles whereas the one with the typical partial depth top detail failed only after a 100 cycles.

Lall et al. (1998) conducted a study for the New York State Department of Transportation (NYSDOT) to evaluate the performance of a full depth shear key configuration in adjacent box beam bridges. The paper describes two studies conducted in 1990 which focused on the ABBB built between 1985 and 1990 and a follow up study performed in 1996. The study conducted in 1990 showed that more than half the bridges built between 1985 and 1990 had incidences of reflective cracking that is, 187 bridges were inspected and 101 bridges displayed longitudinal cracking. This study (from 1990) also focused on details and construction practices employed by other states. Based on the state of NY bridges and the results of the study of construction practices NYSDOT adopted a full depth shear key detail with additional number of transverse PT tendons that is, three for spans up to 50ft and five for longer spans. These details were adopted in May 1992 and a follow up study was conducted in 1996 to observe the effect of the new details.

The NYSDOT details before and after May 1992 are shown in Figure 15. Essentially, pre 1992 detail consisted of partial depth key (depth 12 in.) with grout as the connection material for the bottom 7 in. depth and the top 5 in. filled with asphalt. The new detail proposed the use of a full depth shear key. The

beam cross-section was kept the same but the beam connection was filled to the complete beam depth. A single PT tendon was used at the mid-depth of the beam.
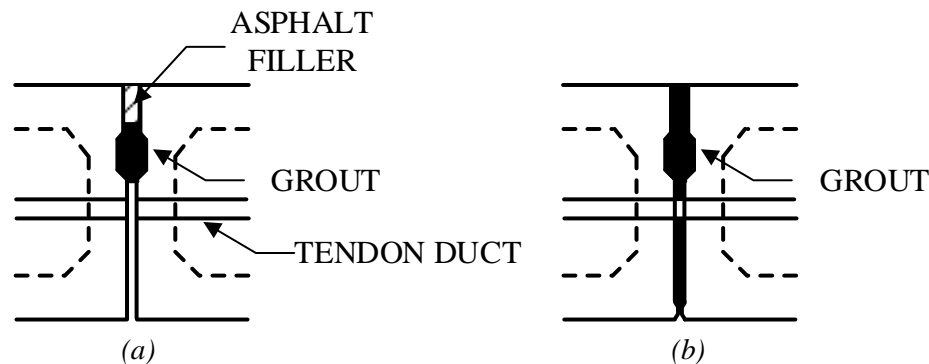
Figure 15: NYSDOT transverse connection details (a) before 1992 and (b) after 1992.
[Reproduced as per "fair use" guidelines.]

The follow up study consisted of inspections of all the bridges built (91 total) with the new connection details. The study found that 21 bridges out of a total of 91 exhibited reflective cracking. The study also showed that a total of 874 joints were inspected (on the 91 bridges) and only 47 displayed reflective cracks on the deck which is 5%. It is to be noted that the 5% figure pertains to shear key failure leading to reflective cracks It is not clear if there were other cracked shear keys that had not yet developed reflective cracks in the deck. Based on this investigation in 1996 it was concluded that the newly adopted shear key detail was directly responsible for reduction in reflective cracks. Moreover, it was also noted that the cracked keyways displayed signs of minor leakage. Other significant observations from this research were as follows,

(a) Bridges with higher average annual daily traffic (AADT) displayed more severe reflective cracking. Of the 21 bridges with reflective cracks the two bridges with the most severe deterioration at the joints had the highest incidence of truck traffic.

(b) Frequency of shear key cracking was unrelated to bridge skew.

(c) Frequency of shear key cracking was not related to bridge span lengths.

(d) Bridges with fixed bearings had more cracks than bridges with expansion bearings.

Miller et al. (1999) studied the effect of shear key location on the incidence of shear key failure. Three experimental tests were performed to ascertain the cause of shear key cracks and to evaluate a new joint detail and also to evaluate a new filler material to replace non-shrink grout. The typical detail and the proposed mid-depth detail are shown in Figure 16.
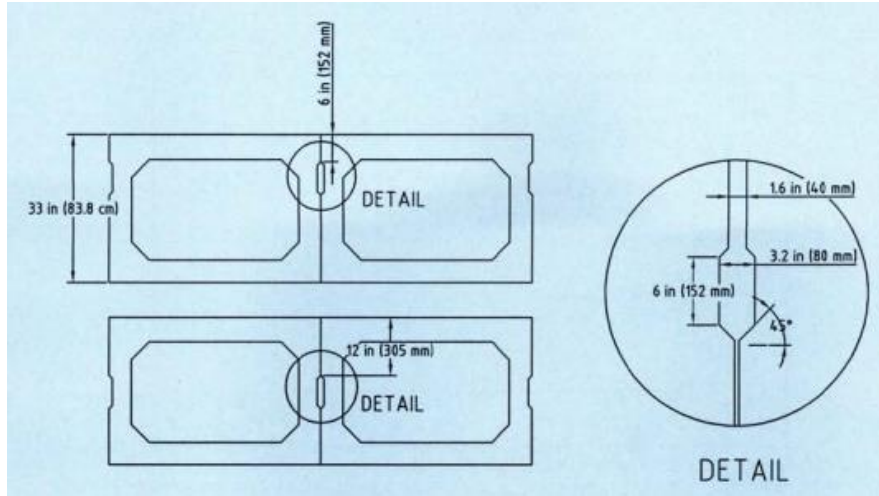
Figure 16: Shear key configurations. Miller et al. (1999).
[Reproduced as per "fair use" guidelines.]

The testing focused on ascertaining causes of shear key failure by using the partial depth shear key located at the beam top and filled with non-shrink grout. The new mid-depth location was also tested with the non-shrink grout. Finally, the use of epoxy was tested with the typical shear key detail at the top of the beam. The experimentation was conducted on a bridge section consisting of four beams and a span length of 75 ft The same beams were used for all the tests i.e. the beams were fabricated with two shear keys one at top and one at the mid-depth. After every test the beam setup was taken apart and the non-shrink grout was removed for beam reuse. The four beams simulated interior beams on a typical ABBB. The transverse connection between beams was provided through a tie rod that was tensioned with a torque wrench. It was noted that by this method the amount of transverse PT achieved was very small. Also, the keyway filler material was placed in the joints after tensioning the transverse tie rods.

The simulated bridge was loaded by a set of four actuators that were placed over the bridge midspan. The schematic of the bridge and the load application is shown in Figure 17.
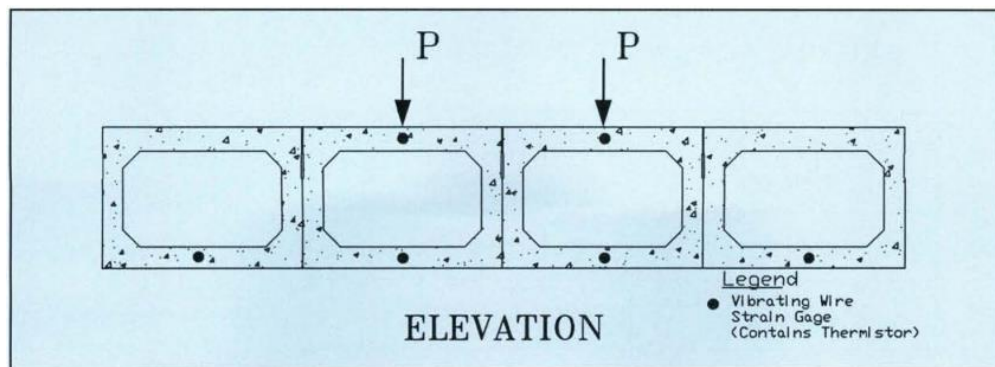
Figure 17: Schematic view of the bridge and load application Miller et al. (1999).
[Reproduced as per "fair use" guidelines.]

The magnitude of load applied via these actuators was 10 kips per actuator, which is 20 kips per pair of actuators that simulated the application of HS20-44 truck load with 25% impact. The testing protocol was as follows,

(a) Prior to tying the beams together each individual beam was subjected to a total load of 20 kips (applied as two 10 kip loads at midspan) and the response was studied to make observations about beam stiffness and strain characteristics.

(b) After connecting the beams and curing filler material as per Ohio Department of Transportation (ODOT) or the manufacturer's specifications the bridge was subjected to three set of static loads. These were,

    i.   20 kips on one interior beam.

    ii. 20 kips on the other interior beam.

    iii. 20 kips on both interior beams.

(c) Loads were applied cyclically. Each cycle consisted of load application of 20 kips on one interior beam alternately to cause a shear reversal on the middle shear key.

(d) Loading was stopped and keys were inspected after 10, 100, 500, 1000, 5000, 10000, 50000, 100000 and then every 100000 cycles till a million cycles. Ultrasonic pulse velocity was used to detect voids in the shear key connection caused by cracking.

Although the traffic loads were simulated on the bridge, the tests were conducted outside of the laboratory. Therefore, the bridge was subjected to environmental effects as well as simulated loading. For the first test which had the typical detail with grout, the shear keys developed cracks before the start of the test. This was attributed to two major factors which were the temperature gradient on the bridge and the beam alignments not being perfect that is the beam axes being at an angle instead of parallel. These effects are shown in Figure 18.
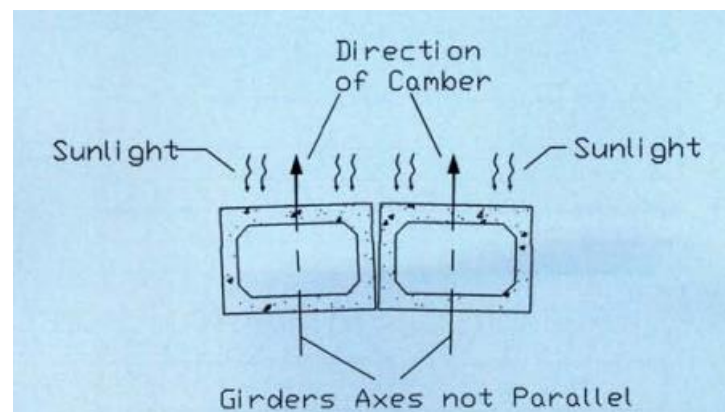
Figure 18: Effect of temperature and misalignment of beam axes Miller et al. (1999).
[Reproduced as per "fair use" guidelines.]

The cumulative effect of these factors causes the top of the joint to develop tensile strains. The strains at joint tops were monitored and found to be 300 με. These strain magnitudes were said to be sufficient to initiate cracking. Cracking monitored during the simulated loading phase indicated that the existing cracks propagated under the loading. New cracks also were observed during loading but the cause of these cracks could not independently be attributed to loading or environmental effects.

The second test was performed on the mid-depth shear key connection. The key itself was grouted, but the gap above the key was not grouted. For this test the adverse effect of temperature seemed to be reduced by the location of the shear key since some full depth (of the key) cracks were observed at beam ends prior to testing. These cracks however were of shorter lengths than the previous test. The loading phase of the test caused only one existing crack to propagate. The performance of this shear key detail was better than the typical detail. The beams had an expanded pocket area at the locations of the transverse tie rod. This pocket was used to access the tie rod during fabrication of the bridge. The access pockets were not grouted in order to allow the reuse of beams. Therefore, there was a periodic gap in the continuity of the shear key and this gap is thought to have assisted in reducing temperature stresses by acting as expansion joints. Moreover, these pockets were also existent during the first test but cracking occurred on both sides of the pocket unlike the second test. The loading itself did not cause a significant deterioration in the joints.

The third test reverted the use of the typical beam top detail but with an epoxy mix instead of non-shrink grout. Throughout this test no instances of cracking were noted indicating a much superior performance. However, it was noted that the co-efficient of thermal expansion of the epoxy was three times higher than that of the beam concrete. Therefore, the epoxy solution would be susceptible to thermally induced cracks if subjected to a wider range of temperature difference.

From the experimental program it was concluded that temperature effects are sufficient to induce cracking in the typical partial depth grouted shear key. The mid-depth key is less susceptible to the effect of temperature cracking. The epoxy connection provides very good results in the testing environment but the difference in thermal expansion could cause severe thermal stresses in the joint. Finally, it was observed that in all tests that the shear keys are able to transfer loads regardless of presence of cracking i.e. the problem of shear key cracking is more or less about bridge durability than that of structural load transfer.

2.4.2. Alternative Shear Key Shapes

The transverse connection and PT detail used in Japan have been covered by Yamane et al. (1994) and El-Remaily et al. (1996). The Japanese ABBB system has reported very few instances of longitudinal cracks at the joints. The Japanese system is similar to the ABBB system used in USA in terms of the size and the shape of the beams. The connection detail is quite different. The Japanese system incorporates a

wider connection (about 6.7 in.) and the beams are connected for the full depth. The increased gap allows for better tolerances to differential camber between adjacent beams. The filler material used in this system is cast in place (CIP) concrete. The typical connection detail used in Japanese ABBBs is shown in Figure 18.
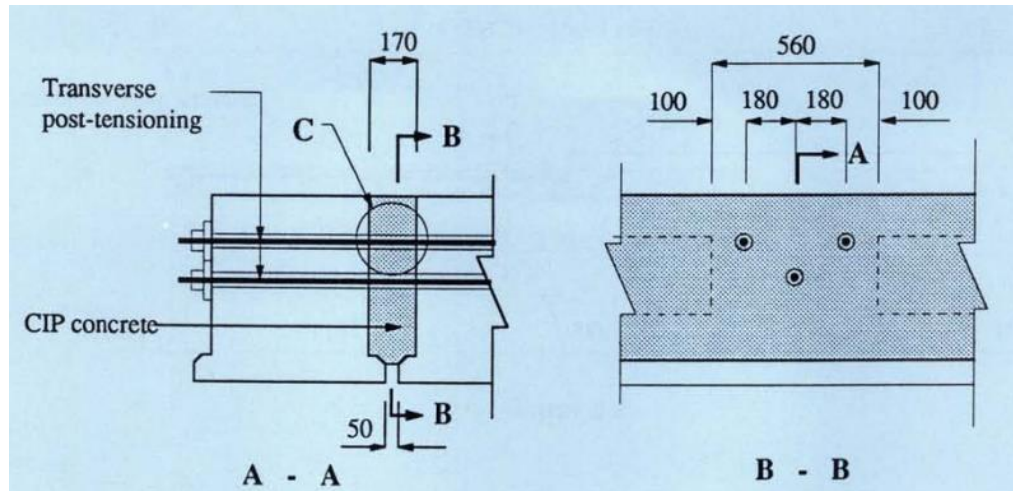
Figure 19: The connection detail used in ABBBs in Japan. El-Remaily et al. (1996).
[Reproduced as per "fair use" guidelines.]

Dong et al. (2007) compared three different longitudinal joint shapes for connection details to be used in the top flanges of adjacent member bridges (not box beams). The connection details are as shown in Figure 20. FEA of full bridge models was performed assuming a fully fixed connection and a hinged connection between adjacent beams to ascertain the nature of forces being imposed on the joints. A sub-assemblage was modeled with the connection details and subjected to the forces and moments as observed in the full bridge analysis. The FEA model of the sub-assemblage is shown in Figure 21. The filler material properties were varied to reflect three different grouts. The bond between the precast element and the filler material was not modeled and a perfect bond was assumed. The stresses at the joint due to applied loads were observed and compared for the three different joints.

22
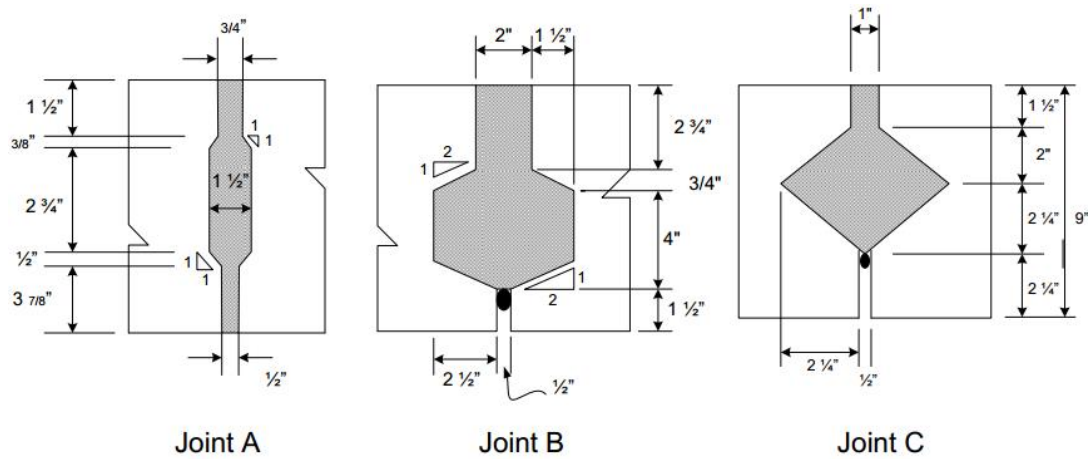
Figure 20: Connection shapes. Dong et al. (2007).
[Reproduced as per "fair use" guidelines.]
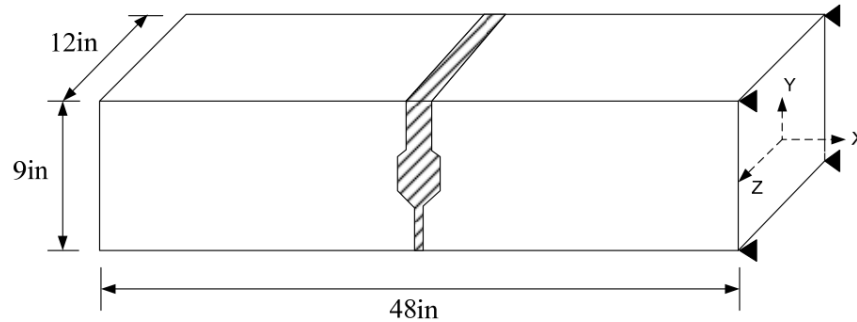
Figure 21: FEA model of sub-assemblages. Dong et al. (2007).
[Reproduced as per "fair use" guidelines.]

The results of this testing suggest that the "Joint A", as shown in Figure 20 was least susceptible to cracking as the stresses at the interface were the least of the three. The partial depth of the Joints B and C caused stress concentrations at the base of the connection detail that were large enough to cause cracking.

2.5. Transverse Post-Tensioning

Annamalai and Brown Jr (1990) performed push off tests on sub-assemblages representing grouted shear key connections (with PT) in precast concrete framed structures. A total of twenty eight sub-assemblage specimens were tested. The number of keys, joint thickness and the amount of PT were varied between different specimens. To clarify, one of the aforementioned aspects was varied while the other two were kept constant. The number of keys tried in the testing were zero, two and three. The joint thickness was varied from 1 to 3 in. and the PT was varied from 0 to 1000 psi and also the PT was applied as uniformly along the depth as well as linearly varying in some specimens. An equation was derived from the test results and to predict the shear strength of the PT connection it is shown in Equation 1.

$$\frac{v_n}{f_c} = 0.16 \, \frac{B}{A_{cr}} + 0.66 \, \frac{N_p}{A_{cr}f_c} \qquad \text{\textit{Equation 1}}$$

Where,

A_{cr} = Area of concrete section resisting shear along crack interface.
B = Area of vertical section through all the concrete keys.
f_c = Compressive strength of grout.
N_p = Prestressing force across connection.
v_n = Nominal shear strength of the connection.

The main conclusions from these tests were that the use of PT greatly enhanced the capacity of connections. Moreover, it was found that the PT with values above 800 psi produced a monolithic behavior without the use of shear keys. Varying the PT force along the depth of the connection did not have a significant bearing on the shear strength. The joint thickness had a bearing on the shear strength of the connections. The thinner connections had the higher shear strength.

El-Remaily et al. (1996) researched the transverse PT used in Japanese ABBB systems. This research showed that Japan used the highest amount of transverse PT to connect adjacent beams. Typically transverse PT was applied in four to seven locations (including end diaphragms) on the basis of bridge span and width. The PT force was applied through multiple strands at each location. The transverse connection in the Japanese ABBB system consisted of a flexural design assuming the bridge deck (in this instance the superstructure) as a slab or a gridwork of beam elements. The amount and location of the PT for diaphragms was determined by flexural design.

The use of carbon fiber reinforced polymer (CFRP) strands was researched by Grace et al. (2010). A half scale bridge model consisting of four adjacent box beams and a 3 in. composite concrete topping. The transverse PT was provided through CFRP tendons. The bridge was constructed with a 30 deg. skew. A total of five equally spaced diaphragm locations, including beam ends, were provided for transverse PT. The internal beams and the external beams were provided a different amount of prestressing so as to simulate the differential camber that is seen in bridge beams. The bridge was instrumented with transverse strain gauges to observe the distribution of transverse PT force. The effect of internal diaphragms was studied by varying the magnitude of transverse PT force per diaphragm and also by varying the number of locations at which the transverse PT was applied. Typically, a non-uniform distribution of PT force was observed. The PT force was highest near the diaphragms and lower between the discrete points of PT force application. The increase in transverse PT forces produced a better transverse distribution of loads. Another important observation was that reducing the number of locations of PT application did not have a significant effect on the transverse strains in the region between PT application locations. It also was noted that the

different variations in transverse PT were unable to produce a uniform compression in the joints as per AASHTO LRFD requirements. Also, the variations in transverse PT did not have any effect on the transverse load distribution while the concrete topping remained uncracked.

Hansen et al. (2012) proposed a simplified method for the construction and maintenance of ABBBs. The use of a modified beam cross-section was proposed. The modified cross-section was based on the "narrow joint" connection detail proposed by Hanna et al. (2011) and details about this beam cross-section are in Section 2.9.1. Essentially, the connection detail involves the use of a grouted joint with high strength bars connecting the beams at the top and bottom flanges (within the box beam void). Although transverse PT was applied, this method negated the use of internal diaphragms. FEA models of the proposed connection details were made and analyzed for typical dead loads and the HL93 load with a 33% impact factor. An 8 ft spacing was assumed between the PT bars. The beam depth was varied in the analysis and the PT force was determined for each case. Bridge sub-assemblage specimens, consisting of four beams, were tested in the laboratory to observe the response of the connection details to fatigue and to verify the ultimate load. Two loading setups were used on the same specimen, one each to impart the worst load effects in the top and bottom PT bars respectively. The boundary conditions and the loads were applied in a manner that the worst effects occurred at the same joint regardless of the test setup with the exception of the location of the worst effects along the beam depth. The specimen was subjected to a fatigue load for five million cycles in both setups. Throughout the fatigue testing no cracks or deterioration was observed in the joints.

2.6. Field Testing of Bridges

2.6.1. Typical methods used in field tests

Hodson et al. (2012) performed a diagnostic test on a CIP box beam bridge to ascertain the distribution factors and load rating of the bridge. The bridge was a two span continuous, CIP prestressed concrete bridge that was built in 1975. A total of fifty three instruments were installed on the bridge. These included forty two uniaxial strain transducer for measuring flexural strains, ten vertical deflection sensors for global deflection measurements and one tilt sensor for bridge rotation. The strain transducers were used to quantify the bridge response near the supports to ascertain bridge fixity as well as to record the maximum strains in the midspan region. Similarly, the tilt sensor was installed to quantify the boundary condition at one end of the bridge. The deflection sensors were installed at the midspan to measure the beam deflections. Two loaded dump trucks were driven across the bridge in different load paths to impart a range of loading effect on the superstructure. A total of sixteen quasi-static tests were performed with the trucks being driven at a speed of 5 mph. The data from the diagnostic tests indicated that the two bridge spans had partial fixity

on the basis of the strains at beam bottom being negative while the truck was in the other span. Also, the tilt sensor readings indicated that boundary conditions of the bridge were stiffer than that of pin – roller supports. The live load distribution factors and the load rating were determined from a parametric study conducted with a FE model.

2.6.2. Relative displacements between adjacent beams

A series of six field tests were performed by Huckelbridge Jr et al. (1995) on five bridges (in Ohio) to investigate the in-situ performance of shear keys in ABBB. The paper describes the tests and results of three field tests on two bridges. One bridge, which displayed considerable joint degradation, was tested twice. Once in the existing deteriorated condition and then again after performing shear key and deck membrane replacement. Beam strains and relative displacements were explicitly measured in this research. Loading was applied through a tandem axle dump truck with a total load of 50 kips for all tests. The main observation in this research was that every bridge structure including the post repair bridge displayed relative displacements that were indicative of a cracked shear key i.e. in terms of magnitude of relative displacement. This was inferred on the basis of field observations and FE analysis (which was not described in this paper). The magnitude of relative displacement between beams connected by a sound shear key should not exceed 0.001 in. according to Huckelbridge Jr et al. (1995). The range of relative displacements measured in this research were 0.003 in. to 0.02 in. indicating some degree of cracking at the joints. The actual degree of cracking was not measured, for instance the length of crack along the bridge. The relative displacements were said to be dependent on the crack length, beam stiffness, magnitude and proximity of load to the cracked joint. A key observation made in this research was that typically joints that cracked were in closest proximity to the typical travel lane for ambient traffic. Moreover, the shear keys in close proximity to lanes that were used by heavy truck traffic were susceptible to failure. It was also noted that the relative displacements between beams were small at the cracked joints when the load was not in close proximity to these joints. Another key observation that was made in this research was that load transfer is possible between beams with cracked joints. Although there was some evidence of loss of load transfer at a severely damaged joint in one particular bridge. Finally, the presence of transverse tie bars did not alleviate the extent of relative displacements between adjacent beams or for that matter these tie bars did not prevent shear key failure.

2.6.3. Beam Distribution Factors from Field Test Results

Girder distribution factors (GDFs) were calculated by Idriss and Liang (2010) from field test of a single span with prestressed concrete beams. Sensors were embedded in the top and bottom flanges of the beams and were installed during beam fabrication. The bridge beams were monitored for two years, from

release of prestress force to the in-service behavior as a bridge. The live load distribution factors for moments were mere calculated for diagnostic tests as well as the ambient traffic by Equation 2.

$$GDF_i = \frac{ES_i\varepsilon_i}{\sum_{j=1}^{k} ES_j\varepsilon_j}$$

Equation 2

Where,

S_i = Section modulus of the ith beam.
ε_i = bottom flange strain at midspan of ith beam.
E = modulus of elasticity
k = number of beams.

The calculation of GDFs for bridge with skew is presented by Collins (2010) and is presented in Equation 3.

$$GDF_i = \frac{R_{max}n}{\sum_{j=1}^{m} R_{peakj}}$$

Equation 3

Where,
R_{max} = response of the maximally loaded girder
R_{peakj} = peak response recorded in the jth girder.
n = number of trucks
m = number of beams.

2.6.4. Effect of transverse post-tensioning forces

The effect of transverse PT forces on transverse load distribution was studied by Fu et al. (2009). The tests were performed to observe the effect of increasing the transverse PT force on adjacent member bridges with spans less than 40 ft. The beam cross-sections were solid slabs connected with a partial depth grouted keyway. Bonded strain gauges were used to measure the flexural strains in the bridge superstructure. A loaded truck was driven over the bridge in multiple configurations of load paths. The PT force was initially kept at 30 kips per location and then increased to 80 kips per location. It was concluded that the magnitude of PT did not affect the load distribution as long as the shear key remained sound. The increase in PT though produced an increase in the transverse compression of the joints that was deemed to increase the resistance of the key to cracking.

2.7. Finite Element Modeling

2.7.1. Modeling bearing pad supports as springs

Sharpe (2010) performed analytical studies to ascertain the causes that initiate cracking in the shear key detail in adjacent box beam bridges. The study involved modeling of thirty nine bridges consisting of

two types of box beam designs, the typical PCI bridge and the TxDOT bridge. The shear key is different between these bridge types. The shear key in the TxDOT bridge detail is larger than the shear key detail in the PCI bridge. The bridges selected in this study were without a slope in the transverse direction, no curvature along the length, a constant cross-section and no skew in order to make a comparison of results. The bridges were modeled in ANSYS and three dimensional solid brick elements were used. The material behavior was modeled as linear elastic isotropic. The analysis of bridge models included realistic idealization of beam supports and loading conditions. The chosen bridges were supported on elastomeric bearing pads. These bearing pads were modeled as linear springs with stiffness equivalent to the bearing pad stiffness. The equivalent stiffness was derived as shown in Equation 4 and Equation 5.

Stiffness in vertical direction:

$$k_{vert} = \frac{E_c \times A}{H} \qquad \text{\textit{Equation 4}}$$

Stiffness in horizontal direction:

$$k_{horiz} = \frac{G \times A}{H} \qquad \text{\textit{Equation 5}}$$

where,

E_c = elastic modulus of bearing pad (psi)
A = cross-sectional area of bearing pad (in.^{2})
G = elastic modulus of bearing pad (assumed 100 psi as per TxDOT recommendation)
H = thickness of bearing pad (in.)

The wheel loads were applied as point loads in place of pressure as recommended by AASHTO. The study also incorporated the effect of temperature and shrinkage stresses. ANSYS does not contain a direct method of applying shrinkage loads, hence the researcher applied converted ultimate shrinkage stress into equivalent change in temperature. This conversion is presented in Equation 6.

$$\epsilon_{sh} = T \times C_{thermal} \qquad \text{\textit{Equation 6}}$$

where,

ϵ_{sh} = shrinkage strain
T = Temperature change
$C_{thermal}$ = Coefficient of thermal expansion

The study concluded that the shear key detail in both bridges was sufficient to resist traffic loads, however the shear key details were problematic in resisting stresses due to temperature and shrinkage. The

study also concluded that the stresses were highest near the support. The study proposed the use of thicker composite deck slabs, transverse post-tensioning and full depth shear keys to prevent cracking.

2.7.2. FEA model calibration for field test results

Fu et al. (2011) created a FEA model of a full scale bridge and calibrated it to match the results of a live load field test conducted in Maryland. A 3D solid model was created in ANSYS. The beams, shear keys, concrete overlay and curbs were modeled by solid elements. Transverse post-tensioning was explicitly modeled by 2D link elements. The transverse force was applied as a uniform reduction in temperature in the link elements to attain the desired level of post-tensioning. The material properties used in the FE analysis were as per typical Maryland DOT standards. After the application of the transverse PT force the compression induced in the cross-section caused the elements in the beams to penetrate into the elements of the adjacent beam as shown in Figure 22. Since this was an unrealistic situation, the gaps between adjacent beams were modeled with "contact elements". These elements prevented the penetration of the elements in adjacent beams as well as provided a means to model shear friction between the surfaces in contact.

ELEMENT
PENETRATION
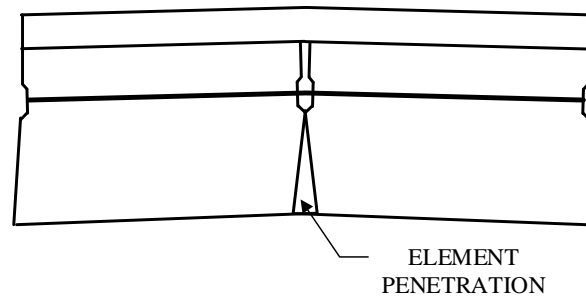
Figure 22: Adjacent beam element penetration in FEA model.

The FEA model was calibrated for two aspects namely, the beam boundary conditions and the composite action between the beams and the concrete overlay. Six different constraint options of boundary conditions and composite action were simulated and these were as shown in Table 3.

Table 3: Constraint conditions simulated in FEA model.

Option	Beam and Topping Behavior	Boundary Conditions
1	Composite	One end pinned, other end sliding.
2	Composite	One end pinned, other end sliding with spring stiffness 110000 kip/ft.
3	Composite	One end pinned, other end sliding with spring stiffness 329000 kip/ft.
4	Composite	One end pinned, other end sliding with spring stiffness 548000 kip/ft.
5	Composite	Both ends pinned.
6	Non composite. Shear forces not transferred. Nodes constrained to displace equally in vertical direction.	Both ends pinned.

[Reproduced as per "fair use" guidelines.]

The boundary conditions were changed from a horizontally flexible support (roller) to completely rigid support (pinned) and also intermediate levels of rigidity afforded by spring resistance to horizontal beam displacement. However, the vertical displacements at the beam ends were rigid for all cases. The maximum beam strains from the lie load test were compared with the maximum beam strains in the FEA model. A typical comparison plot was as shown in Figure 23.
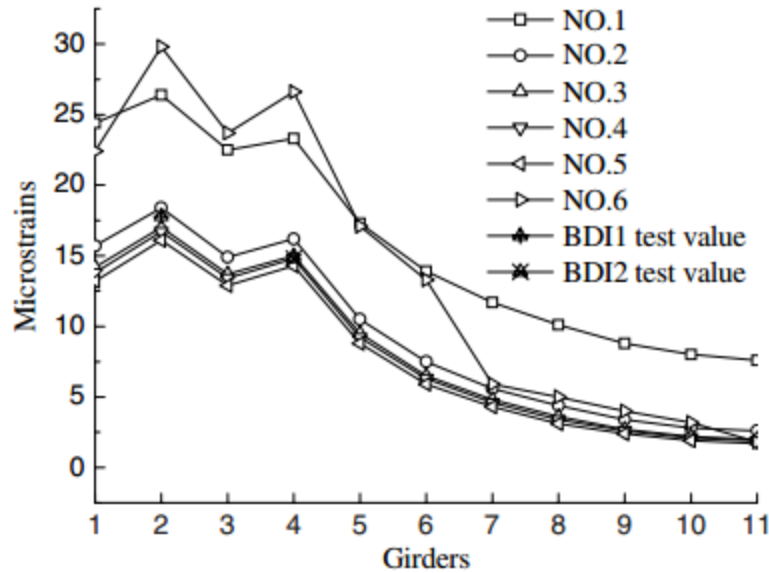
Figure 23: Comparison of strains for different constraint conditions and measured values. Fu et al. (2011).
[Reproduced with permission of the author.]

From the results it was concluded that Option 3, shown in Table 3, was the best option to simulate the behavior of the bridge. It was also noted that modeling the topping as composite or non-composite had a significant bearing on the magnitudes of strains. That is modeling the overlay to be composite with the beams produces strains much smaller in magnitude than the case when overlay is non-composite.

A full bridge FEA model was calibrated to match the live load test results by Hodson et al. (2012). The live load test is described in Section 2.6.1. The bridge superstructure was modeled with eight node solid elements. Six node triangular elements were used to model the beam section that were irregular in shape due to bridge skew. Each node had three translational degrees of freedom (DOFs). The PT strands used to prestress the box beam were modeled as tendon elements that were embedded within the solid model of the concrete bridge superstructure. The tendon elements had six DOFs per node but these were retrained to three after embedment within solid elements. The parabolic drape of the bridge tendons was discretized into a series of short straight sections that followed the profile of the actual tendons. The strains, deflections and the end rotation from the live load test were compared with the FE model. It was found that the boundary conditions of the bridge were stiffer than the assumed pinned – roller supports. The FE model boundary conditions were adequately stiffened by using vertical and longitudinal springs. The comparison of end rotation between the live load test and the FE model is shown in Figure 24.
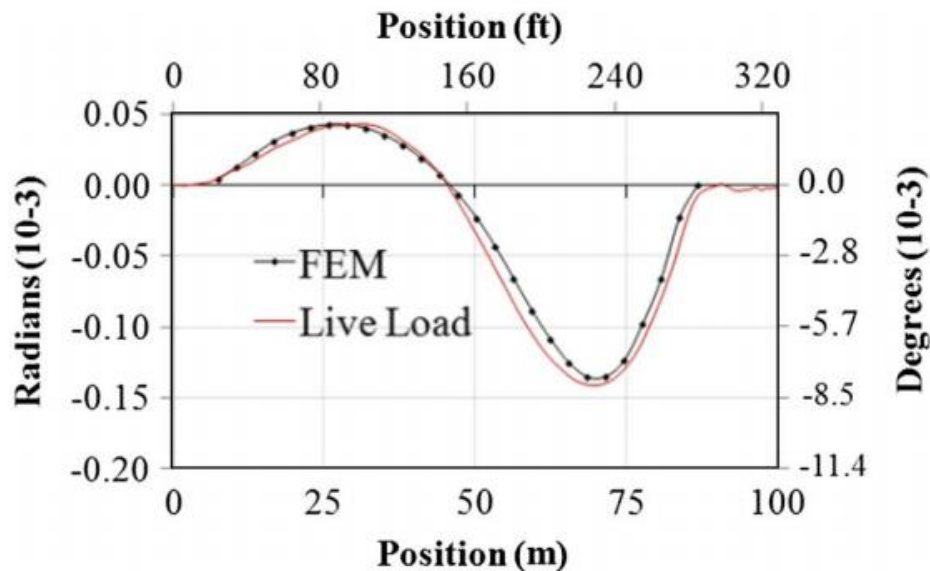
Figure 24: Comparison between FE model and live load test results. Hodson et al. (2012). [Reproduced as per "fair use" guidelines.]

2.7.3. Modeling the effect of PT on ABBB joints

The effect of PT on shear keys was investigated through a series of simple 2D FE models by Sang (2010). A typical bridge was modeled in the plan view with plane stress elements. Joints were not discretely modeled; all elements had the same material properties (concrete). The thickness of elements at the diaphragms and the webs was equal to the total depth of beam section. The thickness of elements at all other locations was the total thickness of the two flanges. The bridge consisted of five diaphragms, two at the ends and three internal. The PT force was modeled as a point load acting along the centerline of the diaphragm elements. The magnitude of the PT force was 30 kips as per Pennsylvania Department of Transportation (PennDOT) specifications. The stresses were studied and the magnitude of stresses was found to be 163.5 psi at the loading point (stress concentration). The influence of the PT force waned towards the middle of the bridge with compressive stresses ranging from 15 to 45 psi. It is to be noted though that the compressive stresses due to transverse PT force are mostly confined to the area near the diaphragm. When the compression eventually spread out and became uniform, the magnitude of compressive stress was as low as 3.5 psi on an average. Although the modeling method used was extremely simplified, the issue highlighted here was the significant difference in the stiffness of diaphragms versus the rest of the beam that cause the locations of the diaphragms to receive highest clamping while the amount of clamping between the diaphragms was very small.

2.8. In situ inspection of existing ABBB

2.8.1. Monitoring a newly constructed bridge

Attanayake and Aktan (2008) studied a bridge (Oakland Drive over I-94) under construction in Portage, MI to study the onset of cracking in the shear key. The bridge consisted of two 79 ft spans and 22 box beams. The beam cross-section was 33x48 in. providing a full bridge width of 93 ft 5 in. The bridge was designed for HS-25 loading and the magnitude of transverse PT applied at each location was 104.5 kips through two tendons. The bottom tendons were continuous for the full width while the top tendons were discontinued at the bridge center line for staged construction. The shear keys on this bridge were closely monitored throughout the construction process. The shear keys were grouted and PT was applied three days after grout placement. Cracks in the shear keys were observed prior to PT application and these cracks did not close after PT application. The bridge had a composite deck. The deck showed signs of cracks over the abutments about two weeks after deck placement. These cracks occurred prior to the placement of barriers of the bridge and the construction of bridge approaches. During this time the bridge was subjected only to intrinsic loads due to heat of hydration and drying shrinkage. The loss of transverse PT during the two week period was deemed to be insufficient to cause tensile stresses high enough to cause cracking. The major findings of this research were that ABBBs in Michigan had the highest level of PT in

the USA but this level is still unable to prevent reflective cracking even though a full depth shear key was used. The cracks appear exclusively at the beam – shear key interface. Reflective cracks in the composite deck were said to initiate at the top of the deck and then propagate for the full thickness of the deck.

2.9. Alternative Connection Options

Most of the research work thus far has focused on investigating and improving the same concept which includes the use of grout as a filler material, use of transverse PT and modification to existing shear keyway detail. Alternative options were found in literature that move away from the presently tried and tested approach. These alternative approaches are now discussed.

2.9.1. The case for non-post-tensioned connections

The use of transverse PT has been quite commonplace in ABBB. Now there is a thought process that says that the ABBB system can be made more economical by replacing the transverse connections with non-PT options. Such research was performed in Nebraska by Hanna et al. (2011). This research proposed the elimination of internal diaphragms and transverse PT. They also proposed two new connection details to replace the currently used PT systems. The proposed specimens were referred to as the wide joint and the narrow joint systems as shown in Figure 25 and Figure 26 respectively. The connections were designed to resist interface shear, torsion and flexure.
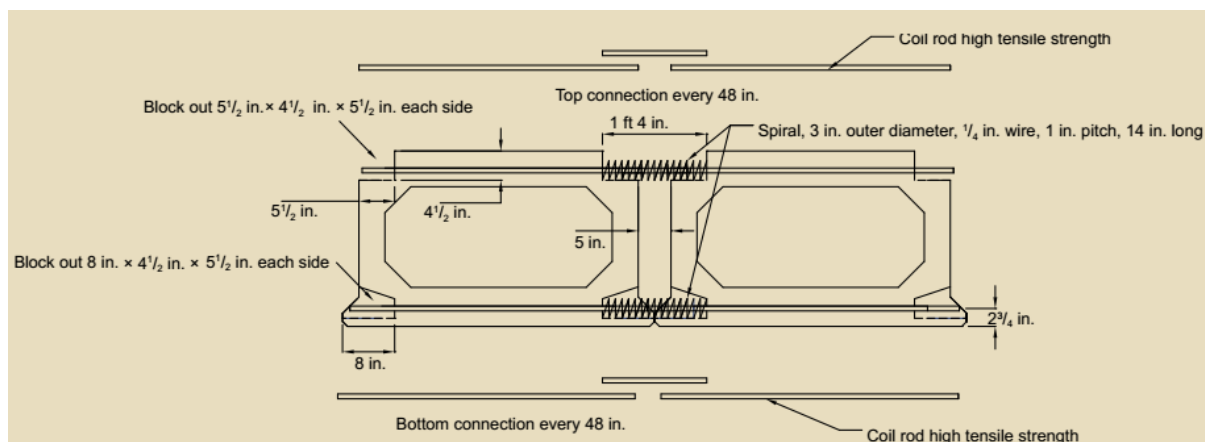
Figure 25: Schematic of the wide connection. Hanna et al. (2011).
[Reproduced as per "fair use" guidelines.]

The beam cross-section would need to be modified to be used in the wide connection. These modifications consist of recesses at the beam bottom and blockouts in the top and bottom flanges of beams spaced at 4 ft intervals. Reinforcing bars protrude from these blockouts and they are spliced between adjacent beams and a ¼ in. thick wire spiral is used to provide confinement to the splice bars. The use of self-consolidating concrete as a filler material was recommended in lieu of grout.
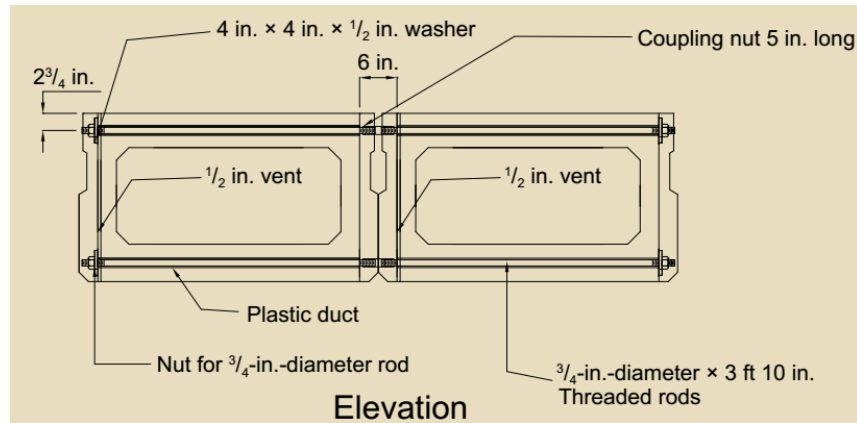
Figure 26: Schematic of the narrow connection. Hanna et al. (2011).
[Reproduced as per "fair use" guidelines.]

Similarly, the beam cross-section was modified for the narrow connection. The modification was that plastic ducts were placed in the beam top and bottom flanges. The bottom duct is located between the two layers of prestressing tendons while the top duct is provided without infringing cover requirements. Threaded rods were inserted in these ducts to connect the adjacent beams through the use of couplers. The use of grout was proposed as connection filler material in this detail.

The connection details were tested experimentally by applying static and fatigue loads. Three specimens were fabricated consisting of two beams each. The length of these specimens was 8 ft and the beam cross-section was 48 in. x 27 in. The three specimens simulated the current typical Illinois Department of Transportation (IDOT) detail and the two proposed details respectively. The magnitude of load applied during cycling was 18.4 kips (i.e. HL93 tire load + 15% impact for fatigue) in upward as well as the downward directions. The existing IDOT connection detail was utilized for the first test. The connection detail used on this test consisted of two threaded rods. The existing IDOT detail failed after 10000 cycles. The interface between the beam and the grout debonded. The IDOT detail was retested with a 5 in. non-composite concrete topping. This specimen was subjected to a load ranging from 0 to 18.4 kips and 18.4 kips to -18.4 kips and back to zero statically to ascertain the stiffness of the system. The cyclic load was applied for 2 million cycles and the stiffness did not deteriorate after the application of cyclic loads. The specimen was tested statically to failure and the ultimate load was 138.7 kips. The wide connection detail was subjected to a load of ±6.4 kips. This load was a third of the 18.4 kips. This was done to simulate a load effect caused on two connections spaced at 4 ft (the specimen consisted of a single connection). Cyclic loads of the same range of magnitude were applied for 2 million cycles and the stiffness was observed to be the same. This connection was then subjected to the calculated 18.4 kips load statically and cyclically and the connection did not display adverse reaction to the fatigue loads, that is the stiffness did not degrade. Ponding tests were performed to observe cracking and no leakage was detected over the course of the full

34

test. The ultimate load that failed the specimen was 162 kips. Finally, the procedure was repeated for the narrow joint specimen and the connection in this specimen also did not lose stiffness or show signs of leakage. The ultimate load to fail this specimen was 156 kips. Therefore, on the basis of experimental testing it was concluded that the new proposed connection details could provide a performance similar to PT connections and these were recommended for practical use.

2.10. Ultra High Performance Concrete – Properties and Bridge Applications

The use of UHPC is becoming more prevalent in bridge construction. UHPC has been promoted for use in prestressed beams, deck waffle slabs and, a factor very relevant to this research, as a connection material for precast concrete elements. UHPC has been known to provide improved compressive and tensile strengths, self-consolidating properties, better bond with reinforcement (non-prestressed and prestressed, steel and composite materials) and an improved bond with concrete. The properties and applications of UHPC that make it relevant to this research are now discussed.

2.10.1. Material properties of UHPC

An extensive testing program was performed by the FHWA to characterize the material properties of UHPC Graybeal (2006). Graybeal performed material characterization tests on UHPC with four different curing regimens. These were as follows,

a) Steam curing at 194 °F (90 °C) and 95-percent relative humidity for 48 hours starting about 24 hours after casting.
b) Steam curing at 140 °F (60 °C) for 48 hours starting about 24 hours after casting.
c) Steam curing at 194 °F (90 °C) for 48 hours starting about 15 days after casting.
d) Curing under laboratory conditions (73 °F (23 °C) and ambient humidity).

Compressive tests were performed on 3 in. x 6 in. cylinders and the procedure of ASTM C39 was followed except for the loading rate which was increased to 150 psi/sec. The typical strength at 28 days averaged from six specimens each was 28.0, 24.8, 24.8, and 18.3 ksi for curing regimens a, b, c and d respectively. Compressive strengths were also tested in cylinders of different sizes (2 in. x4 in., 3 in. x 6 in., 4 in. x 8 in. and 3 in. x 6.5 in.) and cubes of different sizes (2 in. and 4 in.) to study the effect of size and shape on compressive strength. The effect of size was negligible and the cubes had 5% higher strengths than cylinders. Additionally, the effect of fiber orientation was studied on the compressive strengths. The orientation did not have an effect on the compressive strength per se. The presence of fibers prevented explosive failures of specimens.

The tensile strength of UHPC was determined through four different types of tests. These tests include split cylinder tensile strength, flexural test of prismatic sections, axial tensile test of briquettes (dog bone specimens) and axial tensile strength test of cylinders. The flexural strength test was performed in a four point bending setup as per ASTM C1018. The specimen sizes were 4x4x14 in.

A simple test was performed to ascertain the depth of chloride penetration and better understand the durability of UHPC. This was reported by Perry et al. (2012). A series of prisms (6 in. x 6 in. x 21 in.) were placed at the long term exposure test site of the US Army Corp of Engineers (at the Treat Island, Maine USA) in 1996 and 2004. The specimens were kept on a wharf and were subjected to two tide cycles of wet/dry in sea water daily and during winter at low tide were subjected to freeze/thaw. After 13 years, the samples were measured for the depth of chloride penetration. It was observed that high performance concrete (HPC) had a depth of chloride penetration that was five times greater than that of UHPC. The difference in chloride penetration indicated that it would take 1000 years for UHPC to have same level of chloride penetration as HPC in 100 years. Moreover, the UHPC samples displayed sharp corners and edges as opposed to rounded ones on other concrete types (some as early as a 1 year) indicating a much superior freeze/thaw durability.

2.10.2. UHPC bond with reinforcement

Lubbers (2003) performed experiments to determine the development length for prestressing strands in UHPC. Standard 0.5 in. prestressing strands and 0.5 in. oversize strands were cast into UHPC at varying embedment lengths and pull out tests were performed. For comparison, pull out tests were performed on strands cast into conventional normal weight concrete. The specimens consisted of the eight prestressing strands embedded in rectangular prisms. The depth of the prisms that is the length of the prism corresponding the embedment length was varied to obtain prisms of three types i.e. 24 in. deep, 18 in. deep and 12 in. deep. The strands were not prestressed. An attempt was made to cure the prisms by heat treatment, but it was found to be ineffectual. Hence, UHPC in the specimens was not steam or heat cured. The test setup consisted of a pair of load cells to monitor the applied load and a LVDT each to monitor the slip of strand at both ends of the prism, namely the end at which the load was applied and the opposite end. The testing protocol consisted of monitoring load and slip at both ends. It was expected that there would be continuous slip at the end at which the load was applied. The slip at the opposite end indicated that the strand had debonded completely from the concrete. The load at which complete bond was lost was measured as the failure load. The failure loads for conventional concrete are summarized in Table 4 and failure loads for UHPC are summarized in Table 5.

Table 4: Pull out results for conventional concrete prisms.

Embedment Length (in.)	Failure Load (kips)	
	½ in. Standard	½ in. Oversize
24	31.2	30.4

[Reproduced as per "fair use" guidelines.]

Table 5: Pull out results for UHPC prisms

Embedment Length (in.)	Failure Load (kips)	
	½ in. Standard	½ in. Oversize
24	36.5	No Slip
18	28.4	41.8
12	22.6	28.7

[Reproduced as per "fair use" guidelines.]

It can be seen that the strands embedded in UHPC required higher loads to completely debond the strands from concrete. The results from this research have established that strands require smaller development length when bonded with UHPC however, the minimum length or the development length, was not determined.

Basic pullout tests were performed by Perry and Weiss (2009) to determine the development length for No. 4, No. 5 and No. 6 bars in fiber reinforced UHPC i.e. UHPCFRC. The typical schematic of the test specimens is as shown in Figure 27.
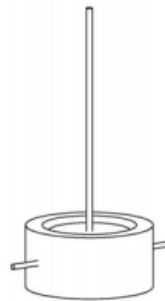
Figure 27: Schematic of pull out test specimens. Perry and Weiss (2009).
[Reproduced as per "fair use" guidelines.]

The embedment lengths for No. 4, No. 5 and No. 6 bars were 2.9 in., 3.9 in and 4.9 in. respectively. The diameter of the UHPCFRC cylinder was 15.7 in. The failure mode for all specimens was the same, reinforcing bar rupture outside of the UHPFRC cylinder.

2.10.3. UHPC bond with concrete

Bond strength between UHPFRC and substrate concrete was investigated by Marcu et al. (2012). The testing was conducted to determine the bond strength for different surface preparation techniques. The bond strength was investigated through three test types, namely slant shear test as per a variation of ASTM C882, splitting tensile strength as per a variation of ASTM C496 and flexural strength test as per a variation of ASTM C78. An example of these respective tests is shown in Figure 28.

(a)   *(b)*   *(c)*
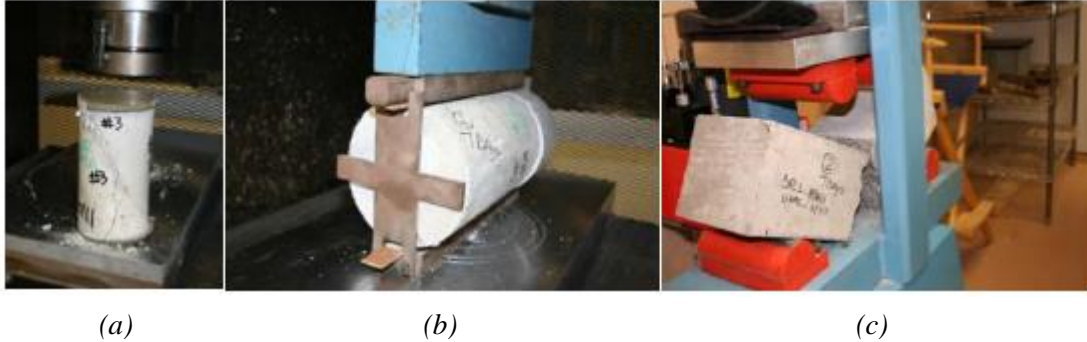
Figure 28: Test types to characterize UHPFRC – concrete bond strength, a) slant shear test, b) splitting cylinder tensile test and c) flexural strength test. Marcu et al. (2012).
[Reproduced as per "fair use" guidelines.]

The concrete half of the specimens was cast first and cured. Once the concrete had developed the expected properties the bond surface was prepared by exposing aggregates in concrete, sand blasting + adhesive epoxy, sand blasting and power wash. Six samples were prepared for each surface preparation technique. Three were tested one day after placing UHPFRC and the remaining three were tested at 7 days. The results from this testing program are summarized in Table 6.

Table 6: Summary of bond strength characterization test results.

Surface Treatment	Average Bond Strength (psi)					
	Slant Shear		Flexural Strength		Splitting Tensile	
	1 Day	7 Days	1 Day	7 Days	1 Day	7 Days
Exposed Aggregates	4840	5630	430	635	655	820
Sand Blasted & Epoxy[#]	580	2360	245	475	550	670
Sand Blasted	1410	3500	335	165	475	650
Power Wash	880	1090	N/A*	45	470	750

NOTES: * - Specimens debonded under self-weight during handling prior to testing.

- Epoxy meeting ASTM C881 requirements.

[Reproduced as per "fair use" guidelines.]

It can be observed that exposing aggregates provides the best method of surface preparation whereas power wash is the poorest.

2.10.4. Application of UHPC as a connection material for precast elements

      Extensive testing was performed in the use of UHPC as a connection material (for closure pours) in precast deck panels by Graybeal (2010). Six deck panel specimens were tested for fatigue and strength. The description of these specimens is found in Table 7. Four of these specimens simulated the transverse connection detail between deck panels and the remaining two specimens simulated the top flange longitudinal connections between top flanges of deck-bulb-Tee beams. The longitudinal connections between the bulb tee flanges are of particular interest since the UHPC connection was subjected to flexural and shear stresses. The test setup for the longitudinal connections is shown in Figure 29.

Table 7: UHPC connection detail test matrix.

Name	Orientation	Depth	Reinforcement
8H	Transverse	8 in.	Alternating #5 headed black reinforcement with 3.6 in. lap length and 18 in. (top) and 7.2 in. (bottom) spacing
8E	Transverse	8 in.	Alternating #4 hairpin epoxy-coated bars with 4 in. lap length and 2.2 in. spacing
8G	Transverse	8 in.	Alternating #5 galvanized straight bars with 6 in. lap length and 18 in. (top) and 7.2 in. (bottom) spacing
8B	Transverse	8 in.	Alternating #5 black straight bars with 6 in. lap length and 18 in. (top) and 7.2 in. (bottom) spacing
6H	Longitudinal	6 in.	Alternating #5 headed black reinforcement with 3.6 in. lap length and 18 in. (top) and 7.2 in. (bottom) spacing
6B	Longitudinal	6 in.	Alternating #5 black straight bars with 6 in. lap length and 18 in. (top) and 7.2 in. (bottom) spacing

[Information available in the public domain.]
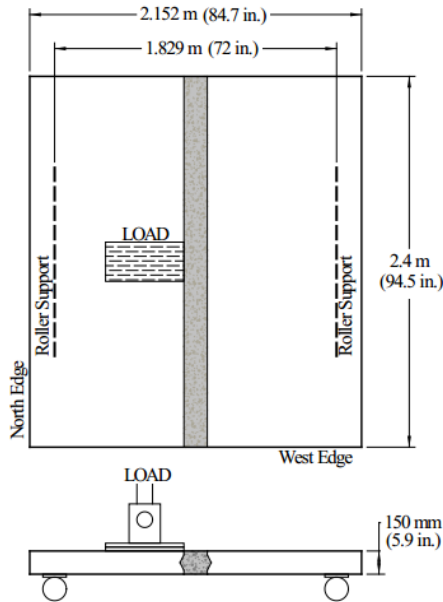
Figure 29: Test setup for longitudinal UHPC joint. Graybeal (2010).
[Information available in the public domain.]

The deck panel specimens were subjected to cyclic loads to impart fatigue in the connection and then the connection was tested for strength. The magnitude of the fatigue loads was such that typical service level stresses would be imparted on the connection. The results of these tests showed that the steel embedded in the UHPC connection did not debond due to fatigue or due to the ultimate strength test. Moreover, it was noted that the reinforcing bars were susceptible to metal fatigue when subjected to cyclic loads of large amplitudes.

2.10.5. Practical applications of UHPC in bridge connections

ABBB was used as a replacement of a fatigued steel beam - concrete deck bridge (Eagle River Bridge) on the TransCanada Highway in Canada. The unique features of the bridge were reported Rajlic et al. (2010). The salient features of this project were the use of UHPC as the connection material and transverse PT not employed. Other salient features include an extensive use of precast elements except the field casting of joints between adjacent beams and adjacent spans. The connections between adjacent beams are discussed here. The cross-section of the bridge superstructure is shown in Figure 30 and the detail of the longitudinal joint is shown in Figure 31.
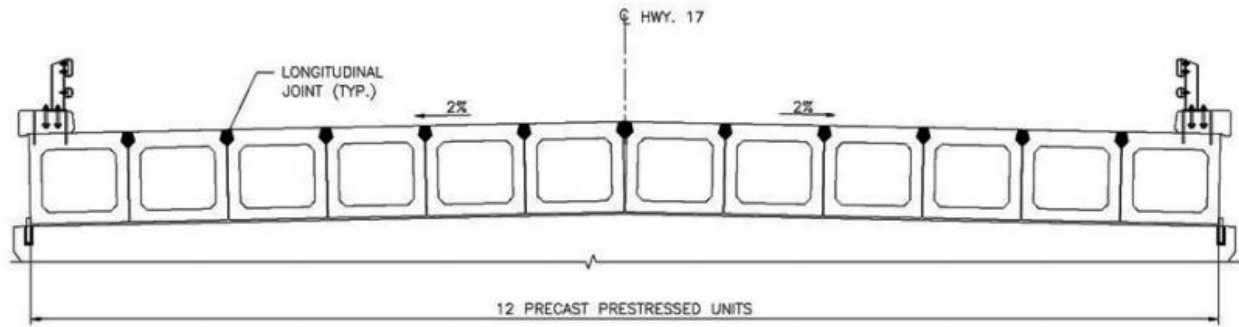
Figure 30: Cross-section of bridge superstructure. Rajlic et al. (2010).
[Reproduced as per "fair use" guidelines.]
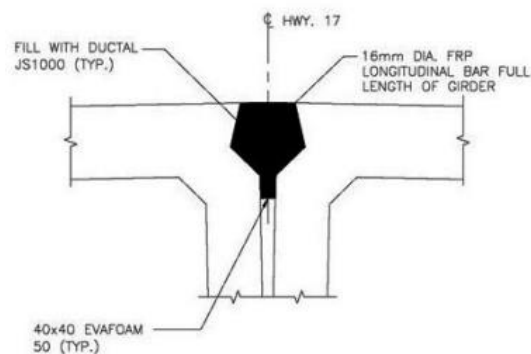
Figure 31: Detail of longitudinal joint. Rajlic et al. (2010).
[Reproduced as per "fair use" guidelines.]

The UHPC option was considered to be more cost-effective than typical concrete topping or distribution slab with transverse PT and grouted joints. The UHPC option for this bridge also was chosen considering the superior mechanical properties of UHPC, shorter splices, low permeability of UHPC and low carbonation depth of UHPC.

2.11. Splice length testing

ACI Committee ACI (2003) reports a typical test specimens used in development length and splice length testing in reinforced concrete. A schematic of a widely used test specimen, as reported by the document, is shown in Figure 32.
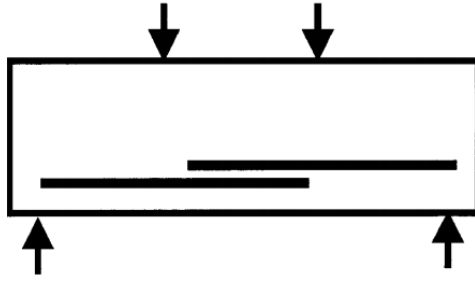
Figure 32: Typical splice test specimen as per 408R-03, ACI (2003) .
[Reproduced as per "fair use" guidelines.].

The splice to be tested is within a constant moment region of the beam. This splice specimen is very easy to fabricate and simulates a realistic state of stress around the reinforcement. Therefore, this splice test specimen is reported to be most commonly used in development length testing as well as splice length testing. The application of such test specimens can be found in Azizinamini (1998), Esfahani and Rangan (1998), Hosny et al. (2012) and Chun and Lee (2013).

2.12. Summary

From the literature that was reviewed the following conclusions were made,

1. Non-shrink grout is the most commonly used shear key forming material. However, this material does not have sufficient bond strength to resist a combination of traffic, intrinsic and environmental load effects.

2. Materials, such as epoxy concrete, polymer concrete and UHPC, present a better alternative to non-shrink grout in terms of material properties and bond with concrete substrate. However, the long term behavior of these materials needs to be studied. The use of proper surface preparation techniques of concrete substrate is very important.

3. Field testing when used in conjunction with finite element modeling presents a very good tool to ascertain the behavior of ABBB system.

4. Transverse PT is widely used in the ABBB system. Transverse PT improves the joint strength, but this is usually at the location of application. The transverse PT forces dissipate to values below AASHTO LRFD requirements at locations between the discrete points of PT application. The magnitude of transverse PT is insignificant in terms of improving the transverse load sharing prior to the joint cracking. After initiation of cracking, transverse PT is able to prevent relative displacements between adjacent beams when applied in a large magnitude. There are several methods to calculate the required transverse PT force, these are dependent on the bridge spans, widths and beam depths. Another important observation is that the use of transverse PT

42

has been insufficient to prevent shear key cracking initiation (prior to applying service level forces on the bridge).

5. The use of UHPC as a connection material for precast elements is becoming prevalent in the accelerated bridge construction practice. The ABBB system can benefit from the use of UHPC as the connection forming material.

6. Most of the joints studied in literature were dependent on bond between the beams and connection forming material. The use of a structural connection with the use of UHPC has not been investigated for the ABBB system.

3. Research Methods

3.1. Introduction

The procedures for carrying out the research work are discussed in this chapter. This chapter provides a logical basis for the progression of all the tasks that were performed in this research. The chapter begins with a description of the live load tests that were performed to quantify the response of in service bridges to traffic loads and the focus of these tests in Section 3.2. Based on the pertinent measurements from the live load tests the development of the FEA model for one bridge tested during diagnostic testing and another full scale bridge model is discussed in Section 3.3. The development of new connection details is discussed in Section 3.4. The details of the proposed specimens are shown in Section 3.5 and the procedures to construct the specimens is described in Section 3.6. Finally, all the experimental work performed in the laboratory to characterize the transverse connection behavior is discussed in Section 3.7. The schematic of the research methods is shown in Figure 33.
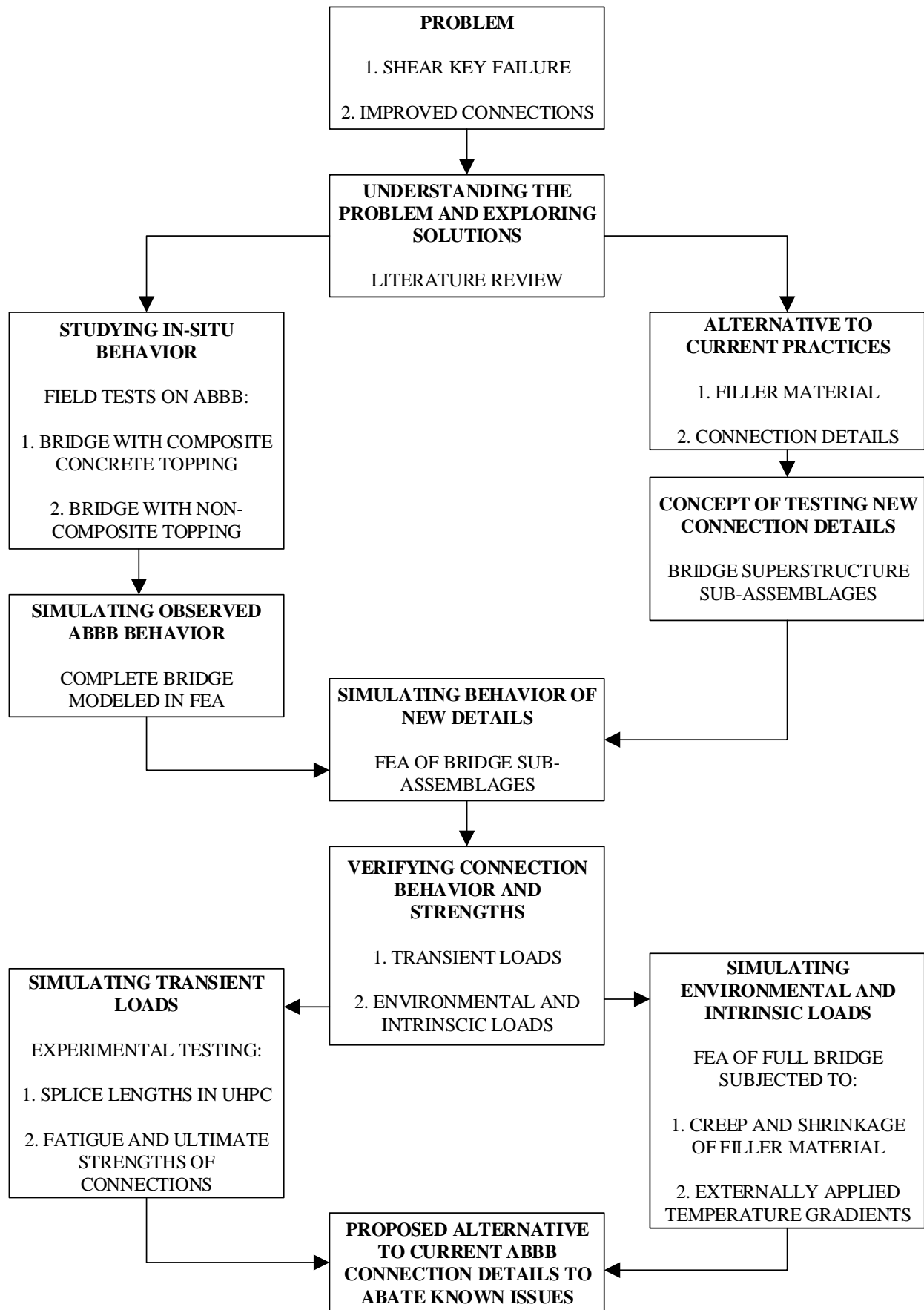
Figure 33: Schematic of research.

3.2. Diagnostic Tests of Adjacent Box Beam Bridges

The live load tests were performed to observe the response of the bridges to transient loads such as live load in the form of loaded tandem axle trucks. These tests were diagnostic in nature that is, the current structural condition of the bridges was ascertained by applying known loads. These loads were intended to impart typical service level load effects on the bridge superstructures. The capacity of the bridge beams or the joints was not sought in these tests. Two bridges were subjected to these diagnostic tests. The first test was performed on the Karr Valley Creek Bridge (KVCB) near Almond, NY and the second diagnostic test was performed on the Aden Road Bridge (ARB) near Nokesville, VA.

Observing the in-situ behavior of the bridges was an important aspect of this research. The understanding of transverse load distribution and relative beam displacements was sought. Thus, the primary focus of these tests was establishing the transverse behavior of ABBB. The relative displacements between adjacent beams are indicative of joint deterioration, especially at the locations where joint deterioration is not conspicuous in the form of reflective cracks in the deck or leakage stains on the beam bottom. Through diagnostic testing other aspects of the bridge behavior such as beam stiffness, end restraints were also studied and used to calibrate the FE models.

Diagnostic tests were carried out in three basic formats i.e. quasi-static or crawl tests, dynamic or full speed tests and static tests. The data recorded during these tests includes longitudinal beam strains, vertical beam deflections, relative vertical and horizontal displacements between beams, beam end displacements and beam end rotations. The testing protocol and the instrumentation used in the diagnostic tests is discussed in the following sections.

3.2.1. Diagnostic Test Measurements

The focus of diagnostic tests was to observe the overall behavior of the bridge as well as focus on the areas where deterioration was known to have occurred. The instrumentation used in these diagnostic tests was located on the bridge superstructure to measure the global response of the bridge and the local response of bridge components. To that end, beam service strains, beam vertical deflections, wheel load distributions, dynamic load allowance and bearing movements were monitored to measure the global response of the bridges. The relative displacements of bridge components that were affected by cracking were measured to study the local response due to deterioration. These aspects of bridge behavior were monitored exclusively for transient loads to study the effect of truck loads on the bridge superstructure since the study was performed in a short duration. The following section describes the instrumentation used in both the diagnostic tests.

3.2.2. Instrumentation

The instrumentation was chosen and positioned on the bridge to capture the specified behavior during testing. Instruments used during the diagnostic test were strain transducers, deflectometers, linear variable differential transducers (LVDTs), tiltmeters, clickers and hand-held thermometers. The description and the purpose of using each instrument type is discussed below.

3.2.2.1. Strain Transducer

Strain transducers, shown in Figure 34, were attached the bottom of the box beams for measuring the strains in beams induced by truck loads. The strain gauges used in the testing were BDI ST350 strain transducers. These gauges consist of four bonded strain gauges in a full Wheatstone bridge configuration. The gauge length of the strain transducers was 3 in. The gauges were mounted on steel tabs that were attached to the concrete. All gauges were bonded to the beams with the use of Loctite 410 glue and Loctite 7452 accelerant. The strain transducers were used in both of the bridge tests for the same purpose.
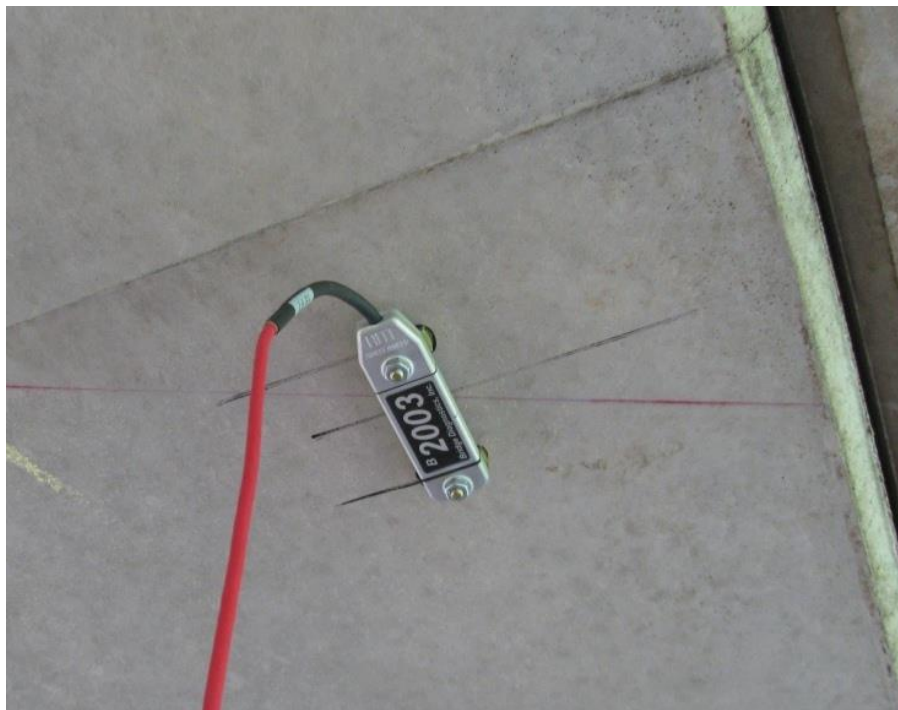
Figure 34: Strain transducer on bottom fiber of box beam.

3.2.2.2. Deflectometer

The deflectometers (also referred as Twangers) used for diagnostic testing, as shown in Figure 35, consisted of a flat aluminum plate that was flexible. This flat plate was attached to a rigid plate and the rigid plate was attached to the beams (directly or indirectly via steel tabs) with the use of the aforementioned glue. A set of four bonded foil strain gauges arranged in a full Wheatsone bridge configuration were

attached to the flexible plate near the connection with the rigid plate. The flexible plate was pre-deflected to induce flexural strains which were measured by the strain gauge apparatus. The data acquisition system was calibrated to interpret these strains as displacement values. The passage of trucks over the bridge superstructure caused a change in deflection of the flexible plate that was equivalent to the global vertical deflection of the bridge beam at that location. These deflectometers were used in both of the bridge tests for the same purpose.
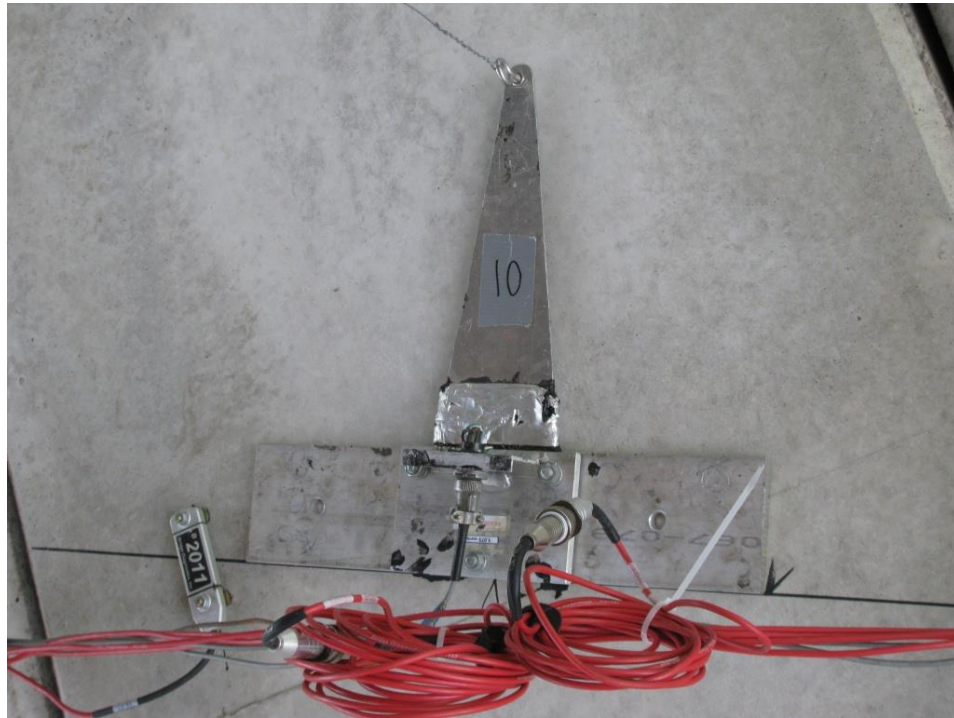
Figure 35: Deflectometers on Beam Bottom.

3.2.2.3. Linear Variable Differential Transducer (LVDT)

LVDTs were used to measure relative displacements between bridge superstructure components. The LVDT setups in the KVCB diagnostic test were used for measuring relative vertical displacements between adjacent beams and the displacements at beam ends. The LVDT setups in the ARB diagnostic test were used to measure the relative vertical and horizontal displacements between adjacent beams.

The approach used to measure relative vertical displacements between adjacent beams used in KVCB test was quite different from the approach used in the ARB test. For the KVCB test, a LVDT was positioned vertically under the web of a beam such that a pair of LVDTs were positioned under a beam. This setup was installed under three adjacent beams to measure the relative vertical displacement between adjacent beams as well as the relative twist which would indirectly indicate the amount of horizontal displacement. This setup provided the global vertical deflection of the bridge beams and the relative

displacements were calculated by subtracting the deflection values between the pair of LVDTs on the either side of the joint. The vertical LVDT setup is shown in Figure 36. The vertical LVDT setup was supported by a scaffold to hold up the LVDTs.

Figure 36: LVDT setup to study relative behavior of beams in KVCB.

For the ARB test, the relative vertical displacements between adjacent beams were measured directly by attaching a LVDT between the webs of adjacent beams. This provided a direct measurement of relative vertical displacement between adjacent beams. The vertical LVDT setup used in the ARB test is shown in Figure 37. The LVDTs were mounted on perforated cold formed angles.
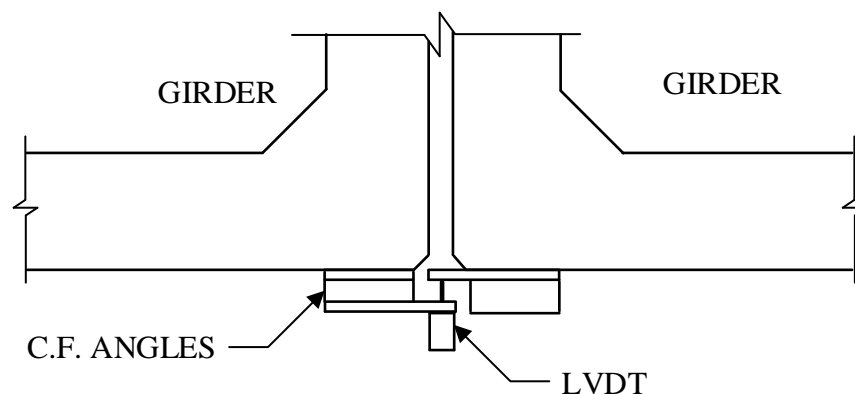
Figure 37: LVDT setup to measure relative vertical displacements in ARB.

A similar setup was utilized to measure the relative horizontal displacements between adjacent beams in the ARB test. The setup consisted of a LVDT mounted on a perforated cold formed angle and

49

attached under a beam web with the LVDT plunger reacting against a block of wood attached on the beam web across the joint. This setup is shown in Figure 38.
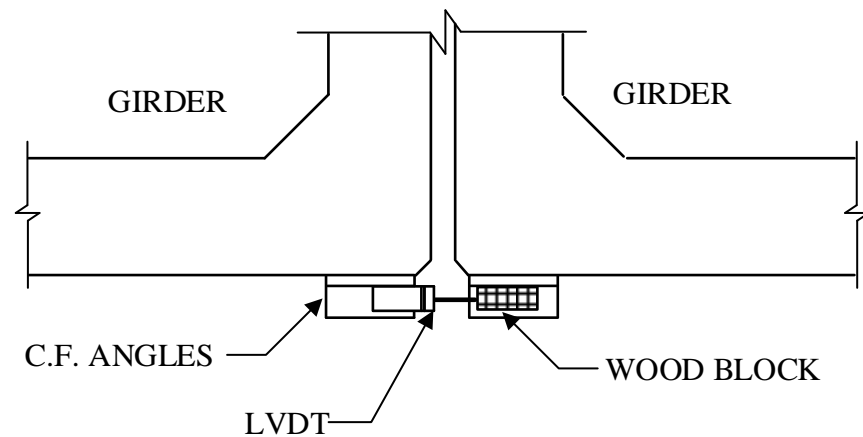
Figure 38: LVDT setup to measure relative horizontal displacements in ARB.

The LVDT setup to measure end rotations and displacements is shown in Figure 39. This setup was used exclusively in the KVCB diagnostic test. In most instances, a single LVDT was attached on the side of a beam above the chamfer at the bottom of the beam(s). This was done to measure the end displacements of beams over the bearing. The setup shown in Figure 39 was used to measure the beam end rotations. The horizontal displacements at beam ends were measured and then the end rotation was calculated using the known vertical distance between the two LVDTs.
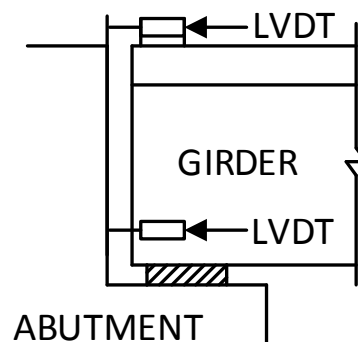
Figure 39: LVDT setup to measure end rotations and displacements in KVCB.

3.2.2.4. Tiltmeter

The tiltmeter was used to measure the beam end rotations. The instrument consisted of a fluid bubble that changed position as per the change in angle of the instrument. Essentially, the fluid bubble operation was similar to that of a spirit level. The change in position of the fluid bubble directly related to the change in the slope at the beam ends due to truck loads. This change in position of the fluid level was

converted into the change of beam end angle by the instrument calibration which was provided by the manufacturer. The accuracy of the instrument was verified in the laboratory by following the procedure as recommended by the manufacturer. The tiltmeters were used in the ARB test only. The tiltmeter setup at the beam end is shown in Figure 40. It is to be noted that the tiltmeter had a very long "settling time" and hence it was meant for a slowly changing response. Therefore, the tiltmeter measurements for the dynamic tests were expected to provide inaccurate results as per the manufacturer.

Figure 40: Tiltmeter attached to beam end in ARB test.

3.2.2.5. Clicker

Clickers were used to locate the position of the trucks on the bridge. The data in the diagnostic tests was recorded with respect to time. To mark the location of the truck in terms of the distance traversed over the bridge the clicker was triggered when the truck reached a predetermined distance on the bridge. The clicker trigger instances then directly indicated the position of the truck on the bridge and the data could be plotted with respect to distance instead of time.

In the KVCB test, a LVDT was used as a clicker. The LVDT plunger was pressed when the truck reached a predetermined location on the bridge. This is shown in Figure 41.

Figure 41: LVDT used as clicker.

In the ARB test an Autoclicker was employed. This system consisted of two parts namely a sensor and a reflective target. The sensor was mounted on the truck near the front wheel and the target was attached on the outside of the front wheel. The rotation of the truck tire caused the target to pass within the field of the sensor. The target was detected by the sensor and a "click" was recorded by the data acquisition system. The distance of the target from the center of the tire was measured which essentially was the radius of the circle formed by the revolution of the target about the center of the tire. The location of the truck was then calculated by multiplying the number of clicker instances times the circumference of the truck tire. The autoclicker system is shown in Figure 42. It is to be noted that the autoclicker could not be used for the dynamic tests. The truck position was marked manually using visual observation of the truck position at the start of the span and at the end.
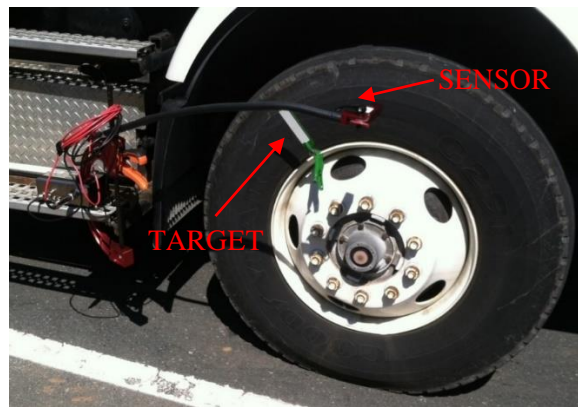
Figure 42: Autoclicker system used in ARB test.

3.2.2.6. Data acquisition system

The data acquisition system (DAQ) and software used for the data collection in KVCB diagnostic test were the Campbell Scientific's CR9000X Datalogger and RTDAQ Software, respectively. The CR9000X was set to sample at a rate of 100 Hz for quasi-static tests and 250 Hz for high speed tests. These rates were selected in order to get the maximum amount of data considering the total time required by the CR9000X to read all instruments. For the high speed test it was determined that because the truck would only be on the bridge for around 5 to 6 seconds, it was important to maximize sampling to adequately retrieve the response. All instruments were connected to the data logger, using an efficient, pre-wired, military connector style system, which can be seen in Figure 43
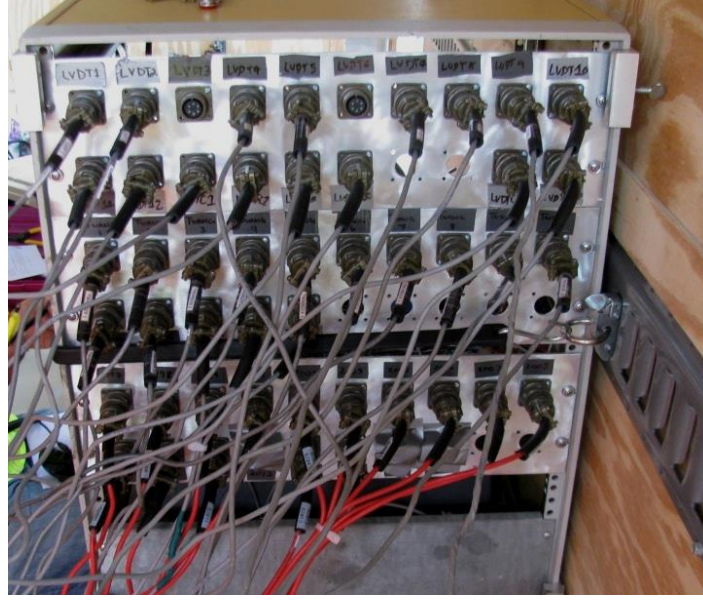
Figure 43: CR9000X data acquisition system used in the KVCB test.

The DAQ used in the ARB test was the Structural Testing System (STS) developed by the Bridge Diagnostics Inc. (BDI). This was a wireless (802.11g broadband) system that incorporated the use of wireless internet for facilitating communication between the DAQ and the instruments and also the computer and the DAQ. The instruments were directly wired to a "node" which communicated to the DAQ "base station". Each node was capable of connecting to four instruments and the base station could connect to a multiple number of nodes (eight in this test) as long as the nodes were within the line of sight of the base station. The pictures of the base station and a typical wireless node are shown in Figure 44.The frequency of data recording was 40 Hz. for quasi-static tests and 100 Hz. for the dynamic test.

(a)

(b)

Figure 44: STS WiFi data acquisition system used in the ARB test, (a) Base Station, (b) Node.

3.2.3. Diagnostic Test of Karr Valley Creek (KVC) Bridge

The KVC Bridge, shown in Figure 45, carried the NY State Route 21. The bridge carried two lanes i.e. one lane each northbound and southbound. The structure was a two span adjacent box girder bridge. The two spans were made continuous for live load with a continuity diaphragm. The bridge superstructure had a skew of 24 degrees. The average daily traffic (ADT) was about 9000 and the average daily truck traffic (ADTT) was about 9% of the ADT as per NBI. The bridge structure was constructed in 1990, hence the diagnostic test was performed after about 20 years of functional life.

Figure 45: The Karr Valley Creek Bridge.

The bridge consisted of 10 box girders. The size of the four interior girders was 36 in. x 39 in. and the remaining girders were 48"x39". The girder connection detail was the typical partial depth grout connection. This girder connection detail was used for the eight interior girders. There was a gap between the fascia girders and the adjacent interior girder to allow for utility lines to traverse the creek. The bridge had a composite concrete topping. Welded wire fabric was utilized to reinforce the concrete topping. The cross-section of the bridge is shown in Figure 46.
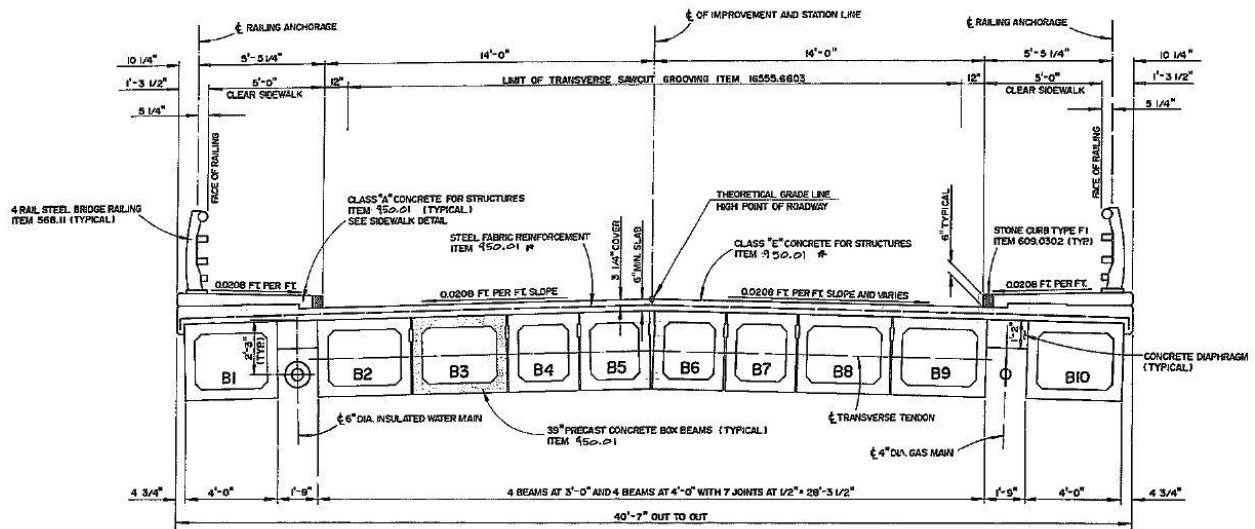
Figure 46: Bridge cross-section.

The concrete topping on the bridge displayed reflective cracks at several locations on the two spans of the bridge. Repair work had been performed on these areas by routing the cracks and refilling with a sealant material. This repair was performed to ensure that water did not leak through the joints. There was one crack in the bridge centerline that had appeared along the whole two spans of the bridge. Reflective cracks of shorter lengths were also noted on several areas of the concrete topping. Observing the bridge superstructure form below a few signs of efflorescence and leakage stains could be observed. The girders themselves did not show any major signs of distress that may accompany corrosion of steel reinforcement.

3.2.3.1. Bridge Instrumentation

The locations of the instruments used in the diagnostic test of KVCB are shown in Figure 47. Most of the instruments that were attached to the bridge were below the bridge superstructure in order to cause minimal interference to the test truck runs as well as the regular traffic on the bridge. The girder and span nomenclature is also shown in Figure 47.

Figure 47: KVC Bridge Layout and Instrumentation.

The instrumentation was kept focused in Span 1 as it was easy to access the girder undersides due to a low clearance. Span 2 was located over the Karr Valley Creek and the only way to access it was by erecting scaffolding in the creek bed. Hence, girders B1 to B9 were instrumented in Span 1 whereas girders B2 to B5 were instrumented in Span 2. Strain gauges and deflectometers were attached at these locations. For the purpose of discussion the locations of instruments are described in terms of single span length which is referred to as "L" and it equals 87 ft 4.875 in. Additional strain gauges and deflectometers were attached on girder B3 in Span 1 at 0.2L and 0.8L to observe the deflected shape of the girder. The vertical LVDT setup for measuring relative displacements between adjacent girders was set up under girders B3, B4 and B5 in Span 1. LVDTs used to measure girder end rotations were attached to the exposed face of girder B9 at the bottom and at the expansion joint over the bridge superstructure. These were attached at 0L and 2L. Additional LVDTs used to measure horizontal displacements at girder ends were attached on the exposed face of girder B9 at 1L outside face of girder B10 at 1L as well.

3.2.3.2. Diagnostic Test Procedure - KVCB

The following sections detail the live load testing procedure for the KVCB.

3.2.3.3. Test Truck Description

Loading of the bridge was provided through the use of two loaded New York State Department of Transportation (NYSDOT) dump trucks. Both three-axle trucks were loaded with gravel to loads of approximately 60 kips. The trucks' axle dimensions and the weights at front and rear axles were measured and recorded when they arrived at the testing site. The axle load distribution and the dimensions of both the trucks can be seen in the sketches in Figure 48 and Figure 49 respectively.
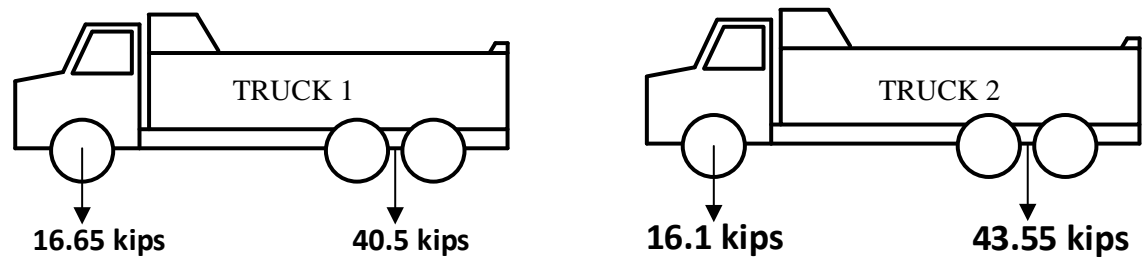
Figure 48: Axle weights of test trucks.
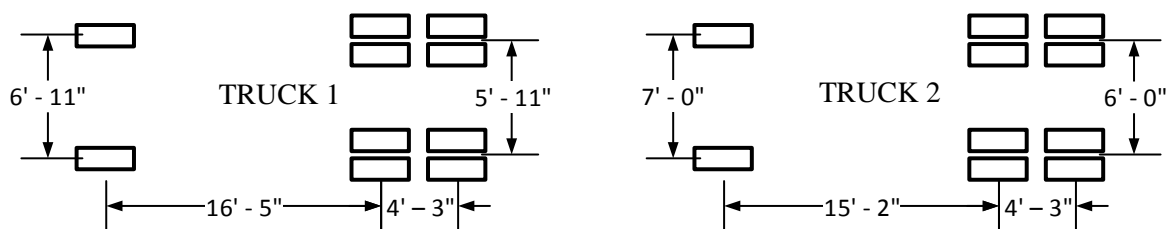
Figure 49: Dimensions of test trucks.

57

3.2.3.4. Truck orientations for Quasi-static tests

For quasi-static testing, two NYSDOT trucks as described above were driven along the bridge at the slowest possible speed (2 to 3 mph) that could be steadily maintained. The truck was driven over the bridge in a number of different orientations to maximize loading on interior and exterior girders and also to simulate the worst conditions at sections where reflective cracking was prevalent. The testing schedule for the southbound lane and the northbound lane is shown in Figure 50 and Figure 51 respectively. Each unique truck orientation was referred to as a "RUN" and the term "PASS" was used to denote the number of times the truck orientation was repeated.

The load pattern for RUN 1 of the truck can be found in Figure 50 and was performed to maximize load on girders B2 and B3. There was a reflective crack in the deck between girders B3 and B4 and RUN 1 imposed load only on one side of the crack. This was done to measure the relative displacement between the girders that led to reflective cracking of the deck. The load pattern in RUN 2 imposed maximum loads on interior girders and also loaded both sides of the reflective crack between girders B3 and B4. The truck orientation in RUN 2 caused one truck to be placed partially in oncoming traffic lane. This orientation was not a typical traffic condition and it was used to impose maximum strains in the girders. The final quasi-static test iteration, RUN 3 was a single truck centered in the northbound lane of traffic, which simulated typical usage of the lane and hence the load was imposed on girders that are most strained under usual traffic conditions.

Load combinations of RUNS 5 through 7 were essentially the same as RUNS 1 through 3 respectively except that the all truck orientations were in the northbound lane. To ensure the quality of the data four passes of the truck were made for each run for a total of twenty four quasi-static passes.

To guide trucks along the correct orientations the left hand side of the wheel path was marked out on the deck with chalk. This allowed for the driver to stay on the correct orientation. Members of the support team guided the trucks by walking in front of the trucks to ensure a uniform pace to the test run. Traffic control was required for the entire duration of the test. One lane was closed throughout the duration of the test for lane and trigger point marking. While performing the test runs traffic on both lanes was halted at a safe distance before the bridge.

Note that RUNS 4 and 8 have been excluded in Figure 50 and Figure 51. These two truck orientations were not actual truck passes. The trucks were parked on the bridge at 0.4L and 1.6L for a static test in the southbound and the northbound lane respectively. The purpose of these truck orientations was to maximize the bending moment on the continuity diaphragm between the two spans. The results from these truck orientations are not discussed.
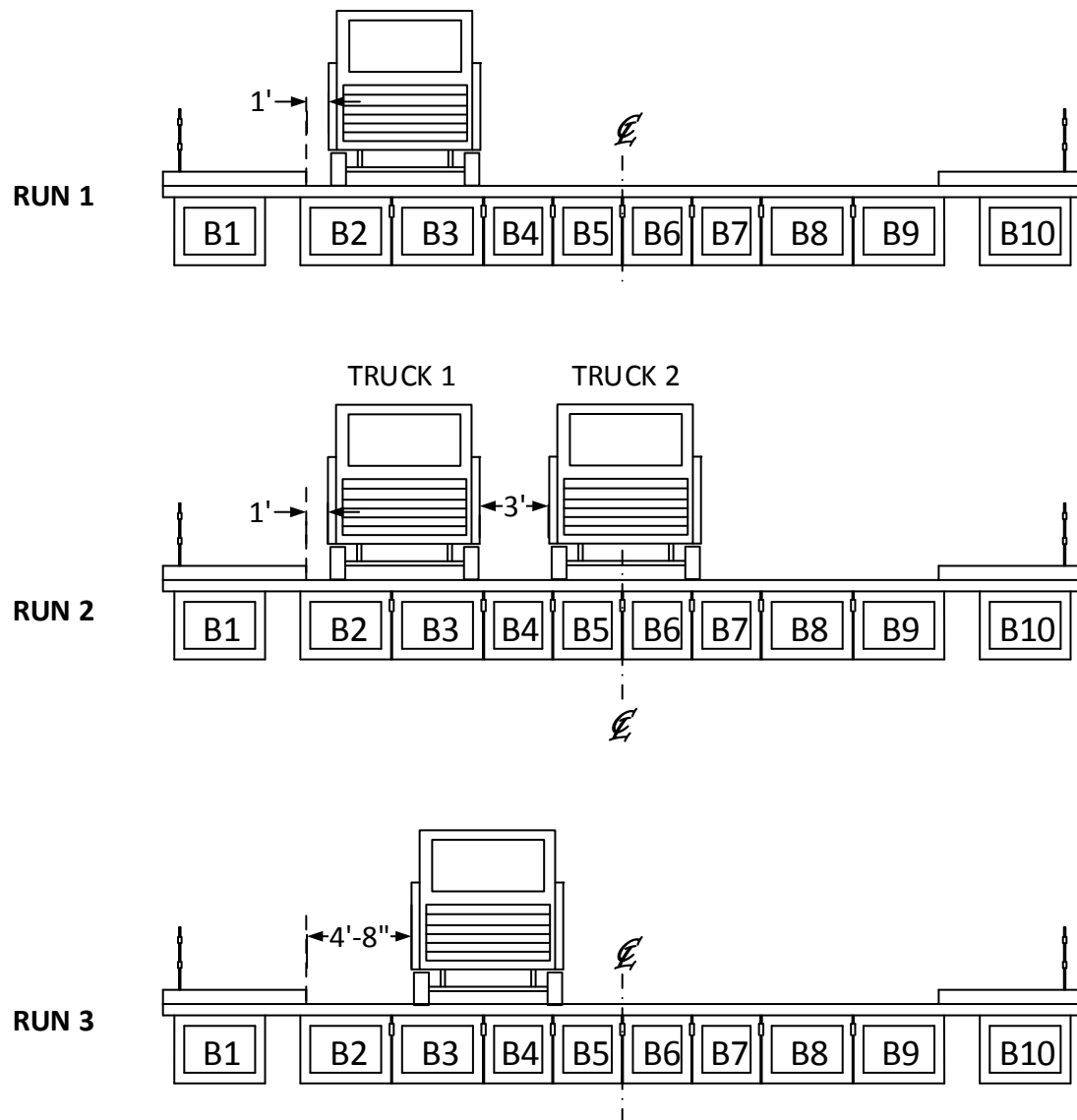
Figure 50: Truck orientations in the southbound lane for quasi-static and static tests.

RUN 5

RUN 6

TRUCK 1   TRUCK 2

RUN 7
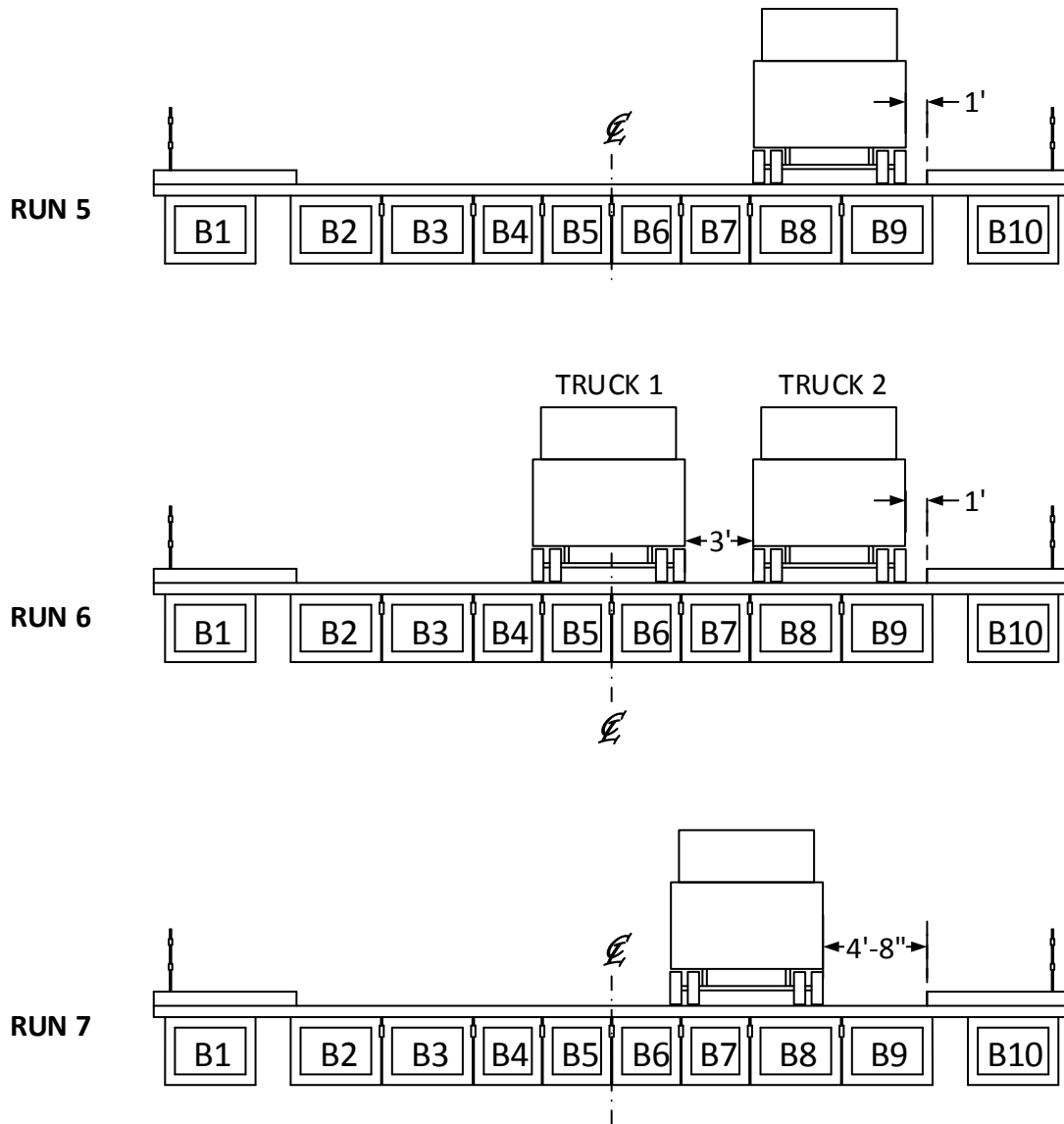
Figure 51: Truck Orientations in Northbound Lane for quasi-static and static tests.

3.2.4. Diagnostic Test of Aden Road Bridge (ARB)

The ARB was a three span adjacent box girder bridge that carried the Route 646 (Aden Road) over the Cedar Run creek. Each of the three spans were simply supported. The bridge had a non-composite asphalt (bituminous concrete) topping of a variable thickness to facilitate a crown on the bridge. The superstructure consisted of nine adjacent box girders. The typical girder size of interior girders was 48 in. × 27in. (BI-48) and the size of the fascia girders was 36 in. × 27in. (BI-36). The adjacent girders were connected by the typical partial depth shear key detail. The transverse PT was applied at the third span locations. Transverse PT was not provided at the span ends. Transverse PT was applied through a single coated (unbonded) Grade 270 strand (with a PT force of 30 kips per location). Solid concrete diaphragms

were provided at the girder ends and at the location of transverse PT. The cross-section details of ARB are shown in Figure 52.
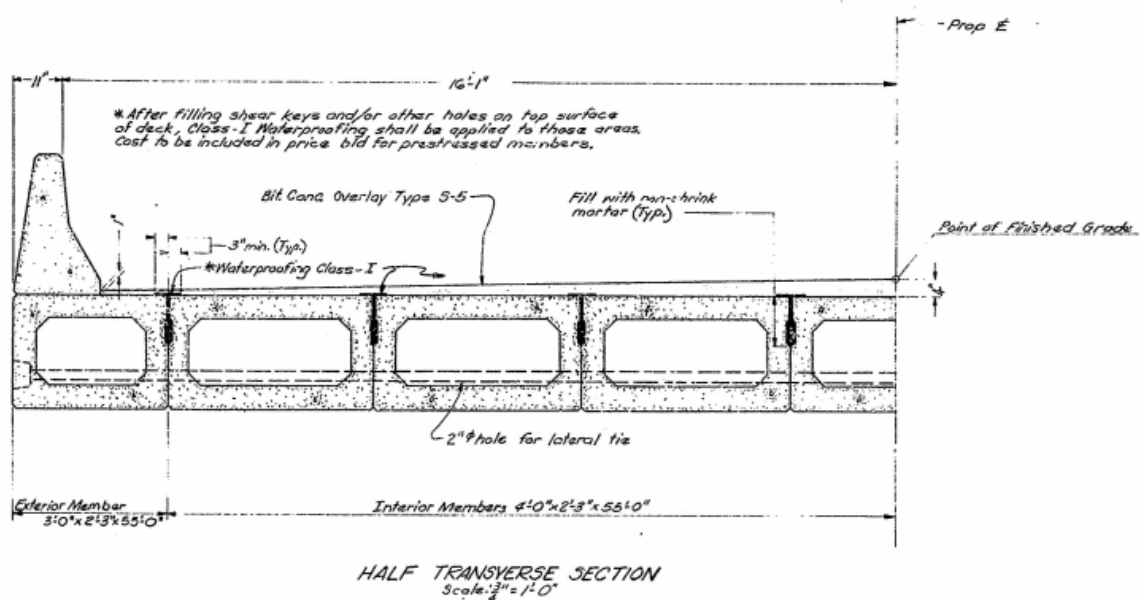
Figure 52: Half cross-section of ARB.

The bridge was constructed in 1982 (as per VDOT Bridge Inventory) and was tested after 31 years of functional life. The bridge superstructure displayed extremely severe deterioration. Every joint in all the three spans displayed signs of failure such as reflective cracks in the asphalt topping as well as leakage through joints. The bridge was visually inspected on a rainy day (prior to testing) and leakage was noted in all the joints. The leakage seemed to be occurring along the full length of the span. The effects of the leakage had consequently led to severe corrosion in the steel reinforcement. Several girders showed spalling and delamination of concrete on the girder underside. Strands were visible at the locations where concrete cover had spalled off from the girder under sides. The visible strands displayed corrosion, as shown in Figure 7, and loss of cross-sectional area in some instances. Similarly, a loss of transverse shear reinforcement cross-sectional area was also noted. At the time of testing the bridge super structure was marked for replacement.

3.2.4.1. Bridge Instrumentation – ARB

Only the first span (western) of the three was instrumented and tested. The detail of the span and the instrument locations are shown in Figure 53. The locations of instruments is described in terms of bridge span "L" which equals 55 ft 0.5 in.

Strain transducers, shown in Figure 34, were attached at 0.5L on the bottom fiber of all the box girders in the superstructure. This facilitated the measurement of the flexural response in each girder for

61

each loading to aid in determination of live load distribution factors. Also, strain transducers were attached on the barriers at 0.5L to measure the contribution of the barriers to the structural response. Additionally, strain transducers were located at 0.25L and 0.75L on girder B7 and B8 to closely observe the behavior at the failed shear key (with the most visible deterioration).

The deflectometers used for live load testing, as shown in Figure 35, were attached adjacent to the strain transducers on the girder underside. Deflectometers were located on the underside of the girders at 0.5L on all girders. Also, deflectometers were located at 0.25L and 0.5L on girders B7 and B8 to study the behavior of the failed shear key.

LVDTs were located at the joint between girders B7 and B8 at 0.25L, 0.5L and 0.75L to measure the relative displacements between the girders with the most visual deterioration. The LVDT setup was as shown in Figure 38 and Figure 39.

Tiltmeters, as shown in Figure 40, were attached to each end of the bridge on the underside of girder(s) to measure the rotations undergone by the superstructure. The tiltmeters were attached at 0L and 1L of the bridge span. The tiltmeters were attached to girder B7 when the trucks were driven in the eastbound lane. For the truck runs in the westbound lane, tiltmeter at 0L was moved over to girder B3.
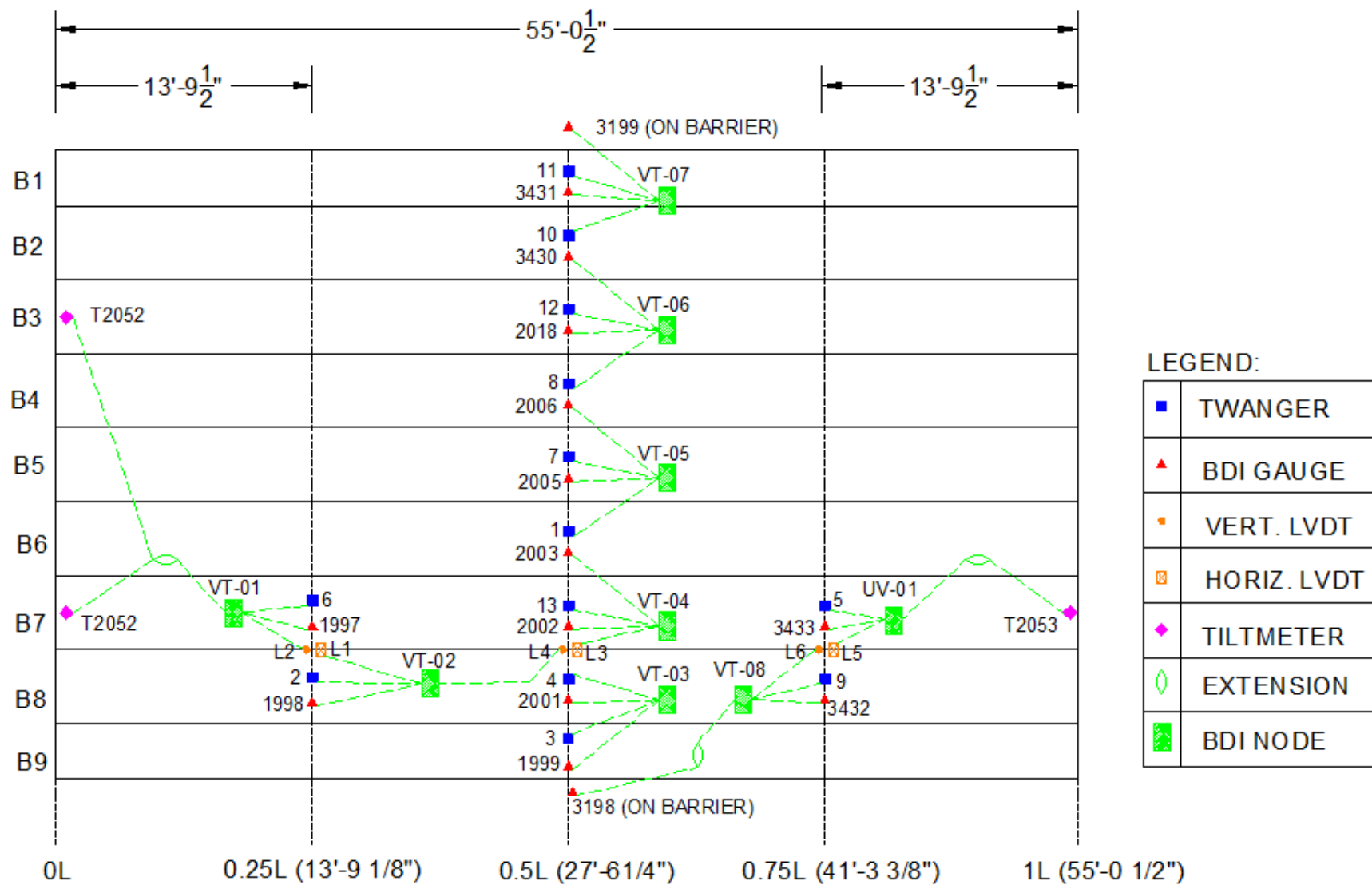
Figure 53: ARB layout and instrumentation.

3.2.4.2. Diagnostic Test Procedure – ARB

The following sections detail the live load testing procedure for the ARB.

3.2.4.3. Test Truck Description

Loading of the bridge was provided through the use of two loaded Virginia Department of Transportation (VDOT) dump trucks. Both three-axle trucks were loaded with gravel to loads of approximately 50 kips. The trucks' axle dimensions and the weights at front and rear axles were measured and recorded when they arrived at the testing site. The axle load distribution and the dimensions of both the trucks can be seen in the sketches in Figure 54 and Figure 55 respectively.
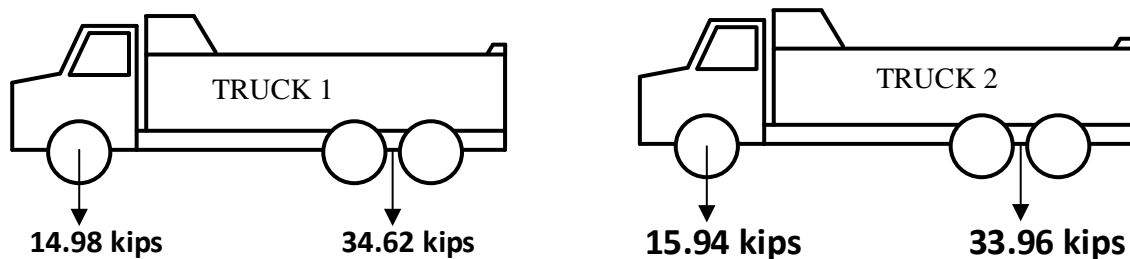
Figure 54: Axle weights of test trucks.
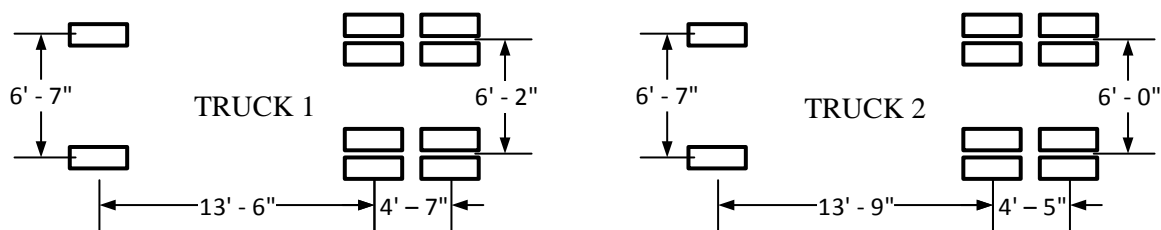
Figure 55: Dimensions of test trucks.

3.2.4.4. Truck orientations for Quasi-static tests

The test procedure for the quasi-static tests was consistent with the previous test. The truck was driven over the bridge in a number of different orientations to maximize loading on interior and exterior girders as shown in Figure 56.

The load pattern in RUN1 and RUN4 imposed maximum load in girder B9 and girder B1 respectively. This orientation was useful in determining the contribution of the barriers to the structural response. This orientation also imparted stresses on the shear key between girders B6 and B7 for RUN1 and shear key between girders B3 and B4 in RUN4.

The second set of quasi-static live load combinations i.e., RUN 2 and RUN 5, shown in Figure 56 maximized the load on girders that are under the traffic lane. RUN 2 placed a single truck centered in the

eastbound lane of traffic, and RUN 5 placed a single truck in the middle of the westbound lane. This orientation also imposed stresses on the shear key between girders B7 and B8 which displayed the worst deterioration amongst all the girders. In comparison the shear key between girders B2 and B3, which displayed comparatively lesser deterioration was stressed in RUN 5.

The final set of quasi-static load combinations i.e., RUNS 3 & 6, as shown in Figure 56, maximized the load on all interior girders of the bridge.

Four passes of the truck were made for each run for a total of 24 quasi-static passes. This was intended to ensure the collection of good quality data.
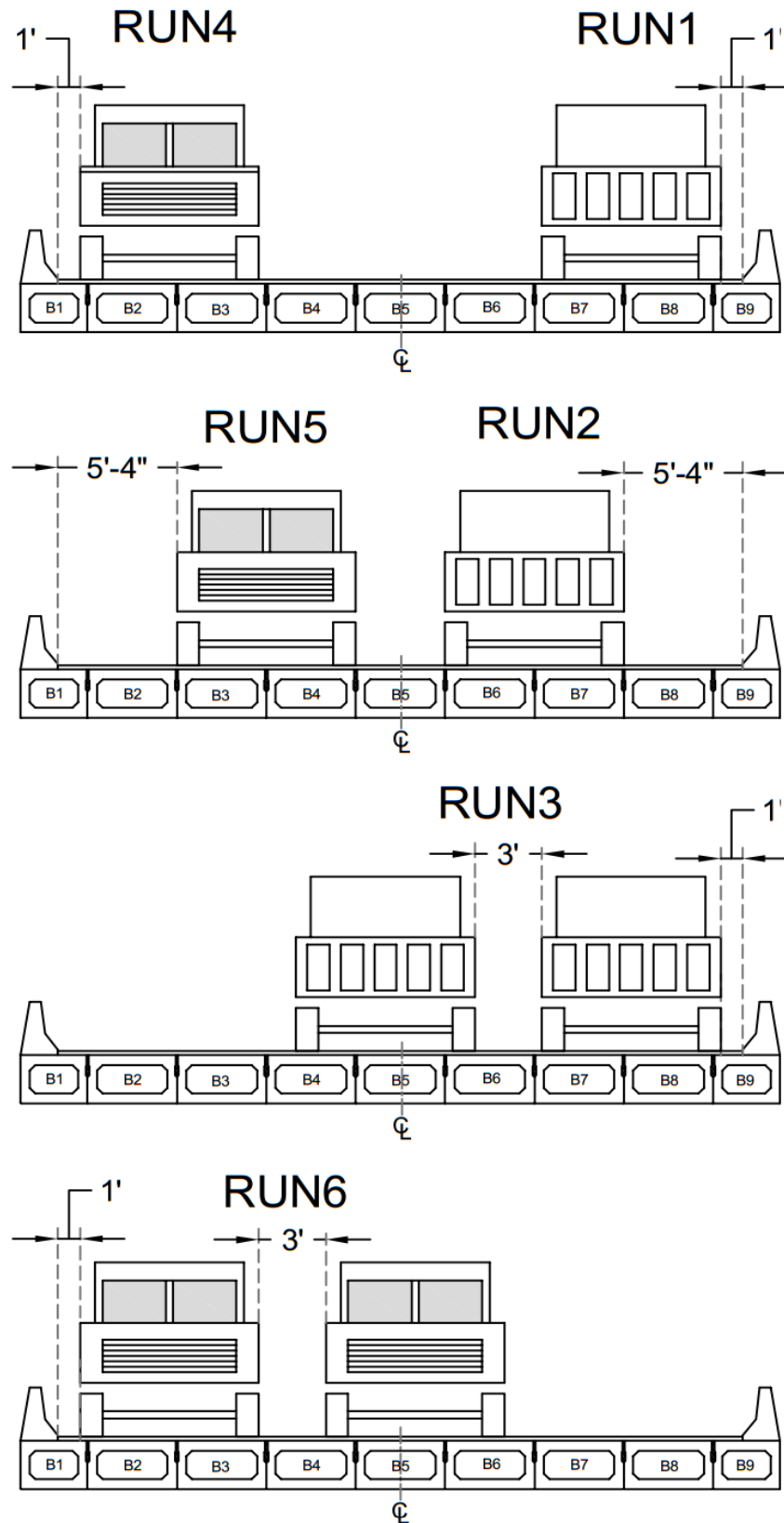
Figure 56: Test truck orientations for diagnostic test of ARB.

The procedure used in the KVCB was repeated for the quasi-static tests of ARB. Loading was provided by a truck traveling through the previously outlined orientations on the bridge. The focus of the testing was to determine the transverse behavior and the GDFs. A total of four truck passes (each truck twice) were performed in each direction. However, the data from all the truck runs was not plotted due to discrepancies in testing such as the autoclicker sensor falling off the tire during loading etc.

3.2.5. Focus of Diagnostic Tests

As mentioned earlier, the focus of the diagnostic tests was to observe the in-situ behavior of the ABBB system. The data collected from the quasi-static tests was used to observe the relative displacements between adjacent beams. These measurements provided the understanding of the magnitude of movement that occurred at a failed joint. The data also was used to calculate the transverse distribution factors of the bridges and compare with the code values to see if any bridge beams were being overstressed due to the failed joints. Finally, all the data that was collected was compared with the FEA models of these bridges. In the following section the FEA analysis procedure is discussed.

3.3. Simulating ABBB Behavior

Finite element analysis (FEA) was performed to quantify the responses of adjacent box beam bridges to typical HS-20 tandem truck (with dynamic load allowance of 33% as per AASHTO). Two basic models were created in ABAQUS with typical material properties assumed for concrete [Type A5, 5000 psi concrete as per VDOT specifications VDOT (2007)], grout that met ASTM C1107 requirements, UHPC properties from FHWA research Graybeal (2006) and topping concrete [Type A4, 4000 psi as per VDOT specifications VDOT (2007)]. These properties were assumed in the initial models of the full scale bridge (FSB). The typical properties used in FEA models is shown in Table 8. The second model utilized the mechanical properties of the materials that were measured in the laboratory.

Table 8: Typical material properties used in FEA models.

Component	Unit Weight (pcf)	Modulus of Elasticity (ksi)	Poisson's Ratio
Topping Concrete	145	3644.1	0.2
Beam Concrete	145.5	4095.4	0.2
UHPC	147	6500	0.19
VHPC	147	5700	0.19
Grout	148	4415.2	0.2
Structural Steel	490	29000	0.3
Prestressing Strands	0.39*	28500	0.3

NOTE: * - indicates unit weight in lb/ft.

3.3.1. Simulation of Aden Road Bridge Test

The ARB diagnostic test was simulated through FEA in ABAQUS. Field tests were performed on this bridge to quantify the actual bridge responses of ABBB. The ARB was selected for FEA simulation since it was a single simply supported span with no skew and without a composite topping. The KVCB model was deemed to be more complex since the bridge had a skew, it was not known whether there was a full composite action between the concrete topping and the bridge beams and finally the full depth cracks at the continuity diaphragm made the two spans partially continuous. On the other hand, the ARB joints and beams were severely deteriorated and it was difficult to know the degree to which the adjacent beams would interact through the cracked shear keys. However, the purpose of modeling the FSB was to compare the flexural strains in the bridge beams, relative displacements between adjacent beams and the transverse distribution factors of a bridge with sound joints. Hence ARB was modeled in ABAQUS. The FEA model of the ARB is shown in Figure 57. The VDOT dump trucks used in the diagnostic tests were modeled as tire patches and the axle weights were applied as pressure.
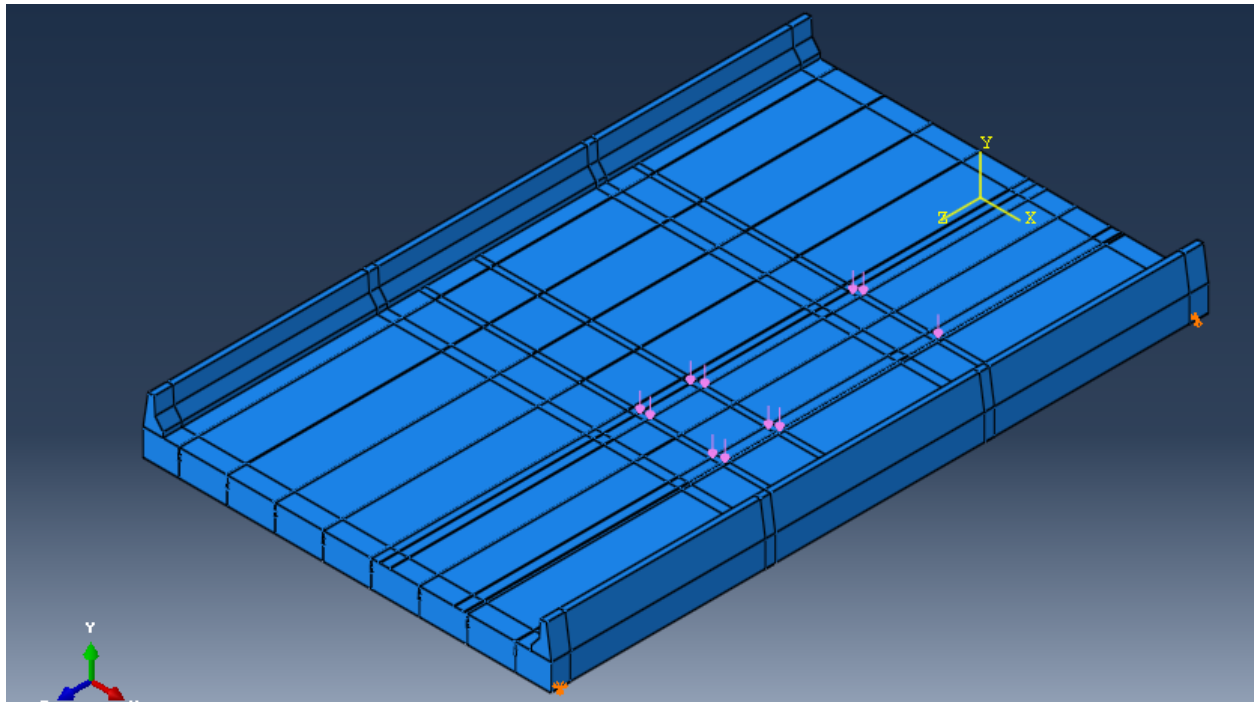
Figure 57: FEA model of the ARB with truck tire patches.

The size of tire patches was calculated as per Section 3.6.1.2.5 of AASHTO (2013), which was as follows,

$$Tire\ Width = P/0.8 \qquad\qquad Equation\ 7$$

$$Tire\ Length = 6.4\ \gamma\ \left(1 + \frac{IM}{100}\right) \qquad\qquad Equation\ 8$$

where,

γ = load factor

IM = dynamic load allowance percent

P = design wheel load (kip)

3.3.2. Full Scale Bridge Model

The FSB model was based on the ARB FEA model. The greatest difference between the two was that concrete barriers and the beam internal diaphragms were ignored in the FSB model. The number of beams, span, beam cross-sections, area of steel etc. were kept the same. The purpose of this model was to simulate the behavior of a full scale bridge that would not have any transverse PT as well as the barriers would not be composite with the beams. As seen in the literature review, the use of transverse PT was not sufficient in abating shear key failures. Therefore, a non-PT option was sought in this research. The FSB model is shown in Figure 58. The FSB model was subjected to a HS-20 design truck load with 33% impact factor. The truck load was also discretized as tire patches with size and pressure as prescribed by AAHSTO LRFD bridge specifications. The design truck was positioned in various locations on the bridge to study the maximum possible stresses at the joints due to truck load. The purpose of the FSB model was to provide a guideline for the state of stress in the joints and the global behavior of the bridge system. These guidelines were then used to formulate the test setup for bridge sub-assemblages for testing the proposed connection details. For the ease of discussion, the beam numbering was also kept the same as that of the ARB.
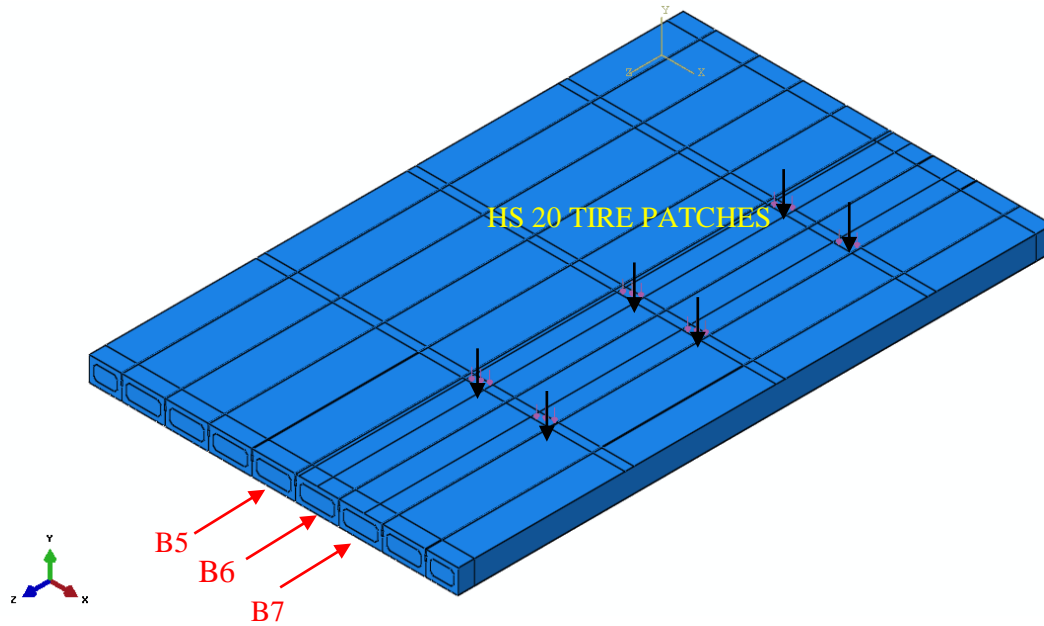
Figure 58: Full scale bridge (FSB) model with truck loads and beams of interest demarcated.

The HS-20 tire loads were applied in the same load paths as the ARB diagnostic test. Figure 58 shows the truck in the middle of the east bound lane and also demarcates the beams of interest for that test run. The stresses between beams B5, B6 and B7 were studied in order to observe the worst effects of the applied loads.

3.3.3. Converting 3D behavior to 2D behavior

The connection details were to be tested for fatigue and strength through the use of bridge superstructure sub-assemblages. The basic idea of the use of the sub-assemblages stemmed from the fact that several connection details were to be tested. It was not feasible to construct and test the connection details on full scale bridge beams. Instead the behavior observed at the ABBB joints was simulated through bridge sub-assemblages. The concept is shown in Figure 59.
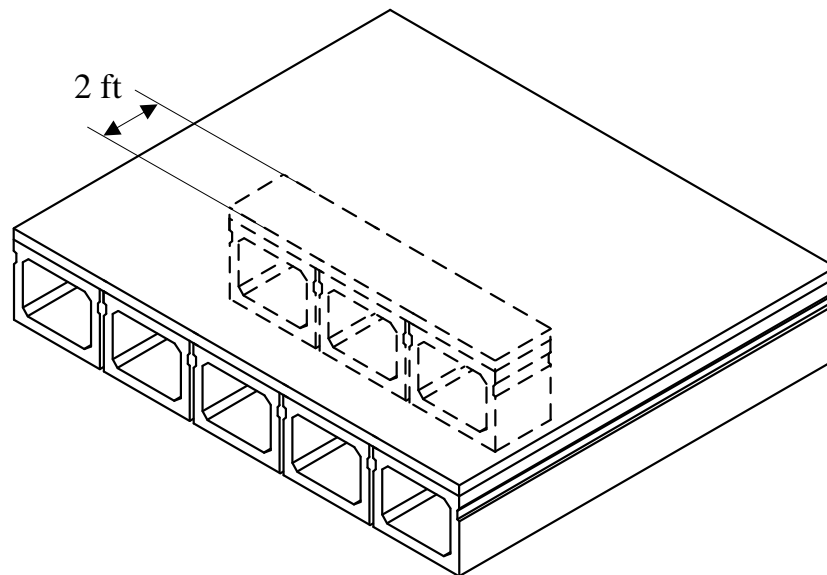
Figure 59: Test sub-assembly extracted from the midspan of a typical ABBB.

The sub-assemblage specimen represented a 2 ft long interior, midspan section from a typical ABBB as shown in Figure 59. The three-dimensional behavior of the bridge was simulated in a specimen that experienced two-dimensional behavior exclusively. In a typical bridge the load distribution between beams induces flexural and shear stresses in the transverse direction across the bridge span. The effect of longitudinal flexure and shear on transverse connections was negligible. The purpose of these tests was to ensure adequate transverse load transfer between adjacent beams; hence longitudinal effects were neglected.

Although the effect of longitudinal stresses was ignored the three-dimensional behavior of the bridge itself was not ignored in terms of beam stiffness. The specimen sub-assemblage sections were to be

supported on steel beams. These steel beams acted as flexible supports to the sub-assemblage beam sections. Essentially, the longitudinal portions of the beams that were missing from the sub-assemblages were simulated by the steel beams. Therefore, the effect of beam longitudinal stiffness on the joint behavior was simulated by the flexible steel beams. FEA models of a test bridge and the sub-assemblages were created and the behavior of the two was compared to ensure that the state of stress in the joints and the relative displacements between beam sections of the sub-assemblages was similar to that observed in a typical ABBB. Based on the above idea the testing setup was envisioned as shown in Figure 60 and Figure 61.
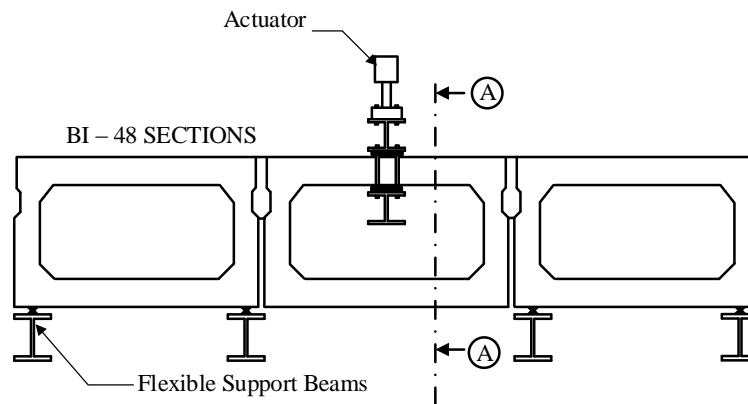
Figure 60: Sub-assembly loading setup.
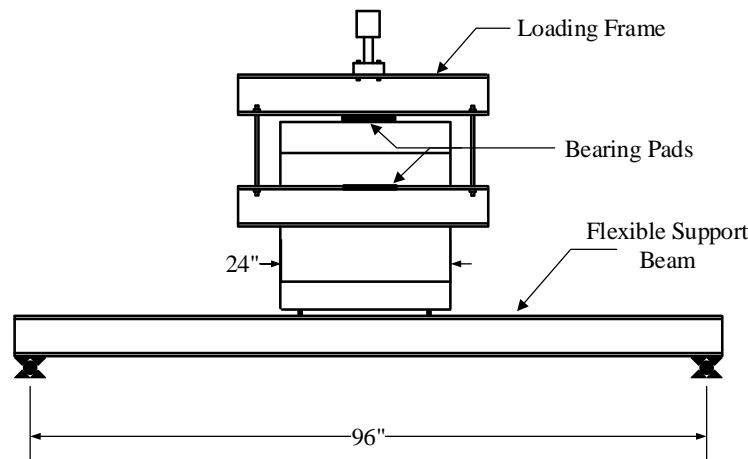
Figure 61: Section A-A from Figure 60 displaying side view of the loading setup.

3.3.4. Stiffness of Support Beams

As described earlier, the replacement of bridge beam stiffness was achieved by the provision of steel beams, one under each web of the exterior sections. Steel beams were used for providing longitudinal stiffness since rolled steel sections have a very good fatigue life and at least six million cycles were expected to be imposed on the flexible support beams considering a million cycles on six specimens. One steel beam was placed under one web of the two exterior sections. The steel beams were used to simulate the

longitudinal stiffness of the concrete box beam beams and it would have been more appropriate to provide two beams per beam section, interior as well as exterior. This possibility was precluded by two circumstances; the width of the column used in the actuator frame and the insufficient number of 10 kip load cells available to measure the vertical reactions transferred from the concrete sections to the steel beams. Hence, the longitudinal stiffness was provided by four steel beams instead of six.

The size of the steel beams was crucial as the stiffness of three concrete beams was to be simulated through four steel beams. The key issue with the size selection was that an appropriate stiffness was essential. If the steel beams were too flexible, the specimen would displace as a rigid body and the worst load effects would not be imposed on the joints. On the other hand, excessively stiff beams would impose excessive stresses on the joints. Practically, it was conservative to err on the side of steel beams being too stiff. The sub-assemblage specimens were modeled in ABAQUS and the supports for the specimens were modeled as vertical springs. Vertical springs were assumed since it was the most practical method for connecting the concrete beam sections to the steel beams. Although rotational springs could also have been included at the supports in the FE model, the realistic application of the rotational spring was deemed to be too difficult as it would involve the use of a moment connection between the concrete beam and the steel beams. Therefore, to convert the vertical spring stiffness into an equivalent steel beam stiffness the vertical stiffness of a single box beam BI-48 section with a span length was calculated assuming a compressive strength of 5000 psi as per VDOT standards. This stiffness value was then mimicked by the steel beams assuming a span of 8 ft (equal to the span between floor beams in the laboratory) and a modulus of elasticity of 29000 ksi. The required moment of inertia for the steel beams was calculated and the W8x15 section was chosen. The moment of inertia of W8x15 was higher than the required value. The stiffness of the three concrete beams was provided through the stiffness of four steel beams instead of six. Therefore, a steel beam with larger moment of inertia was selected. The validation of W8x15 was then performed through FEA.

3.3.5. Sub-assemblage Model

The sub-assemblage (SA) specimens also were modeled in ABAQUS. The sub-assemblages consisting of the beam sections and joints were modeled as linear solid elements (C3D8R in ABAQUS 6.13). The support beams were modeled as beam elements. The two discrete sub-models were connected by rigid one-dimensional spring elements. These rigid connections were established at locations where the beam sections were in actual contact with the steel beams. The spring elements were utilized since the use of tie constraints caused the connection to become too rigid. The boundary conditions for the steel beams restrained any translation in the vertical direction and the direction along the axis of the steel beams. The

direction which was orthogonal to the steel beam axis was allowed to translate. Provisions were made for allowing this translation in the actual specimen tests.
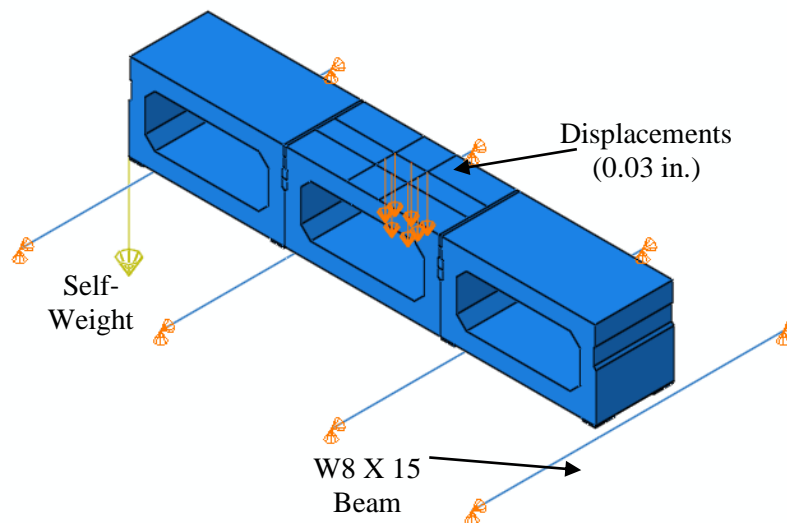
Figure 62: Finite Element model of sub-assemblage specimen (typical partial depth joint detail with grout).

For the purpose of connection between the concrete sections and the steel beams, linear spring elements with a very high stiffness (10^8 kips/in.) were used. In the two horizontal directions, similar linear springs were used to prevent the concrete sections from slipping relative to the steel beams. This was an assumption made during modeling on the basis that the horizontal force caused by loading the specimen was not high enough to overcome the frictional forces between two steel surfaces. The two steel surfaces refer to the load cells used to measure the reactions being transferred from the concrete sections to the steel beams and a steel plate glued to the concrete sections in order to prevent stress concentrations in concrete. More detail about the specimens and the instrumentation is provided in Section 3.7. The steel plates glued to the concrete sections were also modeled to be rigid (very high modulus of elasticity) in order to avoid stress concentrations in concrete due to the springs being attached to a single node on the model.

3.3.6. Comparison of Full Scale Bridge and Sub-assemblage models

The sub-assemblage models were subjected to displacements applied uniformly over an assumed area. The dimensions of the assumed area were based on the rigidity of steel plates that were available in the laboratory. The width of the steel plates was such that the plate would not bend due to the applied loads. Plate bending would prevent the displacements from being applied uniformly. The magnitude of displacements was determined by trial and error method. A displacement was applied statically to the middle specimen section and the effect of the applied displacement on joint stresses and the model

displacements were observed. The magnitude of displacement that produced a state of stress and relative displacements in the joint that were similar to the state of stress and relative displacements in the FSB joint were selected. The comparison of the behavior of the FSB model and the SA model is now presented.

3.3.6.1. Comparison of Transverse Normal Stresses in the Joint

The stress distribution in the FSB and the SA model joints are shown in Figure 64 and Figure 65 respectively. The plots show that the variation in transverse flexural stresses in the joints was quite similar between the two models. The stress distribution caused by the truck loading could be mimicked by the specimen with a total applied displacement of 0.03 in. downward displacement. The magnitude of tensile stress at the base of the keyway was 194 psi for the FSB model and 182 psi for the SA model. The sub-assemblage model could produce the same magnitude of stress for a 0.0305 in. displacement. This additional magnitude of displacement, 0.0005 in., was below the least count for the LVDT in the actuator. Hence, the target displacement was set at 0.03 in. The applied displacement of 0.03 in. was sufficient to produce the same stress variation in the sub-assemblage joints as that induced by the HS-20 truck with 33% impact factor in the FSB model joints. The schematic for the section through joint is shown in Figure 63. The distribution of normal stresses in the keyway are presented for the FSB and the SA in Figure 64 and Figure 65 respectively.
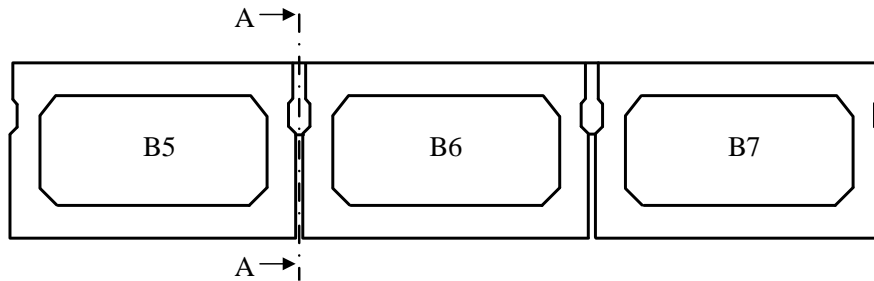
Figure 63: Section through joint for displaying the distribution of normal stress.
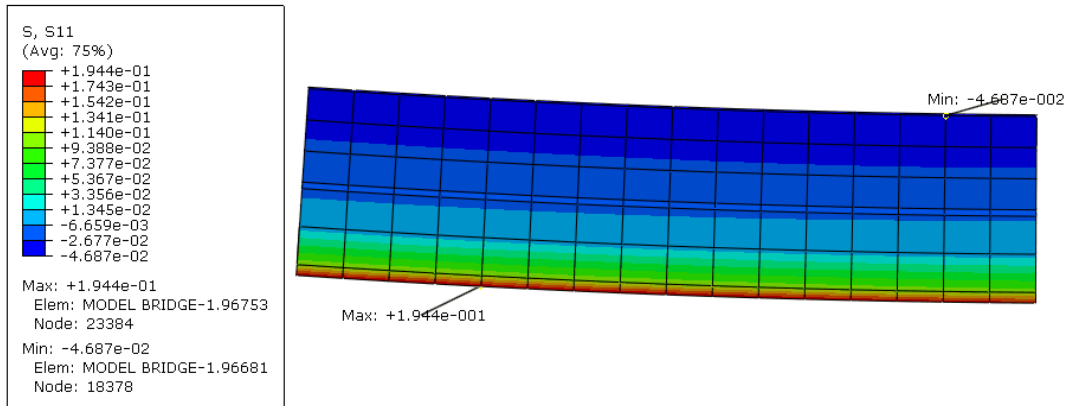
Figure 64: Transverse normal stress distribution in shear key of FSB model (between B5 and B6).

74
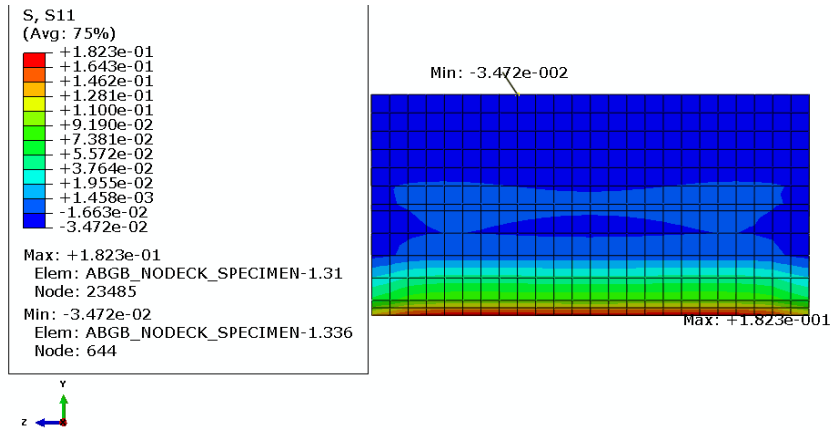
Figure 65: Transverse normal stress distribution in shear key of SA model.

3.3.6.2. Comparison of Global Relative Displacements

The global relative displacements refer to the difference in the global vertical displacements in the adjacent beams. For the sake of a head-to-head comparison the relative deflection between the adjacent beams in the FSB could not be directly parsed from the FEA results. These values could not directly be used since the beams in the FSB model underwent a transverse rotation as shown in Figure 66. Hence, using the results from the FEA model the relative vertical deflection was calculated as shown in Figure 67.
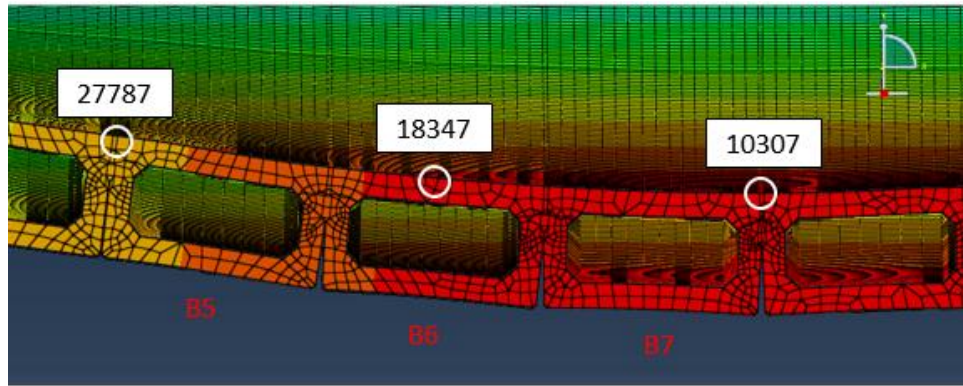
Figure 66: Nodes considered for calculation of relative displacements FSB model.
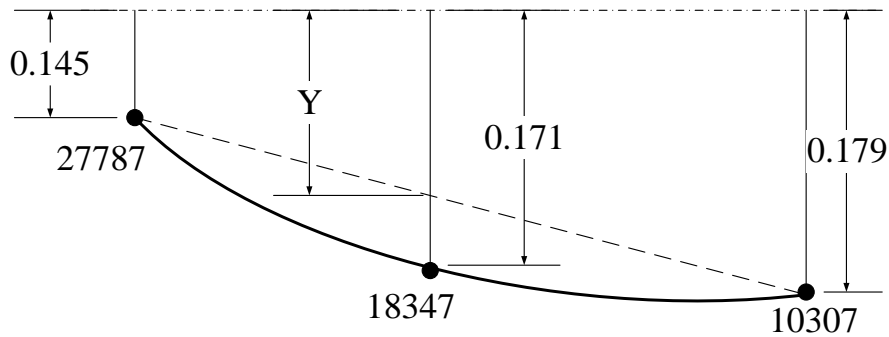
Figure 67: Relative vertical displacement calculations for the beams of interest in FSB.

75

The nodes in the FSB used for calculation of the relative vertical deflection are highlighted in Figure 66. Figure 67 is a schematic of the deflected shape with the values of deflection predicted by the FEA. Assuming a straight line between the two extreme nodes the distance between the straight line and the middle node was calculated as the relative vertical deflection between the adjacent beams in the FSB. The calculations were as follows,

$$\delta = 0.171 - \left(\frac{0.179 + 0.145}{2} \right) = 0.009 \; in.$$

In comparison the magnitude of relative deflection between adjacent beams in the SA model was 0.0106 in. for an externally applied displacement of 0.03 in. Although close, the overall difference in values was 17%. The SA model displayed a higher vertical displacement since the steel beams were allowed to displace in the orthogonal direction. In the FSB the beams outside of the beams of interest would prevent this movement. Hence, the SA was slightly more flexible than the FSB. The nodes considered for calculation of the SA relative deflection are shown in Figure 68.
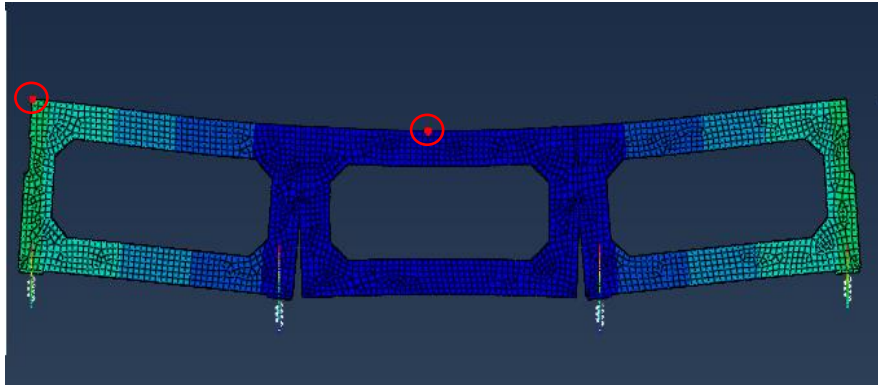
Figure 68: Nodes considered for calculation of relative vertical displacement between SA sections.

3.3.6.3. Comparison of gap opening at joints

The gap opening at the joints were also compared between the FSB and the SA. The nodes considered in this comparison are shown in Figure 69 and Figure 70 for the FSB and SA respectively.
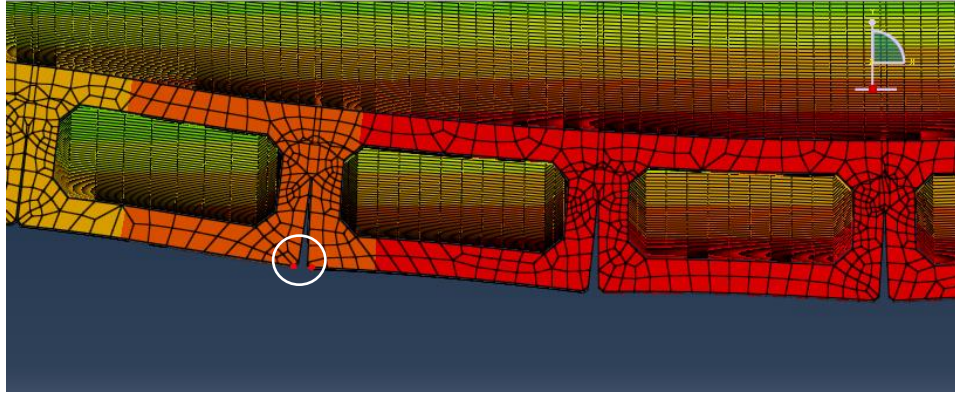
Figure 69: Nodes of interest for measurement of gap opening between B5 and B6 in FSB model.
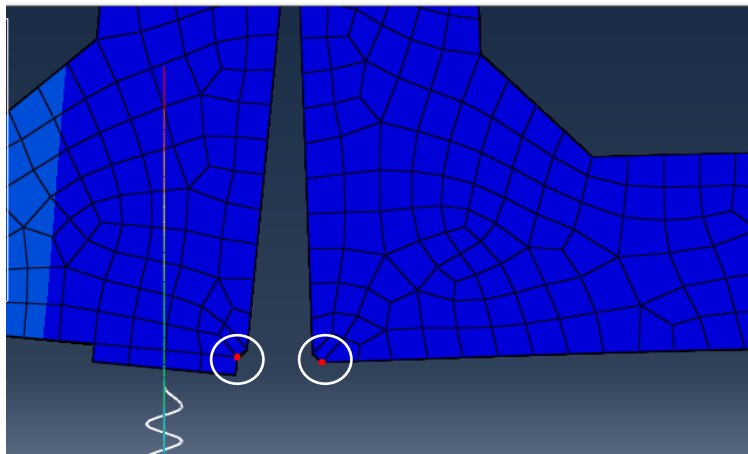
Figure 70: Gap opening measurement in SA model.

The value of gap opening in the FSB was 0.0038 in. and that in the SA model was 0.00387 in. These values were practically the same.

3.3.6.4.   Results of FSB and SA comparison

Overall a close agreement was observed between the behaviors of the FSB and the SA. The SA was slightly more flexible than the FSB due to the fact that it was a three beam assembly. The performance could have been improved by increasing the moment of inertia of the interior pair of steel beams. However, the stress distributions and the gap openings were very close and it was deemed that the performance was sufficient. Moreover, the adjustments required to accommodate beams with unequal depths were deemed to be excessive considering that most of the performance parameters were met by the SA model with W8x15 beams.

3.4. Proposed connection details

Two new connection details were explored in this research. The first connection detail involved absolutely no change to the existing connection detail of a partial or a full depth grouted connection. This detail made use of a Kevlar sheet to reinforce the connection and provide strength and water-proofing to the joint. The second detail is slightly more complicated as it involved the use of blockouts to be cast into concrete at the time of fabrication. The use of ultra and very high performance concrete was proposed as a replacement for grout in these joints. The typical box beam cross-section used in this research is shown in Figure 71. The details of the connections and the fabrication is now described.
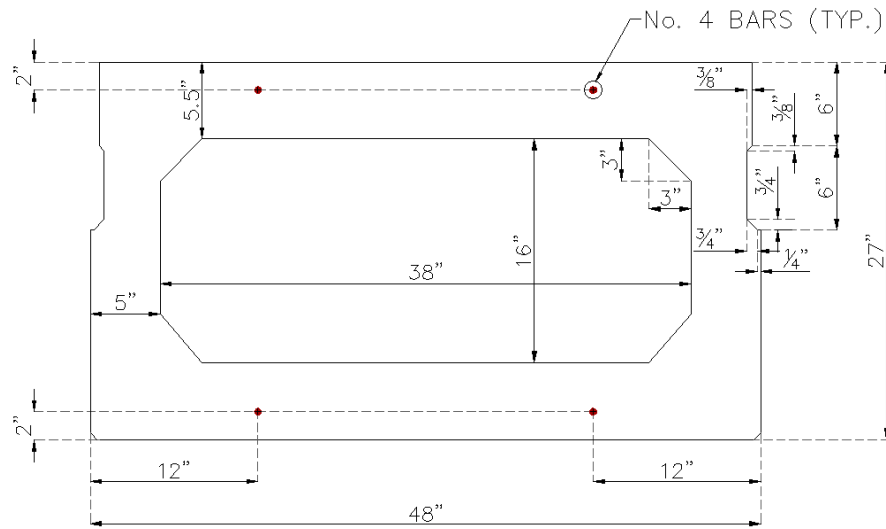
Figure 71: Cross-sectional details of BI-48 beam sections as implemented by VDOT.

3.4.1. Kevlar and epoxy connection

The Kevlar and epoxy (K&E) connection was the simplest detail proposed to be used for longitudinal joints in the ABBB system. The connection detail made no change to existing connection detail or the connection filler material (grout). The K&E sheets were to be attached over the joints to provide resistance to cracking and also to prevent water leakage through the joints in case of occurrence of cracks at the joints. These two aspects were the primary focus of testing this connection detail. The secondary focus was to observe if the K&E sheet presented sufficient capacity to transfer loads between adjacent beams by itself. The typical detail for this connection type is shown in Figure 72.
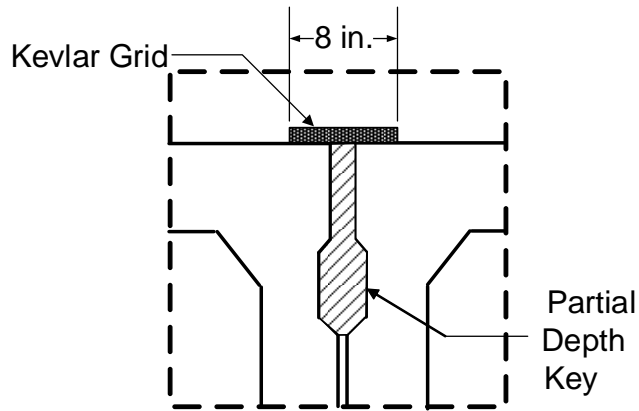
Figure 72: Typical detail of Kevlar and Epoxy connection.

The Kevlar and epoxy (K&E) connection consisted of a sheet with bi-directional Kevlar fibers that were imbued with a specialized epoxy. The details of the Kevlar sheet are presented in Appendix A. The manufacturer had specified the use of this Kevlar sheet for applications such as "heavy duty crack repair, crack control, structural strengthening of concrete where durability, impact resistance and protection of water intrusion is needed". A typical Kevlar sheet is shown in Figure 73.

Figure 73: Kevlar sheet.

The manufacturer specified the epoxy to be used with the Kevlar sheet to achieve the design purposes. This epoxy resin was designed (by the manufacturer) to provide a very good bond with substrate materials, strength to the Kevlar fabric sheet, waterproofing the joint and be flexible to allow temperature and stress related movements at the joints. The K&E combination has been used by VDOT in several repair projects such as joints between segments in a precast box beam bridge and wanted to explore the use of this material in strengthening joints in ABBB. The properties of the epoxy resin are presented in Appendix B.

3.4.2. Top flange splice connection detail

The typical failure mode for the joints in ABBBs has been the propagation of interface crack(s) leading to reflective cracks in the topping material. Usually, the formation and propagation of such cracks is dependent on the bond of the two materials i.e. grout and concrete. Considering all the evidence seen in bridges and other research it can be safely assumed that the bond between the materials is insufficient to prevent interface debonding. Therefore, a structural connection was proposed. This connection was a splice bar (reinforcing bar) that connected two adjacent beams at the top flange. To keep the length of this splice short the use of fiber reinforced ultra high performance concrete (UHPFRC) was proposed. Similarly, a non-proprietary mix of fiber reinforced concrete was also explored with this connection detail. The spliced connection detail is shown in Figure 74.
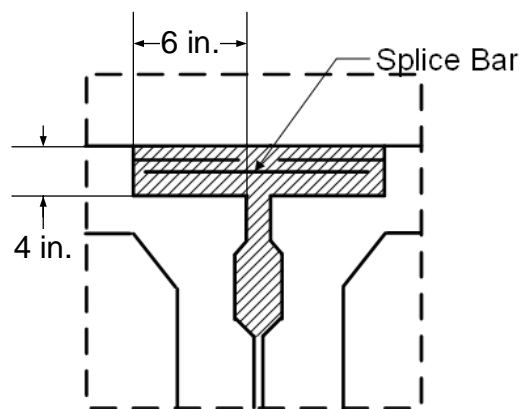
Figure 74: Proposed top flange spliced connection.

The connection essentially remained the same as the traditional detail, the partial depth keyway at the beam top, with an addition of the spliced connection. The spacing between splices was assumed to be 2 ft as the first iteration for this solution. The specimens with the spliced connection detail were tested in this configuration. The minimum required spacing between splices was determined using FEA and is discussed in a later section.

The principal component of this connection detail was the replacement of cementitious grout with a fiber reinforced ultra high performance concrete (UHPC). The use of UHPC as a connection material is becoming prevalent. Several examples of such applications are the use of UHPC as connection material between full depth precast deck panels Graybeal (2010), between flanges of decked bulb-tee beams Perry et al. (2010), and between full depth deck panels and supporting beams Graybeal (2012). The research cited here involved the use of short splices in UHPC.

Two alternative mixes were explored. One of the mixes was a proprietary product named Ductal produced by Lafarge. The use of Ductal has been explored in several researches by FHWA and state DOTs.

The second mix was a non-proprietary mix developed at Virginia Tech. The second mix was based on the mix presented by Morcous et al. (2011) with an addition of 1 in. long steel fibers. The second mix was termed as "Very High Performance Concrete" or VHPC because the properties of this mix did not quite meet the definition of UHPC. Typical UHPC is defined as "cementitious based composite materials with discontinuous fiber reinforcement, compressive strengths above 21.7 ksi pre-and post-cracking tensile strengths above 0.72 ksi and enhanced durability via their discontinuous pore structure" by Russell and Graybeal (2013). The difference in the composition of the two mixes is presented in Table 9.

Table 9: UHPC and VHPC mix proportions.

Constituent	UHPC (lb/cu. ft.)	VHPC (lb/cu. ft.)
Cement	44.44	41.50
Silica Fume	14.44	8.90
Fly Ash	NA	8.90
Ground Quartz	13.15	NA
Fine Sand	63.7	53.70
¼ in. max coarse aggregate	NA	23.00
water	6.82	11.80
superplasticizer	1.92	0.75 – 1.05
Steel fibers	9.74	9.80
Water/cementitious	0.12	0.20

Table 9 shows the comparison of the two materials components and quantities on the basis of 1 cu.ft of concrete. The quantities of the UHPC mix were referred from Graybeal (2006) and the VHPC mix quantities are the modified version of Morcous et al. (2011)). The main difference between the two mixes was that the VHPC mix utilizes coarse aggregates in place of ground quartz and partial replacement of fine sand as compared to UHPC mix. The quantity of cementitious materials in the two mixes is virtually the same but the water/cementitious material ratio is higher in the VHPC. More water is required in the VHPC mix to hydrate the greater amount of aggregates in the mix. It is to be noted that both the materials present a self-consolidating concrete (SCC). The basic properties of the two mixes were compared and the results are discussed in a later section.

3.5. Test Specimens

Two new connection details were to be explored in this research. The connection details were tested through six specimens. The test matrix for the specimen testing is shown in Table 10.

Table 10: Test matrix for sub-assemblage tests.

Connection	Type	Topping	Connection Material	Refer
Partial Depth Keyway	Current Detail	No	Grout	Section 3.5.1
	Kevlar and Epoxy	No	Grout	Section 3.5.2
Partial Depth Keyway with Splices	Splice Bar	No	UHPC	Section 3.5.3
	Splice Bar	Yes	UHPC	Section 3.5.3
	Splice Bar	No	VHPC	Section 3.5.4
	Splice Bar	Yes	VHPC	Section 3.5.4

The details of the test specimens are now discussed.

3.5.1. Existing connection detail

The existing connection detail of partial depth keyway with grout was tested with the SA specimens. This specimen was tested in order to ensure that the behavior observed in the diagnostic bridge tests could be replicated using SA specimens. The specimen with existing connection detail is shown in Figure 75.
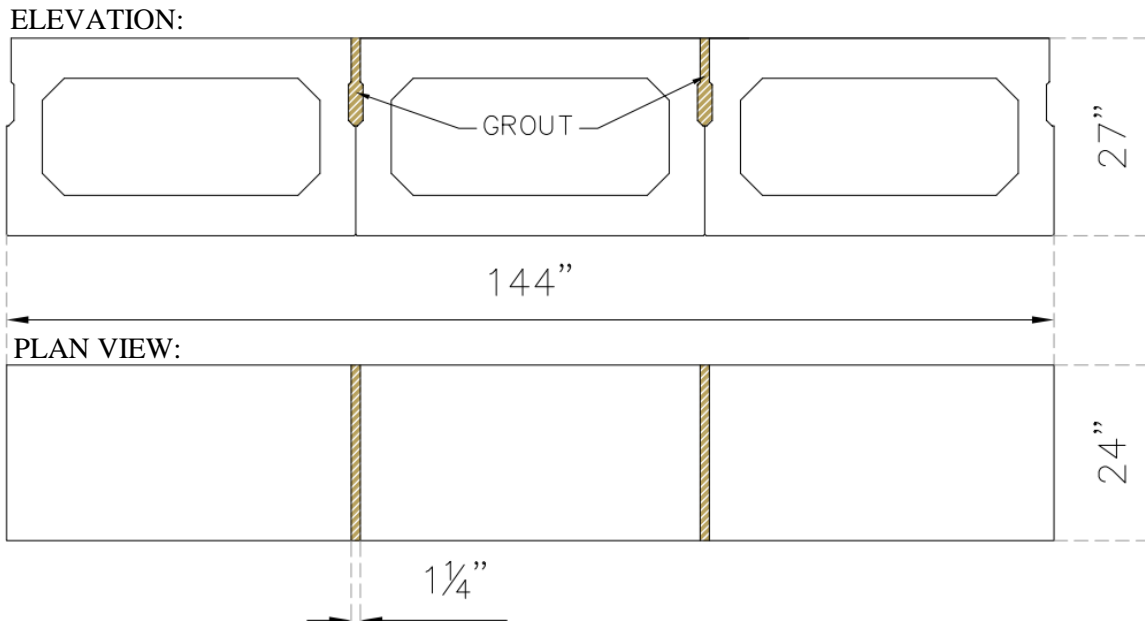
Figure 75: SA specimen with current partial depth grouted keyway.

3.5.2. Existing connection detail with Kevlar and Epoxy

The performance of the K&E was tested using the specimen shown in Figure 76. The focus of this test was to study if the K&E was able to prevent cracking, provide waterproofing and transfer loads across a cracked joint.
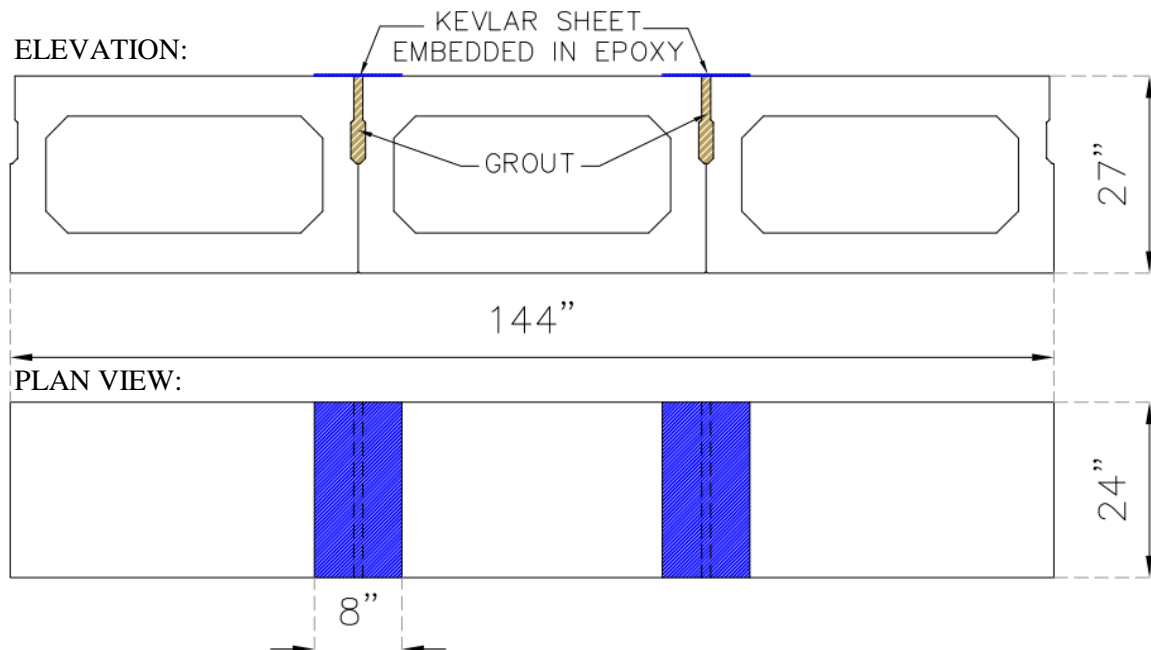
Figure 76: SA specimen with existing connection detail reinforced with Kevlar and Epoxy.

3.5.3. Spliced detail without topping

The spliced connection detail was tested on SA specimen shown in Figure 77. The connection was tested with UHPC and VHPC. An enhanced performance was expected as the splice provided the capacity for the connection to transfer shear as well as moments across the joints.
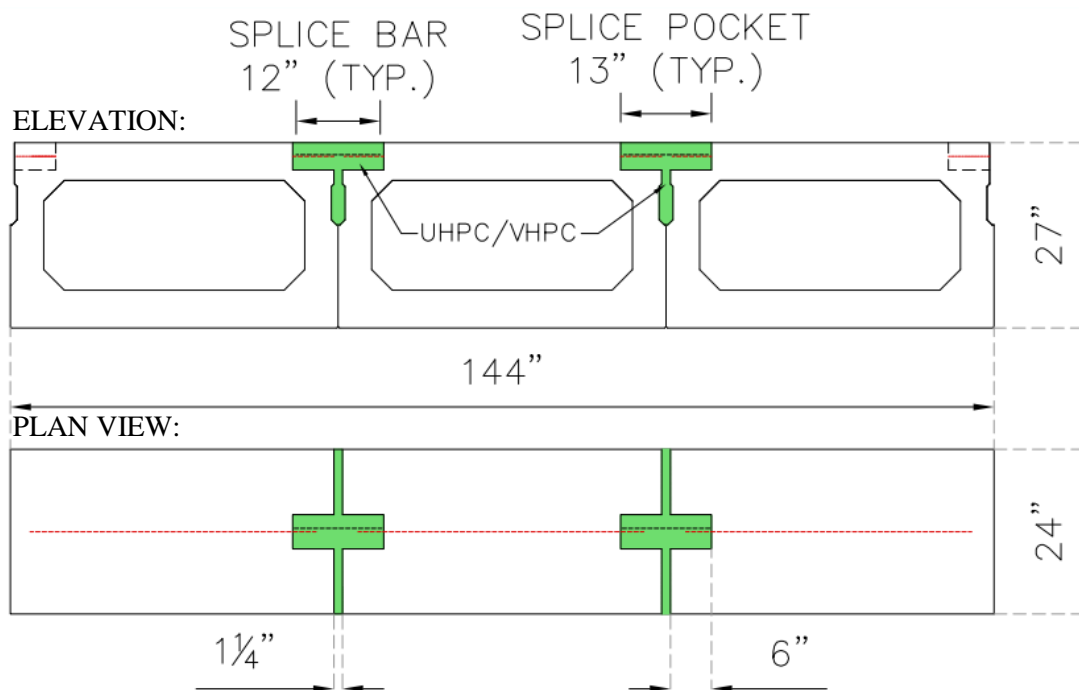
Figure 77: SA specimen with proposed spliced connection detail without topping.

3.5.4. Spliced detail with concrete topping

The spliced connection detail also was tested with a SA specimen that included a concrete topping as shown in Figure 78. The topping was 5 in. deep, which corresponded with ADTT between 100 and 200 as per VDOT specification. Steel reinforcement was extended from the beam sections into the topping for composite action. However, it was decided to study the behavior of bridge specimens in which composite action was not developed. Hence, these bars were cut with oxyacetylene torch and removed. The top surface of the beam sections was roughened, therefore partial composite action still occurred in the specimens.
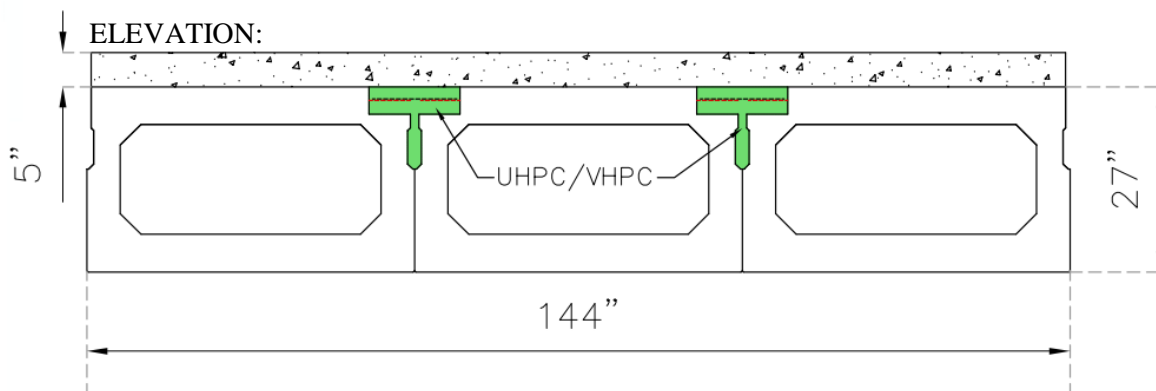
Figure 78: SA specimen with proposed spliced connection detail with topping.

3.6. Fabrication of test specimens

The procedure for fabricating the individual beam sections as well as the joints in the specimens is now described.

3.6.1. Fabrication of beam sections

The beam sections were fabricated by Ross Prestressed Concrete Inc. at their Bristol, TN plant. The plant was the closest to the laboratory and Ross Prestressed Concrete Inc. had a vast experience in fabricating box beam and voided slab beams for the DOTs in Virginia, North Carolina and Tennessee. The box beam sections were fabricated in three batches in a space of about ten days. Each batch of concrete produced two beam sections of three distinct beam types described above. The mix designs for the concrete used in fabrication of the beam sections are presented in Appendix C.

The AASHTO/PCI BI-48 sections were used in this research. This section size was selected since it was a typically used beam size in Virginia. The depth of the keyway in ABBB connections used in Virginia remains the same, regardless of the depth of the beam section. Hence, the section size was incidental to the research considering that the focus of the tests was on the joints and the connections.

The beam sections were designed to ensure the failure would occur at the joints. The amount of steel reinforcement used in the beam sections was much higher than that used at the midspan in typical ABBB beams. Prestressing strands were not used in these sections as they were deemed unnecessary for studying transverse behavior of the beam sections. The typical reinforcement details are shown in Figure 79 and Figure 80 for specimens without and with blockouts for splices respectively.
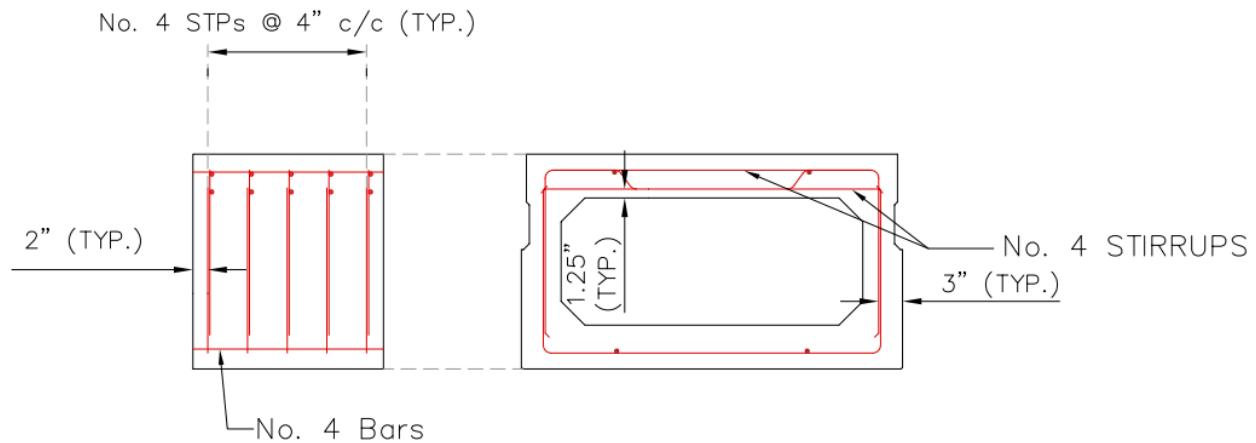
Figure 79: Typical reinforcement detail for specimens with unmodified cross-section.
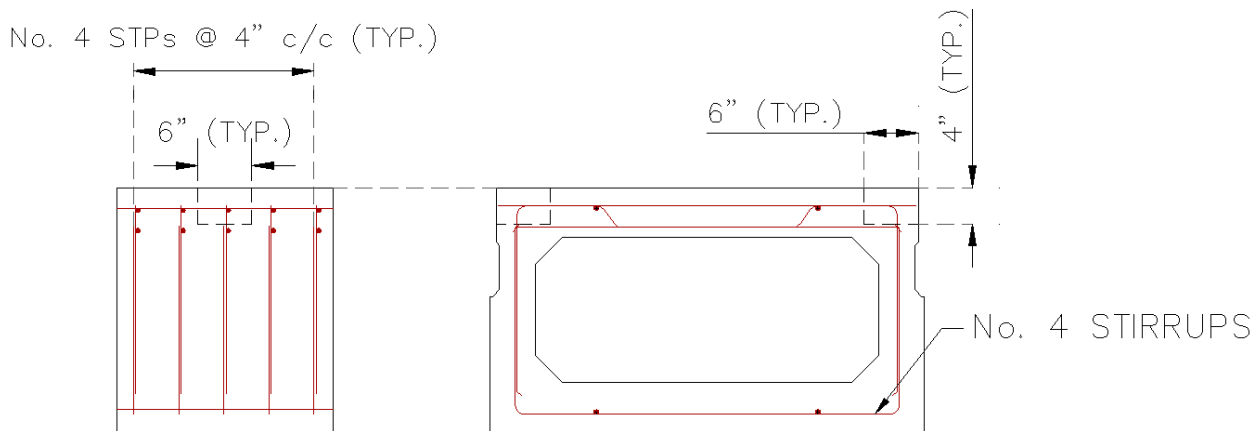
Figure 80: Typical reinforcement detail for specimens with modified cross-section.

Individual 2 ft sections of BI-48 beam sections were fabricated by the precaster, these forms were made of plywood stiffened with 2x4s at the top and the bottom of the forms. The interior void was made with Styrofoam, as prescribed by the VDOT specifications. Threaded rods were passed through the Styrofoam to secure the plywood forms. The steel reinforcement was prevented from moving by securing it to the side of the form or the Styrofoam void with steel chairs. An individual form for a beam section is shown in Figure 81.

Figure 81: Reusable forms individual beam sections.

These forms were placed on the precasting bed and the opens sides were enclosed by steel forms. These steel forms were the same ones that were used by the precaster in construction of box beams for bridges. The gaps in the formwork were sealed with foam. The formwork placement inside the steel forms is shown in Figure 82 and Figure 83 respectively.

Figure 82: Individual beam section forms fitted inside the main formwork.

Figure 83: Box beam sections inside AASHTO/PCI BI-48 forms.

The forms were further secured from movement by inserting threaded rods in the formwork using a frame connected to the external steel forms. The threaded rods provided support to the plywood sides of the forms as well as the Styrofoam voids. The block-outs for the spliced connection bars were also fabricated from Styrofoam. The Styrofoam pieces were covered with duct tape to prevent water from soaking into the block-out. The block-out consisted of two parts that were constructed to fit over the splice bar. A typical blockout is shown in Figure 84 and the block-out connected to splice bar inside the form is shown in Figure 85.

Figure 84: Covered Styrofoam blockout.

Figure 85: Blockout attached to splice bar.

The concrete was placed into the form using a skip suspended from a crane. The concrete placed in the forms was placed from the top. The consolidation was provided by two means. External vibrator was used to consolidate concrete in the bottom of the formwork. An internal needle vibrator was used to consolidate concrete in the webs and the top flange of the specimen sections. The specimen tops were smoothened for specimens without topping and roughened for specimens with composite topping.

Figure 86: Placing concrete from a bucket.

The properties of the fresh concrete were assessed at the site before placement. The concrete workability was checked using the slump cone test and the air entrainment. The properties and the proportions of the fresh concrete are provided in Appendix D. The fresh concrete was steam cured for 24 hours and the forms were released after the compressive strength of the concrete became 3500 psi. Steam curing was not essential for the specimens. Steam curing was applied to the specimen sections to expedite the strength gain and consequently the specimen section fabrication. The sections for the six specimens were constructed in three separate batches. Twenty four 4 in. x 8 in. cylinders were cast for each batch. All specimen sections were delivered to Thomas M. Murray structures and materials laboratory at the same time.

3.6.2. Construction of specimen joints

The specimen joints were constructed at the laboratory prior to starting the testing program. The specimens were to be prepared and the joints were constructed a week prior to the planned start of the testing. The preparation of the specimen included sand-blasting the shear keys to enhance the bond between specimen sections and the keyway. The sand blasting was done using a portable sand blaster. Typically, the sand blasting was done less than 24 hours prior to the joint placement. This was done to avoid concrete

88

carbonation from reducing the bond strength. Prior to the placement of the joint material the keyway was saturated with water. This was done to avoid the beam concrete from absorbing the water from the connection material mix.

The joints were constructed after placing the individual sections on the test setup. The specimen sections were placed in a sequential manner. The placement of the middle section was the most important as the position of the rest of the sections was dependent on the middle section. The middle section was carefully centered under the actuator and the loading beam. The middle section was placed over screw jacks and raised to the required height. The exterior sections were then placed on the steel support beams. The reactions recorded by the load cells were monitored to ensure a uniform load distribution between the interior and exterior support beams.

Strips of neoprene were used to seal the joints from leakage. The neoprene strips were glued to the specimen sides using silicone. Silicone could have been used by itself to seal the joints. However, the silicone is a very good water proof material and leaving it in the joint would prevent the water from leaking during ponding tests. Therefore, the neoprene strips were used. These strips were made longer than the specimen thickness so as to pull them out after the joint had cured.

The joint sides were formed with plywood sheets. A pair of plywood sheets was used to seal the specimen sides. Threaded rods were passed through both the sheets and tightened so that the forms would remain stable during placement. Silicone was used around the joint sides to prevent leakage of material from the form sides. The connection filler material was placed from the gap at the top of the joint.

Figure 87: Formwork for joint fabrication.

3.6.2.1. Grouted connections

The grout material was selected on the basis of VDOT Bridge Specifications. VDOT required the use of a grout that would meet ASTN C1107 requirements. VDOT did not specify the brand of the grout to be used in the testing. Therefore, Quikrete Non Shrink Precision Grout was selected to be used for the grouted specimens. The grout was available as packaged premix that was to be mixed with water. The quantity of water was determined on the basis of workability. A trial batch of the premix was made to assess the properties of the material prior to using it in the specimens. The trial batch confirmed that the grout product met the ASTM C1107 standards. The grout was mixed with water using a pan mixer with a rotating drum. The grout was mixed until the required consistency and flowability was achieved. The fresh grout was placed in the joints using hand held buckets. The grout was poured directly into the exposed keyway and leveled with the joint. The grout was also placed in 2 in. x 2in. cube molds for compressive strength, 4 in. x 8 in. cylinders for modulus of elasticity and 1 in. x 1in. x 12 in. bars for measuring shrinkage.

3.6.2.2. Kevlar and Epoxy connection

The joints in the specimen with K&E connection were placed using the procedure described above. The K&E connection was attached to the joint two days prior to start of the testing. The epoxy had a curing time of 10 hours and the test could have been started after that. The surface above the joint had to be prepared prior to the application of K&E connection. The surface was ground with a concrete grinder until aggregates were visible. The ground surface is shown in Figure 88.

Figure 88: Surface preparation for K&E connection.

Ideally, sand blasting or shot blasting is recommended for the K&E connection. However, the specimen was within the test setup in the lab and these operations could not be performed. Instead the grinder was used. The area was cleared of any dust and particles with compressed air.

The epoxy consisted of two parts. These were the epoxy resin and the hardener. The two parts had to be mixed in equal proportions with a mixing tool able to impart 600 rpm. The procedure for attaching the K&E sheet to the specimen is shown in Figure 89 and was as follows,

1. The resin and the hardener were proportioned in equal amounts and mixed as per instructions.
2. The epoxy was poured and spread evenly over the joint.
3. Kevlar sheet was placed on the epoxy and was gently pressed into the epoxy until the fibers were completely covered with the epoxy.
4. Aggregates were broadcast over the surface and the epoxy was allowed to cure for half hour.
5. Another layer of the mixed epoxy was poured over the previous layer and spread out evenly.
6. Another layer of aggregate was broadcast over the surface.

(a)

(b)

(c)

(d)

Figure 89: Procedure for attaching the K&E sheet to the specimen.

3.6.2.3.   UHPC connections

The procedure for the formwork described above was followed for the top flange spliced connections. The keyways as well as the splice block-outs were sand blasted and sprayed with water. The splice bar was tied to the reinforcing bar in the pocket with a single tie on each side. The UHPC was then mixed and placed. The procedure for mixing UHPC was as follows,

1. The premix was placed in the pan mixer and dry mixed for two minutes or until the hardened lumps broke down.
2. The superplasticizer was mixed in with the water and poured into the premix.
3. The premix and the fluid combination was allowed to mix for $20 - 30$ minutes. During this stage the dry premix starts clumping into small balls of partially hydrated paste. On mixing further and with the material hydrating the UHPC paste is formed. This paste is self-consolidating.
4. Finally, the fibers were added and the mixture allowed to mix for another $2 - 3$ minutes.
5. The flowability of the mix was measured using the flow test.

The UHPC mix was placed from the top of the joint and allowed to flow till the joint was completely filled up. The UHPC also was used to form cubes for compression strength tests, cylinders for modulus of elasticity and split tensile cylinder strength 1in. x in. x 12 in. shrinkage bars. The joints and the material test specimens were covered with plastic sheets. The forms were released after three days. The UHPC was allowed to air cure as per expected in the field conditions.

3.6.2.4.   VHPC connections

The procedures for preparation of the UHPC specimens were repeated for specimens with VHPC connections. Only the mixing procedure was different, it was as follows,

1. The coarse and fine aggregates were placed in the pan mixer drum and an arbitrary amount of water from the batched quantity was added to the drum. The dry contents and water were allowed to mix till the aggregates appeared to be wet.
2. The cement was added to the drum followed by another arbitrary quantity of water and mixed for $3 - 4$ minutes.
3. The silica fume and fly ash were added and the remaining quantity of water was added and mixed for $5 - 6$ minutes or until the material appeared to be sticking to the drum.
4. The mixing was stopped and the dry and unhydrated or unmixed material was extracted from the pan sides and mixed with the partially hydrated material.

5. The superplasticizer was added in measured doses. The initially assumed value was added and the mix was observed. If needed, additional quantities of superplasticizer in form of 10% of the total required superplasticizer were added to the mix until the desired flowability was achieved.

3.7. Sub-assemblage Testing

The experiments performed in the laboratory consisted of the splice length testing performed to ascertain the minimum length of splice required for one of the proposed connection details. And the proposed connection details were tested for fatigue and strength using aforementioned sub-assemblages.

3.7.1. Durability and strength of proposed connection details

The laboratory component of sub-assemblage tests consisted of a series of static and cyclic loads. The testing program is now explained.

3.7.1.1. Test Concept

The purpose of the cyclic loads was to impart fatigue into the joints. A total of 1 million cycles were planned to be applied to the specimen unless the joint failed prior to completion. The testing program involved the application of predetermined total displacements of 0.03 in. Then the specimen was displaced for the half of the static displacement and then repeated displacements of +/- 0.015 in. were applied to induce fatigue in the joints. The magnitude of displacement to be applied to the sub-assemblage specimens was determined by FEA models of the sub-assemblages as explained earlier. The frequency of displacement application was 2 Hz for the fatigue tests.

The purpose of the static tests was to observe the performance of the specimens over the duration of induction of fatigue in the specimens. The initial static tests measured the baseline reference behavior of the specimens. Static tests performed later in the duration of the test would indicate any change in performance. The main focus of the static tests was to observe any degradation of stiffness that would occur with any fatigue in the joints. The static tests determined the overall behavior of the specimen sub-assemblages and the change in it over a period of predetermined number of cycles. The static tests were performed with a logarithmic frequency i.e. static tests were performed after 10, 100, 1000, 10000, 100000 until one million cycles, with additional static tests after every 100000 cycles after the first 100000 cycles until a million. Finally, the specimens were to be loaded statically until failure to measure the strength of the specimens. The schedule for load application is shown in Table 11. Note that the test designations in Table 11 are also used in the sub-assemblage test results presented in Chapter 6.

Table 11: Schedule of displacement application for sub-assemblage tests.

Test Name	Type	Load Application	Test Purpose
Baseline	Static	Monotonic Ramp	Reference response for all tests
Baseline 2/3	Static	Monotonic Ramp	New reference after clamp beam adjustments
10 Cycles	Cyclic	Sine Wave	Connection fatigue
After 10 Cycles	Static	Monotonic Ramp	Condition assessment after fatigue cycles
100 Cycles	Cyclic	Sine Wave	Connection fatigue
After 100 Cycles	Static	Monotonic Ramp	Condition assessment after fatigue cycles
1000 Cycles	Cyclic	Sine Wave	Connection fatigue
After 1000 Cycles	Static	Monotonic Ramp	Condition assessment after fatigue cycles
10000 Cycles	Cyclic	Sine Wave	Connection fatigue
After 10000 Cycles	Static	Monotonic Ramp	Condition assessment after fatigue cycles
100k Cycles	Cyclic	Sine Wave	Connection fatigue
After 100k Cycles	Static	Monotonic Ramp	Condition assessment after fatigue cycles
200k Cycles	Cyclic	Sine Wave	Connection fatigue
After 200k Cycles	Static	Monotonic Ramp	Condition assessment after fatigue cycles
300k Cycles	Cyclic	Sine Wave	Connection fatigue
After 300k Cycles	Static	Monotonic Ramp	Condition assessment after fatigue cycles
400k Cycles	Cyclic	Sine Wave	Connection fatigue
After 400k Cycles	Static	Monotonic Ramp	Condition assessment after fatigue cycles
500k Cycles	Cyclic	Sine Wave	Connection fatigue
After 500k Cycles	Static	Monotonic Ramp	Condition assessment after fatigue cycles
600k Cycles	Cyclic	Sine Wave	Connection fatigue
After 600k Cycles	Static	Monotonic Ramp	Condition assessment after fatigue cycles
700k Cycles	Cyclic	Sine Wave	Connection fatigue
After 700k Cycles	Static	Monotonic Ramp	Condition assessment after fatigue cycles
800k Cycles	Cyclic	Sine Wave	Connection fatigue
After 800k Cycles	Static	Monotonic Ramp	Condition assessment after fatigue cycles
900k Cycles	Cyclic	Sine Wave	Connection fatigue
After 900k Cycles	Static	Monotonic Ramp	Condition assessment after fatigue cycles
1 Million Cycles	Cyclic	Sine Wave	Connection fatigue
After 1 Million Cycles	Static	Monotonic Ramp	Condition assessment after fatigue cycles
Final Static Test	Static	Monotonic Ramp	Specimen failure

The displacement application for the static and cyclic tests is explained in Figure 90.
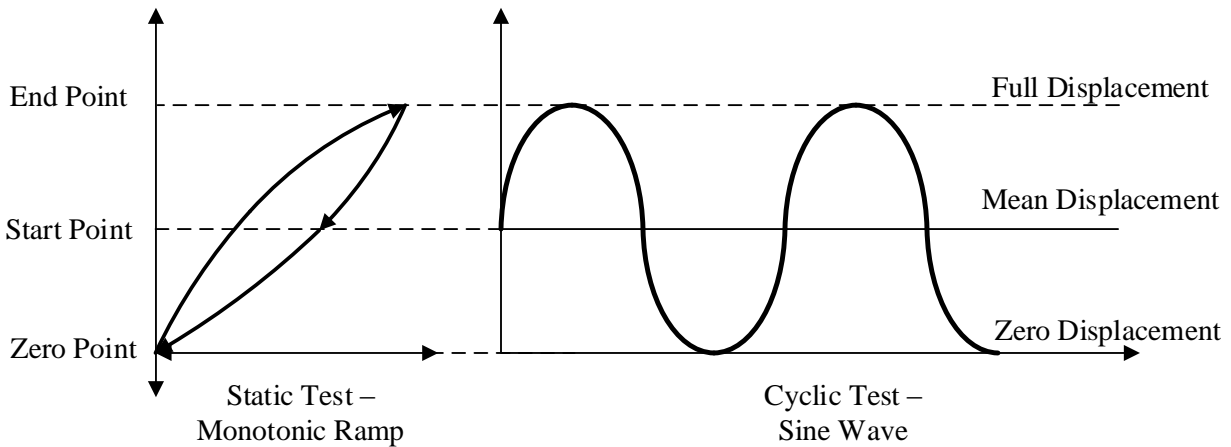
Figure 90: Scheme for displacement application to sub-assemblage specimens.

The nomenclature used in   Figure 90 is as follows,

a. Zero Point: Theoretically the point at which the stress in joint due to actuator was zero. The baseline static tests started from the zero point.

b. Start Point: The point from which all static and cyclic tests started with the exception of the baseline static tests. The magnitude of displacement at the start point was equal to half of the total target displacement.

c. End Point: The point at which the state of stress in the sub-assemblage joint was equivalent to that in the full scale bridge due to HS-20 tire patch. The displacement at the end point was equal to the target displacement of 0.03 in.

The procedure in which the tests were performed was as follows,

a. Attach specimen to the actuator using clamping beams. Release temporary supports under middle section.

b. Perform first baseline test - displace actuator until the target displacement was achieved. Note that the actuator displacement was slightly larger than the displacement imparted to the specimens. The actuator displacement consisted of the displacement applied to specimen plus the flexibility of the frame supporting the actuator. Hence, the specimens were displaced until the target displacement was achieved. The target displacement corresponded with the "end point" of   Figure 90.

c. Unload specimen and return it to "zero point".

d. Displace specimen to the "start point" or till half of the target displacement was achieved.

e. Begin application of planned number of displacement cycles as per Table 11.

f. Perform a static test after applying planned number of cycles. The specimen returned to the "start point" after the cyclic displacements. The specimen would then be displaced to the "zero point", then to the "end point" and finally returned to the "start point". The cycling regimen was continued.

g. Observe specimen for out-of-plane movements and for any other source of flexibility.

h. Adjust clamp beam tightness if needed. Unload specimen and displace it to zero point. Perform another baseline static test and return specimen to "start point".

i. Continue specimen test until failure or until the application of 1 million cycles.

j. Perform final static test – displace the specimen until failure.

3.7.1.2. Test instrumentation

The sub-assemblage specimens were instrumented extensively to measure different performance parameters of the joints and the specimens. The instrumentation was primarily focused on measuring strains and displacements in the specimens. The strains and stresses in the joint could not be directly measured. Therefore, the instrumentation was applied such that the state of stress in the joint could be gleaned indirectly from the response of the instruments. The instrumentation used in the testing was as follows.

3.7.1.2.1. Actuator

MTS actuator was used to apply the loads and displacements to the specimen. The actuator had a 10 in. total stroke and 55 kip capacity. The actuator was equipped with an internal LVDT and load cell to measure the respective responses.

3.7.1.2.2. Gap displacements

The relative displacements were measured between adjacent beam sections using LVDTs. A pair of LVDTs were used. One was placed about 1 in. below the joint and the other was attached 1 in. above the bottom of the beam. The pair of LVDTs were the closest indicators of joint behavior. The increment in LVDT values indicated occurrence of cracks and corresponding propagation. The location of these LVDTs is shown in Figure 91.

3.7.1.2.3. Vertical displacements

The vertical displacements were measured to observe the actual displacements being imposed on the specimen sections. Wire potentiometers (WPs) and LVDTs were used for this purpose. The WPs were used on the first two specimens and the LVDTs were used for the rest of the specimens. Two of these sensors were used under each exterior beams section. These were attached 1 in. from the tip of the flanges

of the steel support beams. The locations of these sensors is shown in Figure 91. In the first test specimen, an additional WP was attached in the middle of the specimen, under the middle beam section. This was replaced in remaining specimens with a pair of LVDTs and attached to the loading beam in order to measure the displacements applied to the specimens and to ensure that the displacement was applied evenly. These pair of sensors also ensured that the specimen did not twist during loading. The location of the sensor pair is shown in Figure 92.

3.7.1.2.4. Surface strains

The surface strains were measured with BDI strain transducers. The strain transducers were used to measure strains in the specimen sections. These strains were observed to see any change in behavior before and after cracking at the joints or in the beam sections. The locations of these strain transducers are shown in Figure 91.

3.7.1.2.5. Load distribution

The load distribution was measured prior to and after the commencement of the loading program. Prior to testing, the sensors were used to ensure an equal load distribution between the two support beams. After starting testing, the load distribution was monitored to observe the change in response brought about by deterioration in the joints. The load distribution between adjacent specimen sections was measured by load cells placed on steel beams. Four load cells were used per exterior section for the first specimen. However, it was very difficult to balance the self-weight of the individual specimen sections equally on the four load cells. Therefore, three load cells were used to make the load balancing easier. The load cell locations are shown in Figure 91. Additionally, strain gauges were bonded to the steel beams to measure load distribution in case any load cell did not work. Location of the bonded strain gauges are shown in Figure 92.
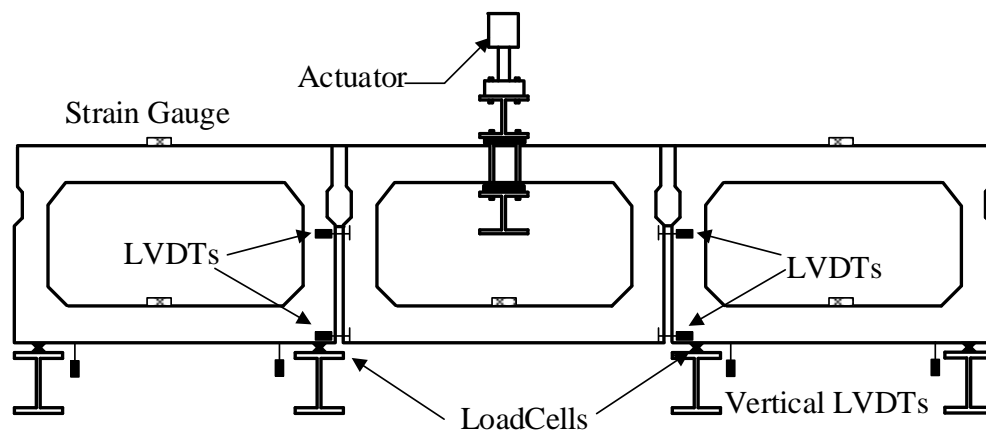
Figure 91: Setup for sub-assemblage tests – front view.
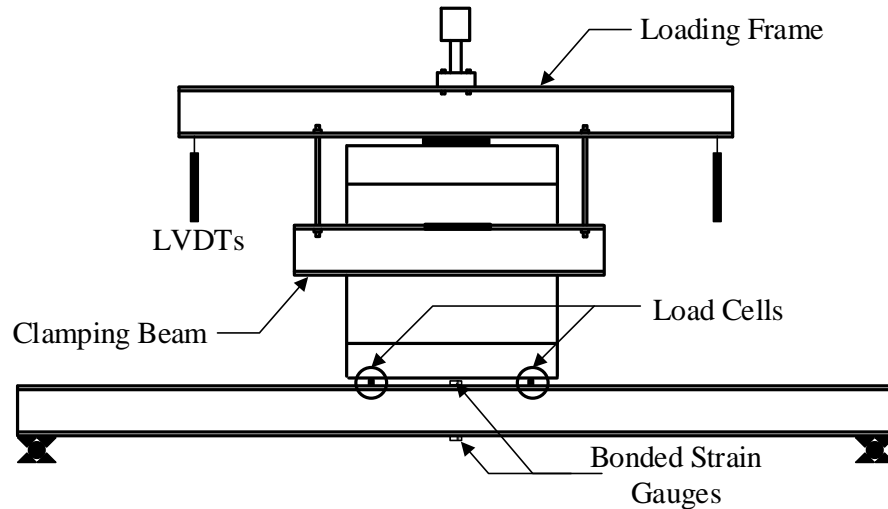
Figure 92: Setup for sub-assemblage tests – side view.

3.7.1.3. Data record for sub-assemblage tests

The data record varied between the static and cyclic tests. For the static tests all the instruments were used to measure responses and all the data was recorded for the full duration of the tests. The data was recorded at 10 Hz for the static tests. On the other hand, several instruments were disconnected for the fatigue tests. Instruments such as LVDTs, externally mounted concrete strain gauges were disconnected for the fatigue tests as these instruments were not meant to be subjected to so many loading and unloading cycles. However, Load cells, bonded strain gauges on steel beams and the load cell and the LVDT on the actuator could not be disconnected and hence were monitored periodically (5 seconds every 5 minutes at 50 Hz.) till end of the fatigue tests.

3.7.2. Determining the length of splice with UHPC/VHPC

Beam splices were tested in order to ascertain the minimum tension splice length required to develop the connection that is to transfer tensile stresses across the joints in adjacent box beam bridges. The purpose of these tests was to simulate a connection detail between adjacent box beams subjected to tensile stresses. The focus of these tests was to establish the lower bound of splice length that would be sufficient to transfer forces across the longitudinal joints in adjacent box beam bridges in the transverse direction.

3.7.2.1. Test Concept

The testing program was devised such that a tensile stress gradient could be induced in the region of the splice. A tensile gradient was envisioned on the basis of transfer of forces that would occur between adjacent box beams connected rigidly at the top flange. The basic assumption for this connection detail was that UHPC and VHPC spliced connections would be established at the top flanges of the beams. Figure 93 shows a typical cross-section of an adjacent box beam bridge connected at the top flanges with truck wheel

98

loads. The deflected shape of that bridge cross-section which shows the location of tensile stresses is shown in *Figure 94*. Similarly, the location of tensile stresses in the spliced connection when used with a composite topping is shown in Figure 95.
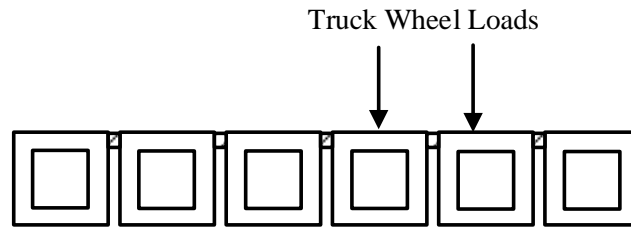
Figure 93: Cross-section of a typical adjacent box beam bridge with top flange connections.
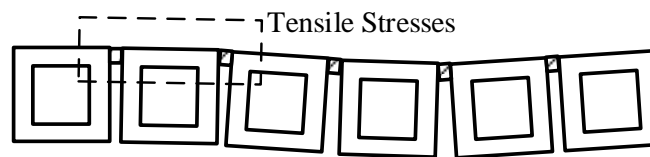
Figure 94: Deflected shape of the typical cross-section.
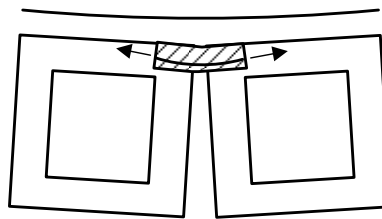
Figure 95: Tensile stresses at the bottom of the connection in an ABBB with composite topping.

The connection detail subjected to a tensile gradient would be critical in determining the minimum length of splice required to form the connection. This critical connection detail was isolated and incorporated into a simply supported beam to be subjected to a tensile gradient. The specimen was not an exact representation of the proposed joints in the bridge since the size of the pocket in the proposed connection details was not the same as that in the splice test specimens. However, the splice test specimens were consistent in terms of the required splice lengths and the area of influence of stresses induced by the splice bars in UHPC. The test was devised to be a simply supported beam with a pocket in the midspan where the splice was cast. The details of the specimen are discussed in greater detail in the following sections.

3.7.2.2. Specimen Details

The specimens were 8.5 ft long simply supported reinforced concrete beams with a block-out pocket at midspan. The tension reinforcing bars were not continuous at the midspan, and a bar was placed across

the discontinuity to form the splice connection. The cross-sectional size of the pocket was kept consistent between specimens. The length of the pocket was varied according to the splice length under consideration. The main tension reinforcement was either two No. 4 bars or No. 6 bars depending on the specimen. These bar sizes were considered for forming the connections between adjacent beams in bridges based on results of experimental testing reported by Perry and Weiss (2009). In the first four specimens tested, the area of steel in compression was the same as that in tension. This was, however, revised in later tests after observing the test results from initial specimens and is discussed in greater detail in the analysis of results. The typical details of the test specimens are summarized in Table 12. The typical details of the initial test specimens with UHPC are shown in Figure 96 and the typical details of the modified (greater area of compression reinforcement) test specimens with UHPC are shown in Figure 97. Figure 98 presents the details of the specimens with VHPC.

Table 12: Splice length specimens test matrix.

Specimen Designation	Tension Steel	Splice Length, in	Pocket Length, in	Pocket Filler	Compression Steel	Concrete Strength, ksi
U-4-5-I-E	2 No. 4s	5	11	UHPC	2 No. 4s	8
U-4-6-I-E		6	13			8
U-4-3-I		3	7		2 No. 7s and 1 No. 6	5
U-4-4-I		4	9			5
U-4-5-II		5	11			5
V-4-5-I		5	11	VHPC	2 No. 8s	5
V-4-6-I		6	13		2 No. 8s	5
V-4-5-II		5	15		2 No. 8s	5
V-4-3-I		3	17		2 No. 8s	5
V-4-4-I		4	21		2 No. 8s	5
V-4-4-II		4	9		2 No. 8s	5
U-6-5-I-E	2 No. 6s	5	11	UHPC	2 No. 6s	8
U-6-6-I-E		6	13			8
U-6-7-I		7	15		2 No. 8s and 1 No. 7	5
U-6-8-I		8	17			5

The specimen nomenclature was as follows,

U/V-BR-SL-No-DS

Where,

        U/V = Material used in pocket. U = UHPC, V = VHPC

        BR = Tension reinforcing bar size, in

        SL = Length of splice, in

        No = Serial number for each specimen type on the basis of splice lengths

        DS = Specimen design. E = equal area of steel in tension and compression

L (VARIES)

12" (TYP.)

5" (TYP.)

102" (TYP.)

ELEVATION W/O POCKET

3" (MIN.)

#3 BAR (TYP.) LIFTING HOOK

½" (TYP.)

2 − #4/#6 BARS (TYP.)

2 − #3 BARS (TYP.)

#3 − 2L STPs at 6.5" c/c (TYP.)

2 − #4/#6 BARS (TYP.)

#3 − 2L STPs at 3" c/c (TYP.)

SECTIONAL ELEVATION W/O POCKET

12" (TYP.)

5" (TYP.)

¾" FOAM (TYP.)

102" (TYP.)

ELEVATION WITH UHPC POCKET POCKET

A B C D

A B C D

SECTIONAL ELEVATION WITH UHPC POCKET POCKET

TENSION REINFORCING (TYP.)

10"

12" (TYP.)

COVER 2" (TYP.)

SIDE COVER 2½" (TYP.)

COMPRESSION REINFORCING(TYP.)

DETAIL A−A

4" (TYP.)

4" (TYP.)

DETAIL B−B

5"

7"

DETAIL C−C

SPLICE BARS (TYP.)

5"

7"

8"

DETAIL D−D

Figure 96: Typical details of initial UHPC test specimens.

UHPC SPLICE TEST SPECIMEN:

ELEVATION W/O POCKET

SECTIONAL ELEVATION W/O POCKET

ELEVATION WITH UHPC POCKET POCKET

SECTIONAL ELEVATION WITH UHPC POCKET

DETAIL A—A

DETAIL B—B

DETAIL C—C

DETAIL D—D

VIRGINIA TECH

SIMPLY SUPPORTED BEAM SPECIMENS — MODIFIED COMPRESSION REINFORCEMENT

UHPC SPLICE TESTS

SPECIMENS WITH 6" SPLICE	DRAWING NO.	DATE
	UTC–2	2/18/2013
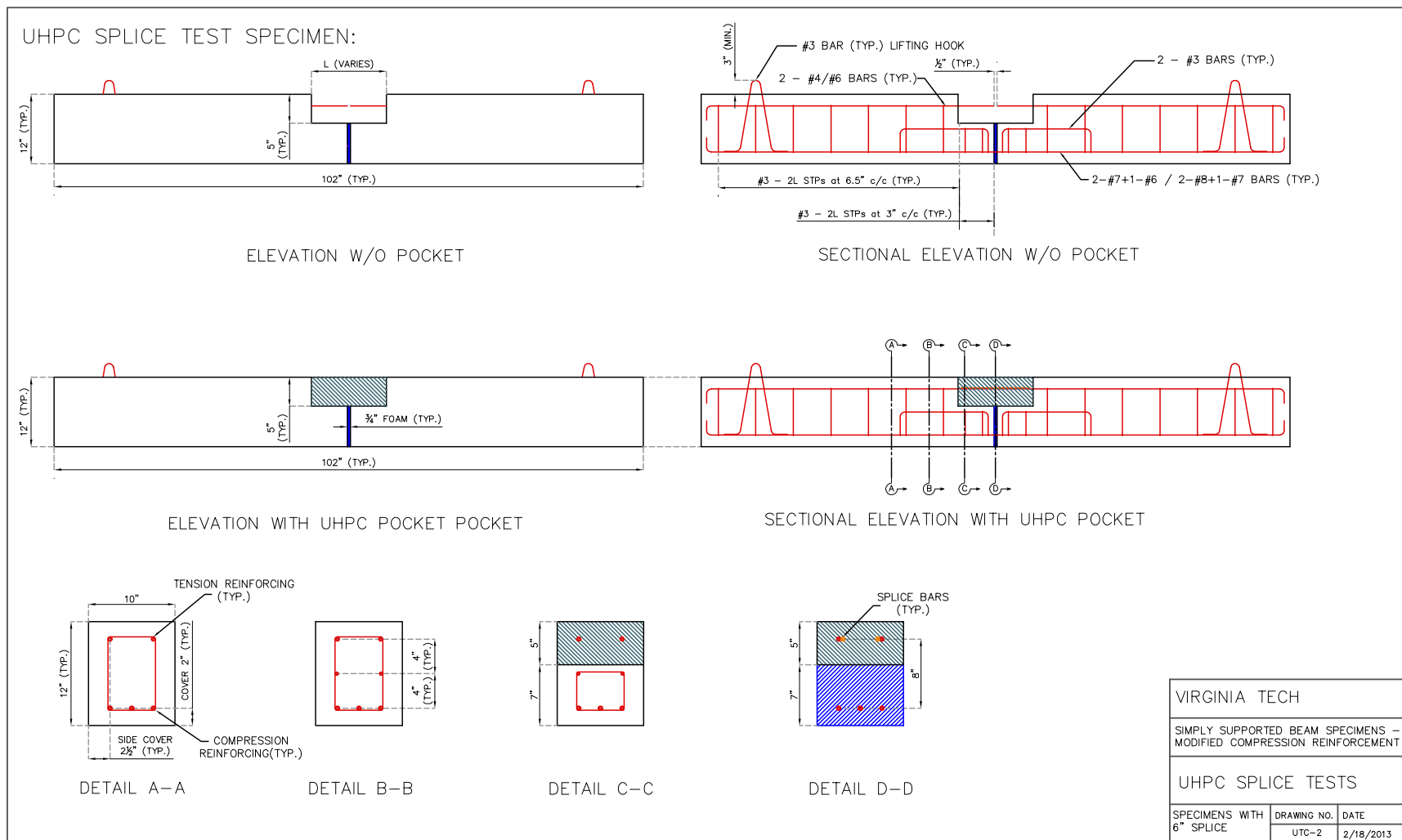
Figure 97: Typical details of modified UHPC test specimens.
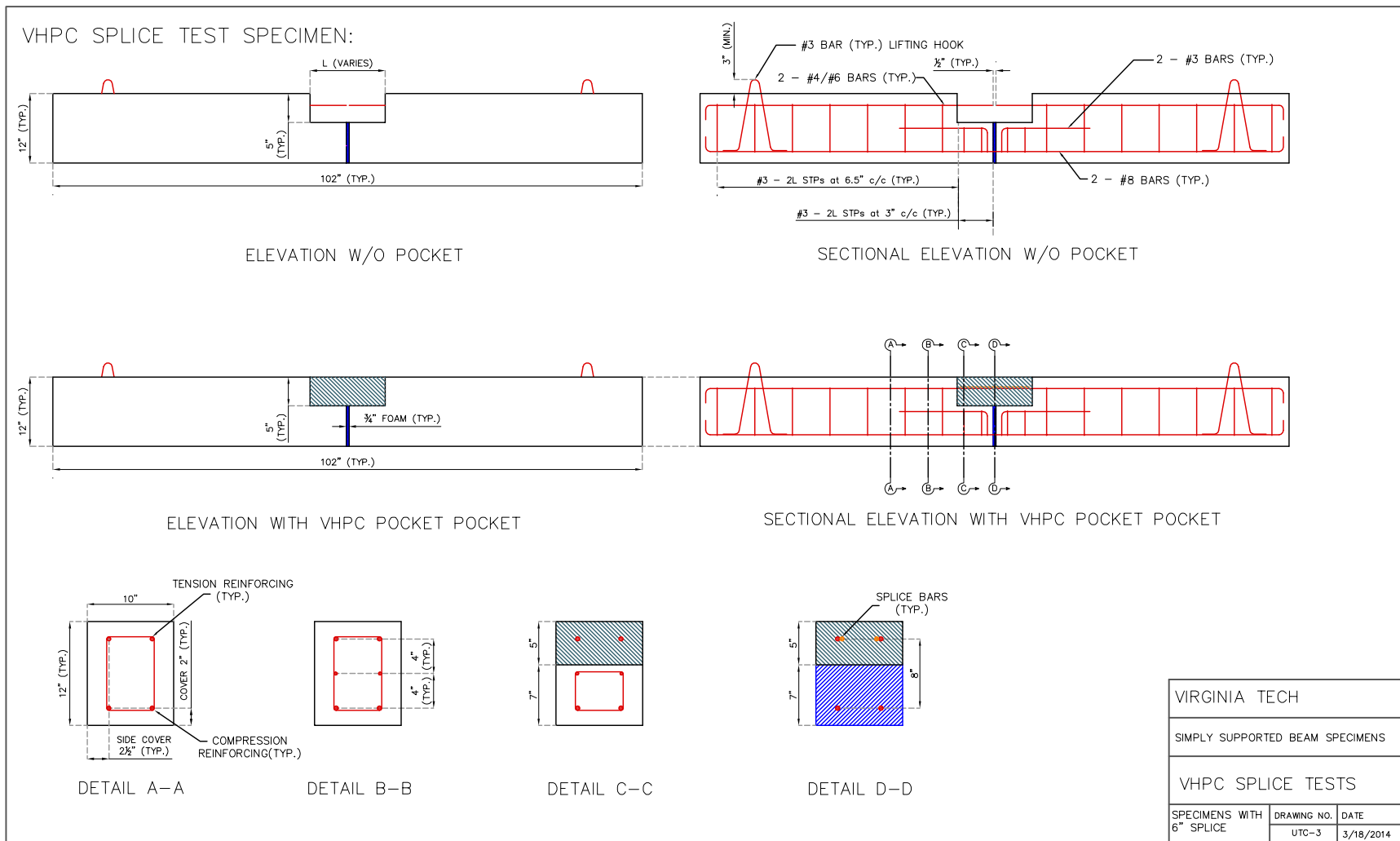
Figure 98: Typical details of VHPC test specimens.

Critical information sought from this testing was the stress and strain in the spliced reinforcing bars. To determine if a splice length was adequate to develop the yield strength of the bar, the stress in the bar must be known. Typically stresses are measured indirectly by measuring the strains and then calculating the stresses. Unfortunately, this measurement could not be made directly with a bonded electrical resistance strain gage on the tension steel, because the water proofing required to protect the gage from the concrete destroys the bond between the bar and the concrete. With the splice lengths being very short, any length of reinforcement lost to strain gauge waterproofing was undesirable. Therefore, another method was used to determine the forces in the spliced bars during the tests.

At the midspan of the beam, beneath the splice pocket, a ¾ in. thick foam pad was placed vertically to separate the left and right sides of the precast element. In this way, the bottom layer of reinforcement alone carried the compression at this location. This was expected to simplify the calculation of the stress in the tension reinforcement, by eliminating the uncertainty in determining the moment arm between the tension and compression forces in the beam. Therefore, there was no need to assume a stress block and a location of the centroid of the compression block. Also, since the total tension must equal the total compression, after the pocket filler material had cracks with widths too wide to allow the fibers to carry tension, all tension must be in the reinforcing steel alone. The compression bars were strain gaged to allow the calculation of the compressive force. The gap in the concrete facilitated the calculation of tensile force which would indicate whether the reinforcing steel in tension yielded prior to the failure of the specimen. The mechanics of the specimen section at the area of interest are shown in Figure 5.
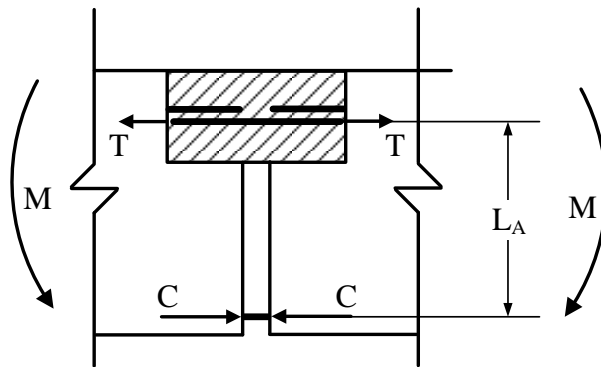
Figure 99: Beam mechanics – tension equals compression for equilibrium.

The section of the precast element under the UHPC or VHPC pocket was reinforced with longitudinal No. 3 bars and stirrups as shown in Figure 96, Figure 97 and Figure 98. These were included to ensure that no premature failure would occur in the precast section of the specimen.

3.7.2.3. Test Setup

The test setup is shown in Figure 100. The test simulated a simply supported beam with a splice in the region of maximum bending moment. The test setup was a four point bending setup which placed the splice pocket in the region of constant moment. The specimens were tested in an inverted configuration so that the cracking patterns in the UHPC/VHPC pocket could easily be observed. The specimens were loaded monotonically till failure.

The load applied through the actuator was measured by a single load cell (maximum capacity 50 kips). Vertical deflections were measured by three wire potentiometers connected to the beam ends and midspan of the beam. The interface between UHPC/VHPC and beam concrete was instrumented with LVDTs (on the east face) to observe the occurrence of cracks at the concrete – UHPC/VHPC interface. The reinforcement in the compression zone was instrumented with strain gauges. In the specimens which had two compression bars, both reinforcing bars were instrumented (see Figure 96 and Figure 98). In the specimens which had three compression bars, the two outermost reinforcing bars (see Figure 97) were instrumented. Additionally, locating discs for a portable extensometer, called as DEMEC (Demountable MEChanical) gauge were attached to the top of the UHPC/VHPC pocket and the west face of all specimens to measure surface deformations at different depths at midspan (top fiber, tensile reinforcement depth, mid-depth of beam and compressive reinforcement depth).
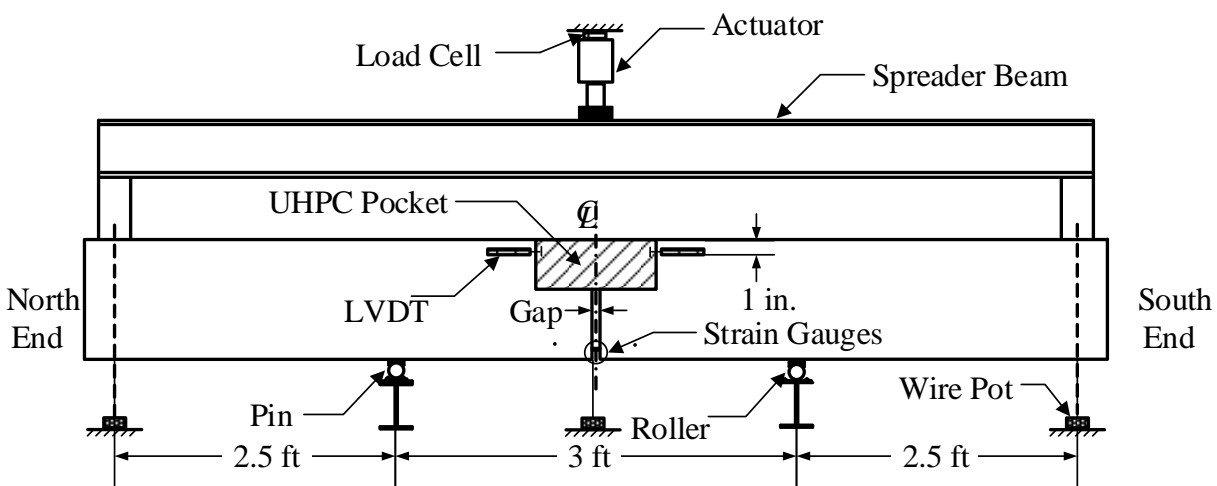
Figure 100: Setup for splice tests.

3.7.2.4. Test Procedure

The testing program consisted of loading each beam statically to failure in a four point loading setup. The spacing of the bolt patterns on the floor beams did not allow for a uniform distance between supports and loading points. Hence, the spacing between the supports was increased to 3 ft. The corresponding reduction in distance between the support and loading point caused the span to be at the threshold of the

deep beam definition per ACI (2008). ACI 318 defines a deep beam as one having a ratio of the clear span between a support and the nearest loading point to the depth of the beam less than 2.0. The ratio in the test beam was 2.5.

The loading on the beams was applied monotonically at pre-determined increments with pauses to mark cracks and make DEMEC measurements. Load increments of 1000 to 2000 lb were applied to specimens with No. 4 bars until the first crack in the UHPC/VHPC pocket was observed. The load application was then increased to 2500 to 3000 lb. Similarly, load increments of 2000 to 3000 lb were applied to specimens with No. 6 bars followed by increments of 5000 to 6000 lb after first UHPC crack was observed. The actual rate of loading during load application was difficult to control due to the nature of the manually operated electric hydraulic pump. Hence, the load application was accomplished in small steps. To ensure correct load application the responses from wire potentiometers, strain gauges on compression reinforcement and the DEMECs were monitored for the first three load application steps. If the corresponding increase in deflections at the ends and/or the increases in strains were found to be unequal then the beam was unloaded and the actuator was repositioned to ensure equal load application at both ends of the specimen and across the cross-section of the specimen.

The System 5000 data acquisition system (DAQ) was used to record data. The DAQ was programmed to read and record data at 10 Hz. Although the test itself was static it was important to record response of the specimen to instantly changing conditions such as the occurrence of cracks or tension reinforcement slip. The data recording was started after the specimen was positioned on the supports prior to the placement of the spreader beam. Hence, the test data does not directly include the effect of self-weight of the specimen on the test results. Similarly, the baseline reading for DEMEC readings was made after the beam was positioned on the supports. The effect of self-weight was found to be small in comparison to applied loads on the results of the splice tests.

3.8. Summary of Research Methods

This chapter provided the protocols and procedures for all the experimental and analytical work done in this research. The details of the different specimens and models were also provided. The purpose of this chapter was to provide a background information to all the analyses and experiments performed in this research. Many of the details in this chapter may be repeated in the following chapters. However, if any information is missing from the following chapters, it can be found in this chapter.

4.   Results of Diagnostic Tests

The results from the diagnostic tests of two bridges, Karr Valley Creek and Aden Road, and the FEA of one bridge are now discussed. This chapter is sub-divided into two parts, the diagnostic test results and the FEA results. Finally, the experimental and FEA results for the ARB are compared.

4.1.   Results from KVCB Diagnostic Test

All results pertaining to the transverse behavior of the KVCB are now discussed. The transverse bridge behavior was studied by plotting the maximum responses recorded by the instruments along the width of the bridge. Girder strains, girder deflections and relative vertical displacements between adjacent girders were studied.

4.1.1.   Transverse Girder Strain Distributions in KVCB

The transverse girder strain distributions were plotted at the 0.4L location on the bridge (shown in Figure 47). From the data recorded during the quasi-static truck runs, and the absolute maximum magnitude of strain, amongst all girders, induced by the trucks was noted for every pass. The data for all the girders from the instant at which the absolute maximum strain was induced was plotted. The data for truck runs 1, 2, 3, 5, 6 and 7 is plotted in Figure 101, Figure 102, Figure 103, Figure 104, Figure 105 and Figure 106, respectively. Note that in the following figures the following nomenclature is adopted,

$$TRx - p$$

where,

TR = Test Run

x = Truck position along bridge width (as per Figure 50 and Figure 51)

p = Indicator for truck pass in the same position (A, B, C and D signify Pass number 1, 2, 3 and 4 respectively).
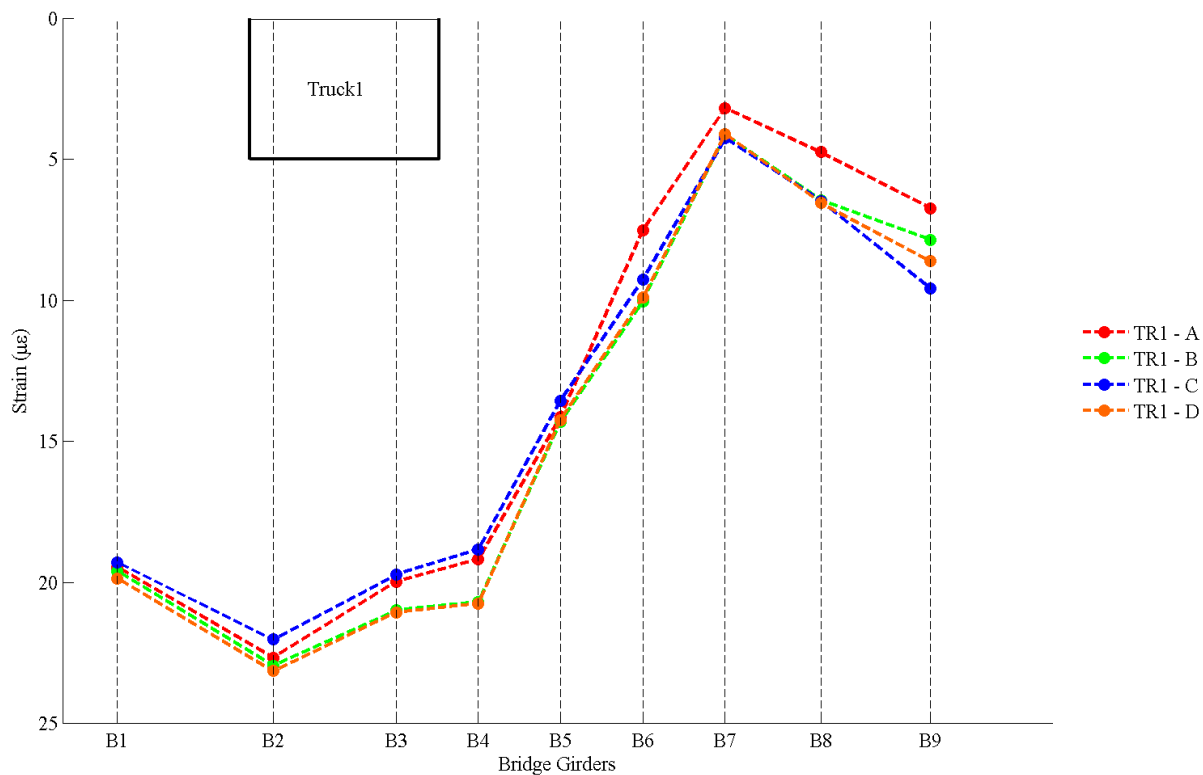
Figure 101: Strain distribution in transverse direction for all passes in Run 1.
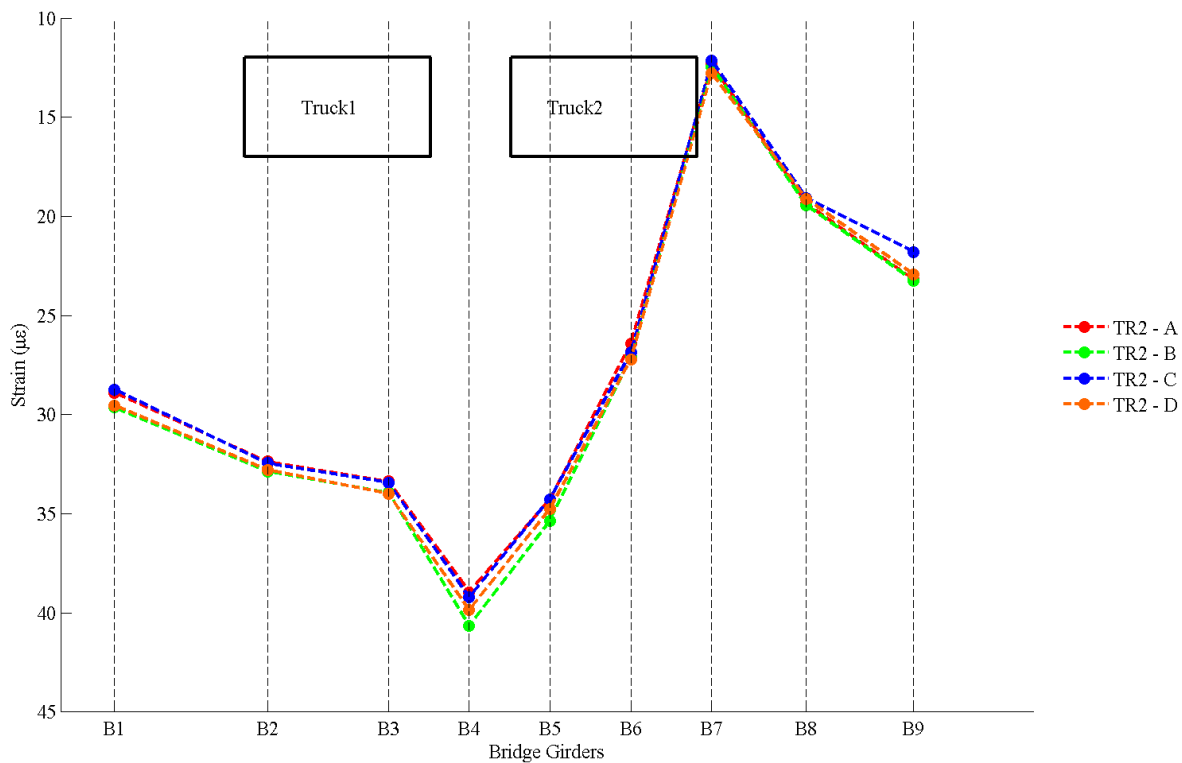
Figure 102: Strain distribution in transverse direction for all passes in Run 2.

108
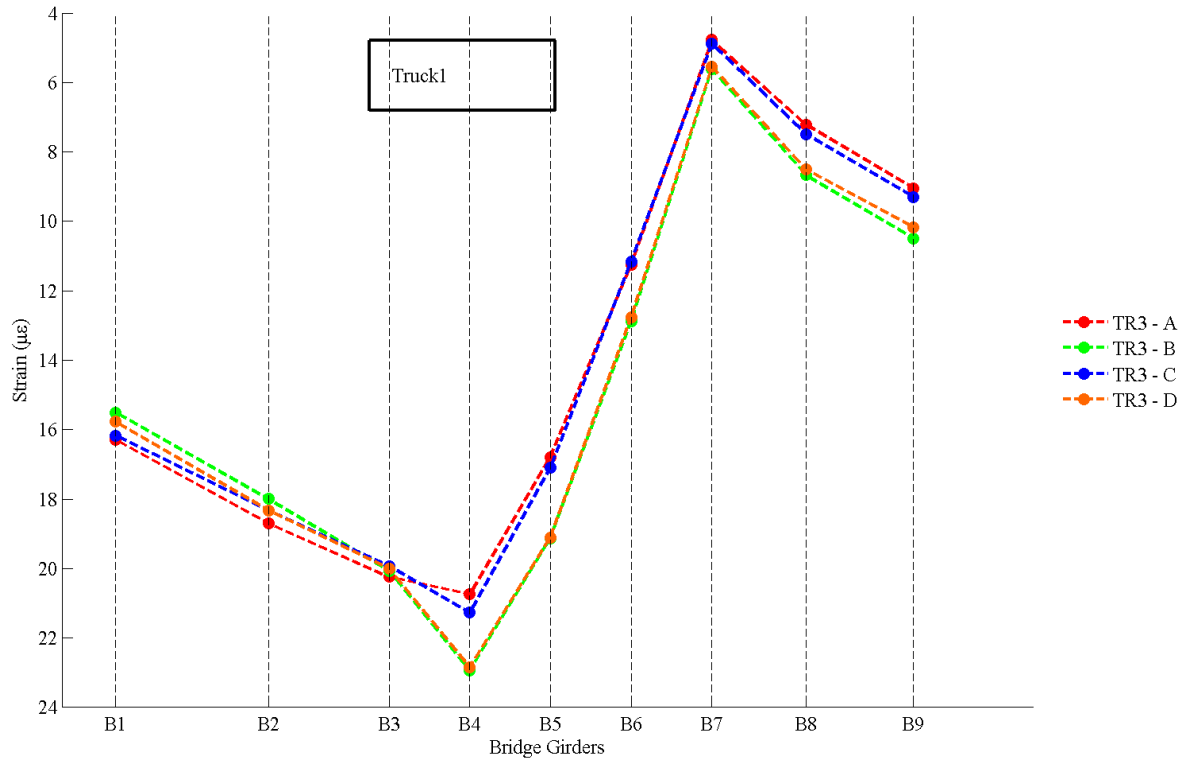
Figure 103: Strain distribution in transverse direction for all passes in Run 3.
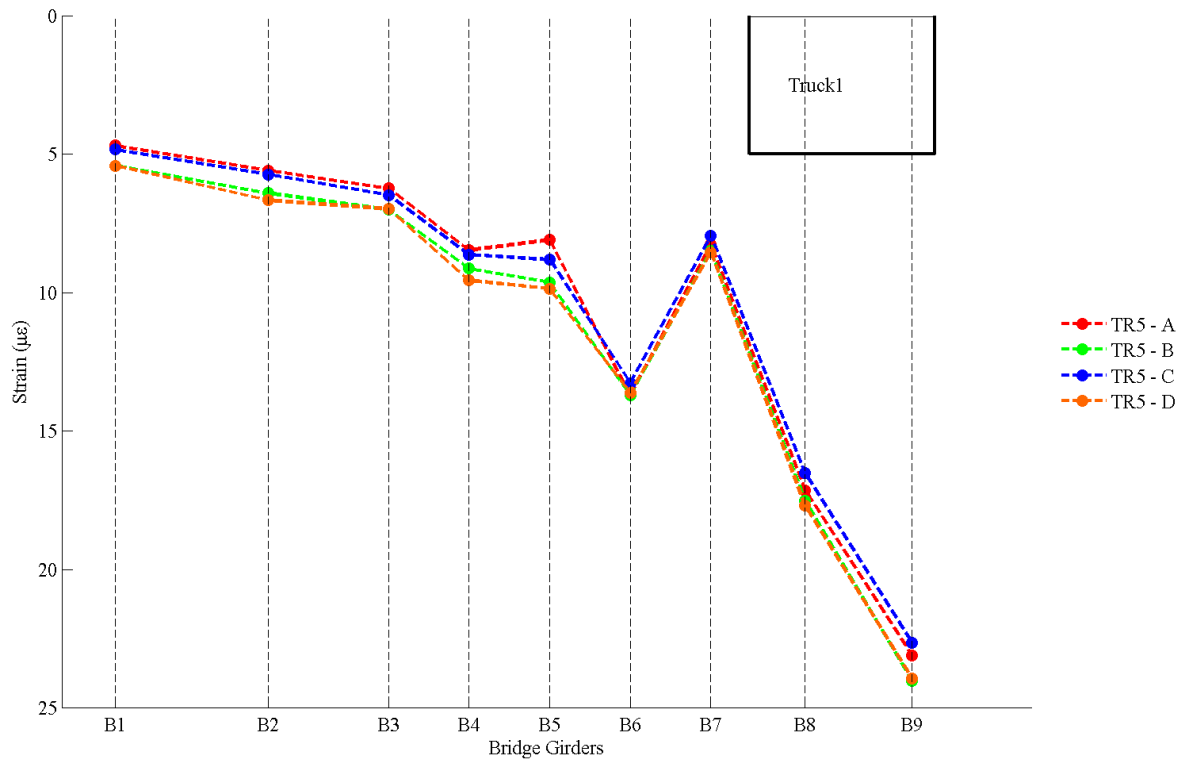
Figure 104: Strain distribution in transverse direction for all passes in Run 5.
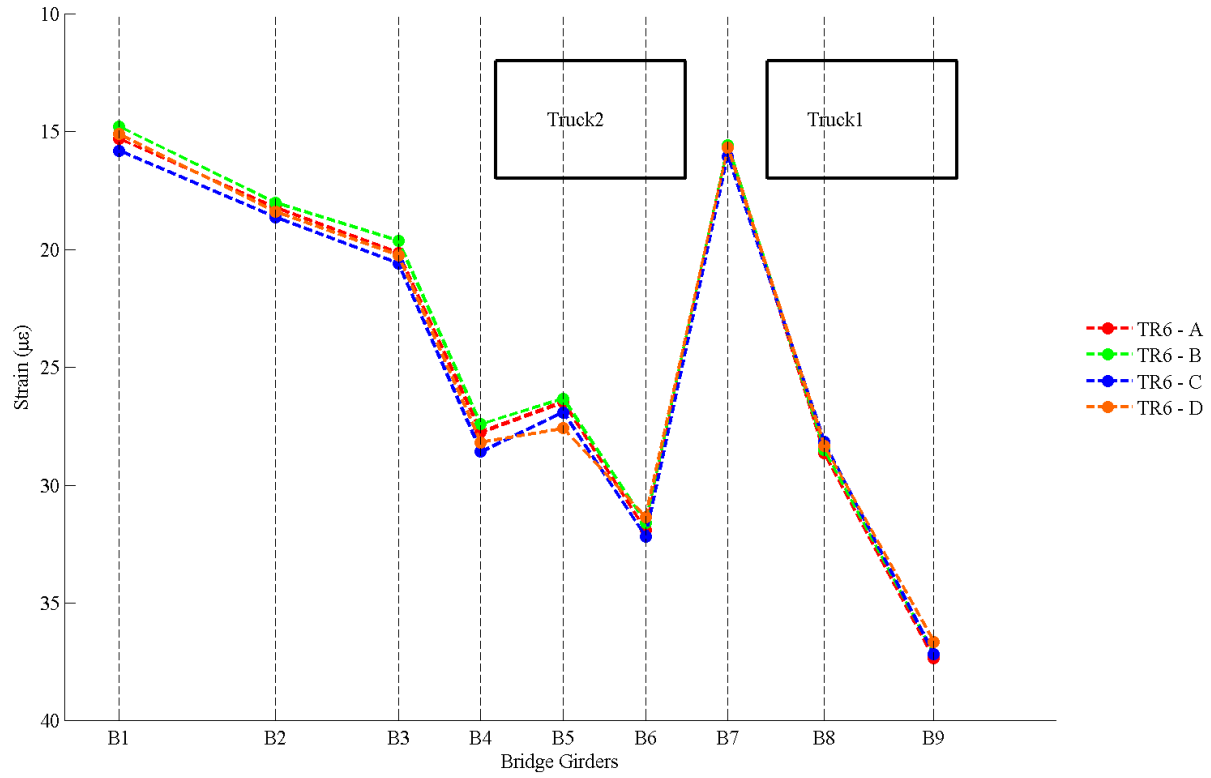
Figure 105: Strain distribution in transverse direction for all passes in Run 6.
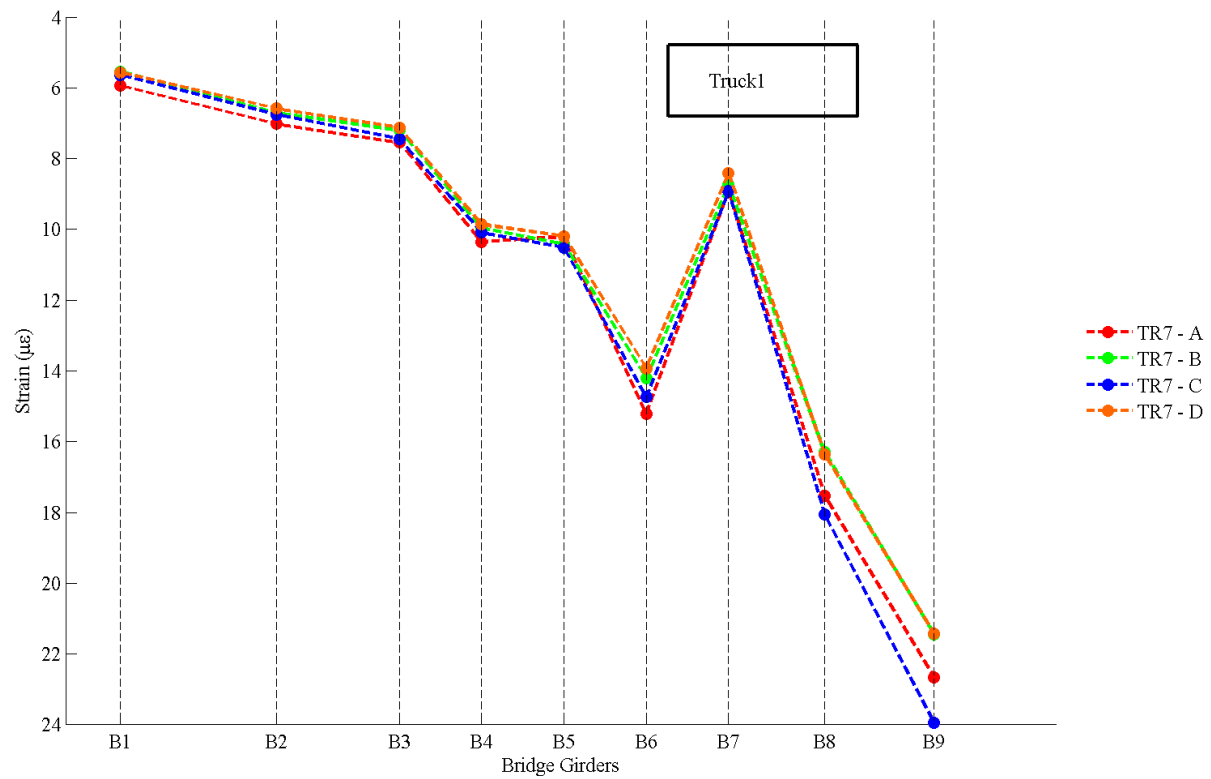
Figure 106: Strain distribution in transverse direction for all passes in Run 7.

The strain distribution did not appear to be uniform from the transverse plots of data. For all test runs the distribution of strains in girders B7 through B9 was haphazard and seemed to be erroneous. The magnitude of strain in girder B7 was much smaller than that of adjacent girders B6 and B8 whereas the magnitude of strain in girder B9 was larger as seen in transverse strain plots of Truck Runs 1, 2 and 3. Generally for test runs with a single truck configuration there was a sharp change in strain between girder B5 and B6 which could be attributed to a possible shear key crack in Span 1. This conclusion was further reinforced by the presence of a reflective crack on the deck over this location. The strains at girder B7 were consistently small and did not follow a logical pattern, even when the truck load paths were over this location. The strain gauge calibration was checked after the field tests and no problems were found. Hence, the lower strains may indicate that the girder location may have a concrete delamination. Considering, that strain measurements are affected by local effects this seemed to be a possibility. The possibility of shear key failure causing the lower strains at B7 could be neglected since girders B8 and B9 displayed higher strains than B7, especially for Runs 1, 2 and 3, when the trucks were not positioned directly over the location.

4.1.2. Transverse Deflection in KVCB

To observe the transverse behavior of the bridge, deflections were plotted along the width of the bridge at the mid-width of each girder. The values were plotted at the instant at which absolute maximum girder deflection occurred. These plots are presented in Figure 107, Figure 108, Figure 109, Figure 110, Figure 111, and Figure 112.
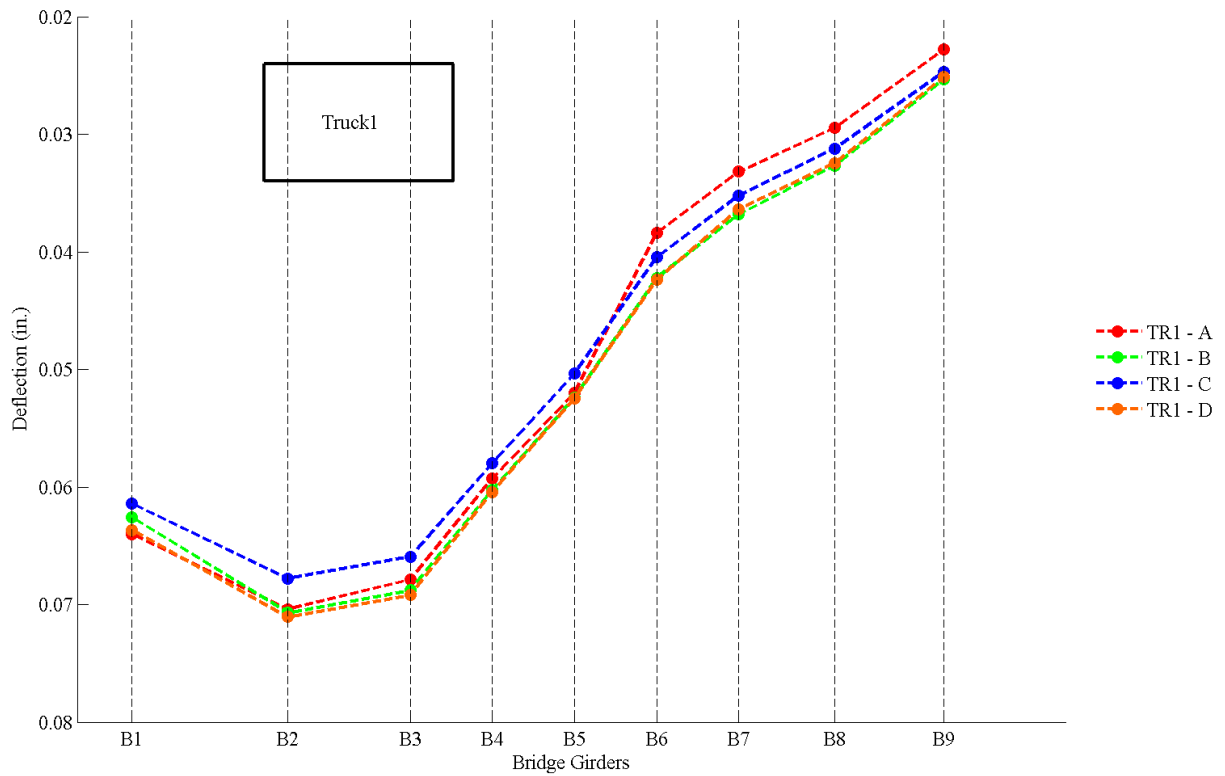
Figure 107: Distribution of girder deflection in transverse direction for all passes in Run 1.
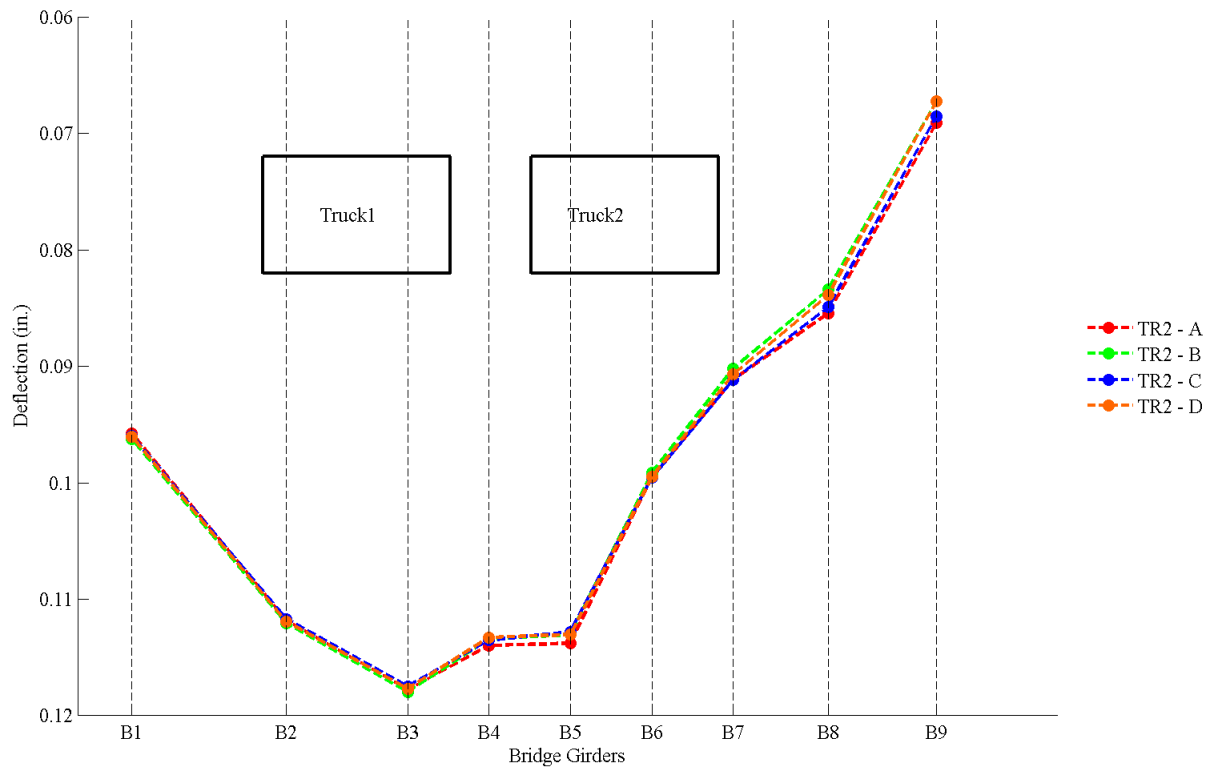
Figure 108: Distribution of girder deflection in transverse direction for all passes in Run 2.

112
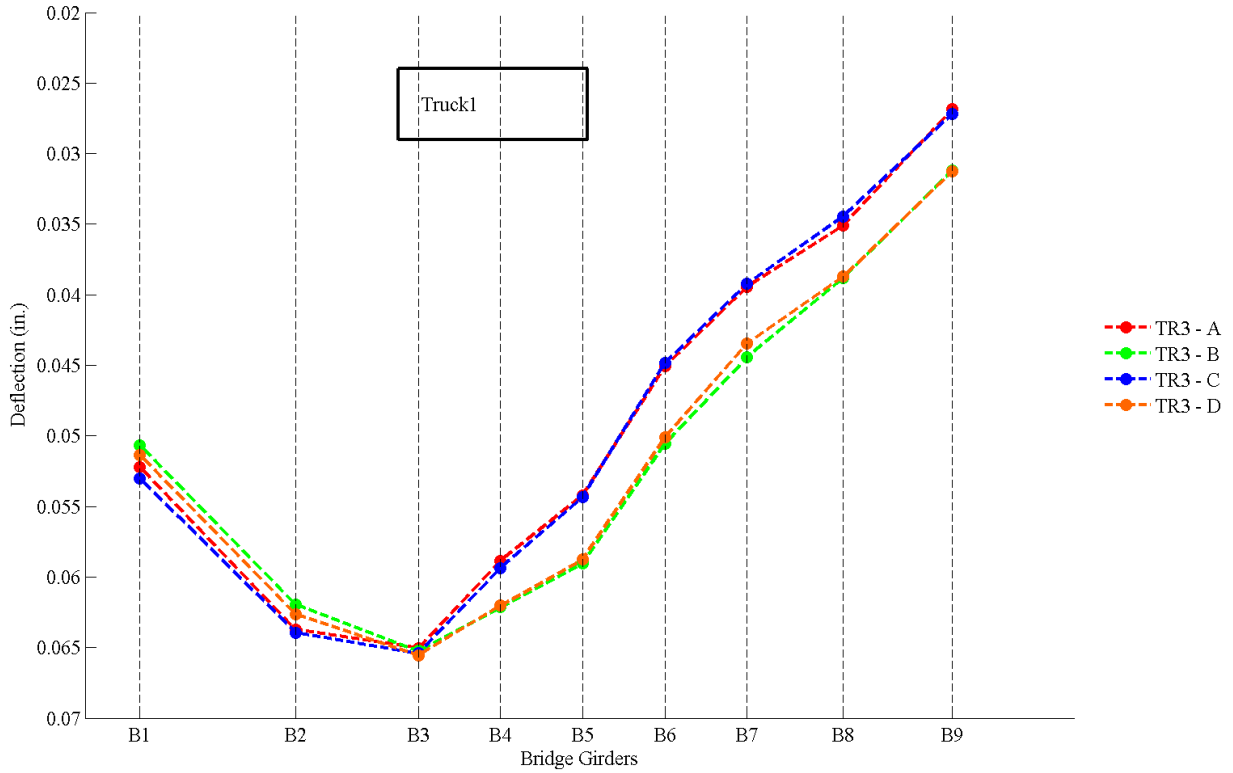
Figure 109: Distribution of girder deflection in transverse direction for all passes in Run 3.
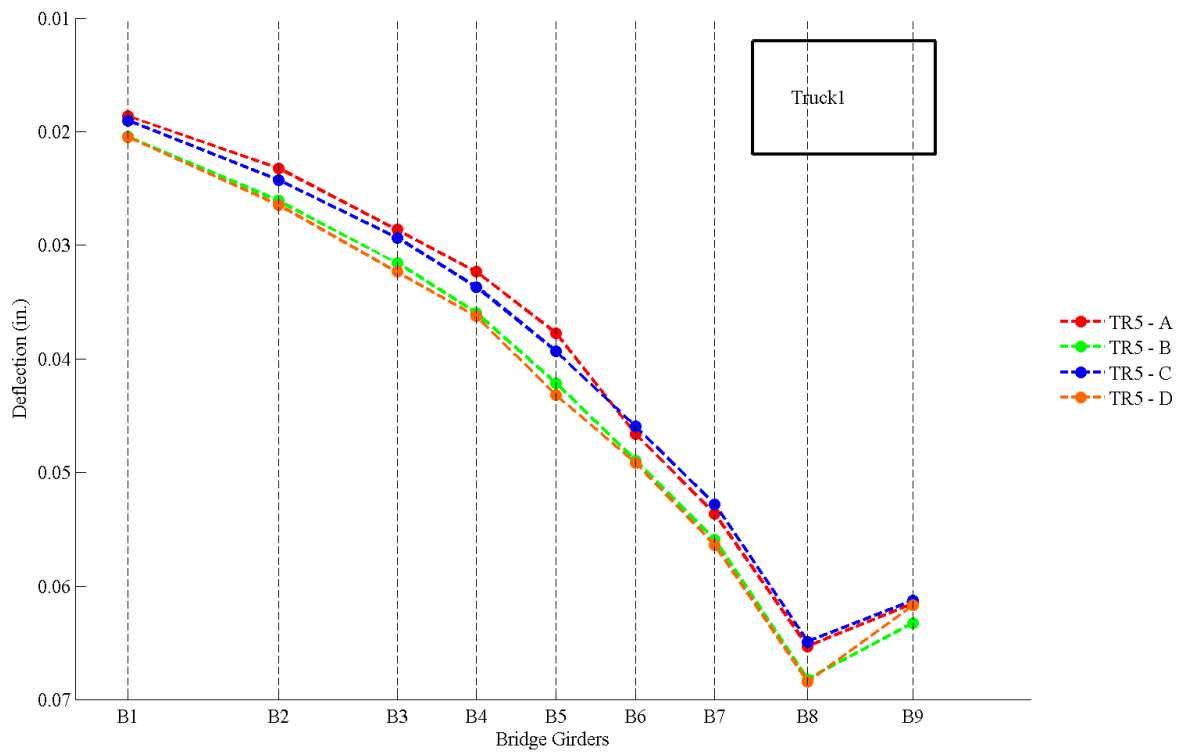
Figure 110: Distribution of girder deflection in transverse direction for all passes in Run 4.

113
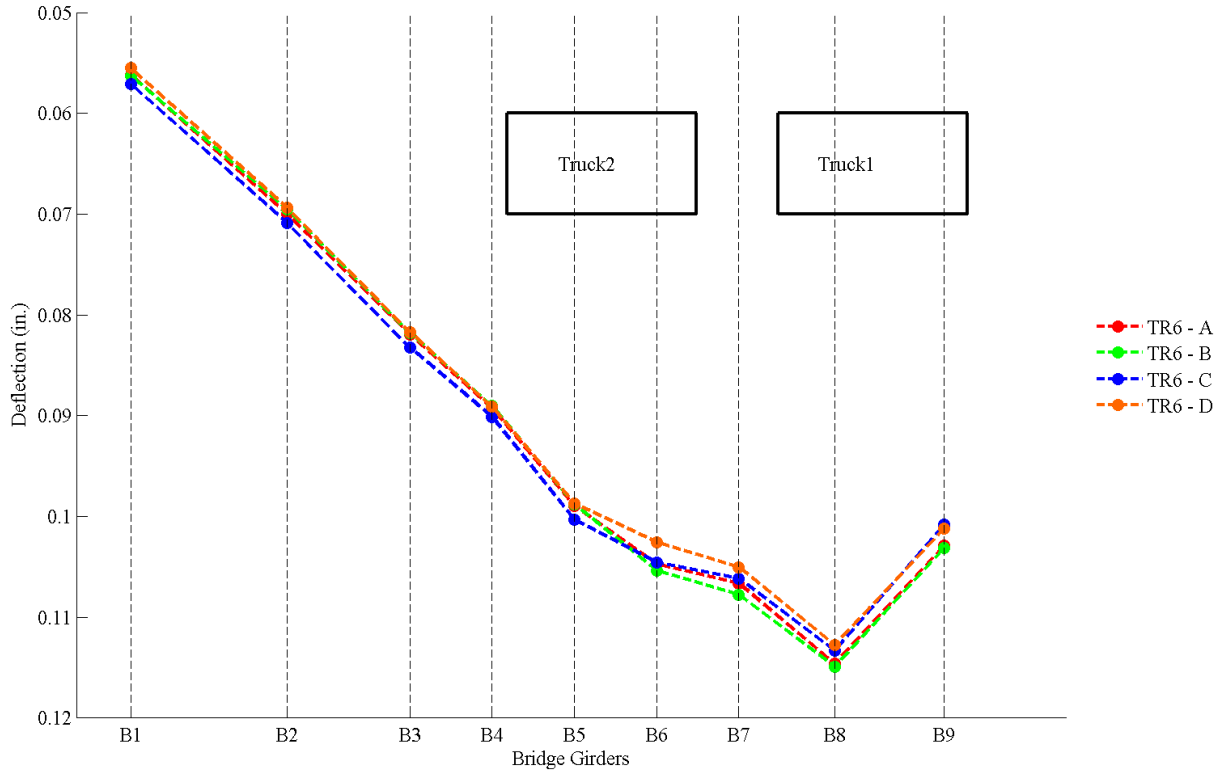
Figure 111: Distribution of girder deflection in transverse direction for all passes in Run 6.
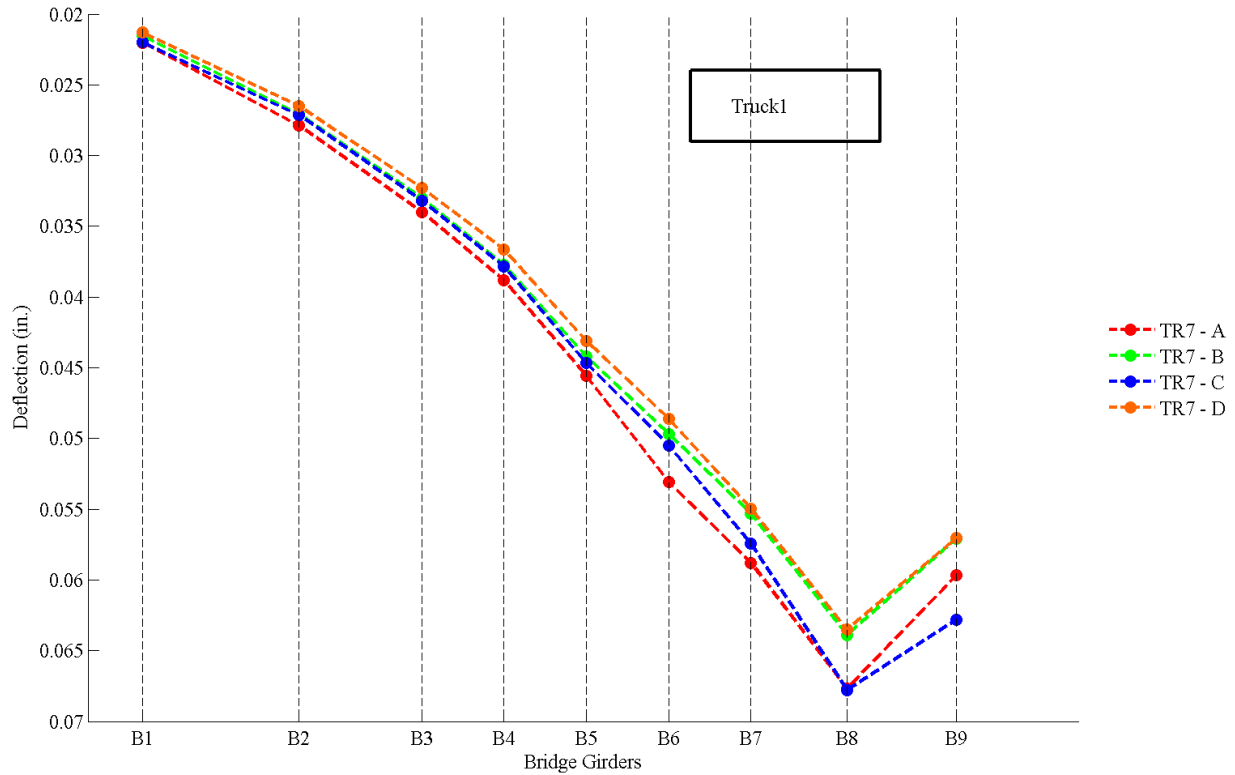
Figure 112: Distribution of girder deflection in transverse direction for all passes in Run 7.

The plots showed the girder deflection variation along the cross-section of the bridge. The girders directly in the loaded path displayed higher displacements as compared to those in the non-loaded path. The transverse response of the bridge appeared to be essentially linear, that is the magnitudes of deflections reduced almost linearly for girders that were away from the loaded path. The linear appearance to the cross-section deflection indicated that the load was being transferred into adjacent girders regardless of presence of reflective cracks and shear key failure in some joints. This was particularly true for test runs 5, 6 and 7. The plots of test runs 1, 2 and 3 appear less linear, especially between girders B5 and B6 where difference in magnitude of deflection appeared to be more drastic than at other joints. Similarly, for Run 2 the variation of deflection between girders B3, B4 and B5 indicated that there was significant relative displacement between girders. The relative displacements between these three girders were studied closely and are discussed in the following section.

4.1.3. Relative Vertical Displacements between Adjacent Girders in KVCB

The measurement of relative displacements between girders was an essential part in the live load test of the KVCB. The bridge was known to have the problematic partial depth shear key detail. Consequently, the KVCB displayed the signs of shear key failure through reflective cracks on the deck notably between girders B1 and B2, B5 and B6, B8 and B9 in the south span and girders B2 and B3, B7 and B8 in the north span. To observe the transverse displacements between the adjacent girders a cluster of LVDTs were attached vertically to the underside of girders B3 through B5. Girders B3 through B5 were selected on the basis that there were no visible signs of deterioration at these joints, which allowed for closer examination of the transverse behavior of the adjacent girders under load. The LVDT cluster, as shown in Figure 36, was positioned such that the displacement of each girder was recorded at center of each web. Recording displacements of the girder webs allowed for studying the relative vertical deflection and also relative rotation between the boxes. The measurements of displacements made by the LVDT cluster are presented in Figure 113 through Figure 118. The displacements are presented for instances when the magnitude of relative displacement was the highest, which typically was when the rear axles were closest to the instrumented locations. In these plots the axis of individual LVDTs is plotted but not individually demarcated. Instead the girder designation is shown between the vertical LVDT axes.
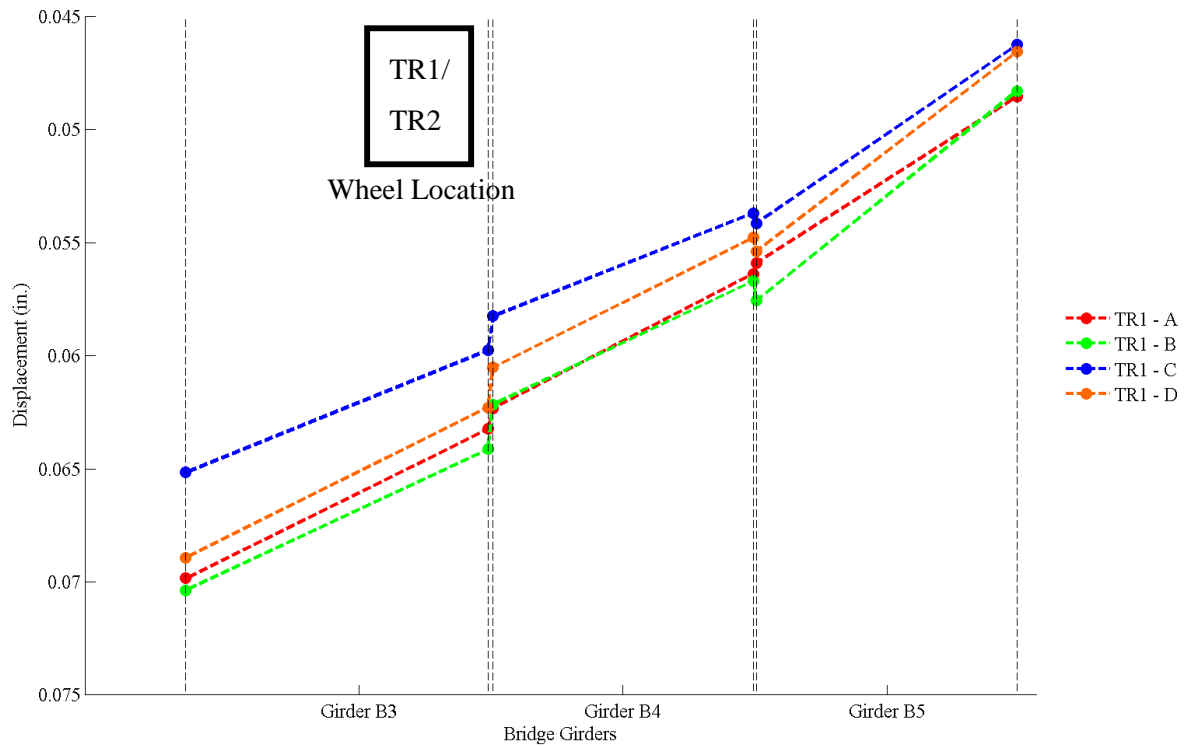
Figure 113: Relative vertical displacement between adjacent girders for all passes during Run 1.
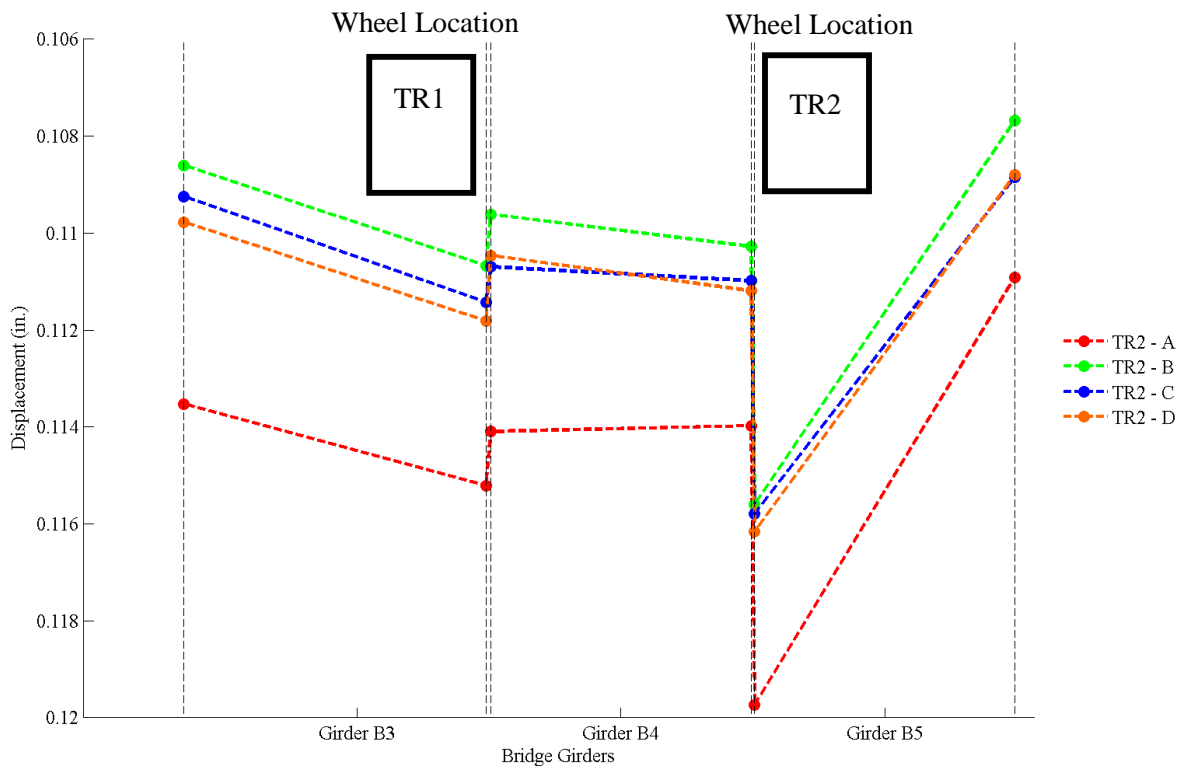
Figure 114: Relative vertical displacement between adjacent girders for all passes during Run 2.
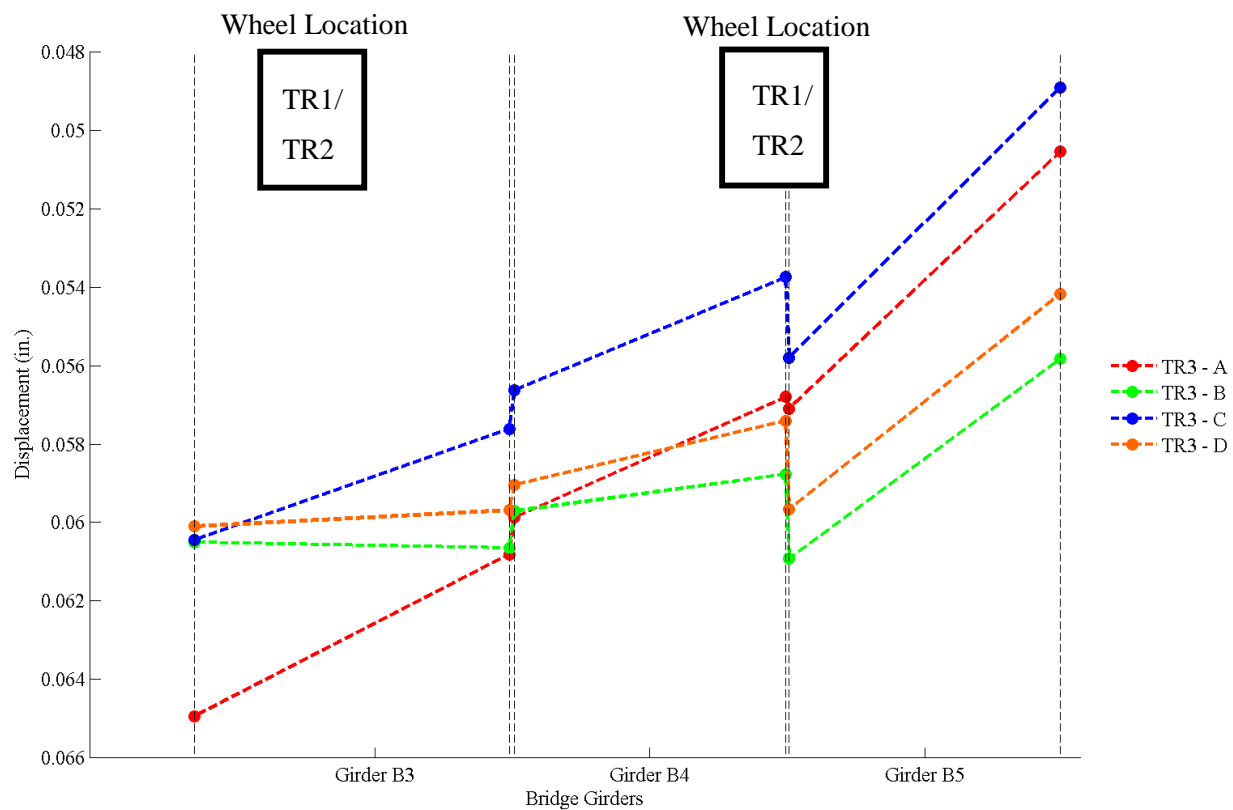
Figure 115: Relative vertical displacement between adjacent girders for all passes during Run 3.
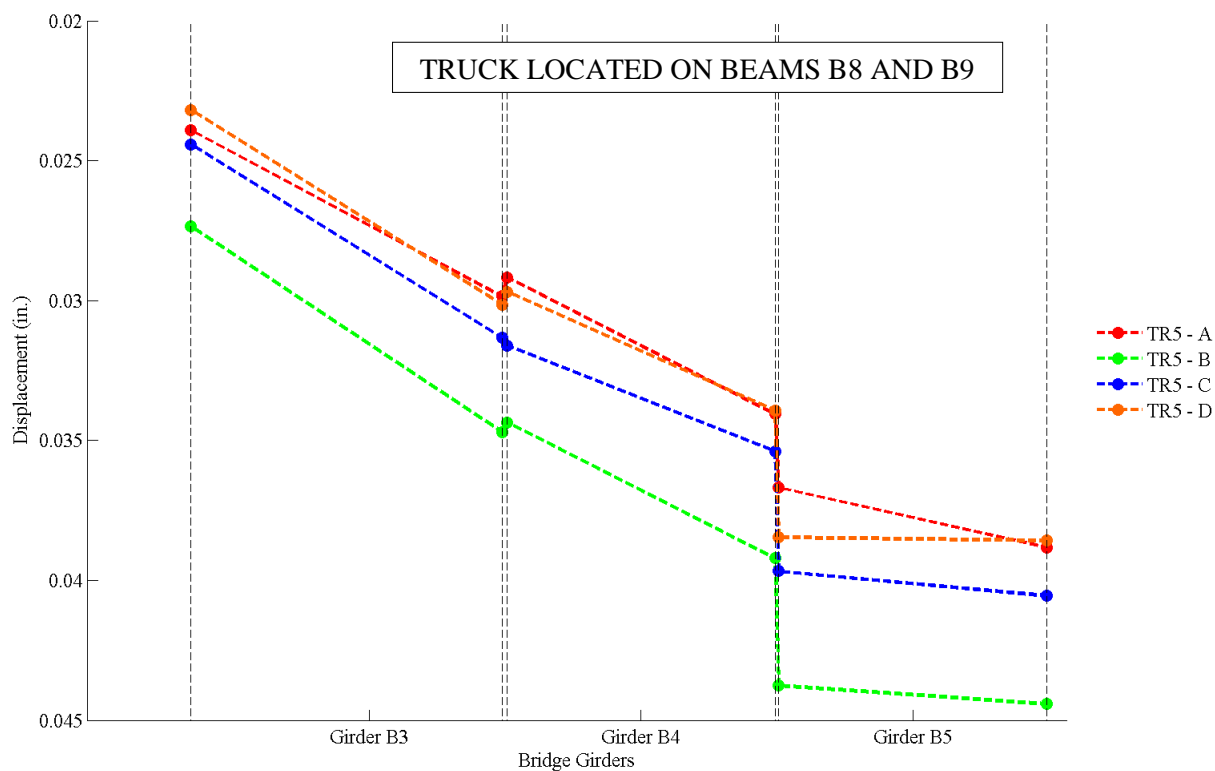
Figure 116: Relative vertical displacement between adjacent girders for all passes during Run 5.

117
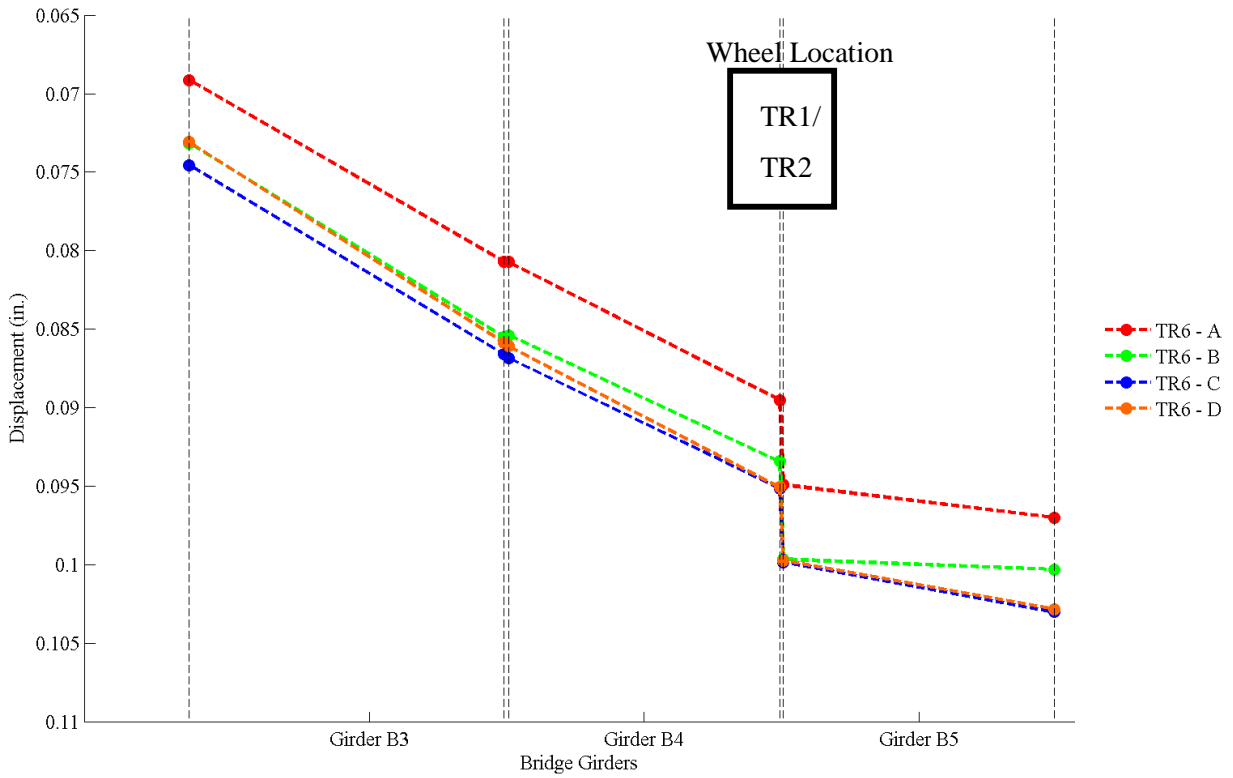
Figure 117: Relative vertical displacement between adjacent girders for all passes during Run 6.
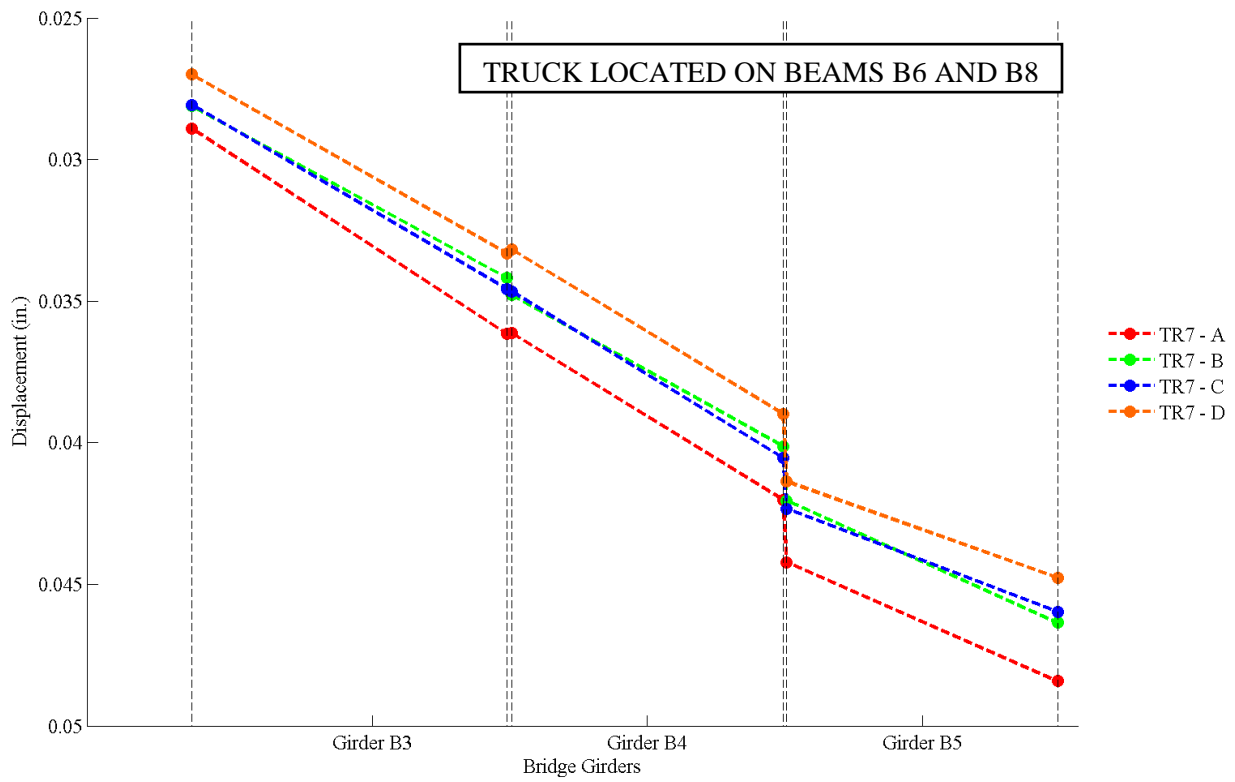
Figure 118: Relative vertical displacement between adjacent girders for all passes during Run 7.

In the above figures it can be observed that the girders do not deform as a single unit (there is relative vertical displacement and relative twist between the girders for certain test truck configurations). Although the magnitude of relative vertical displacement appears to be extremely small the difference in the slope between displacements of web deflections for each girders i.e. the difference in twist is more conspicuous. Girders B3, B4 and B5 were in the wheel load path for test runs 1, 2 and 3. The difference in relative vertical deflections and relative twist can be better observed in these plots i.e. Figure 113, Figure 114 and Figure 115. The plot for Test Run 1 displays the behavior that is to be expected of an adjacent box girder bridge i.e. negligible relative vertical displacement and twist. However, this behavior is not exhibited for Test Runs 2 and 3. In Test Run 2, the trucks were placed primarily over girders B2 and B3 and girders B5 and B6 leading to slightly lesser deflection in girder B4 than girder B3 and B5 thereby exacerbating the relative displacements at the joints. In Test Run 3 the trucks were placed B3 and more or less over the joint between girders B4 and B5 causing smaller deflection in girder B4 and a larger twist in girder B5. The results for northbound test runs presented in Figure 116, Figure 117 and Figure 118 exhibit higher relative displacements between girders B4 and B5. These results indicate that the worst effects of load transfer are in the immediate vicinity of the applied load. The girders that are not directly in the loaded path display smaller relative displacements. Moreover, the magnitude of relative displacements between girders B4 and B5 might indicate a shear key failure that may precipitate reflective cracks in the concrete topping.

4.1.4. Girder Distribution Factors from KVCB Test Data

Girder distribution factors (GDF) are a critical parameter in design of bridges. GDFs characterize the transverse distribution of load that is expected to be occur on the girder. To clarify, GDFs can be defined as the fraction of live load carried by a single beam in a bridge. Essentially GDFs preclude the necessity of using more complicated analysis methods like Finite Element Modeling for the design of highway bridges. GDFs are affected by various factors including girder stiffness, topping conditions as well as skew. Deterioration in the deck and superstructure conditions affects the distribution of load between girders and hence experimental means are necessary to ascertain the GDFs. There are different distribution factors for moment and shear, however, the focus of this investigation was on the distribution factors for moments as the bridge was instrumented to measure flexural strains and vertical deflections. The shear distribution factors can be measured in diagnostic tests by measuring beam strains at the supports with instruments attached to the beam webs in a "rosette" pattern. For the ABBB system, it was not possible to access the beam webs as the gap between the adjacent beams was too small to access. Hence, the shear distribution factors were not measured in this testing program.

Distribution factors were calculated from experimental results as well as available AASHTO methods. The AASHTO formulae for calculating GDFs consider the ideal condition of the bridge i.e. the

condition of bridge at the start of its serviceable life. After the onset of bridge deterioration the conditions that were assumed in design do not exist. For example, the KVCB had several reflective cracks between girders at various points along the bridge spans which would cause a departure from assumed behavior. Also, the KVCB had a gap between the fascia girders and the interior girders to allow for utility pipes to span the creek. This was a deviation from a typical cross-sectional detail of adjacent precast box girder bridges. The effect of deterioration and deviation from typical bridge details over the load distribution can be better studied by calculating GDFs from experimental data and comparing against GDFs calculated by AASHTO.

4.1.4.1. GDFs by AASHTO Method – KVCB

The KVCB was classified as a category (f) in cross-section type for calculation of GDFs by AASHTO method. The category (f) structure may be broadly defined as precast solid, voided or cellular concrete boxes with shear keys and cast-in-place concrete overlay. The following formulae were used to calculate GDFs for bending moments in interior girders,

One design lane loaded;

$$k \left(\frac{b}{33.3L} \right)^{0.5} \left(\frac{I}{J} \right)^{0.25}$$

Equation 9

and; factor for number of beams,

$$k = 2.5(N_b)^{-0.2} \geq 1.5$$

Equation 10

where, $N_b =$ number of girders in bridge cross-section
$b =$ girder width (in.)
$L =$ span length of girder (ft)
$I =$ moment of inertia (in.^{4})
$J =$ St. Venant torsional inertia (in.^{4})

Two or more design lanes loaded;

$$k \left(\frac{b}{305} \right)^{0.5} \left(\frac{b}{12.0L} \right)^{0.2} \left(\frac{I}{J} \right)^{0.06}$$

Equation 11

The range of applicability of Equation 9 and Equation 11 is

$$35 \, ft \leq b \leq 60 \, ft$$
$$20 \, ft \leq L \leq 120 \, ft$$
$$5 \leq N_b \leq 20$$

GDFs for bending moments in exterior girders were calculated as,

One design lane loaded;

$$g = e g_{interior}$$

Equation 12

and; the exterior girder factor, $\qquad e = 1.125 + \dfrac{d_e}{30} \geq 1.0$ $\qquad\qquad$ *Equation 13*

where, $\quad$ $g_{interior}$ = $\quad$ GDF for interior girder as calculated by Equation 9 and/or Equation 11

$\qquad\qquad$ d_e = $\quad$ horizontal distance from the centerline of the exterior web of exterior beam at the deck level to the interior edge of curb or traffic barrier (ft)

Two or more design lanes loaded; $\qquad\qquad\qquad g = e\, g_{interior}$ $\qquad\qquad\qquad\qquad$ *Equation 14*

and; $\qquad\qquad\qquad\qquad e = 1.04 + \dfrac{d_e}{25} \geq 1.0$ $\qquad\qquad\qquad$ *Equation 15*

The range of applicability of Equation 13 and Equation 14 is $d_e \leq 2.0$

For category (f) structures with skew greater than 10° the bending moment may be reduced as,

$$r = 1.05 - 0.25\tan(\theta) \leq 1.0$$

If $\theta > 60°$, use $\theta = 60°$ $\qquad\qquad\qquad$ *Equation 16*

where, $\qquad$ θ = $\quad$ skew angle (deg.)

The range of applicability of Equation 16 is $0° \leq \theta \leq 60°$

The results of calculations by AASHTO formulae is presented in Table 13.

Table 13: Distribution factors by AASHTO LRFD formulae.

Distribution Factors For	Girder Type	Distribution Factors	
		Single Lane	Multiple Lanes
Interior Girders	BIII-48	0.166	0.252
	BIII-36	0.153	0.206
Exterior Girder	BIII-48	0.143	0.167

4.1.4.2. Experimental Calculations of GDFs – KVCB

For calculation of GDFs from experimental data, the results of strain and deflections at 0.4L of the bridge span were used. The KVCB was extensively instrumented at this section and the strains and deflections were measured for nine out of ten girders. For GDF calculation the following formulae were referred from Idriss and Liang (2010) and is shown in Equation 2.

Equation 2 is effective for calculating GDFs of bridges with very small to no skew. For making adjustments to distribution factors for skew the formula presented in Collins (2010) and was modified for

individual section sizes as presented in Idriss and Liang (2010). See Section 2.6.3 for explanation of Equation 17.

$$g_i = \frac{R_{max}W_i n}{\sum_{j=1}^{m} R_{peakj}W_j}$$

Equation 17

where,

R_{max} = response of maximally loaded girder
W_i = section modulus of girder with the maximum response
R_{peakj} = peak response recorded in girder j
W_j = section modulus of girder j
n = number of trucks on bridge
m = total number of beams in bridge

For calculation of GDFs by Equation 16 and Equation 17 the type 39 in. × 48 in. girder was considered as the typical girder in calculation of section modulus ratios. GDFs were calculated for all the girders although girder B10 was not instrumented. The response of girder B10 was estimated on the basis of adjacent girder readings. For deflections the girder B10 response was linearly extrapolated from the deflections of girders B8 and B9. For estimating strains, linear extrapolation was not possible due to the haphazard distribution of strains in girder B7 through B9. Instead, the strain in girder B10 was estimated by averaging the strains in girders B6 through B9.

Maximum values of GDF calculated from experimental results were used for comparison with AASHTO GDFs. Maximum value of GDF calculated from strain and deflection were selected for tests with a single truck configuration and for tests with two truck configurations. The summary and comparison of GDFs is presented in Figure 119 through Figure 122. The girder sections 39 in. × 48 in. are denoted as BIII – 48 and the 39 in. × 36 in. girder sections are denoted as BIII – 36 in the following plots.
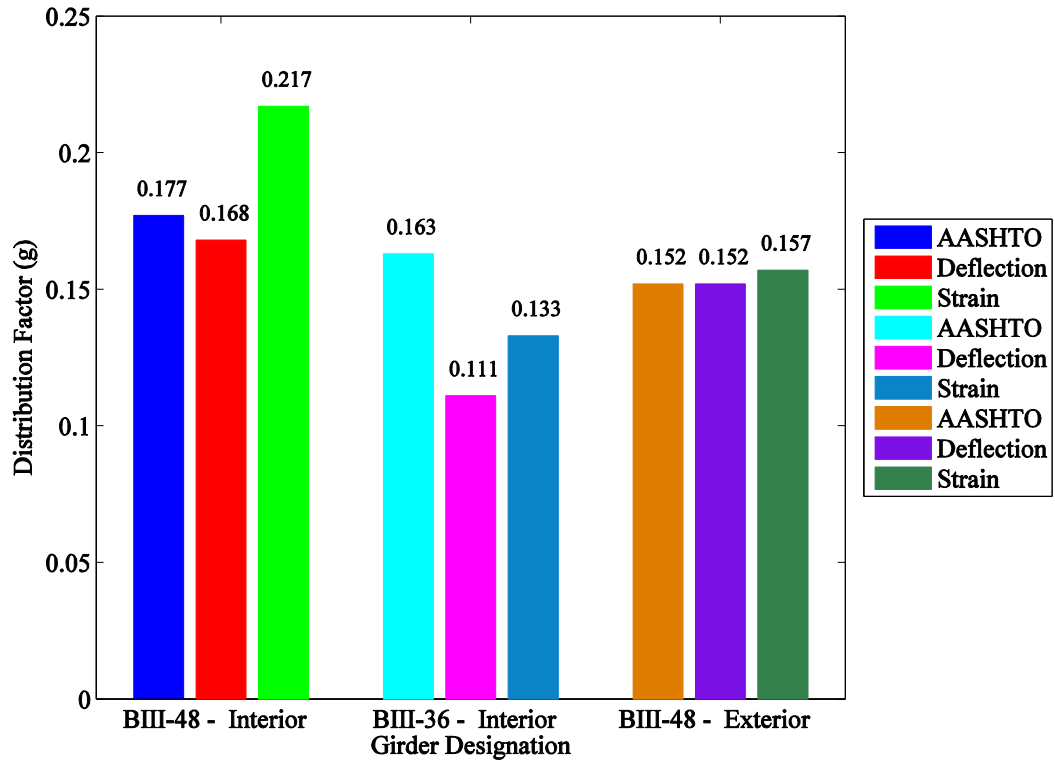
Figure 119: Comparison of GDFs calculated for single lane configuration.
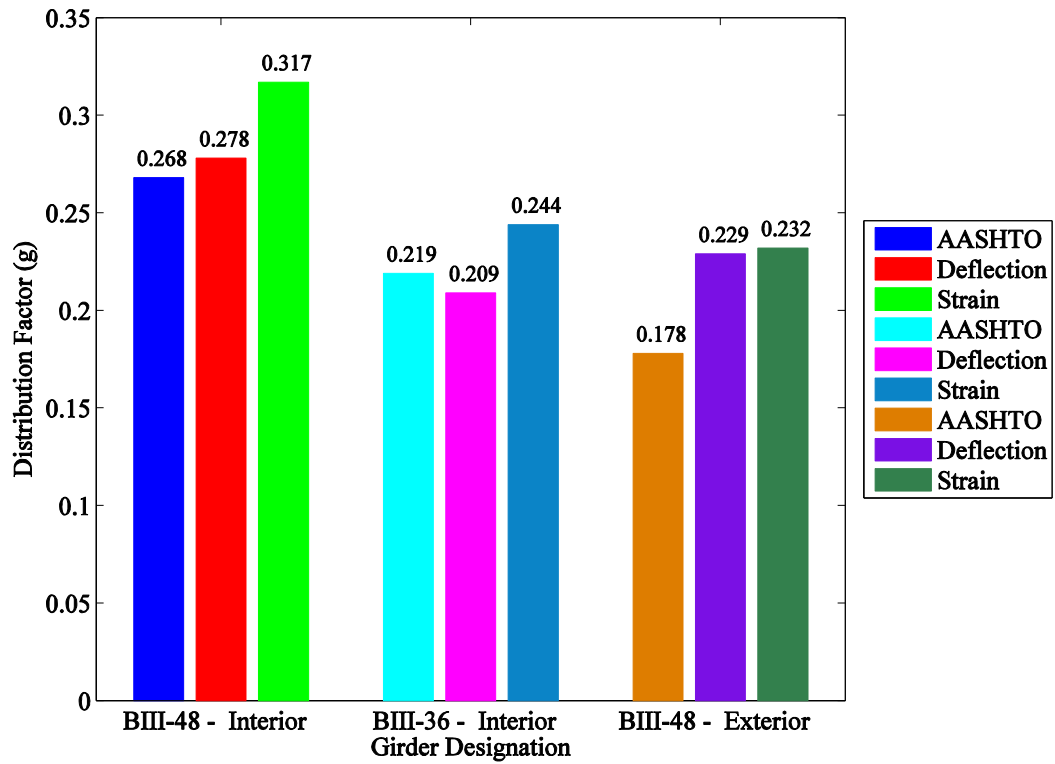
Figure 120: Comparison of GDFs calculated for multiple lane configuration.
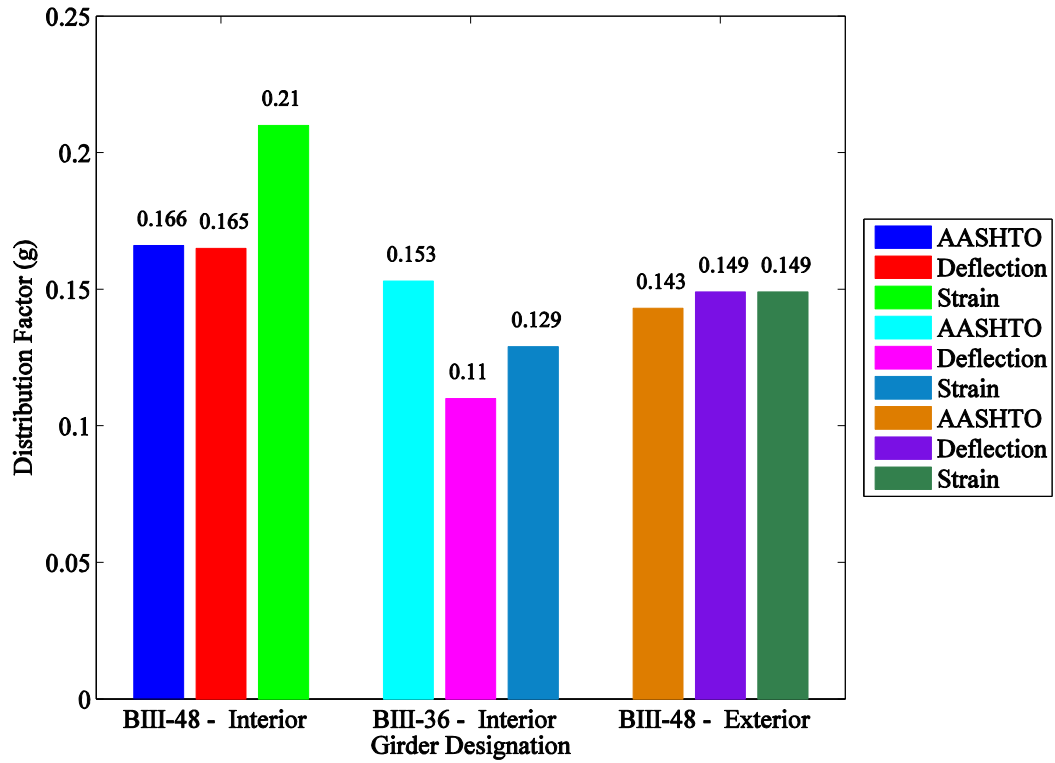
Figure 121: Comparison of GDFs calculated for single lane configuration with skew correction.
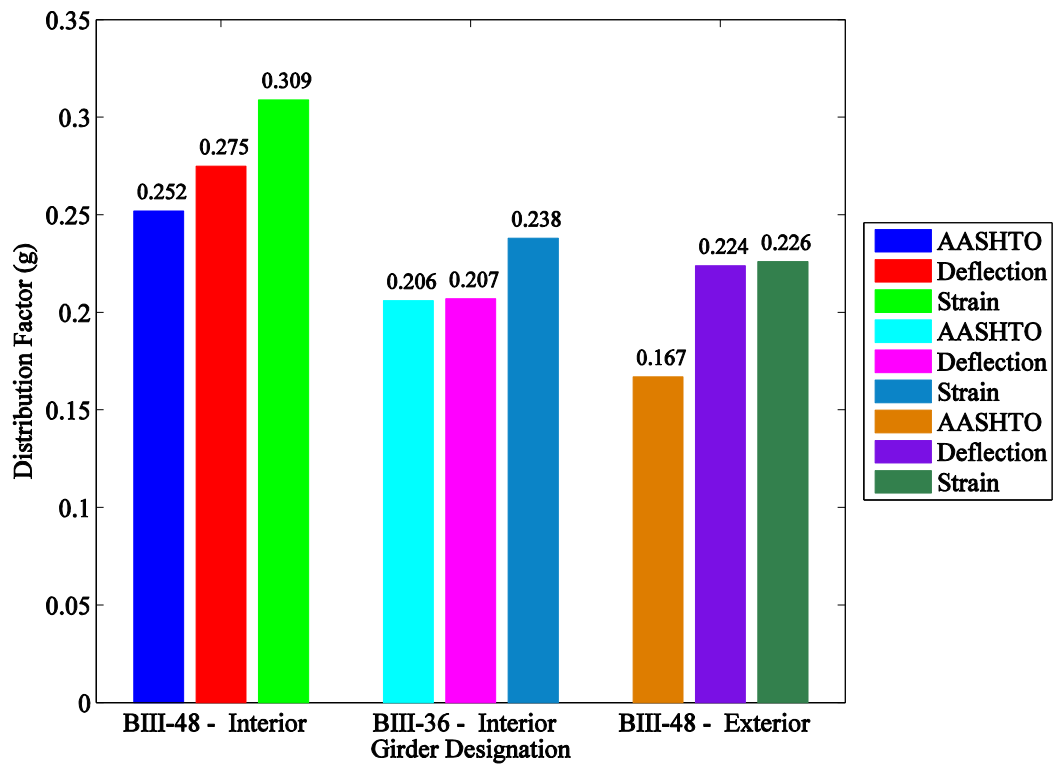
Figure 122: Comparison of GDFs calculated for multiple lane configuration with skew correction.

In above bar charts the comparison between the GDFs calculated from AASHTO and the experimental results is shown. It can be observed that for the most part the values of GDFs calculated from strain for interior girders are much higher than those calculated by AASHTO and deflections. This particular behavior is attributed to the strains in girder B9 for test runs in the northbound lane being significantly higher than strains in other girders leading to higher GDFs from strain values. However, the GDFs calculated from strain for exterior girders do not appear to excessively higher than those calculated by deflections and AASHTO. As for GDFs calculated from deflections for single truck configuration are close in comparison to AASHTO GDFs for design truck in single lane. Based on results of deflections alone it can be observed that AASHTO estimate of GDFs for bending in internal girders is close to experimental results for the larger 39 in. $\times$ 48 in. type girders. However, the same equations seem to over predict GDFs in the smaller 39 in. $\times$ 36 in. girders. For multiple truck configurations, the AASHTO method tends to under predict GDFs as compared to GDFs from strains and deflections calculated for interior as well as exterior girder. In case of the KVCB the fascia girders seem to be receiving a significant amount of truck load, even though the fascia girders were not directly subjected to traffic loads. The AASHTO equations grossly under predict GDFs for exterior girders. The amount of cracking observed on the fascia girders may be explained on the assumption that the same GDFs were used in design of fascia girders. Overall, it could be concluded that the AASHTO method for GDFs under predicted GDF for multiple truck configurations but performed well for single truck configuration. This should not be a concern as the two truck configuration used in this testing would be an extremely rare event on a bridge with a single lane of travel in each direction.

4.2.   Results from ARB Diagnostic Test

The transverse distributions of strains, variations in deflection and relative displacements are presented and discussed.

4.2.1.   Transverse Girder Strain Distributions in ARB

The transverse strains from the ARB test are presented. The methods described in the KVCB data reduction were utilized for the ARB data analysis as well. The transverse strain distributions are presented in Figure 123, Figure 124, Figure 125, Figure 126, Figure 127 and Figure 128.
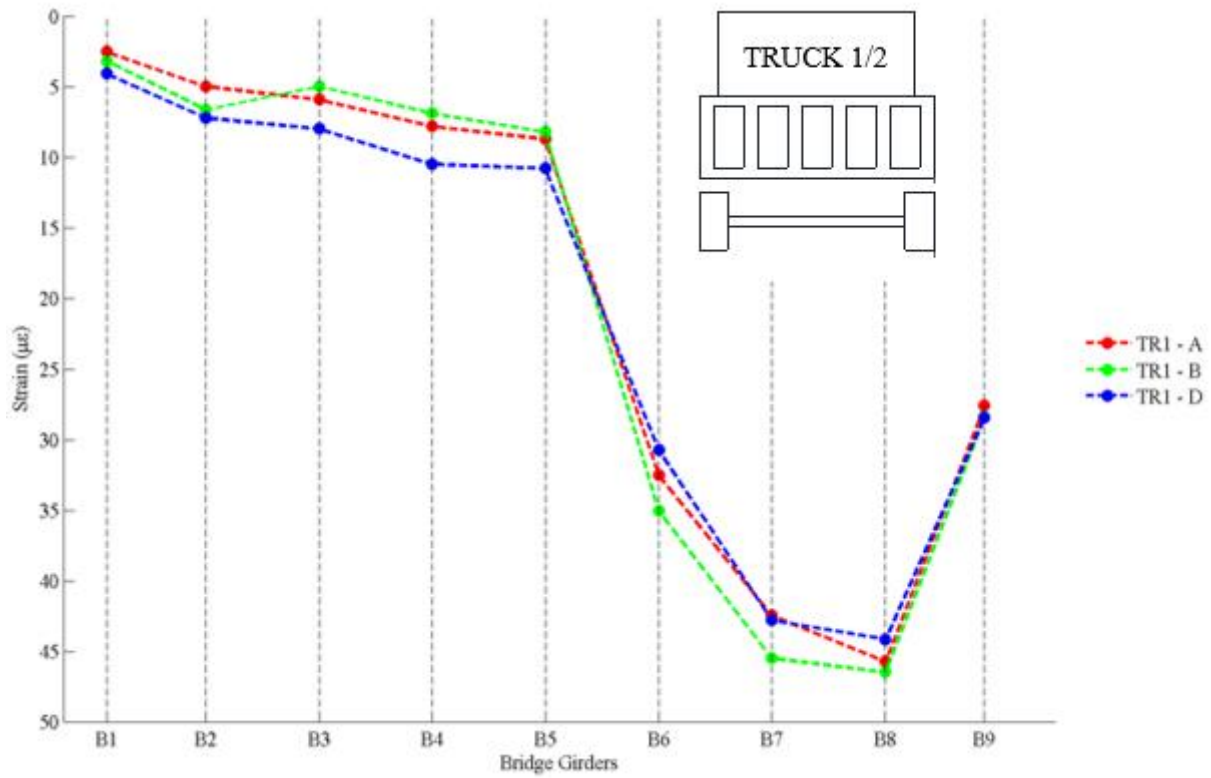
Figure 123: Transverse strain distributions for all reported truck passes in Run 1.
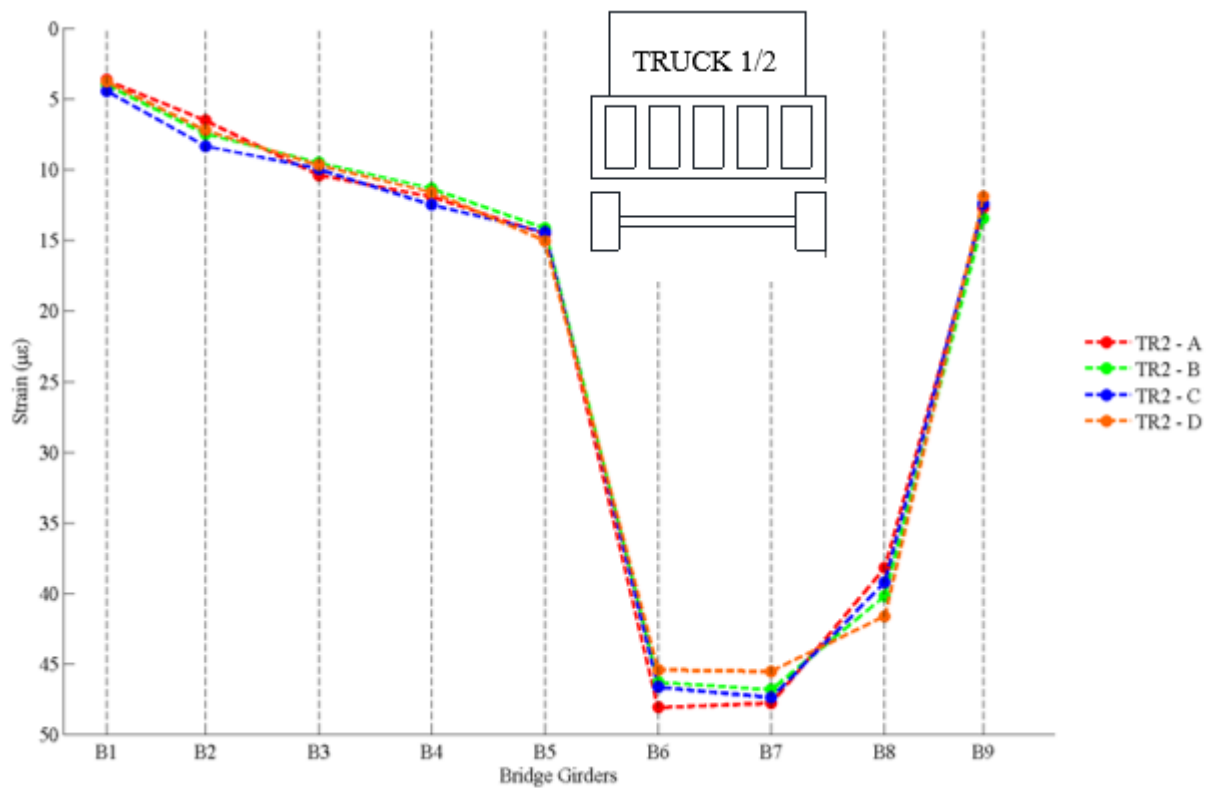
Figure 124: Transverse strain distributions for all reported truck passes in Run 2.

126
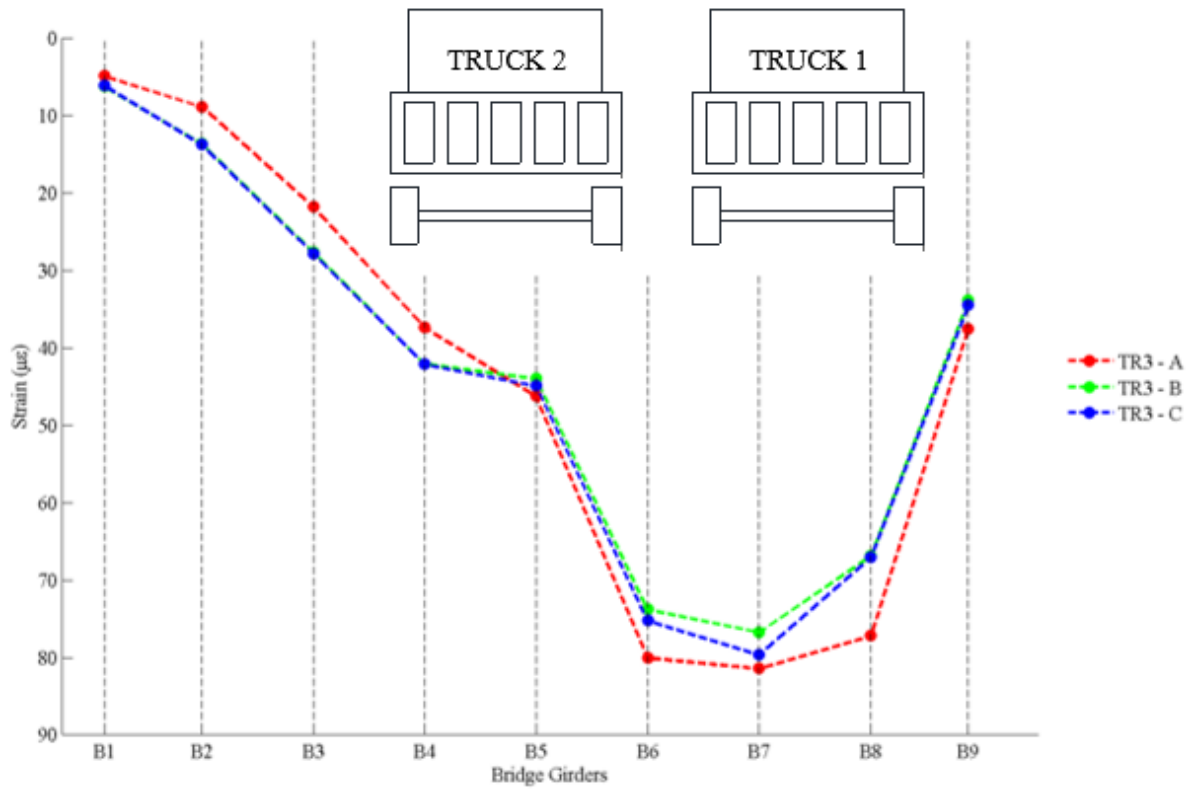
Figure 125: Transverse strain distributions for all reported truck passes in Run 3.
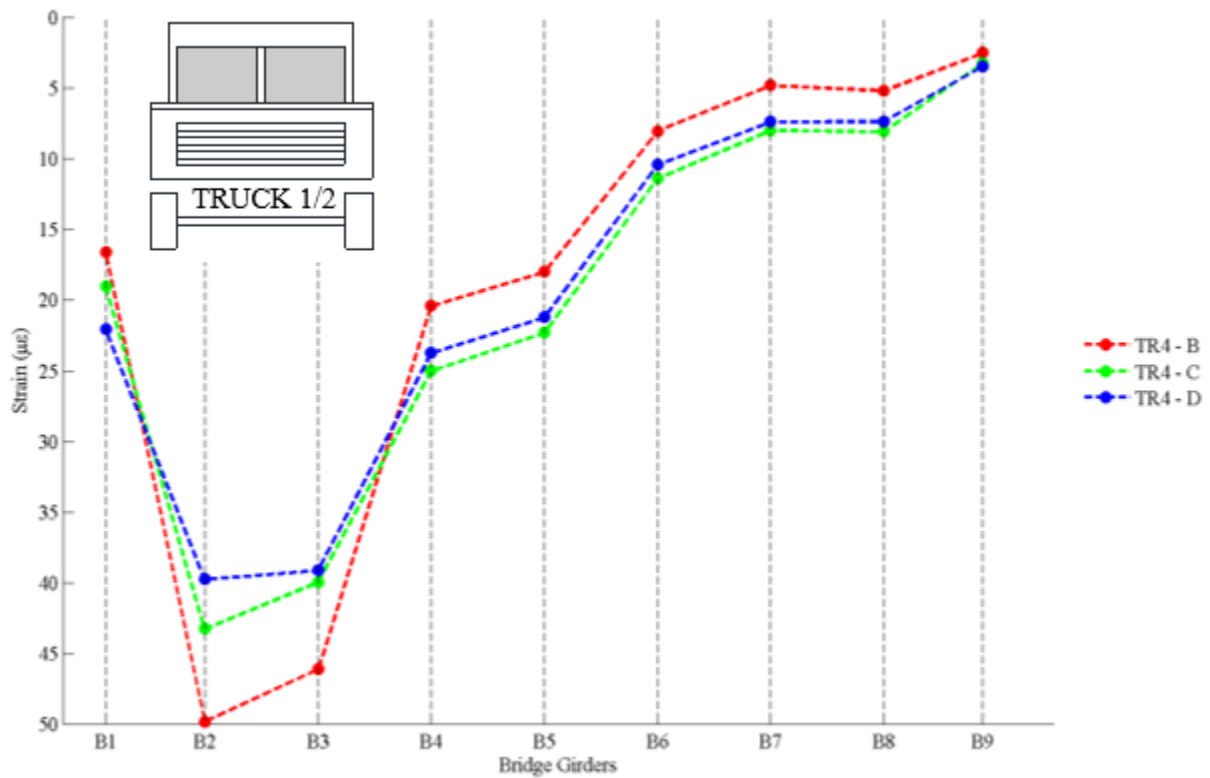
Figure 126: Transverse strain distributions for all reported truck passes in Run 4.
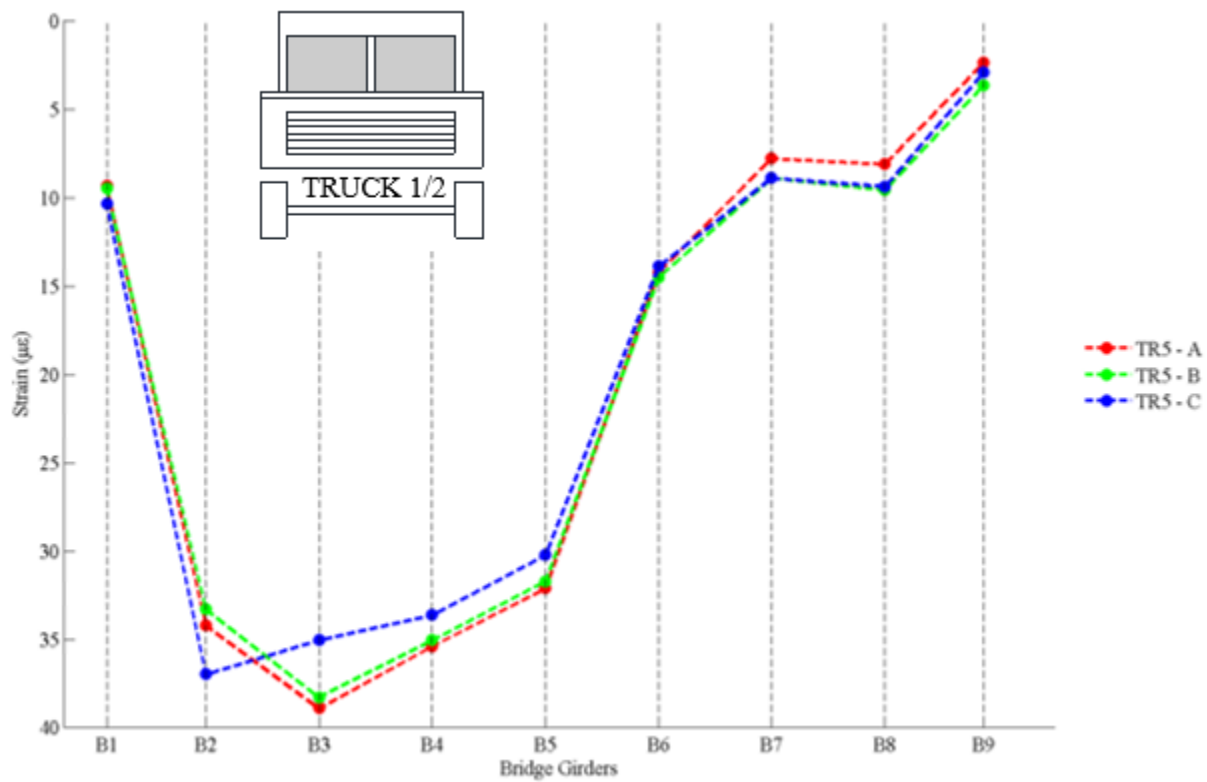
Figure 127: Transverse strain distributions for all reported truck passes in Run 5.
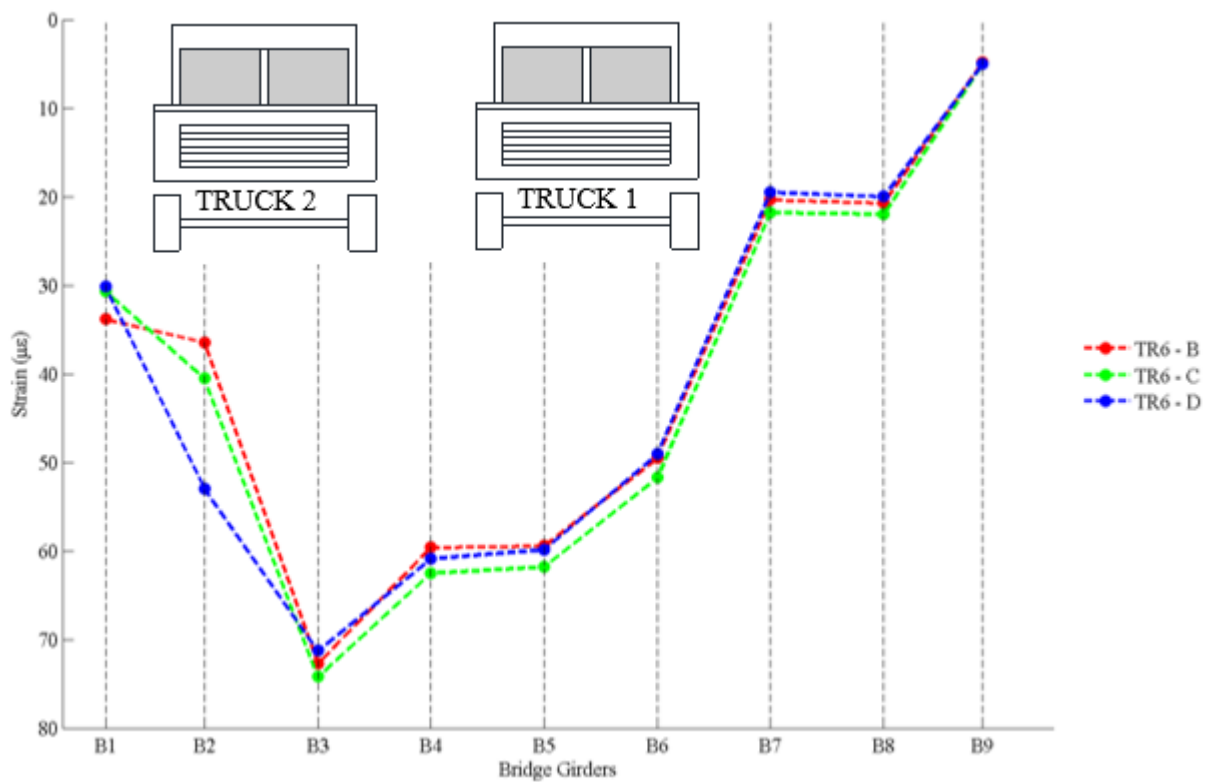
Figure 128: Transverse strain distributions for all reported truck passes in Run 6.

128

The transverse strain distribution plots show that the stresses are concentrated over the girders that are in the load path of the truck(s). This is not a surprising observation considering the amount of deterioration that was noted on the bridge superstructure, particularly the visible signs of joint deterioration. Another important observation that can be made from these plots is the smaller magnitude of strain values in the fascia girders. Even with a truck in close proximity the magnitude of strain in significantly lower than the adjacent interior girders. This can certainly be attributed to the presence of concrete barrier rails on the bridge superstructure. Although, these barriers are designed to be non-composite a degree of composite action still occurs since reinforcing bars are typically continued from the girder in to the barrier rails. Although, the barrier rails are made discontinuous at certain intervals, the sections that bond with the girder concrete allow for added stiffness in the fascia girders. The presence of concrete barrier rails can cause the joint distress by exacerbating the relative displacements between the fascia girder and the adjacent girder. Overall, a very poor load transfer could be observed in the adjacent girders in ARB.

4.2.2. Transverse Deflection in ARB

The variations in transverse direction of the super structure are presented in Figure 129, Figure 130, Figure 131, Figure 132, Figure 133 and Figure 134.
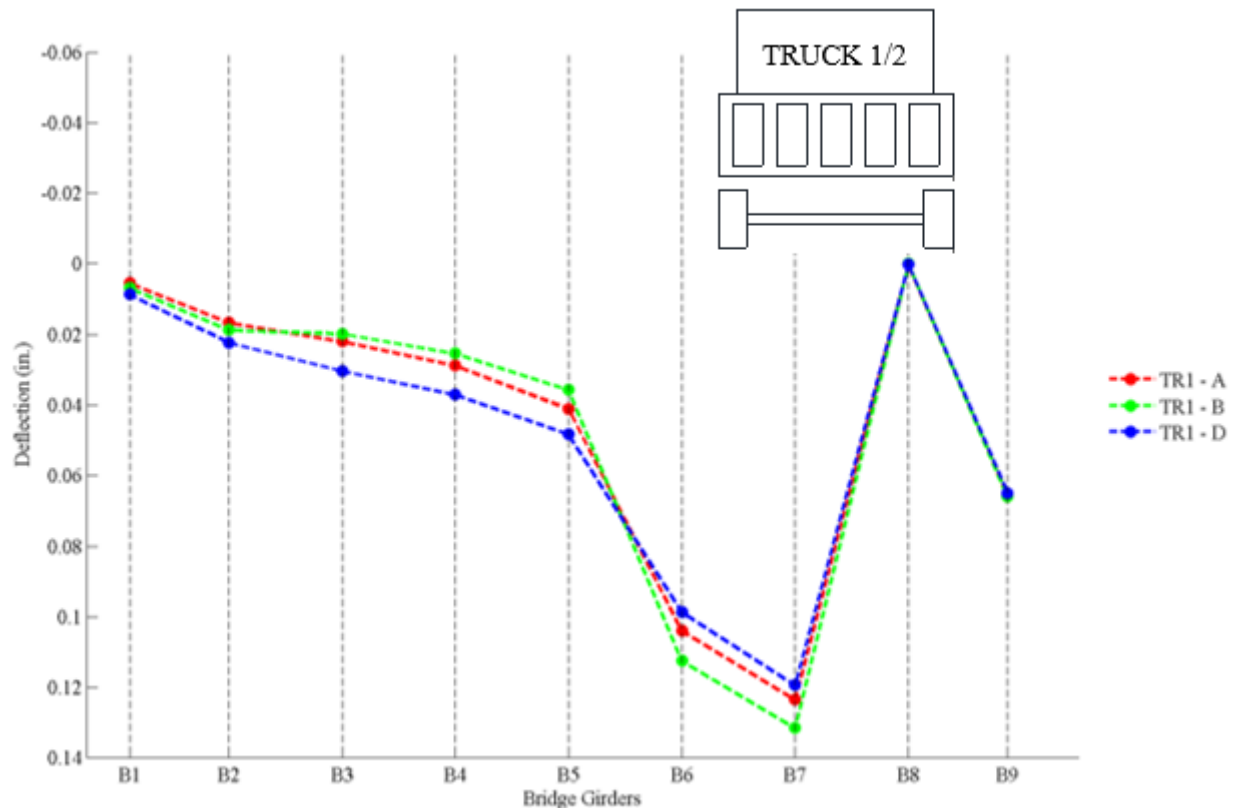
Figure 129: Transverse variations in girder deflections for all reported truck passes in Run 1.
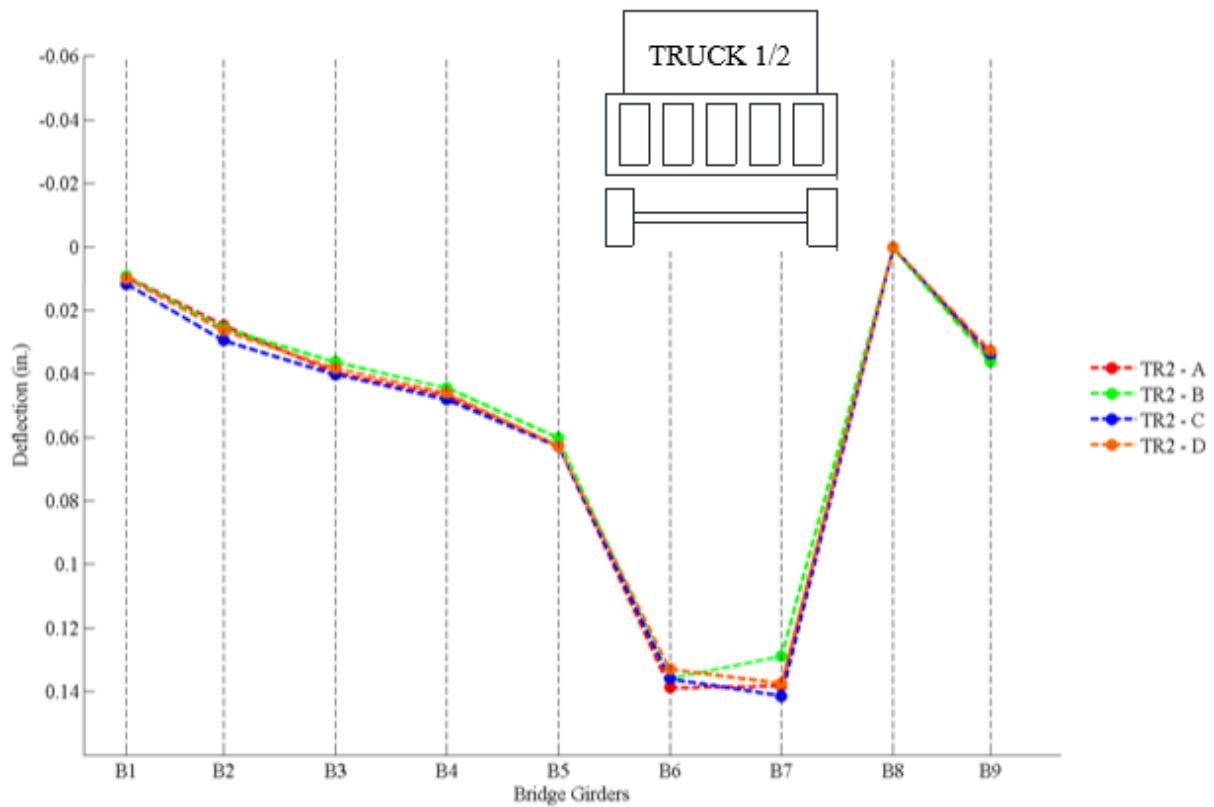
Figure 130: Transverse variations in girder deflections for all reported truck passes in Run 2.
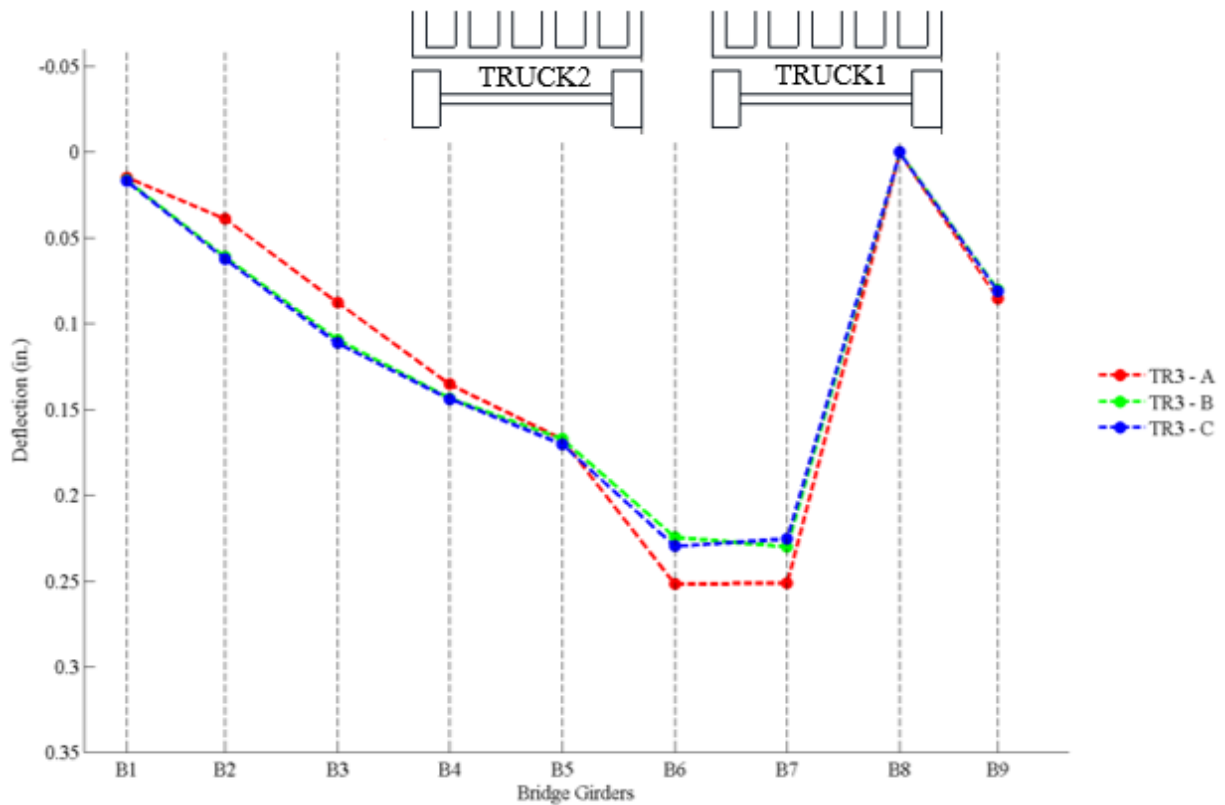
Figure 131: Transverse variations in girder deflections for all reported truck passes in Run 3.
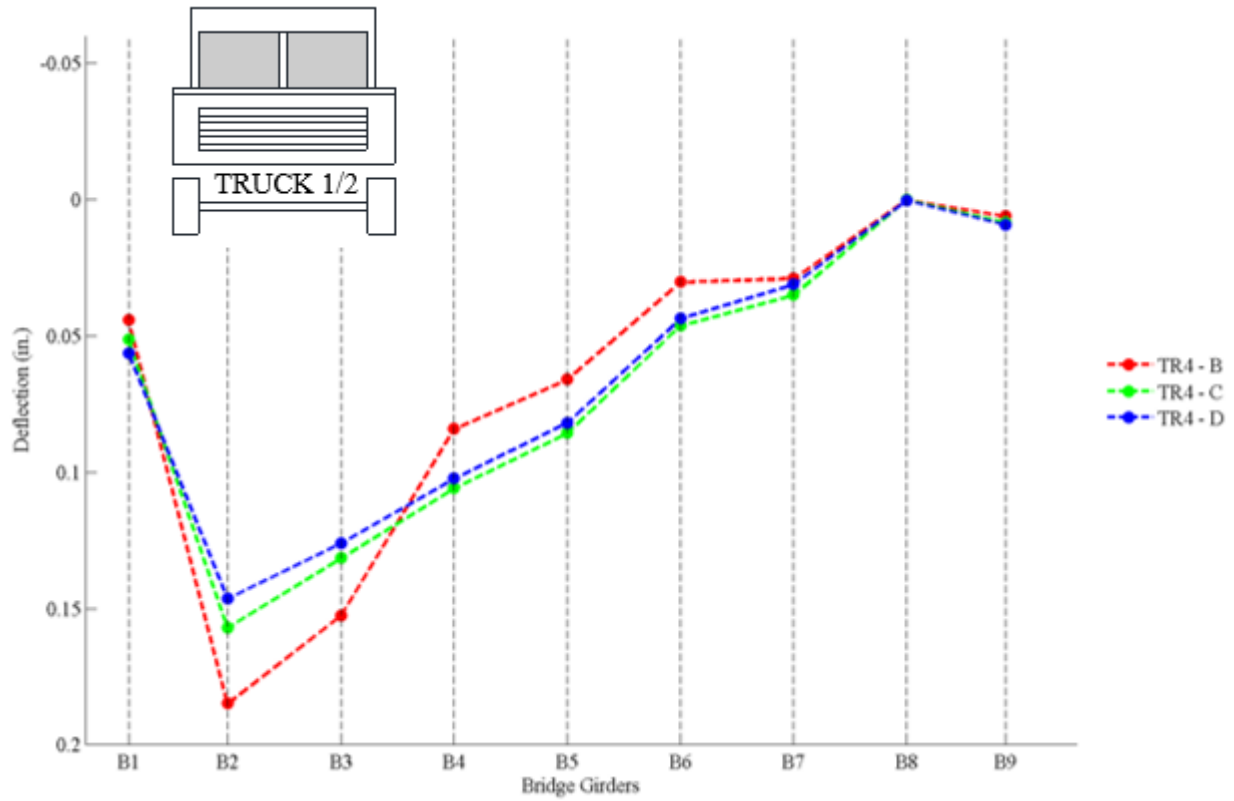
Figure 132: Transverse variations in girder deflections for all reported truck passes in Run 4.
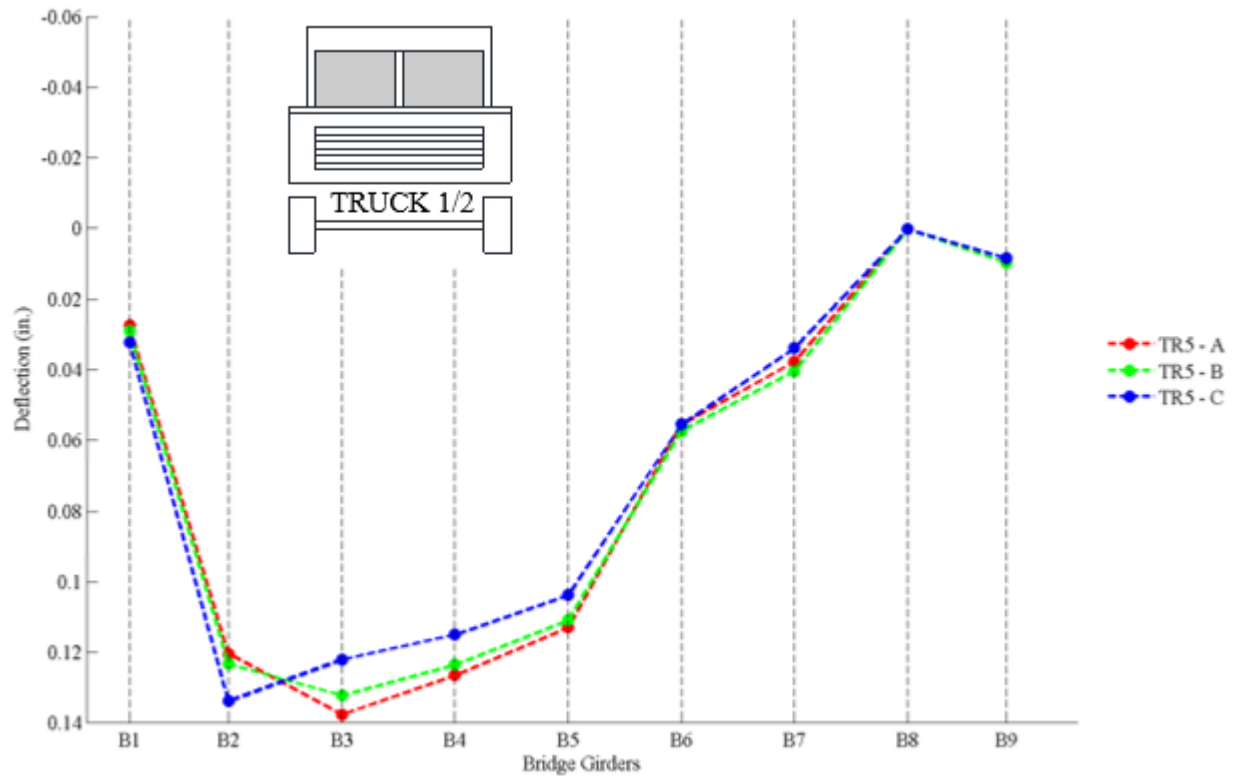
Figure 133: Transverse variations in girder deflections for all reported truck passes in Run 3.

131
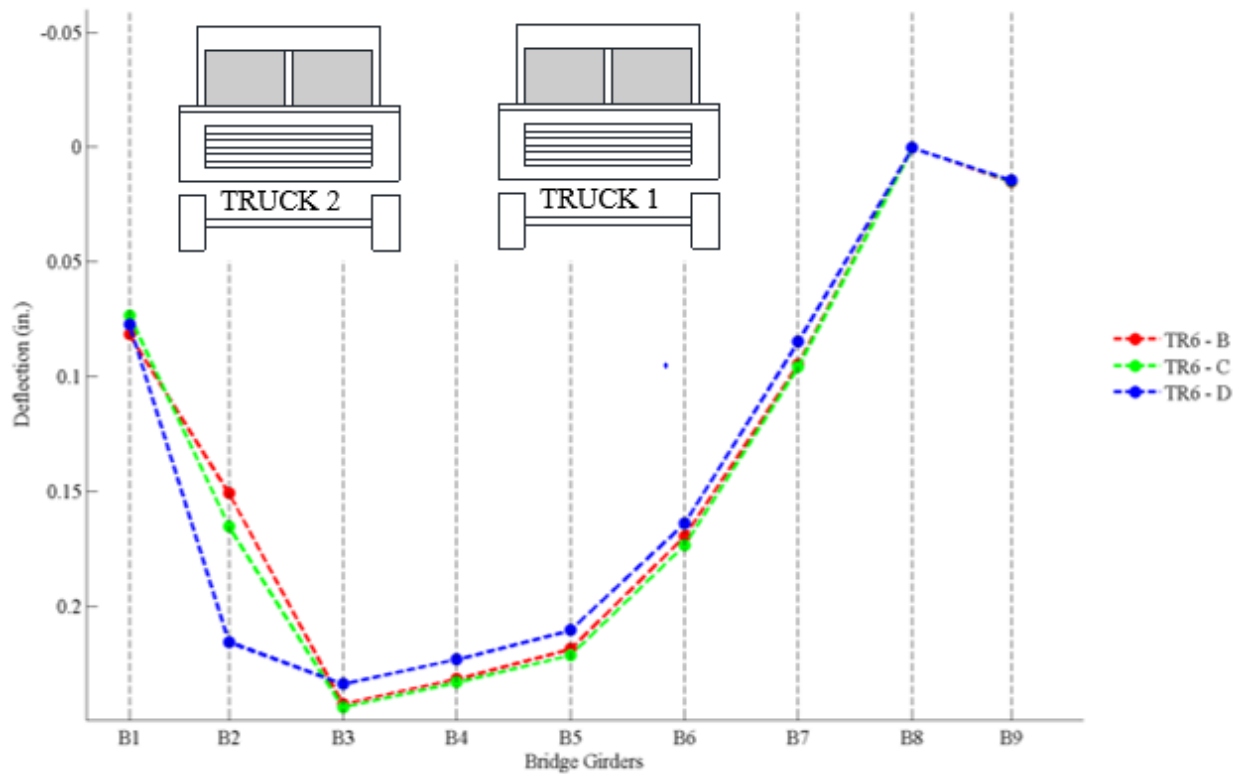
Figure 134: Transverse variations in girder deflections for all reported truck passes in Run 3.

The deflectometer on girder B8 did not work in these tests and hence displayed a zero response for all the test runs. However, observations about transverse deflection variation could be made from the remaining instruments. The behavior as described in the strain distributions can also be seen in the deflections. The girders in the load paths displayed higher deflections than those in the non-loaded path indicating severe joint deteriorations.

4.2.3. Relative Displacements between Adjacent Girders in ARB

The vertical and horizontal displacements between adjacent girders were measured during the diagnostic test as shown in Figure 37 and Figure 38 respectively. The data was plotted as an influence line of relative displacements between adjacent girders. The data for vertical displacements was not useful since the LVDT plungers of the vertical LVDTs would remain stuck thereby recording no response or at best a partial response. A typical partial response that was recorded by these LVDTs is shown in Figure 135.
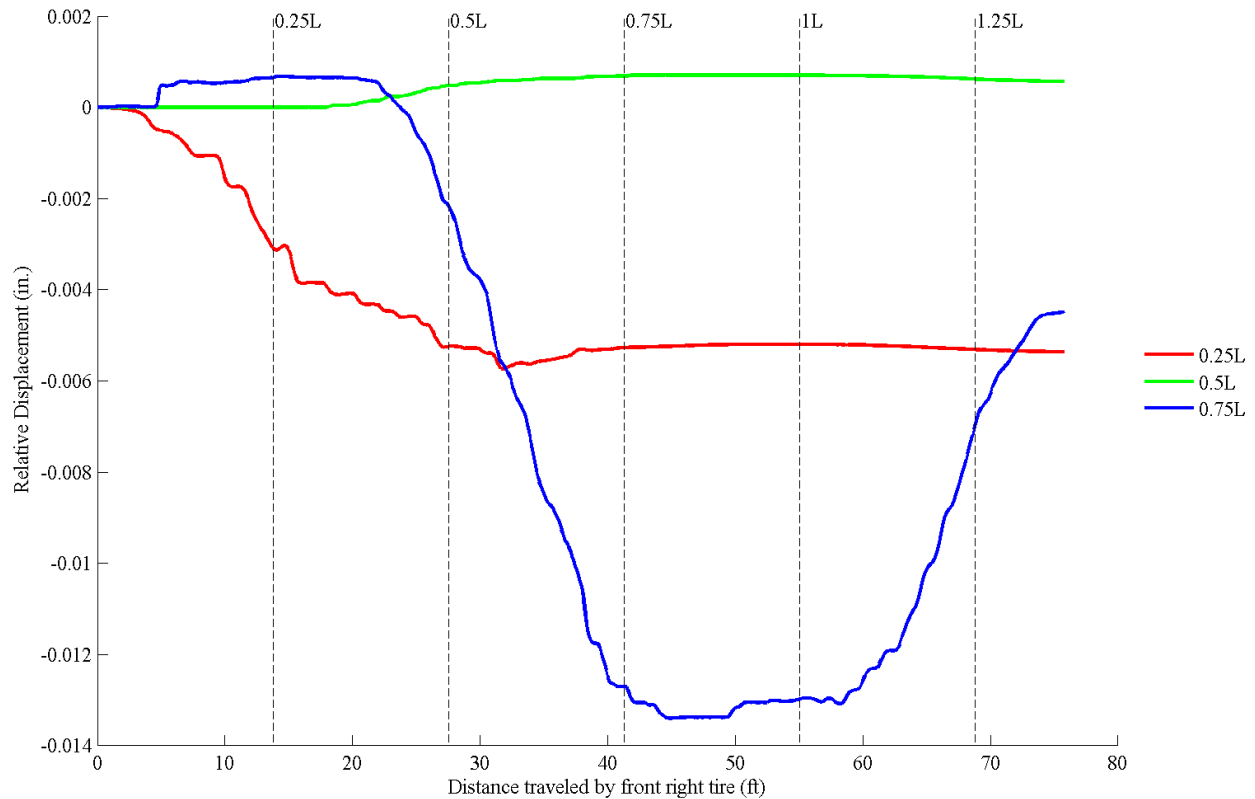
Figure 135: Partial response recorded by vertical LVDTs.

Typically, the LVDT plungers would compress to some displacement and then recover only a partial amount of extension after the removal of truck load (as shown by 0.25L and 0.75L traces in Figure 135). Therefore, the next test run response would then be flat (as seen for the 0.5L trace in Figure 135) since the plunger was not in contact with the target. Therefore, useable data was not obtained from these instruments.

On the other hand, the horizontal LVDTs did not have the same issues. The typical plots for horizontal displacements when truck was in proximity to the instrumented joints are shown in Figure 136 and Figure 137.

It can be observed that a constant horizontal displacement was seen as a response to Truck Run1 in which the truck tires were on the opposite sides of the instrumented joint. A smaller response was expected at the 0.25L and 0.75L since those locations were closer to the supports. However, the equal response indicated that the girder ends also rotate transversely even when two bearing pads were used to support the beam, one bearing pad under each web.

133
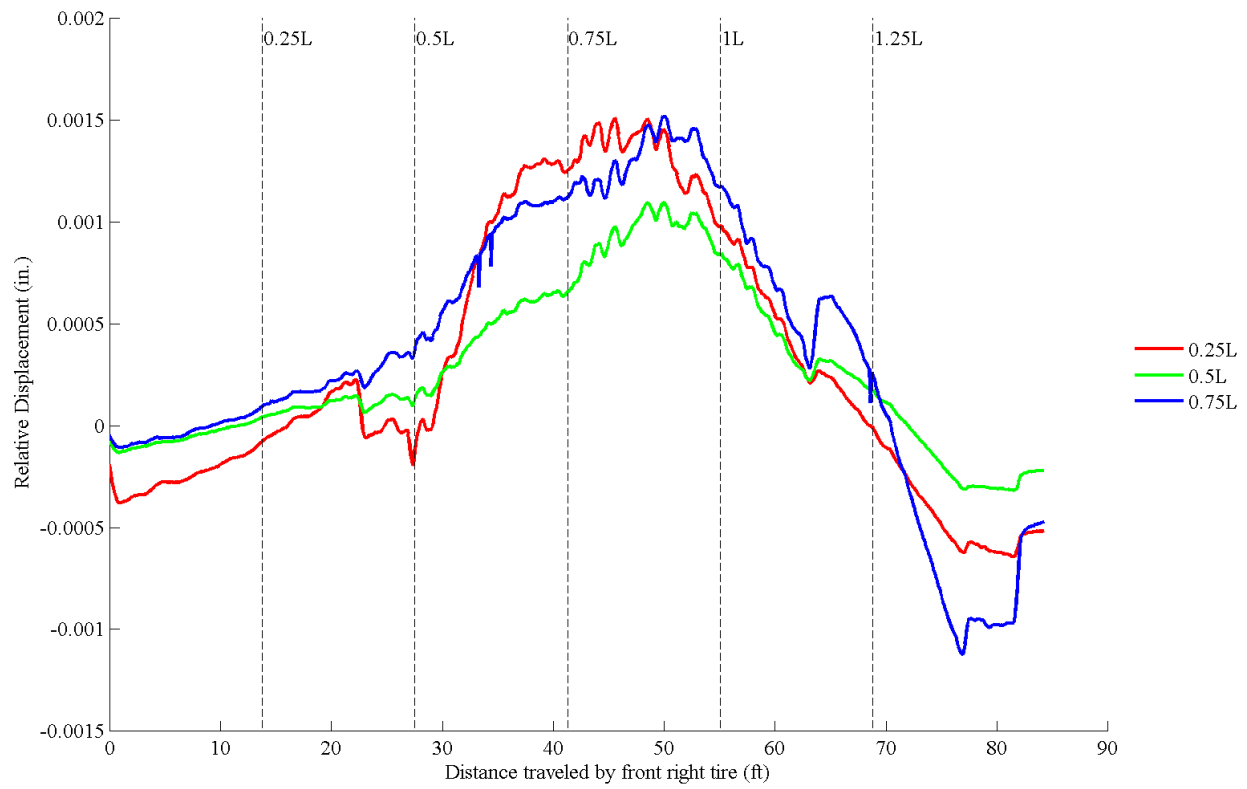
Figure 136: Typical horizontal displacement response for Run 1.
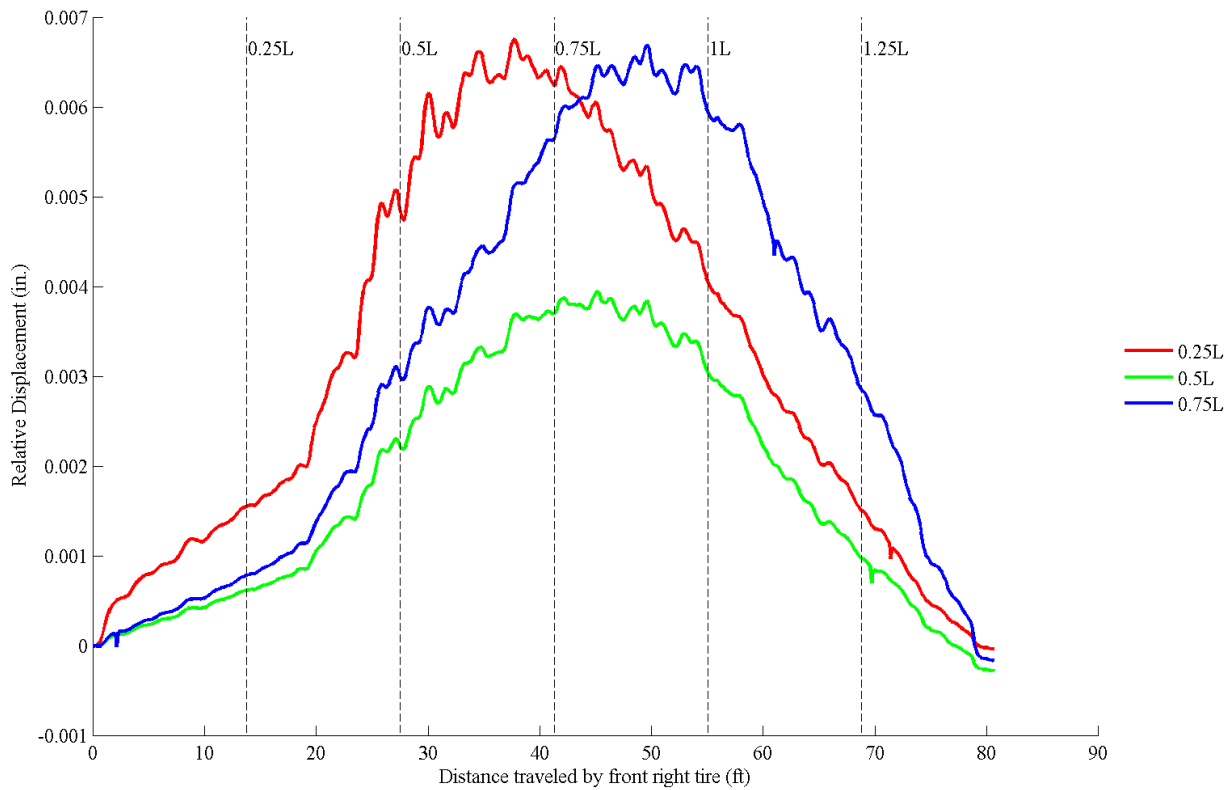
Figure 137: Typical horizontal displacement response for Run 2.

134

Moreover, the response at 0.25L and 0.75L was higher than that at 0.5L for the Truck Run 2, in which the truck was driven in close proximity on one side of the joint as shown Figure 56.
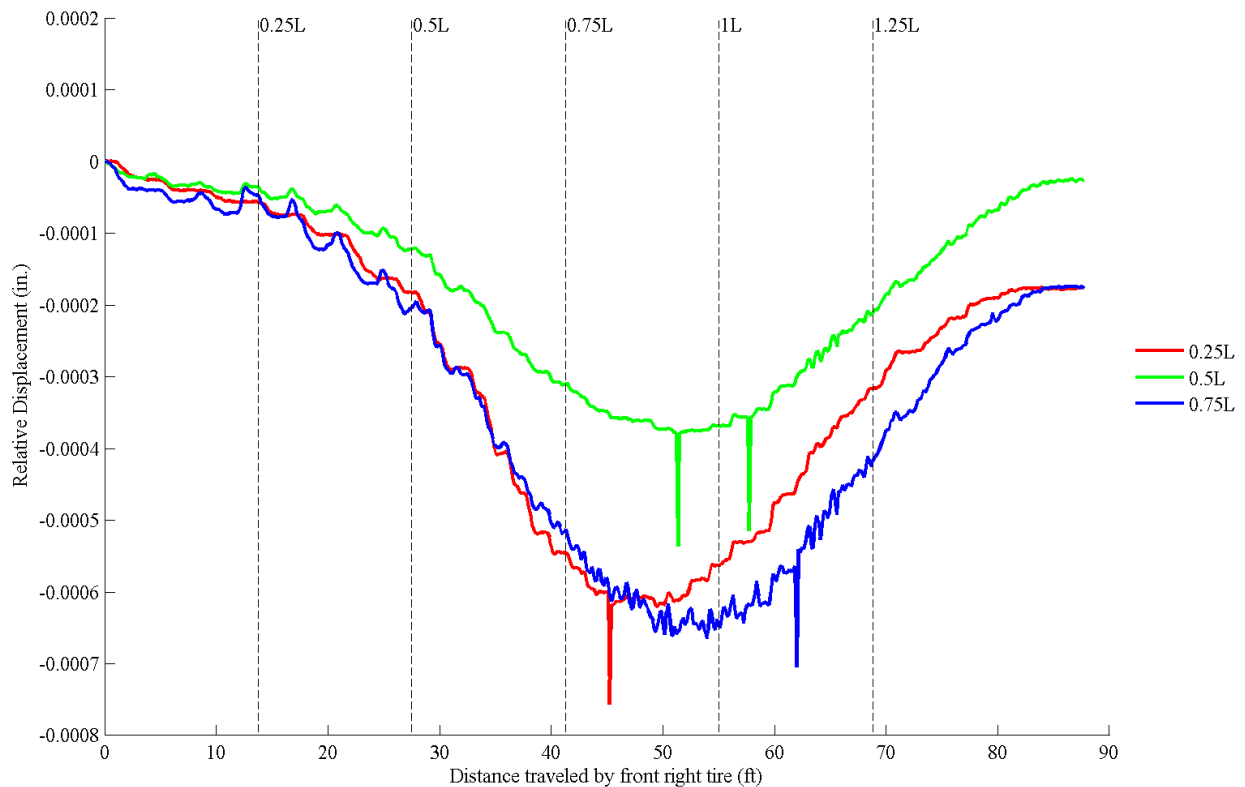
Figure 138: Typical horizontal displacement response for Run 5.

With the trucks placed in the eastbound lane the nature of the gap displacement changed as seen in Figure 138. With the trucks placed in the westbound lane the gap between the adjacent beams reduced. Therefore, for the joints in the unloaded path, the tension is induced at the top of the joint.

4.2.4. Girder Distribution Factors from ARB Test

The distribution factors for the ARB diagnostic test were calculated as per the methods described in Section 4.1.4.2. Similarly, the GDFs calculated from experimental data were compared against the AASHTO LRFD specifications. In the ARB, the effect of barriers on the GDFs was studied by calculating section modulus of the fascia girders with and without the barrier. The barrier area was converted into an equivalent rectangular area for the ease of calculations. All the rounded corners on the barriers were considered as sharp corners. The distance of the center of gravity (CG) of the barrier cross-section was determined from the top of the beam. The equivalent rectangular area of barrier was then calculated with a depth that was twice the distance of the CG, so that the radius of gyration would be the same as that of the actual barrier rail and the moment of inertia (MI) of the girder section would be realistic.
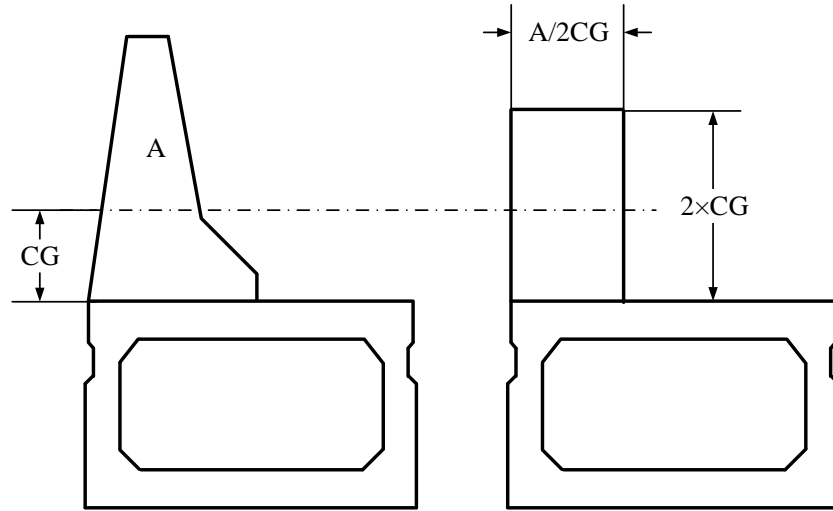
Figure 139: Equivalent area of barrier for calculating the section modulus for fascia girders.

4.2.4.1. GDFs by AASHTO method − ARB

The ARB could be classified as a category F structure if perfect transverse connection was assumed and also as category G structure assuming that the adjacent girders were subjected to the same level of vertical displacements but the boxes were free to rotate independently. Practically, the category G is more applicable to the ARB since relative horizontal displacements were measured between the bridge girders. However, the assumption of same vertical displacements would still be incorrect on the basis of the deterioration observed in the joints of the bridge. The GDFs for category F superstructure assumption were calculated as shown in Section 4.2.4.1. The GDFs for a category G superstructure were calculated as follows,

Distribution factors, $GDF = \dfrac{S}{D}$ *Equation 18*

Where, $D = 11.5 - N_L + 1.4 N_L (1 - 0.2C)^2$ when, $C \leq 5$ *Equation 19*

And, $D = 11.5 - N_L$ when, $C > 5$ *Equation 20*

Here, $C = K\dfrac{W}{L} \leq K$ *Equation 21*

Also, $K = \sqrt{\dfrac{(1 + \mu)\, I}{J}}$ *Equation 22*

Finally,
S = center to center girder spacing (ft), assumed as 4 ft
W = edge to edge width of bridge (ft), 34 ft
L = span length (ft), 55 ft
N_L = number of design lanes, 2 lanes assumed.

μ = Poisson's ration, μ = 0.2 assumed for concrete.
I = Moment of inertia (in.^{4})
J = St. Venant's Torsion (in.^{4})

The GDFs calculated by both the methods are presented in Table 14.

Table 14: Distribution factors by AASHTO LRFD formulae.

Superstructure Category	Distribution Factors	Single Lane	Multiple Lanes
F	Interior Girders	0.468	0.362
	Exterior Girders	0.542	0.391
G	Interior Girders	0.421	0.421
	Exterior Girders	0.488	0.455

4.2.4.2. Experimental Calculations of GDFs – ARB

The methods described in Section 4.1.4.2 were used to calculate the distribution factors from experimental results. The strain values were used to calculate the GDFs from the ARB data. The deflection values were not used since the deflectometer on girder B8 did not record any response and averaging the value of girder B8 from the basis of girder B7 and B9 deflection values would not be sensible considering the amount of deflection imparted on individual girders that were in the load paths. The results of the distribution factors calculated from strain data and comparison with AASHTO calculations are presented in Figure 140 and Figure 141 for single lane configurations and multiple lane configurations respectively.
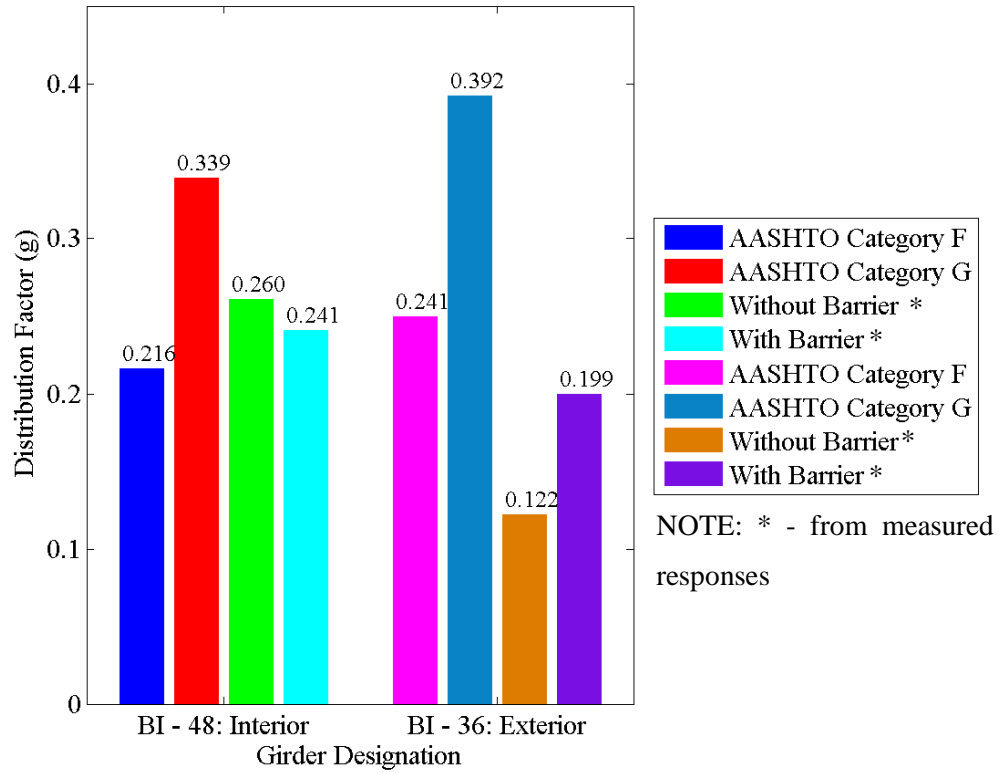
Figure 140: GDFs for single lane configuration.
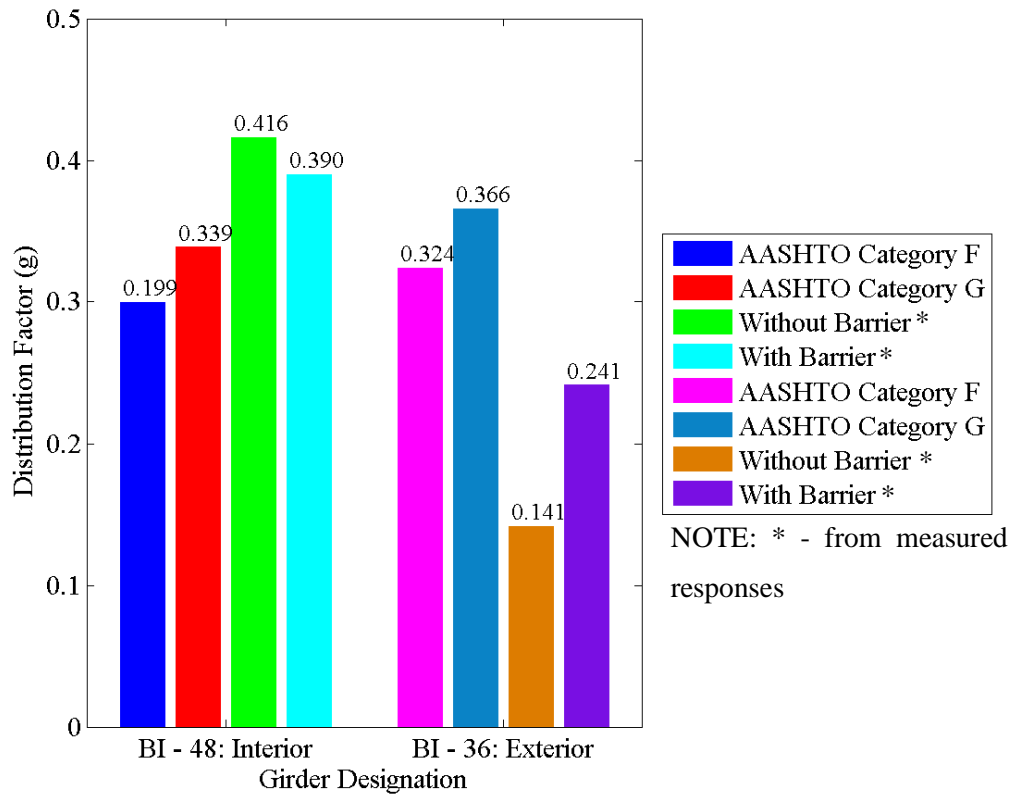
Figure 141: GDFs for multiple lane configuration.

138

In above bar charts the comparison between the GDFs calculated from AASHTO and the experimental results is shown. It can be observed that for most part the values of GDFs calculated from strain for interior girders are higher for single and multiple lane configurations as compared to category F factors regardless of the contribution of the barriers. The single lane GDFs from strain were lower than the AASHTO design values for a category G structure for the single lane configuration. The GDFs from strain calculated for the multiple lane configuration were much higher than the AASHTO values for category F and G classification regardless of barrier contribution. The multiple lane configuration tested on the ARB was a situation that would not typically occur on the bridge since there was a single lane of travel in each direction. On the other hand, if the interior girders were designed as per category F then the joint failures prevented the assumed load distribution from occurring and thereby exposing the girders to a potentially dangerous situation when exposed to loads closer to the design loads.

The GDFs for the fascia or exterior girders calculated from strains were smaller than the AASHTO values. The GDFs calculated with the assumption of barrier contribution were significantly higher than the assumption of barrier not contributing. Regardless of the truck loading configurations the load being transferred into the exterior girders would not reach the level of load to cause a failure. However, the assumption of barrier not contributing to the bridge superstructure is untrue. The presence of concrete barrier rail changes the load distribution of the ABBB superstructure as described in Kasan and Harries (2013). Moreover, the behavior of the fascia girder changes due to the presence of a connection between the girder and the concrete barrier. The composite action, possibly partial, causes biaxial flexure on the girder cross-section since the neutral axis of the section rotates and is inclined with respect to the transverse axis of the girder. Unsymmetrical bending is not considered in design and consequently the girder capacity is overestimated for fascia girders as per Kasan and Harries (2013).

4.3. Summary of Diagnostic Test Results

The diagnostic tests were performed to study the behavior of in service ABBB bridges. The bridges with varying levels of deterioration were instrumented and the response of each bridge to trucks with known loads was recorded. The instruments used in these tests were used to capture various aspects of bridge behavior. However, the above discussion was kept strictly focused on the transverse bridge behavior. The diagnostic tests served to provide an understanding into the transverse behavior of in service ABBBs.

4.4. Finite Element Analysis of Diagnostic Test

The ARB was further studied with the use of FEA. The in-situ behavior of the bridge was studied through the field tests. The bridges instrumented and studied in the diagnostic tests had deteriorated joints.

139

The study of an ABBB system without joint deterioration was sought in order to improve the understanding of the bridge behavior. The ARB was modeled in ABAQUS and the truck loads imposed on the bridge were simulated using tire patches. The response of the bridge model was compared with the response recorded during the diagnostic tests to observe the effect that the deterioration has on the overall bridge behavior.

4.4.1. Description of the FEA model

The ARB was modeled in ABAQUS 6.13 using 3D solid elements. The elements used in the models are designated as C3D8R in ABAQUS. The C3D8R term stands for a general purpose, 3D continuum elements with eight nodes, reduced integration and hourglass control as per ABAQUS (2013). The C3D8R elements possess three translational degrees of freedom (DOFs) at each node. Considering the overall size of the bridge model elements with reduced integration were used to save on computational effort. The C3D8R elements consist of a single integration point, which is located at the centroid of the element. The usage of a single point of integration produces an element that is able to resist constant strain states but it also has zero energy modes corresponding with bending deformation as per Cook et al. (2001). These zero energy deformation modes are also referred to as spurious modes or "hourglass" modes by Cook et al. (2001), ABAQUS (2013) and Koutromanos (2014). The modes associated with flexure cause the element to deform in a manner that the strain energy at the integration point is zero. Therefore, the reduced integration used in these elements produces a stiffness matrix that is unable to resist the deformation modes associated with flexure. There are 12 spurious deformation modes in the eight node solid elements with a single integration point as per Cook et al. (2001). Some of these spurious deformation modes are reported in Flanagan and Belytschko (1981) and Koutromanos (2014).

Hourglass control is provided by ABAQUS by default when using the reduced integration linear elements that alleviates the distortion due to spurious zero energy modes. The hourglass control entails the introduction of artificial stiffness to resist the spurious deformation modes. ABAQUS uses hourglass control schemes as derived by Flanagan and Belytschko (1981) for linear problems. Also, the documentation recommends the prevention of formation of stress concentrations by spreading out point loads and boundary conditions over larger areas. The use of a fine mesh is recommended by the ABAQUS documentation as it further alleviates the probles associated with hourglassing. Generally, the reduced integration linear isoparametric elements with hourglass control are able to accurately model the flexural behavior when used with the hourglass control as per ABAQUS documentation.

The bridge model itself was constructed from a single part consisting of girders, joints and the barriers. The individual components such as girders, joints and the barriers were then defined by partitioning the single part into individual components. The original cross-section of the entire bridge model is shown

in Figure 142. The cross-section was sketched in ABAQUS using the plans provided by VDOT and the cross-section was extruded for the full span of the bridge.

Figure 142: Cross section of ARB model.

The voids in the box beams were included for the sections between internal and end diaphragms. The partitions were sketched on one end of the bridge model using the dimensions provided in the bridge plans and extruded for the complete span of the bridge. The extruded partitions created separate sections within the monolithic part and each section was assigned properties corresponding to the material used in the bridge. The use of partitions is shown in Figure 143.
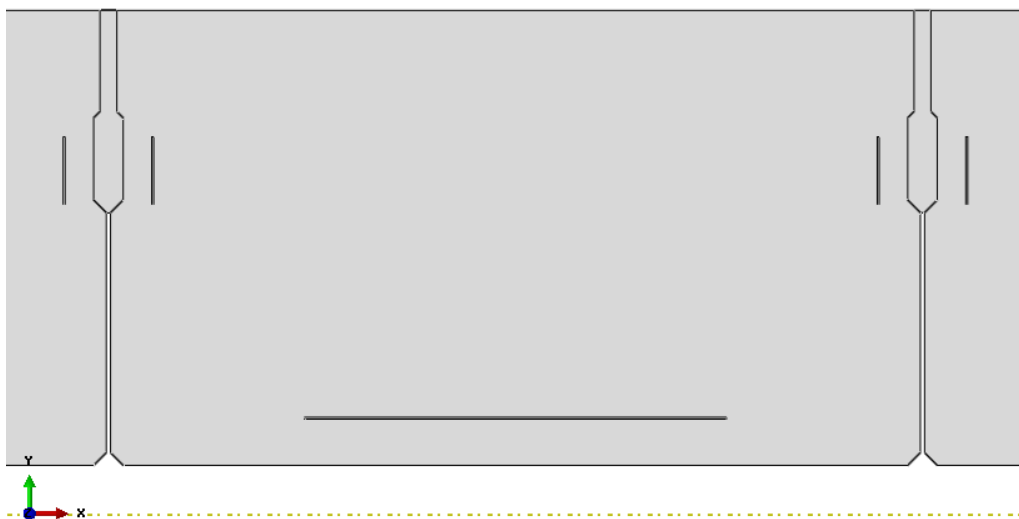
Figure 143: Partitions in FEA model of ARB showing joints and steel areas.

The steel prestressing was included in the ARB model as an equivalent area. Since a linear elastic approach was taken to the ARB model the effect of modeling actual strands as truss elements and the effect of using equivalent areas was considered to be the same. A simple analysis was performed with a single beam and the results of the two approaches were compared. The results did not show any significant difference. Hence, the equivalent steel areas approach was adopted as it saved time in terms of modeling each strand and embedding it within the concrete model. The area of prestressing steel was calculated from the number and size of strands. The corresponding center of gravity of the strand pattern was also calculated. The equivalent area of steel was modeled such that the area of steel in the individual webs and flange

remained the same as that of the actual bridge. The center of gravity of the equivalent area of steel also was the same as that of the actual strand pattern.

The effect of prestress was not explicitly included in the model. The effective prestressing force and its associated camber had already occurred prior to the placement of joints and the application of truck loads via the diagnostic test. The effect of camber was nullified in the diagnostic tests as the sensors were attached to the bridges long after the occurrence of camber and placement of joints. Therefore, the actually measured deflections and strains in the diagnostic tests pertained purely to the imposed truck load effect. Hence, modeling the prestressing force and imposing a camber in the ARB model would have provided incorrect results. Essentially, the steel areas added stiffness to the beams in the ARB model.

The most important aspect of the model was the joints. These were the main focus of the entire investigation. The discretization of the joint into smaller elements was carefully studied prior to application in the investigation. The shape of the joint was such that purely quad elements could not be used. The shape of the keyway potentially could give rise to distorted elements. On the other hand, providing very small elements caused stress concentrations at the joint. Hence, the joints were further partitioned to prevent distortions. These partitions are shown in Figure 144. By making these partitions the elements could then be assigned as quad and non-quad (hex) areas within the joint.
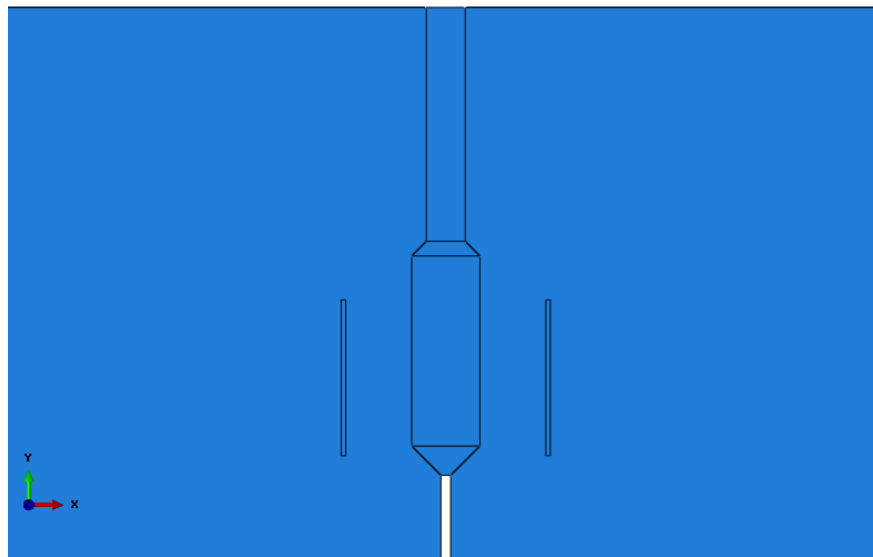
Figure 144: Joint area partition.

The partitioned joint was then further discretized in to smaller elements. The element size was based on the prevention of distortion as well as avoiding stress concentrations due to the use of very small elements. The joint discretization used was as shown in Figure 145.
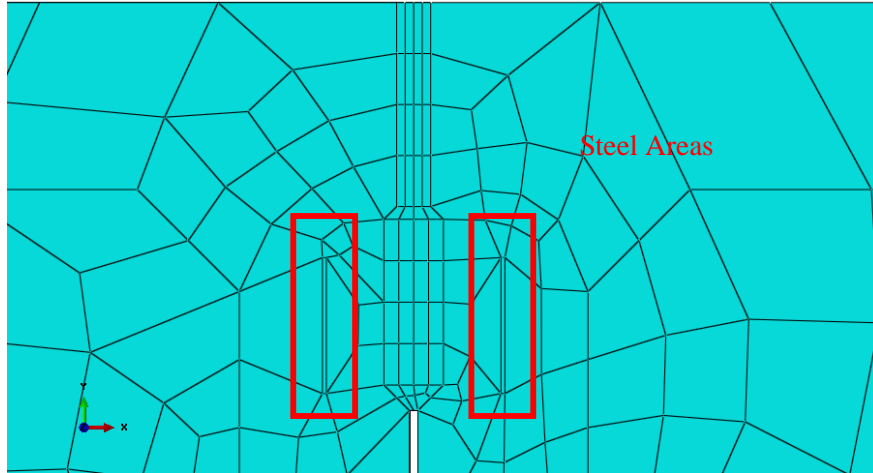
Figure 145: Discretization of joints in smaller elements.

For the analysis of the ARB model, the joint discretization was not the most important since the overall global effect of the truck loads was compared. The state of stress in the joints was not the main focus of the ARB model. However, the joint was thus discretized for the sake of consistency between the ARB model and the model of the full scale bridge that was to be used for comparison with the sub-assemblage models.

4.5.   Comparison of Diagnostic Test with FEA

The trucks were placed on the ARB model in the same orientations as the actual diagnostic tests. The front right tires of the truck were placed at a distance of 0.1 times the span and the response was compared to the results of the diagnostic tests. The results presented here pertain to comparison between the maximum responses recorded in the diagnostic tests. These responses were recorded with the truck positioned roughly at the location which would cause the absolute maximum bending moment along the longitudinal span of the bridge. Therefore, the trucks in the ARB model were also located at the position which analytically produced the absolute maximum bending moment in the longitudinal direction. The comparison of the FEA and the diagnostic tests is presented in Figure 146 through Figure 157. The FEA was performed with the truck(s) placed in the east bound lane only (Runs 1 through 3). Since, the structure was symmetrical and the analysis was linear elastic, the FE response for the truck loads in west bound direction was the mirror image of the response of the truck loads in the east bound lane.

The magnitudes of the strains and deflections for the ARB model were selected from the nodes closest to the actual location of the sensors. Therefore, the girder deflection values were selected from the exact centerline of the girder whereas the strain values were selected from nodes offset by 12 in. from the center of the girder.

143

The dimensions of tire patches calculated from Equation 7 and Equation 8 are shown in Table 15. For the purpose of simulation of the quasi-static tests the live load multiplication factor and the impact factor were ignored.

Table 15: Tire patch dimensions and pressure in ARB model.

Tire	Axle Weight (kip)	Truck 1 Tire Patch (in.)		Pressure (ksi)	Axle Weight (kip)	Truck 2 Tire Patch (in.)		Pressure (ksi)
		Width	Length			Width	Length	
Front	14.98	18.725	6.4	0.125	15.94	19.925	6.4	0.125
Rear	34.62*	21.6375	6.4	0.125	33.96*	21.225	6.4	0.125

NOTE: * - Rear axle weight in Table 15 is combined for the two rear axles.

4.5.1. Comparison of girder strains

The strain results for Run 1, 2, 3, 4, 5 and 6 are shown in Figure 146, Figure 147, Figure 148, Figure 149, Figure 150 and Figure 151 respectively. The FEA model predicted a gradual change in strains along the transverse direction. The transvers strain distribution of the ARB model showed that the response lay between the two extremes of strain distribution measured in the diagnostic tests. The two extremes meaning the much higher strains in the girders in the loaded path and the lower strains in the girders in the unloaded path. Overall, the general trend of the two responses, measured and predicted, was similar. The distribution of strains essentially appeared to be the average of the strains measured in the diagnostic tests.
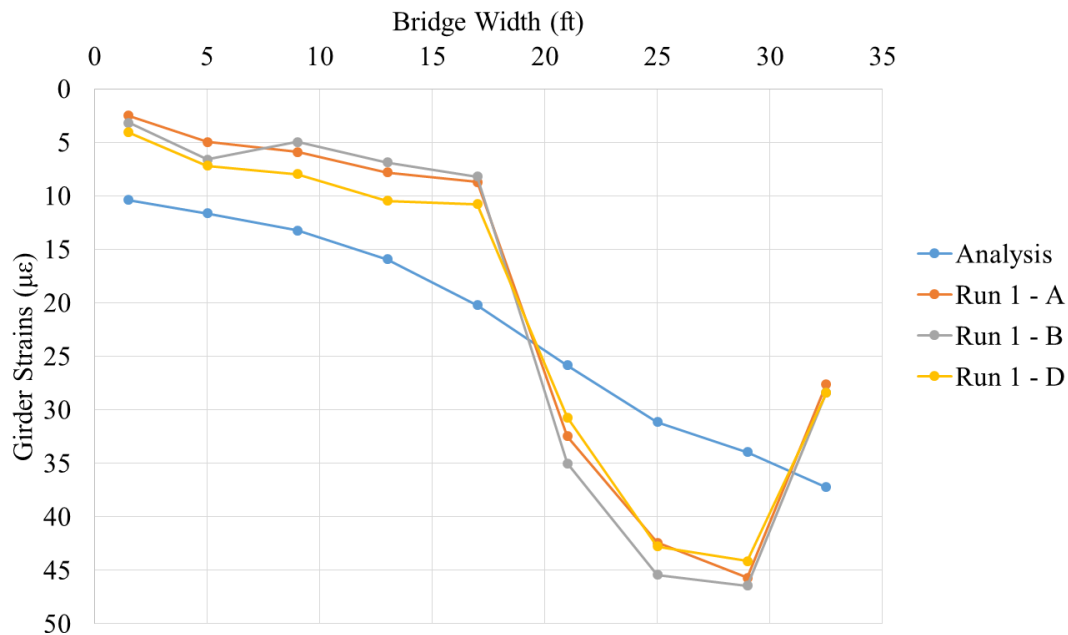
Figure 146: Comparison of girder bottom strains in Run 1.
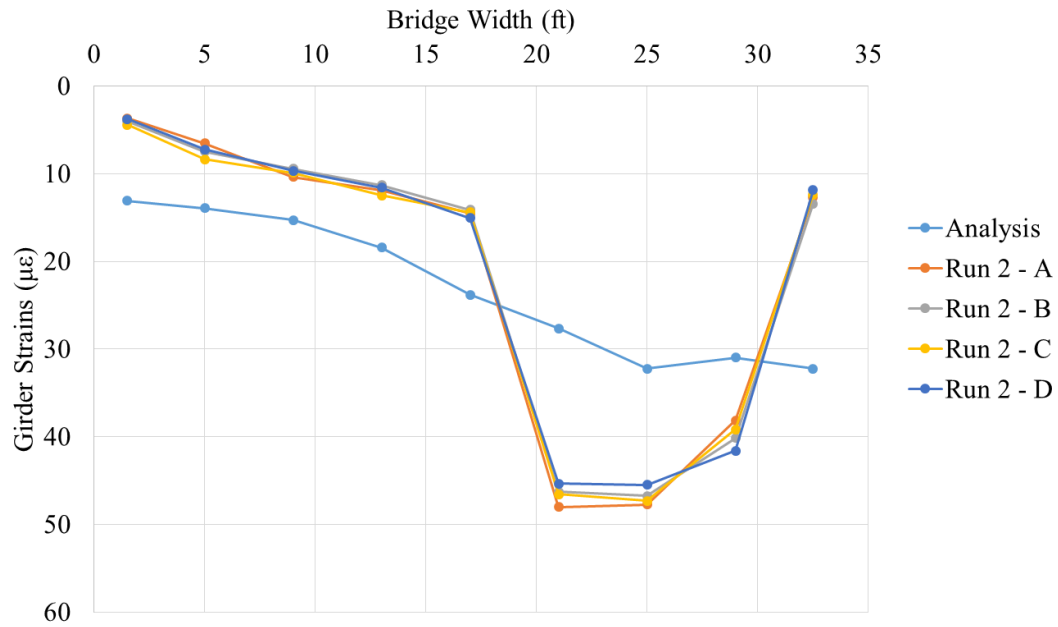
Figure 147: Comparison of girder bottom strains in Run 2.
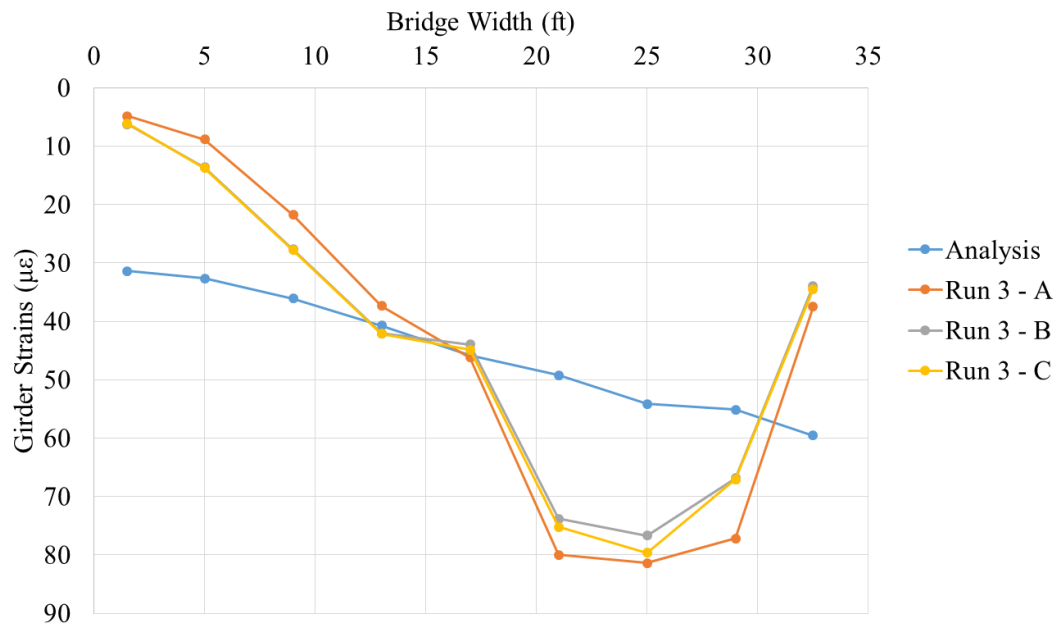
Figure 148: Comparison of girder bottom strains in Run 3.
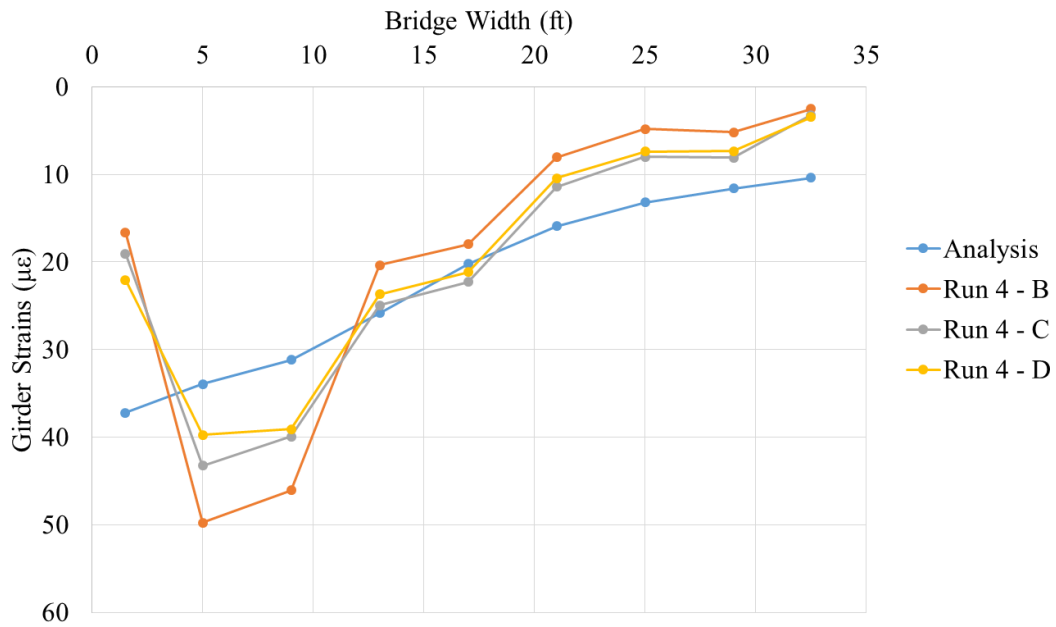
Figure 149: Comparison of girder bottom strains in Run 4.
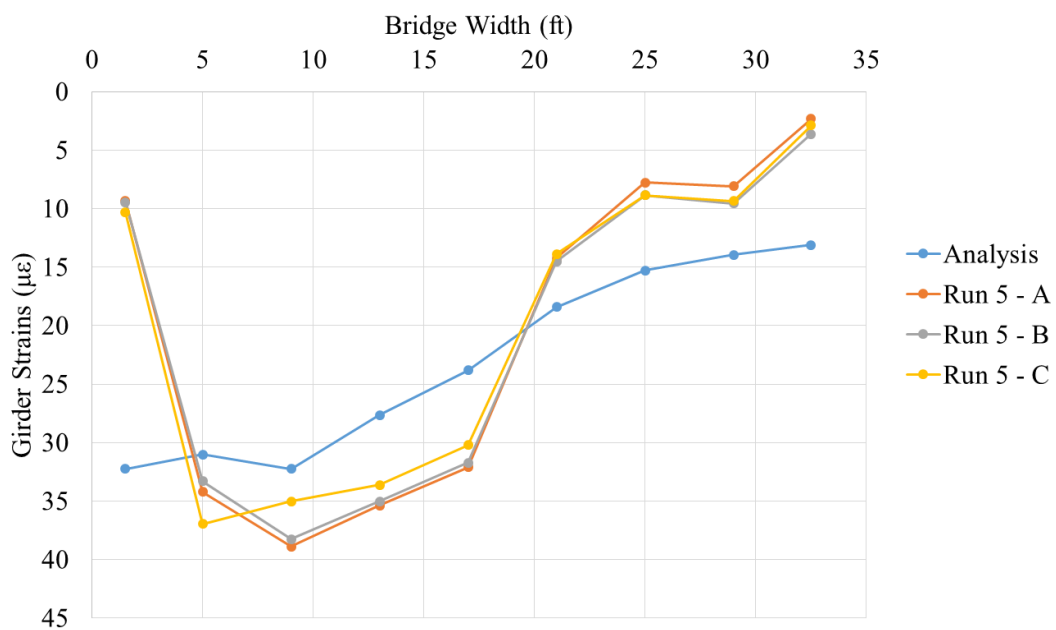
Figure 150: Comparison of girder bottom strains in Run 5.
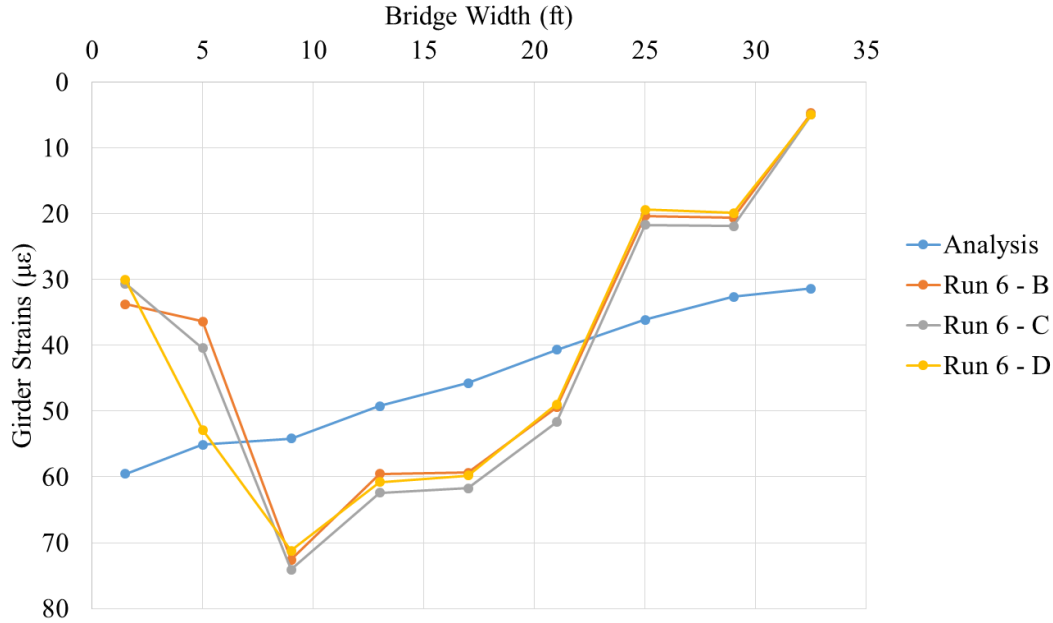
Figure 151: Comparison of girder bottom strains in Run 6.

Additionally, the average value of strains was calculated for both the model response as well as the measured response. Basically, a single average value was calculated from the diagnostic tests per run and for the corresponding FEA response. The responses between the ARB model and the diagnostic tests were expected to be very different due to the great difference in the condition of the joints between the two. The average value represented a condition in which the joints were completely rigid and all the girders shared load equally.

Table 16: Comparison of average strains.

| Test Run | Strain (με) | | Difference (%) |
	FEA	Test Result	
1	22.2	20.9	5.92
2	23.1	21.5	6.93
3	45	43.4	3.52
4	22.2	19.5	12.16
5	23.1	20.3	12.1
6	45	40.5	9.86

The single average value calculated from the strains recorded from the ARB model and that calculated from the diagnostic tests varied from 4 to 7% for the east bound trucks and 10 to 12% for the west bound trucks. The FEA model consistently predicted higher average values than the diagnostic tests.

This indicated that the FEA model was slightly more flexible than the actual bridge. This could be attributed to the assumed boundary conditions and the material properties in the ARB model.

4.5.2. Comparison of girder deflections

The comparison of girder deflections showed a similar trend to that seen in the comparison of the girder strains. The measured values of deflections bounded the values predicted by the ARB FEA model. The general trend displayed by the distribution of girder deflections was similar to that displayed by the measured values. The comparisons of Truck Runs 1, 2, 3, 4, 5 and 6 are shown in Figure 152, Figure 153, Figure 154, Figure 155, Figure 156 and Figure 157 respectively. The comparison of average deflection values is shown in Table 17.
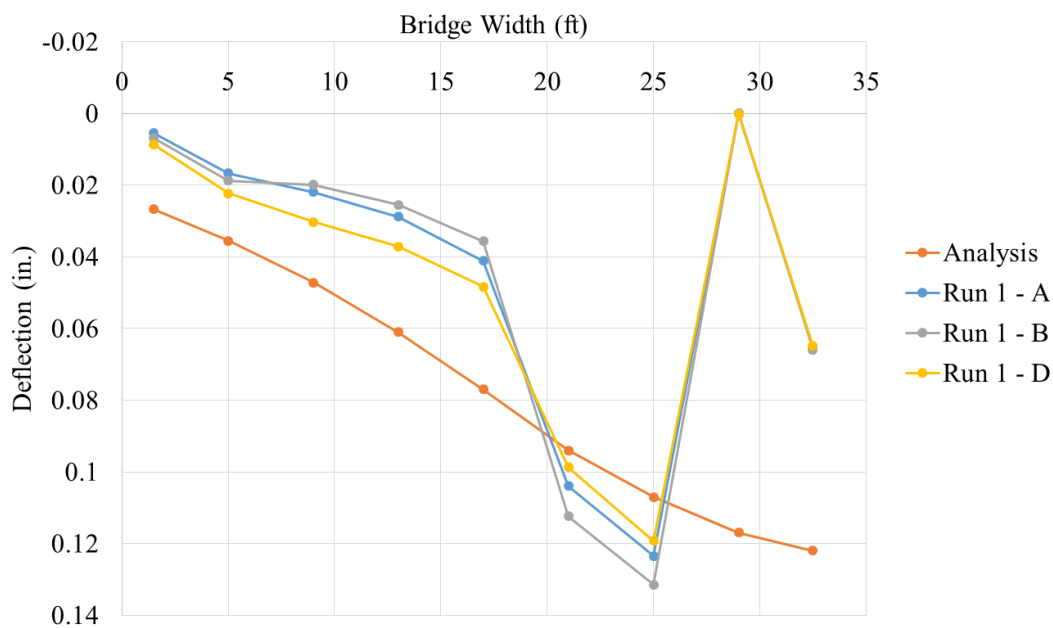
Figure 152: Comparison of girder deflections in Run 1.
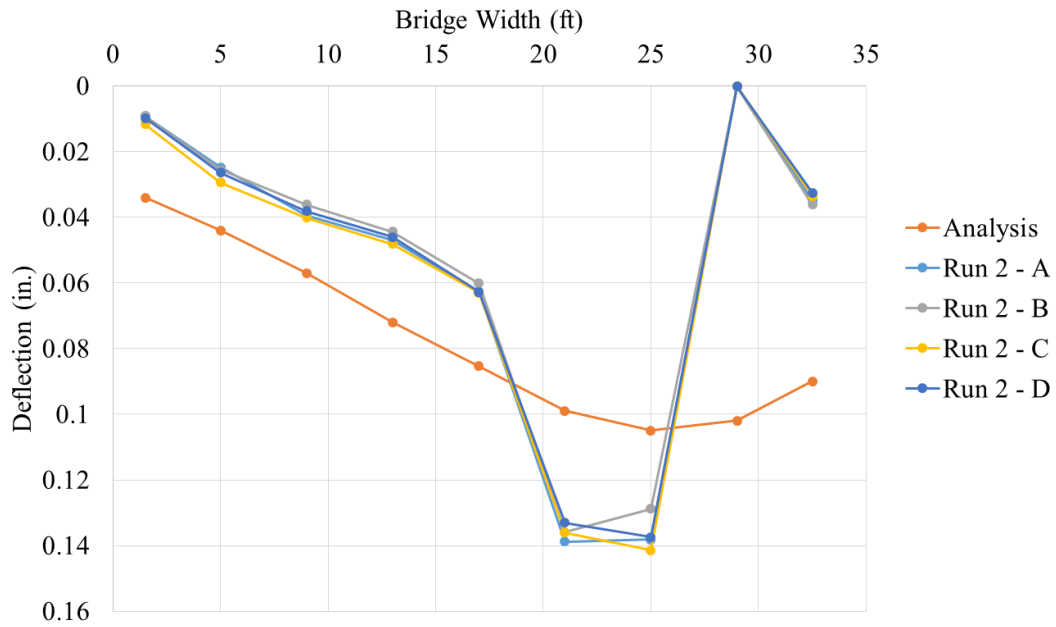
Figure 153: Comparison of girder deflections in Run 2.
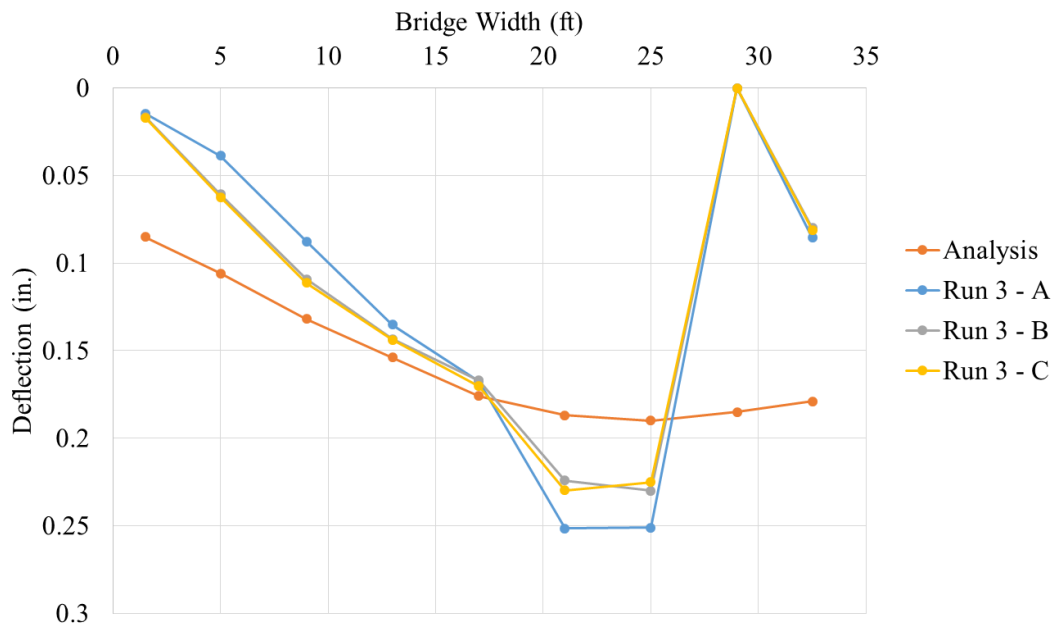
Figure 154: Comparison of girder deflections in Run 3.
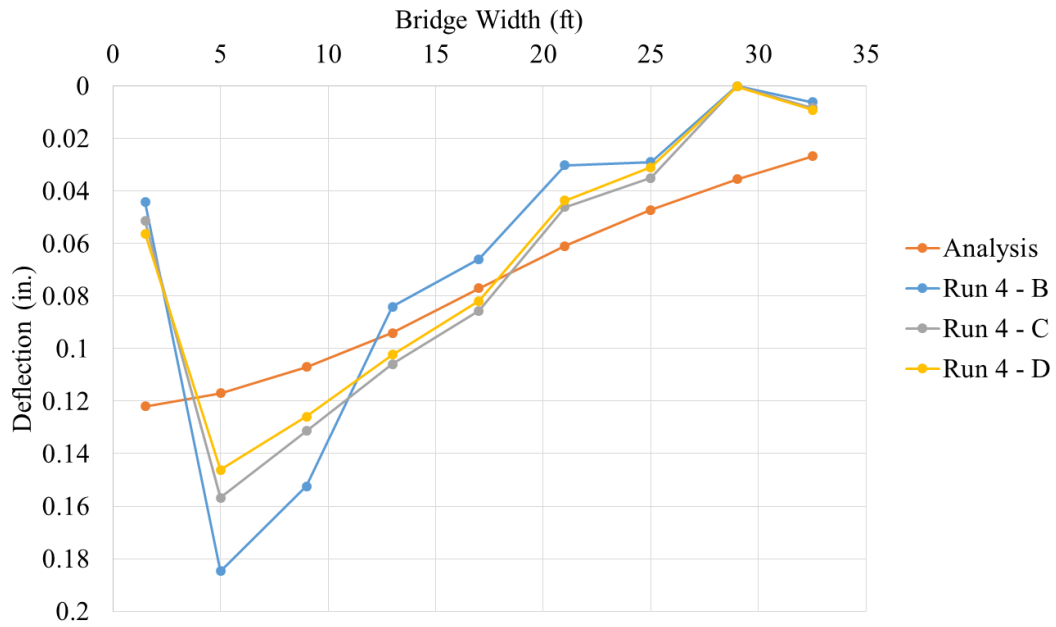
Figure 155: Comparison of girder deflections in Run 4.
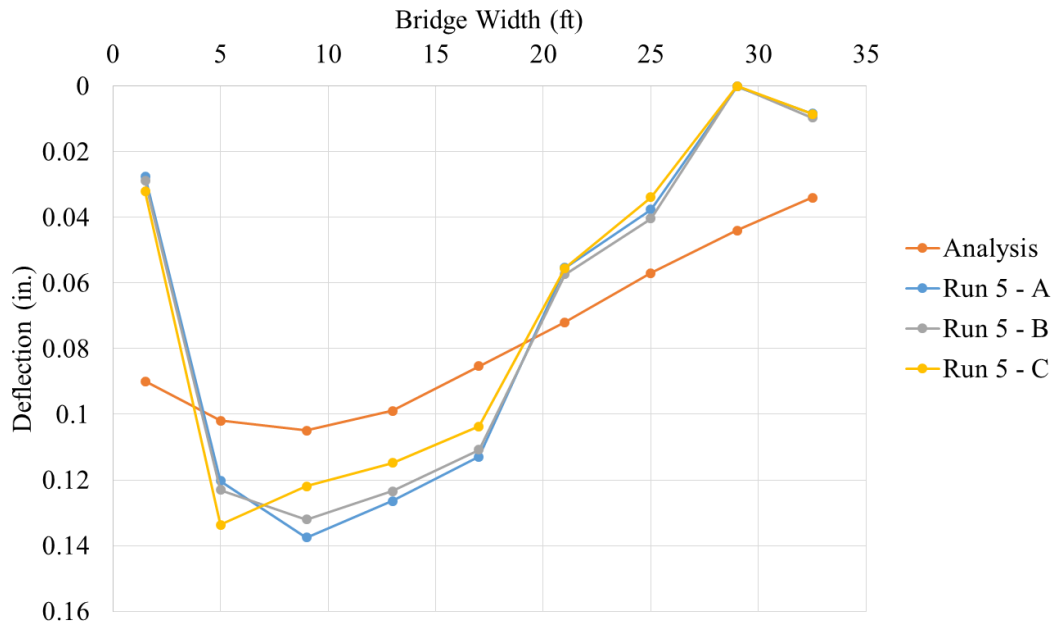
Figure 156: Comparison of girder deflections in Run 5.
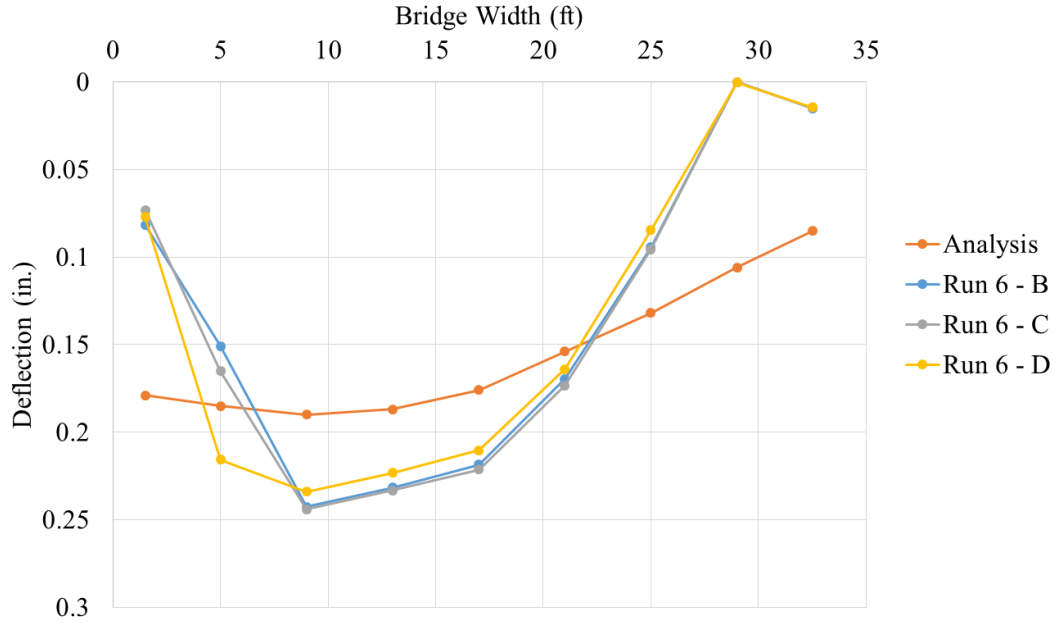
Figure 157: Comparison of girder deflections in Run 6.

The comparison of the average values for deflections showed a much higher difference than the comparison of strains. This difference can be attributed to the fact that one deflectometer did not work during the testing. Therefore, the higher differences were seen for the east bound truck configurations where the significant portion of the actual bridge response was missing for beam B8. The difference in the westbound response was much smaller and comparable to the difference in corresponding strain values. Therefore, the deflection values also showed a more flexible ARB model as compared to the actual bridge.

Table 17: Comparison of average deflection values.

Test Run	Global Deflection (in.)		Difference (%)
	FEA	**Test Result**	
1	0.076	0.046	39.27
2	0.077	0.055	28.76
3	0.155	0.115	25.76
4	0.076	0.067	12.04
5	0.077	0.069	10.07
6	0.155	0.135	12.72

4.6.   Discussion on FEA – Diagnostic test comparison

The FEA of ARB was a mathematical of the ABBB system. The ARB model was used to simulate the behavior of an ABBB system with sound joints. This simulation was an important aspect of this research

as the behavior studied in this analysis was extrapolated for another ABBB model, also known as the FSB model. The ARB model was developed on the basis of material properties as prescribed by the drawings and as-built plans that were provided by VDOT prior to the diagnostic tests. Especially, the compressive strengths of concrete and grout and the tensile strength of prestressing steel were as per specified in the drawings. The actual strengths of these materials were not accessible for this research. ABAQUS required the input of modulus of elasticity for linear elastic modeling. Therefore, in lieu of the actual bridge component material properties, the modulus of elasticity for concrete was calculated by usual means and the typical steel modulus of elasticity was assumed. The properties used in the FEA models are reported in Table 8. Another important aspect of the ARB model was that the supports were idealized as springs and the stiffness of the supports was calculated with an assumed shear modulus. The actual shear modulus of the elastomeric bearing pads was unknown. Therefore, considering the uncertainty in the actual material properties, the ARB model provided responses that were close to those measured in the diagnostic test with the assumed properties.

5. Splice Length Testing

The appropriate length for the spliced connection was ascertained by testing simply supported beams in a four point bending setup with the splices cast in the region of constant bending moment. The beams were tested monotonically until failure. The focus of these tests was to measure the stress and the strain in the tension reinforcement. The ultimate goal of these tests was to determine the minimum length of splice at which the tension steel yields. The spliced connections were proposed to be used as an accelerated bridge construction technique for ABBB construction. Testing was typically performed within seven to nine days of placing the joints. The splice lengths of were investigated for No.4 and No. 6 bars. The results of these tests are now discussed.

5.1. Material Properties

Tests were performed to determine the material properties of the reinforcing steel, conventional concrete, UHPC and VHPC used in the tests. The compressive strengths and the modulus of elasticity for precast concrete and for the filler material were performed with three 4 in. x 8 in. cylinders each. The splitting tensile strength for the filler material was also performed with three 4 in. x 8 in. cylinders. Additional research was performed to quantify the tensile properties of UHPC and VHPC using a direct tension test and a modulus of rupture test. These results are not reported here but can be referred at Halbe et al. (2014). The testing of steel reinforcement was performed after the end of all splice beam tests. Samples of No. 4, No.6, No. 7 and No. 8 bars were tested for every respective batch. The steel yield strength, ultimate strength and the modulus of elasticity were sought.

5.1.1. Properties of precast concrete

The precast beams were cast on three occasions. For each placement, specimens were made to determine compressive strength, splitting tensile strength and modulus of elasticity. Additionally, steel reinforcement samples from each batch were also saved for later testing. The precast beams were moist cured for seven days prior to removal from the forms. After stripping the forms, the beams were stored in the lab until placement of the connection filler material and subsequent testing. The properties of the concrete are presented in Table 18. For the specimens with VHPC, splitting tensile strength and modulus were only tested at the end of the testing program. The age of precast concrete at the time of testing was more than ninety days and all the specimens with VHPC filler were tested within a period of ten days. Therefore, a single set of material property tests were performed for the precast concrete.

Table 18: Properties of concrete in precast beams.

Specimen Designation	Compressive Strength, (psi)	Splitting Tensile Strength, (psi)	Modulus of Elasticity, (ksi)
U-4-5-I-E	7360	816	4090
U-4-6-I-E	7360	816	4090
U-4-3-I	7360	816	4090
U-4-4-I	3900	-	3590
U-4-5-II	3900	-	3590
V-4-5-I	4700	-	-
V-4-6-I	4700	-	-
V-4-5-II	4640	-	-
V-4-3-I	4890	-	-
V-4-4-I	4890	-	-
V-4-4-II	4640	-	-
End of Test VHPC	4720	351	3400
U-6-5-I-E	7360	816	4090
U-6-6-I-E	7360	816	4090
U-6-7-I	3900	-	3590
U-6-8-I	3900	-	3590

5.1.2. Reinforcing steel properties

The bars used for the splices and as the compression reinforcing were tested to determine the stress-strain behavior. Samples of each bar size, 30 in. in length, were placed in the Satec Universal test machine, and gripped at each end with hydraulically operated grips. For initial samples, strains were measured only with a clip-on 2 in gauge length extensometer. The clip on extensometer was removed at its maximum extension of 3% strain. After removal of the gauge, the cross-head displacement, and the measured distance between the cross-heads was used to calculate the strains. The strain at the ultimate stress was calculated from the cross-head displacements and plotted with a straight line approximation from the last point recorded by the extensometer.

Figure 158, Figure 159, Figure 160 and Figure 161 present the stress-strain plots for the No. 4, No. 6, No. 7 and No. 8 bars, respectively. The dotted lines in these plots indicate the straight line approximation of stress-strain behavior. It is to be noted that the strains for the No. 8 bars in Figure 161 are calculated from the full length of the bar. The diameter of the No. 8 bars was too large for the extensometer to grip the bar specimens. Therefore, the strains for No. 8 bars were calculated from the full 24 in. gauge length of the bar

Table 19 presents the key properties of the reinforcement. Note that bars designated U-bars were used in the UHPC pockets and those designated V-bars were used in the VHPC pockets.

Table 19: Reinforcing steel properties.

Bar Size	Filler Material	Modulus of Elasticity (ksi)	Yield stress (ksi)	Strain at onset of strain hardening	Ultimate Strength, ksi	Ultimate Strain
No. 4	UHPC	29,000	62.0	0.0077	102	0.140
No. 6	UHPC	29,000	60.0	0.0077	102	0.164
No. 7	UHPC	29,000	62.0	0.0072	102	0.136
No. 8	UHPC	29,000	69.5	0.0055	104	0.176
No. 4	VHPC	29,000	69.0	0.0062	109	0.106
No. 8	VHPC	29,000	69.5	0.0055	104	0.176
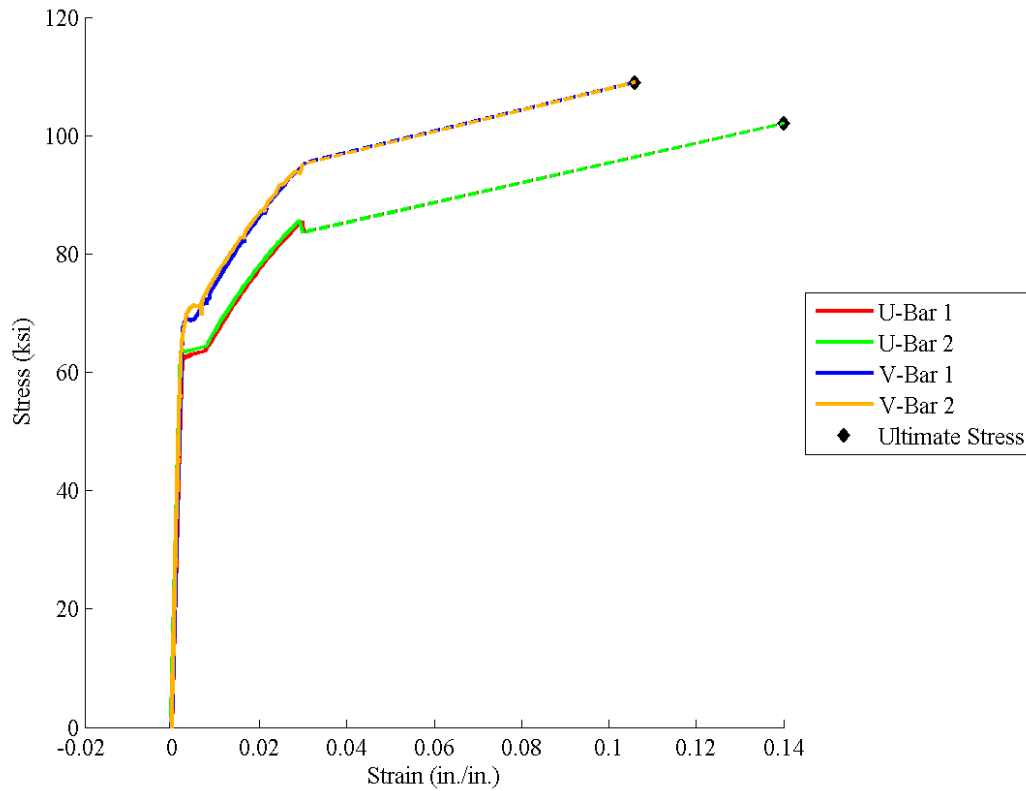
Figure 158: Stress vs. strain plot for No. 4 bars.
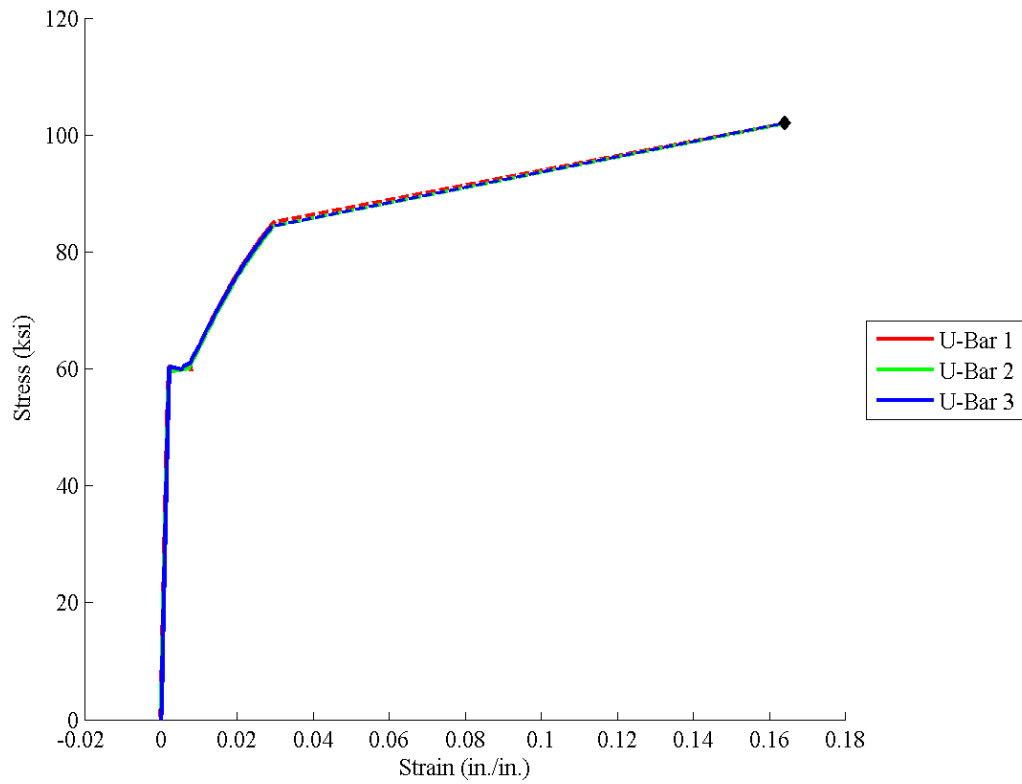
Figure 159: Stress vs. strain Plot for No. 6 bars.
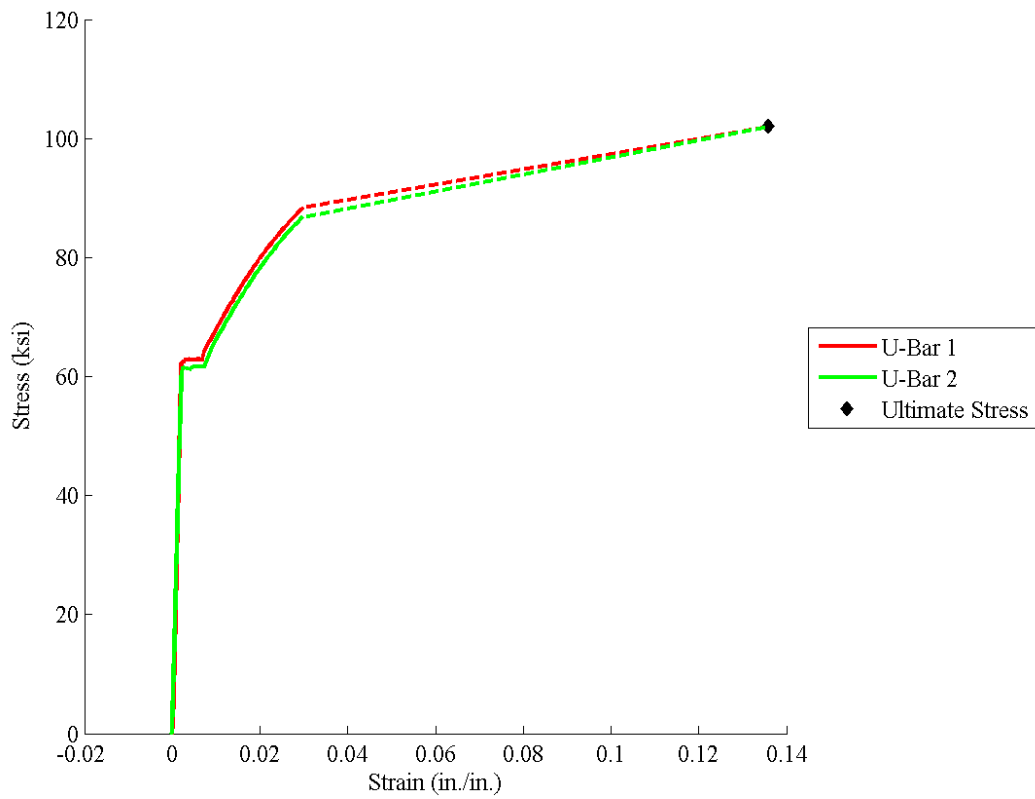
Figure 160: Stress vs. strain plot for No. 7 bars.

156
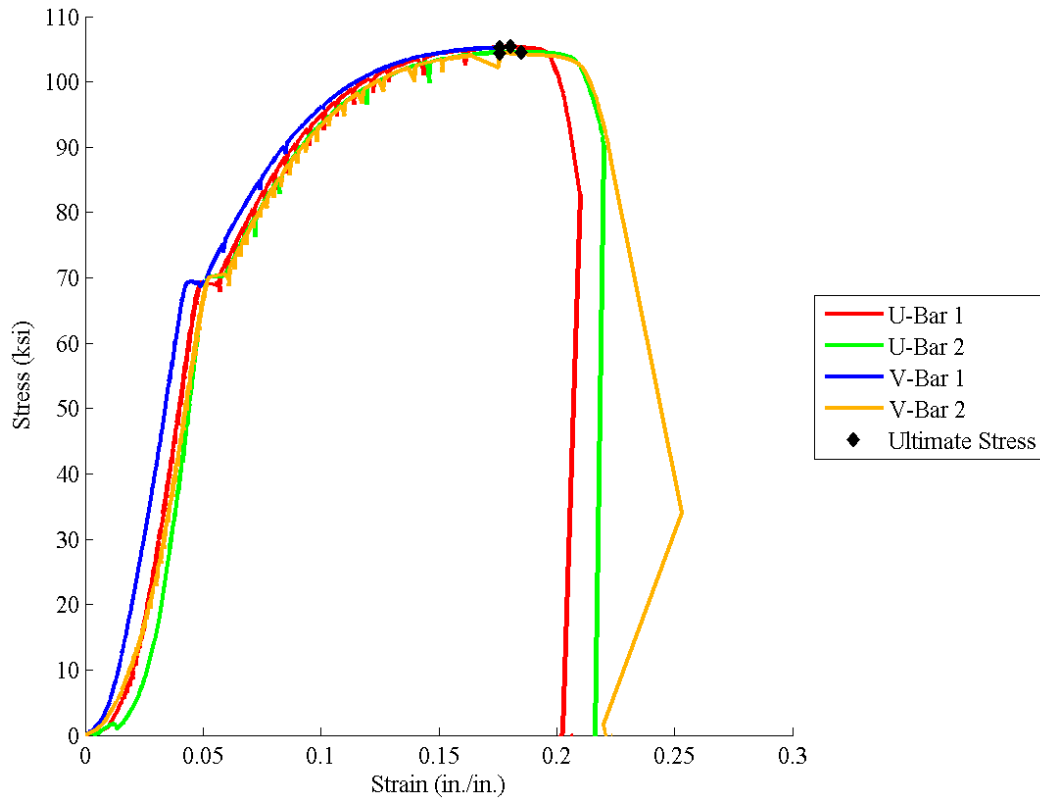
Figure 161: Stress vs. strain plot for No. 8 bars.

5.1.3. Splice Pocket Filler Properties

The splice pockets were filled two at a time, and tested typically seven to nine days after placement, depending upon the schedule of the splice test.   Samples were made from each batch to determine compressive strength, splitting tensile strength, and modulus of elasticity. The UHPC compressive strength was measured with 2in. $\times$ 2in. $\times$ 2in. cubes. The VHPC compressive strength was measured with 4 in. $\times$ 8 in. cylinders due to the presence of aggregates in the mix. The properties of the connection filler material are reported in Table 20.

Table 20: Properties of connection filler material.

Placement	Specimens	Age at Testing, days	Compressive Strength, ksi	Splitting Tensile Strength, ksi	Modulus of Elasticity, ksi
10/19/12	UHPC	7	14,000	3680	6840
11/6/12	UHPC	7	13,200	3070	6460
11/22/12	UHPC	14	23,800	N/A	8530
12/13/12	UHPC	8	13,500	3140	6670
6/6/13	UHPC	7	20,200	2200	8080
6/19/13	UHPC	8	20,700	2100	8150
6/19/13	UHPC	9	20,500	2390	8280
6/4/13	UHPC	7	19,300	2670	8210
6/6/13	UHPC	9	20,700	2390	8090
1/13/14	VHPC	8	12,400	1660	5440
1/13/14	VHPC	9	13,500	N/A	5680
2/3/14	VHPC	7	12,900	1620	5750
2/11/14	VHPC	10	13,800	1750	5250

5.2. Splice Test Results for No. 4 Bars and UHPC and VHPC

The splice lengths tested with No. 4 bars ranged from 3 in to 6 in. As discussed earlier, the UHPC tests were performed in two stages. Specimens U-4-5-I-E and U-4-6-I-E were the first beams tested. The reinforcement details of these beams are shown in Figure 96 and, to reiterate, both the tension and compression reinforcement was two No. 4 bars. The remaining specimens were tested in the second phase of testing. The second stage UHPC beams, shown in Figure 97, contained two No. 4 bars as tension reinforcement and a combination of two No. 7 bars and one No. 6 bar as compression reinforcement. After observing the results from the UHPC tests, the VHPC specimens were designed with two No. 4 bars as tension reinforcement and two No. 8 bars as compression reinforcement Figure 98. Table 21 presents the cracking load, maximum load, and failure mode measured for each specimen.

Since there was no direct measurement of bar slip, a slipping failure deemed was characterized by a significant widening of a crack, or the pocket-to-precast interface opening, with a decreasing load. If there were no slip, increased crack width would be associated with increasing bar strain, bar stress, and therefore, applied load. The crack or interface opening wider with a decreasing load indicated that the bar must be slipping or debonding in the vicinity of the crack. The slipping was accompanied by splitting cracks in some of the specimens, and these are noted in Table 21 as slip/split failures. One specimen failed by rupture of the bar. Also note that the first two tests, U-4-5-I-E and U-4-6-I-E, which had equal amount

of tension and compression reinforcement, had very ductile failures, since both top and bottom bars had yielded, and were strain hardening significantly. For both specimens, with a small load application the displacement was increasing significantly, so the tests were halted before any obvious slipping or splitting occurred.

Table 21: Summary of test results with No. 4 bars.

Specimen Designation	Splice Length, in	Compression Reinforcement	First Cracking Load, lbs	Maximum Load, lbs	Failure Mode
U-4-5-I-E	5	2 No. 4s	7200	28,000	-
U-4-6-I-E	6	2 No. 4s	6900	26,500	-
U-4-3-I	3	2 No.7s and 1 No. 6	5800	15,700	slip
U-4-4-I	4	2 No.7s and 1 No. 6	7500	24,500	slip/split
U-4-5-II	5	2 No.7s and 1 No. 6	9000	29,600	slip/split
V-4-5-I	5	2 No. 8s	3,200	24,500	slip/split
V-4-6-I	6	2 No. 8s	3,000	28,700	slip/split
V-4-5-II	5	2 No. 8s	1,500	28,300	rupture
V-4-3-I	3	2 No. 8s	1,000	21,300	slip/split
V-4-4-I	4	2 No. 8s	2,000	21,800	slip
V-4-4-II	4	2 No. 8s	1,500	23,800	slip/split

The nominal strength of the specimens was calculated based on the nominal yield strength of the tension reinforcement and the moment arm between the compression and tension reinforcement. For this basic calculation, the contribution of the UHPC/VHPC to flexural strength was ignored.

$$A_s = 0.2\,in^2 \times 2 = 0.4\,in^2 \qquad\qquad \textit{Equation 23}$$

$$M_n = A_s f_y \times moment\ arm = 0.4\,in^2 \times 60\,ksi \times 8\,in = 192\,in\text{-}k \qquad \textit{Equation 24}$$

Based on the loading diagram presented in Figure 6, the applied load to result in a 192 in-k moment was:

$$M = \frac{P_{applied}}{2} \times 30\,in \qquad\qquad \textit{Equation 25}$$

$$P_{applied} = \frac{M}{15\,in} = \frac{192\,in\text{-}k}{15\,in} = 12.8\,kips \qquad\qquad \textit{Equation 26}$$

It is apparent in comparing this load to the failure loads presented in Table 21 that all specimens exceeded the yield moment, indicating all tension reinforcement had yielded at the maximum load. For the UHPC specimens, repeating the same calculations with the measured ultimate strength of the No. 4 reinforcing bars, of 102 ksi (see Table 19) indicates that the bars would be expected to rupture at an applied

load of 21.8 kips. Interestingly, four of five specimens exceeded this capacity, and none failed due to bar rupture. For the VHPC specimens, the measured ultimate strength of the No. 4 reinforcing bars was 109.5 ksi (see Table 19), indicating that the bars would be expected to rupture at an applied load of 23.4 kips. With four of the six test specimens exceeding this capacity, only one failed due to bar rupture.

5.2.1. Load vs. Displacement

The load vs. deflection behavior of the specimens with No. 4 bars is shown in Figure 162, Figure 163 and Figure 164. For the UHPC beam, specimen U-4-3-I failed at the lowest load and specimen U-4-5-II failed at the highest load. However, in terms of ductility specimens U-4-5-I-E and U-4-6-I-E had the best response. For these beams, the displacement was increasing with no significant increase in load, so the tests were stopped before any bar slip was noted. The specimen with the shortest splice length, specimen U-4-3-I with 3 in splice length had the poorest performance. As seen in the load vs. deflection plots, the curve for U-4-3-I drops off before any significant inelastic behavior was observed. The sudden drop in load, with the significant increase in displacement and crack opening indicated reinforcement was slipping relative to the UHPC. In comparison the specimen with 4 in splice length, U-4-4-I, displayed inelastic behavior prior to failure although the reinforcing steel in tension also was deemed to be slipping relative to the UHPC. Beam U-4-5-II displayed the maximum capacity. Specimen U-4-5-II and specimen U-4-5-I-E had the same splice length and the same area of steel in tension. The difference between the two was the area of steel in compression. Specimen U-4-5-II was tested to ensure that the performance shown by U-4-5-I-E could be repeated even with the increase in the area of steel in compression.

For the VHPC, the specimens performed as expected. Specimen V-4-3-I failed at the lowest load and V-4-6-I failed at the highest load. Unlike the UHPC specimens, inelastic behavior was observed with all of the VHPC specimens. Specimens V-4-5-I and V-4-5-II both had a 5 in. splice length, with the same compression and tension reinforcement configuration. The large difference in ductility observed can be attributed to the extra VHPC present in the larger pocket for V-4-5-II. The larger pocket in specimen V-4-5-II allowed for the stress to increase enough to rupture the tension steel. To avoid having the VHPC pocket contribute more tensile strength than present in the previous tests where the pocket length was designed for the splice length, the final two specimens tested, V-4-3-I and V-4-4-I, had an initial crack cast into the VHPC pocket at the end of the both sides of the splice. This crack was created on both sides by placing a piece of cardboard at the end of the splice. This prevented the VHPC from carrying tensile stress across the face of what was the interface between the precast member and the pocket on the other specimens. In specimen V-4-5-II, which had a long pocket (15 in) but a short splice (5 in), the tension reinforcing steel ruptured at the interface of the precast member and the VHPC pocket rather than inside the pocket at the end of the splice.
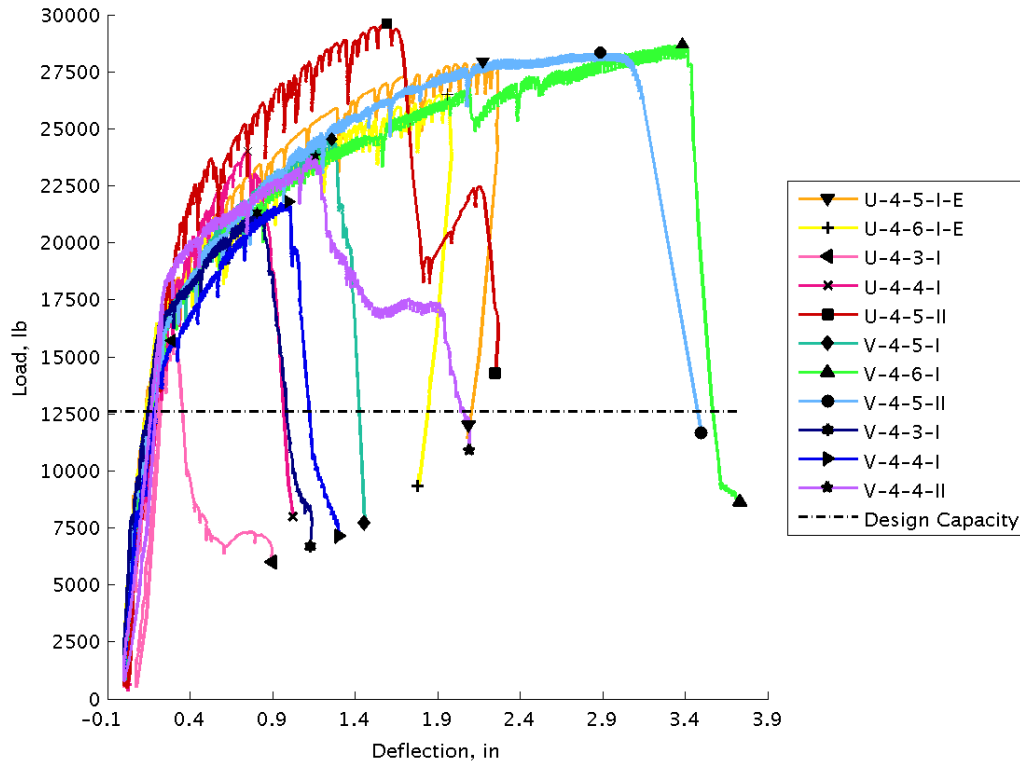
Figure 162: Load vs. south end deflection for all specimens with No. 4 bars.
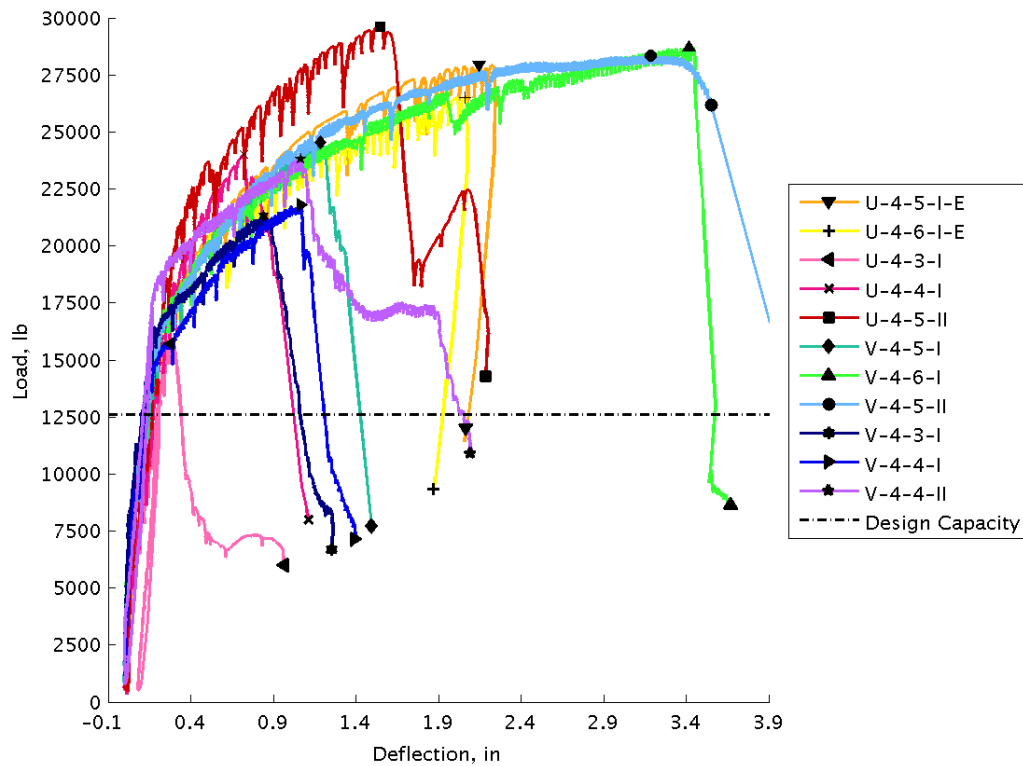
Figure 163: Load vs. north end deflection for specimens with No. 4 bars.

161
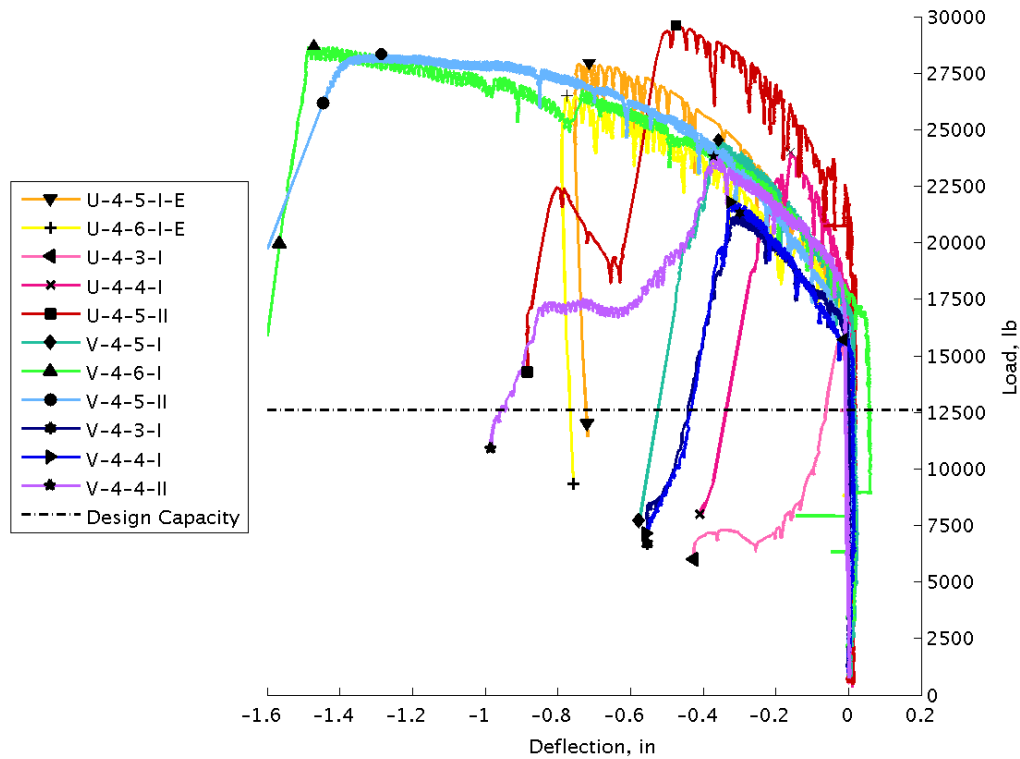
Figure 164: Load vs. midspan deflection for specimens with No. 4 bars.
(Note that upward displacement is negative).

Observing Figure 162 and Figure 163, the load vs. deflection plots show that the magnitude of deflection at the south end and the north end respectively were nearly equal, indicating that the spreader beam distributed the loads equally to both ends from a single actuator for all test specimens. In all specimens with No. 4 bars, the midspan did not show significant deflection until the specimens had cracked, as seen in Figure 164. Midspan deflections showed significant increases after the interfaces of the precast element and the pocket debonded.

5.2.2. Load vs. Strain

The strains measured in the compressive reinforcement were plotted with respect to externally applied loads to observe the change in strains over the period of testing (shown in Figure 165 and Figure 166). The actuator load applied externally to the beam and not the load directly applied to the compressive reinforcing steel through flexure. Hence, the load vs. compressive strain plots do not represent the typical stress vs. strain behavior of a steel reinforcing bar.

162
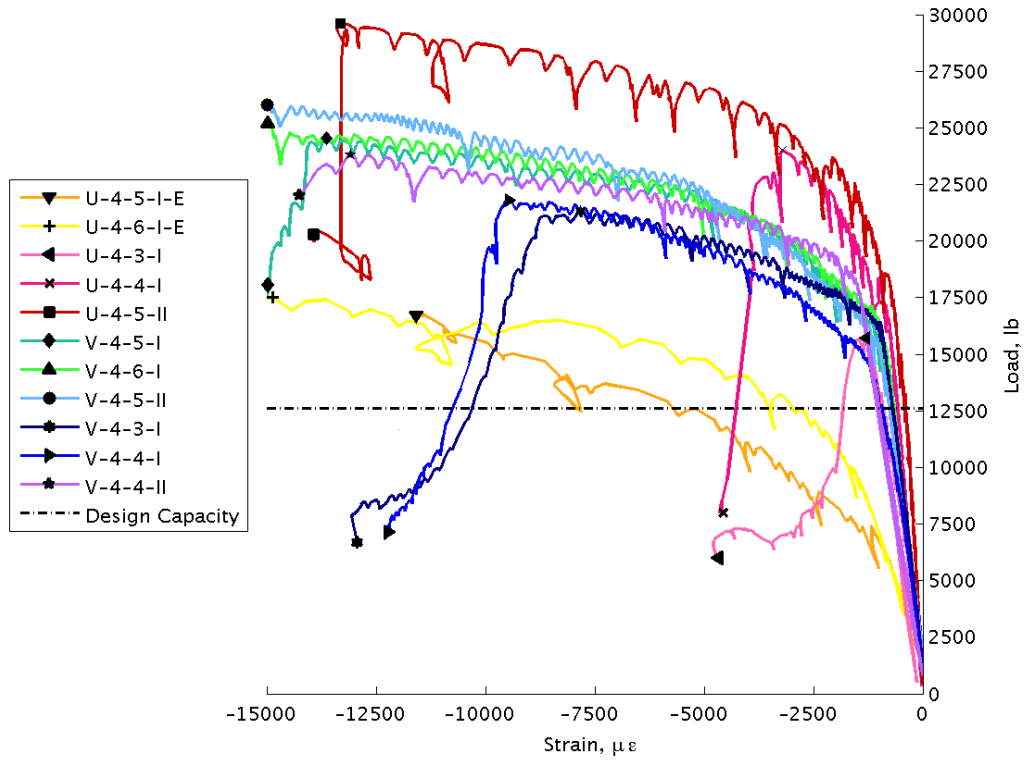
Figure 165: Load vs. reinforcement bar (East) strain for specimens with No.4 bars.
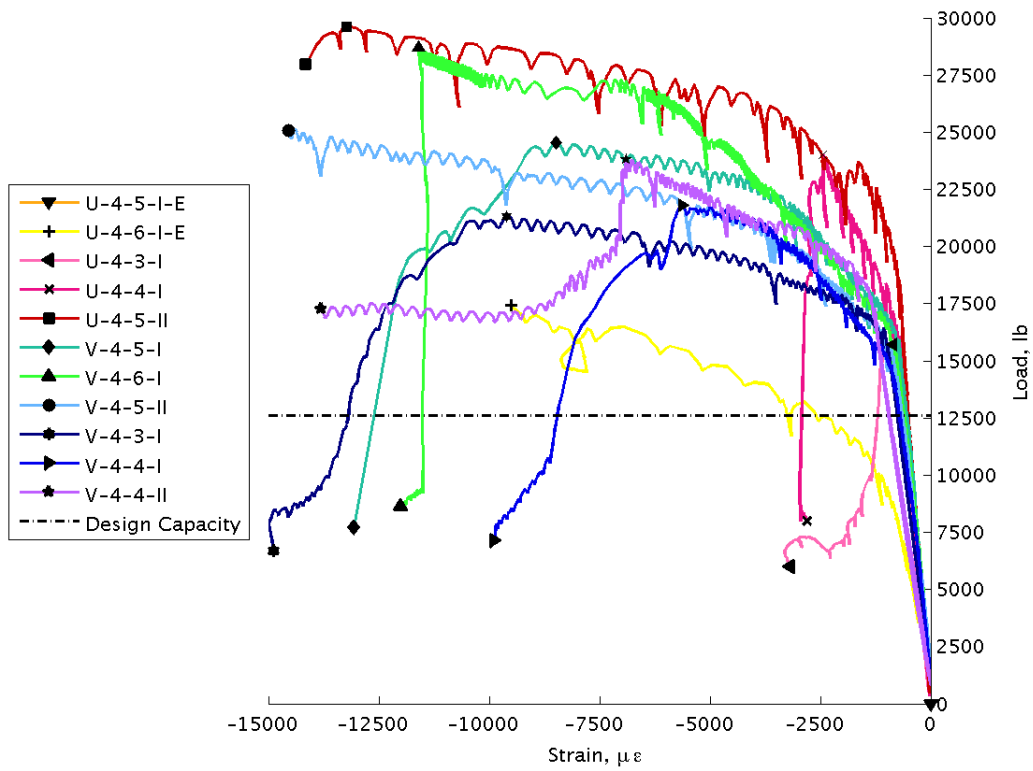
Figure 166: Load vs. reinforcement bar (West) strain for specimens with No. 4 bars.

Using a simple model, the force in the reinforcing steel in compression can be calculated as shown in Figure 167 and Figure 162.
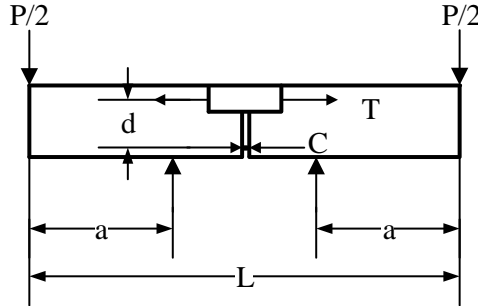
Figure 167: Force in compressive reinforcement from externally applied loads.

From Figure 167,
$$C = \frac{P \times a}{2 \times d}$$
Equation 27

Based on this simplistic model, the compression reinforcement in the specimens with the larger amount of compression reinforcement (two No. 7 bars and one No. 6 bar or 2 No. 8 bars) should not have yielded. However, the strain gauges indicated that they yielded. This was because the strain gauges were placed on the bottom of the reinforcing bars, and the strain gradient through the bars was large enough that the bottom fibers of the bars did yield in compression while the top of the bar was in tension. This is discussed in greater detail in the Section 5.5 of this chapter.

From the load vs. strain plots in Figure 165 and Figure 166, the difference in behavior exhibited by the specimens with the smaller amount of compression reinforcement (U-4-5-I-E and U-4-6-I-E) and those with the larger amount of compression reinforcement was very noticeable. As would be expected, the smaller amount of compression reinforcement yielded at a much lower applied load. The compression reinforcement in Specimen U-4-3-I did not yield prior to achieving the peak load, due to the slipping failure of the tension reinforcement.

5.2.3. Load vs. Interface Opening

The displacements at the interface of the precast element and the pocket were measured by LVDTs. Typically, the interface between the pocket and the precast concrete opened before any cracks were observed in the UHPC or VHPC pockets. After the interface opened completely, the crack would either propagate diagonally into the precast concrete below the pocket, or the interface would continue to debond along the bottom of the pocket. A schematic representation of the cracks in the precast element under the pocket is shown in Figure 168.
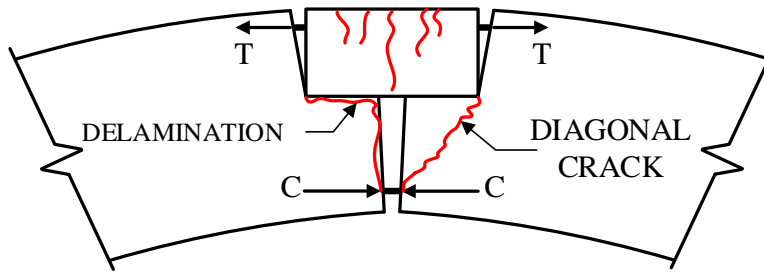
Figure 168: Schematic representation of cracks in the precast element under the splice pocket.

The measurements were plotted with respect to the externally applied load as shown in Figure 169 and Figure 170. It can be observed that the load vs. interface displacement plots for all specimens are very similar prior to the interface debonding. After debonding the interface gaps at either end widened at different rates. Except for specimen U-4-3-I, all specimens showed evidence that the tension reinforcement had yielded and begun to strain harden. Slip was indicated when the gap opened considerably as the load dropped off. Note that slip occurred at the south interface for most specimens, but at the north and south for specimen V-4-4-I. The north interface of specimens U-4-5-I-E and U-4-6-I-E widened more than the south interface. Potentially, the reinforcement could have pulled out or ruptured at this end but both tests were stopped prior to the occurrence of failure.
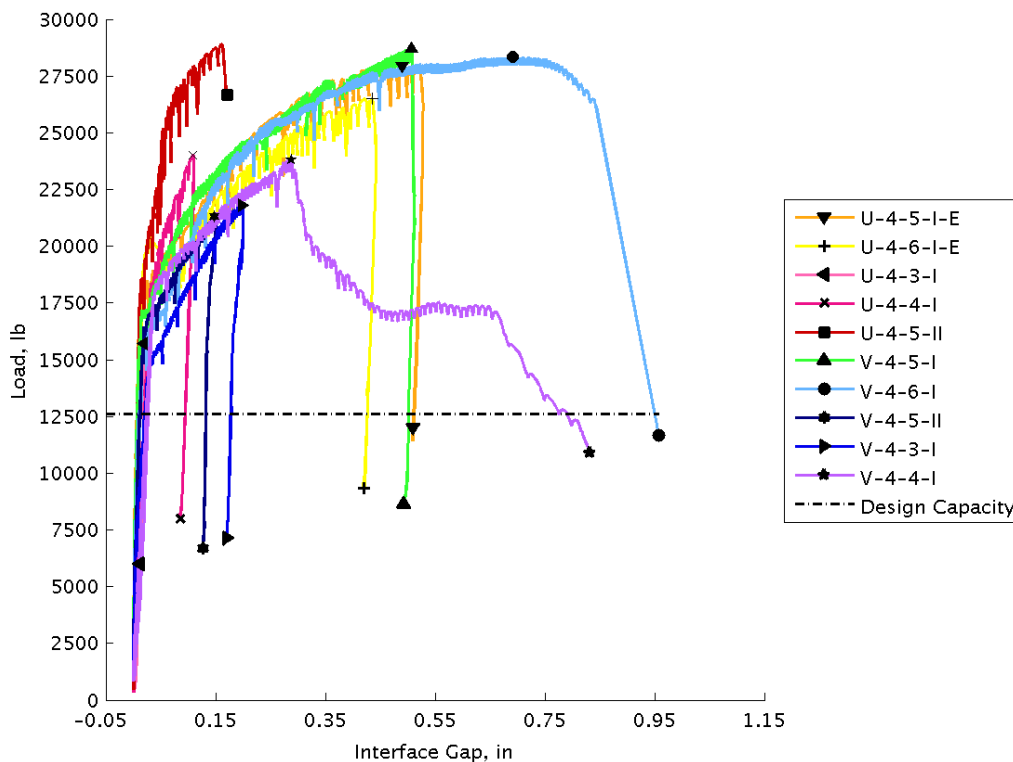
Figure 169: Load vs. north interface displacement for specimens with No. 4 bars.
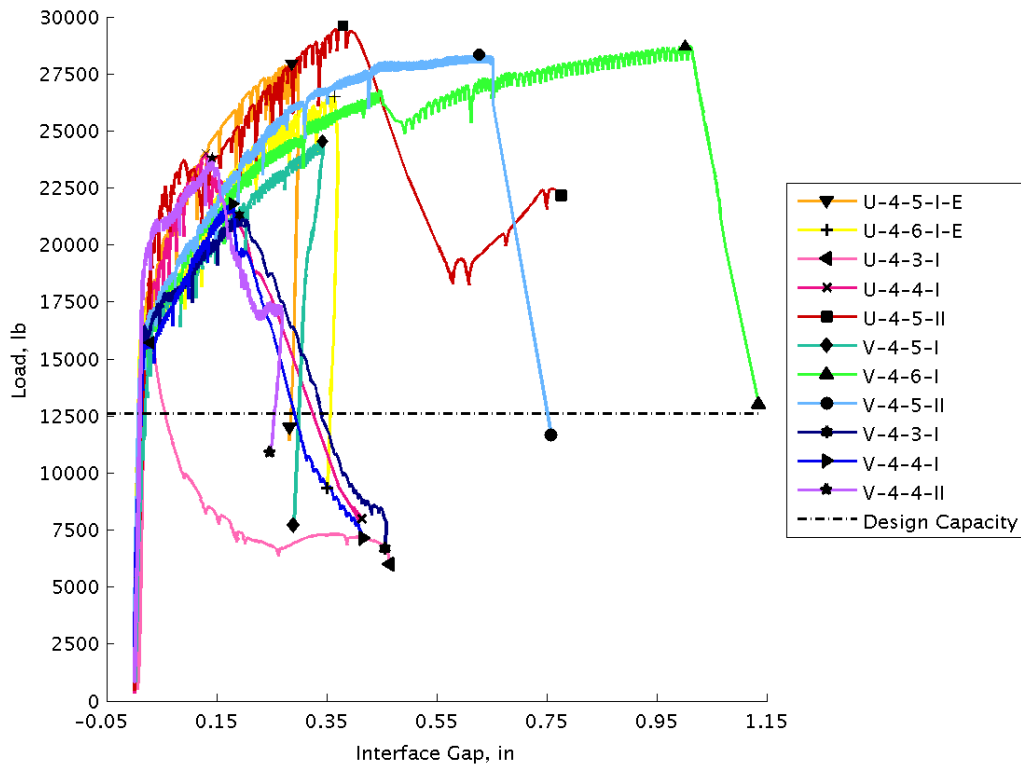
Figure 170: Load vs. south interface displacement for specimens with No.4 bars.

5.2.4. Load vs. DEMEC Strain Measurements

The surface strains were measured by a DEMEC gauge. Locations and designations of the locating discs for the DEMEC gauge are presented in Figure 171. DEMEC measurements of surface strain for Specimen U-4-5-I-E are shown in Figure 172. The surface strains confirm that in the specimens with No. 4 bars, most of the deformation in the beam occurred at one interface. The surface strains measured within the UHPC/VHPC pocket were very small as compared to the interface strains. The measurements can be easily understood by comparing the tensile strength of the UHPC/VHPC (typically around 1 ksi) to the bond strength of UHPC to precast concrete (typically around 0.3 ksi) and VHPC to precast concrete (typically around 0.2 ksi). Because the bond strength was lower, it can be expected that the interface will crack first in the region of constant moment. Once the interface cracked, the total tension force is carried across the interface by the reinforcing bar only. Within the pocket, the tension force was shared by the reinforcing bar and the filler material up to the limiting strain. It was therefore not a surprise that the strains within the pocket wee much smaller than the strains across the interface.

166
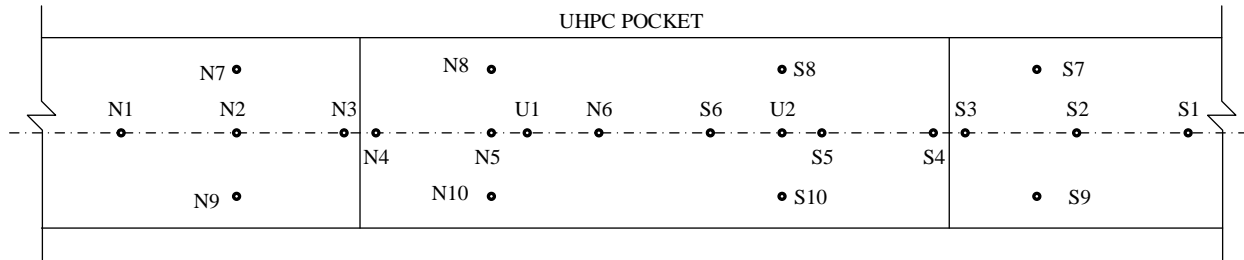
Figure 171: Locations and designations of locating discs for DEMEC gauge.
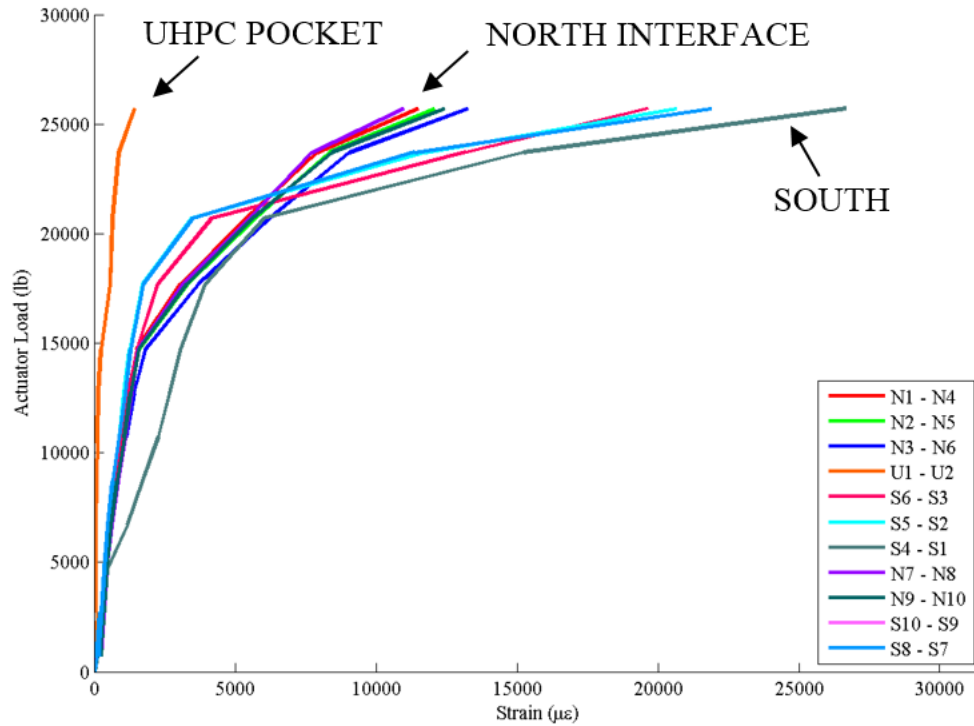
Figure 172: DEMEC strain measurements at the top of the beam for specimen U-4-5-I-E.

5.2.5. Crack Patterns and Failure Modes

Figure 173 shows the UHPC pocket in specimen U-4-5-I-E which exhibited few flexural cracks. Most of the deformation occurred at the interface after the precast element and the UHPC pocket debonded. The flexural cracks in the UHPC pocket formed and propagated until the interface debonded. This behavior can also be seen in the load vs. surface strain relation plotted using the DEMEC measurements (Figure 172), which indicated the strains in the pocket were very small relative to the strains across the interfaces. The UHPC pocket did not show any signs of splitting cracks.

167

Figure 173: UHPC pocket in specimen U-4-5-I-E showing interface separation and flexural cracks.

Several flexural cracks can be observed in the UHPC pocket of specimen U-4-6-I-E at the time of failure, shown in Figure 174. The UHPC pocket in U-4-6-I-E displayed more flexural cracks than specimen U-4-5-I-E.   Splitting cracks were not observed in the UHPC pocket. The overall observed cracking pattern and the behavior were very similar to beam U-4-5-I-E.

Figure 174: UHPC pocket in specimen U-4-6-I-E at end of load application showing flexural cracks.

Specimen U-4-3-I did not show any flexural cracks at failure as shown in Figure 175. The predominant cracking observed was at the interfaces and at the corners of the UHPC pocket. Splitting cracks were observed prior to failure and only these continued propagating until the reinforcing bars slipped. The slip occurred at the south interface, as illustrated in Figure 170 by the gap widening considerably as the load dropped off.
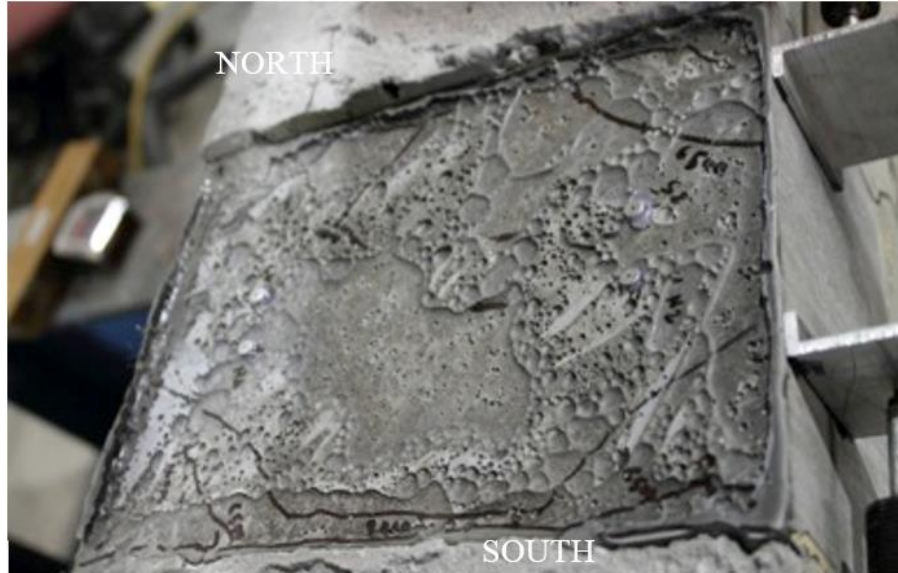
Figure 175: UHPC pocket in specimen U-4-3-I showing cracks near the interfaces and the corners.

Several flexural and splitting cracks could be observed in specimen U-4-5-II as seen in Flexural cracks occurred and propagated until a total applied load of 20,000 lb. Splitting cracks in the UHPC pocket started forming at loads over 20,000 lbs, and propagated until failure. The south interface cracked at about 15,000 lbs and widened until failure. The failure occurred after reinforcing bars at south interface slipped relative to the UHPC pocket. Most of the splitting cracks were concentrated near the south interface.

Figure 176: UHPC pocket in specimen U-4-5-II after failure showing south interface separation.

In specimen U-4-4-I the flexural cracks could be observed in the UHPC pocket over the location of the foam block-out as shown in Figure 177. Some splitting cracks were observed at the south interface at loads above 23,000 lbs. Failure occurred after reinforcing bars slipped relative to the UHPC pocket at the south interface. Flexural cracks stopped forming and propagating in the UHPC pocket after the interfaces debonded, as also seen in U-4-5-I-E and U-4-6-I-E tests.
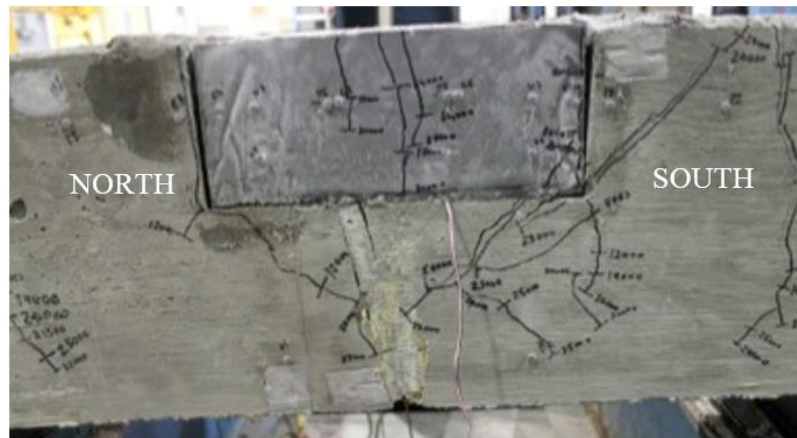
Figure 177: Side view of UHPC pocket in specimen U-4-4-I after failure showing interface separation.

In specimen V-4-5-I, large splitting cracks formed on top of the VHPC pocket above both the east and west reinforcing bars at the north interface at 12,000 lbs as shown in Figure 178. This crack propagated downward towards the foam pad at midspan. These splitting cracks indicate that the reinforcing bars extending from the precast into the pocket at the north end of the member slipped relative to the VHPC pocket. This slip led to the specimen failure at 24,500 lbs.

Figure 178: VHPC pocket in specimen V-4-5-I showing interface separation and splitting cracks.

170

The cracking pattern of specimen V-4-6-I was very similar to specimen V-4-5-I. The main difference was that the main crack formed at the south end instead of the north as shown in Figure 179. The splitting cracks formed at 19,500 lbs and the specimen failed at 28,700 lbs. At the peak load, the south gap opened to over 1 in in width. At this time, the load dropped off suddenly, indicating the bars were slipping.
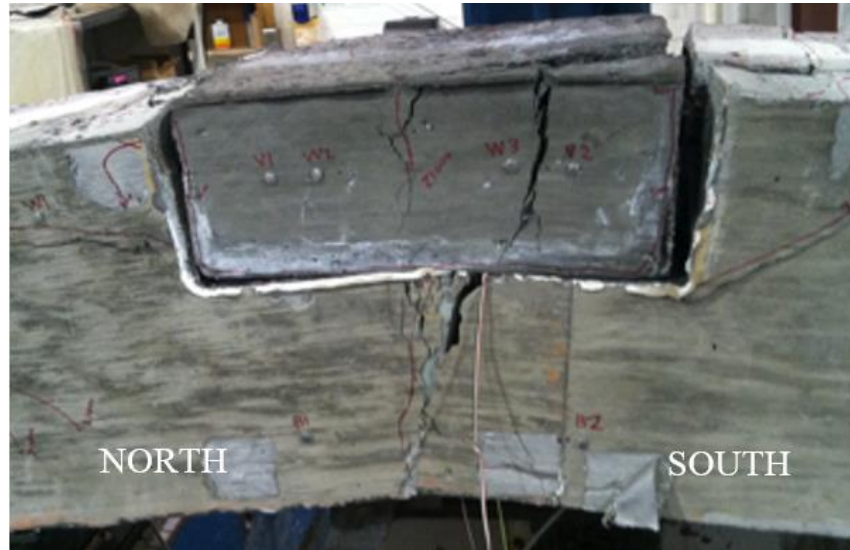
Figure 179: VHPC pocket in specimen V-4-6-I showing interface separation and splitting cracks.

Specimen V-4-5-II failed due to the reinforcing bars rupturing as shown in Figure 180. Cracks formed at the interface around the entire pocket at 1,500 lbs. The pocket continued to separate until the north face was completely detached. The reinforcing bars ruptured at 28,300 lbs causing the specimen to fail as shown in Figure 180.

Figure 180: VHPC pocket in specimen V-4-5-II showing interface separation and reinforcing bars ruptured.

Figure 181: Specimen V-4-5-II at end of load application showing the reinforcing bars ruptured.

Specimen V-4-4-II initially separated at the south interface and then formed a splitting crack on the east side of the pocket at the height of the reinforcing bars as shown in Figure 182. This splitting crack continued into the precast member at the same level, indicating that the reinforcing bar slipped both in the precast element and the VHPC pocket.

Figure 182: VHPC pocket in specimen V-4-4-II showing interface separation and splitting cracks.

Similar to specimen V-4-4-II, specimen V-4-3-I also had an initial splitting crack form on the east side of the VHPC pocket at the artificial south interface as shown in Figure 183. This indicates that there was also some slipping of the reinforcing bar within the VHPC pocket.

Figure 183: VHPC pocket in specimen V-4-3-I at end of load application showing interface separation.

Specimen V-4-4-I did not exhibit many cracks within the VHPC pocket as shown in Figure 184. Instead, the artificial south interface widened and the specimen failed at 21,800 lbs.

Figure 184: VHPC pocket in specimen V-4-4-I at end of load application showing interface separation.

In summary, all of the specimens in this series exhibited behavior and carried loads indicating that the tension reinforcing bars had yielded. An attempt was made to measure the tensile stresses through equilibrium and measuring compressive strains. The magnitudes of strains on the compression bars were much higher than expected. Therefore, an alternative method was sought to calculate the stress in tension steel. This analysis is presented in the Section 5.5.

5.3. Splice Test Results with No. 6 Bars and UHPC

The splice lengths tested with No. 6 bars ranged from 5 in to 8 in. As described previously, the tests were performed in two stages, with the first two tests having an equal area of compression and tension reinforcement (two No. 6 bars), and the second two tests having a greater amount of compression reinforcement (two No. 8 bars and one No. 7). The typical details are shown in Figure 96 and Figure 97. Table 22 presents the cracking load, maximum load measured for each specimen, and failure mode.

Table 22: Test results for specimens with No. 6 bars and UHPC.

Specimen Designation	Splice Length (in.)	Compression Reinforcement	First Cracking Load (lb.)	Maximum Load (lb.)	Failure Mode
U-6-5-I-E	5	2 No. 6s	7800	35,080	slip
U-6-6-I-E	6	2 No. 6s	8000	35,710	slip
U-6-7-I.	7	2 No.8s and 1 No. 7	9000	43,200	slip/split
U-6-8-I.	8	2 No.8s and 1 No. 7	9300	43,480	slip/split

The nominal strength of the specimens was calculated based on the nominal yield strength of the tension reinforcement and the moment arm between the compression and tension reinforcement. For this basic calculation, the contribution of the UHPC to flexural strength was ignored.

$$A_s = 0.44in^2 \times 2 = 0.88in^2 \qquad \text{\textit{Equation 28}}$$

$$M_n = A_s f_y \acute{} \ moment\ arm = 0.88in^2 \acute{} 60\,ksi \acute{} 8in = 422in\text{-}k \qquad \text{\textit{Equation 29}}$$

Based on the loading diagram presented in Figure 167, the applied load to result in a 422 in-k moment was;

$$M = \frac{P_{applied}}{2} \acute{} 30\,in \qquad \text{\textit{Equation 30}}$$

$$P_{applied} = \frac{M}{15in} = \frac{422in\text{-}k}{15in} = 28.2\,kips \qquad \text{\textit{Equation 31}}$$

It is apparent in comparing this load to the failure loads presented in Table 22 that all specimens exceeded the yield moment, indicating all tension reinforcement had yielded at the instant of failure. Repeating the same calculations with the ultimate strength of the No. 6 reinforcing bars, of 102 ksi (Table 19) indicated that the bars would be expected to rupture at an applied load of 47.8 kips. None of the four specimens exceeded this capacity, and none failed due to bar rupture.

Typically the first flexural crack in all specimens with No. 6 bars was in the precast element over the supports between applied loads of 7000 and 10,000 lb. The first UHPC crack in these specimens was between total applied loads of 10,000 and 15,000 lb. Another typically observed feature of all No. 6 specimens was the occurrence of splitting cracks in UHPC at higher loads. Moreover, at higher loads the propagation of splitting cracks was more prevalent than propagation of flexural cracks. Eventually, the failure mode for all No. 6 specimens was slip/splitting type failure.

5.3.1. Load vs. Deflection

The load vs. deflection behavior of the No. 6 specimens is shown in Figure 185, Figure 186 and Figure 187. All specimens with No. 6 initially bars displayed very similar linear load vs. deflection behavior. The specimens with equal amounts of tension and compression reinforcement displayed non-linear behavior at lower loads than the specimens with the greater area of compression reinforcement. The specimens with greater compression reinforcement also failed at higher loads than those with equal areas.
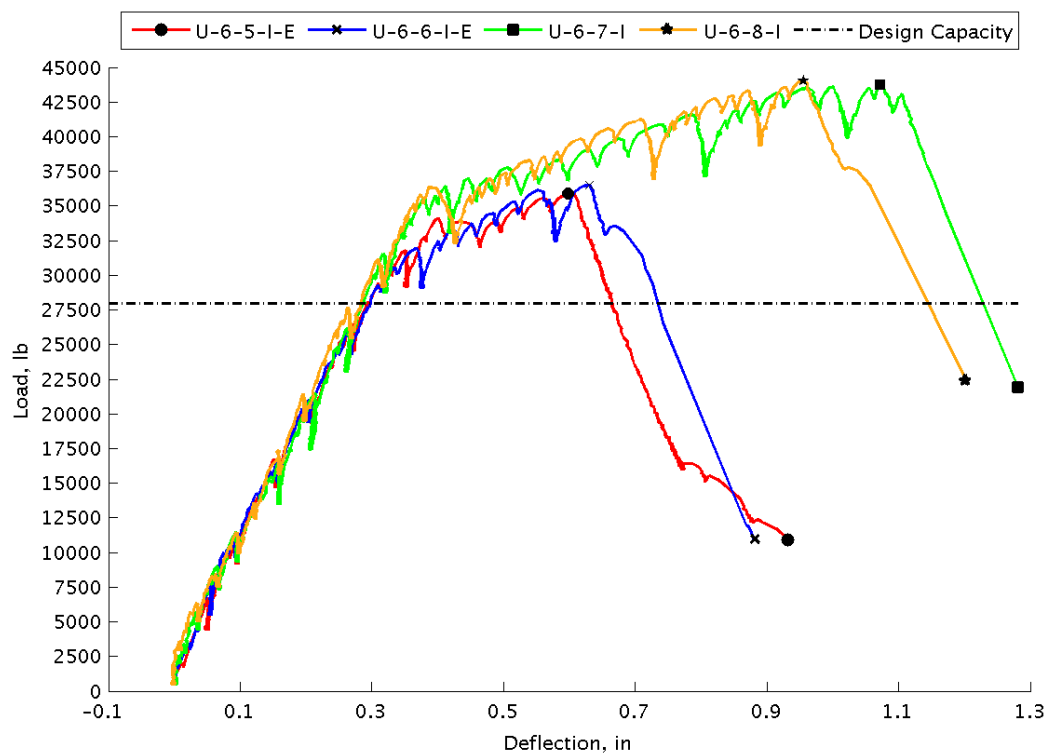
Figure 185: Load vs. south deflection for all specimens with No. 6 bars.
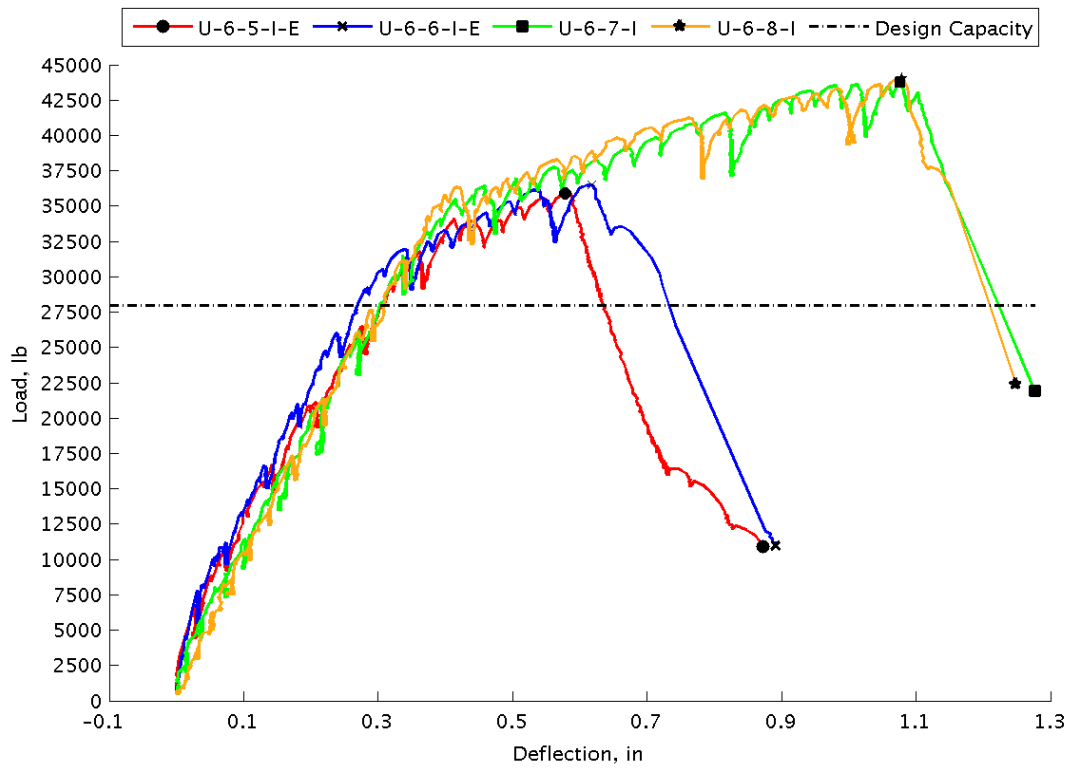
Figure 186: Load vs. north deflection for all specimens with No. 6 bars.
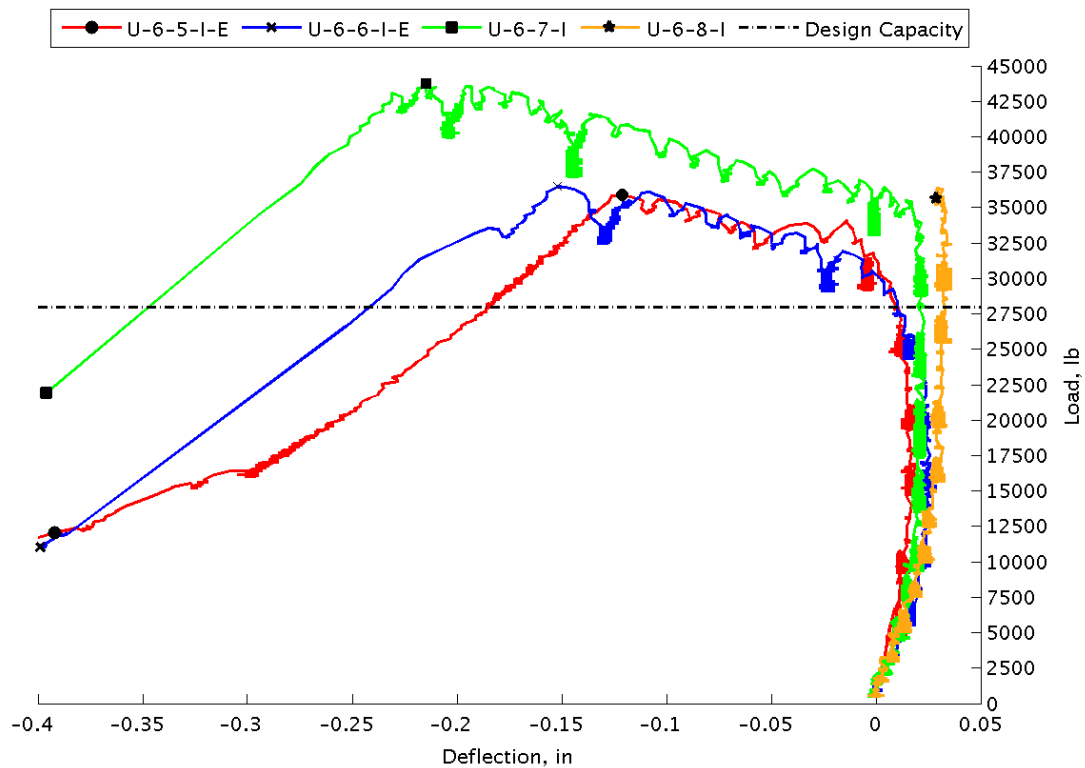
Figure 187: Load vs. Midspan Deflection for All Specimens with No. 6 Bars.
(Note: upward deflection is negative)

176

The magnitudes of deflections at the north and south ends of all of the specimens were very similar, indicating that the actuator load was distributed equally by the spreader beam. The only time when any significant difference occurred was close to failure when the reinforcing bars on one side of the pocket slipped relative to the UHPC. The midspan deflections did not increase until the specimen had cracked significantly. The midspan deflections increased rapidly after the interface between the precast element and the UHPC pocket debonded.

5.3.2. Load vs. Strain

The load vs. compressive strain plots for all specimens with No. 6 bars are shown in Figure 188 and Figure 189. The specimens which had an equal amount of tension and compression reinforcement (U-6-5-I-E and U-6-6-I-E) displayed non-linear behavior at lower loads than the specimens which had a greater amount of compression reinforcement (U-6-7-I and U-6-8-I.).
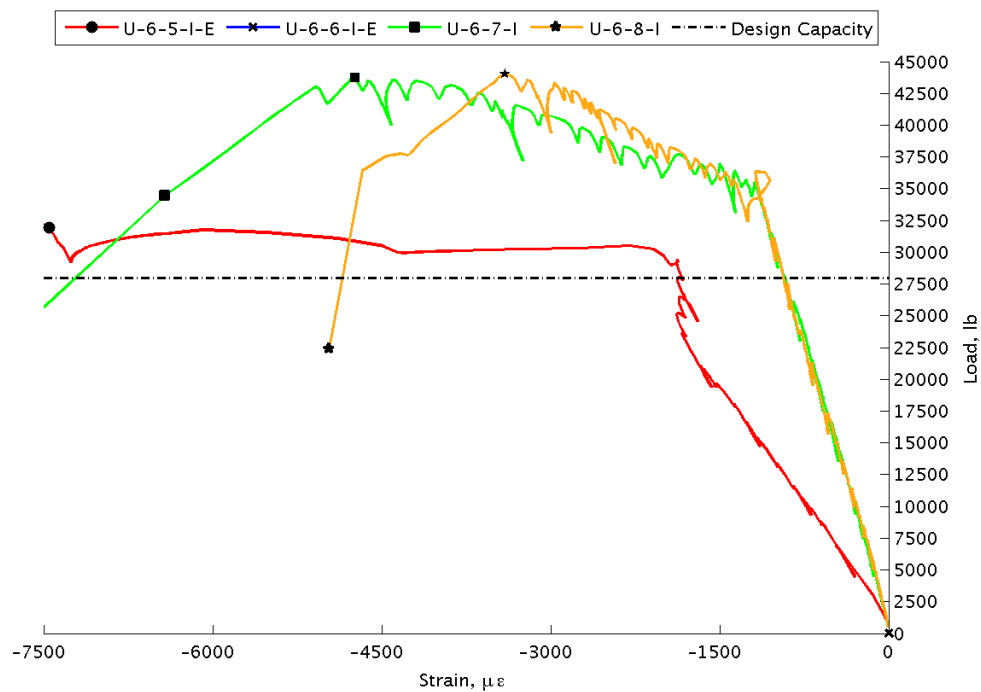
Figure 188: Load vs. reinforcement strain (East) for all specimens with No. 6 bars.
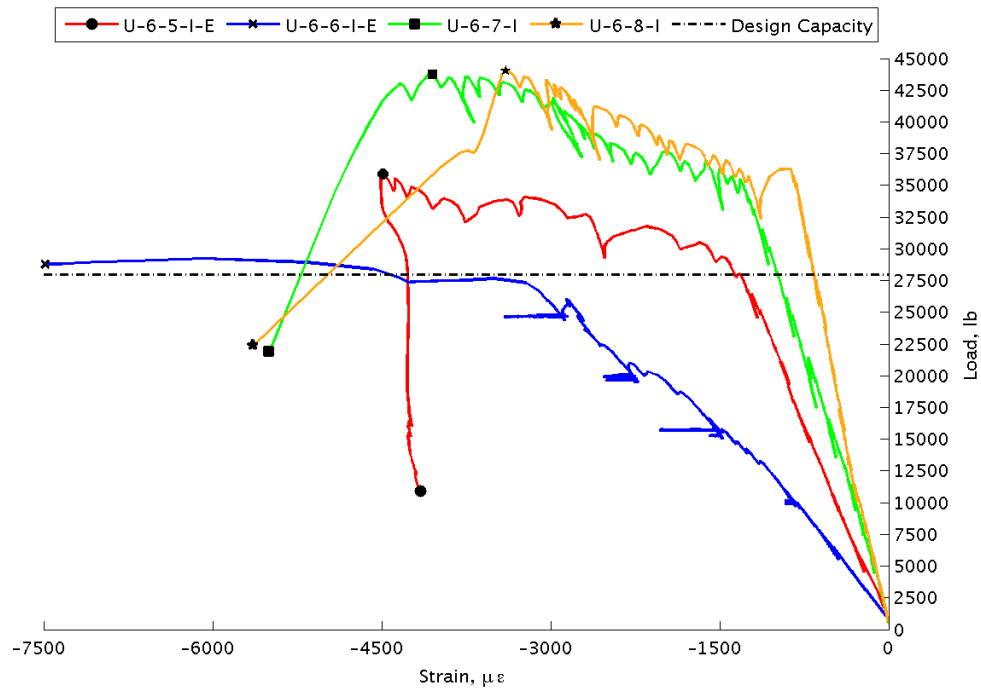
Figure 189: Load vs. reinforcement strain (West) for all specimens with No. 6 bars.

The loading on specimen U-6-5-I-E, albeit equal at north and south ends, was applied unsymmetrically on the specimen cross-section. This was not noticed during the loading and hence there was a substantial difference in the strains in the compressive reinforcement bars on the east side and the west side of the specimen cross-section. The strain gauge on the east reinforcing bar was possibly damaged during the concrete placement and was unable to record any strains during the test. The nature of unsymmetrical loading on U-6-5-I-E and only one working strain gauge on U-6-6-I-E caused the load vs. compressive strain plots of these specimens to be dissimilar. The strain increases were carefully monitored for specimens U-6-7-I and U-6-8-I, and unsymmetrical loading was avoided. Also, the overall increase in strain was much smaller in the specimens with the greater cross-sectional area of reinforcement in compression.

5.3.3. Load vs. Interface Opening

The displacements at the interface of the precast element and the UHPC pocket are plotted in Figure 190 and Figure 191. Typically, cracks at the interface would become discernible after the applied load was above 15,000 lbs for all specimens with No. 6 bars. In specimen U-6-5-I-E the north interface cracked and widened at failure. The south interface did not undergo significant widening since the failure occurred due to slip of the reinforcing bars near the north interface. Similar behavior could be observed in specimen U-

6-5-I-E, and the predominant widening of the interface occurred at the north interface. The displacements at the interface for specimens U-6-7-I and U-6-8-I were of similar magnitude until peak load was applied to the specimens. The displacements at the north and south interfaces of all specimens were unequal after the application of peak load.
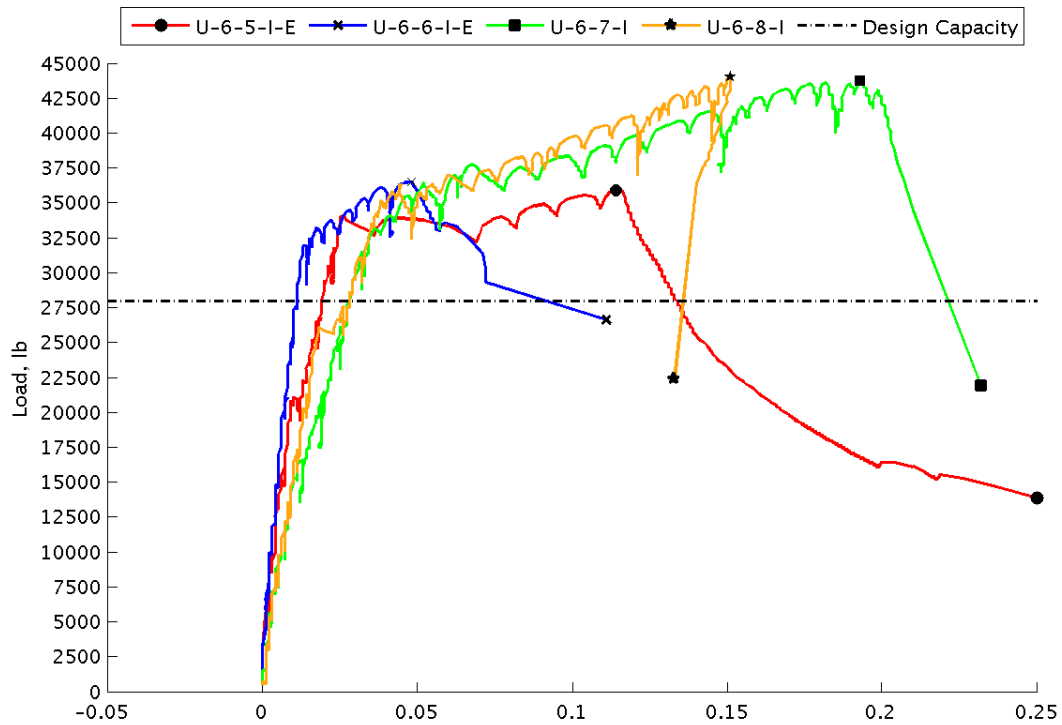
Figure 190: Load vs. north interface displacement for all specimens with no. 6 bars.
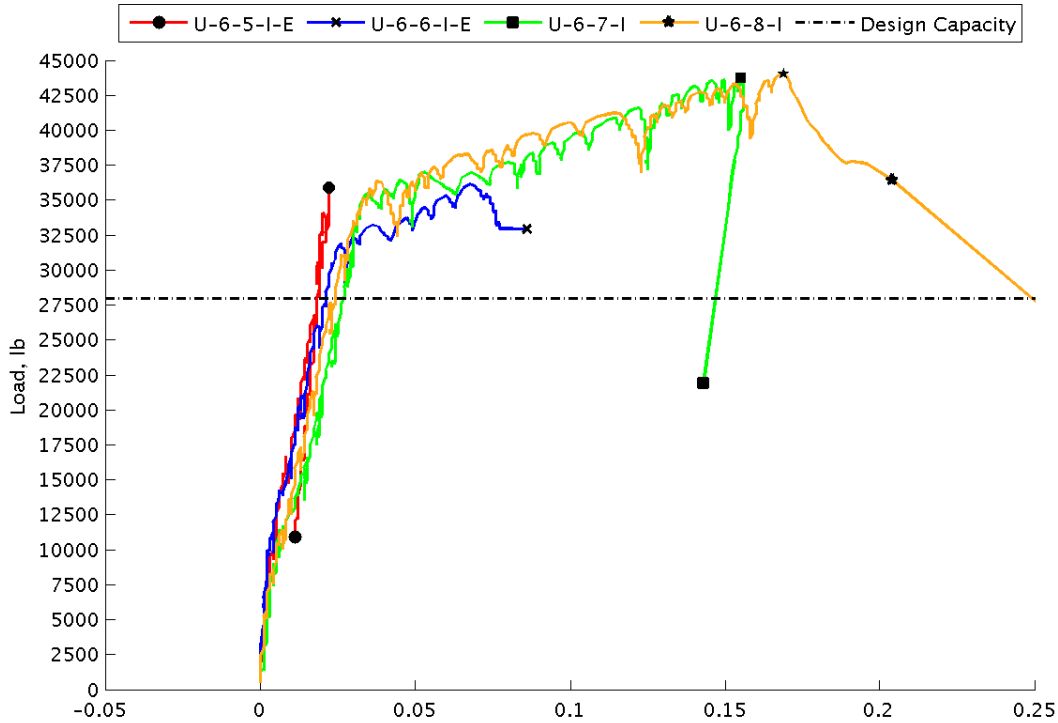
Figure 191: Load vs. south interface displacement for all specimens with No. 6 bars.

It is noteworthy that in the specimens with equal tension and compression reinforcement, the interfaces that were closer to the roller support experienced the most deformation resulting in the widest gaps. However, the same behavior was not observed in the other two specimens. Moreover, an observation can be made that the values of interface displacement measured in all specimens with No. 6 bars at the peak were smaller than those measured in the specimens with No. 4 bars at the application of the peak load.

5.3.4. Load vs. DEMEC Strain Measurements

Figure 192 presents the surface strain measurements made with the DEMEC gauge at the top of the UHPC pocket for the specimen U-6-8-I. The numbering of the DEMEC points is as shown in Figure 172. The plot is typical for specimens with No. 6 bars. As seen in the specimens with No. 4 bars, the cracks, and hence the strains, at the interface were very large compared to the cracks within the UHPC pocket.
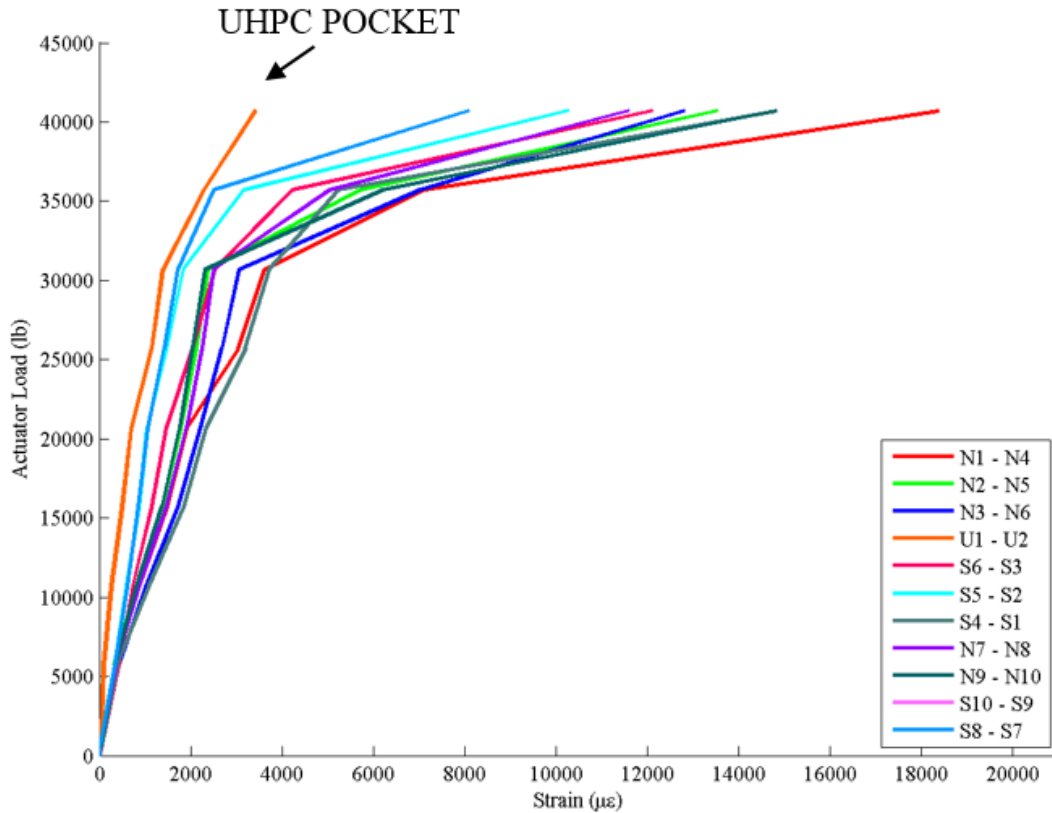
Figure 192: Strain variation observed at the top of the UHPC pocket in U-6-8-I.

5.3.5. Crack Patterns and Failure Modes

Throughout the testing program various failure modes were encountered. The significance of these failure modes is important to the discussion of the splice test results since several key conclusions can be made by observing the crack patterns in the UHPC pocket at failure.

Flexural cracks in the UHPC pocket of specimen U-6-5-I-E were observed at the midspan. Splitting cracks were observed at the north interface where the reinforcing bars appear to have slipped. As seen in Figure 193, splitting cracks can be observed at the top of the UHPC pocket predominantly closer to the eastern face which was the side with the higher load based on strain measurements. This crack was observed prior to failure and it opened up at failure. A single splitting crack was also observed at the depth of the reinforcing bar on the western face at the north interface. This crack occurred at the same instant that the specimen failed, and it may have been triggered by slipping of the reinforcing bars.
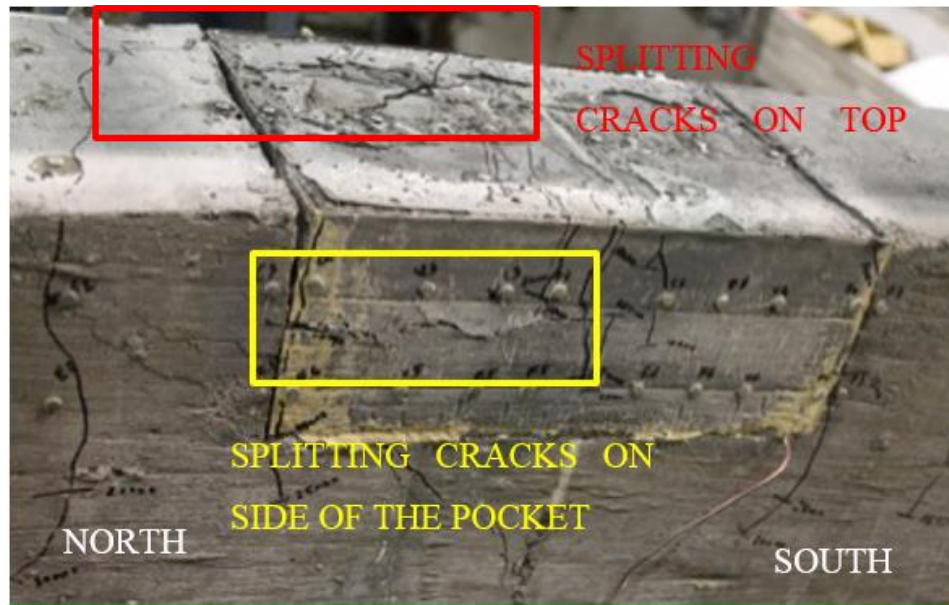
Figure 193: side view of the UHPC pocket in specimen U-6-5-I-E after failure showing splitting cracks.

Specimen U-6-6-I-E exhibited several flexural cracks during loading, and eventually the north interface separated. Prior to failure several splitting cracks were observed in the UHPC pocket over the location of the reinforcing steel. The eventual failure mode in this specimen was unique as compared to all specimens with No. 4 bars, but somewhat similar to the failure mode observed in specimen U-6-5-I-E. Splitting cracks occurred at the level of reinforcement and connected with the interface opening and the existing flexural cracks over the section with the foam. This mode of failure was caused by the short length of the splice reinforcement because the stiffness of the reinforcing bars projecting from the precast element and the splice bars was sufficient to precipitate splitting cracks and then separate the pocket into two parts. Essentially the short length of the reinforcement caused a "prying" action on the UHPC pocket as shown in Figure 194. The stiffness of the bars in the UHPC pocket was high enough to prevent the reinforcing bars from deforming with the UHPC in the pocket in a compatible manner.

Figure 194: Side view of UHPC pocket in specimen U-6-6-I-E after failure showing the effect of prying action.

The failure mode of the specimens with the greater area of compression reinforcement was different as compared to the failure mode of the specimens with equal areas. Specimen U-6-7-I displayed several flexural cracks followed by splitting cracks in the UHPC pocket. The eventual failure was not at the interface as seen in previous specimens. Instead, the north interface began debonding prior to failure and the reinforcing bars projecting from the north into the pocket began to slip. At failure, as the bars projecting from the north slipped out, and an existing flexural crack widened. This flexural crack occurred at the tip of the splice bars and propagated at an angle to the beam axis, close to the bars projecting from the north. The failure mode and associated cracking can be seen in Figure 195. The width of the primary crack in the UHPC, compared to the opening of the north interface, indicate that at failure the bars projecting from the north slipped as the diagonal splitting crack developed.

Figure 195: Top of the UHPC pocket in specimen U-6-7-I after failure.

183

The failure mode of specimen U-6-8-I was similar to that seen in specimen U-6-7-I. An existing flexural crack widened at failure. In this case the location of the crack indicates that failure was initiated between the bars projecting from the precast element into the UHPC pocket. The width of the crack also indicates that the splice bars slipped relative to the UHPC pocket. The failure mode of specimen U-6-8-I can be seen in Figure 196. The crack highlighted in Figure 196 occurred after applying an additional load increment to the specimen after failure.

Figure 196: Specimen U-6-8-I after failure.

5.4. Discussion of test results

The test results of the beams with No. 4 and No. 6 bars are discussed. The main focus of the discussion is on the strains in compression reinforcement and the consequent strains in the tension steel.

5.4.1. Strains in compression reinforcement

The principal answer sought in this testing was what splice length was sufficient to yield the uncoated No. 4 and No.6 reinforcing bars in the UHPC and VHPC pockets. The magnitude of strain in tension was not measured directly so the stress in the tension reinforcement must be determined indirectly. The strain in compression was measured in the tests via strain gauges and a summary of strains recorded at different loads during the test are presented in Table 23. The strains presented in these tables for each test are the average of the two values measured directly by strain gauges on the two extreme reinforcing bars in compression.

Table 23: Average strain gauge measurements splice tests specimens.

Specimens	Load (lb)						
	6000	12000	15000	20000	30000	40000	Peak
	Strain (µε)						
U-4-4-I-E	-1315	-5993	-10755	-	-	-	-
U-4-5-I-E	-905	-3144	-7030	-	-	-	-
U-4-3-I	-372	-811	-1097	-	-	-	-3509
U-4-4-I	-359	-596	-757	-1704	-	-	-3152
U-4-3-I	-257	-473	-639	-1122	-	-	-4795
V-4-5-I	-292	-632	-903	-2907	-	-	-11103
V-4-6-I	-627	-987	-1177	-3305	-	-	-12382
V-4-5-II	-728	-1141	-1541	-4144	-	-	-
V-4-3-I	-375	-764	-994	-6006	-	-	-399
V-4-4-I	249	-227	-633	-4162	-	-	194
V-4-4-II	-1849	-2339	-2585	-4367	-	-	-11426
U-6-5-I-E	-436	-828	-1033	-1338	-3449	-	-8047
U-6-6-I-E	-690	-1181	-1560	-2339	-10382	-	-
U-6-7-I	-212	-410	-514	-690	-1079	-2905	-7072
U-6-8-I	-194	-391	-465	-603	-884	-2503	-9018

Based on steel properties presented in Table 19, and the measured strains in Table 23, it is clear that all compression bars exceeded their yield strain at some point during testing. The specimens with a greater amount of compression steel than tension steel were not expected to yield, based on an average stress in the bars. However, the strain gauge was placed on the bottom of the bars, and there was a significant strain gradient through the depth of the bars. Therefore, even if the strain at the center of the bar was less than yield, the strain gage on the bottom of the bar could indicate yielding. To get a better understanding of the behavior of the cross-section, and thereby determine the forces in the spliced bars, a strain compatibility analysis was performed on the four tested cross-sections. The following section describes the assumptions made in the analysis.

5.5. Strain Compatibility Analysis

To perform a strain compatibility analysis, the constitutive relationships for each material must be known. For the reinforcing steel, the material properties determined during testing were averaged for all bar sizes to result in a single stress-strain relationship used for all bars. The relationship is presented in Figure 197, and the equations for various strain ranges are presented in Table 24.
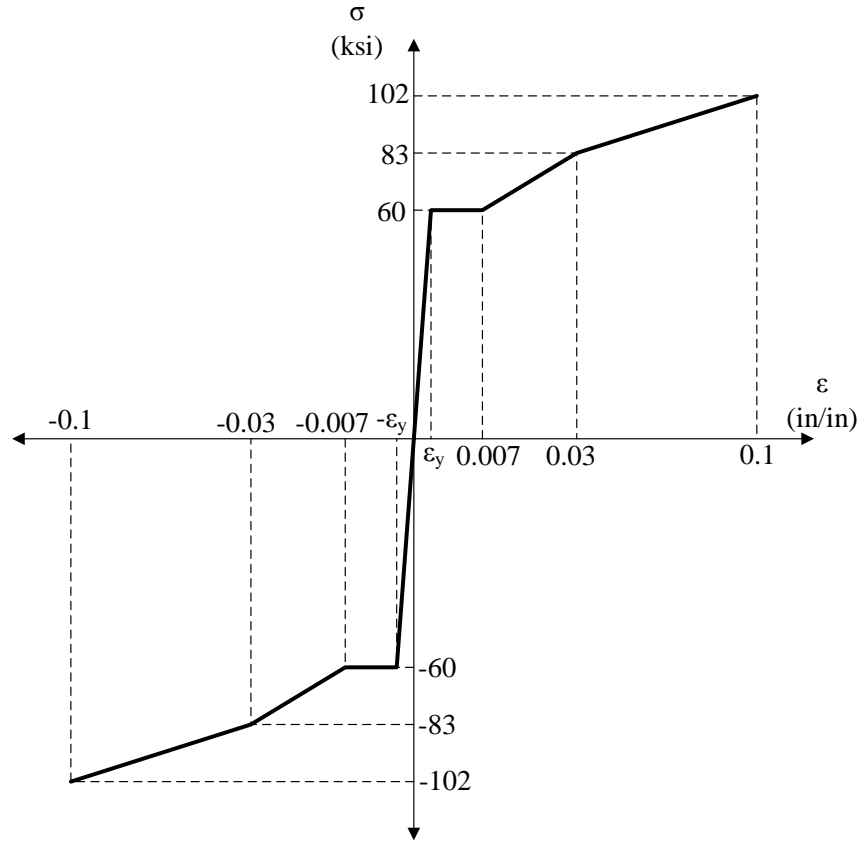
Figure 197: Stress-strain relationship for reinforcing steel.

Table 24: Equations for steel stress and strain.

Strain Range	Equation
$\varepsilon_s > 0.03$	$F_s = 85 + (\varepsilon_s - 0.03)214 \leq 102$ ksi
$0.007 \leq \varepsilon_s < 0.03$	$F_s = 60 + (\varepsilon_s - 0.007)1087$
$\varepsilon_y \leq \varepsilon_s < 0.007$	$F_s = 60$
$-\varepsilon_y \leq \varepsilon_s < \varepsilon_y$	$F_s = \varepsilon_s E_s$
$-0.007 < \varepsilon_s \leq -\varepsilon_y$	$F_s = -60$
$-0.03 < \varepsilon_s \leq -0.007$	$F_s = -60 + (\varepsilon_s + 0.007)1087$
$\varepsilon_s < -0.03$	$F_s = -85 + (\varepsilon_s + 0.03)214 \geq -102$ ksi

Since the strain gradient for the cross-section at high loads was very steep, it was possible that part of the compression reinforcing bar could be yielded while the rest of the bar was elastic. At higher loads, it would be possible that part of the bar was strain hardening, while other parts were at yield. Therefore, a computational approach was needed to determine the total force in a bar, based on the strain distribution through the depth of the bar.

The approach adopted was to split the bar into 20 slices. For each slice, the location of the center of the slice relative to the center of the bar was calculated. Then, based on the curvature assumed for a given

iteration, the strain at the center of each layer was calculated. Based on the relationships in Table 24, the stress in each layer was determined. The width of the layer was determined, and the area was calculated as the width of the layer times the thickness. This was not a precise calculation for the circular bar, but with 20 slices, was within 98% of the actual area of each slice. Finally, the force in each layer could be calculated as the stress times the area, and all the forces were summed to determine the total force in the bar.

A constitutive model was also needed for the UHPC in the splice pocket. Figure 197 presents the model used, which was adopted from Russell and Graybeal (2013). For the UHPC in compression, the stress is simply the strain times the modulus of elasticity. On the tension side, the stress is the strain multiplied by the modulus up to the cracking stress. For strains larger than the cracking strain, but less than a limiting strain, the stress is assumed to be constant, and equal to the cracking stress. At strains larger than the limiting strain, the stress in the UHPC drops to zero.

The modulus, cracking stress and limiting strain were selected based on material tests, but there was some uncertainty related to these numbers. The analysis was performed using a high value for each parameter, and a low value. In this way, the behavior could be bracketed between two possibilities, one with very good UHPC performance and contribution to strength, and the other with lower performance. The lower performance standards are more similar to the interface between the UHPC and the concrete. This was the location that typically cracked first, and once cracked carried no tension. It is expected that the measured behavior would fall between these two extremes. The high and low values for the UHPC parameters are presented in Table 25. The same values were used for the VHPC.

Table 25: Parameters for UHPC constitutive model.

Parameter	High Value	Low Value
Modulus of Elasticity	8000 psi	6000 psi
Cracking stress	1.0 ksi	0.25 ksi
Limiting Strain	0.010	0.0005
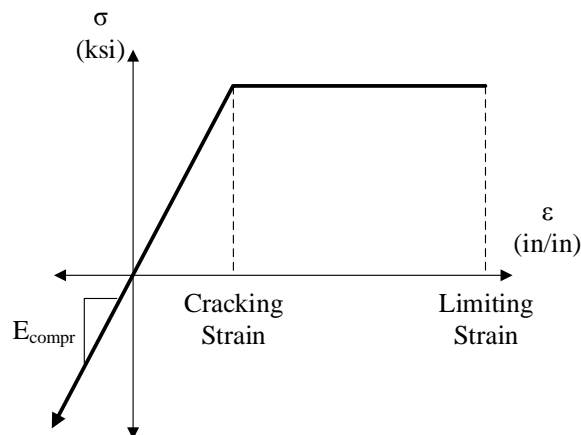
Figure 198: Constitutive model for UHPC.

The calculations for the UHPC/VHPC pocket were also done by splitting the cross-section of the pocket into 20 strips of 0.25 in thickness. Based on the assumed curvature for a given iteration, the strain at the center of each strip was calculated. Then the stress and the force were calculated. To determine the internal moment, the centroid of the force in the UHPC/VHPC, relative to the top of the beam was also calculated.

The process to calculate one point on the load vs. strain-at-the-bottom-of-the-bar curve was as follows:

1. Select the strain at the centroid of the compression bar for the point to be calculated.
2. Select a neutral axis depth, c, measured from the center of the compression bar.
3. Based on strain and c, calculate the curvature, $\phi = \varepsilon/c$.
4. Based on the strain and curvature, determine the strain at each layer of steel and UHPC/VHPC.
5. Based on strains and constitutive relationships, determine the stresses and forces in the UHPC/VHPC and steel bars.
6. Sum stresses, and iterate on c, until the forces sum to zero.
7. Based on c, calculate internal moment.
8. Based on internal moment and the statics of the beam specimens, calculate the externally applied load.

This process was repeated for increasing levels of strain at the center of the compression bar for four different cross-sections, representing the four combinations of compression and tension reinforcement tested in this program. For each cross-section, the analysis was done using the high and low values for the UHPC constitutive model shown in Table 25. Then, the calculated plots of load vs. strain-at-the-bottom-of-the-bar were compared to measurements from tests. The comparisons are shown in Figure 199, Figure 200, Figure 201, Figure 202 and Figure 203. The same calculations were performed for the VHPC specimens and the comparison of calculated vs. measured values is shown in Figure 60. Plots are shown for the analyses using the lower properties, because these calculations matched the measured values better.
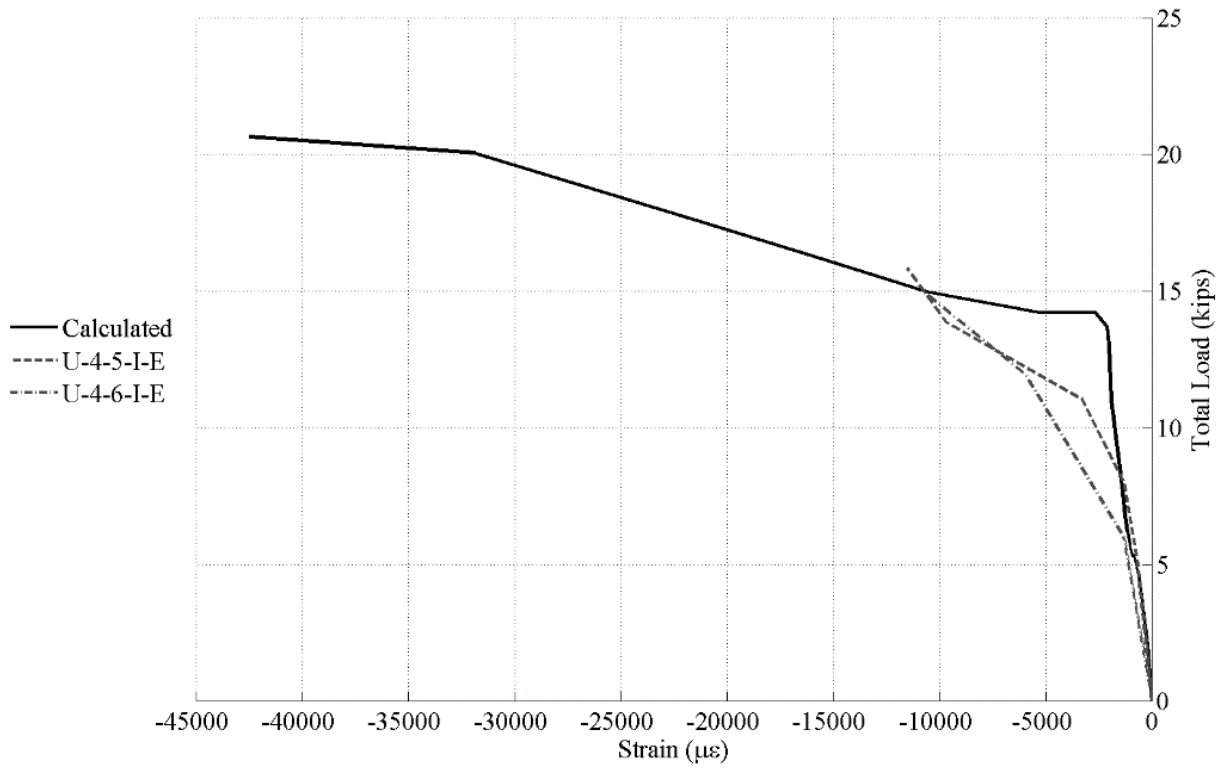
Figure 199: Load vs. strain at bottom of compression reinforcement for specimens with two No. 4 bars at top and bottom of beam.
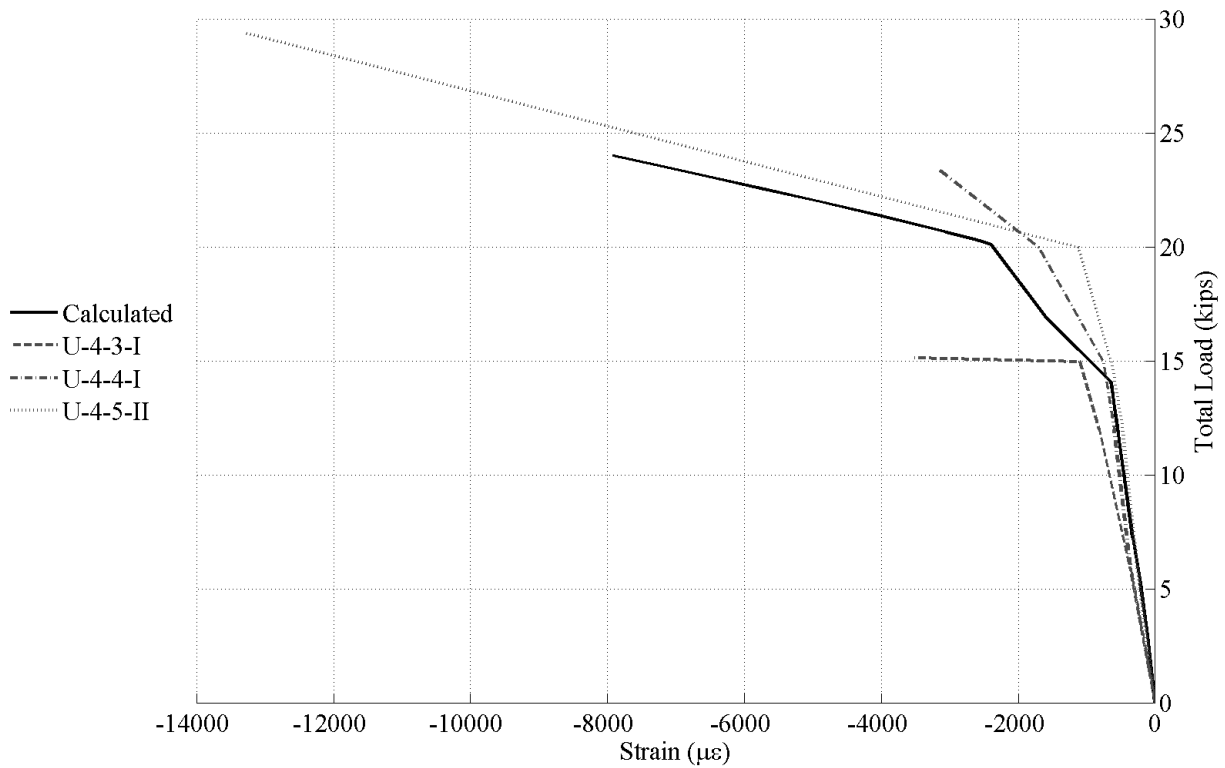
Figure 200: Load vs. strain at bottom of compression reinforcement for specimens with two No. 4 bars at top and two no. 7 plus one no. 6 at bottom of beam.
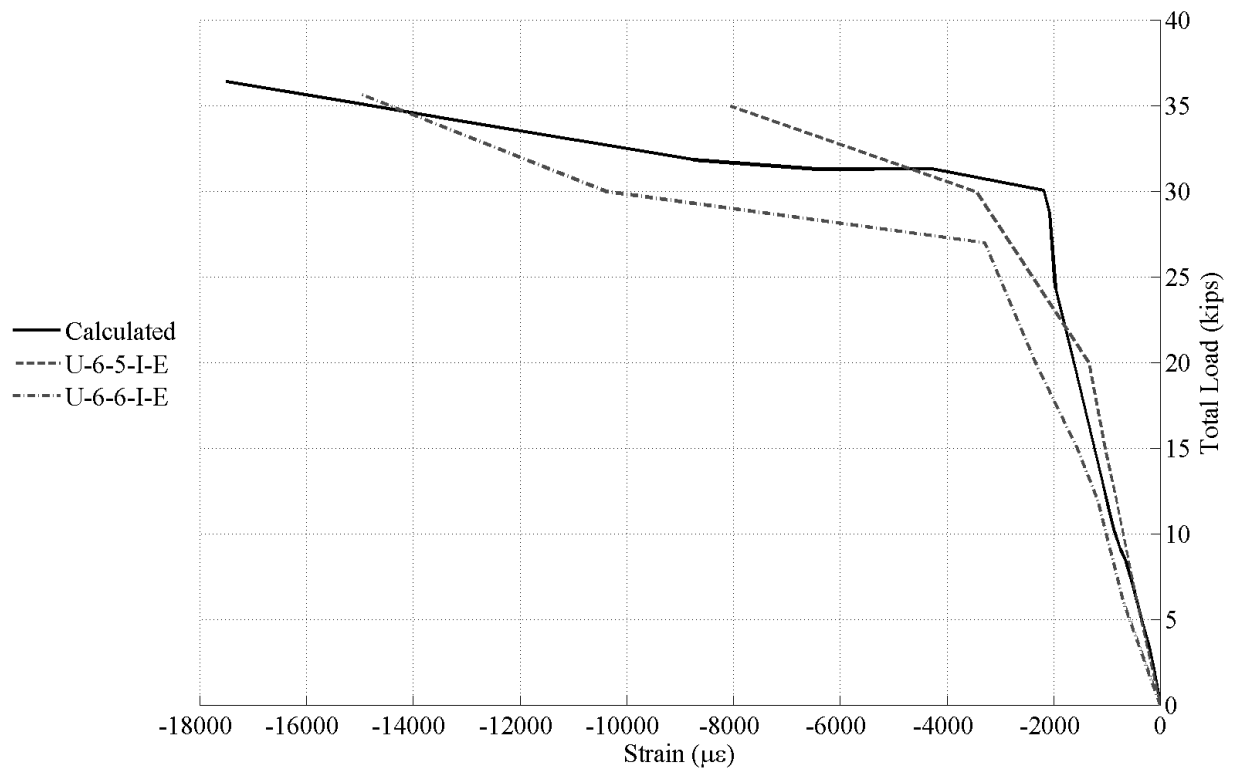
Figure 201: Load vs. strain at bottom of compression reinforcement for specimens with two No. 6 bars at top and bottom of beam.
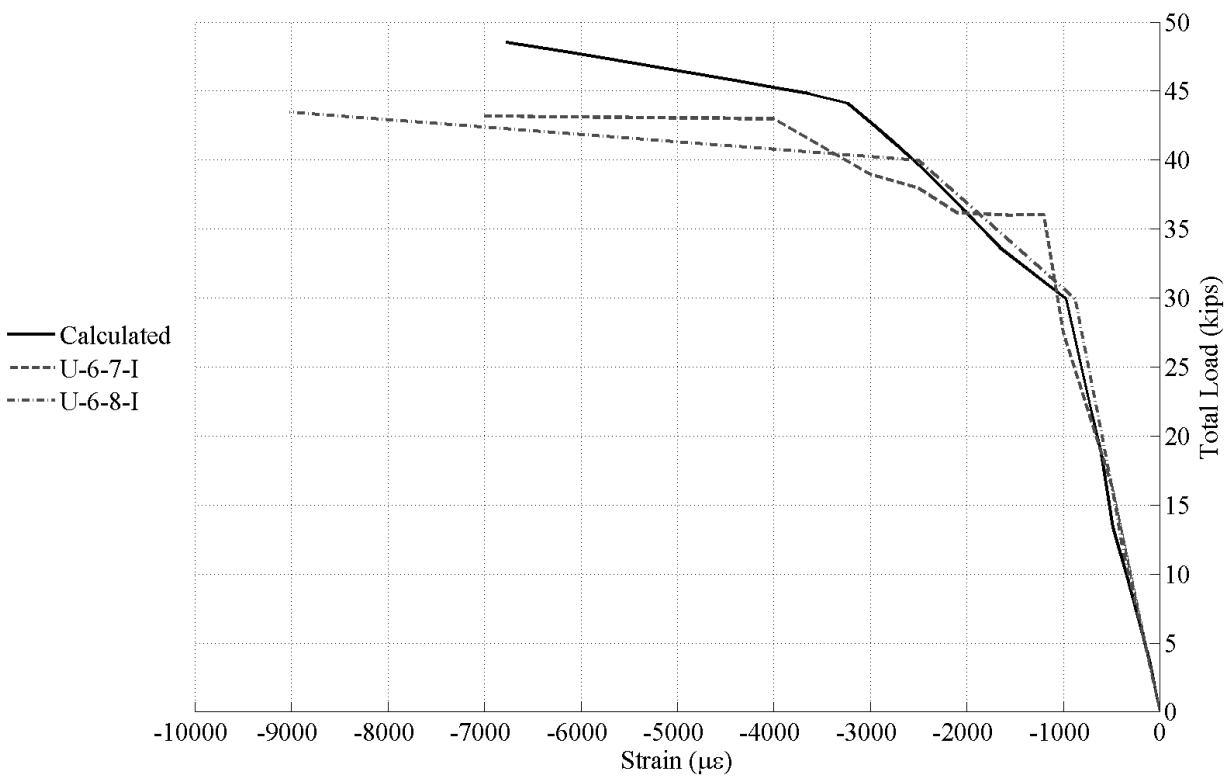
Figure 202: Load vs. strain at bottom of compression reinforcement for specimens with two No. 6 bars at top and two No. 8 plus one No. 7 at bottom of beam.
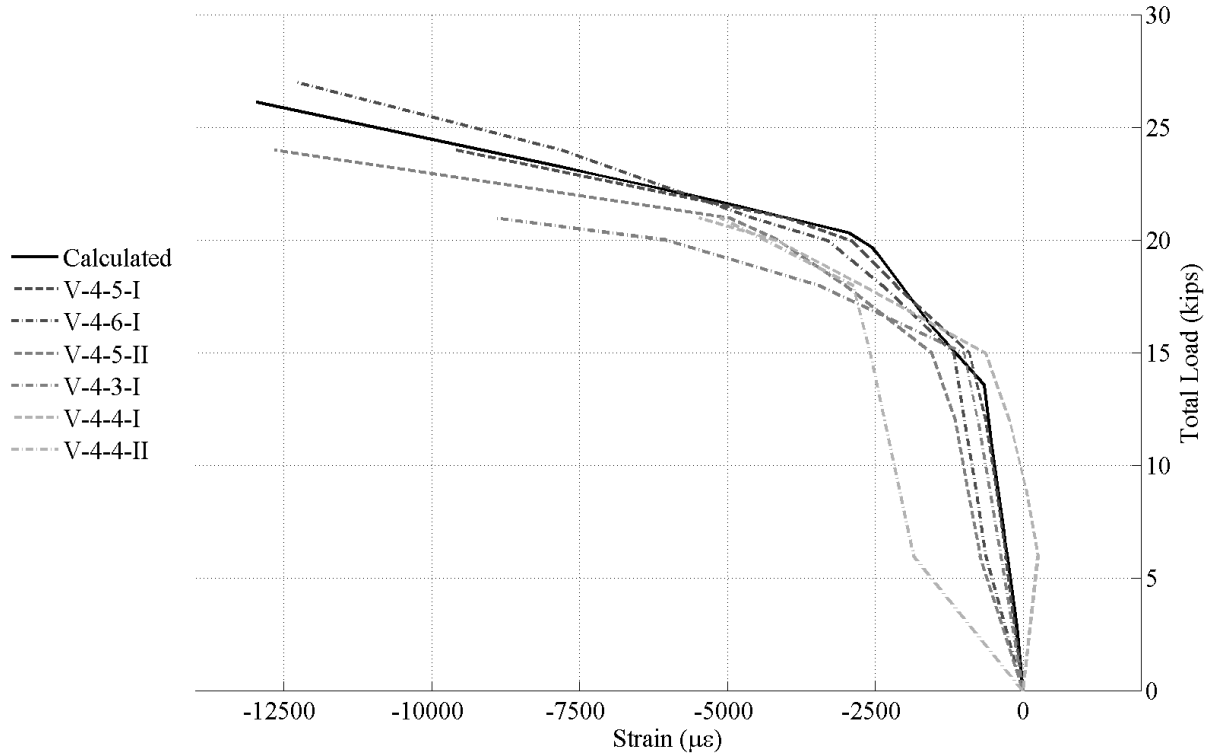
Figure 203: Load vs. strain at bottom of compression reinforcement for specimens with Two No. 4 bars at top and two no. 8 at bottom of beam with VHPC.

Overall, a good agreement was observed between the strain compatibility analysis and the measured data. Differences between predicted and observed behavior were most likely caused by the averaging of steel material properties and the inherent variability in the bond strength between the pocket filler material and the concrete in the precast element.

Because the agreement between measured and calculated compression strains was good, the model was used to determine the strain in the tension reinforcement. For most specimens, the strain that was calculated for the tension reinforcement at the maximum measured compressive strain was selected as the maximum tension strain. For some specimens (U-4-5-II and U-6-8-I), the measured compressive strain was higher than predicted by the model. In this case, the model's maximum tension strain was selected to represent the maximum tested tensile strain. The scheme of selection of ultimate compressive strains is shown in Figure 204.

Based on the maximum tension strain determined from the analysis, the stress in the tension steel was calculated from the constitutive model shown in Figure 197. The strains and stresses in the tension steel were calculated and are reported in Table 26.
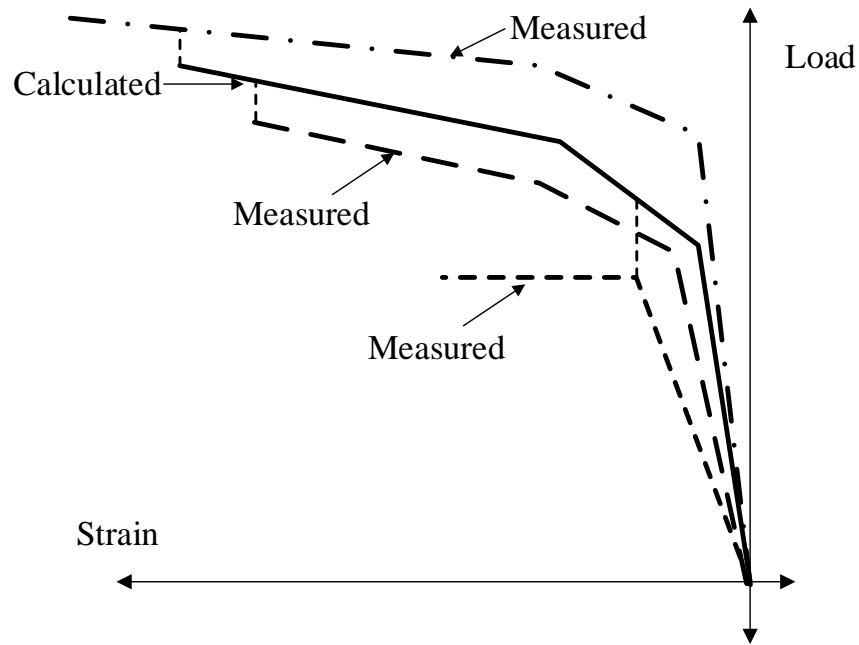
Figure 204: Method for selecting strain in compression bars at ultimate.

As observed in Table 26, the tension reinforcement in all specimens attained the yield stress. Therefore, based solely on the criteria of yield stress, a 3 in splice length is adequate for a No. 4 bar in UHPC or VHPC, and a 5 in splice length is adequate for a No. 6 bar in UHPC. However, ductility should also be considered. ACI 318-11 requires that for a beam to be considered tension controlled, the tension reinforcement must reach a strain of at least 0.005, which was exceeded by all the specimens.

There are, however, several other factors that need to be considered in making the splice length recommendation. First is the inherent variability in construction. The actual splice length may be shorter than specified due to construction error, or there may be improper mixing or placing of the UHPC or VHPC around the splice which would reduce the bond strength. These possible problems would reduce the strength and ductility of the splice. The scope of this research project did not allow for multiple repetitions of splice lengths to be tested, so the inherent variability is unknown. Based on the expected variability in field splices, a 5 in splice is recommended for No. 4 bars for UHPC and VHPC. A 6 in splice is recommended for No. 6 bars, in UHPC only.

Table 26: Maximum strains and stresses in tension reinforcement.

Specimen Designation	Splice Length (in.)	Selected Strain in Compression (in. /in.)	Maximum Strain in Tension Steel (in. /in.)	Maximum Tension Stress (ksi.)
U-4-5-I-E	5	0.012	0.010	63.3
U-4-6-I-E	6	0.011	0.009	62.2
U-4-3-I	3	0.001	0.016	69.8
U-4-4-I	4	0.003	0.040	87.1
U-4-5-II	5	0.008	0.100	100
V-4-5-I	5	0.008	0.11	102.3
V-4-6-I	6	0.008	0.14	108.6
V-4-5-II	5	0.008	0.145	109.5
V-4-3-I	3	0.008	0.104	100.8
V-4-4-I	4	0.005	0.066	92.6
V-4-4-II	4	0.005	0.062	91.8
U-6-5-I-E	5	0.008	0.008	60.9
U-6-6-I-E	6	0.015	0.013	66.5
U-6-7-I	7	0.007	0.067	92.9
U-6-8-I	8	0.007	0.067	92.9

5.6. Summary of splice tests

Testing was performed to ascertain the performance of UHPC and VHPC as a filler material to allow the use of short splice lengths in longitudinal joints between adjacent box beam bridges. Based on the results of the static tests performed on simply supported beam specimens it was determined that the minimum splice length for No. 4 bars was 4 in. with UHPC and VHPC. The minimum splice length for No. 6 bars was 6 in. with UHPC only.

6. Characterization of Connection Behavior

The connection behavior was studied through laboratory testing of the sub-assemblage (SA) specimens to observe response to transient traffic loads and through finite element analysis for long term effects of creep, shrinkage and temperature. The results of the laboratory tests and the finite element analysis are now discussed.

6.1. Results of material property tests

Material properties were assessed for beam section concrete, connection materials and topping concrete. The material properties tested, the specimens and the corresponding ASTM standards referred for those tests are shown in Table 27.

Table 27: Details of material property tests.

Test	Specimen	Material	Standard	Reference
Compressive Strength	4 in. × 8in. Cylinders	Normal Concrete and VHPC	C39	ASTM (2009)
Compressive Strength	2 in. × 2 in. Cubes	Grout and UHPC	C109	ASTM (2013)
Splitting Tensile Strength	4 in. × 8in. Cylinders	UHPC and VHPC	C496	ASTM (2011)
Modulus of Elasticity	4 in. × 8in. Cylinders	All cementitious materials	C469	ASTM (2014)
Free Shrinkage	1 in. × 1 in. × 12 in. Bars	Grout and UHPC	C157 and C490	ASTM (2008) and ASTM (2011)
Free Shrinkage	3 in. × 3 in. × 12 in. Bars	VHPC	C157 and C490	ASTM (2008) and ASTM (2011)
Joint – beam concrete bond	2 in. diameter × 1in. high stub cylinders	Grout, UHPC and VHPC	N/A	Wallenfelsz et al. (2007)

Typically, the material property tests were performed on the first day and the last day of fatigue testing except for the beam section concrete and shrinkage readings. Typically, the final static test was performed right after the completion of fatigue testing. The shrinkage readings were first taken after the formwork was released and continued until the last day of testing. The specifics of material testing are now discussed.

6.1.1. Beam section concrete

The concrete beam sections were fabricated in three different batches. Each batch consisted of six beam specimen sections with two beam sections each for the unmodified cross-section, top flange splice without topping and top flange splice with topping. Therefore, each specimen consisted of concrete from two different batches. The specimen section usage based on the batches is shown in Table 28. Note that the age of concrete batches shown in Table 28 is the age on the day of testing. In the three beam setup of the sub-assemblages the sections from the same batch were used as exterior beams for the sake of symmetry. Also, Batch 1, 2 and 3 are referred to as B1, B2 and B3 respectively.

Table 28: Beam section concrete as per batch.

Specimen	Type	Exterior Sections		Middle Section	
		Batch	Age (Days)	Batch	Age (Days)
1	Existing Detail	B2	76	B3	72
2	UHPC Top Connection	B3	96	B2	100
3	UHPC Top Connection with Topping	B3	128	B2	132
4	Existing Detail with K&E	B1	170	B3	163
5	VHPC Top Connection	B1	187	B2	184
6	VHPC Top Connection with Topping	B1	211	B2	208

The beam section concrete properties were determined from two cylinders for each batch used in each specimen since a limited number of cylinders were available for testing. The results for the material properties testing are presented as averaged results for compressive strengths and moduli of elasticity for each batch used in the corresponding specimen. The results are presented in Table 29. The beam section concrete properties were assessed only on the last day of testing. Considering the age of concrete a significant change in material properties was not expected between the start of the test and the end of one specimen test, which typically was six to seven days.

Table 29: Summary of material properties for beam section concrete.

Specimen	Compressive Strength (psi)		Modulus of Elasticity (ksi)	
	Exterior	Middle	Exterior	Middle
1	7381	9450	5634	6220
2	9569	7659	6389	5801
3	10026	7619	5879	5566
4	7301	10086	5139	6315
5	7421	7620	5214	5791
6	7380	7539	5231	5710

6.1.2. Joints

The connection material properties were tested twice in the course of fatigue testing. The properties were initially tested at the start of testing, which typically was seventh day after fabrication of specimen joints. The exceptions to start of testing on the seventh day were Specimen 2 and 6. The reasons for these exceptions are explained in Sections 6.2.2 and 6.2.4 respectively. The material properties were also tested on the last day of testing, which was typically the sixth day after start of testing for all specimens. The compressive strength, modulus of elasticity and the splitting tensile strength were measured for the materials used in joints. Three cylinders each were used for compressive strengths and modulus. Splitting tensile strength test results were based on two or three cylinders depending upon the quantity of completely mixed material from each batch. These results are presented in Table 30.

Table 30: Summary of material properties for joints.

Specimen	Material	Compressive Strength (psi)		Modulus of Elasticity (ksi)		Tensile Strength (psi)
		Test Start	Test End	Test Start	Test End	Test End
1	Grout	7417	7833	2957	3094	N/A
2	UHPC	15167	17583	7341	7774	2036
3	UHPC	14042	17167	6941	7516	2195
4	Grout	8208	8792	3142	3262	N/A
5	VHPC	12839	13488	5019	5549	1671
6	VHPC	13063	13980	5271	5263	1900

Free shrinkage was recorded by measuring the change in length of 12 in. long bars. It is to be noted that the actual gauge length for measuring shrinkage was 11 in. The measurements were started after removal of joint formwork and stopped after the completion of the sub-assemblage specimen tests. The exception to this was Specimen 1 which failed on the third day of testing. These measurements are presented in Table 31, which shows the average value of shrinkage at the start and end of testing. Two shrinkage specimens were used for each sub-assemblage test. Shrinkage was recorded for all specimens except Specimen 4 in which the 1 in. x 1 in. cross-section bars broke during release from molds.

Table 31: Summary of shrinkage for joints.

Specimen	Type	Shrinkage (µε)	
		Test Start	Test End
1	Grout	687	764
2	UHPC	170	315
3	UHPC	199	320
4	Grout	NA	NA
5	VHPC	117	279
6	VHPC	202	308

6.1.3. Topping concrete

Concrete topping was used with Specimens 3 and 6 only. The age of the concrete topping in both the specimens at the start of testing was four days. Typically, in the field conditions the bridge is not opened to traffic until the twenty-eight day target strength is not achieved as per VDOT (2007). This protocol was not followed in this research in order to start loading the specimens seven days after placing the joints. The specimens were analyzed in FEA to ensure that the stresses in the topping do not exceed the compressive strength of the concrete. Similarly, the bearing strength of the topping was also checked under the location of displacement application. The FEA models confirmed that the stresses did not exceed the capacity of the topping concrete.

The material properties for the topping concrete were ascertained at the start of testing as well as at the end of testing. Three cylinders were each used for compressive strength and modulus of elasticity. Three additional cylinders were used for testing the splitting tensile strength. The properties of topping concrete are summarized in Table 32.

Table 32: Summary of material properties for topping concrete.

Specimen	Compressive Strength (psi)		Modulus of Elasticity (ksi)		Tensile Strength (psi)
	Test Start	Test End	Test Start	Test End	Test End
3	3833	4506	3681	4293	494
6	2162	3475	2794	3920	N/A

6.1.4. Joint – beam concrete bond

Bond strength was studied for the specimens using the simple pull off test. The pull off test was conducted for all specimens except the first one. That is because the need for performing a study on bond strength between the joint material and the actual beam concrete was made necessary after performing tests on Specimen 1. For Specimen 1, the joint cracked unexpectedly during initial adjustments prior to the start of testing. To avoid the repeat of such occurrences and to gain the knowledge of bond between the beam

concrete and the joint materials the bond strength was tested with a simple pull off test. The tests on Specimen 1 are discussed in Section 6.2.1. The bond strength was tested for Specimens 2 to 6 on the first and the last days of testing. A total of three to four specimens were tested at the start and the end of the each sub-assemblage test. The summary of averaged values is presented in Table 33.

Table 33: Summary of joint-beam concrete bond.

Specimen	Type	Bond Strength (psi)	
		Test Start	Test End
1	Grout	N/A	N/A
2	UHPC	195	204
3	UHPC	79	93
4	Grout	68	74
5	VHPC	35	86
6	VHPC	97	93

6.1.5. Discussion on material properties

The material property testing showed that UHPC possessed the best properties among the three materials. Grout possessed the lowest values of compressive strength and modulus of elasticity. Also, the bond strength was poor and the values for shrinkage were the highest. Therefore, the replacement of grout from ABBB joints seems logical. UHPC possessed the best properties in terms of strengths and stiffness. However, the shrinkage and bond values were comparable with the VHPC values. Therefore, based purely on material properties, any of the two fiber reinforced mixes can be used in the ABBB joints. The data presented in the previous discussion was only a summary of the test results. The complete material property test results are presented in Appendix E.

6.2. Results of sub-assemblage tests

As discussed earlier, six specimens were tested to study the behavior of existing and proposed connection details in the laboratory. The data recorded by the instruments is plotted with respect to the load cell on the actuator. Although the actuator location was manipulated in displacement control the load cell values were used as a reference. The target displacement for all specimens was 0.03 in. as per the ABAQUS model of the sub-assemblage specimens. This displacement was to be applied to the middle section of the three beam sub-assemblage setup at the top flange. To reiterate, the target displacement was derived from the comparison of the finite element models of the sub-assemblage specimens and the full scale bridge. The target 0.03 in. displacement applied to the sub-assemblage specimen produced the same effect at the joints

as that observed in the full scale bridge model with a HS-20 truck including a 33% impact factor. The displacements recorded by the actuator consisted of the displacement applied to the specimen and the displacement of the test frame. The target displacement of 0.03 in. was to be applied to the specimen itself.

A total of thirty-five sensors were used in this testing program. The data presented in the following sections pertains to those instruments that display the behavior directly related to the main concern of this research, the behavior at the joints. The most important aspect of this research was the magnitude of stresses in the joints and the connections. The stresses could not be directly measured. Hence, the data from the instruments that indicated the condition of the joints is presented. The data not presented in the following section is provided in Appendix F.

6.2.1. Specimen 1 – Existing Detail

This was the first test performed in the program. The bond strength between grout and the concrete was unknown and a previous study by Wallenfelsz et al. (2007) showed that bond strength between grout and concrete could vary between 50 – 200 psi for a smooth surface with saturated surface dry (SSD) conditions. With a wide margin of bond strength, it was not known if the joints would crack during the static load application. The FEA model had indicated that the stress in the joint could go as high as 190 psi at the interface for a displacement of 0.03 in. Therefore, the specimen was planned to be loaded with short increments of 0.01 in. leading to a total of 0.03 in.

6.2.1.1. S1 – Fatigue tests

The load distribution for the S1 test was problematic from the construction of the specimen to testing. The self-weight of the specimen was not distributed equally on the four load cells. The majority of the load would be supported by three load cells with one load cell not in contact with the specimen. Therefore, thin shims were inserted prior to joint fabrication to balance the load better. However, this load balance was lost after joint fabrication. The loss of balance was caused by the formwork used to place the joints. The load distribution was attempted to be rectified prior to the commencement of testing. A hydraulic jack was used to lift the exterior beam specimens and readjust the shims. During the process of readjustment of the shims, cracks developed at both the joints. These cracks developed for about the one third to half the depth of the joint. Cracks seen after the shim readjustment are presented in Figure 205. These cracks were marked and the test proceeded as per plan.

Figure 205: Cracks in joint after shim readjustment.

The specimen was loaded in 0.01 in. displacement increments. The total externally applied displacement was targeted at 0.03 in. However, in the first static test, the total applied displacement needed to be 0.06 in. to match the vertical deflections simulated by the finite element model. As described earlier, the target displacement to be applied to the specimen did not necessarily equate the displacement of the actuator due to other sources of flexibility in the test setup. Therefore, the actuator displacement application was monitored through the wire-potentiometer (WP) measurements. The displacements, at the locations of the WPs, were noted from the sub-assemblage (SA) model prior to test start. For the baseline static test the displacements were applied such that the measurements at the WPs matched those noted from the FE model. These specimen displacements were achieved after applying a total displacement of 0.06 in. To simplify the explanation for the need for additional displacements the first baseline test is presented schematically in Figure 206 and Figure 207. The behavior simulated by the finite element model is shown in Figure 206 and the actual behavior observed during the baseline static test is shown in Figure 207.
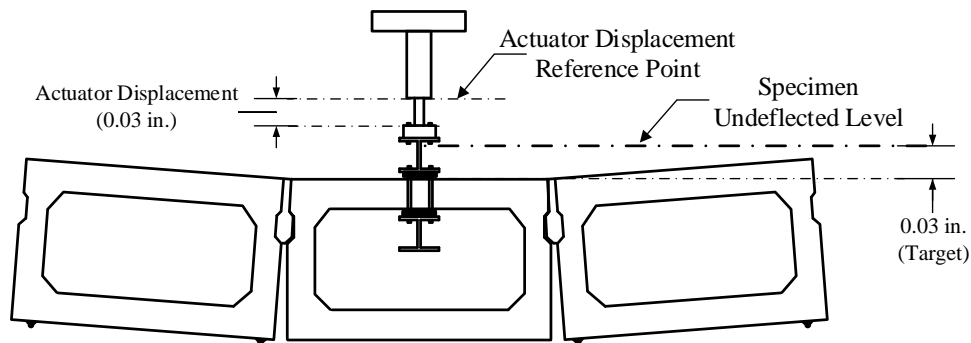
Figure 206: Behavior of the test setup as per finite element model.
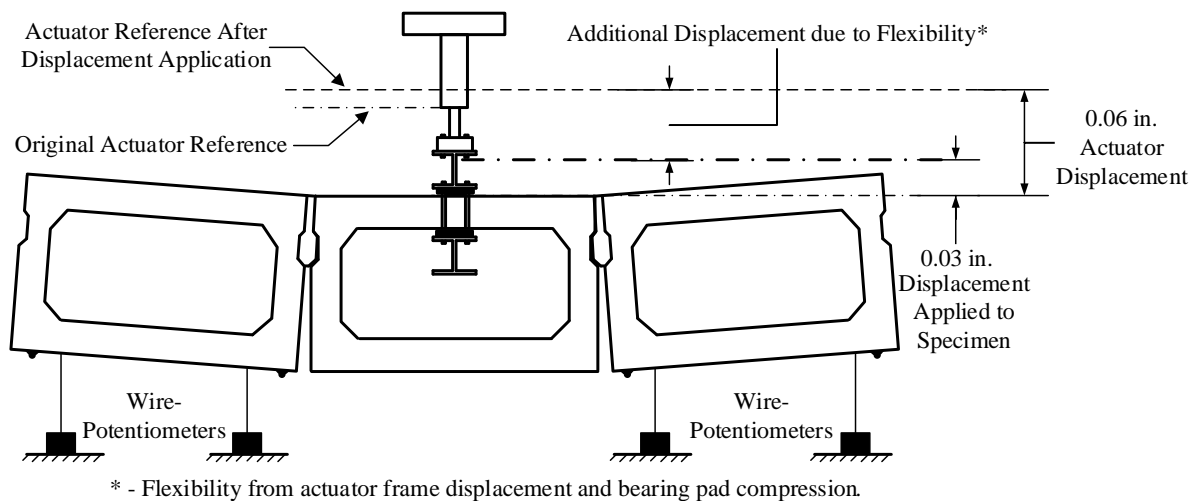
Figure 207: Actual behavior during testing.

The actuator load vs. actuator displacement plot is shown in Figure 208 and the variation of WP data is shown in Figure 209. The procedure of observing the WP measurements continued for every static test until the application of 100 cycles. As seen in the WP plot variation, it was very difficult to make definite observations of the actual displacements being imparted to the specimen. For every static test until the application of 100 cycles the specimen response seemed to be getting softer without any appreciable change to the depth of the cracks in the joints as seen in the load vs. displacement plot. An additional static test, denoted as Baseline 2 static test, was performed. For this test, the total actuator displacement required to produce the same level of expected specimen deflection was almost 0.14 in. This indicated that the neoprene pad used under the actuator to prevent stress concentrations was providing an additional amount of flexibility to the test setup. Moreover, the clamp tightness also seemed to be reducing with increasing number of cycles. Therefore, the test was paused and the clamps were retightened until neoprene pads in the clamps were crushed and it was not possible to tighten the clamps any further.

The effect of clamp tightness can be observed in Figure 208. All tests up to Baseline 2 test show a very flexible response. After the clamp retightening, the actual specimen response was seen. The magnitude of the total applied displacement was increased after clamp retightening until the expected reading at the WP was achieved. However, this target deflection was surpassed during the static test after the application of 100000 cycles due to the variation in the WP response. Consequently the specimen was overloaded and the depth of cracks increased during this static test.
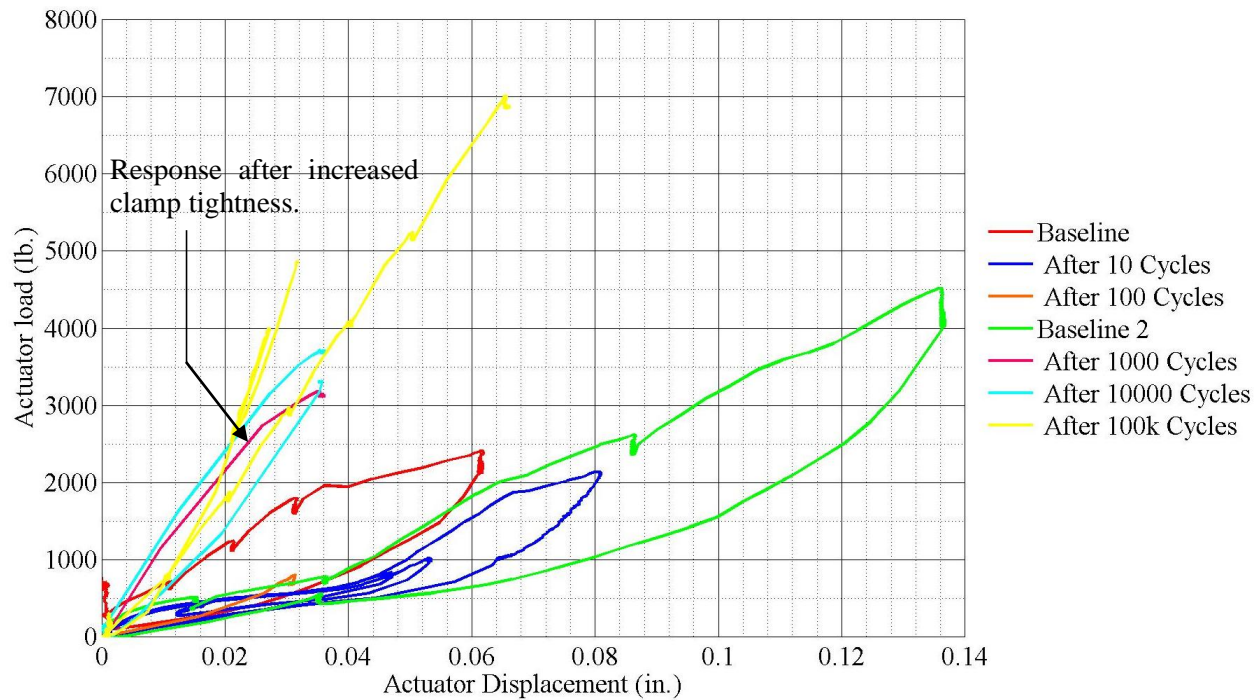
Figure 208: S1 - actuator load vs. actuator displacement.
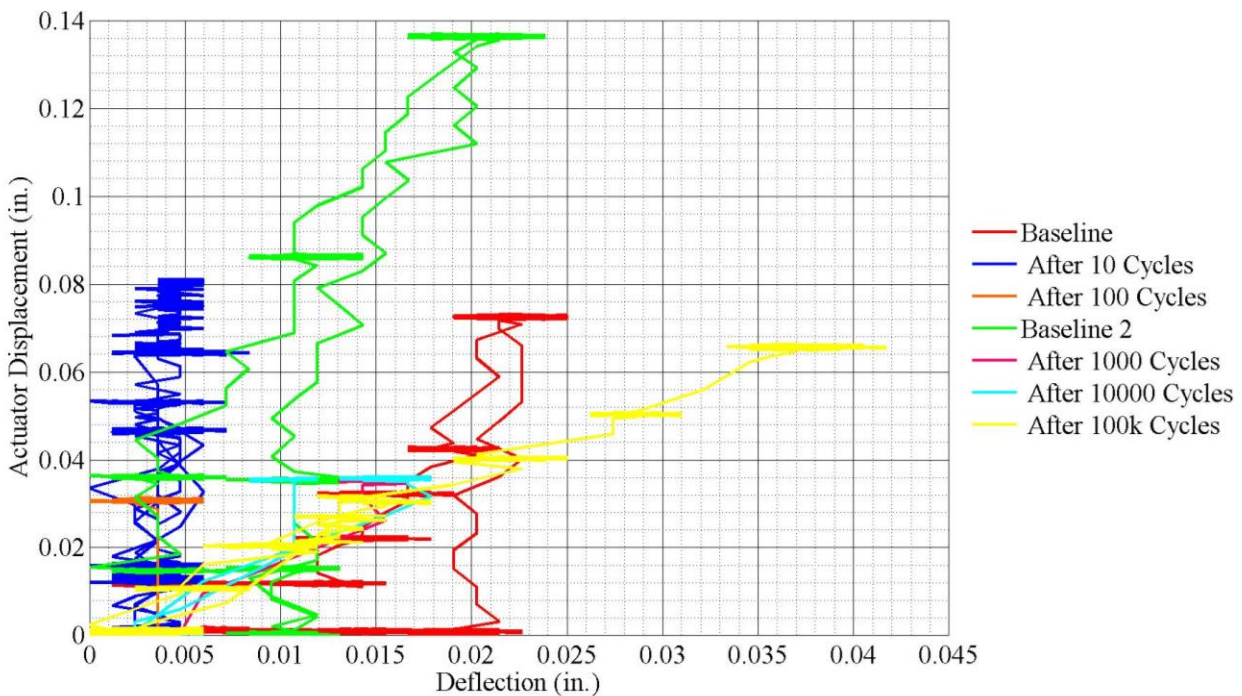
Figure 209: S1 – variation in vertical displacement near interior north support beam.

The existing cracks did not propagate in the first 100000 cycles as seen in the displacements recorded by LVDTs across the gaps between beams in Figure 210 and Figure 211. The existing cracks

propagated further after about 103000 cycles and completely debonded after about 106000 cycles at the south joint. The change in response after failure is shown in Figure 212.
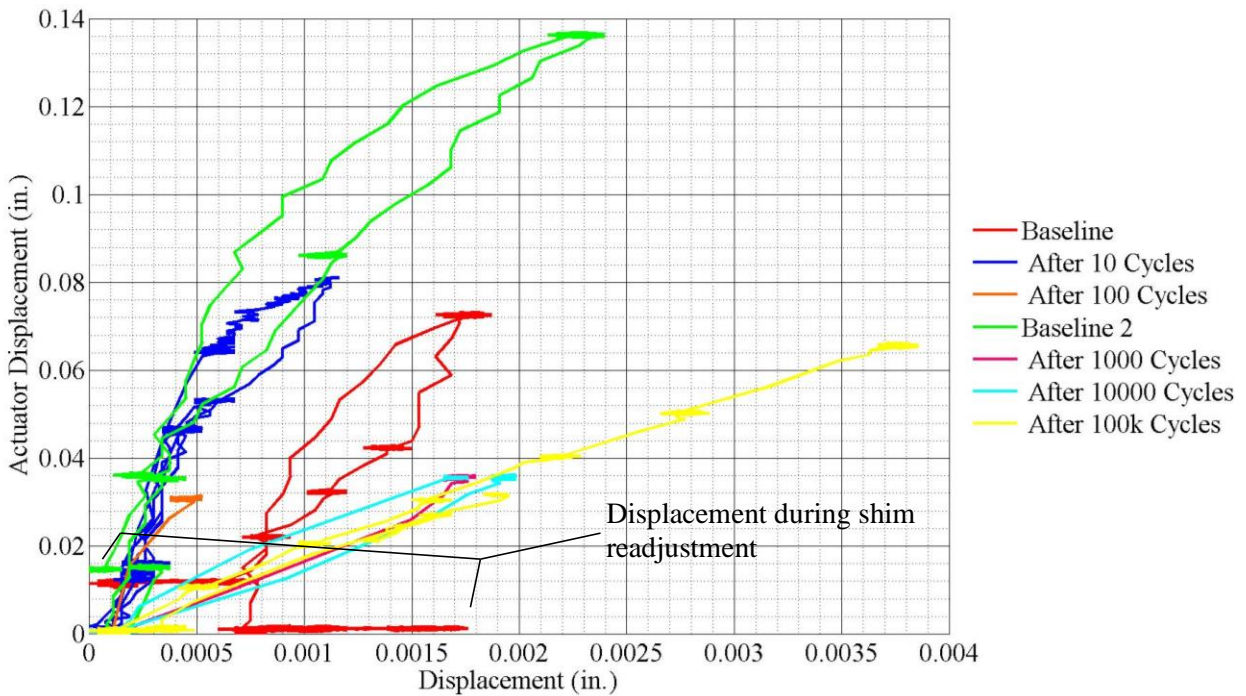
Figure 210: S1 – variation in north joint displacements during fatigue testing.
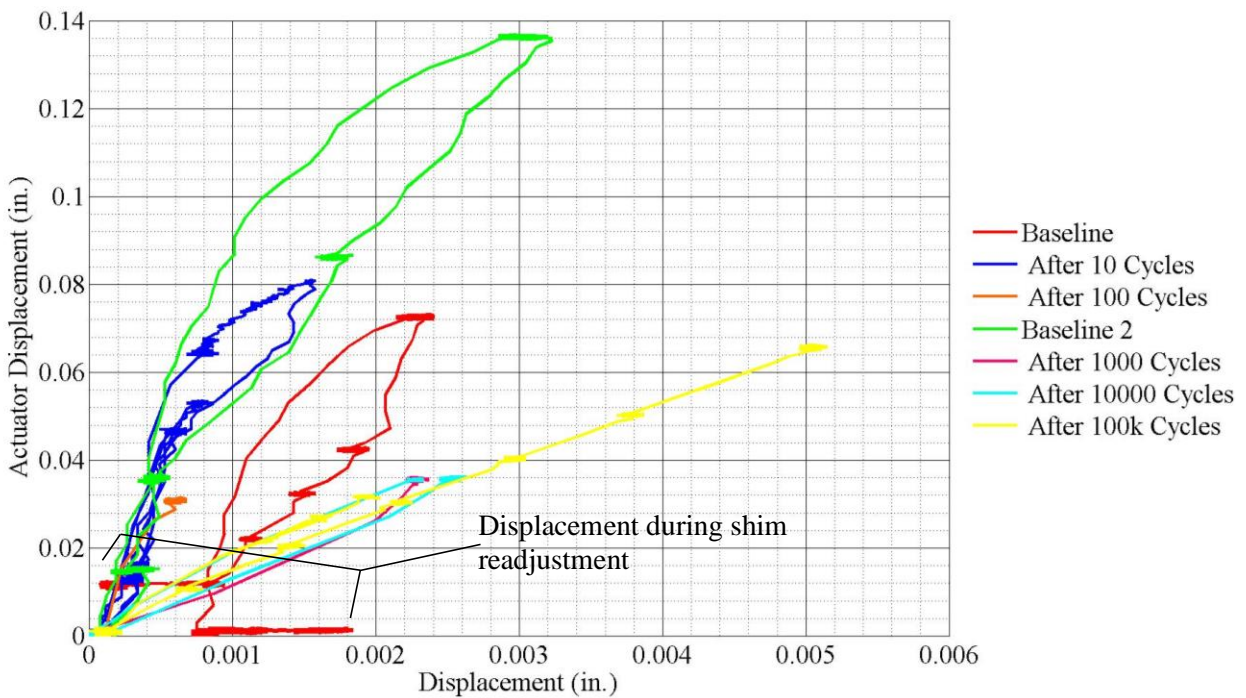
Figure 211: S1 – variation in south joint displacements during fatigue testing..

Figure 212: S1 – change in behavior after joint failure.

Figure 212 is plot of actuator load recorded during the application of 100000 cycles between cycle numbers 100000 to 200000. The data was recorded for 6 seconds every 2 minutes. The vertical lines seen in Figure 212 are the 6 second records of the actuator load cell data. Each individual line is a sine curve. A portion of data from Figure 212 is magnified and shown in Figure 213.

Figure 213: S1 – sample of recorded data.

Figure 214: S1 – cracks propagated for the full depth of south joint.

The grout completely debonded from the middle section. The grout came cleanly off the joint surface and also the grout did not remove any concrete from the precast girder sections. The joint after failure is shown in Figure 215.

Figure 215: S1 – no trace of grout in the joint.

6.2.1.2. S1 – Ponding test

The ponding test was performed for S1 after 1000 cycles. The joints did not leak until after complete joint failure.

6.2.1.3. S1 – Ultimate strength test

Only a single joint in S1 had failed during cycling. Therefore an attempt was made to fail the other joint. The loading protocol of 0.03 in. displacement was used. The specimen was loaded up to a total displacement of 0.15 in. The loading was stopped at this point since the gap at the joint began to close instead of opening. After failure of the joint, the assumed boundary conditions ceased to exist. Therefore, the gap behavior indicated closure instead of opening or in other words, the top of the joint was in tension and the bottom in compression. The loading was stopped also because the north beam section began lifting off of the supports. The load vs. displacement behavior of S3 is shown in Figure 216.
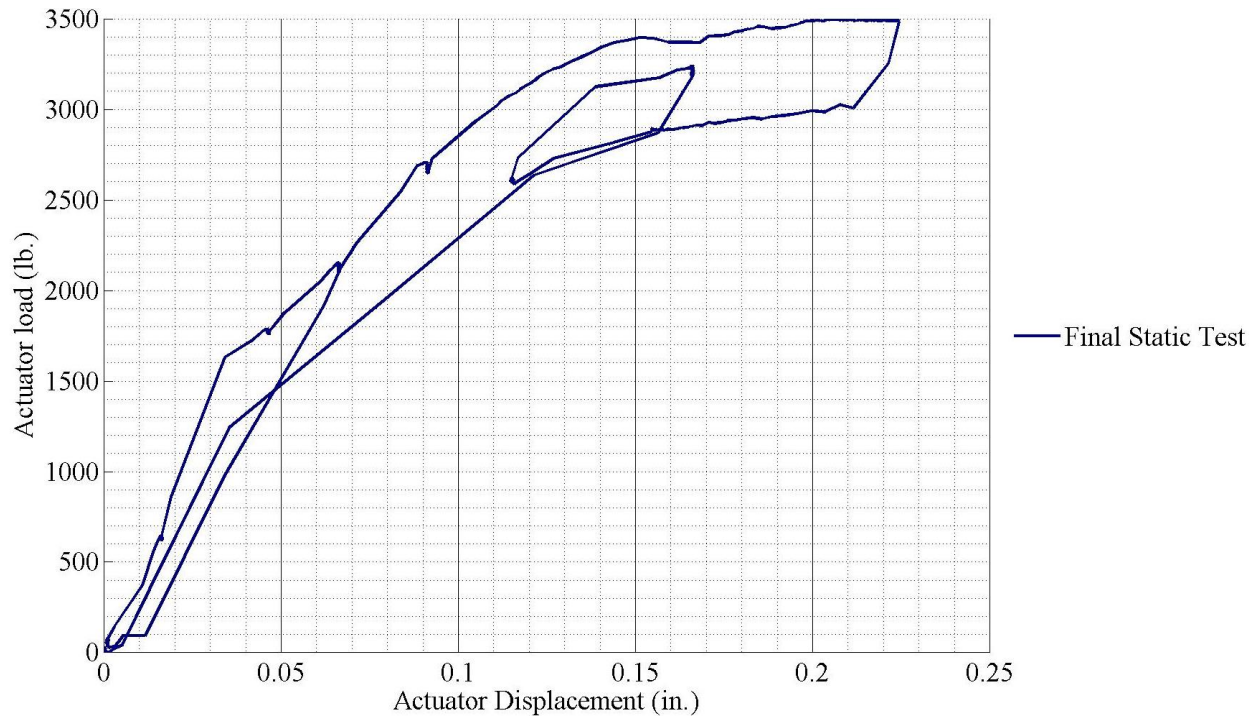
Figure 216: S1 – actuator load vs. displacement, final static test.

6.2.1.4. Summary of S1 Test

This test did not progress exactly as per plan due to the joints in this specimen cracking prior to the start of the testing during support readjustments. This key issue led to a major change in the test setup. The four load cell setup was changed to a three load cell setup. The load cells were placed in the corners of the exterior beam sections. In the new setup, the exterior load cell pair was reduced to a single load cell. The change in setup is shown in Figure 217.

Four Loadcell Setup   Three Loadcell Setup
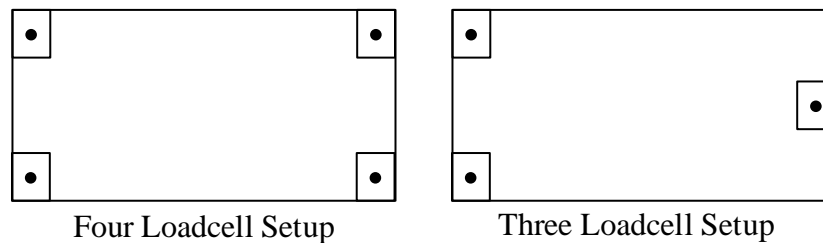
Figure 217: Change in load cell setup (Plan View).

The tightness of the clamps were not thought to be such an important factor initially in this testing. Increasing clamp tightness ensured that the flexibility of the test setup reduced. The reduction in flexibility at the clamps consequently nullified the requirement of applying small displacement increments to reach the target increment. Moreover, with the WPs being very sensitive to electrical noise and providing data unfit to observe and make changes to the displacement application an additional pair of vertical LVDTs

were attached to loading beam. The vertical LVDTs measured only the displacements imparted to the specimen and were not affected by the additional flexibility of the actuator frame.

Cracks were observed at the top of the keyway prior to the start of the testing. These cracks were present for the full length of the joint. The most probable cause of these cracks would be shrinkage, especially considering the shrinkage strains measured for the grout. It is to be noted that there was no leakage observed at the joints until after one joint had completely failed during loading. Therefore, the initial cracks were superficial in nature.

6.2.2. Specimen 2 – Spliced UHPC connection without topping

Several changes were made to the testing protocol after S1 test. The most important change was that the exterior beams were balanced on three load cells as opposed to four initially. By doing so, the problems with the self-weight distribution were precluded. The location of the load cell on the exterior support beams now coincided with the location of the bonded strain gauges. Therefore, these strain gauges were removed for this specimen test.

Another modification to the testing protocol was made necessary because of equipment issues. The MTS actuator was unable to hold a constant level causing a fluctuation in the magnitudes of loads and displacements. This is referred to as a dither problem by MTS. This problem occurred only while the actuator was expected to maintain a constant displacement. The actuator was able to change locations and apply cyclic loads without the problem of dither. This was observed and confirmed by running several trial runs of displacement application and few cycles of 0.015 in. displacement. The joints were observed for cracking during the trial phase and none were found. To fix the dither issue, the rate of displacement application was changed to 0.04 in./min instead of 0.1 in./min for static tests. This change was enforced to slow down the displacement application sufficiently such that the occurrence of cracks could be observed and displacement application could be stopped to mark the cracks. In lieu of occurrence of cracking, the complete displacement was applied and then removed with a minimal delay between the two to completely preclude the dither issue.

6.2.2.1. S2 – Fatigue Tests

The testing program progressed as per plan for this test. The static tests were performed followed by the cyclic tests. The specimen would typically be attached rigidly to the actuator clamping beams prior to the start of testing. With the application of the initial cycles, typically ranging from 10 to 100 cycles, the specimen clamping connection would loosen or any flexibility allowed by the neoprene pads would be discovered during the application of the initial cycles. The clamp tightness or the flexibility would be

rectified prior to continuing the cycling of the specimens. Therefore, the response of the specimens would change after the application of the first 10 – 100 cycles.

The load vs. applied displacement plot is shown in Figure 218. The plot shows the overall response of the specimen to applied displacements. The resistance of the specimen, indicated by magnitude of load, to the applied displacements did not change after the clamps were tightened to the ideal amount. This indicates that the joints in the specimen did not undergo any deterioration during the fatigue testing of the specimen S2.
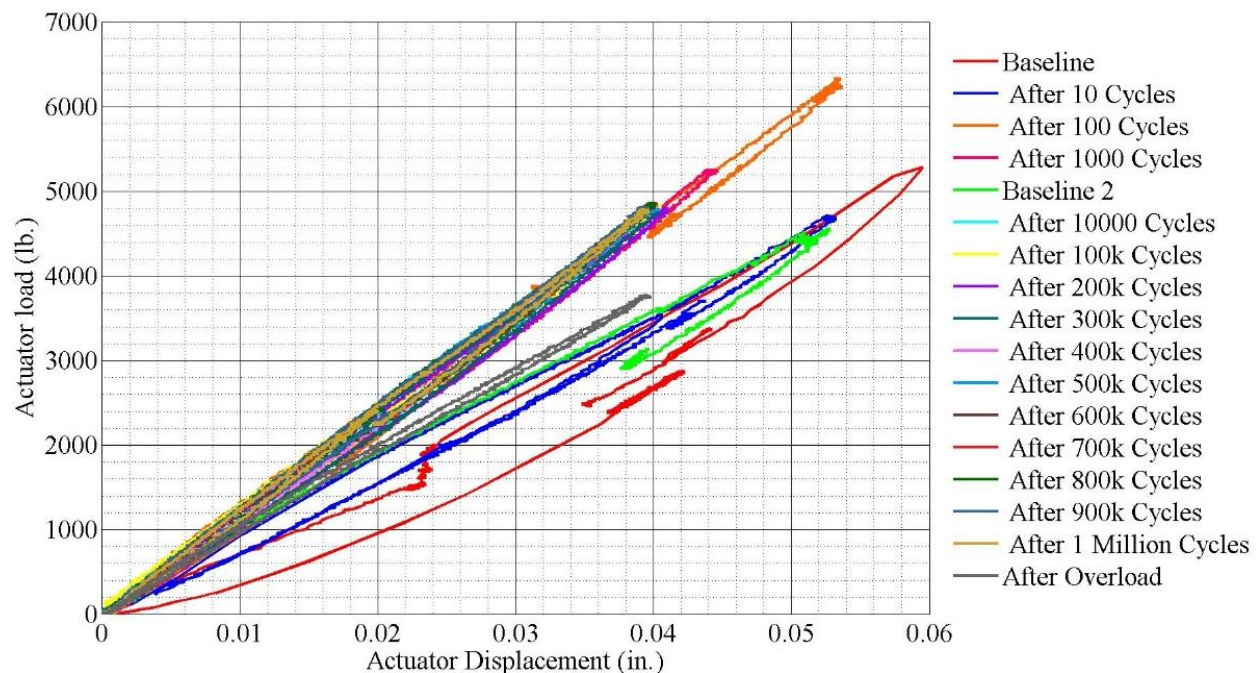
Figure 218: S2 - actuator load vs. actuator displacement.

The displacements applied to the specimen were smaller than the actuator displacements. These displacements were measured by externally mounted LVDTs. These LVDTs measured the relative displacement of the loading beam with respect to the ground as opposed to the actuator displacements, which were with respect to the load frame. The point of difference here was that the load frame and the neoprene pads in the test setup contributed to the total actuator displacements. The external LVDT displacements were not affected by the test setup flexibility and were direct measurements of displacements imparted to the specimens. The application of the target displacement of 0.03 in. could be verified through the measurements of the external LVDTs. The variation of the actual displacements applied to specimen S2 is shown in Figure 219.
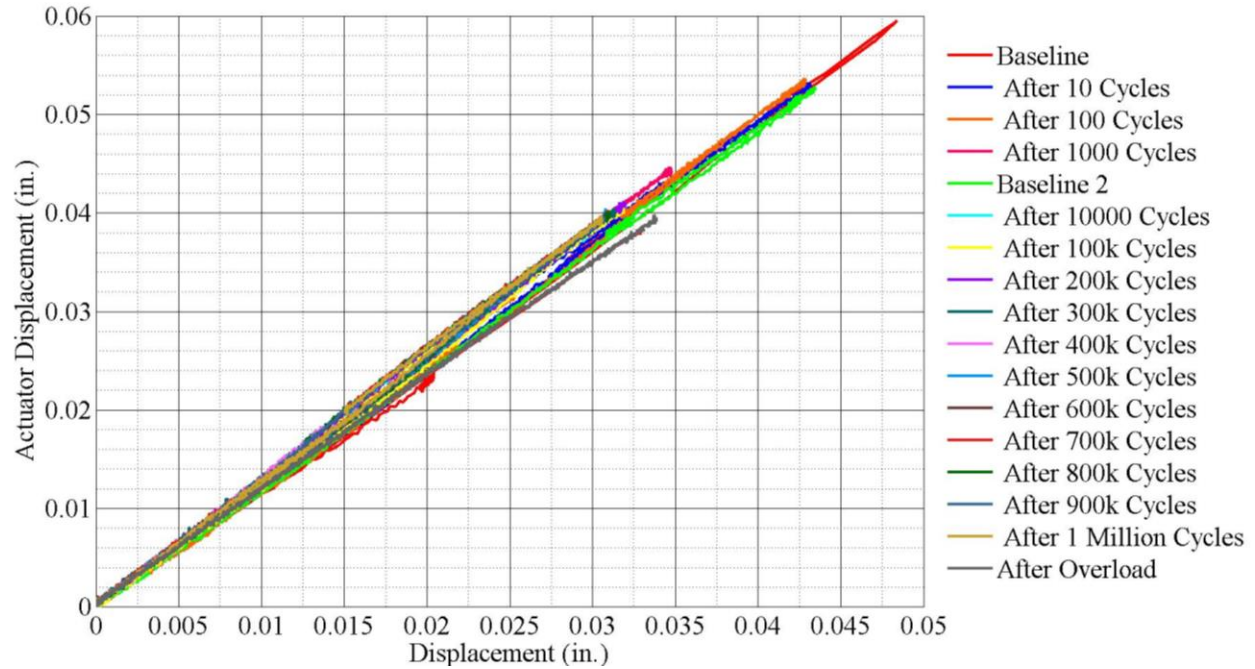
Figure 219: S2 – actual specimen displacements plotted with respect to actuator displacements.

After the initial adjustments to the actuator levels (two baseline tests), there was no change in the behavior of the specimen. This meant that there was no change in the stiffness of the specimen over the duration of application of a million cycles. There was no cracking observed in the specimen joints. The response at the base of the specimen was measured by four LVDTs. These responses are shown in Figure 220, Figure 221, Figure 222 and Figure 223. The response at the gaps did not change at all indicating that a crack was never initiated across the joint. Moreover, the specimen was loaded for an additional 100000 cycles after the conclusion of the ultimate strength to observe the change in response with cracked joints. This response is also included in Figure 220, Figure 221, Figure 222 and Figure 223. The change in response recorded by the gap LVDTs prior to and after cracking is quite drastic. The typical displacement at the gap between adjacent beams was approximately 0.0035 in. prior to cracking. After cracking, the magnitude of gap openings increased to 0.0085 in. which represents an increase by 2.4 times.
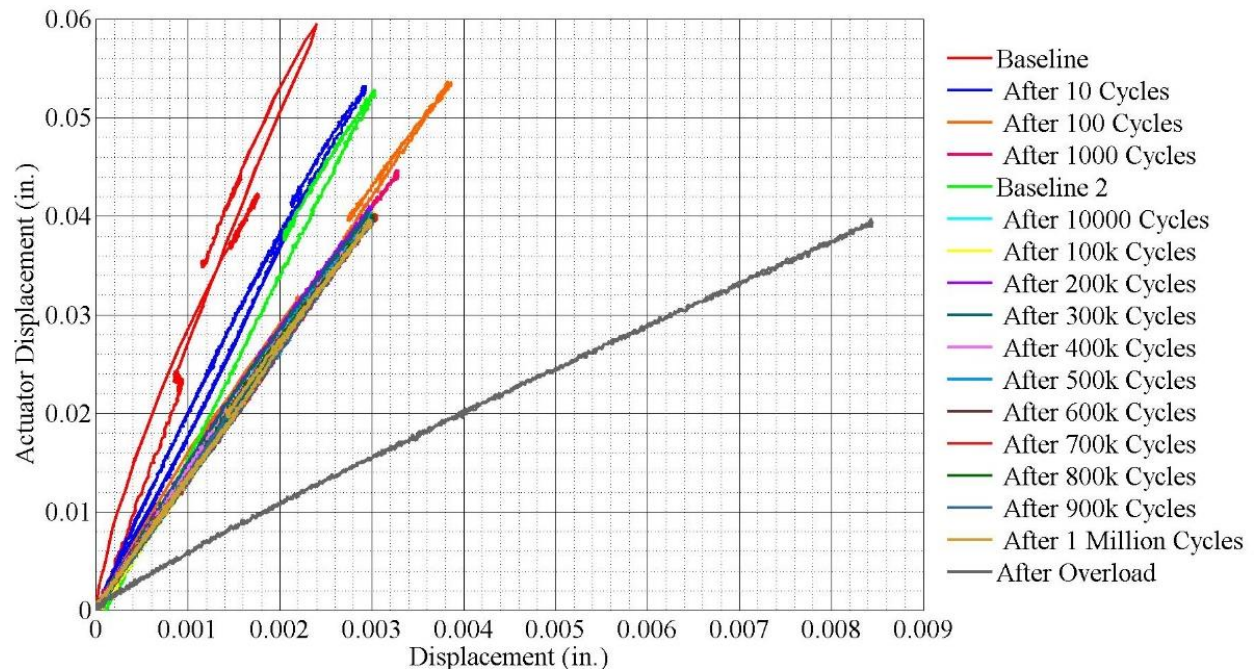
Figure 220: S2 – variation in NE joint displacements during fatigue testing.
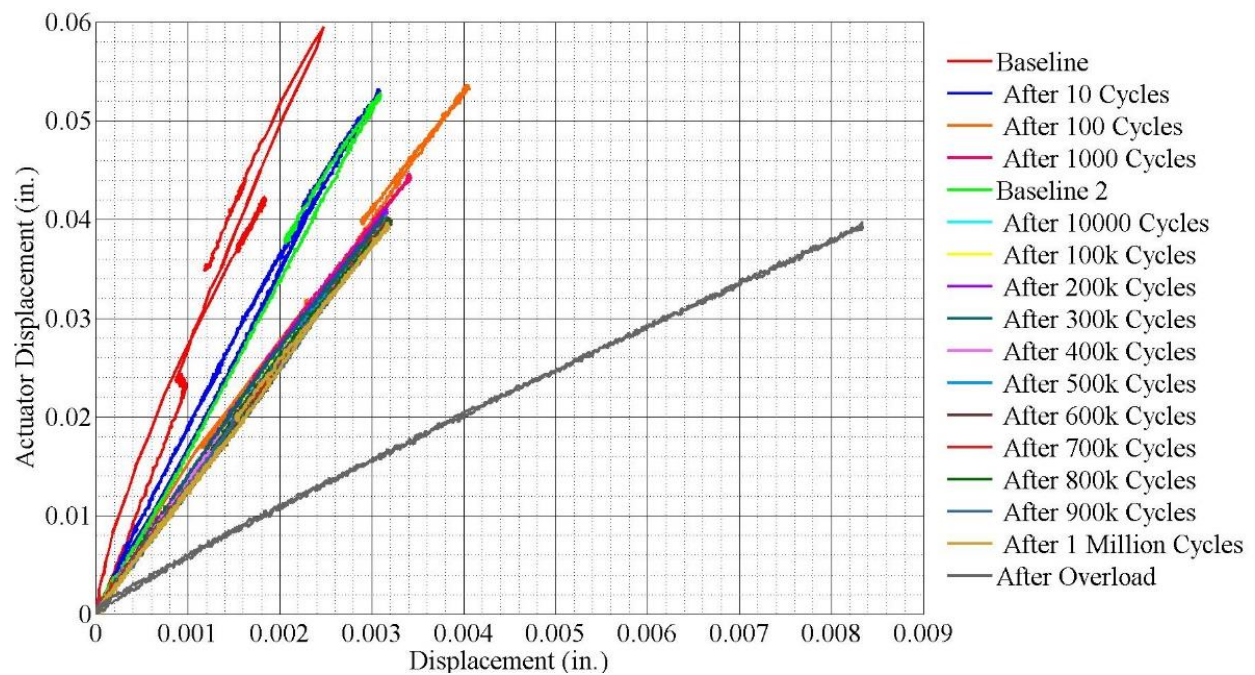
Figure 221: S2 – variation in NW joint displacements during fatigue testing.
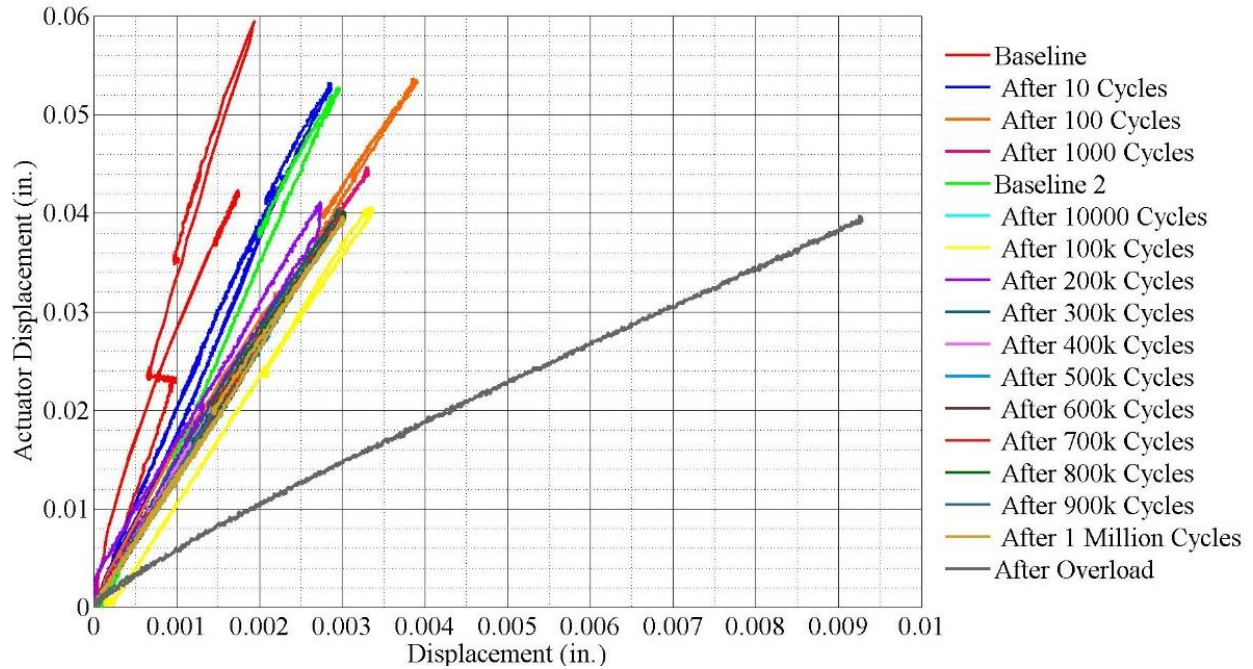
Figure 222: S2 – variation in SE joint displacements during fatigue testing.
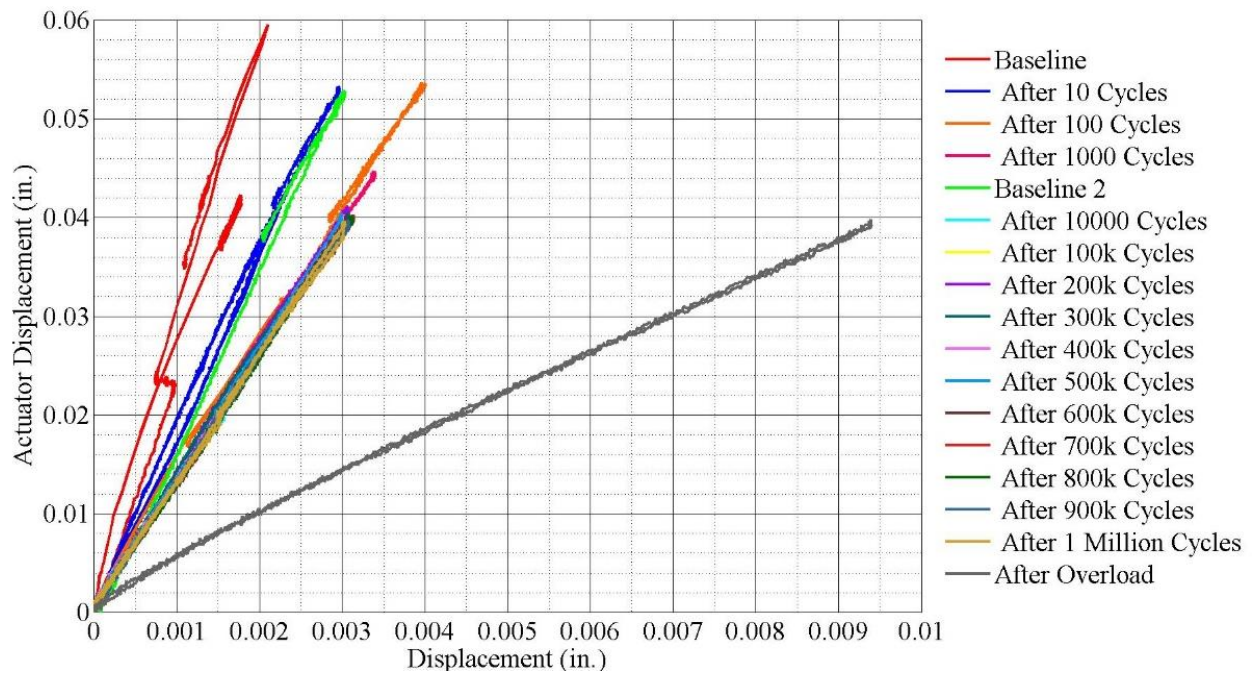
Figure 223: S2 – variation in SW joint displacements during fatigue testing.

The displacements were also measured at the specimen underside by externally connected WPs. The WPs produced highly distorted data as these instruments had a tendency to fluctuate due to electrical noise. Therefore, the data produced by these sensors did not provide a clear picture of the vertical displacements. The typical response recorded by the WPs is shown in Figure 224 and Figure 225.
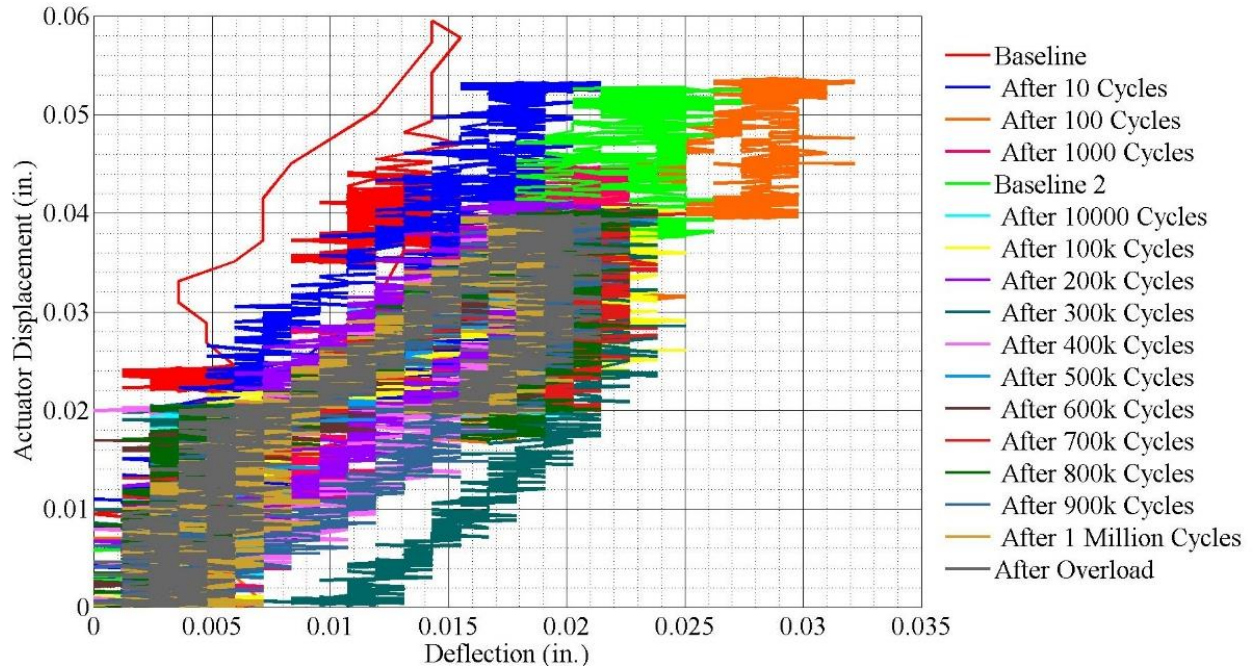
Figure 224: Response recorded by WP4 in S2 static tests.
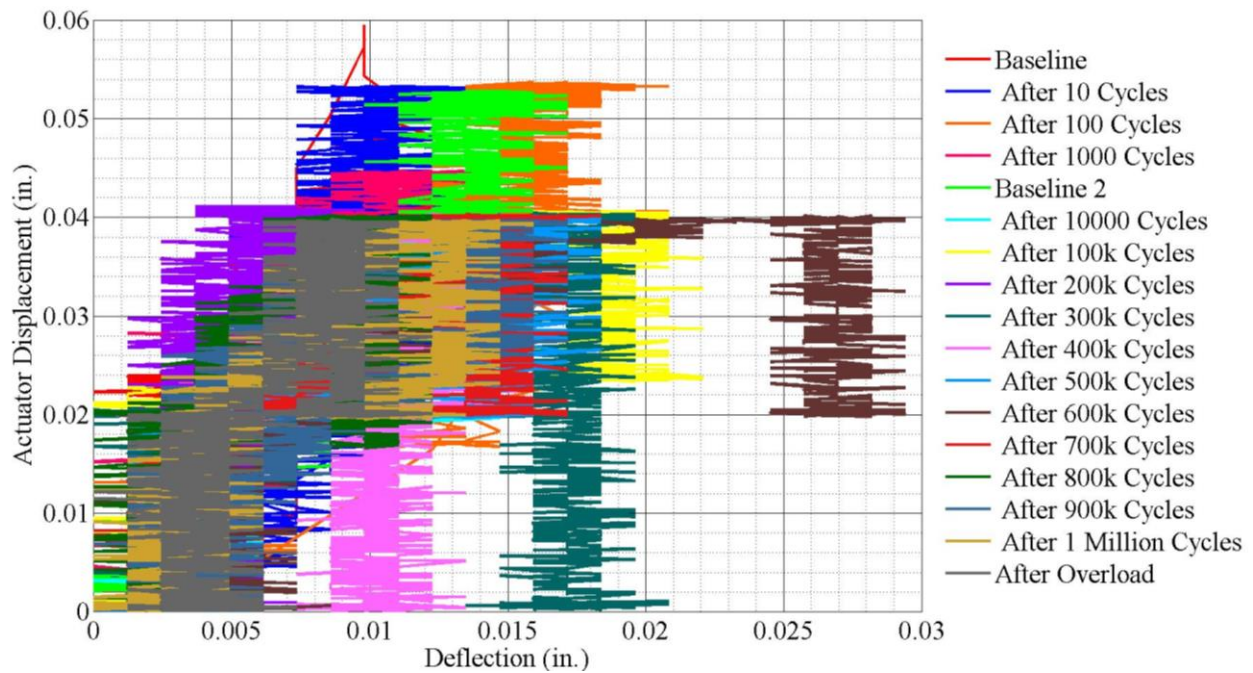
Figure 225: Response recorded by WP5 in S2 static tests.

The displacements could be verified using the reactions recorded by the load cells. The typical reactions were 1.6 kips and 1 kip for the interior support beams and exterior support beams respectively. The steel beam deflection due to these reactions were 0.023 in. and 0.013 in. respectively. Half of the total reaction recorded at interior north beam by one load cell is shown in Figure 226. The actual displacements

in the WPs would be slightly smaller than the calculated values since the WPs were offset from the support beams. The magnitude of those values appear to be in the same range as that seen in Figure 224 and Figure 225. Therefore, the WPs were providing the correct magnitude of displacements, but the data still was quite unclear due to the noise. Hence, the WPs were replaced with LVDTs that were more sensitive and stable for such small displacements.
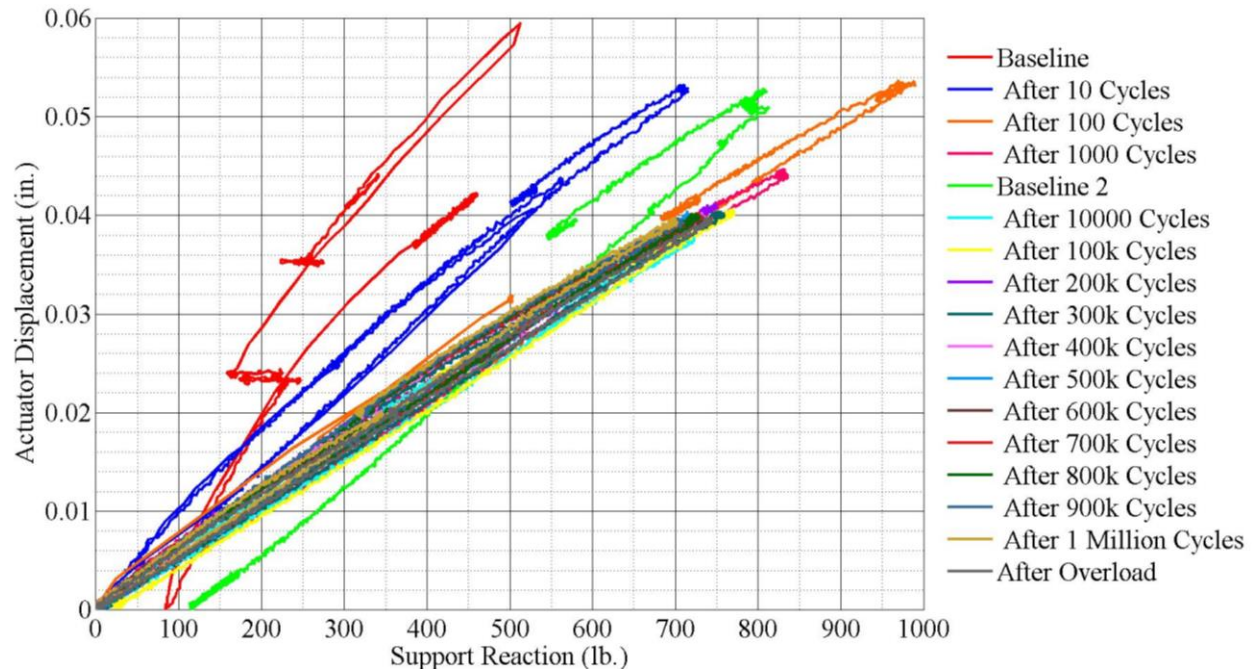
Figure 226: S2 – Variation in reaction during static tests at interior north support beam.

6.2.2.2. S2 – Ponding Tests

The joints on S2 were ponded in order to observe any leakage through the joints from 10000 cycles onwards. No leakage was seen in the joints.

6.2.2.3. S2 – Final Static Test

At the conclusion of application of 1 million cycles the specimen S2 an attempt was made to measure the ultimate capacity of the connection by loading it statically to failure. Displacement increments were applied in increments of 0.02 in. until first crack was observed. Following displacement increments were increased to 0.04 in.

The first crack in the joint was observed at an applied displacement between 0.08 in and 0.10 in. Basically, at this applied displacement, both joints displayed a crack and it is not known which one occurred first. Moreover, some of the cracks had propagated into the concrete section. These cracks had initiated at the base of the joint and debonded it for about 1.5 in. and then continued into the concrete of beam sections. The strength of bond was assumed to be lower than the tensile strength of concrete and hence this behavior

214

was not expected. These initial cracks are shown in Figure 227. The answer to this issue was found via the FEA model for S2. The shear stress distribution at the interface was studied. This plot is shown in Figure 228. High shear stresses in concrete coupled with high bond strength caused the cracks to propagate into concrete instead of continuing along the interface. Note that the magnitude of stresses shown in Figure 228 are not relevant to this discussion. The figure is used for purpose of studying the nature of stresses and not the magnitude.

Figure 227: Initial cracks in north joint of specimen S2.
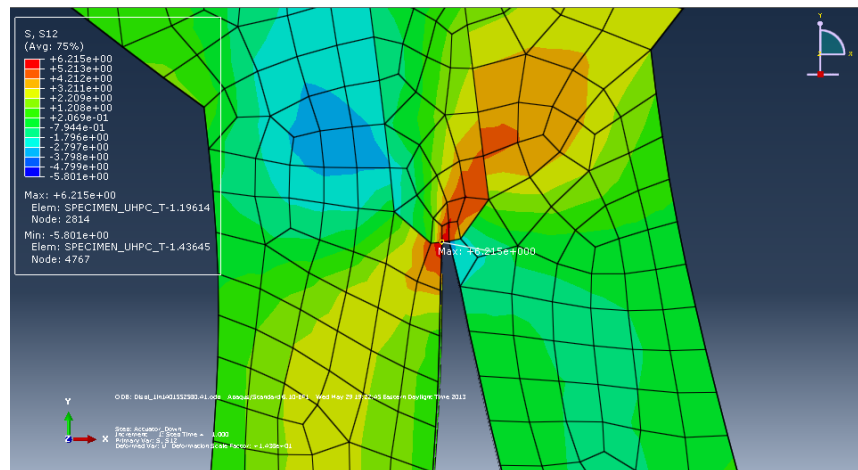
Figure 228: Shear stress distribution at the joint as per SA model of S2.

Additional displacements that were applied to the specimen caused the existing cracks to propagate further in beam concrete. Displacements were applied to the specimen until the magnitude of forces being applied to the support beams reached a magnitude that was close to yielding for the steel beams. The steel beams were to be reused in the remaining tests and the yielding of steel would change the behavior of the

215

specimens. Moreover, the top flange of the interior north support beam displayed transverse bending due to an unintended eccentricity between the axis of the support load cell and the web of the support beam. Hence, further displacements were stopped. Consequently, the ultimate capacity of the connections could not be measured. The total displacement applied to S2 was 0.44 in. The load vs. displacement plot for the final static test is shown in Figure 229.
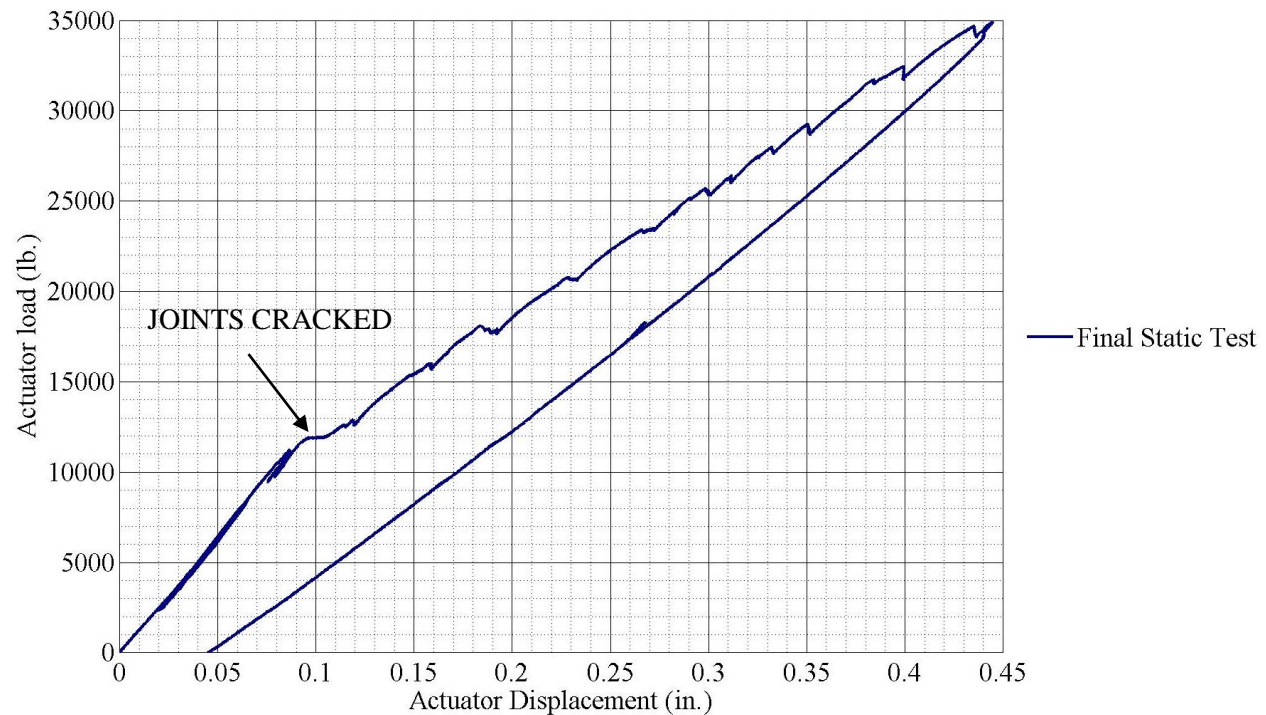
Figure 229: Load vs. displacement for S2 – final static test.

Since the specimen did not completely fail and the joints were relatively undamaged after the final static test, additional 100,000 cycles were applied to the specimen to see the difference in behavior with the cracks in the beam section. The previous plots show the effect of the existing damage on the behavior of the specimen.

6.2.2.4. Summary of S2 Test

The tests on specimen S2, spliced connection detail with UHPC, displayed that the proposed connection detail had sufficient strength and durability to resist traffic loads. Moreover, the service level loads were insufficient to break the bond between the UHPC and the beam concrete. Also, at the final static test, the cracks did not propagate as per expected pattern of joint debonding. Therefore, the spliced connection by itself was not loaded in this test. Moreover, the inability to fail the specimen meant that a failure mode or at least the formation of cracks within the splice pocket could not be observed. It can be said that the propagation of cracks into the beam section webs may be detrimental for bridge health. It is to

be noted that these cracks propagated into the webs at a load thrice that of the service level load. Hence, such a deterioration would not occur for typical traffic loads.

6.2.3. Specimen 3 – Spliced UHPC connection with topping

The top flange spliced connection detail was tested with a specimen consisting of a 5 in. concrete topping. VDOT specifies the use of a 5 in. concrete topping for ABBB with an ADTT between 100 and 200. Hence, to study the effect of fatigue on a connection on a bridge with higher volume of traffic. Slight modification was made to the test setup. Web stiffeners were welded to the beams in order to prevent the transverse bending of the flange due to eccentricity. This had no bearing on the behavior of the joints.

The beam sections in S3 were initially designed to accommodate a 7 in. composite concrete topping. VDOT was more concerned about the application of these bridges with a 5 in. non-composite topping. Therefore, the reinforcing steel extending from the beam sections was torched off. These beam sections had a roughened top surface to provide bond with the topping material. Removing the surface roughness was not feasible. Hence, the concrete topping had at least a partial composite action with the beam sections.

6.2.3.1. S3 – Fatigue Tests

The protocol for this test was the same as previous tests. Displacements of 0.03 in. up to 0.04 in. were applied in a cyclic manner to induce fatigue in the joints. The performance of this specimen was expected to exceed that of S2. S3 was the same specimen as S2, albeit with an additional capacity due to partial composite action with the concrete topping. However, the north joint debonded to about one-fourth of the depth during the second baseline static test. The crack further propagated to about one-third of the depth during cycling between 3400 and 3500 cycles. The change in the stiffness of the specimen over the duration of the 10000 cycles is shown in Figure 230. The plot shows the change in the actuator load, or realistically the resistance the specimen offers to the applied displacements. The actuator load could be observed to be degrading gradually till about 1200 seconds. After that point the load dropped rapidly over a period of 300 seconds. Following this rapid drop, the load stabilized as a consequence of loss of stiffness causing the magnitude of load applied to the specimen to reduce for the same range of displacements. Basically, the drop in load during or after the end of application of cycles indicated a loss of stiffness, with the joint cracking being the most probable cause for it.
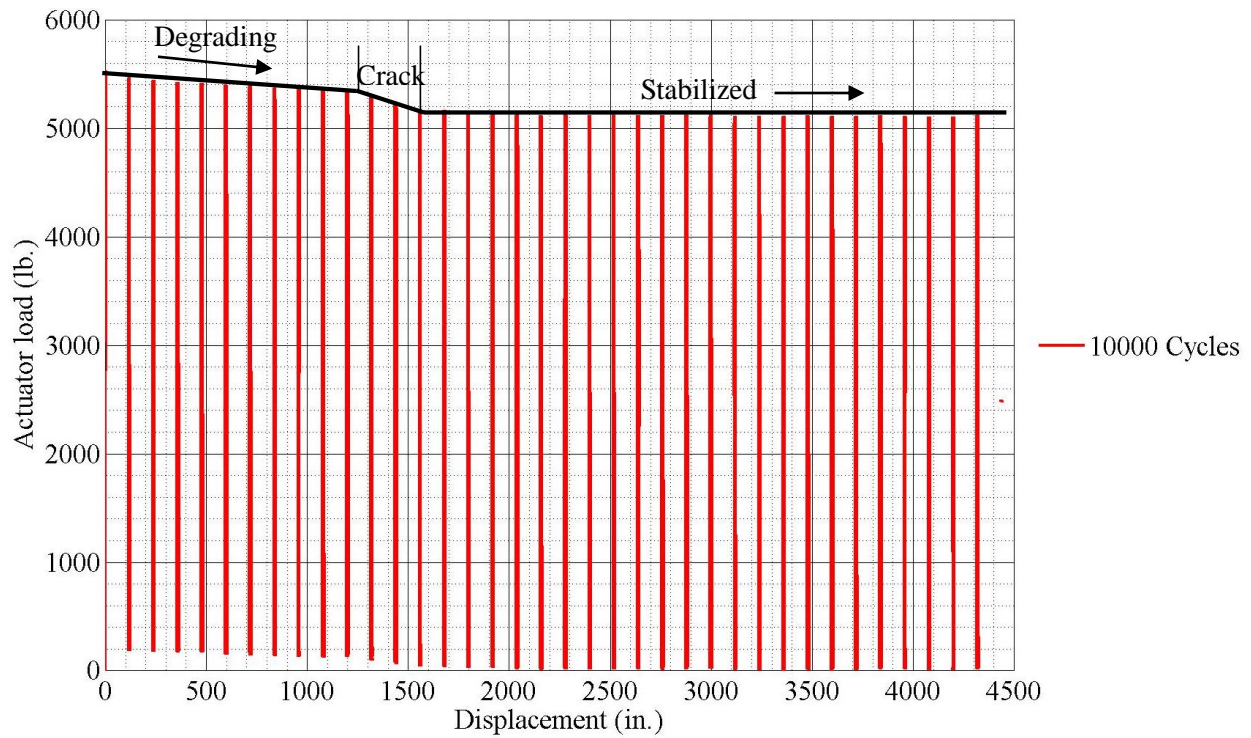
Figure 230: Change in magnitude of actuator load during fatigue test due to crack propagation.
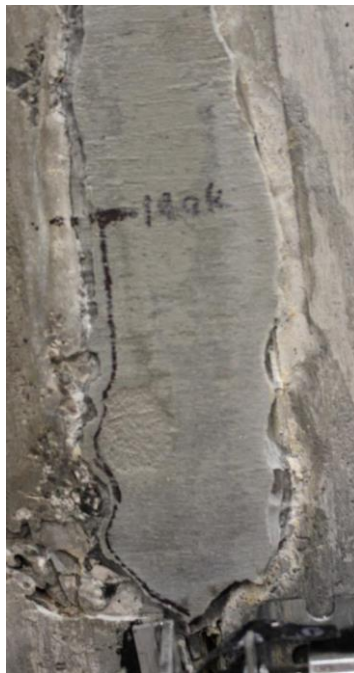
Figure 231: Debonded length of north joint after 10000 cycles.

The same change in response was not conspicuous in the global behavior of the specimen as seen in the load vs. displacement plot, which is shown in Figure 232. That simply meant that even with the

presence of the crack at the joint, the specimen was able to provide the same level of resistance after the magnitude of displacements was modified to include the effect of the cracked joint.
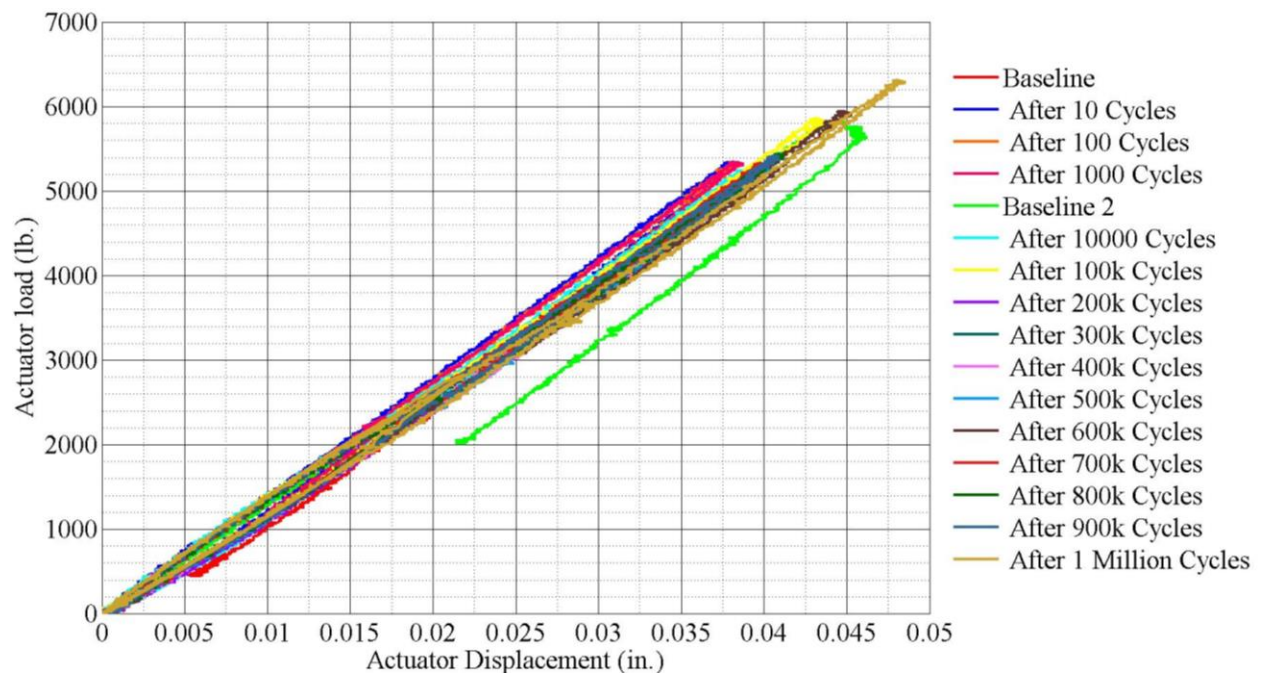
Figure 232: S3 – actuator load vs. actuator displacement.

The actual displacements imparted to the specimen S3 are plotted with respect to the actuator displacements and are shown in Figure 233.
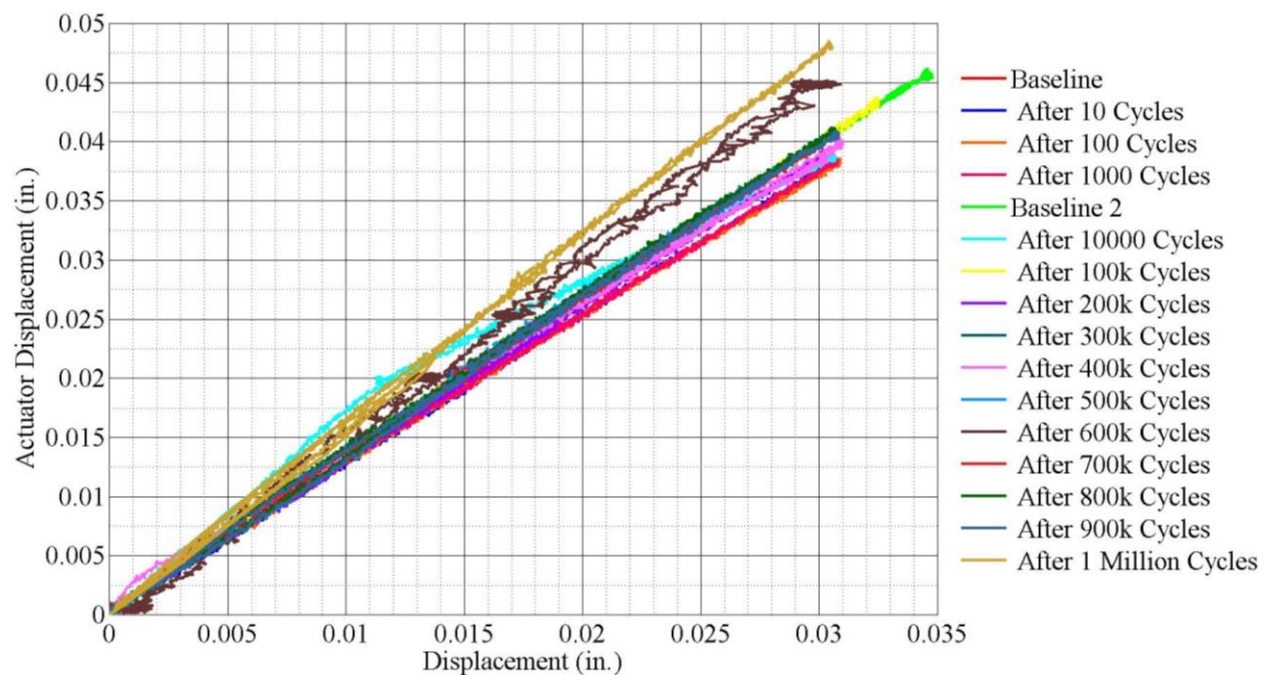
Figure 233: S3 – actual displacements imparted to specimen.

The change in behavior at the north joint could be best observed from the LVDT data plots at the NE, NW, SE and SW as shown in Figure 234, Figure 235, Figure 236 and Figure 237. The LVDTs on the north joints display non-linear behavior after 1000 cycles whereas the behavior did not change at the LVDTs at the south joint. The occurrence of crack in the north joint is also seen in Figure 234 and Figure 235.
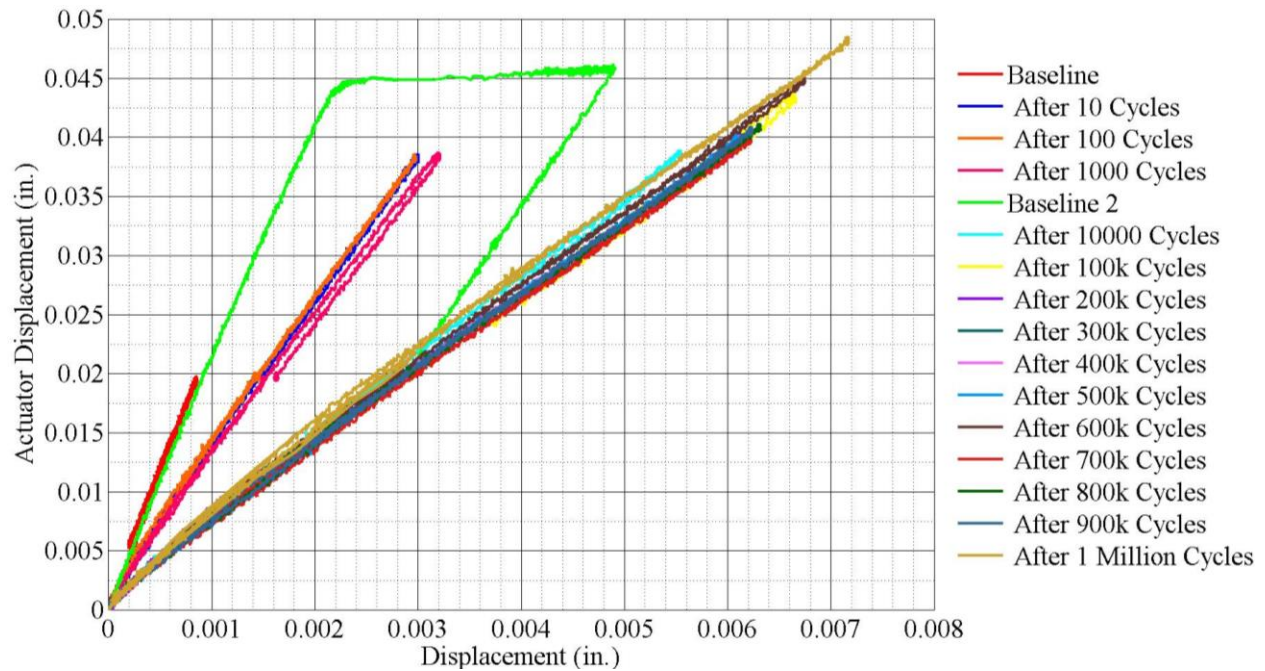
Figure 234: S3 - variation in NE joint displacements during fatigue testing.
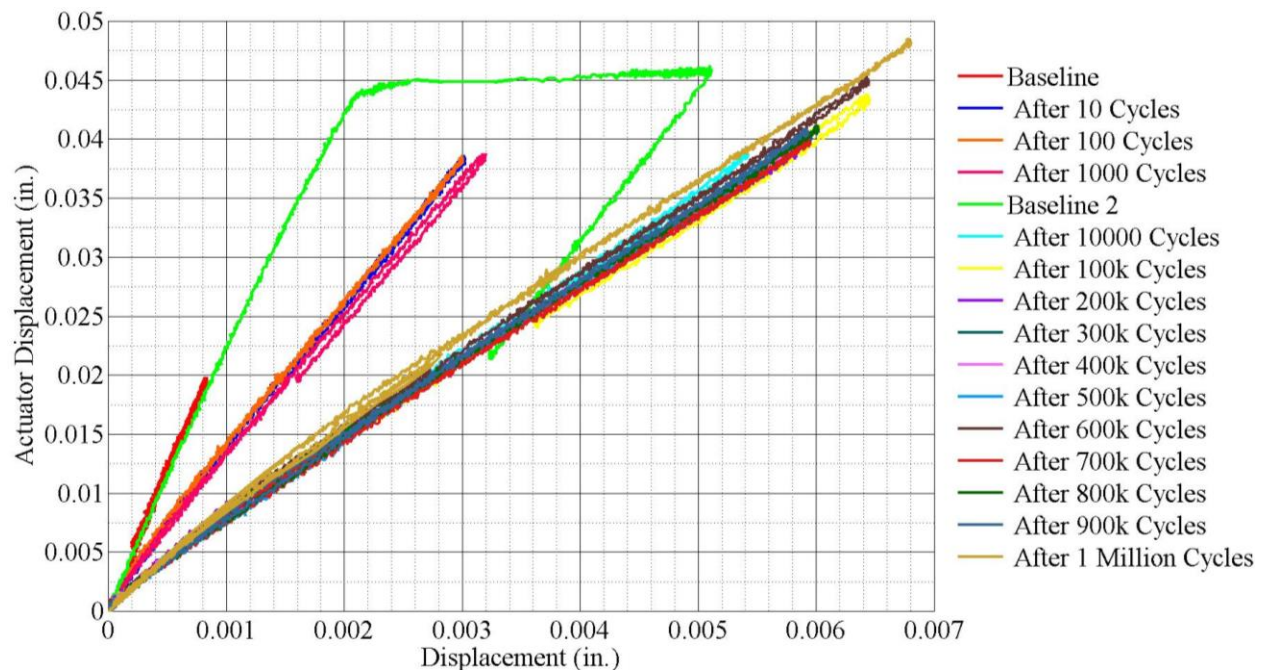
Figure 235: S3 - variation in NW joint displacements during fatigue testing.
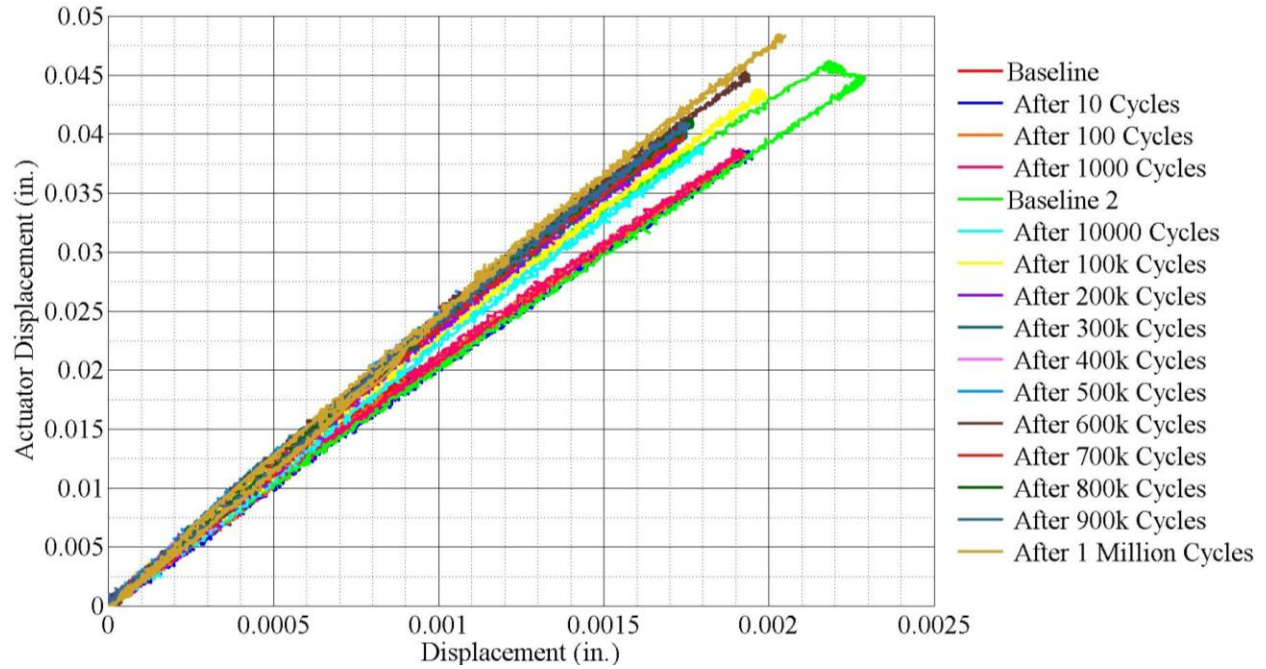
Figure 236: S3 – variation in SE joint displacements during fatigue testing.
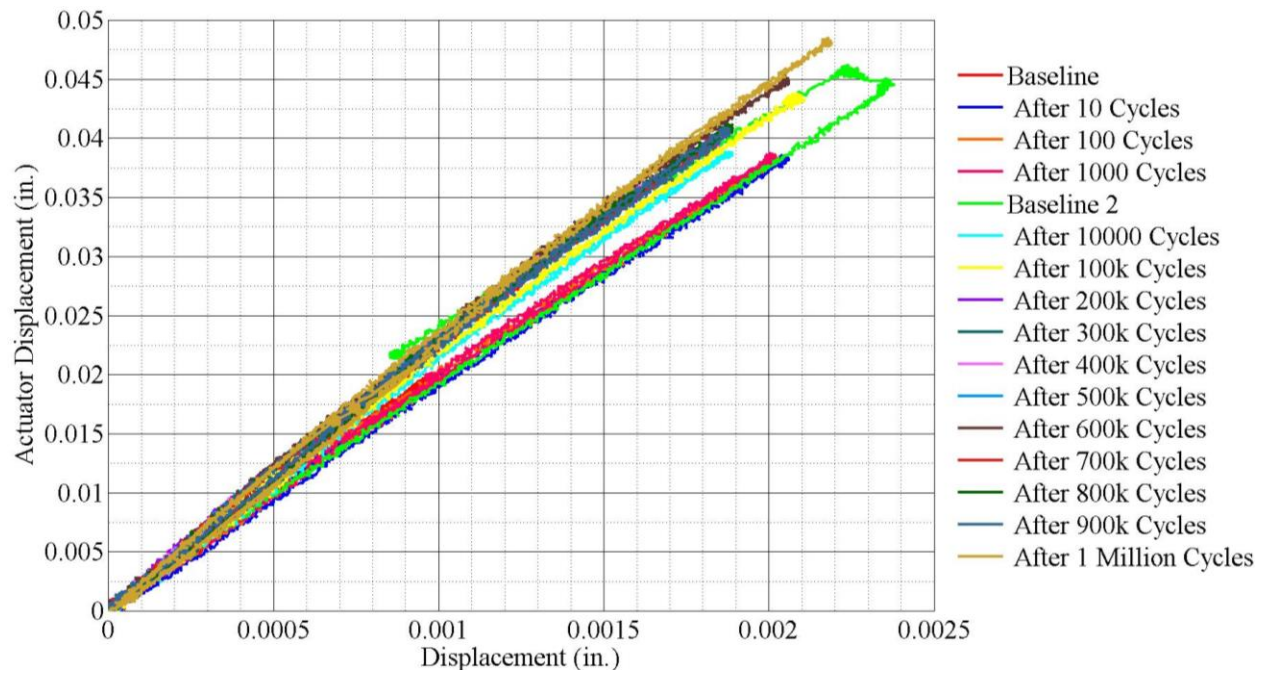
Figure 237: S3 – variation in SW joint displacements during fatigue testing.

6.2.3.2. S3 – ponding tests

Ponding tests were performed on specimen S3. There was no leakage observed under the specimen owing to the fact that the crack in the north joint did not propagate for the full depth as well as the presence of concrete topping.

6.2.3.3.   S3 – Ultimate strength test

The ultimate strength test for S3 was expected to have the same result as S2, the connection was not expected to fail prior to the onset of steel beam yielding. The increments were applied in 0.02 in. until the south joint cracked, followed by 0.04 in. displacements till the end of the test. The existing crack in the north joint began propagating after the application of 0.12 in. total displacement and had reached the topping by application of 0.14 in. displacement. The crack propagated around the corner of the middle beam section and began debonding the topping from the beam section. This effect is shown in Figure 238. Eventually, the crack at the north joint began propagating into the topping.
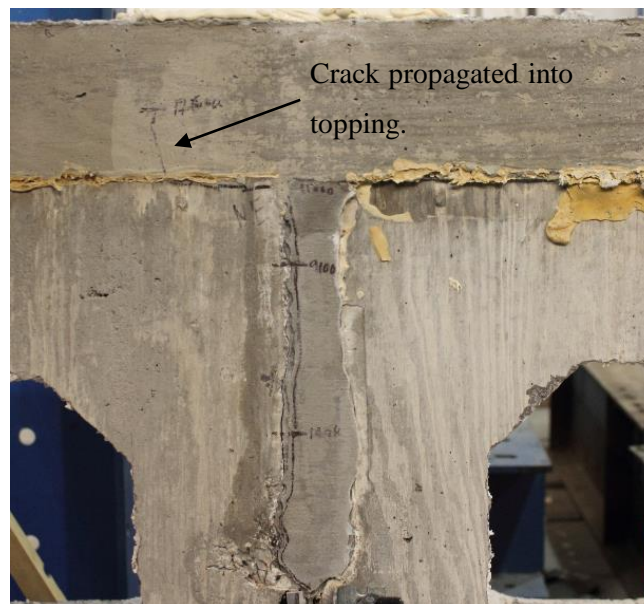
Figure 238: S3 – Crack propagation at the north joint after final static test.

The south joint cracked at an applied displacement of 0.23 in., at which the applied load was about 25000 lb. The full depth of the joint cracked in an instant and the load reduced by 2000 to 3000 lb. On continued application of displacements the crack at the south joint began mimicking the behavior of the cracks at the north joint. The displacement application was completely halted after applying a total displacement of 0.33 in. The loading had to be halted since load cells on the interior support beams were close to their full capacity of 10 kips. The global load vs. displacement plot is shown in Figure 240.

Figure 239: S3 – Crack propagation at the south joint after final static test.
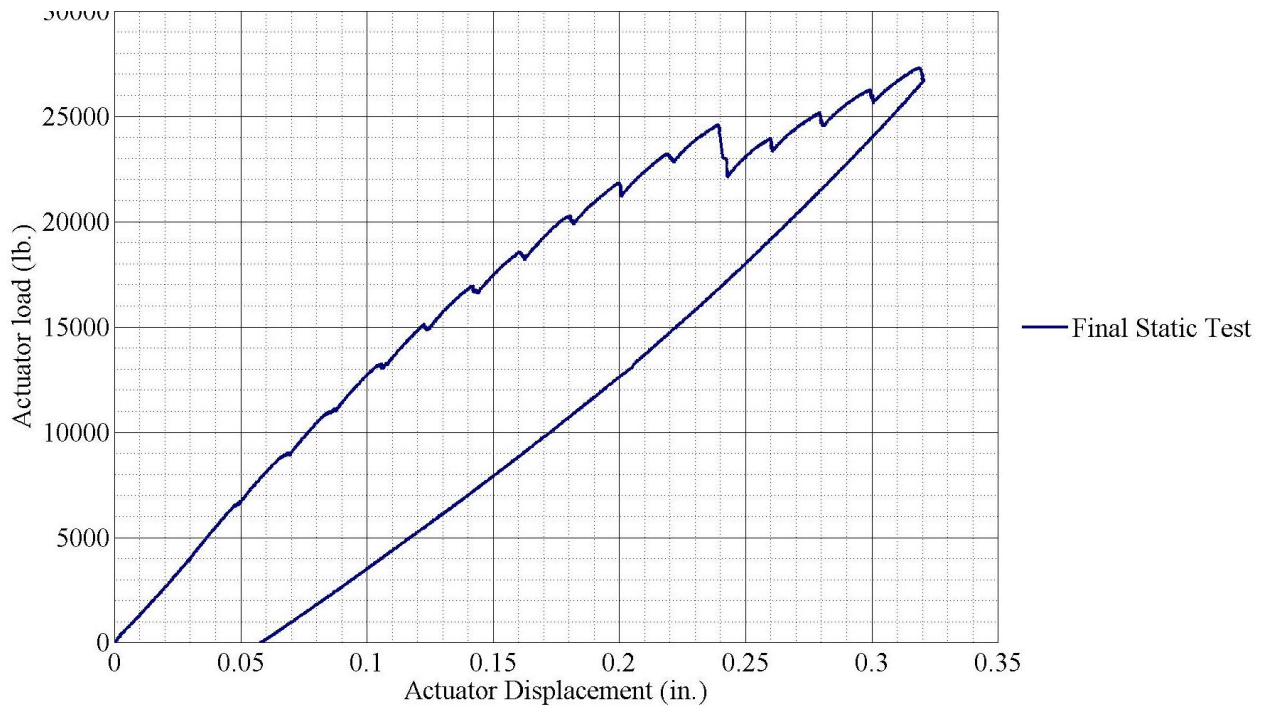
Figure 240: S3 – load vs. displacement plot for final static test.

6.2.3.4.   Summary of S3 Test

The S3 test showed that the joints with UHPC can crack during service level loading. Although S2 and S3 had the same connection detail, the bond strengths measured for both the tests were significantly

different. The bond strength in S2 was almost twice of that measured in S3. This result indicates that the shear key was totally dependent upon the strength of bond between the pocket material and the beam concrete. The crack did not propagate for the full depth of the joint during the fatigue testing of S3. The crack propagated for the full depth during the final static test. The cracks also continued into the deck, but the action was dissimilar from that of a joint crack propagating as a reflective crack. The joint crack propagated transversely along the topping – beam top interface and then proceeded into the topping. This transverse propagation may be attributed to the use of the spliced connection. The spliced connection reduced the relative rotation between the adjacent beam sections over the joints. Therefore, the crack propagated transversely until the flexural stress in the concrete topping surpassed the modulus of rupture. The important point of observation here is that the crack propagation into the topping occurred at an applied load magnitude that was four times the service level load. Hence, the use of spliced connection alleviated the stresses in the concrete topping over the joints. Overall, the use of concrete topping also provided a stiffer response to the applied displacements as expected.

6.2.4. Specimen 4 – Kevlar and Epoxy connection

Specimen 4 (S4) had the Kevlar and Epoxy (K&E) connection. This specimen was expected to behave very similarly to S1. The basic connection detail was the same. Therefore, until the initiation and propagation of the joint crack for the full depth the behavior was expected to be the same. However, an important aspect of this specimen test was to observe if the K&E connection prevented the cracks from occurring.

6.2.4.1. S4 – Fatigue tests

The test protocol of applying a total displacement of 0.03 in. up to 0.035 in. was repeated in this test. This was followed up to the application of 10 cycles to the specimen. After 10 cycles, the clamping beams were retightened and another baseline static test was run. In this test, the displacement increment was incorrectly input to a higher value due to switching of two input digits. This resulted in the north joint cracking for the full depth. Essentially, the north beam section would have completely separated if the K&E connection was not present. The behavior of the specimen completely changed after the joint cracked. The initial assumptions for the boundary conditions became irrelevant. The K&E connection being flexible for out of plane (orthogonal to the Kevlar grid) movements, acted as a hinge. Therefore, the loads generated by the applied displacements were transferred only as vertical shear at the interior north support beam. The exterior north support beam did not receive any of the imposed load. The north beam section rotated about the north beam. The load vs. displacement plot for S4 is shown in Figure 241.
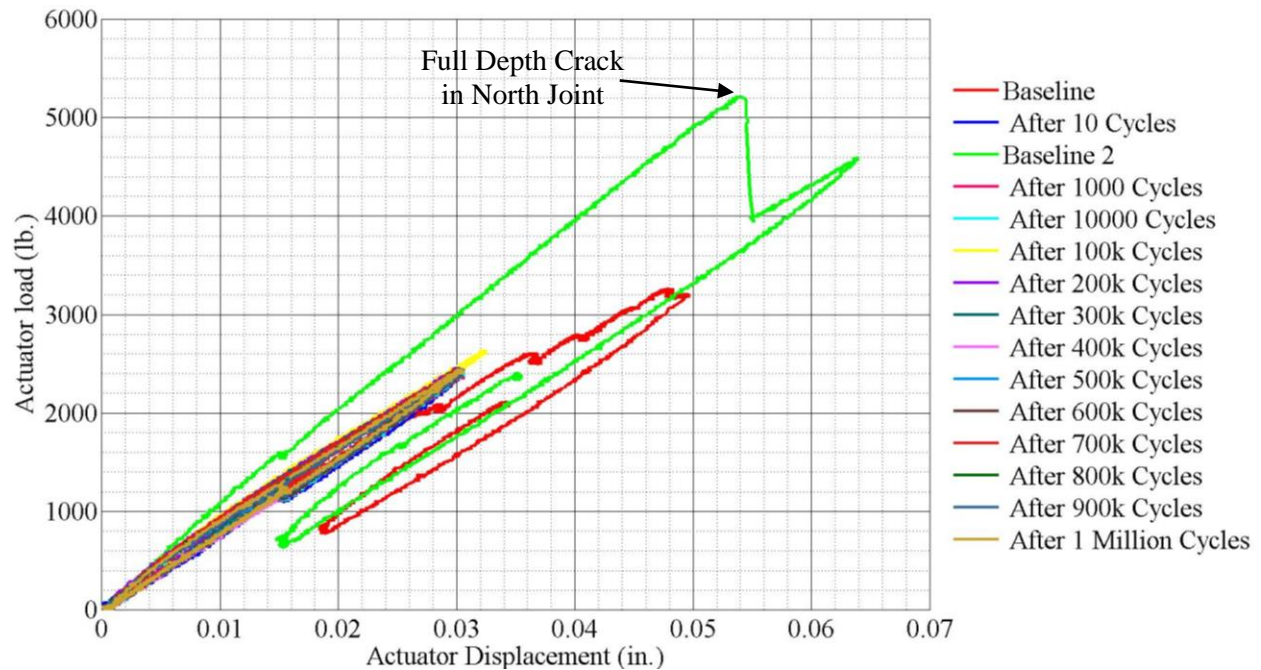
Figure 241: S4 – actuator load vs. actuator displacement.

The displacements applied to the specimen, as measured by external LVDTs, are presented in Figure 242.
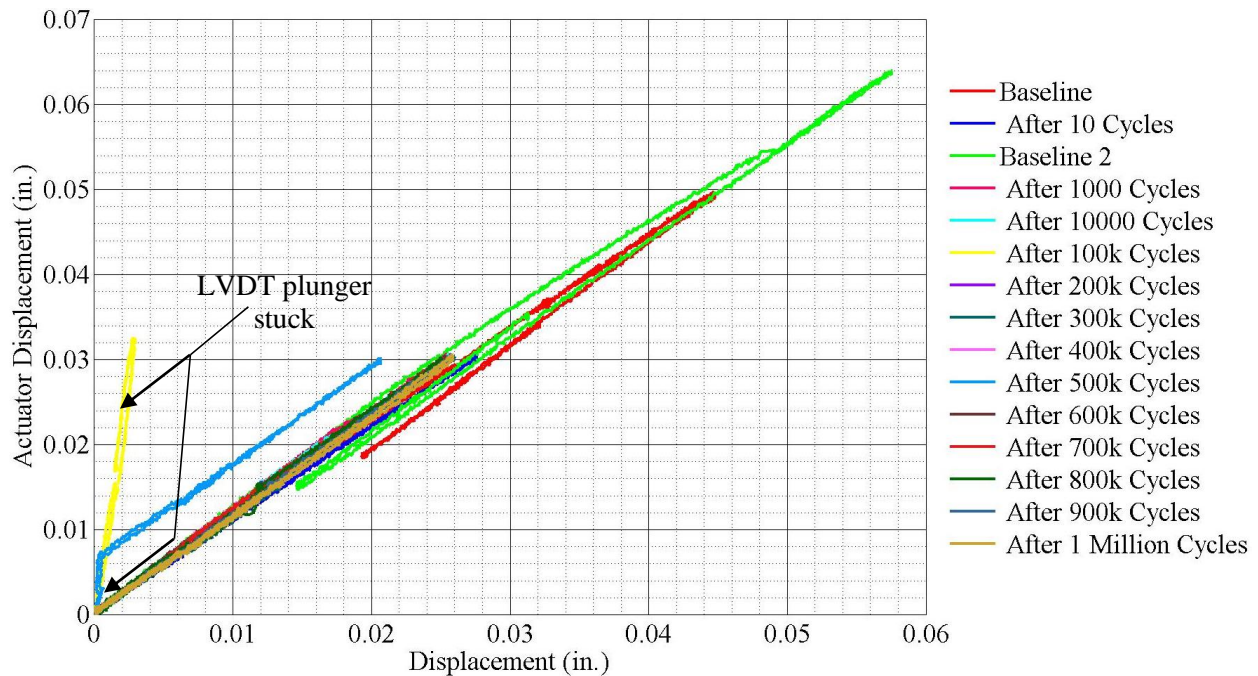
Figure 242: S4 – actual displacements imparted to the specimen.

The rest of the testing proceeded as per protocol. The applied displacements were adjusted such that the imposed load was raised to the desired level. From the application of 100 cycles to 1 million there was no significant change in the behavior of the specimen. The south joint remained sound for the duration of the fatigue testing.

The gap displacements for the NE, NW, SE and SW joints are shown in Figure 243, Figure 244, Figure 245 and Figure 246 respectively. The joint displacements at the north joint increased drastically after the joint cracked for the full depth. On the other hand, the magnitude of displacements reduced at the south joint. The reduction in displacements was caused by the added flexibility at the north joint. The initially designed boundary conditions would cause both the joints to widen when a downward displacement was applied. However, the unsymmetrical distribution of loads caused the south joint displacements to be smaller than the expected magnitudes.
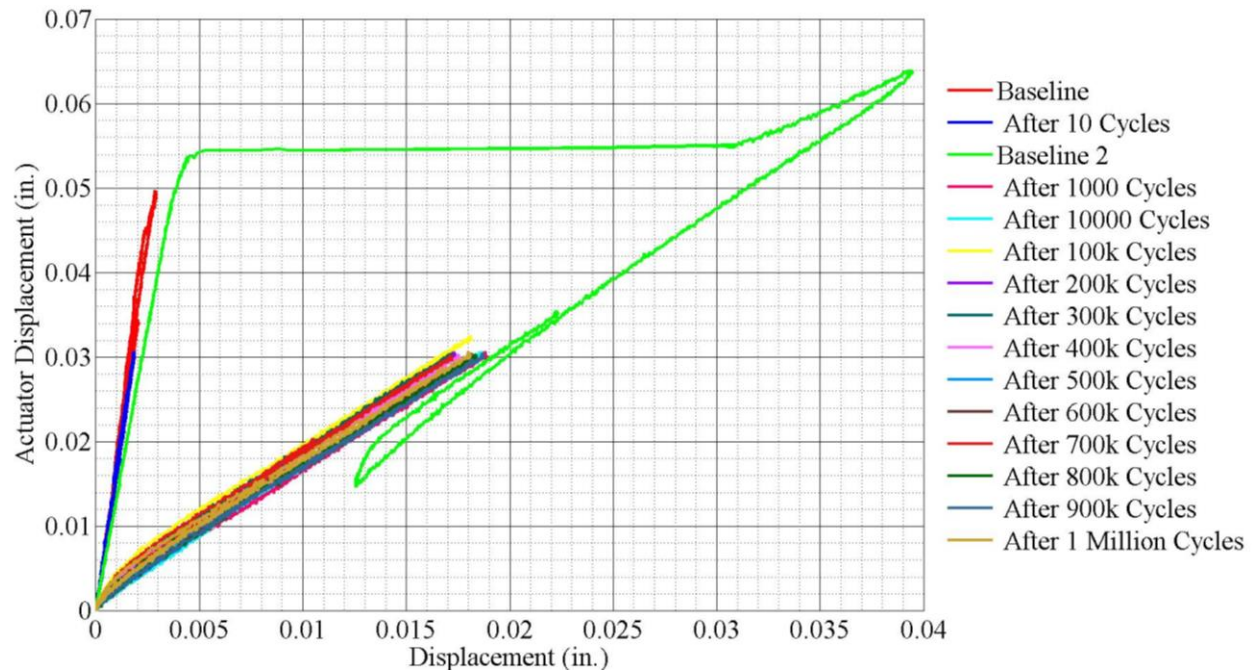
Figure 243: S4 – variation in NE joint displacements during fatigue testing.
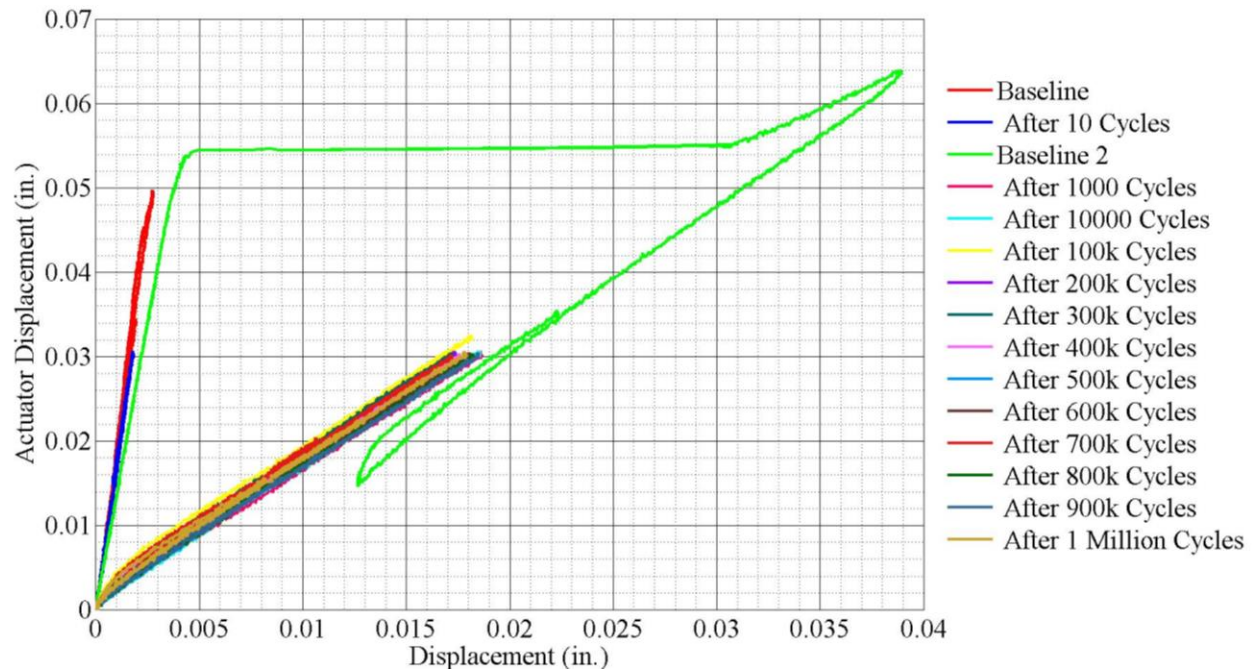
Figure 244: S4 – variation in NW joint displacements during fatigue testing.
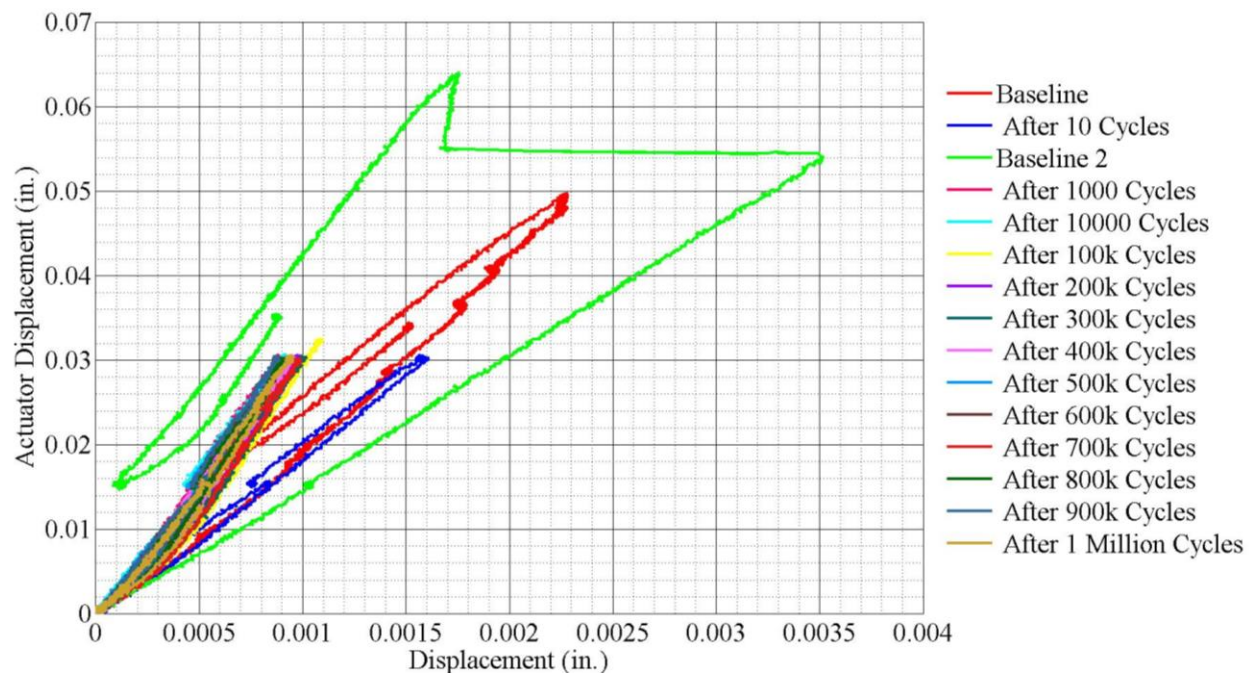
Figure 245: S4 – variation in SE joint displacements during fatigue testing.

227
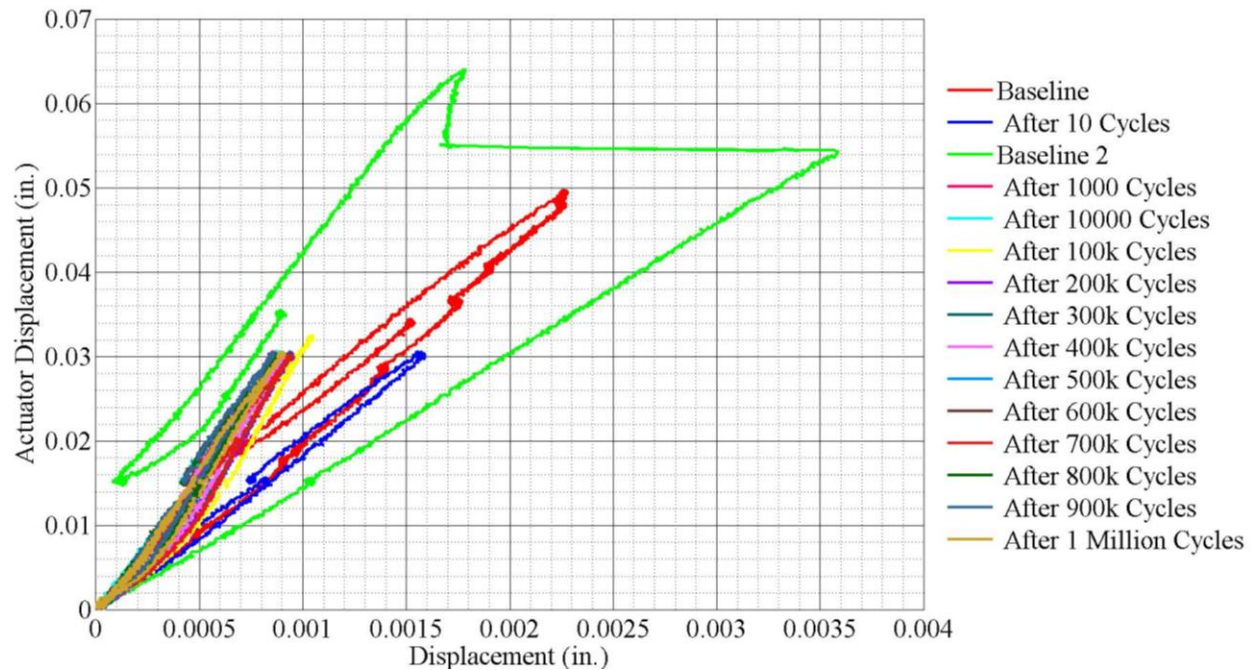
Figure 246: S4 – variation in SW joint displacements during fatigue testing.

The vertical deflection effectively imparted to S4 near the interior south, exterior south, interior north and exterior north is shown in Figure 247, Figure 248, Figure 249 and Figure 250 respectively. The magnitude of deflection reduced at all locations except at interior north where the deflection magnitude remained the same virtually. An exaggerated view of the S4 displacement is shown in Figure 251.

With the deviation from the design boundary conditions and the added flexibility of the specimen the K&E connection served as the only link between the middle section and the north section. Also, since the displacements and the gap openings reduced at all other locations the worst load effects were concentrated at the K&E connection. Therefore, after full depth cracking of the north joint, the entire test for S4 essentially became the fatigue testing of the K&E joint exclusively.
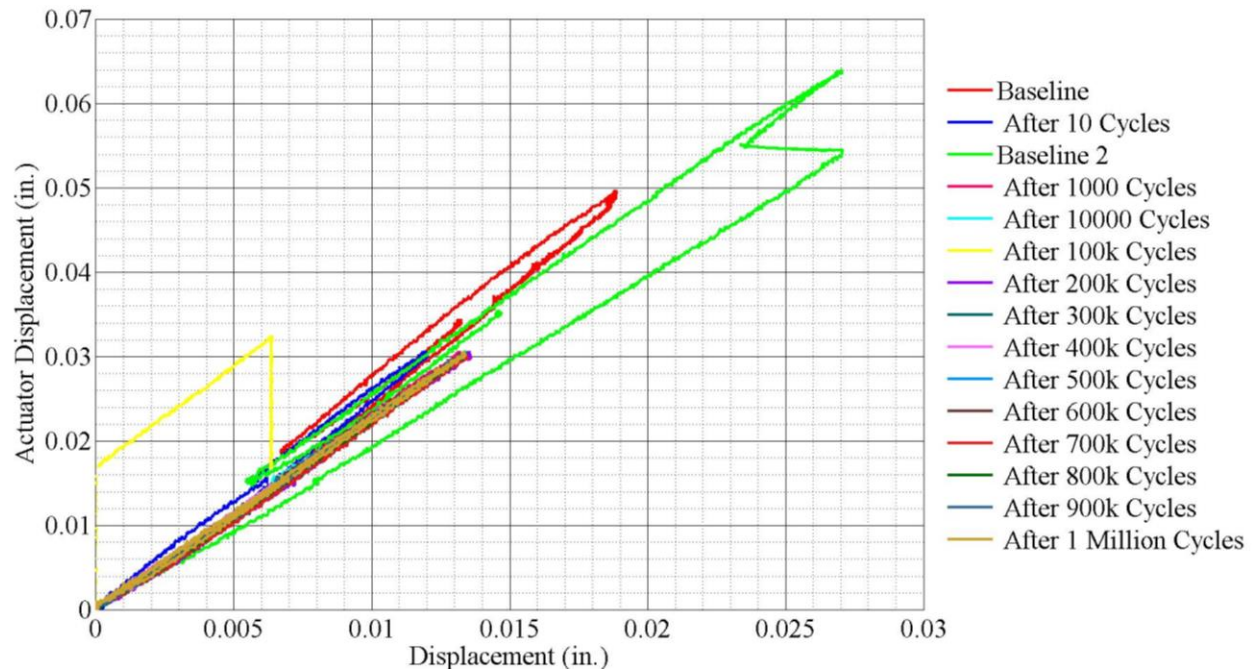
Figure 247: S4 – variation in vertical deflection near interior south support beam during fatigue.
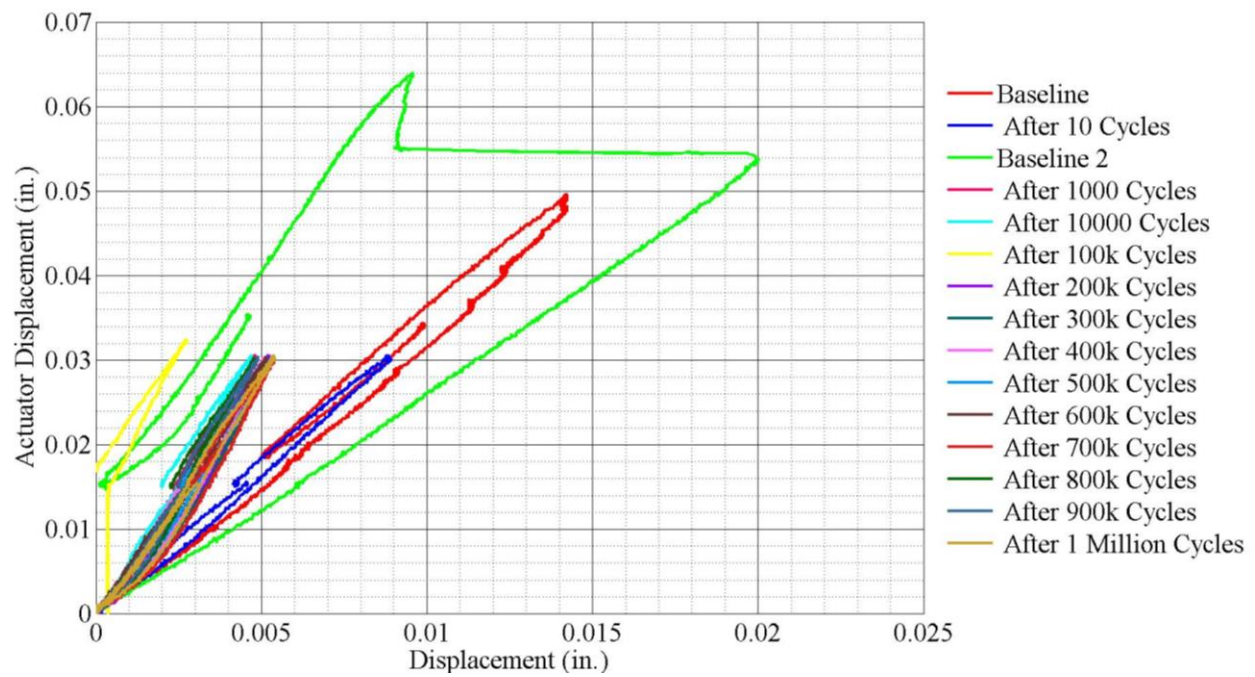
Figure 248: S4 – variation in vertical deflection near exterior south support beam during fatigue.
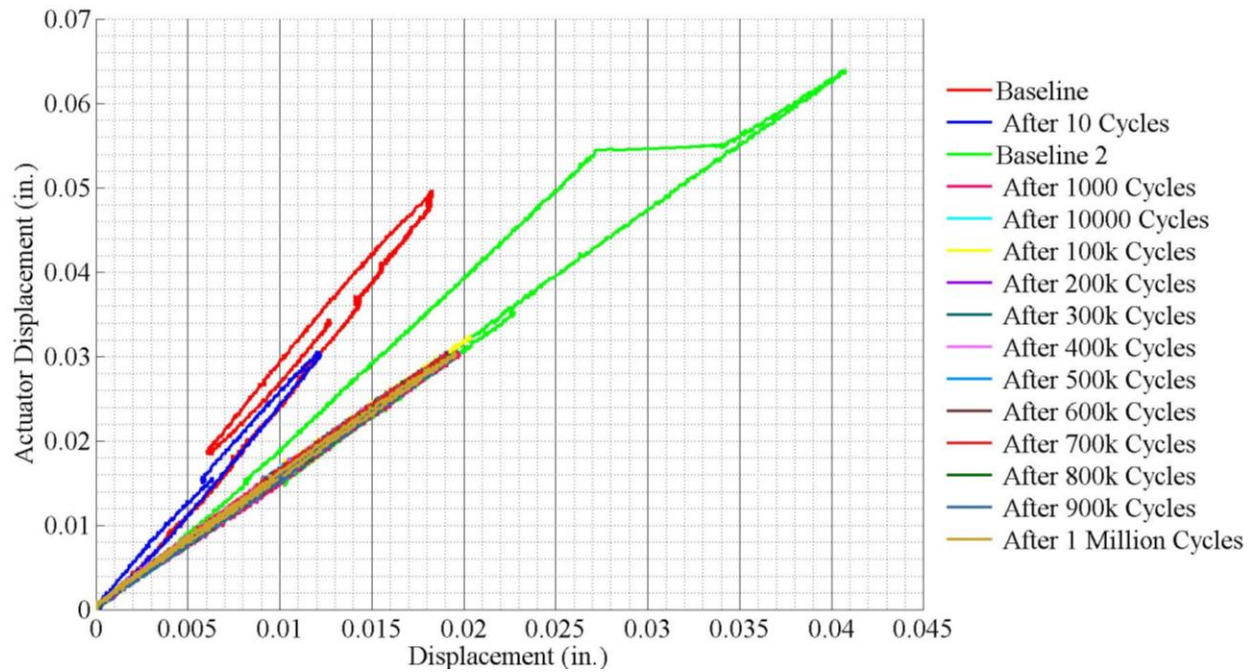
Figure 249: S4 – variation in vertical deflection near interior north support beam during fatigue.
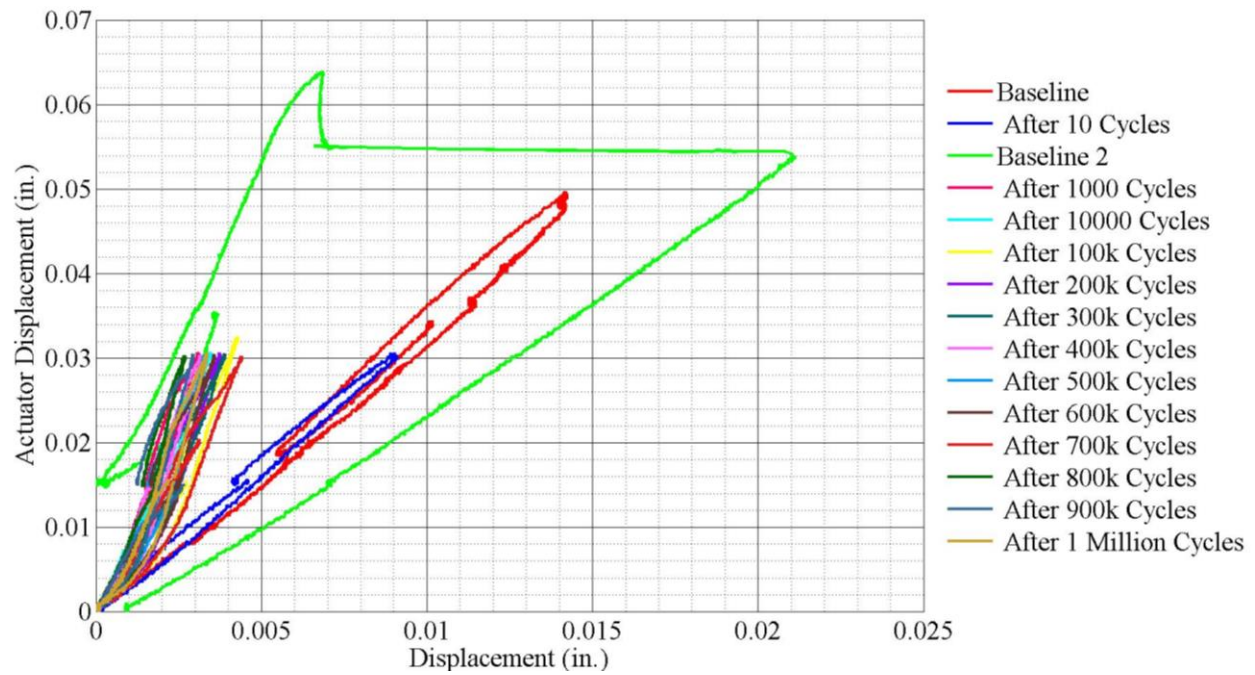
Figure 250: S4 – variation in vertical deflection near exterior south support beam during fatigue.

South   North

Undeflected level

Reduced gap opening

Rotating about support
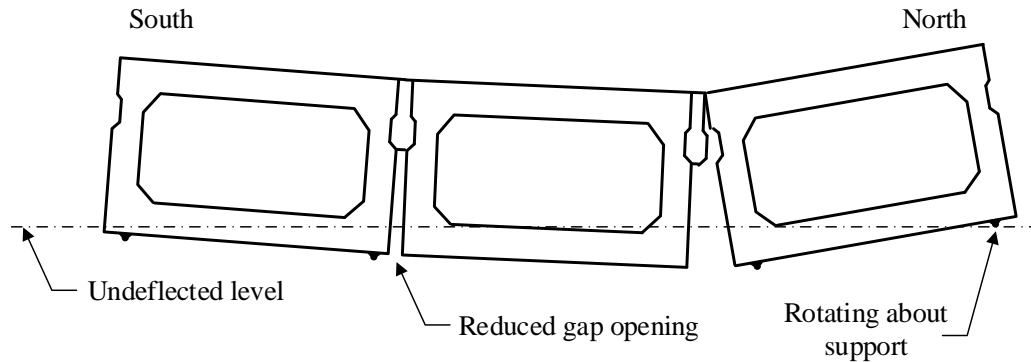
Figure 251: S4 – schematic of deflected shape after north joint failure.

In that regard, the K&E joint did not show any signs of damage or degradation. The failure of the K&E joint was not expected to occur through the grid of the connection. The Kevlar grid when embedded in the epoxy resin provided a capacity of 4 kips/ft as per the manufacturer. Hence, a close watch was kept on the bond between the K&E sheet and the beam concrete. The bond did not degrade over the remaining duration of fatigue testing.

6.2.4.2. S4 – Ponding test

The ponding test was performed for S4 immediately after the north joint failed and was continued until the end of the testing program. Water was ponded over the K&E connection as well as around the edge of the epoxy. The joint did not leak for the entire duration that the specimen was ponded during fatigue testing.

6.2.4.3. S4 – Ultimate strength test

For the ultimate strength test the displacements were applied uniformly in 0.03 in. increments. The focus of this test was the strength of the K&E connection and the south joint to observe any cracking there. The south joint did not crack in this test. The trend seen in the LVDT plots for the vertical deflection continued in the ultimate strength test. The north joint was the weaker among the two joints and as such was subjected to the worst load effects. The north beam section lost contact with the exterior north beam at above 0.08 in. total displacement. This rotation of the north beam section increased with increment in displacement. Cracking sounds were heard after applying a total displacement of 0.15 in. indicating that the K&E connection at the north joint might be failing. The displacement increment was then halved to 0.015 in order to prevent a sudden failure. After application of a total displacement of 0.18 in. the K&E connection began to debond from the middle beam section and failed completely with the displacement being held constant at 0.18 in. As seen in the failure of S1, the grout completely debonded from one side and remained bonded to the other side of the keyway. The debonded keyway and the failed connection is shown in Figure 252. The load vs. deflection plot for S4 is shown in Figure 253.
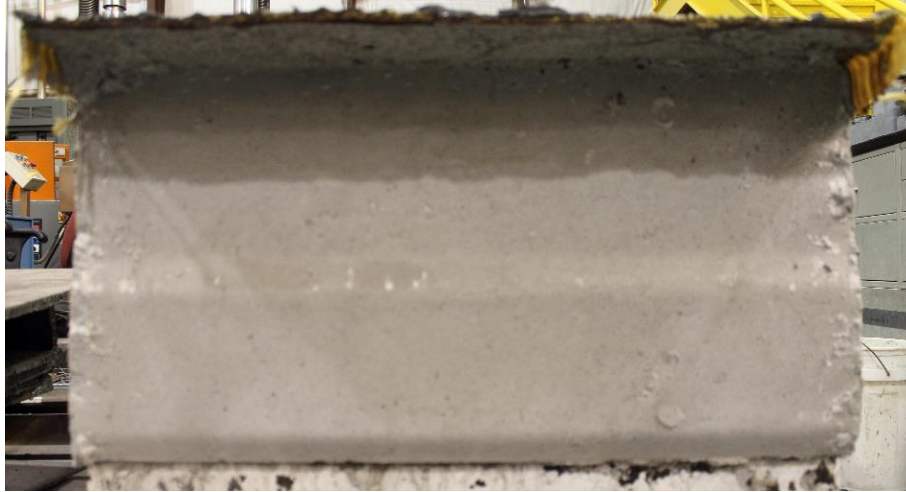
Figure 252: S4 – K&E connection debonded from the middle section.
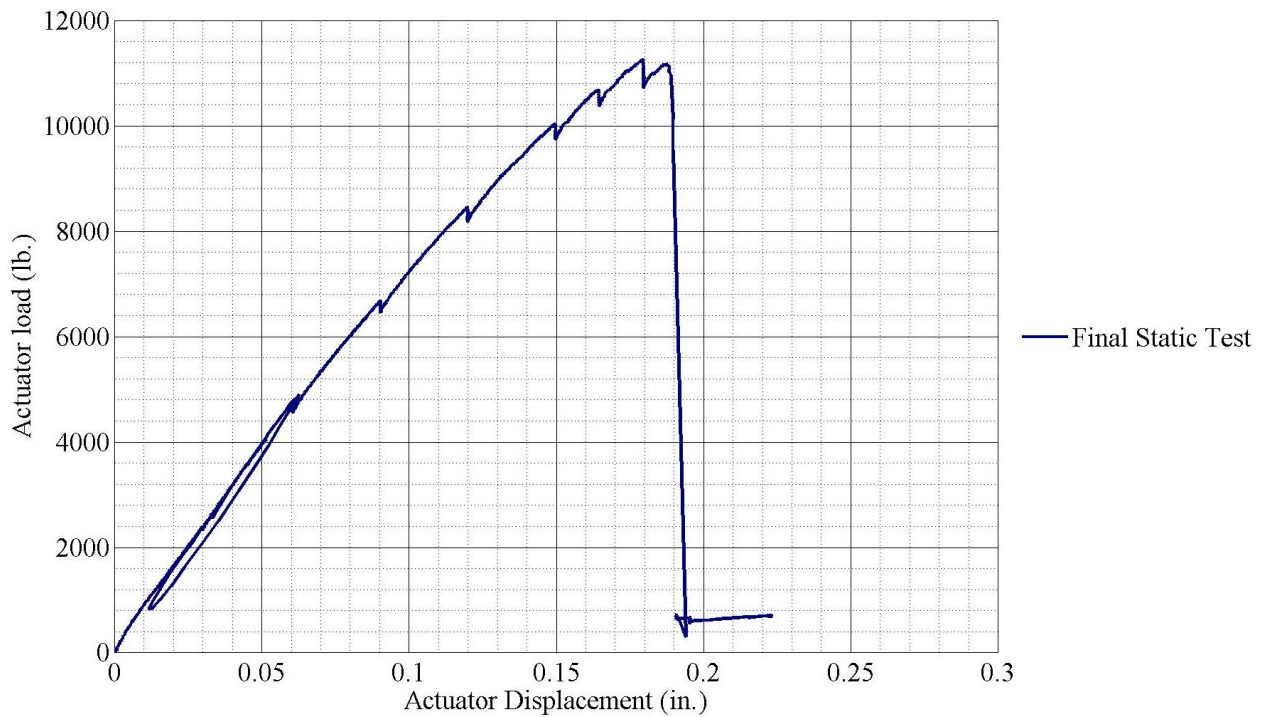
Figure 253: S4 – load vs. deflection, final static test.

6.2.4.4.   Summary of S4 Test

The purpose of this test was to observe the effect of addition of the K&E connection to the existing partial depth grouted detail. The K&E connection was unable to prevent the joint from cracking. The K&E connection was not engaged until the joint cracked for the full depth. Hence, the position of the K&E connection precluded it from preventing cracking. However, the K&E connection allowed the transfer of shear across the fully cracked joint. The K&E sheet debonded from the beam sections during the final static

test of S5. The use of sand-blasting or shot-blasting for preparing the concrete surface may provide a better bond than grinding.

6.2.5. Specimen 5 – Spliced VHPC connection without topping

The top flange splice connection was also tested with VHPC connection. The connection details were exactly the same as S2. The VHPC used in this mix did not have the required flowability due to the super-plasticizer being under used. The dosage rate for the VHPC mix was to be determined on the basis of flowability during mixing. The dosage used for this mix was deemed to be flowable after mixing. However, the mix quickly became stiff during placement and lost its' plasticity. Therefore, voids were introduced in the joint. Moreover, the bond was expected to be poor for the connection in this specimen (and as seen in Table 33). A picture of a joint in the specimen is shown in Figure 254.

Figure 254: S5 – Poor consolidation of VHPC in joint.

6.2.5.1. S5 – fatigue test

The fatigue test for the specimen 5 (S5) was as per the planned protocol of applying 0.03 in. up to 0.04 in. displacement. The focus of this test was on the performance of the VHPC with respect to that of UHPC which had provided an excellent performance in S2 and S3. However, with the joint being poorly consolidated, it was expected that this specimen would not perform as well as S2, which was directly comparable to S5 in terms of the construction.

The north joint cracked in the baseline static test for the specimen. The crack in the north joint was quite fine and not very conspicuous owing to the poorly defined surface of the VHPC connection. The load vs. deflection plot for S5 is shown in Figure 255. There were no further instances of crack occurring in

either joint as the behavior of the specimen became stable after the application of the first 10 cycles and retightening the clamping beams.
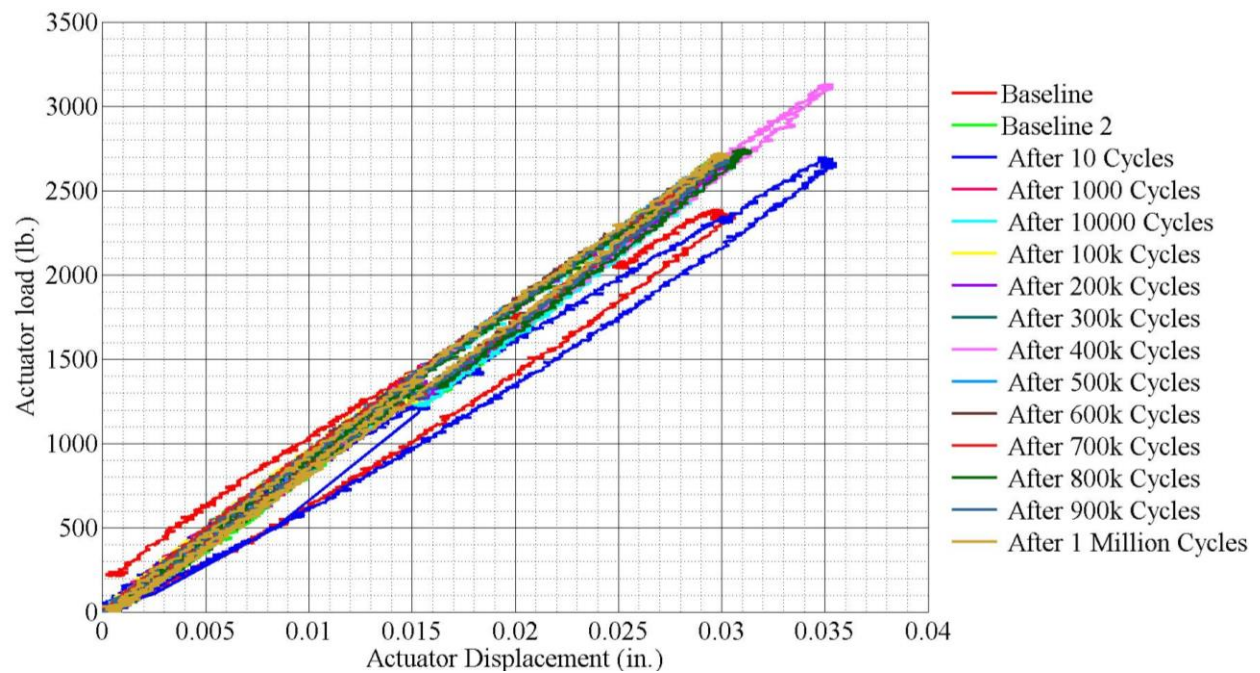
Figure 255: S5 – actuator load vs. actuator displacement.

The actual displacements applied to the specimen are shown in Figure 256.
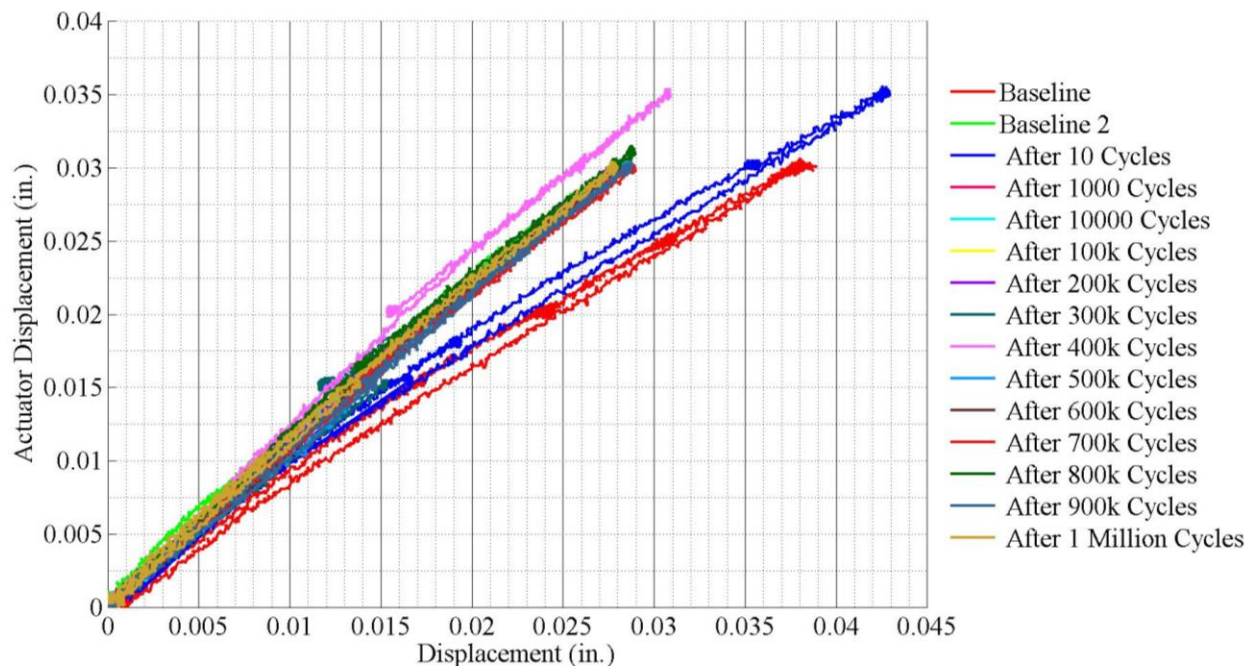
Figure 256: S5 – actual displacements imparted on specimen.

The displacements recorded at the gap between the middle section and the north beam section display the occurrence of the crack at the north joint. Figure 257 and Figure 258 display the displacements at the north gap. The crack propagation continued for the rest of the test as indicated by the gradual reduction of slope of the load vs. displacement plots which basically was a softening of the specimen response.
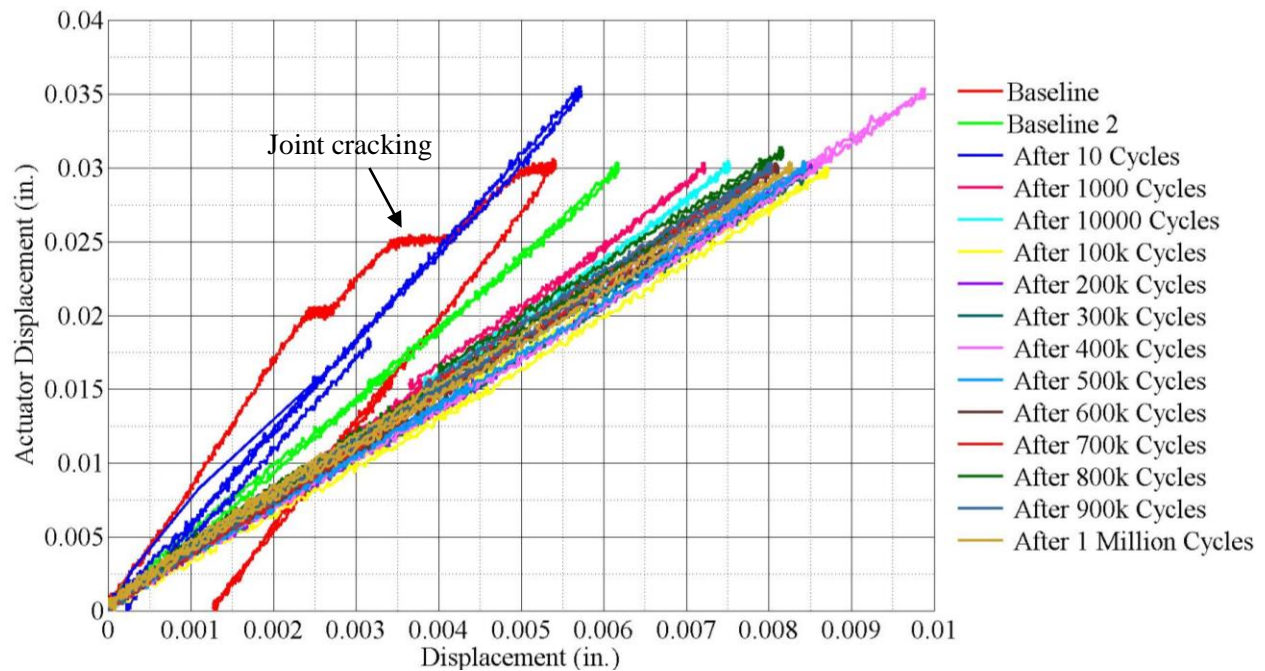
Figure 257: S5 – variation in NE joint displacements during fatigue testing.
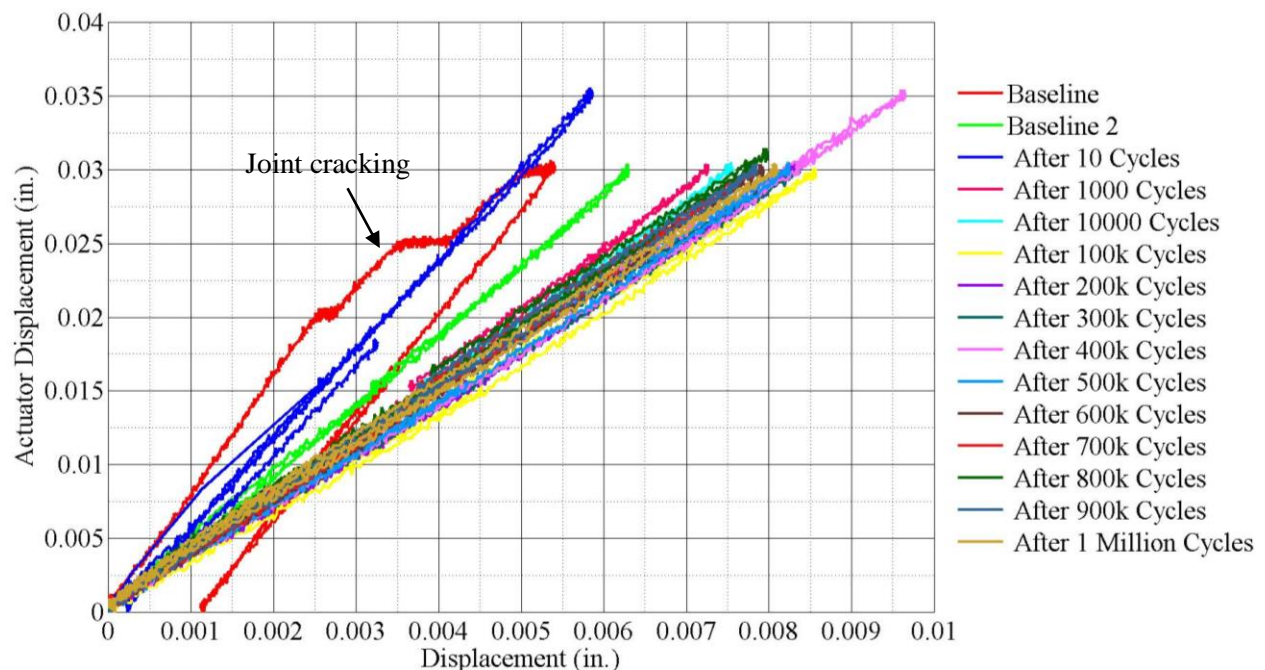
Figure 258: S5 – variation in NW joint displacements during fatigue testing..

The gap displacements on the south joint indicated an exact opposite response after the specimen softened at the north joint. The gap displacements became smaller over the duration of cycling. The response at the south joint is shown in Figure 259 and Figure 260. The reduction in joint displacements at the south joint corresponded with the increment in joint displacements at the north joint.
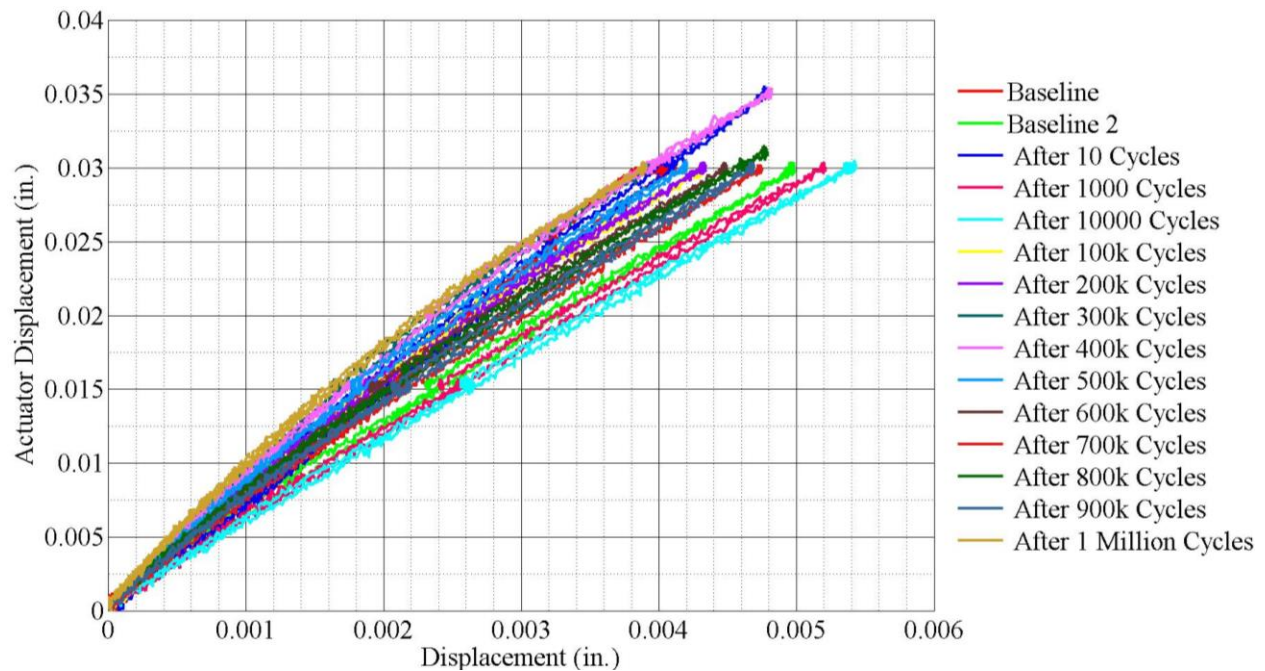
Figure 259: S5 - variation in SE joint displacements during fatigue testing.
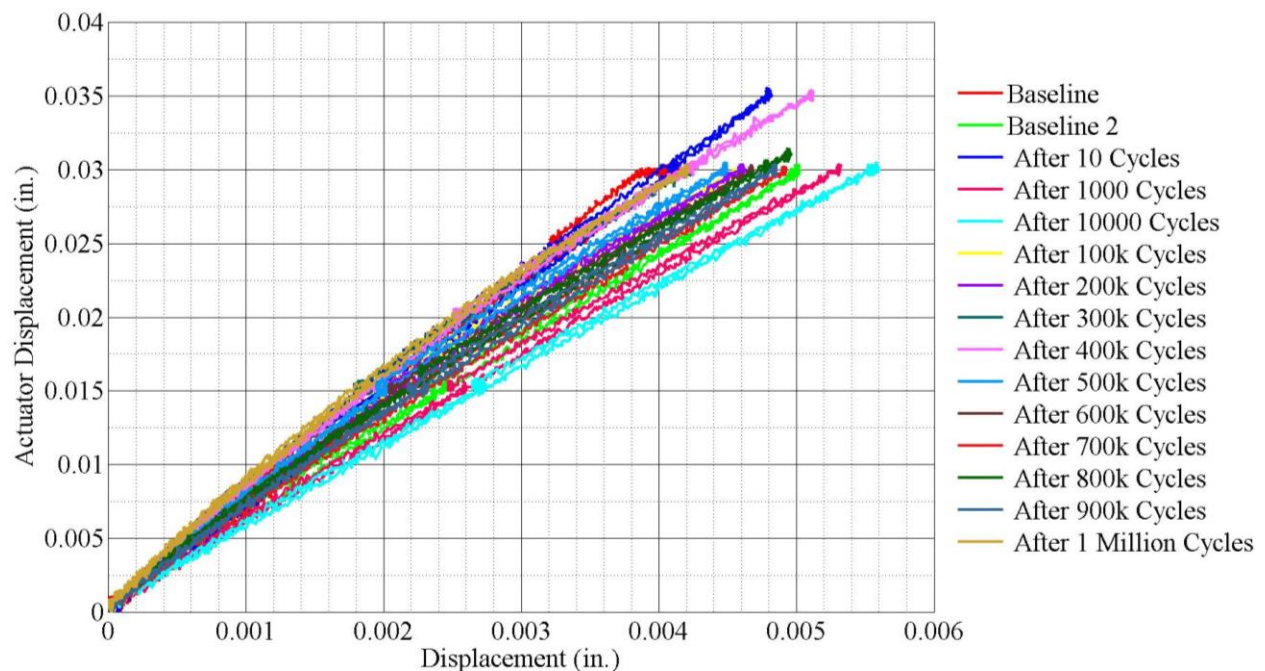
Figure 260: S5 – variation in SW joint displacements during fatigue testing.

6.2.5.2. S5 – ponding test

The ponding test was performed for specimen S5 after the application of 1000 cycles. The specimen displayed leakage after the first ponding test at both the joints. This did not necessarily indicate a full depth crack or a failure of the splice. The water seemed to be seeping through the existing voids in the connection. Figure 261 displays water seeping through a void at the corner of the pocket. Water seepage is indicated by a bubble as shown in the highlighted area of Figure 261.

Figure 261: S5 – water seepage through a pre-existing void.

6.2.5.3. S5 – ultimate strength test

The ultimate strength test was performed for S5 with application of constant 0.03 in. displacements to the specimens. The existing crack at the north interface kept propagating for the duration of the final static test. There were no cracks seen either visually or through the LVDTs at the south joint in this test. The existing crack at the north joint could definitely be seen after application of 0.12 in. total displacement. At that point, the crack had propagated for the full depth of the key way and the splice was providing the resistance at the joint. The north beam section lost contact with the exterior support beam after a total displacement of 0.15 in. The increments in displacement applied from this point on simply exacerbated the rotation of the north beam section. At total displacement of 0.34 in. the concrete in the middle beam section began displaying distress in the form of cracks on the girder top. These cracks were for the full thickness of the specimen and were propagating from the specimen sides to the corner of the pocket. At this point the specimen failure was expected. Therefore, additional 0.04 in displacements were applied. The specimen began losing stiffness and the displacement kept increasing without any appreciable increase in the load. The specimen failed completely after application of a total displacement of 0.5 in. The concrete at the top

of the middle beam section crushed. Figure 262 displays the crushed concrete at the top of the middle beam section. The load vs. displacement plot for S5 is shown in Figure 263.

Figure 262: S5 – concrete crushing over the middle section.
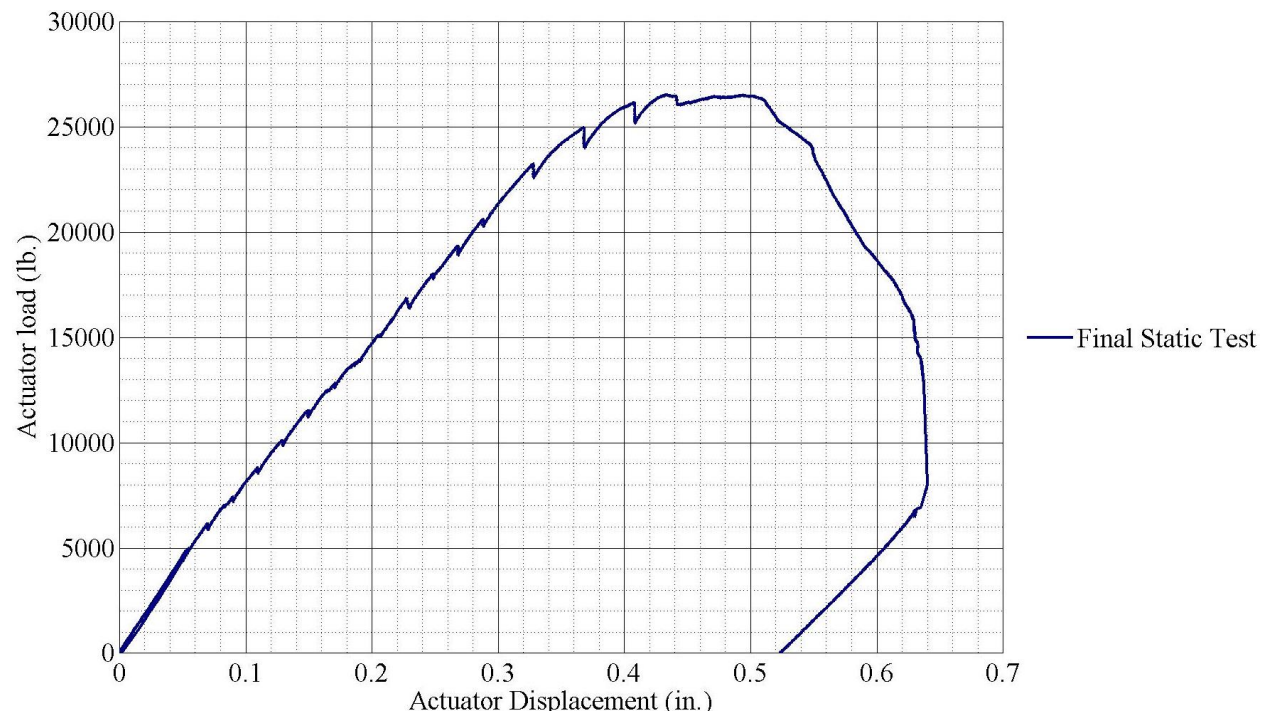
Figure 263: S5 – actuator load vs. displacement, final static test.

6.2.5.4. Summary of S5 Test

In this test the beam concrete crushed. The performance of the joint was the focus of this testing. Therefore, the crushed concrete was cleared from the specimen and the north splice was exposed. The interface crack had propagated to the splice and continued into the splice as a diagonal shear crack in a short beam. The fibers could be seen to have been pulled out at this crack. The reinforcing bar from the middle beam section remained bonded to the VHPC. The deflected shape of the bar indicated that the bar had provided a dowel action. A schematic view of the failure surface is shown in Figure 265.

Figure 264: S5 – failure surface in VHPC splice pocket.
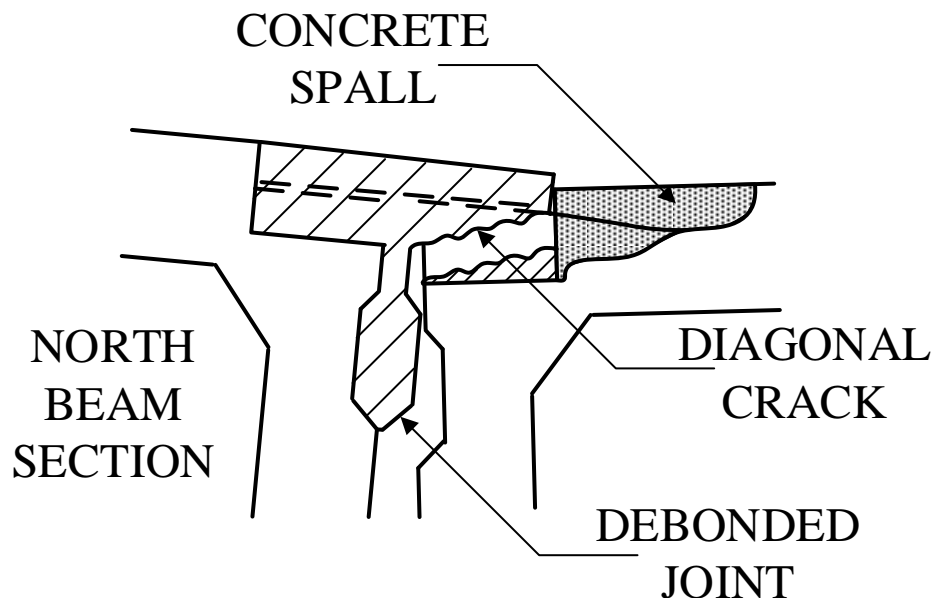
Figure 265: S5 – schematic of failure mode.

The failure mode clearly shows that the cracks propagated into the splice from the joint. The crack propagated in a manner that the reinforcing steel from the beam section was not engaged until complete failure of the specimen. This can be attributed to the poor quality of the VHPC in the joint. However, to ensure that the splice bars also provide resistance to the applied loads, the splice bars could be placed lower in the pocket.

6.2.6. Specimen 6 – Spliced VHPC connection with topping

Specimen 6 (S6) consisted of the top flange spliced connection as well as a concrete topping. S6 was directly comparable to S3. The issues with the superplaticizer dosage were fixed for the VHPC mix in this specimen. The dosage was increased to produce self-consolidating concrete. Care was taken to ensure that the superplaticizer was not overused to prevent segregation of the aggregate and fibers from the concrete paste.

6.2.6.1. S6 – fatigue testing

The testing protocol for the fatigue testing was repeated with displacements of 0.03 in to 0.04 in. applied to the specimen. The clamp beams had to be retightened twice in this test. The specimen response did not appear to change for the duration of the entire testing program. The actuator load vs. displacement plot is shown in Figure 266.
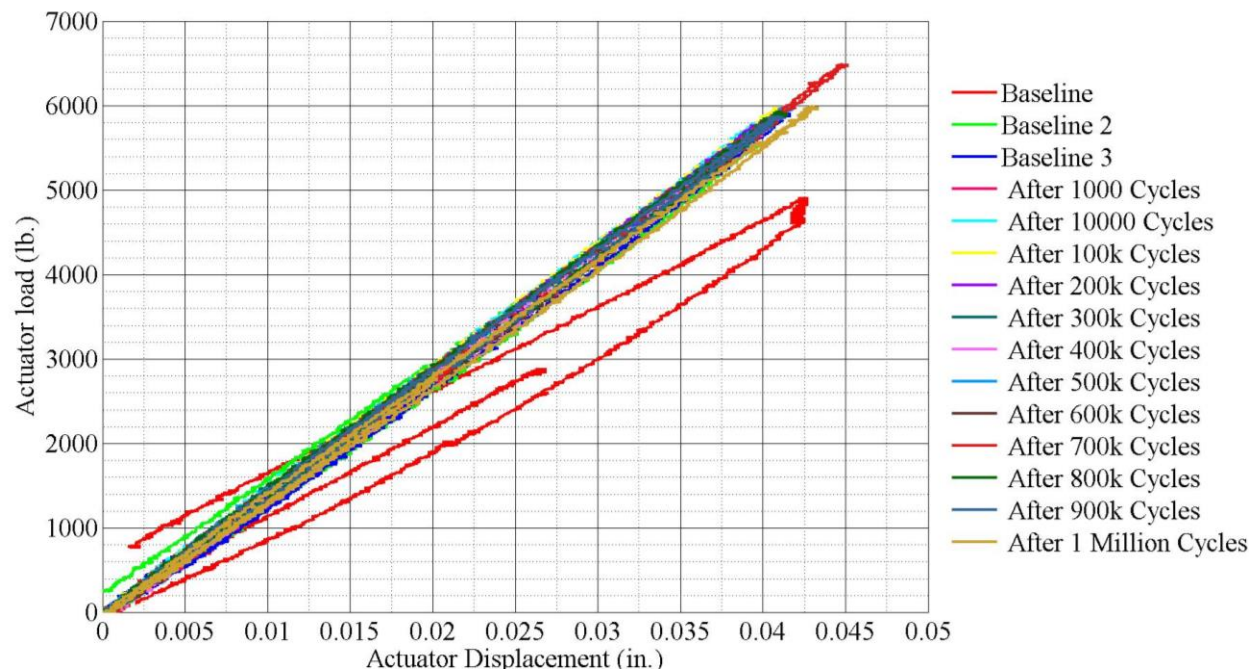
Figure 266: S6 – actuator load vs. displacement.

The actual displacements applied to the specimen are plotted with respect to the actuator displacements and are shown in Figure 267.
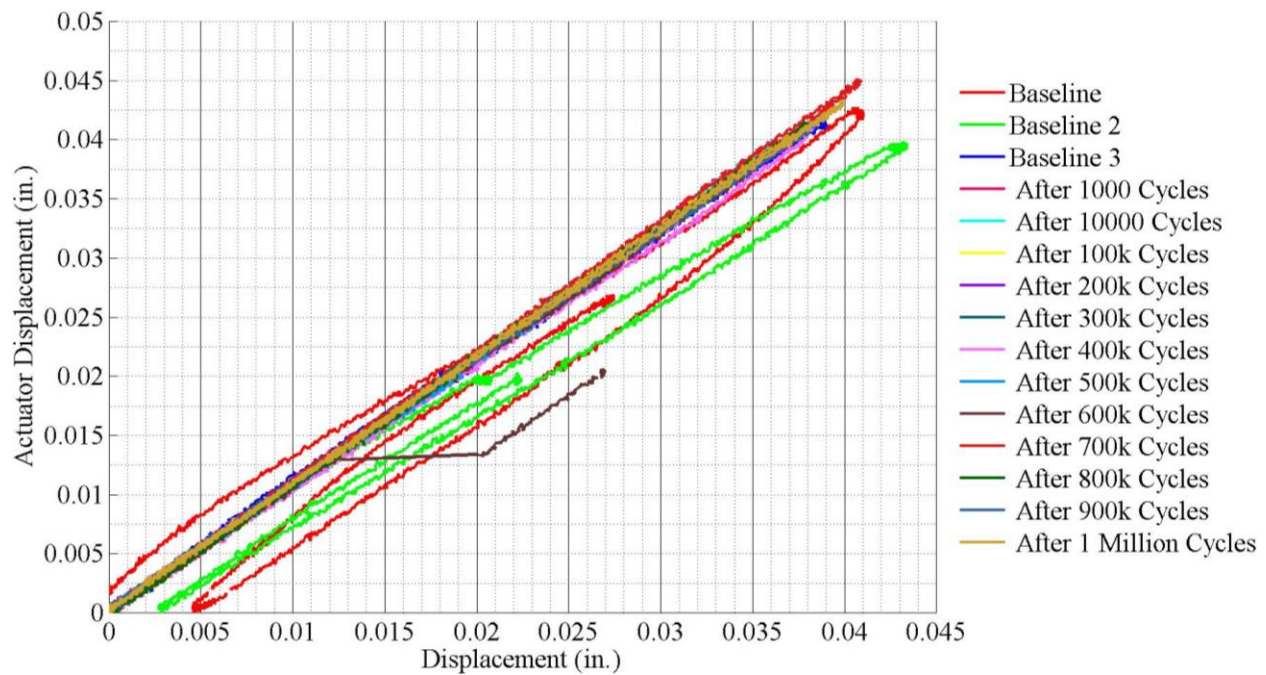
Figure 267: S6 – actual displacements applied to the specimen.

The displacements observed at the north joint, shown in Figure 268 and Figure 269, displayed a similar trend as the load vs. global displacement plots. The displacements at the south joint also showed the same trend for the first 900,000 cycles. The south joint cracked during cycling in the last 100,000 cycles. The displacements observed at the south joint are shown in Figure 270 and Figure 271. The drop in load due to south joint cracking is shown in Figure 272.
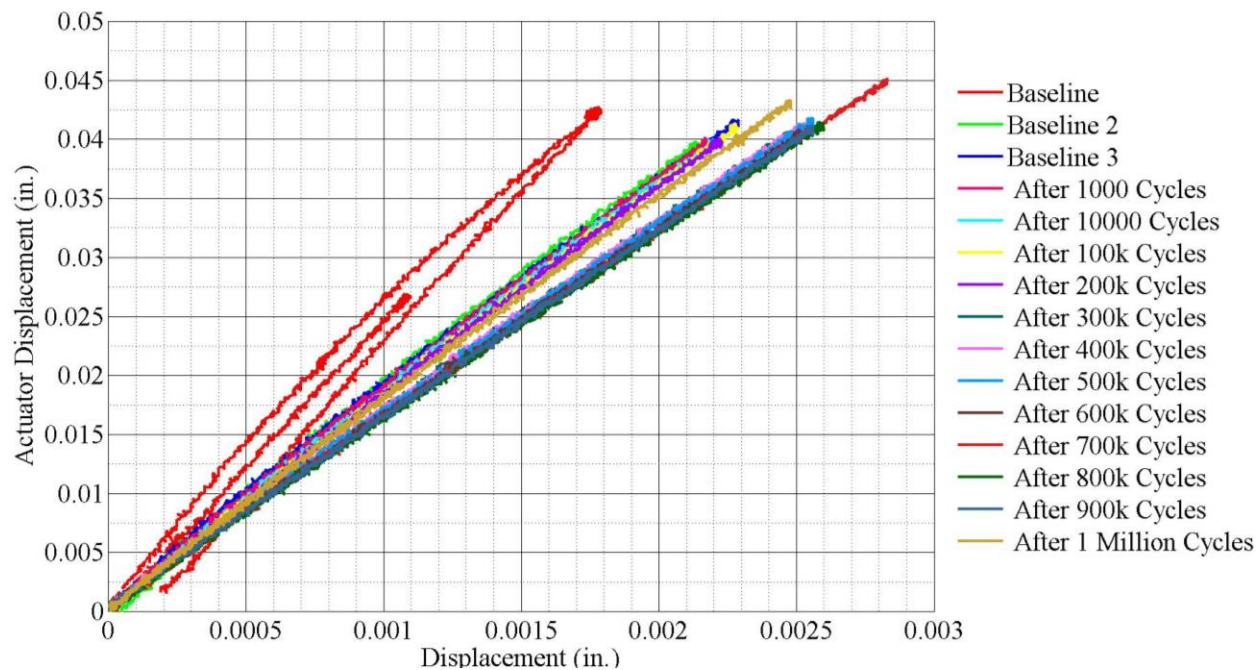
Figure 268: S6 – variation in NE joint displacements during fatigue testing.
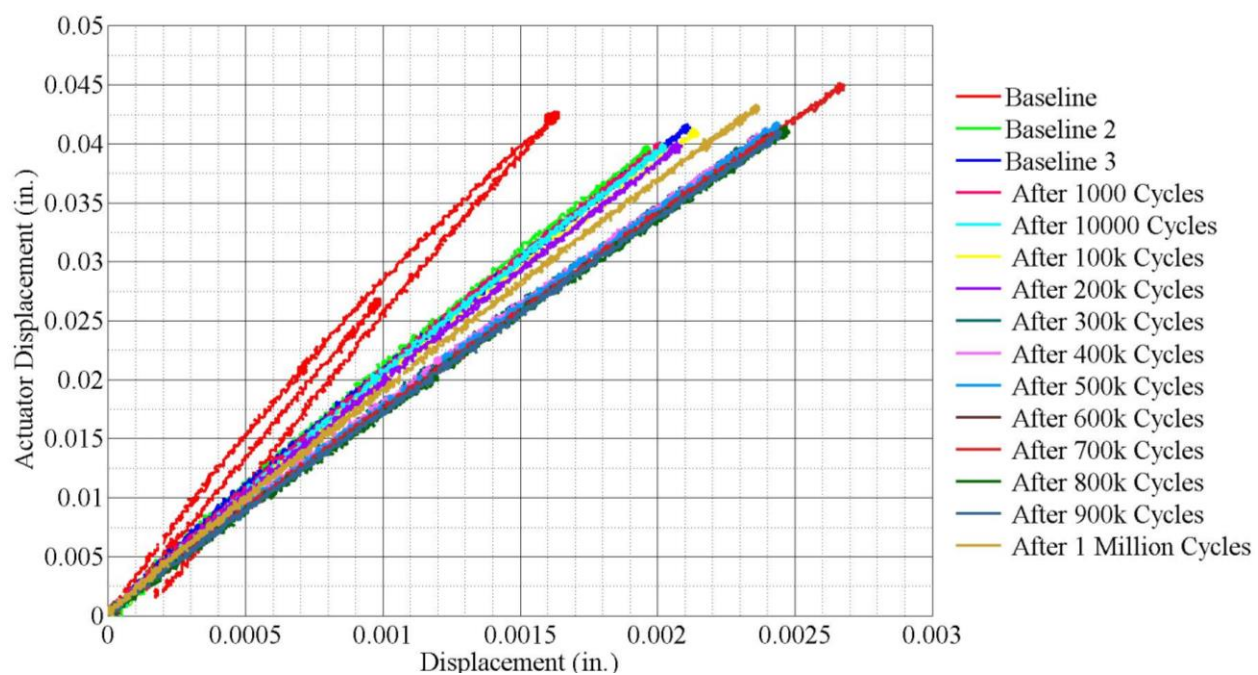
Figure 269: S6 – variation in NW joint displacements during fatigue testing.
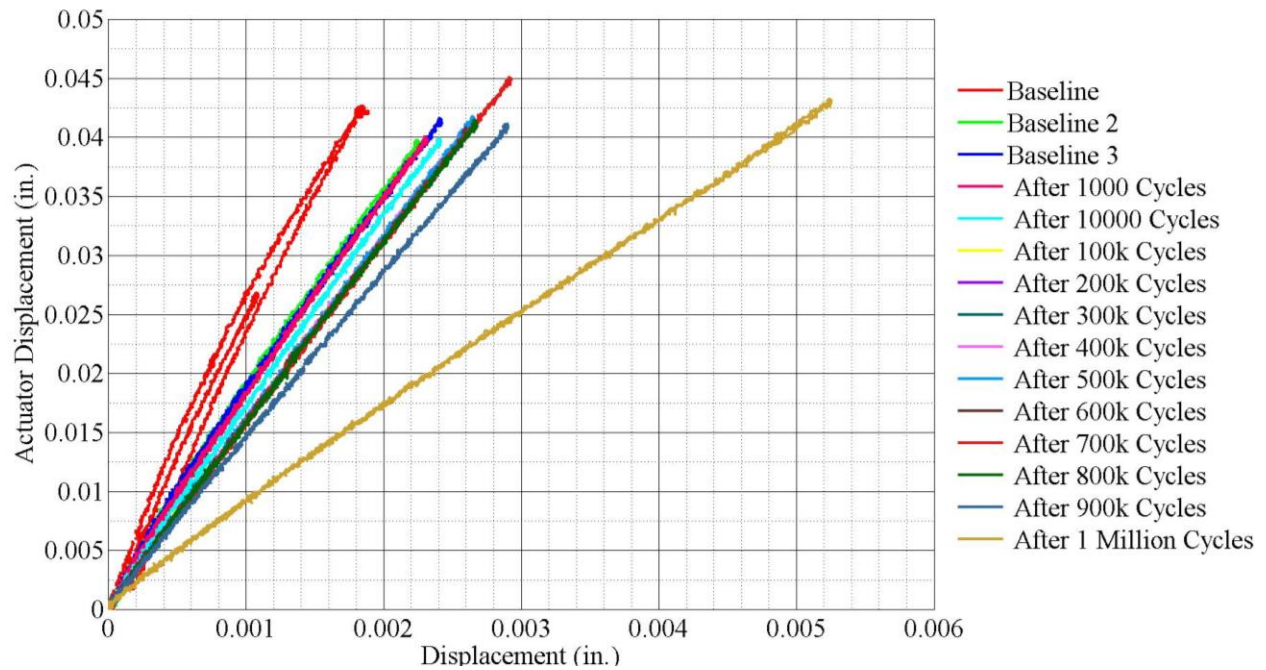
Figure 270: S6 – variation in SE joint displacements during fatigue testing.
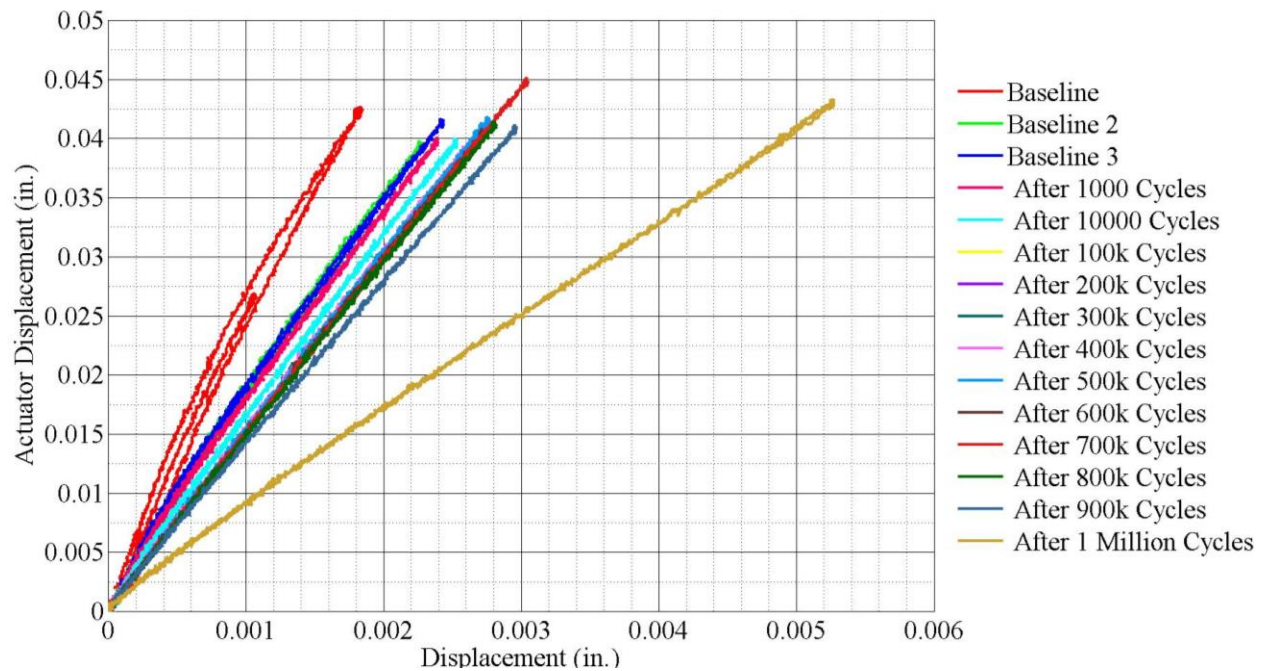
Figure 271: S6 – variation in NW joint displacements during fatigue testing.
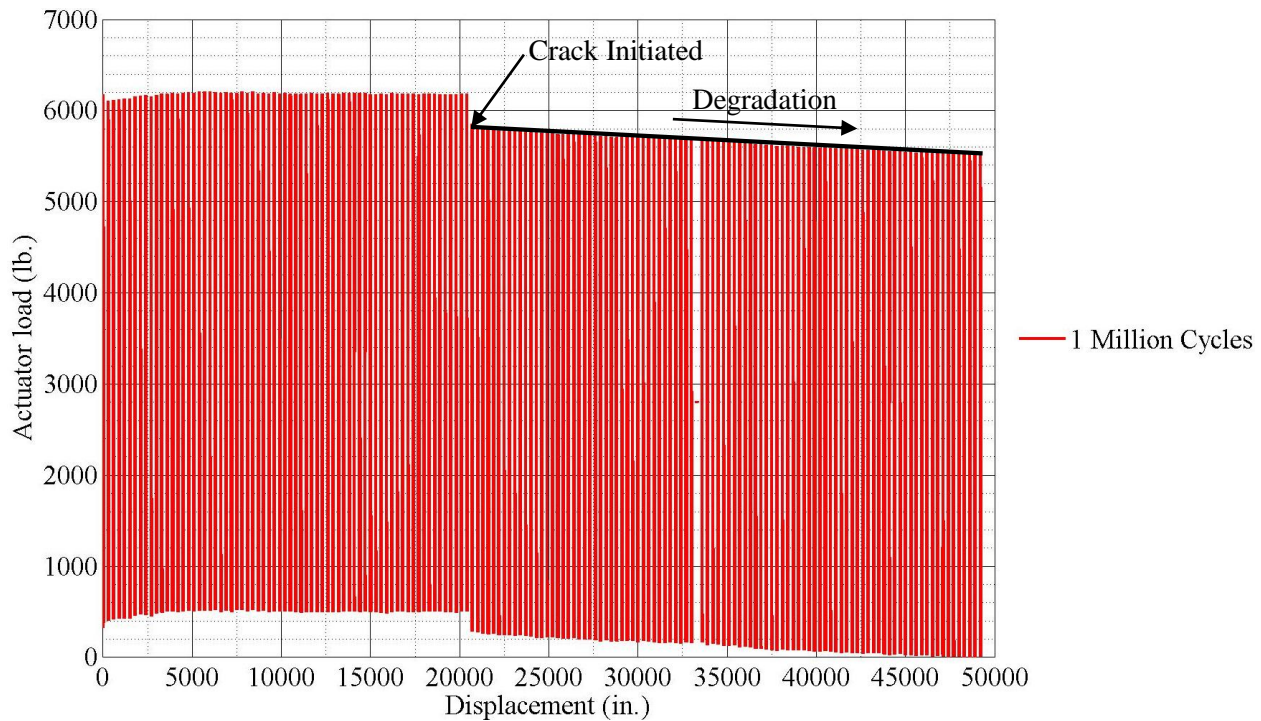
Figure 272: S6 – drop in load after south joint cracking.

6.2.6.2. S6 – Ponding test

The ponding test was performed for S6 and there was no joint leakage for the duration of the testing.

6.2.6.3. S6 – Ultimate strength test

The displacements were applied in 0.02 in. increments until the north joint cracked and then were increased to 0.04 in. The existing crack in the south joint propagated for the full depth for a total displacement of 0.12 in. The next 0.02 in. increment in deflection propagated the crack at the south joint in to the interface between the beam section and the topping. The north joint cracked at a total applied displacement of 0.18 in. Both the exterior beam sections lost contact with the exterior support beams after application of 0.24 in. displacement. The specimen then was continuously displaced by 0.153 in. to a total of 0.393 in. since a drastic failure was not expected in this specimen. The displacement was stopped after applying another 0.04 in. displacement (0.433 in. total). The support load cells were close to maximum capacity at this point. The load vs. displacement plot for the final static test of S6 is shown in Figure 273.
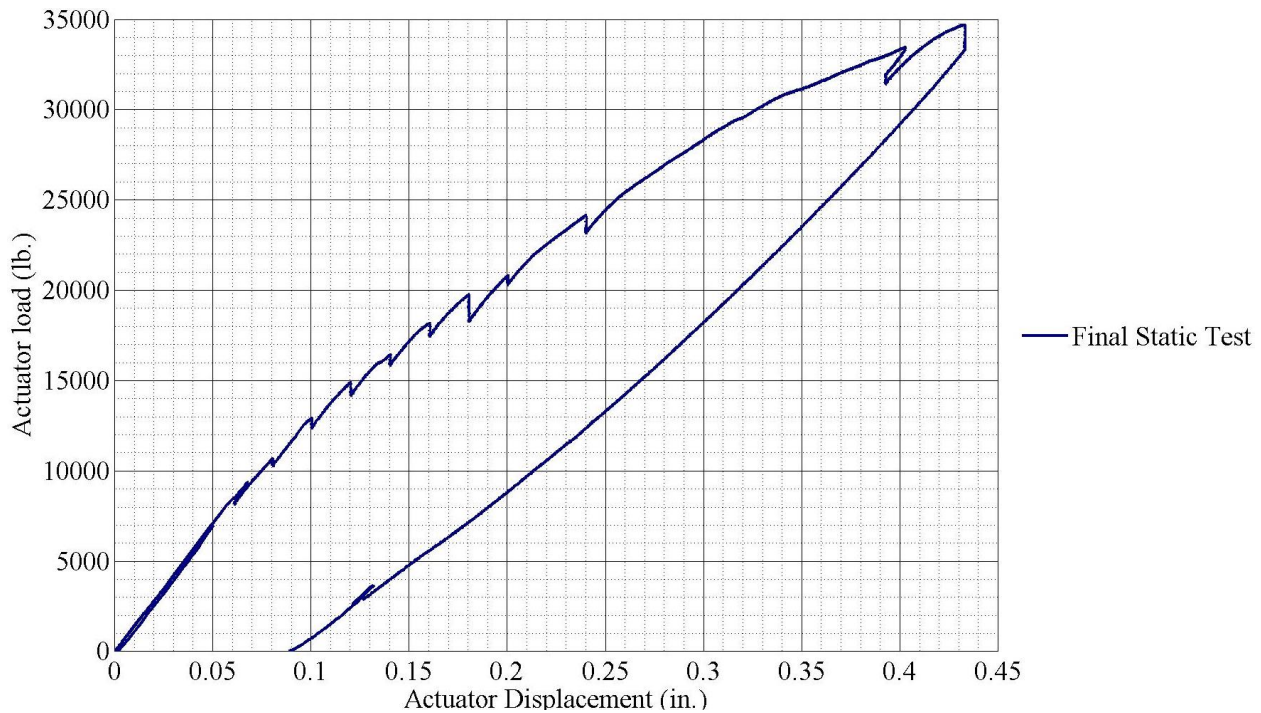
Figure 273: S6 – load vs. displacement, final static test.

6.2.6.4. Summary of S6 Test

The VHPC connection in the keyway debonded during the application of the last 100000 cycles. The plot of the load magnitude plotted with respect to time shows that the joint condition was deteriorating over the remaining period of fatigue test. The stabilization seen in S3 after crack propagation was not seen in the S5 test at least for the remaining period of testing. Possibly, this crack could have propagated until the splice connection with further fatigue testing.

The connection with VHPC provided a performance very similar to the connection with UHPC. The "reflective cracks" did not propagate over the joint, but transversely until the modulus of rupture of the topping was exceeded.

The S6 test provided a better performance from the VHPC used in the testing. The quantity of VHPC in the mix for S6 was increased by 30% over the quantity used in S5. The increased quantity provided the flowability necessary to fill the joint without voids. The additional quantity of super-plasticizer did not cause the aggregates and the fibers to segregate from the cementitious paste.

6.2.7. Summary of sub-assemblage test results

The results for the sub-assemblage tests are summarized in Table 34. The results are presented in terms of the number of cycles applied to the specimens, maximum load applied, failure mode and the ponding tests.

Table 34: Summary of sub-assemblage test results.

Specimen	Material	First Crack Load (kips)	Number of Cycles	Maximum Load (kips)		Failure Mode	Ponding Test
				Cycling	Static		
S1	Grout	N/A[#]	105000	5.4	7	Crack propagation for full depth of keyway	No leak until failure
S2	UHPC	11.8[A]	1000000	5.4	33.7	No distinct failure mode. Test stopped.	No leak
S3	UHPC	5.8[B]	1000000	5.6	28.4	No distinct failure mode. Test stopped.	No leak
S4	Grout	5.2[B]	1000000	3.4	11.8	Kevlar reinforcement debonded from beam concrete.	No leak
S5	VHPC	1.8[B]	1000000	3.8	24.5	Beam concrete crushing.	1000 Cycles
S6	VHPC	6.2[C]	1000000	6.2	36	No distinct failure mode. Test stopped.	No leak

NOTE: A = Cracked during final static test.
         B = Cracked during intermediate static test during fatigue loading.
         C = Cracked during fatigue test.
         # = Cracking load not known. Specimen cracked during initial handling.

6.3. Comparison of connection performance

The connection behavior is now compared by plotting the results of the six specimen tests together. The comparison is made in terms of connection durability and connection strength. The focus of comparison was on the basis of the results that pertain to the joint behavior. The results of the LVDTs at the gaps and the overall behavior measured by the actuator LVDT are compared.

For the purpose of comparison the responses of different specimens, the method of plotting was modified in the following figures. For the comparison plots, the data from x and y axes was analytically zeroed. The first value recorded for each instrument was subtracted out from all values for the respective instrument. This ensured that the starting point for all plots was zero. Therefore, the magnitudes of ordinates in these plots appear to be different from the previous series of plots. However, the constant in both the plots is the range of displacement or load applied to the specimens. These results are now discussed.

6.3.1. Comparison of connection durability

Connection durability was compared by plotting the results of the two baseline tests and the final static test performed after the end of 1 million cycles. The first baseline test was the first ever displacement application to the specimens. This test provided the baseline response of the specimens. Often, the response

changed without the occurrence of cracks since the beams clamping the specimens would not be tight enough during the first set of cycles applied to the specimens. Therefore, a second baseline test was also performed. The second base line test provided the true comparative response to the change in response over further cycles. Typically, the second baseline test was performed after 1000 cycles.

6.3.1.1. Comparison of global behavior

The displacements applied by the MTS actuator and the resistance measured by the MTS load cell provided the overall global response of the specimens. Basically, the actuator load vs. displacement response provided the best indicator of specimen stiffness. The global responses of the specimens to first base line test, second base line test and the static test after 1 million cycles is shown in Figure 274, Figure 275 and Figure 276 respectively.
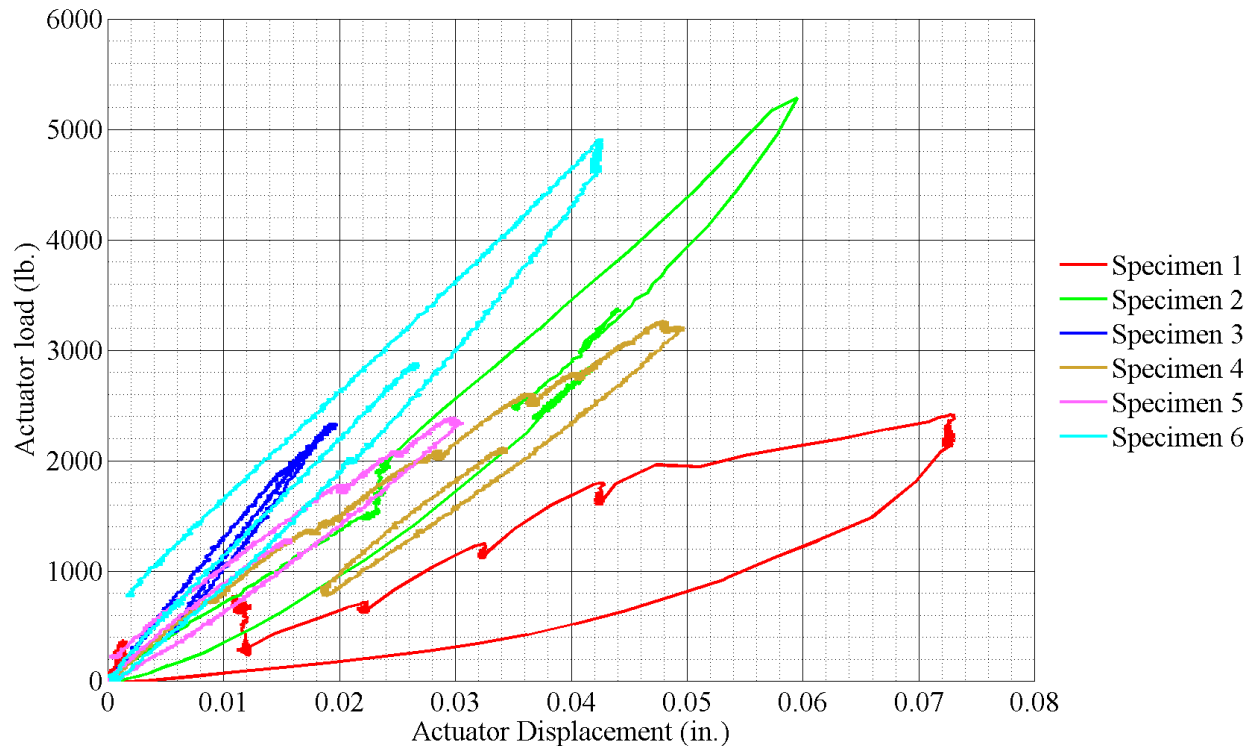
Figure 274: Comparison of actuator displacements for first baseline static test.
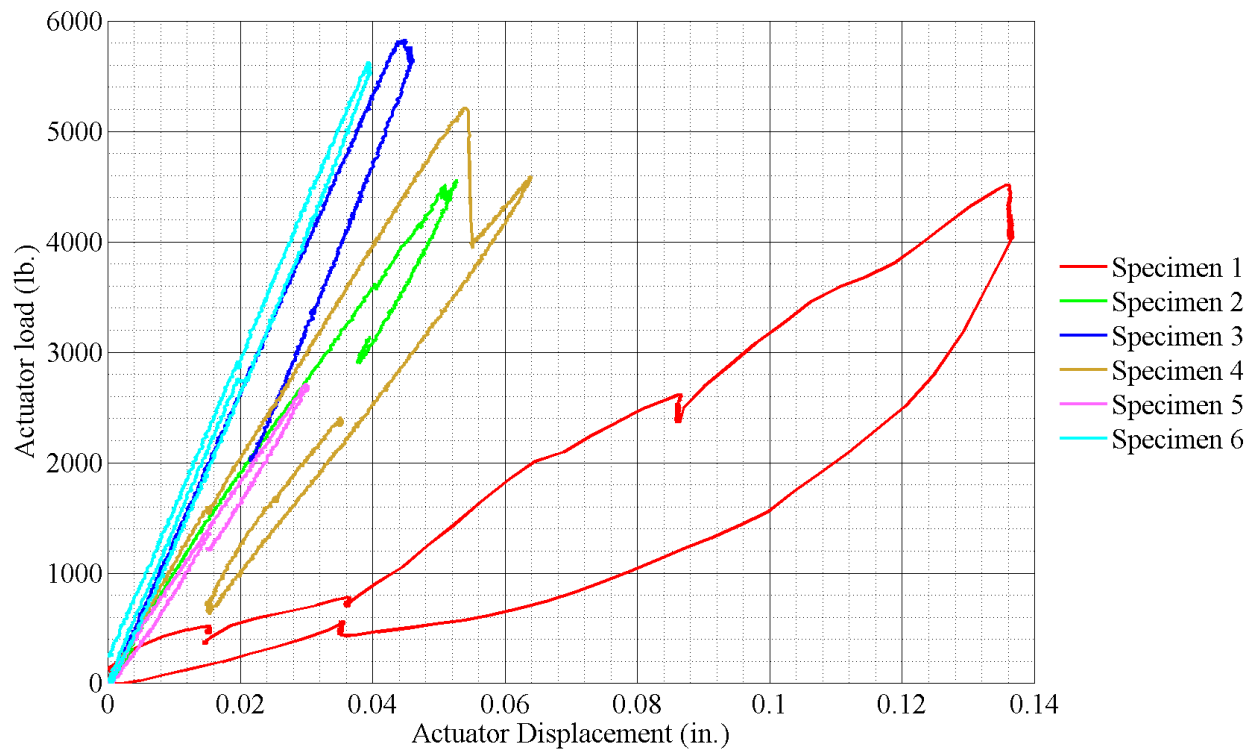
Figure 275: Comparison of actuator displacements for second baseline static test.

Figure 276: Comparison of actuator displacements for static test after 1 million cycles.

The above plots show the degradation of stiffness over a duration of 1 million displacement cycles, except for S1 which failed early. The stiffness degradation is indicated by the change of the slope of the plot. The reduction in slope was equivalent to the reduction in the stiffness of the specimen.

The specimens with grouted connections, S1 and S4, provided the most flexible responses. Joints in S1 had already cracked when the first base line test was performed. Therefore, the response of S1 was non-linear throughout. These cracks propagated with increasing number of cycles. Therefore the softening of the specimen response was expected. As for S4, one joint cracked for the full depth during the second baseline test. Therefore, the softening observed between at the end of 1 million cycles was also logical. Moreover, the only point of difference between specimens S1 and S4 was the presence of the K&E connection. Hence, it can be said that the K&E connection provided a more durable solution than the existing connection.

Specimens with spliced connection without concrete topping, S2 and S5, were stiffer than the grouted specimens. Between the two specimens, S2 with UHPC performed better than S5 with VHPC. Although a fair head to head comparison cannot be made considering the poor quality of the VHPC in the S5 joints. However, the response of S2 did not change at all since the joints did not crack for the entire duration of fatigue testing. On the other hand, S5 joints cracked during the first baseline static test. This was clarified from the joint and gap LVDTs. The actual crack(s) were inconspicuous owing to the irregular and voided surface of the joints. Moreover, the bond strength of the joint and beam concrete was poor. Therefore, the cracks continued to propagate during fatigue testing causing a continual degradation of stiffness. Overall, in terms of stiffness, specimens S2 and S5 provided a stiffer response than specimens S1 and S4 as seen by the higher resistance values for comparable magnitude of global displacement.

Spliced specimens with concrete topping, S3 and S6 provided the stiffest response as expected. S3 and S6 were not only similar in terms of the construction but also were comparable in terms of the bond strength between the joint and beam concrete. The results from fatigue testing show very similar results in terms of global behavior of the specimens S3 and S6. The slope of the load vs. deflection curves was almost identical from the second base line test and remained so until the end of testing. In terms of stiffness, there was not much difference between specimens S3 and S6.

6.3.1.2. Comparison of gap displacements

The displacements recorded at the gaps provided an insight into the condition of the joints over the fatigue cycling period. The gap displacements were measured by a pair of LVDTs at each joint except for S1 in which a single LVDT was used per joint at the middle of the specimen. The measurements of displacements recorded for a pair of LVDTs were averaged. The difference between the measurements

from a LVDT pair on the same joint was negligible. The discussion also focuses on the two base line static tests and the final static test after 1 million cycles.

The gap displacements for north joint and the south joint for the first baseline static test are presented in Figure 277 and Figure 278 respectively. The results for the second baseline test are presented in Figure 279 and Figure 280 and finally, the results for the final static test performed after 1 million cycles are shown in Figure 281 and Figure 282.

For the first baseline test, the maximum displacements at the gaps were recorded for S5. Considering the overall stiffness, the grouted connections were expected to have the most displacements at the gaps. However, the bond strength for S5 was very low due to the poor quality of the mix. Therefore, the gap displacements were highest for S5. The lowest gap displacements were recorded for specimens S3 and S6 as expected. These specimens had the stiffest response as seen above.

Figure 277: Comparison of north gap displacements for first baseline static tests.

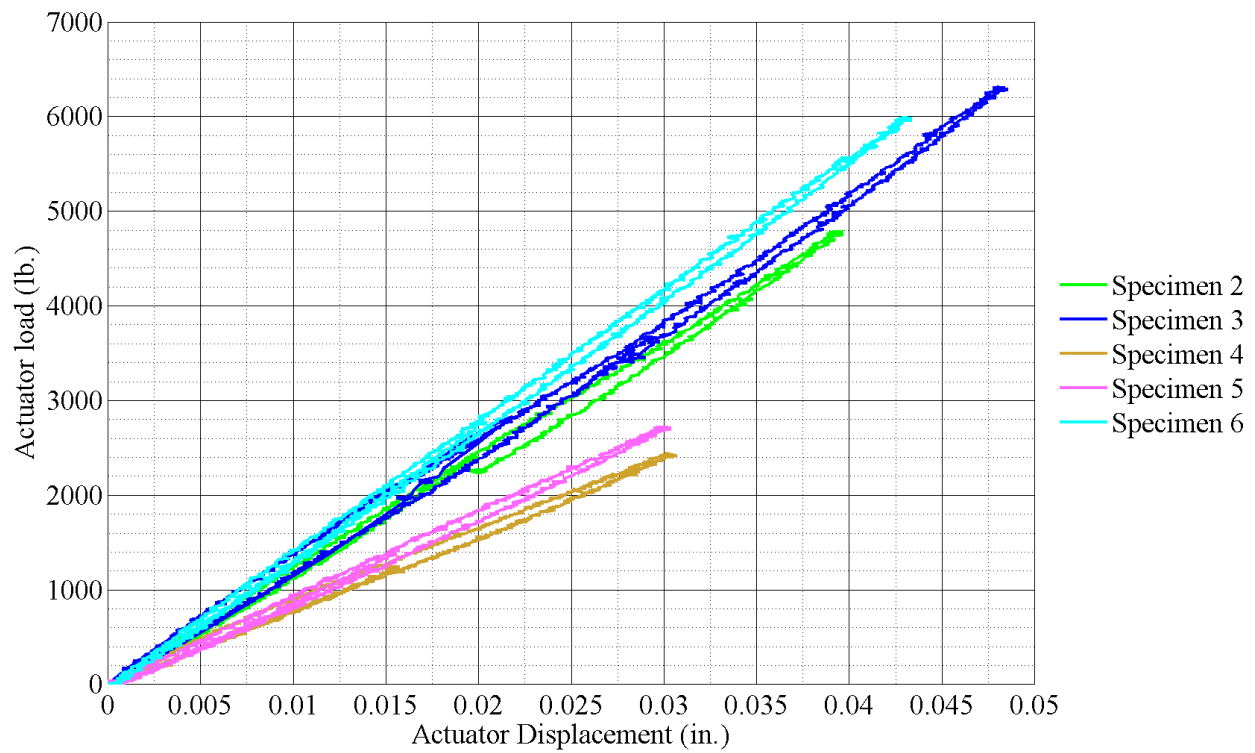*Figure 278: Comparison of south gap displacements for first baseline static test.*

The magnitudes of displacements recorded for the second baseline show a similar trend to that observed in the first static test. The only exception was that the north joint in S4 cracked during the second base line static test. The response of the rest of the specimens remained the same as the first baseline test. The surprising result here was that S1 had smaller gap displacements at the north joint and a comparable response at the south joint with S2 even though the joint had cracked in S1.
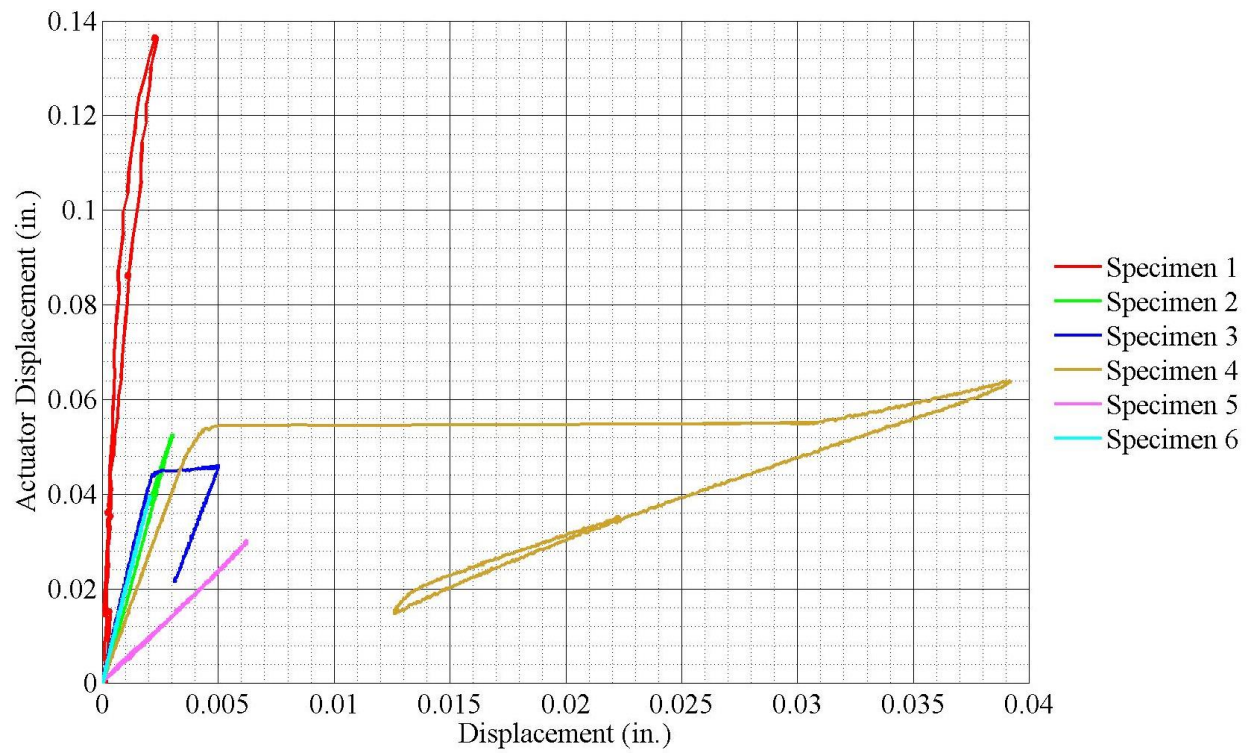
Figure 279: Comparison of north gap displacements for second baseline static test.
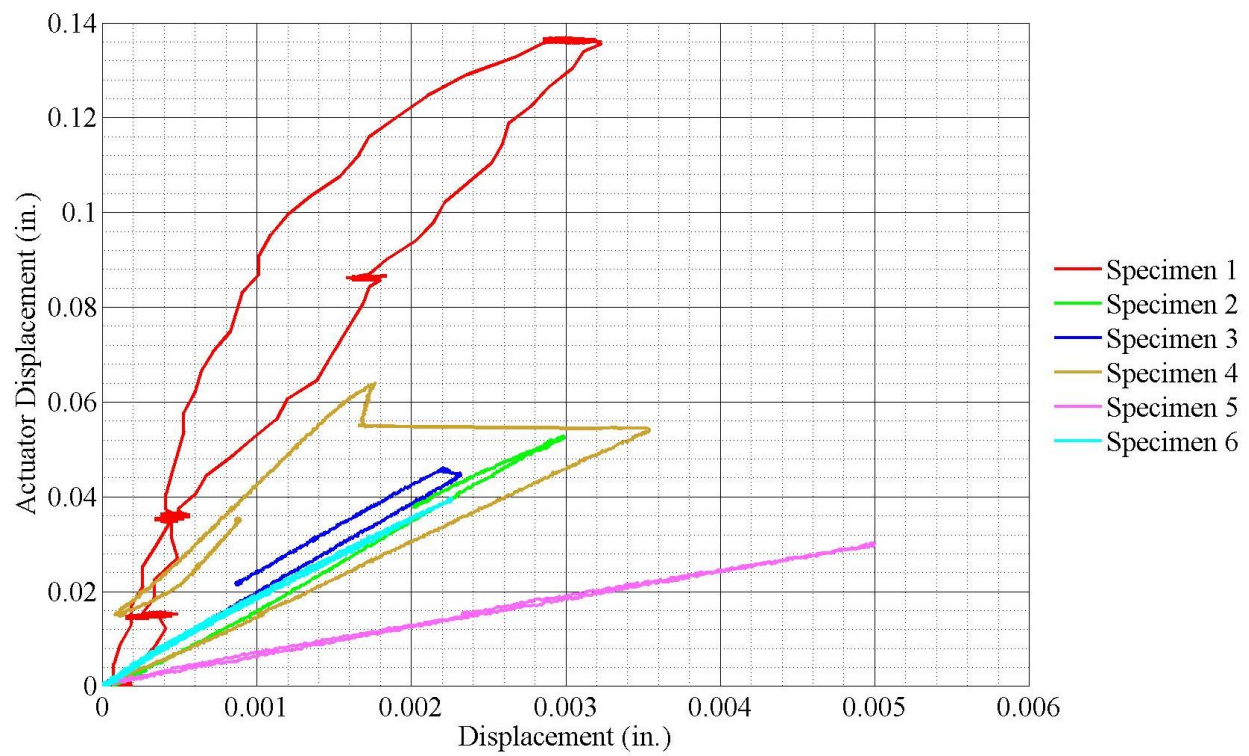
Figure 280: Comparison of south gap displacements for second baseline static test.

252

The gap displacements after 1 million cycles showed that the failed joint in S4 produced the most displacement at the gap. The high magnitude of displacement can be attributed to the K&E connection at the top of the joint acting as a hinge. On the other hand, the sound joint in S4 produced very small displacements in comparison.
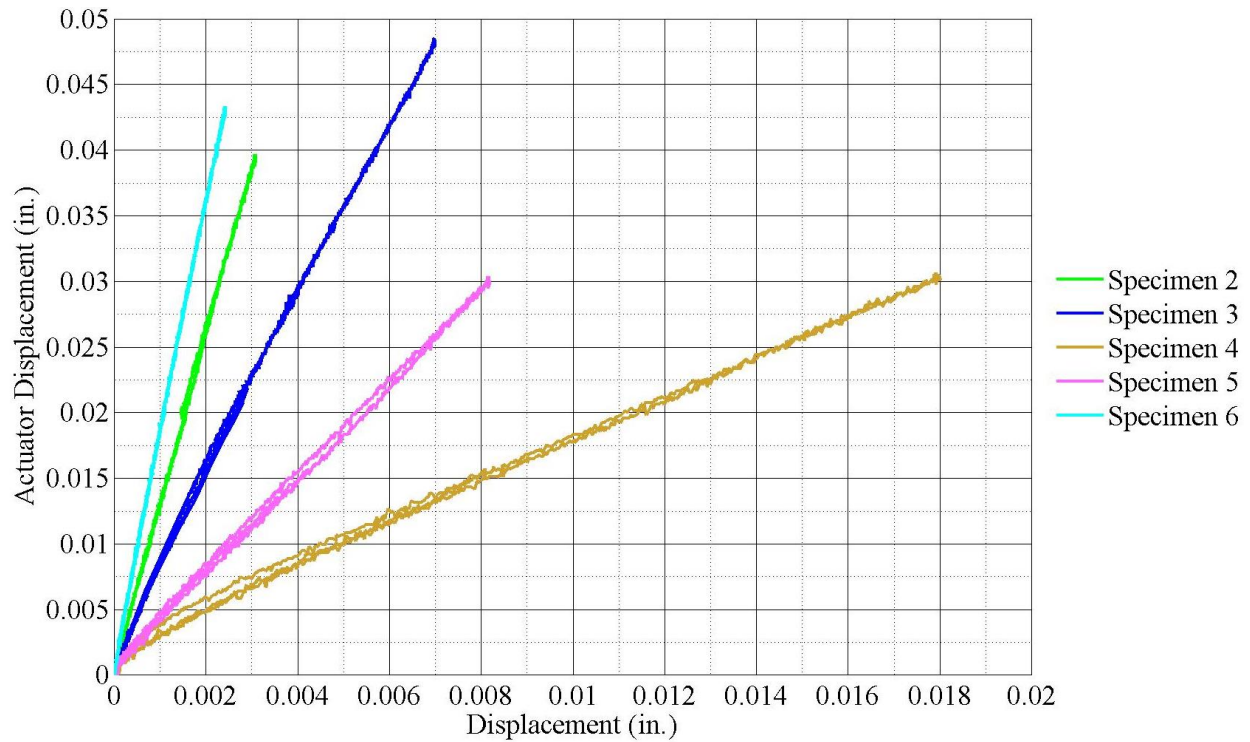
Figure 281: Comparison of north gap displacements for static test after 1 million cycles.
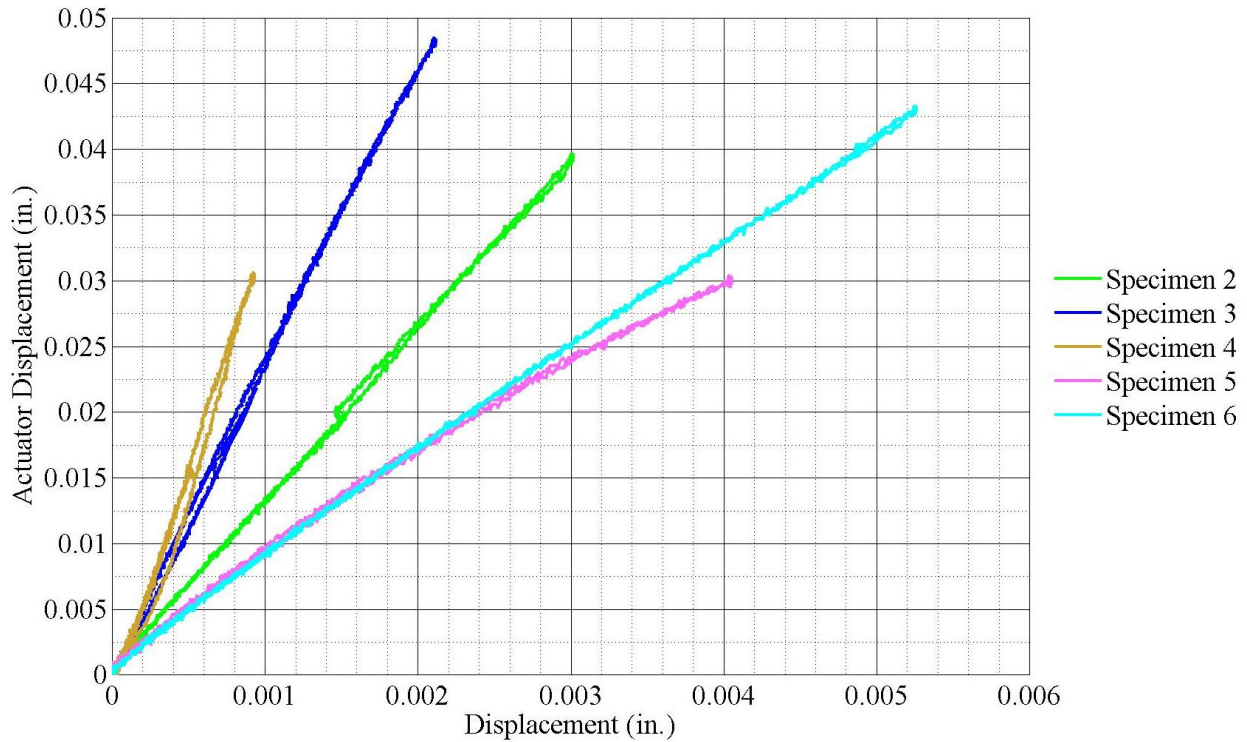
Figure 282: Comparison of south gap displacements for static test after 1 million cycles.

To observe the smallest gap displacement, the LVDT values for the smallest displacement in the joints were compared between specimens. The results were plotted for static test after completion of 1 million cycles. These results are presented in Figure 283. The location of the smallest displacements corresponded with the joints that did not have any cracks, except for S1 which failed early and was ignored here and S5 in which cracks were present for the entire duration of testing. The smallest measured displacement was seen in S4. This however, does not mean that the grouted joint and the K&E connection displayed least displacements. The displacements at the sound joint in S4 were reduced due to the increased displacements at the cracked joint as explained in Section 6.2.4.1. For a fair comparison, the load which corresponded with the displacement value was also taken in to consideration.

In terms of the smallest displacement with respect to load, the smallest displacement was observed in specimen S3 followed closely by S6. The difference in the gap displacements between S3 and S6 may be attributed to the difference in modulus of elasticity. UHPC consistently had a higher modulus of elasticity than VHPC in the all the experimentation that was performed in this research.
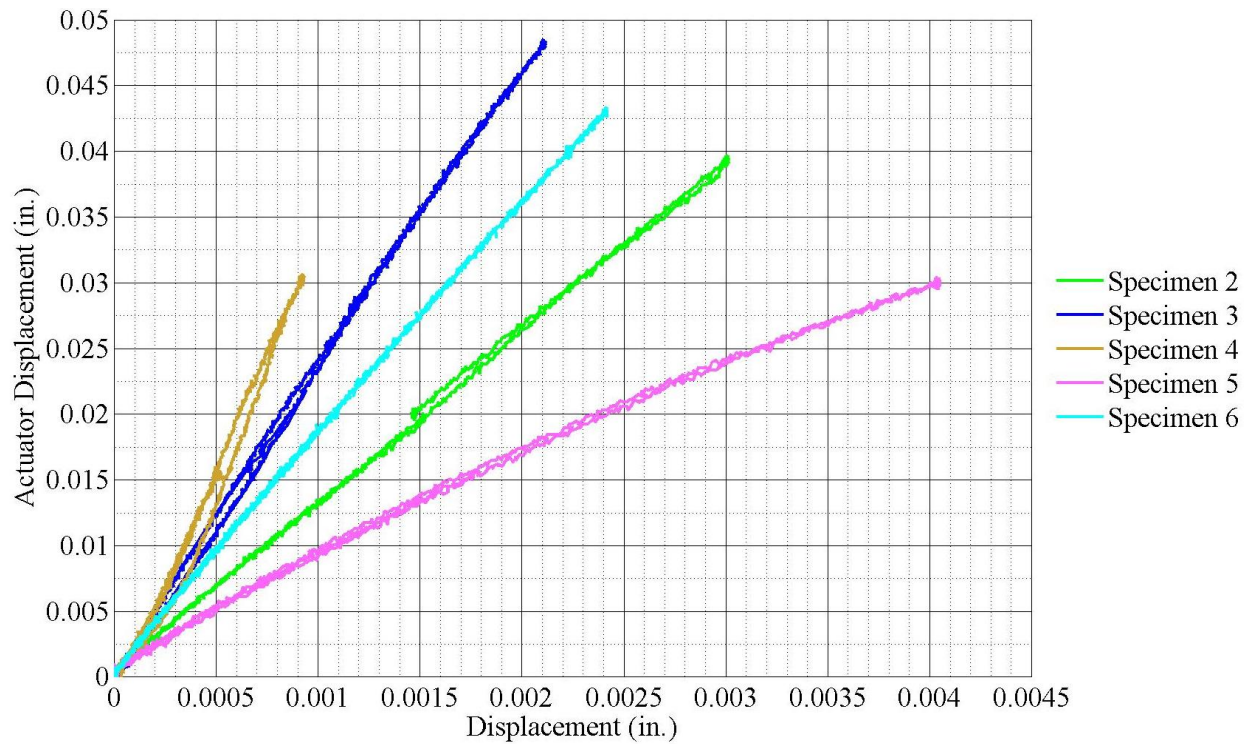
Figure 283: Comparison of minimum gap displacements in all specimens after 1 million cycles.
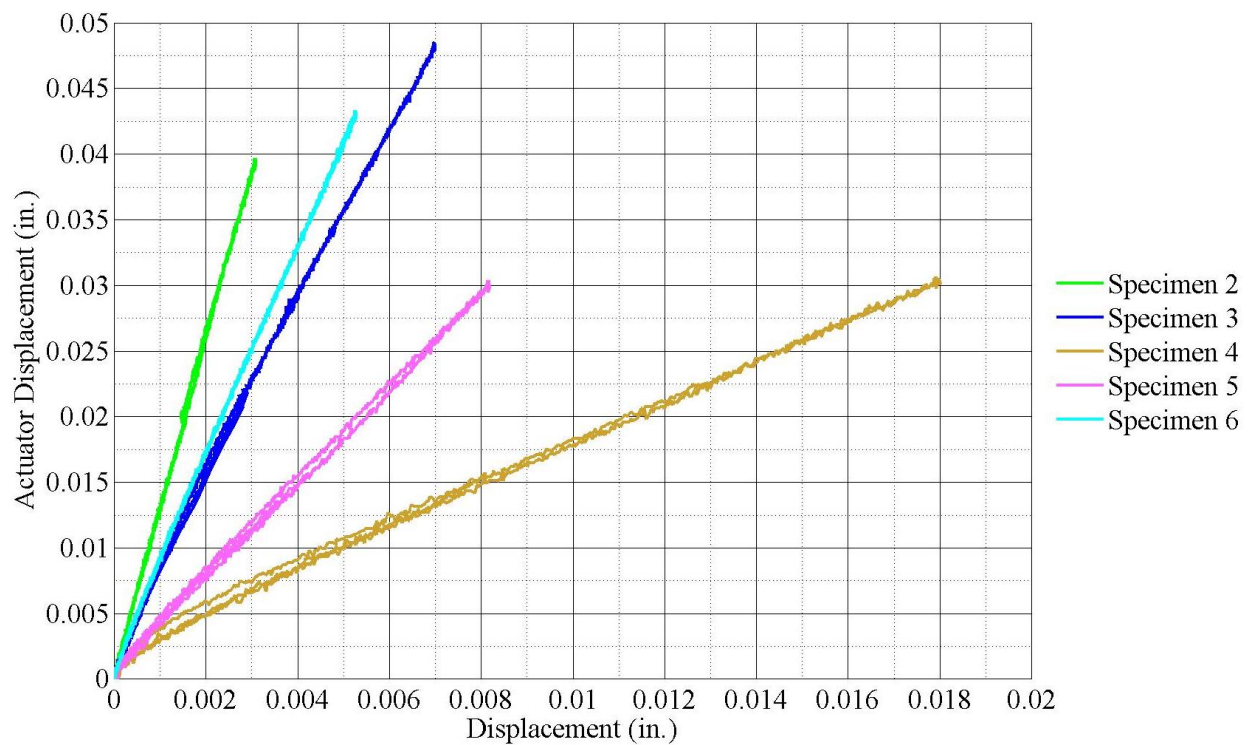
Figure 284: Comparison of maximum gap displacements in all specimens after 1 million cycles.

6.3.2. Comparison of connection strength

As discussed in earlier Sections, all specimens were subjected to a final static test to "overload" the specimens and to measure the capacity and observe the behavior past service level truck loads. The results are presented in Figure 285. The slope of the load vs. deflection curve is a good indicator of the specimen stiffness. In that regard, grouted specimens had the lowest stiffness and the spliced specimens with topping had the highest stiffness as seen in earlier results. Comparing specimens in terms of strength, it is quite obvious that the spliced connections provided the best performance. Except S5, none of the spliced specimens failed during the ultimate strength test.
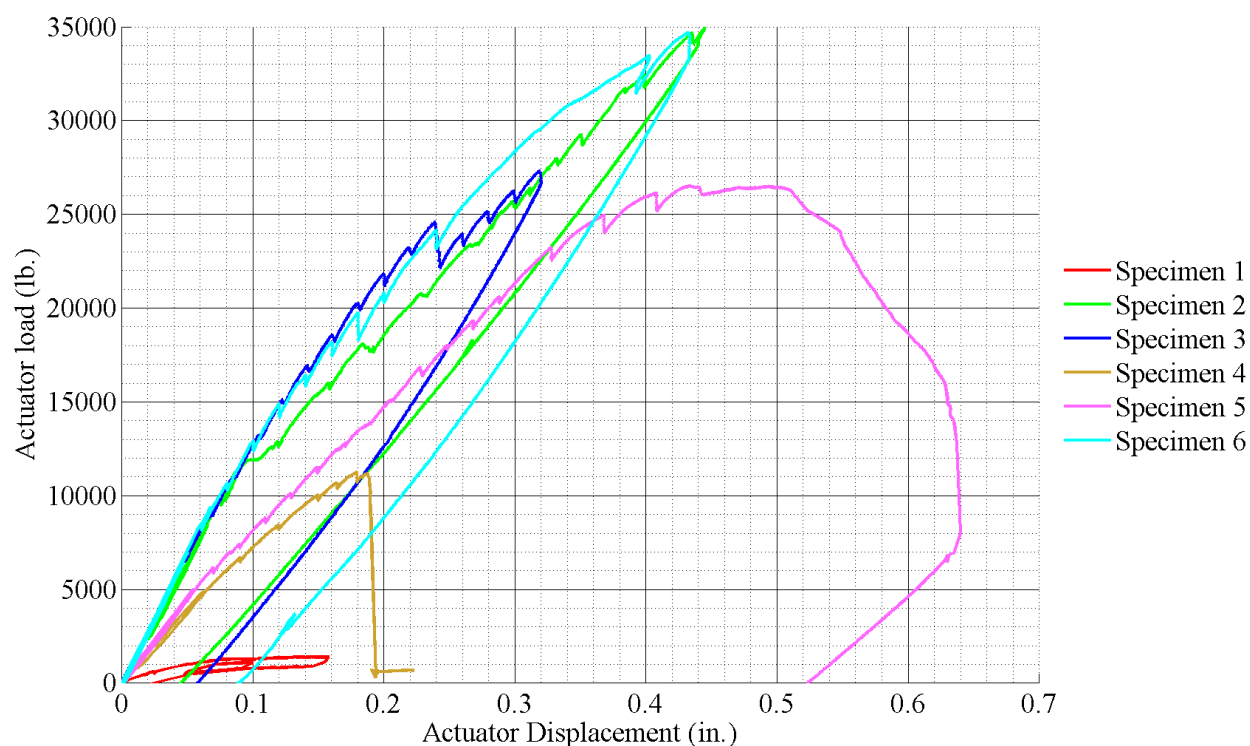
Figure 285: Comparison of load vs. deflection behavior for the ultimate strength test.

The occurrence of cracks in the joints during the ultimate strength test was compared. The variation in the gap displacements over the duration of the ultimate tests for the north and the south joints is presented in Figure 286 and Figure 287. In these plots, the joints in specimens S1, S5 were already cracked. S1 actually had failed in fatigue test prior to the ultimate strength test. Similarly, one joint each of specimens S3 and S6 was partially cracked prior to the ultimate strength test. In S4 one joint had completely cracked prior to the ultimate strength test. Only S2 cracked during the ultimate strength test.
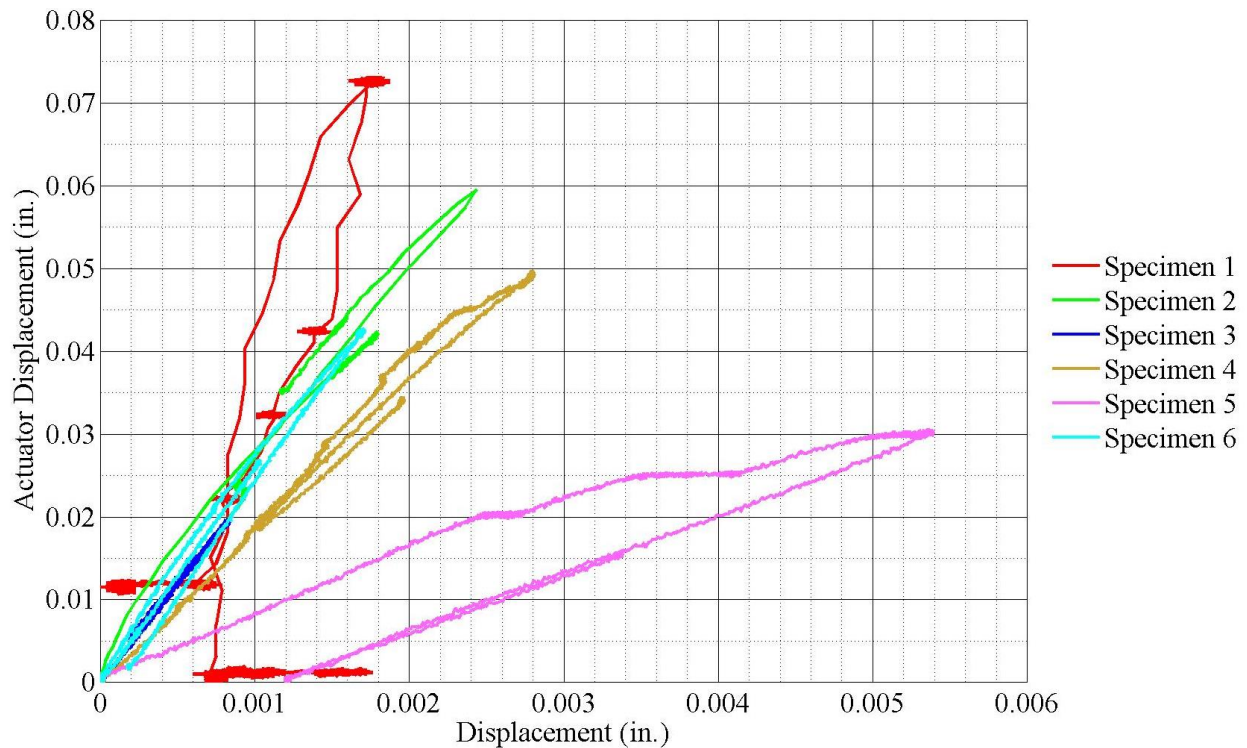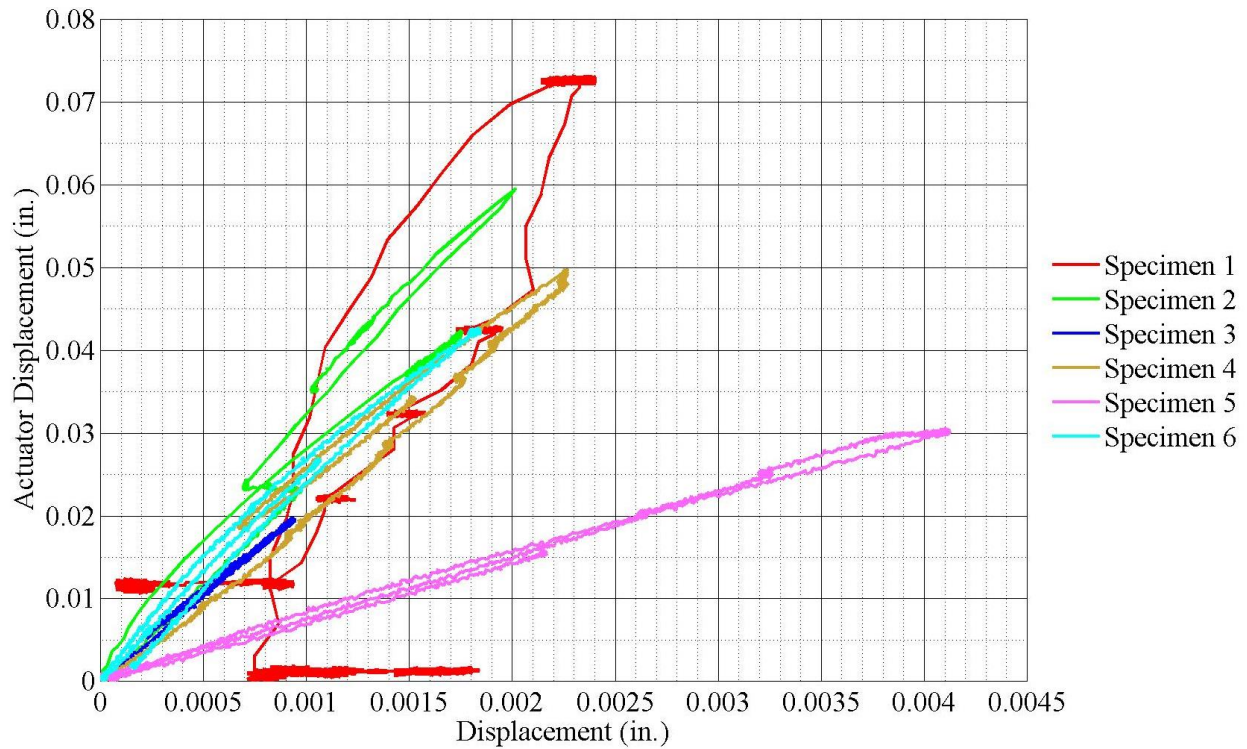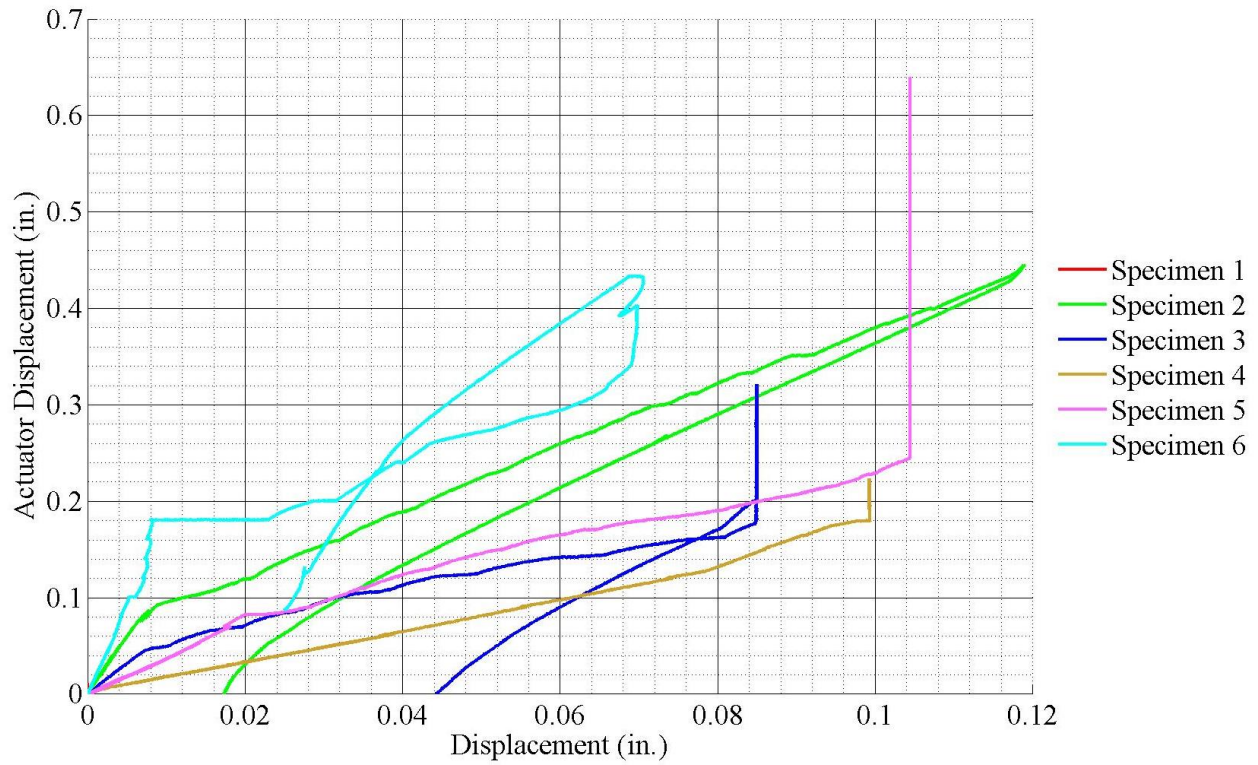
Figure 286: Comparison of north gap displacements for the ultimate strength test.
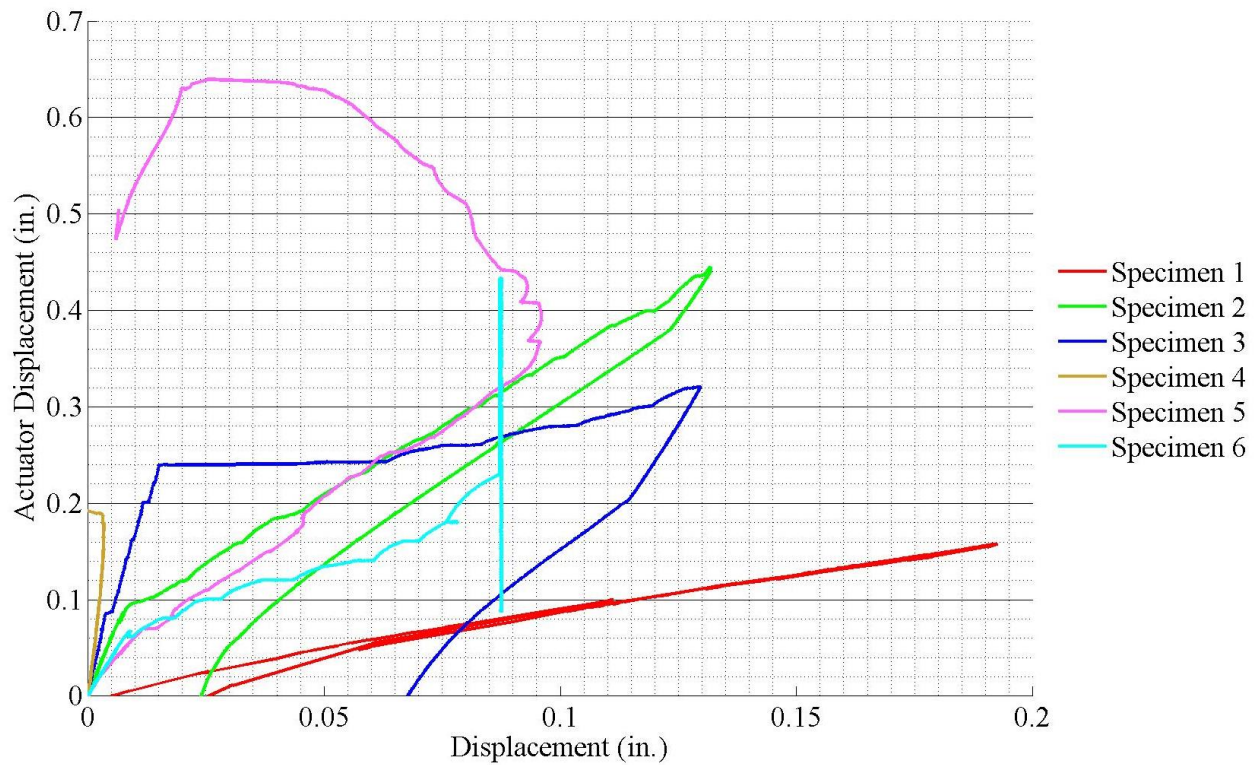
Figure 287: Comparison of south gap displacements for the ultimate strength test.

In terms of loads at cracking, S1 and S5 had the lowest loads. In the cracking loads observed during ultimate strength test, S2 had the lowest load followed by S6 and then S3. Although S2 had the highest bond strength it appears as if S3 and S6 had higher cracking load. However since S3 and S6 had cracked during fatigue testing, it can be said that S2 had the highest cracking load at about 11000 lb. The S3 and S6 loads appear higher since the crack propagation occurred on the deteriorated joint and the sound joint simply cracked at a higher overall applied load. The explanation for this is similar to what was observed in S4. The deteriorated joint has higher displacements and consequently the displacements at the sound joint become less severe.

6.4.   Summary of connection testing

The testing performed in the laboratory was to evaluate the durability of the connections when subjected to cycles of simulated truck loads. This testing was performed to establish the minimum threshold requirement for the connections in ABBB, the capacity to resist traffic loads without any significant deterioration. In regards to ABBB, significant deterioration would be the debonding failure of ABBB and a subsequent loss in load transfer as well as allowing water to leak though the joint. The other aspects that were focused on were the selection of an appropriate connection forming material, ultimate strength of these connection details and the constructability of the connections.

The specimens with the proposed connection details met the requirements of long term fatigue testing. All specimens lasted for 1 million cycles with varying levels of deterioration in the joints. The worst deterioration was seen in S4 in which one joint cracked for the full depth. However, the K&E connection performed very well in order to maintain some load transfer across the joint as well as preventing water leakage through the joint. The K&E connection was also the weakest connection among the proposed details. The K&E sheet debonded from the specimen at a load about three to four times the simulated truck load.

Specimens with top flange splice but without a concrete topping also performed very well. In terms of the main performance parameters S2, with UHPC connection, was perfect. There was no deterioration observed during fatigue testing and consequently no leakage during ponding tests. The strength of the connection could not be ascertained due to the nature of the test setup. In comparison S5 showed leakage from the very beginning of ponding tests and also the specimen failed during the ultimate load test. The leakage issue though is easily fixable with the correct super-plasticizer dosage. Moreover, the poor quality of VHPC in terms of flowability marred the results of S5. These results should have been very similar to S2.

Finally, S3 and S6 provided a stronger connection than S2 and S5. There was no leakage and the ultimate strength could not be ascertained. There was some joint deterioration observed in these tests. This joint deterioration occurred in a single joint and for S3 the cracks arrested and did not propagate after the first 10000 cycles. Whereas in S6, the first crack occurred during the application of last 100000 cycles in fatigue testing. Therefore, the progression of the cracks could not be observed. However, it is to be noted that the crack in the S6 joint did not propagate to the full depth of keyway in the first 1 million cycles. Hence, all the experimental performance parameters were met by the proposed connections.

6.5. Splice pocket spacing

Throughout this research the spliced connections were spaced at a center-to-center spacing of 2 ft. The 2 ft spacing was an initial assumption of the proposed connection detail. Moreover, the laboratory specimens were 2 ft in length, therefore the actual experimental work also was based on a 2 ft spacing. The experimental results showed that a spliced connection with a 2 ft spacing exceeded the performance parameters for the proposed details. Therefore, the spacing of splices has the potential to be increased in order to reduce the construction time and reduce material and labor costs. Spacings of 3 ft and 4 ft were investigated through FEA. A comparison was made between the results of a 2ft, 3ft and 4ft spacing.

The FSB model, as described in Section 3.3.2, was used for this analysis with one modification. The keyway between the adjacent beams was not modeled. Instead only the spliced connections were modeled. This was done to induce the worst load effects directly on the spliced connections. As observed in the testing, the splices in ABBB connections are not engaged until a crack propagates to the depth of the connection. Therefore, to simulate the worst case scenario, the keyway connection was ignored. Moreover, including the keyway connection in the model, the splices would be in compression due to the fact that a linear elastic model with a perfect bond was assumed.

The FSB model was modified by removing portions of the keyways in the horizontal and vertical directions to ensure that the only connection between the adjacent beams was equivalent to the size of the cross-section of the splice pocket. All the keyway material below the top 4 in. of the splice pocket was removed along. Also, the portion of keyway between adjacent splices was removed up to a depth of 4 in. from the top. The horizontal and vertical voids are shown in Figure 288 and Figure 289 respectively.
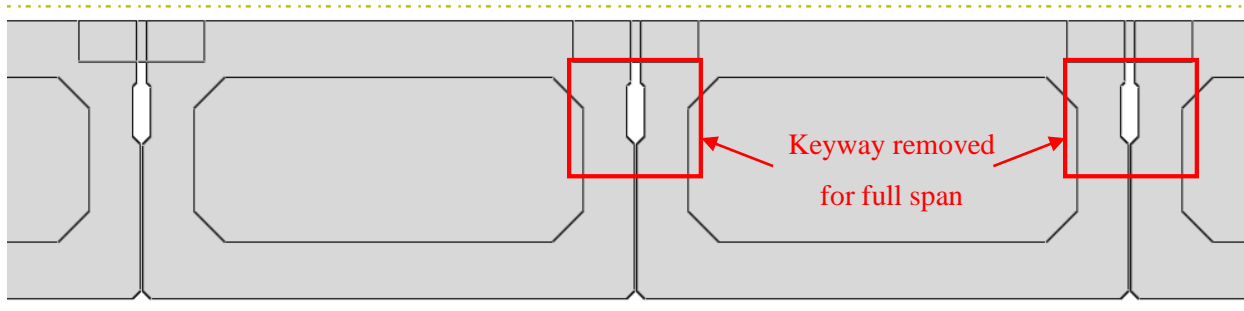
Figure 288: Horizontal voids in joints of FSB model.
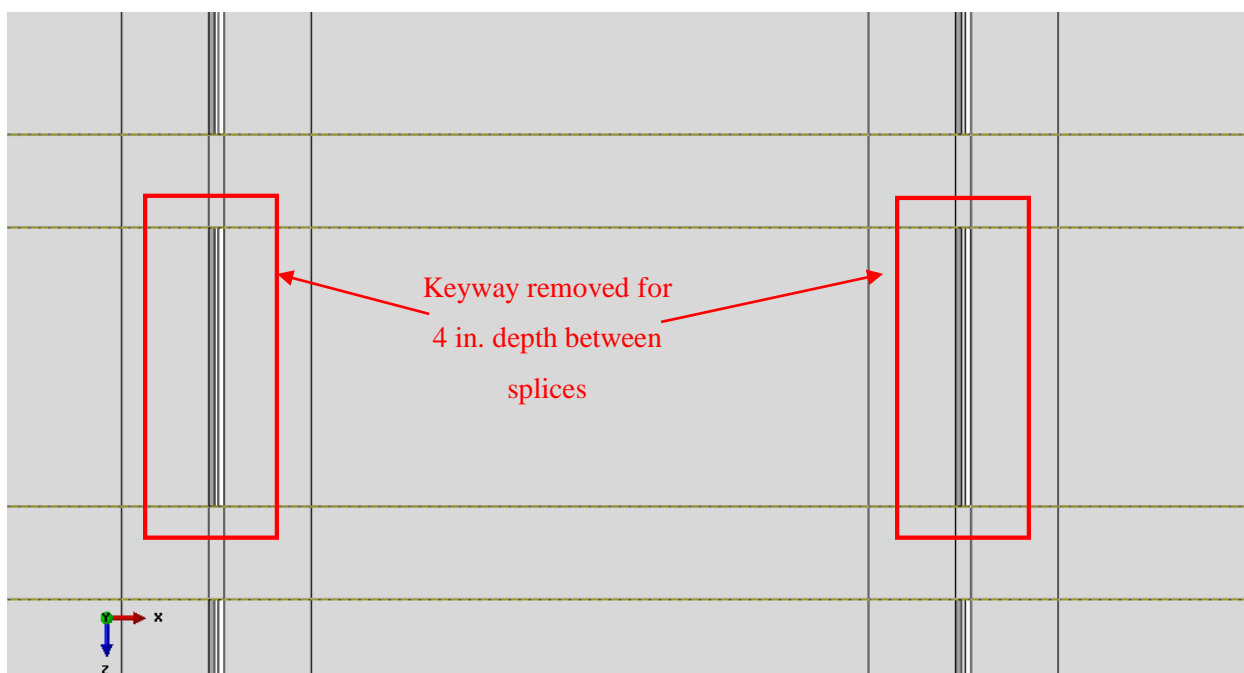
Figure 289: Vertical voids in joints of FSB model.

The truck load paths were assumed to be the same as those assumed in the initial FSB analysis. In terms of truck tire positions, two approaches were adopted. The first approach was to place the tire patch adjacent to a splice at the midspan to induce the worst shear in the connection. The second approach was to place the tire patch equidistant from two adjacent splices at the midspan. The HS-20 truck with dynamic load allowance was used in this analysis. The results are presented in Table 35. The results signify the absolute maximum stresses induced by the truck tire between the different load paths that were used for the analysis. Also, the stresses reported in Table 35 pertain to the state of stress in the splices.

Table 35: Results of splice spacing analysis.

Splice Spacing (ft)	Location of Tire Patch	Flexural Stresses (psi)		Absolute Maximum Shear Stress (psi)
		Compression	Tension	
2	Next to Splice	547	494	231.6
	Between Splices	530	476	224.7
3	Next to Splice	579	509	276.8
	Between Splices	597	519	274
4	Next to Splice	632	542	346.4
	Between Splices	601	517	354.8

The results show that worst stresses induced in the splices for any spacing were less than the cracking strength of UHPC. The cracking strength of UHPC ranges from 0.9 to 1.5 ksi as per Russell and Graybeal (2013). Therefore, potentially a spacing larger than 4 ft is possible if the loads under consideration are purely due to transient traffic loads. However, intrinsic loads such as shrinkage and external temperature effects were not explicitly considered in this analysis. Therefore, this analysis shows the potential for larger spacing between splices. The recommended spacing for these connections can be made only after all the loads are considered on the connections.

6.6. Long term behavior analysis

The ABBB system and the proposed connection details were examined for the short term effects of live loads trough experimental testing. The proposed connection details proved to be excellent in resistance to live load effects. It was not possible to study the long term effects of using experimental methods. Therefore, FEA models were used to predict the effect of shrinkage and temperature stresses on the joints and the connections. These analyses are now discussed.

6.6.1. Connection shrinkage

Shrinkage is a major contributor to the failure of shear keys in ABBB system. The evidence to this particular aspect was discussed in Chapter 2. Cracking has been observed to initiate within grouted shear keys within a few days of construction as discussed by Attanayake and Aktan (2008). Therefore, simple analyses was performed to simulate the worst shrinkage effects on the keyways and the proposed spliced connections of the ABBB system.

6.6.1.1. FEA simulation of shrinkage on spliced connections

The analysis was performed with FEA and two models were considered. The first model was the FSB model and the second model was the modified FSB model as explained in Section 6.5. These linear

elastic models with perfect bond at the interface were used to observe the state of stress at the interface between the beam and the connections. The models were not capable of predicting the age at which cracking would occur or generally, these models were incapable of predicting the occurrence of cracks. Only the state of stress induced by the simulation of shrinkage was studied. Moreover, the focus of shrinkage effects was on the interface between joints/connections and the beams.

Shrinkage cannot be directly applied to a model in ABAQUS. Therefore, the approach adopted by Sharpe (2010), introducing shrinkage strain as an autogenous, temperature induced strain. This was achieved by converting the ultimate shrinkage strain, as a worst case scenario, into an equivalent uniform decrease in temperature. The same approach was adopted by Lange et al. (2003) to model the shrinkage of composite concrete bridge decks in ABAQUS. Emulating shrinkage strain as uniform temperature change was said to be appropriate in situations where the three strain components in the 3D model were equal as per Lange et al. (2003).

The ranges of co-efficient of thermal expansion (CTE) and of ultimate shrinkage values were reported by Russell and Graybeal (2013). The range of CTE was 6.7 to 8.7 $\mu\varepsilon/^\circ$F and the ultimate shrinkage strain value for UHPC was reported to be up to 900 $\mu\varepsilon$. Therefore, for this analyses a CTE of 7 $\mu\varepsilon/^\circ$F and the ultimate shrinkage strain of 900 $\mu\varepsilon$ were assumed. This led to a uniform temperature decrease of 128.57 $^\circ$F. Another assumption in these analyses was that the beam concrete had ceased to shrink. Therefore, the uniform temperature decrease was applied exclusively to the joints and the connections. The result of this application is shown in Figure 290.

Figure 290: State of stress in joints and spliced connections due to application of ultimate shrinkage strain.

The maximum principal stress in the joint was predicted by ABAQUS as 6.134 ksi due to the differential shrinkage between beam concrete and the joints. This value is literally impossible to achieve at the interface. The only reason that such a value could be attained can be attributed to the fact that a perfect bond was assumed at the interface and a linear elastic model was used for the analysis. However, the upshot of this analysis is that shrinkage by itself can cause the joints to debond.

Another observation that was made in this analysis was that the splices were subjected to compressive stresses due to application of shrinkage. This again is the effect of assuming a perfect bond at the interface. Therefore, a second analysis was performed to observe the effect of differential shrinkage on the splices only. This analysis was performed on the modified FSB model and the result was as shown in Figure 291.
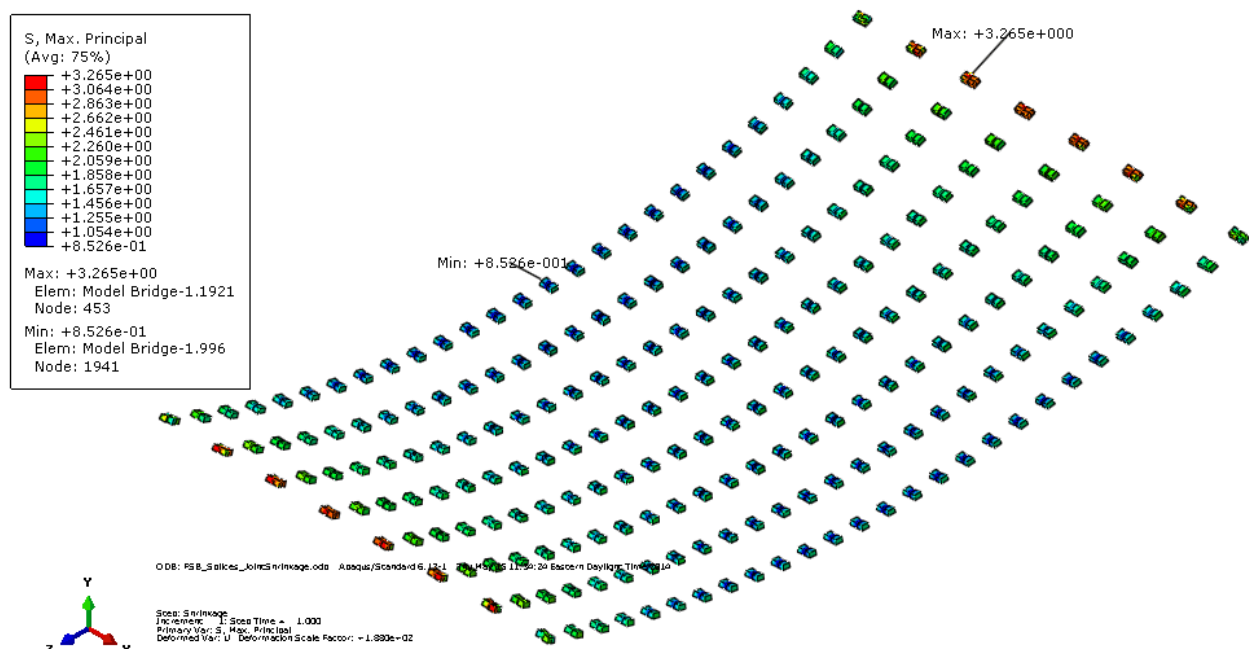
Figure 291: Maximum principal stresses in spliced connections due to application of ultimate shrinkage strain.

The results of this analysis show that the shrinkage causes a net tensile stress in all splices. Moreover, the maximum stress is predicted to occur at the interface. Hence, both the analyses show that UHPC connections can be susceptible cracking at the interface due to differential shrinkage.

The above analyses was very simplified in that the free shrinkage strain was directly applied to a connection that was definitely restrained by beam concrete. Moreover, the effect of steel reinforcement within the splices was ignored. The steel reinforcement also restrains shrinkage from within the splice. This effect can be modeled by applying a factor to free shrinkage to convert it into a restrained shrinkage. This

263

conversion is known as the Dischinger equation and it can be referred in Oesterle et al. (1989). Also, the effect of tensile creep was not considered in the above simplified analyses. The tensile stresses caused by restrained shrinkage are reduced by the occurrence of tensile creep. Tensile creep can reduce tensile stresses by about 50% as per D'Ambrosia (2011), based on an experimental and analytical research. Therefore, the magnitude of shrinkage strains can be reduced on the basis of analytical methods and experimental results.

The above discussed analytical methods were not explored in this research. Instead an argument is presented that shows that the proposed connections can be durable in the long terms regardless of occurrence of interface cracks due to shrinkage. Assuming the free shrinkage strain is applied to the keyway and the splices. The splice is 13 in. long and the free deformation in the splice due to shrinkage would be 0.0117 in. This can be assumed to be the crack width for the sake of this argument. Similarly, the thickest portion of the keyway is 1 in. in the transverse direction. Therefore, the deformation and by assumption the crack width would be 0.0009 in. For comparison, article 5.7.3.4 of AASHTO (2013), provides the specifications of reinforcement spacing to control cracking in concrete members in bridges. The commentary to this article states that a crack width of 0.017 in. is allowable for Class 1 exposure condition. Class 1 exposure condition applies to concrete members in which corrosion is not the greatest concern. By that logic, the connections in ABBB cannot be allowed to corrode and hence can be considered a part of Class 2 exposure conditions. The Class 2 exposure condition allows a maximum crack width of 75% of Class 1 exposure condition or 0.0127 in. Which is greater than the exaggerated crack width calculated for the splices. Moreover, the connections, even when used without a concrete topping would be covered by asphalt. Typically VDOT uses a water proof membrane on ABBB systems when asphalt is used as a topping. Therefore, there is potentially protection available to prevent the ingress of water where cracks could form.

This raises the issue that a similar argument can be made about using the existing grouted details. To that effect, the greatest difference between the existing connection details and the proposed connection details is the use of splices. In the event of complete loss of bond at the interface due to intrinsic or temperature loads there exists a set of discrete connections that are capable of transferring loads across the joints as well as keeping the relative displacements between adjacent box beams under control. Basically, "under control" means that the relative displacements would be smaller than those observed in current grouted detail. To verify this assertion, the relative displacements measured in the two diagnostic tests were compared with the results of the FEA of the modified FSB model. The maximum relative displacements measured from the FEA, as discussed in Section 6.5, are presented in Table 36 and the maximum relative girder displacements measured in the two diagnostic tests are presented in Table 37.

Table 36: Maximum relative displacements measured in splice spacing analysis.

Splice Spacing (ft)	Location of Tire Patch	Relative Displacement (in.)	
		Vertical	Transverse
2	Next to Splice	0.0016	0.0097
	Between Splices	0.0016	0.0094
3	Next to Splice	0.0018	0.0101
	Between Splices	0.0015	0.0093
4	Next to Splice	0.002	0.0108
	Between Splices	0.003	0.0103

Table 37: Maximum relative displacements measured in diagnostic tests.

Bridge	Maximum Relative Displacement (in.)	
	Vertical	Transverse
Karr Valley Creek	0.0017	N/A
Aden Road	0.0100	0.007

Comparing the relevant values in Table 36 and Table 37 it can be observed that the vertical relative displacements in the tested bridges was higher than the vertical relative displacements predicted by the modified FSB model. To reiterate, the modified FSB model did not include a composite concrete topping. Therefore, the displacements predicted by the model were equivalent to those measured in the Karr Valley Creek Bridge. To make a note of comparison, the KVCB had 39 in. deep beams with a concrete composite topping as opposed to the modified FSB which had 27 in. deep beams without a composite concrete topping. The Aden Road Bridge on the other hand was perfectly comparable to the modified FSB model, since the ARB was the starting point of the modified FSB model. In that regard, the relative displacements were greater by at least three times for the maximum predicted relative vertical displacement. Moreover, the modified FSB was a worst case scenario assumption of loss of bond between the joints and the beams. However, the UHPC material would still be existing in the joints and would provide additional resistance through shear friction. Similarly, the horizontal relative displacements would be attenuated by the presence of UHPC in the joints and make the model values smaller than the measured values.

6.6.1.2. FEA simulation of interface cracks

The occurrence of shrinkage cracks was determined in the previous analysis. The worst case scenario of deformation due to free shrinkage was assumed in the argument. Instead of assuming the worst

case scenario a FEA of a single splice subjected to ultimate shrinkage strain was performed to simulate the crack widths in the splice connections. The details of the single splice model are shown in Figure 292.
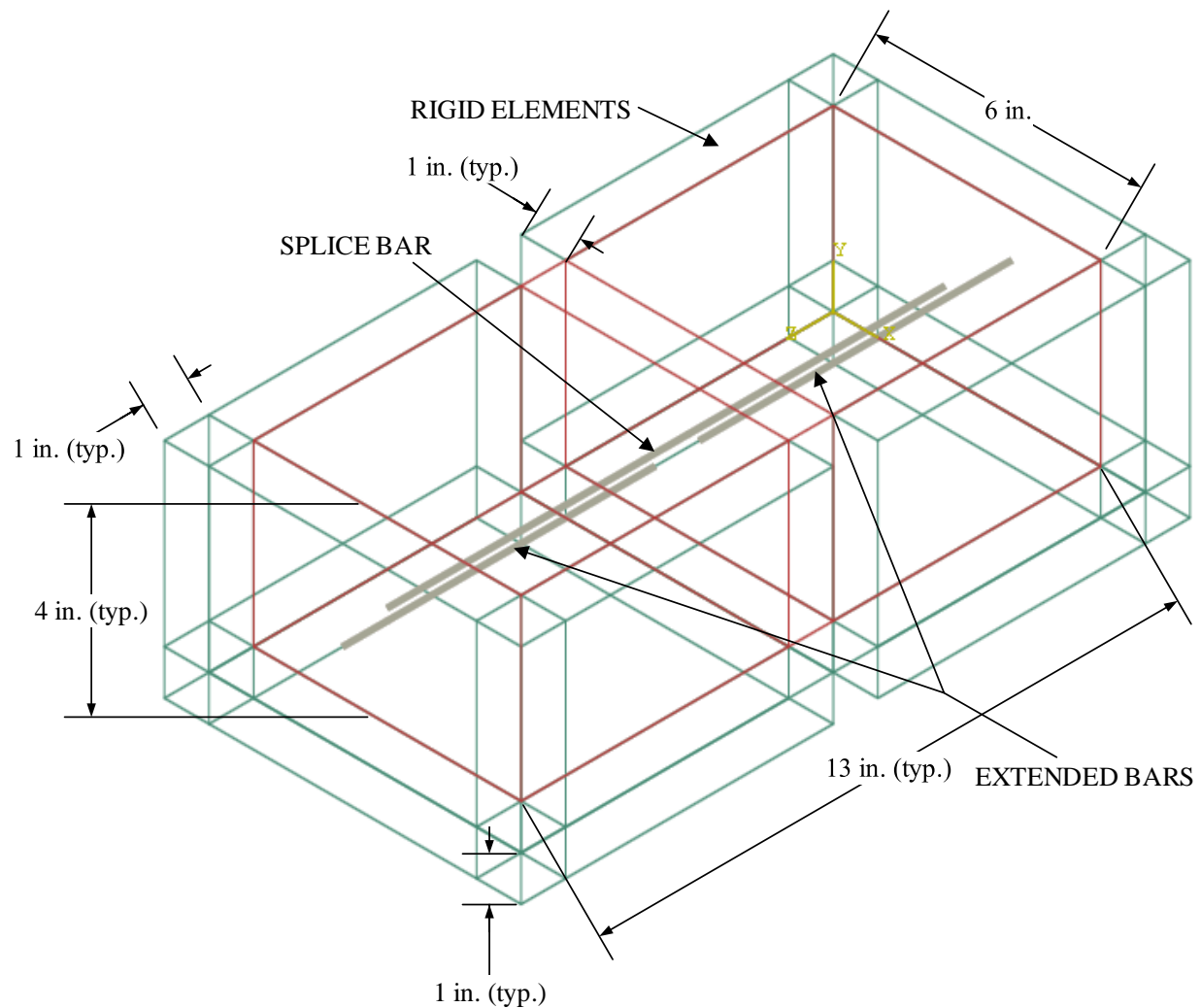
Figure 292: Details of single splice model.

The single splice was modeled with C3D8R continuum elements. The precast beams were not explicitly modeled. Instead a 1 in. thick layer of continuum elements were modeled around the splice. A gap was left in the rigid elements. The width of the gap was equal to the distance between the top of two adjacent beams in the ABBB system. Bars extending from the precast beams and the splice bar were modeled as beam elements. The extended bars were partially embedded inside the rigid elements and a length equal to the length of actual extended bars, 6 in., was embedded inside the splice. Similarly, the splice bar was completely embedded inside the splice. By embedding the beam elements inside the continuum elements a perfect bond was assumed between the steel reinforcement and UHPC. The rigid elements were all restrained from movement with all degrees of freedom restrained by pin supports. These

restraints were applied on the outside of the model. All the faces of the splice in contact with the rigid elements were connected by individual face to face tie constraints.

Shrinkage was simulated as uniform temperature decrease of 128.5714 °F and applied only to the splice as described earlier. The cracks were simulated by removing the tie constraints along the splice – rigid element interfaces. There were a total of eight interfaces constrained together. The constrained faces and their designations are shown in Figure 293. The assumed directions are also shown in Figure 293. Note that the z direction is in the plane of the paper. The maximum crack width in each direction due to the shrinkage simulation is shown in Table 38.
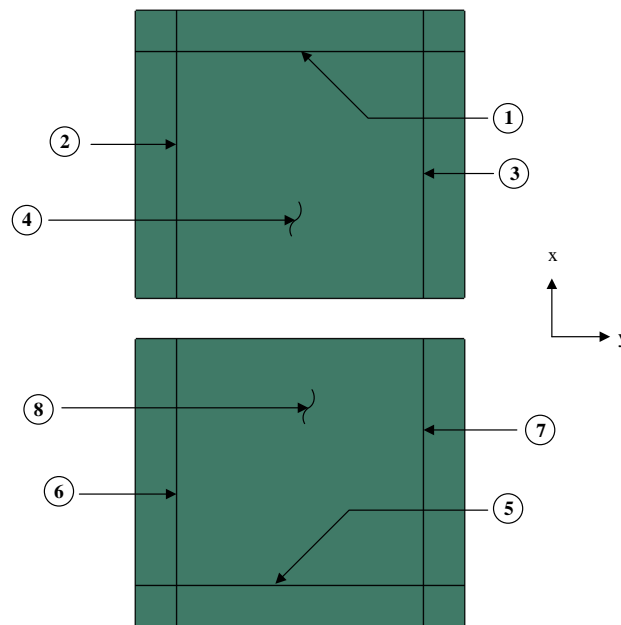
Figure 293: Numerical designation of constrained faces.

Table 38: Simulated crack widths due to shrinkage.

	Crack Widths (in.)		
Crack Location	**x**	**y**	**z**
1 and 5	0.0043	N/A	N/A
1, 2, 3 and 5, 6, 7	0.0051	0.0032	N/A
1 through 8	0.0059	0.0032	0.0023
1 only	0.0044	N/A	N/A
1 through 3	0.0058	0.0037	N/A
1 through 4	0.0036	0.0035	0.009

All crack widths calculated from the FEA simulation were less than the crack width allowed in Section 5.7.3.4 of AASHTO (2013) for exposure class 2.

6.6.2. Temperature effects

The effect of temperature on the proposed connection details also was studied with the FSB model. The temperature gradient specified in Section 3.12.3 of AASHTO (2013) was applied to the FSB. The AASHTO temperature gradient is shown in Figure 294 and the temperature values corresponding to the figure are shown in Table 39.
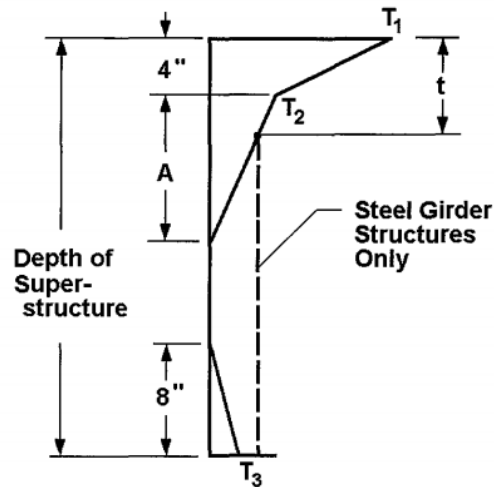
Figure 294: Temperature gradient as per AASHTO (2013).

Table 39: Temperatures as per zone for AASHTO temperature gradient.

Zone	T_1 (°F)	T_2 (°F)
1	54	14
2	46	12
3	41	11
4	38	9

As per Table 39, Virginia falls into Zone 3 and the corresponding temperatures wre adopted in the analysis. The beam concrete CTE was assumed to be 6 με/ °F on the basis of range of values presented in FHWA (2011). The CTE of UHPC connection was assumed to be 7 με/ °F as per the previous analysis. Also, from Figure 294, the magnitude of dimension "A" was 12 in. as per Section 3.12.3. The worst stress at the joint was as shown in Figure 295

268
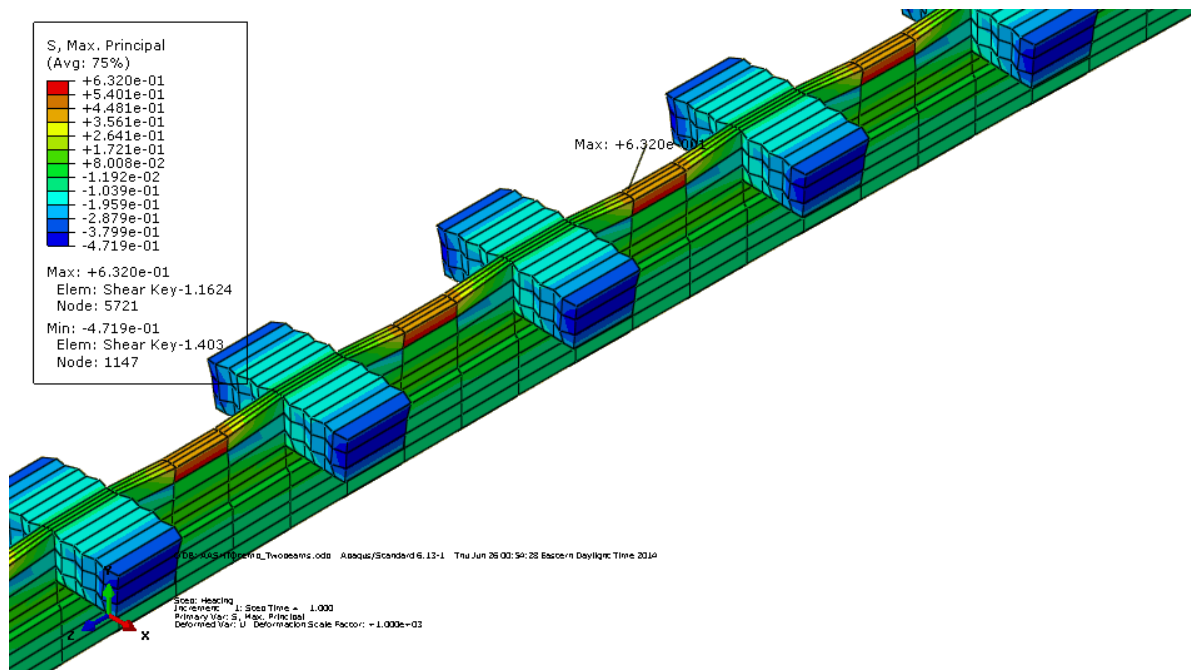
Figure 295: Effect of temperature gradient on proposed connections.

The maximum stress at the joints was 632 psi. This occurred at the joint between two adjacent splices. The magnitude of stress is obviously greater than the bond strength between the joint and the beam in direct tension. However, the worst effects are between the splices and the splices can control relative displacements as shown in Section 6.6.1.

6.7. Summary of long term analysis

The long term analysis was performed to ascertain the durability of the proposed connection details. The techniques used in the analyses were very simplified with the highest reported value of ultimate free shrinkage strain imparted on the connections and the keyway. The results of this analysis show that the state of stress induced by shrinkage is very high and it can easily cause a crack at the interface. What this analysis fails to address is the instance in time at which this crack would be initiated. The occurrence of a crack is very much possible considering the amount of shrinkage that can occur with UHPC. Therefore, working on the assumption that a crack would definitely form at the interface a solution was sought so that the proposed connection details meet the crack width requirements of AASHTO (2013). Also, by comparing the FEA results with those from field testing, it was demonstrated that the proposed details do not allow the same magnitude of relative displacement as the current shear key detail does even with the keyway debonded from the new details.

7. Conclusions and Recommendations

The objective of this research was to provide a solution to alleviate the shear key failures and reflective cracks in the ABBB system. The approach adopted was to provide new connection details and the use of fiber reinforced UHPC and VHPC as an improvement for the existing details. From the analytical and experimental work performed, the following conclusions were made.

7.1. Conclusions from literature review

From the literature that was reviewed the following conclusions from Chapter 2 are reiterated,

1. Non-shrink grout is the most commonly used shear key forming material. However, this material does not have sufficient bond strength to resist a combination of traffic, intrinsic and environmental load effects.

2. Materials, such as epoxy concrete, polymer concrete and UHPC, present a better alternative to non-shrink grout in terms of material properties and bond with concrete substrate. However, the long term behavior of these materials needs to be studied. The use of proper surface preparation techniques of concrete substrate is very important.

3. Field testing when used in conjunction with finite element modeling presents a very good tool to ascertain the behavior of ABBB system.

4. Transverse PT is widely used in the ABBB system. Transverse PT improves the joint strength, but this is usually at the location of application. The transverse PT forces dissipate to values below AASHTO LRFD requirements at locations between the discrete points of PT application. The magnitude of transverse PT is insignificant in terms of improving the transverse load sharing prior to the joint cracking. After initiation of cracking, transverse PT is able to prevent relative displacements between adjacent beams when applied in a large magnitude. There are several methods to calculate the required transverse PT force, these are dependent on the bridge spans, widths and beam depths. Another important observation is that the use of transverse PT has been insufficient to prevent shear key cracking initiation (prior to applying service level forces on the bridge).

5. The use of UHPC as a connection material for precast elements is becoming prevalent in the accelerated bridge construction practice. The ABBB system can benefit from the use of UHPC as the connection forming material.

6. Most of the joints studied in literature were dependent on bond between the beams and connection forming material. The use of a structural connection with the use of UHPC has not been investigated for the ABBB system.

7.2. Conclusions from diagnostic tests

Diagnostic tests were performed on two bridges, KVCB in NY and ARB in VA, to observe the in-service behavior of the ABBB system. The bridges were subjected to trucks with known loads to induce a response from the bridge and to study it. Both bridges were instrumented extensively. The following conclusions were made from the diagnostic tests.

1. Presence of shear key cracks disrupted the transverse load distribution of ABBB. However, shear key failure did not lead to complete loss of load transfer. This was attributed to the fact that grout remained in the keyway and allowed some load transfer through shear friction and mechanical interlock.

2. Concrete topping improved the bridge performance in terms of load distribution after shear key failure and also durability. The KVCB had higher traffic volume and a longer span than ARB, yet the deterioration in KVCB joints was lesser than that in ARB. Moreover, the KVCB was exposed to higher quantities of deicing salts than ARB since the KVCB was located in a colder region than ARB.

3. Girder distribution factors (GDFs) calculated from the diagnostic test measurements show that the actual load distribution per girder can be unconservative when compared to design values. Moreover, for an ABBB with deteriorated joints the disruption of load distribution causes higher forces on the beams while, potentially, the capacity is decreasing due to deterioration.

4. Concrete barriers can be detrimental to the ABBB system. The barriers provide additional stiffness to the fascia beams, which is not assumed in design. The added stiffness attracts higher forces and moments towards the fascia beams. The fascia beams can resist these forces, however the joints are susceptible to fail.

5. Beams in ABBB system rotate along the longitudinal axis. This produces additional stresses at the base of the joint, thereby exacerbating the joint deterioration.

6. The gaps between adjacent beams open when truck loads are over the joint or in close proximity under consideration. The gaps not in the loaded path tend to compress and close.

7.3. Conclusions from Finite Element Analysis

Finite element analysis played a very important role in this research. Finite element analysis was used to develop a model and compare its behavior with a bridge that was tested in the field. Finite element analysis also was used to simulate the behavior of bridge and the connection sub-assemblages. The Finite element analysis showed that,

1. For load transfer, the shear key in ABBB needs to transfer some tensile stresses through the keyway in the vicinity of the truck loads. Typically, the highest tensile stress was found at the base of the joint.
2. The highest stresses in the joints were found to be at the location closest to the rear (heavier) tires of the simulated truck loads. This indicated that the truck loads caused a local increment in joint stresses.
3. The knowledge of actual material properties and boundary conditions is important to accurately model the actual measured response of the bridge.

7.4. Conclusions from splice tests

The tests on inverted simply supported specimens was performed to ascertain the performance of UHPC and VHPC as connection forming materials to facilitate the use of short splice lengths in longitudinal joints between adjacent beams of ABBB. The experimental results were then verified with a strain-compatibility analysis. From the test results, the following conclusions were made,

1. Splice lengths with No. 4 bars of 4 in. and longer were sufficient to yield the tension reinforcement prior to failure. However, a splice of 4 in. length is very short and variability in length fabrication, such as cutting the bar to a smaller length than 4 in. could cause a bond failure in the connection. Moreover, considering the variability in the properties of concrete, a safety factor for the short splice lengths is desirable. Therefore, a minimum 5 in. splice is recommended for No. 4 bars.
2. Splice lengths with No. 6 bars of 5 in. and longer were sufficient to yield the tension reinforcement prior to failure. However, for the reasons stated above, a 6 in. splice is recommended. This splice length for No. 6 bars is applicable when used with UHPC. The use of No. 6 bars with VHPC was not investigated.
3. Strain compatibility analysis provided a logical method to verify the strains and stresses in the tensile steel in the splice test beams.

4. The difference in the performance of UHPC and VHPC as a means to develop a short splice was almost negligible. Both materials provided the same results for No. 4 bars.

5. No. 6 bars have the potential to cause additional stresses in the connection due to prying action. The use of transverse reinforcement may be advisable when using No. 6 bars with short splices.

7.5. Conclusions from sub-assemblage tests

Two new connection details were proposed as part of this research. The structural performance of the proposed connection details was assessed through laboratory testing. A total of six sub-assemblage specimens were tested with five specimens incorporating the proposed details and the use of UHPC and VHPC as a connection filler material. The proposed connections were subjected to fatigue for a million cycles and then to a static overload. These loading protocols established two basic test criteria, durability and strength of the proposed connections. Ponding tests were also performed to observe any leakage at the joints. From the testing program the following observations were made,

1. The existing detail, the partial depth grouted shear key, is the weakest connection for the ABBB system. Although this has been established through several examples of joint failures in bridges, the test on the specimen with the existing detail reinforced this conclusion.

2. The Kevlar and Epoxy (K&E) connection provided an upgrade over the existing connection detail. K&E connection is incapable of preventing shear key failures. However, the K&E connection provides resistance against further deterioration by bridging the crack and providing a post full depth crack capacity. The K&E connection successfully resisted fatigue for almost 1 million cycles without any signs of deterioration. The K&E connection also provides a very good protection against water leakage through joints. Finally, surface preparation is extremely important for the successful application of the K&E connection. Shot-blasting or sand-blasting are the ideal surface preparation techniques for the K&E connection. Poor surface preparation can make the K&E connection weak.

3. Spliced connections when used with a 2 ft center to center spacing provide sufficient resistance to fatigue and overloads.

4. The spliced connection in the top flanges of ABBB beam with UHPC provided the best resistance to the applied loads, fatigue as well as overload. The joints in this specimen did not leak throughout the test.

5. The spliced connections with VHPC also provided a very good performance. Although S5 joint was not well consolidated and it leaked due to the voids in the VHPC, it was able to last for the full fatigue cycles. S5 failed in the ultimate strength test. The cracks propagated from the base

of the splice diagonally under the reinforcing steel and the splice bars. This also could be attributed to the weak VHPC mix in the joint.

6. The spliced connections when used with a concrete topping provided an enhanced performance over the specimens without topping. The specimens with topping were stiffer and most probably were stronger than the specimens without topping. Which leads to the conclusion that the use of concrete topping on ABBB would present a stronger and more durable bridge.

7. In terms of head-to-head performance in the experimental testing, there was no difference in the performance of UHPC and VHPC. This conclusion is based on specimens S3 and S6 only.

8. For most part, the assumption of adhesive failure at the joints holds true for the ABBB system. All specimens, except S2, had some level of debonding in the joints. However, the spliced connections are advantageous in this situation as the free propagation of the cracks is halted by the shape of the splice pocket and the presence steel reinforcement.

7.6. Conclusions from long term analysis of proposed connections

A simplified analysis was performed to study the outcome of long term load effects on the proposed connections. The effects of restrained shrinkage and AASHTO temperature gradients on the joints and connections were studied. Shrinkage was studied by applying the ultimate free shrinkage strain as an equivalent drop in temperature. Based on these analyses the following conclusions were made,

1. Restrained shrinkage produces the worst load effects in ABBB joints. The magnitude of stresses observed in the model leave no doubt that a crack would be initiated at the interface of the beam and the joint/connection.

2. Temperature stresses caused by the AASHTO positive temperature gradient can cause the joint to crack.

3. Although a crack may seem unavoidable, the exaggerated crack width calculated in the simplified analysis was within the maximum acceptable width for a Class 2 exposure condition as per AASHTO. Therefore, providing a layer of protection such as water-proofing membrane for an asphalt topping or a concrete topping will ensure a more durable joint.

4. Providing a concrete topping on an ABBB will attenuate the magnitude of temperature stresses by imposing the worst temperature effects on the topping instead of the connections at the top of the bridge beams.

7.7. Recommendations

On the basis of conclusions made in this research, the following recommendations are made,

1. The use of spliced connections is recommended for the ABBB system. The recommended center to center spacing is 2 ft.

2. The use of UHPC is recommended for ABBB system. There is significant experience in using UHPC as a connection material for precast elements. UHPC also is easy to work with. The basic steps in mixing UHPC are not too dissimilar from mixing grout. Also, the material properties of UHPC and its durability are well researched. The only deterrent to the use of UHPC is the cost of the material.

3. VHPC has proven to be a very good alternative to UHPC in terms of the performance observed in this testing program. However, the testing on the VHPC mix used in this testing is not complete. The long term durability of VHPC such as resistance to freeze thaw cycles etc. has not yet been studied. Therefore, until such a study is completed, VHPC represents a potential mix for use in ABBB joints.

4. K&E connections are ideal for use with existing bridges. In the cases where shear key failure has already initiated the K&E connection will prevent the ingress of water and deicing salts into the joints.

5. The use of transverse post-tensioning does not prevent shear key cracks in the ABBB system. Therefore, the use of a non-PT option is recommended for this bridge system.

6. The use of self-consolidating materials, UHPC and VHPC, as connection materials has been researched here. Prior to using these materials, a thorough inspection of the joints and any formworks is recommended. Since, these materials can leak through gaps. This problem is more prevalent for UHPC as it tends to stay plastic for more than 12 hours and there is no aggregate to prevent or impede the leak.

7.8. Future work

As mentioned in the introductory chapter of this dissertation, there is a new found interest in improving the connections and overall the ABBB system. Although this research has looked at comprehensive ways to deal with the reflective cracking issue, it was not possible to pursue every idea. Therefore, the following topics may be looked at for future research in ABBB,

1. The spliced connections tested in this research were never tested to the ultimate capacity. Therefore, only the ultimate capacity testing of the spliced connections should be explored.

Although it was seen in this research that the connections had a much higher capacity than service loads, the possible failure modes in these connections could not be verified.

2. The effect of skew on the connections was not studied in this research. The nature of forces induced on the connections will change on the basis of alignment of the spliced connections.

3. The durability of VHPC as a material needs to be studied before practical application as a connection material.

4. The finite element analysis performed in this research was all linear elastic. To study the effect creep and shrinkage over the long term a more stringent analysis is recommended. The use of non-linear FEA to predict the occurrence and propagation of cracks in the interface of the proposed connections is a worthwhile venture.

5. The use of alternate keyway shapes or even the use of alternate pocket shapes can be explored. Preferably, a pocket shape that also provides a mechanical interlock is encouraged.

References

AASHTO (2013). AASHTO LRFD Bridge Design Specifications, Customary U.S. Units (6th Edition) with 2012 and 2013 Interim Revisions; and 2012 Errata, American Association of State Highway and Transportation Officials (AASHTO).

ABAQUS (2013). ABAQUS 6.13 Documentation. Providence, RI, Dassault Systemes.

ACI (2003). Committee 408R-03: Bond and Development of Straight Reinforcing Bars in Tension (Reapproved 2012). Farmington Hills, MI, ACI.

ACI (2008). Committee 318-08: Building code requirements for structural concrete and commentary. Farmington Hills, MI, American Concrete Institute.

Annamalai, G. and R. C. Brown Jr (1990). "Shear-transfer behavior of post-tensioned grouted shear-key connections in precast concrete-framed structures." *ACI Structural Journal* 87(1): 53-59.

ASTM Standard C157/C157M - 08 (2008), "Test Method for Length Change of Hardened Hydraulic-Cement Mortar and Concrete" *ASTM International*, West Conshohocken, PA, DOI: 10.1520/C0157_C0157M-08, www.astm.org

ASTM Standard C39 (2009), "Test Method for Compressive Strength of Cylindrical Concrete Specimens" *ASTM International*, West Conshohocken, PA, DOI: 10.1520/c0039_c0039m-09a, www.astm.org

ASTM C490/C490M - 11 e1 (2011), "Standard Practice for Use of Apparatus for the Determination of Length Change of Hardened Cement Paste, Mortar, and Concrete" *ASTM International*, West Conshohocken, PA, DOI: 10.1520/C0490_C0490M-11E01, www.astm.org

ASTM Standard C496/C496M (2011), "Test Method for Splitting Tensile Strength of Cylindrical Concrete Specimens" *ASTM International*, West Conshohocken, PA, DOI: 10.1520/c0496_c0496m-11, www.astm.org

ASTM Standard C109/C109M (2013), "Test Method for Compressive Strength of Hydraulic Cement Mortars (Using 2-in. or [50-mm] Cube Specimens)" *ASTM International*, West Conshohocken, PA, DOI: 10.1520/c0109_c0109m-13, www.astm.org

Attanayake, U. and H. M. Aktan (2008). Issues with Reflective Deck Cracks in Side-by-Side Box Beam Bridges. *NCBC Concrete Bridge Conference, Proceedings*, St. Louis, Mo.

Azizinamini, A. (1998). "Behavior of tension splices for reinforcing bars embedded in high-strength concrete." *Transportation Research Record*(1624): 125-131.

Chun, S. C. and J. G. Lee (2013). Anchorage strengths of lap splices anchored by high-strength headed bars. *8th International Conference on Fracture Mechanics of Concrete and Concrete Structures, FraMCoS 2013, March 11, 2013 - March 14, 2013*, Toledo, Spain, International Center for Numerical Methods in Engineering.

Collins, W. N. (2010). Live load testing and analysis of the southbound span of u.s. route 15 over interstate-66. *Masters Thesis*, Virginia Tech.

Cook, R. D., D. S. Malkus, M. E. Plesha and R. J. Witt (2001). Concepts and Applications of Finite Element Analysis, John Wiley & Sons.

D'Ambrosia, M. D. (2011). Early age creep and shrinkage of emerging concrete materials. *Doctoral Dissertation*, University of Illinois at Urbana-Champaign.

Dong, H., Y. Li and T. M. Ahlborn (2007). Performance of joint connectionsbetween decked prestressed concrete bridge girders. *PCI National Bridge Conference*, Phoenix, AZ.

El-Esnawi, H. H. (1996). Evaluation of improved shear key design for multi-beam prestressed concrete box girder bridges. *Ph.D. Dissertation*, Case Western Reserve University.

El-Remaily, A., M. K. Tadros, T. Yamane and G. Krause (1996). "Transverse design of adjacent precast prestressed concrete box girder bridges." *PCI Journal* 41(Compendex): 96-113.

Esfahani, M. R. and B. V. Rangan (1998). "Bond between normal strength and high-strength concrete (HSC) and reinforcing bars in splices in beams." *ACI Structural Journal* 95(3): 272-279.

FHWA. (2011). "Thermal Coefficient of Portland Cement Concrete." *Portland Cement Concrete Pavements Research* Retrieved 9/5, 2013, from http://www.fhwa.dot.gov/publications/research/infrastructure/pavements/pccp/thermal.cfm.

Flanagan, D. P. and T. Belytschko (1981). "UNIFORM STRAIN HEXAHEDRON AND QUADRILATERAL WITH ORTHOGONAL HOURGLASS CONTROL." *International Journal for Numerical Methods in Engineering* 17(5): 679-706.

Fu, C. C., Z. Pan and M. S. Ahmed (2011). "Transverse posttensioning design of adjacent precast solid multibeam bridges." *Journal of Performance of Constructed Facilities* 25(3): 223-230.

Fu, C. C., Z. Pan, M. S. Ahmed and S. K. Jeong (2009). Behavior and Analysis of an Instrumented MD335 over Wallace Creek Slab Bridge Impact of the Transverse Post-tensioning Force Required to Tie Precast, Prestressed Concrete Slab Beams as a Single Unit Slab Bridge, Maryland State Highway Administration and Federal Highway Administration.

Grace, N. F., E. A. Jensen, T. Enomoto, V. A. Matsagar, E. M. Soliman and J. Q. Hanson (2010). "Transverse diaphragms and unbonded CFRP posttensioning in box-beam bridges." *PCI Journal* 55(2): 109-122.

Graybeal, B. A. (2006). Material Property Characterization of Ultra-High Performance Concrete. United States**:** 190p.

Graybeal, B. A. (2010). Behavior of field-cast ultra-high performance concrete bridge deck connections under cyclic and static structural loading.

Graybeal, B. A. (2012). Ultra-High Performance Concrete Composite Connections for Precast Concrete Bridge Decks. United States**:** 110p.

Gulyas, R. J., G. J. Wirthlin and J. T. Champa (1995). "Evaluation of keyway grout test methods for precast concrete bridges." *PCI Journal* 40(1): 44-57.

Halbe, K., C. Field, T. E. Cousins and C. L. Roberts-Wollmann (2014). Splice lengths for no. 4 and no. 6 bars in UHPC and VHPC. Charlottesville, VA, Virginia Center for Transportation Innovation and Research.

Hanna, K., G. Morcous and M. K. Tadros (2011). "Adjacent box girders without internal diaphragms or post-tensioned joints." *PCI journal* 56(4): 51-64.

Hansen, J., K. Hanna and M. K. Tadros (2012). "Simplified transverse post-tensioning construction and maintenance of adjacent box girders." *PCI Journal* 57(2): 64-79.

Hodson, D., P. Barr and M. Halling (2012). "Live-Load Analysis of Posttensioned Box-Girder Bridges." *Journal of Bridge Engineering* 17(4): 644-651.

Hosny, A., H. M. Seliem, S. H. Rizkalla and P. Zia (2012). "Development length of unconfined conventional and high-strength steel reinforcing bars." *ACI Structural Journal* 109(5): 655-664.

Huckelbridge Jr, A. A., H. El-Esnawi and F. Moses (1995). "Shear key performance in multibeam box girder bridges." *Journal of Performance of Constructed Facilities* 9(Compendex): 271-285.

Idriss, R. and Z. Liang (2010). "In-Service Shear and Moment Girder Distribution Factors in Simple-Span Prestressed Concrete Girder Bridge." *Transportation Research Record: Journal of the Transportation Research Board* 2172(-1): 142-150.

Issa, M. A., C. L. Ribero do Valle, S. Islam, H. A. Abdalla and M. A. Issa (2003). "Performance of transverse joint grout materials in full-depth precast concrete bridge deck systems." *PCI Journal* 48(4): 92-103.

Kasan, J. and K. Harries (2013). "Analysis of Eccentrically Loaded Adjacent Box Girders." *Journal of Bridge Engineering* 18(1): 15-25.

Koutromanos, I. M. (2014). "Finite Element Analysis Notes." Retrieved 8/1/2014, from http://www.researchgate.net/publication/264310128_Finite_Element_Analysis_Notes.

Lall, J., S. Alampalli and E. F. DiCocco (1998). "Performance of full-depth shear keys in adjacent prestressed box beam bridges." *PCI Journal* 43(Compendex): 72-79.

Lange, D. A., J. R. Roesler, M. D. D'Ambrosia, Z. C. Grasley, D. R. Cowen and C. J. Lee (2003). High Performance Concrete for Transportation Structures. Illinois Cooperative Highway and Transportation Series No. 287. Transportation Engineering Series No. 126.

Lubbers, A. R. (2003). Bond Performance Between Ultra-High Performance Concrete and Prestressing Strands. *MS Thesis*, Ohio University.

Marcu, S., G. Greene and B. A. Graybeal (2012). Performance of deck-level connections between precast concrete components – concept and early results. *PCI National Bridge Conference*, Nashville, TN.

Miller, R. A., G. Hlavacs, T. Long and A. Greuel (1999). "Full-scale testing of shear keys for adjacent box girder bridges." *PCI Journal* 44(6): 80-90.

Morcous, G., M. Maguire and M. K. Tadros (2011). "Welded-wire reinforcement versus random steel fibers in precast, prestressed concrete bridge girders." *PCI Journal* 56(2): 113-120.

Oesterle, R. G., J. D. Glikin and S. C. Larson (1989). Design of Precast Prestressed Bridge Girders Made Continuous. United States**:** 106p.

Perry, V., D. Dykstra, P. Murray and B. Rajlic (2010). Innovative field cast UHPC joints for precast bridge systems- 3-span live load continuous. *2010 Annual Conference of the Transportation Association of Canada: Adjusting to New Realities, TAC/ATC 2010, September 26, 2010 - September 29, 2010*, Halifax, NS, Canada, Transportation Association of Canada (TAC).

Perry, V., R. Krisciunas and B. Stofko (2012). Mackenzie river twin bridges – the largest field-cast uhpc connections project in north america. PCI National Bridge Conference. Nashville, TN.

Perry, V. and G. Weiss (2009). Innovative Field Cast UHPC Joints for Precast Bridge Decks–Design, Prototype Testing and Projects. *Proceedings of the International Workshop on Ultra High Performance Fibre Reinforced Concrete—Designing and Building with UHPFRC: State of the Art Development*.

Rajlic, B., P. Murray, D. Dykstra and R. Krisciunas (2010). The Eagle River Bridge Superstructure Replacement. *Proceedings of the 8th International Conference on Short and Medium Span Bridges*.

Russell, H. G. (2009). Adjacent Precast Concrete Box Beam Bridges: Connection Details. A Synthesis of Highway Practice. United States**:** 86p.

Russell, H. G. and B. A. Graybeal (2013). Ultra-High Performance Concrete: A State-of-the-Art Report for the Bridge Community. United States**:** 176p.

Sang, Z. (2010). A Numerical Analysis of the Shear Key Cracking Problem in Adjacent Box Beam Bridges. *MS Thesis*, The Pennsylvania State University.

Sharpe, G. P. (2010). Reflective cracking of shear keys in multi-beam bridges. *Masters Thesis*, Texas A&M University.

VDOT (2007). Road and Bridge Specifications. Richmond.

VDOT (2008). Manual of Structure and Bridge Division. 5.

VDOT (2013). Instructional and Informational Memorandum (IIM-S&B-80.4).

Wallenfelsz, J. A., C. Lijeron and C. L. Roberts-Wollmann (2007). Recommendations for the Connection Between Full-Depth Precast Bridge Deck Panel Systems and Precast I-Beams. United States**:** 80p.

Yamane, T., M. K. Tadros and P. Arumugasamy (1994). "Short to Medium Span Precast Prestressed Concrete Bridges in Japan." *PCI Journal* 39(2): 74 - 100.

Appendix A

Fortec 5680-BD Kevlar®

Kevlar® fiber bi-directional fabric for crack repair, water-proofing and structural reinforcement

FORTEC STABILIZATION

Product Description Fortec 5680-BD Kevlar® is a bi-directional fabric system comprised of highly durable 5,680 denier Kevlar® yarns, producing a superior and dense weave. The system is designed for heavy duty crack repair, crack control, and structural strengthening of concrete and masonry structures where durability, impact resistance and protection of water intrusion is needed. The system of Fortec 5680-BD Kevlar® textile used with Fortec Lo-Mod 526 Flexible epoxy resin is the best alliance of strength and bonding that seals out moisture, transfers loads and allows temperature and stress related movements to occur without brittleness.

PRODUCT USE

Target Applications
- ❖ Transverse cracks in bridge decks
- ❖ Post-tensioned segmental bridge joints
- ❖ Longitudinal cracks and joints
- ❖ Rigid pavement joint and dowel protection
- ❖ Cast-in-place water storage structures
- ❖ Cyclical loading applications
- ❖ Where crack control with water protection is needed

Repair Applications
- ❖ Collision and impacts
- ❖ Excessive movement
- ❖ Elastomeric joint failures
- ❖ Age
- ❖ Overuse

Key Features
- ❖ 0° and 90°, equal bi-directional strength
- ❖ High bond strength
- ❖ Conforms to irregular surfaces
- ❖ Easy gun-applied epoxy resins
- ❖ Strongest duty Kevlar® system available
- ❖ Excellent crack control

Benefits
- ❖ Protection from corrosion
- ❖ Increased strength
- ❖ Water and chloride prevention
- ❖ Ride quality
- ❖ Long term repairs
- ❖ Increased service life

SPECIFICATIONS

Typical Data

Base Material	5,680 denier Kevlar® yarns woven into a dense, bidirectional weave
Storage	Product shall be kept from direct sunlight
Shelf Life	Unlimited
Color	Yellow
Filament Tensile Strength, ksi (MPa)	522 (3,600)
Filament Tensile Modulus, ksi (MPa)	17,985 (124,000)
Fabric Nominal Width, in (mm)	8 (200)
Fabric Nominal Thickness, in (mm)	0.040 (1.0)
Primary Fiber Direction	0° and 90°, bidirectional plain weave
Fabric Weight, oz/yd² (g/m²)	26.6 (900)

Mechanical and Physical Properties

0° / 90°	Ultimate Tensile Strength[1] f_{fu}^* ksi (MPa)	Modulus of Elasticity[1] E_f ksi (GPa)	Ultimate Tensile Strength per Unit Width p_{fu}^* kips/in (kN/mm)	Tensile Elastic Modulus per Unit Width $E_f t_f$ kips/in (kN/mm)	Ultimate Strain at Rupture ε_{fu}^* in/in (mm/mm)
Average Values	100 (0.69)	3,450 (23.8)	4.0 (0.69)	138 (23.8)	0.029 (0.029)
Design Values	60 (0.41)	2,070 (14.3)	2.4 (0.41)	82.8 (14.3)	0.029 (0.029)

[1] ASTM D3039

281

Appendix B

EPOXY MULTI-LAYER RAPID SET
SKID RESISTANT / HI-FRICTION POLYMER OVERLAY
FOR BRIDGE AND PARKING DECKS

526

FORMULATED AND LABELED FOR PROFESSIONAL USE ONLY
NOT FOR SALE TO OR USE BY THE GENERAL PUBLIC

PRODUCT DATA   **PRODUCT DATA**   **PRODUCT DATA**   **PRODUCT DATA**

Formulated to comply with the Rapid Strength development and minimum closure requirements as established by AASHTO Task Force 34 Epoxy Polymer Concrete Bridge Deck Overlays and ACI 548 Type EM (Epoxy Multi-Layer) Polymer Overlay for Bridge and Parking Garage Decks. Meets and exceeds the requirements of ASTM C 881 Type III (Exception an improved gel time) for use in bonding skid-resistance, high-friction surfacing overlay materials.

DESCRIPTION

E-Bond 526 is a 2-component 100% solids, Zero VOC, Moisture-Tolerant Epoxy polymer that provides long term impermeable protection of the underlying reinforcing from the corrosive effect from chloride ions penetration. E-Bond 526 provides a Skid-Resistant High–Friction wearing surface for bridge and parking decks with a unique Low–Modulus of Elasticity allowing the 526 Epoxy Polymer Overlay to accommodate variations in stress due to thermal and mechanical movement of the substrate.

E-Bond 526 is recommended as a Multi-Layer Polymer Overlay as a minimum for the necessary impermeable protection. The 1st layer is applied as a penetrating sealer/bonding agent to bond the broadcast aggregate to the substrate while also filling fissures and voids in the substrate which creates out gassing (releasing of air from the concrete), through the 1st layer leaving minute pinholes. The 2nd layer is necessary to seal any remaining pinholes/voids and to encapsulates the 1st lift aggregate and securely bonds the 2nd layer of broadcast aggregate.

E-Bond 526 has a highly successful 20 year track record with more than 12 million square feet in place across United States and Canada as a waterproofing and anti-skid overlay with deicing capability to reduce or prevent frost and ice formation on Bridge and Parking Decks. There are thousands of bridges with E-Bond 526 Overlay in place exposed to extremes of weather with over 15 years of service life while maintaining waterproofing integrity indicated by low levels of chloride ions and retention of skid/friction properties measuring in the 50's.

FEATURES

- Rapid strength development in warm /cool weather

- Provides a highly impermeable system to protect the reinforcing steel from the corrosive effect of Chloride ions penetration.
- Skid Resistant
- Unique Low Modulus

- Self Priming
- Light-weight protective overlays
- Withstands vehicular traffic
- Simple 1 to 1 mix ratio by volume
- Good chemical resistance
- VOC

BENEFITS

- Minimizes bridge closure time and traffic disruption. Excellent for heavy traffic industrial flooring, safety for vehicles and pedestrians
- ¼ inch of 526 polymer overlay is 20 times more impermeable than 2 inches of concrete.

- Retains skid number above 50 for extended period of time
- Accommodates variations in stress due to thermal and mechanical movement, excellent for thin-set mortar and grouting
- Reduces closure time
- Limits dead load in suspended structures
- Extends the service life of decks
- Convenient easy to use
- Long-term protection to icing solutions and automotive fluids
- Fully Reactive- no low boiling Constituents

WHERE TO USE

- When an impermeable waterproof/skid resistant overlay is required to protect new and existing bridge decks against the damaging effects of the intrusion by chloride ions. - As a rapid set overlay installation when quick turnaround times are required throughout a wide temperature range - As a skid-resistant system for parking decks, loading docks and ramps - As a skid-resistant coating for steel decks, warehouse floors - Airport runways - As a low modulus patching mortar for spalls and deck delamination's - As a single coat system for skid proofing asphalt surfaces - A Hi Friction/Skid resistant single coat surfacing for asphalt surfaces.

1

EPOXY MULTI-LAYER RAPID SET
HI-FRICTION SKID RESISTANT POLYMER OVERLAY
FOR BRIDGE AND PARKING DECKS

PHYSICAL PROPERTIES
(Material and curing conditions @ 75°F (24°C) and 50% R.H.)

Mixing Ratio: Component A/B	1:1 by volume
Viscosity: ASTM-D-2393 (poises)	15-30
Gel Time: ASTM-C-881 (60 g) (minutes)	15-30
Tensile Properties: (ASTM-D-638) Type I 7 day	
Tensile Strength	2500-5000 psi (17-34 MPa)
Elongation at Break	30-80%
Adhesive Strength ASTM C 1583 – 04 (mixed with aggregate) min. 250 psi (MPa 1.7)	250+ psi(Mpa)
Bond Strength: (ASTM-C-882) 2 day (moist cure) Plastic concrete to hardened concrete	1600 psi (11) min.
VOC mixed	0 g/l
Compressive Properties: (ASTM-C-579) Method B 3 hour Minimum	
1 day	1000 psi (6.g/19 Mpa)
7 day	5000 psi (34 Mpa)
	6500 psi (45 Mpa)
Compressive Modulus ASTM D 695 14 day	130,000 psi (896 Mpa) max.
Thermal Compatibility ASTM C 884 (Mixed with aggregate) 7 days	
	No delaminations
Water Absorption: (ASTM-D-570) 7 days	
	0.4%
Permeability of Chloride Ions AASHTO T277 28 days (less than 100 coulombs)	73 (negligible)

For Best Performance

- Precondition the components to 70°F (23°C) to 80°F (27°C) for 24 hours before use.

- Minimum ambient, surface, aggregate and epoxy temperatures should be 50°F (10°C) and rising at the time of application.

- Store at 40ºF (4.4ºC)-95ºF(35ºC)

- Protect from moisture.

- Protect from freezing.

- Do not add solvents or water to epoxy material.

- Do not alter or change the recommended proportions when blending the components.

Rapid Set times Minimum Closures times in Warm and Cool Weather Applications

Layers	Average Temperature of Deck, Epoxy, and Aggregate Components in °F (°C)									
	85+ (29+)	84-80 (29-27)	79-75 (26-24)	74-70 (23-21)	69-65 (21-18)	64-60 (18-16)	59-55 (15-13)	*54-50 (12-10)	*49-45 (9-7)	*44-40 (7-4)
Hours	1	1½	1 ¾	1 ¾	2	2	2 ¼	2 ½	2 ¾	3

*It is highly recommended that all components be conditioned in advance of use to 75°F (24°C). This may take 48 hrs. It is to the contactors benefit to maintain the components at elevated temperatures. At lower temperatures (<55°F), the resin will be become difficult to remove from containers and to mix properly.

Minimum Epoxy & Aggregate Coverage Rates (2 Layer System for Concrete & Steel)

	Epoxy Rate Gallons/100 ft² (Liters/sq m²) *	Aggregate Rate**
Layer 1	2 ½ per gallons per 100 ft² (1 gal./ 40 ft² 1 L/M²)	10 lbs/yd² (5.4 kg/M²)
Layer 2	5 gallons per 100 ft² (1 gal. /20 ft² 2 L/M²)	14 lbs/yd² (7.6 kg/M²)

*Total epoxy applied must equal no less than 7 ½ gal/100 ft² (3 L/M²) more or less if aggregate used is larger or smaller than as specified in Aggregate Chart. A grooved deck may require more epoxy polymer.

Minimum Epoxy & Aggregate Coverage Rates for 1 Layer Applications on Asphalt

	Epoxy Rate ft²/ gal. (mils)	Aggregate Rate**
Layer 1	4 gallons per 100 ft² (64 mils – 1/16")	15 lbs/yd²

2

283

Appendix C

Concrete Batch I Mix Design:

PULL WEIGHT SUMMARY BASED ON MOISTURE

25-Jun-13

MIX NO: Virginia Pull
(BRISTOL PLANT)
SSD

Free Moist F.A.= 2.7 Percent
Free Moist C.A.= 2.8 Percent
Total Free Moist= 10.6 Gal./CY

Item	(1 C.Y.)	
Cement	635	POUNDS
Fine	1452	POUNDS
Coarse	1744	POUNDS
Water	30.0	GALLONS
200N	25.0	OUNCES
S. Fume	0.0	POUNDS
Air Ent	3.0	OUNCES
Super	45.0	OUNCES

Item	1/4 CY	1/2 CY	3/4 CY	1 CY	1.25 CY	1.5 CY	1.75 CY	2 CY
Cement	159	318	476	635	794	953	1111	1270
Fine	373	746	1118	1491	1864	2237	2610	2982
Coarse	448	896	1345	1793	2241	2689	3137	3586
Tot.Agg.	821	1642	2463	3284	4105	4926	5747	6568
Water	4.9	9.7	14.6	19.4	24.3	29.1	34.0	38.9
200N	6.3	12.5	18.8	25.0	31.3	37.5	43.8	50.0
S. Fume	0.0	0.0	0.0	0.0	0.0	0.0	0.0	0.0
Air Ent	0.8	1.5	2.3	3.0	3.8	4.5	5.3	6.0
Super	11.3	22.5	33.8	45.0	56.3	67.5	78.8	90.0

Item	2.25 CY	2.5 CY	2.75 CY	3 CY	3.25 CY	3.5 CY	3.75 CY	4 CY
Cement	1429	1588	1746	1905	2064	2223	2381	2540
Fine	3355	3728	4101	4474	4846	5219	5592	5965
Coarse	4034	4482	4930	5378	5827	6275	6723	7171
Tot.Agg.	7389	8210	9031	9852	10673	11494	12315	13136
Water	43.7	48.6	53.4	58.3	63.2	68.0	72.9	77.7
200N	56.3	62.5	68.8	75.0	81.3	87.5	93.8	100.0
S. Fume	0.0	0.0	0.0	0.0	0.0	0.0	0.0	0.0
Air Ent	6.8	7.5	8.3	9.0	9.8	10.5	11.3	12.0
Super	101.3	112.5	123.8	135.0	146.3	157.5	168.8	180.0

Concrete Batch II Mix Design:

PULL WEIGHT SUMMARY BASED ON MOISTURE

28-Jun-13

MIX NO: VIRGINIA
(BRISTOL PLANT)
SSD

Free Moist F.A.= 4.4 Percent
Free Moist C.A.= 1.9 Percent
Total Free Moist= 11.6 Gal./CY

Item	(1 C.Y.)	
Cement	635	POUNDS
Fine	1452	POUNDS
Coarse	1744	POUNDS
Water	30.0	GALLONS
200N	30.0	OUNCES
S. Fume	0.0	POUNDS
Air Ent	3.0	OUNCES
Super	45.0	OUNCES

Item	1/4 CY	1/2 CY	3/4 CY	1 CY	1.25 CY	1.5 CY	1.75 CY	2 CY
Cement	159	318	476	635	794	953	1111	1270
Fine	379	758	1137	1516	1895	2274	2653	3032
Coarse	444	889	1333	1777	2221	2666	3110	3554
Tot.Agg.	823	1647	2470	3293	4116	4940	5763	6586
Water	4.6	9.2	13.8	18.4	22.9	27.5	32.1	36.7
200N	7.5	15.0	22.5	30.0	37.5	45.0	52.5	60.0
S. Fume	0.0	0.0	0.0	0.0	0.0	0.0	0.0	0.0
Air Ent	0.8	1.5	2.3	3.0	3.8	4.5	5.3	6.0
Super	11.3	22.5	33.8	45.0	56.3	67.5	78.8	90.0

Item	2.25 CY	2.5 CY	2.75 CY	3 CY	3.25 CY	3.5 CY	3.75 CY	4 CY
Cement	1429	1588	1746	1905	2064	2223	2381	2540
Fine	3411	3790	4169	4548	4927	5306	5685	6064
Coarse	3999	4443	4887	5331	5776	6220	6664	7109
Tot.Agg.	7409	8233	9056	9879	10702	11526	12349	13172
Water	41.3	45.9	50.5	55.1	59.6	64.2	68.8	73.4
200N	67.5	75.0	82.5	90.0	97.5	105.0	112.5	120.0
S. Fume	0.0	0.0	0.0	0.0	0.0	0.0	0.0	0.0
Air Ent	6.8	7.5	8.3	9.0	9.8	10.5	11.3	12.0
Super	101.3	112.5	123.8	135.0	146.3	157.5	168.8	180.0

Appendix D

Sub-assemblage Concrete Batch I – Fresh Concrete Properties:

ROSS PRESTRESSED CONCRETE, INC.
P.O. Box 276
Bristol, Tennessee 37620-276
Phone (423) 323-1777
Fax (423) 323-9461

ROSS PRESTRESS

PRODUCTION REPORT

COUNTY, ST.	VIRGINIA TECH
RPC JOB NO.	B13-18
POUR NO.	#1
POUR DATE	6-25-2013
AIR TEMP.	74°
INSPECTORS	VA TECH
PLANT:	BRISTOL

CONCRETE PROPERTIES

LOAD NO.	1.	4
STATION	LE	DE
SLUMP	3¼	
AIR CONTENT	6.9	
PLACEMENT TEMP.	72°	
COMP. STRENGTH @ DET.	4377	
COMP. STRENGTH @ 28 DAYS		
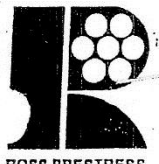
MEMBERS CAST:
2-SPEC 1   2-SPEC 1
2-SPEC 2   7-SPEC 2
2-SPEC 3   2-SPEC 3
1-SPEC 7   1-SPEC 1

DESCRIPTION: VOIDED SLABS
BOX BEAMS

REQUIRED PROPERTIES

TYPE MIX	ON FILE
COMP. STRENGTH @ DET.	3500
COMP. STRENGTH @ 28 DAYS	5000
ADMIXTURES	30 oz 7700
AIR CONTENT	3 oz

PRE-POUR INSPECTION

STRAND	NA	FORM COND.	✓
RE-STEEL	✓	SKEW	30
HEIGHT	✓	BLOCKOUTS	✓
WIDTH	✓	INSERTS	NA
LENGTH	✓	PLATES	NA
VOIDS	✓	DEFL. PTS.	NA
FORM ALIGN.	✓	END DETAILS	

POST-POUR INSPECTION

HEIGHT	✓
WIDTH	✓
LENGTH	24' 11
CAMBER	NA
SKEW	30
INSERTS	W
DOWEL HOLES	NA
TIE ROD HOLES	NO
FINISH	✓
MISC.	Keyway Study

TENSION DATA

MFG.	
SIZE/TYPE	
INIT. TENSION	N/A
PRELOAD	
BED LENGTH	
NET ELONG.	
MAX GAUGE	
MIN GAUGE	
STRESS DATE	
REEL NO.	
TENN: YES ___ NO ___	
MACHINE	

AMBIENT CURING TEMP

LOCATIONS & TEMP

TIME			
	SEE CHARTS		

REMARKS: _____ QUALITY CONTROL SUPERVISOR _____

7-5

286

Sub-assemblage Concrete Batch II – Fresh Concrete Properties:

ROSS PRESTRESSED CONCRETE, INC.
P.O. Box 276
Bristol, Tennessee 37620-276
Phone (423) 323-1777
Fax (423) 323-9461

ROSS PRESTRESS

PRODUCTION REPORT

COUNTY, ST.	VIRGINIA TECH
RPC JOB NO.	B13-18
POUR NO.	#3
POUR DATE	6-28 2013
AIR TEMP.	74
INSPECTORS	ROBERT G. SADDER
PLANT:	BRISTOL

CONCRETE PROPERTIES

LOAD NO.	1.	4
STATION	LE	DE
SLUMP	8"	
AIR CONTENT	54	
PLACEMENT TEMP.	80°	
COMP. STRENGTH @ DET.	4151	
COMP. STRENGTH @ 28 DAYS		

MEMBERS CAST: 2-SPEC 1,2,3 1-SPEC 4
2-SPEC 1,2,3 1-SPEC 4

DESCRIPTION: VOIDED SLABS
BOX BEAMS

REQUIRED PROPERTIES

TYPE MIX	ON FILE
COMP. STRENGTH @ DET.	3500
COMP. STRENGTH @ 28 DAYS	5000
ADMIXTURES	45 OZ 7700
AIR CONTENT	3 OZ

PRE-POUR INSPECTION

STRAND	N/A	FORM COND.	✓
RE-STEEL	✓	SKEW	✓
HEIGHT	✓	BLOCKOUTS	✓
WIDTH	✓	INSERTS	NA
LENGTH	✓	PLATES	NA
VOIDS	N	DEFL. PTS.	NA
FORM ALIGN.	N	END DETAILS	NA

POST-POUR INSPECTION

HEIGHT	✓
WIDTH	✓
LENGTH	28/16
CAMBER	NA
SKEW	50✓
INSERTS	NA
DOWEL HOLES	N
TIE ROD HOLES	N
FINISH	✓
MISC.	

TENSION DATA

MFG.	
SIZE/TYPE	
INIT. TENSION	N/A
PRELOAD	
BED LENGTH	
NET ELONG.	
MAX GAUGE	
MIN GAUGE	
STRESS DATE	
REEL NO.	

TENN: YES _____ NO _____

MACHINE _____

AMBIENT CURING TEMP

LOCATIONS & TEMP

TIME			
	SEE CHARTS		

REMARKS: Rough Bottom on angle _____ QUALITY CONTROL SUPERVISOR _____

7-5

287

Appendix E

Material test data from sub-assemblage tests is presented here.

Compressive strength of precast beam concrete

Table 40: Compressive strengths of sub-assemblage section concrete – Batch I.

Specimen	Age (Days)	Cylinder	Failure Load (lb)	Strength (psi)	Average Strength (psi)	Time (sec)	Average Load Rate (lb/sec)
S4	170	BB-S4-B1-Cy1	91000	7241.55	7301.233	183	497.3
		BB-S4-B1-Cy2	92500	7360.916		191	484.3
S5	187	BB-S5-B1-Cy1	94500	7520.071	7420.599	199	474.9
		BB-S5-B1-Cy2	92000	7321.127		188	489.4
S6	211	BB-S6-B1-Cy1	92000	7321.127	7380.81	195	471.8
		BB-S6-B1-Cy2	93500	7440.494		192	487

Table 41: Compressive strengths of sub-assemblage section concrete – Batch II.

Specimen	Age (Days)	Cylinder	Failure Load (lb)	Strength (psi)	Average Strength (psi)	Time (sec)	Average Load Rate (lb/sec)
S1	76	BB-B2-S1-Cy1	91500	7281.339	7380.81	191	479.1
		BB-B2-S1-Cy2	94000	7480.282		197	477.2
S2	100	BB-B2-S2-Cy1	98500	7838.381	7659.332	202	487.6
		BB-B2-S2-Cy2	94000	7480.282		191	492.1
S3	128	BB-S3-B2-Cy1	100000	7957.747	7619.543	206	485.4
		BB-S3-B2-Cy2	91500	7281.339		189	484.1
S5	184	BB-S5-B2-Cy1	96500	7679.226	7619.543	202	477.7
		BB-S5-B2-Cy2	95000	7559.86		198	479.8
S6	208	BB-S6-B2-Cy1	95000	7559.86	7539.965	200	475
		BB-S6-B2-Cy2	94500	7520.071		195	484.6

Table 42: Compressive strengths of sub-assemblage section concrete – Batch III.

Specimen	Age (Days)	Cylinder	Failure Load (lb)	Strength (psi)	Average Strength (psi)	Time (sec)	Average Load Rate (lb/sec)
S1	72	BB-B3-S1-Cy1	119500	9509.508	9449.825	249	479.9
		BB-B3-S1-Cy2	118000	9390.142		240	491.7
S2	96	BB-B3-S2-Cy1	121000	9628.874	9569.191	243	497.9
		BB-B3-S2-Cy2	119500	9509.508		238	502.1
S3	132	BB-B3-S3-Cy1	124000	9867.606	10026.76	252	492.1
		BB-B3-S3-Cy2	128000	10185.92		280	457.1
S4	163	BB-B3-S4-Cy1	126000	10026.76	10086.44	263	479.1
		BB-B3-S4-Cy2	127500	10146.13		271	470.5

Modulus of elasticity of precast beam concrete

Batch I concrete:
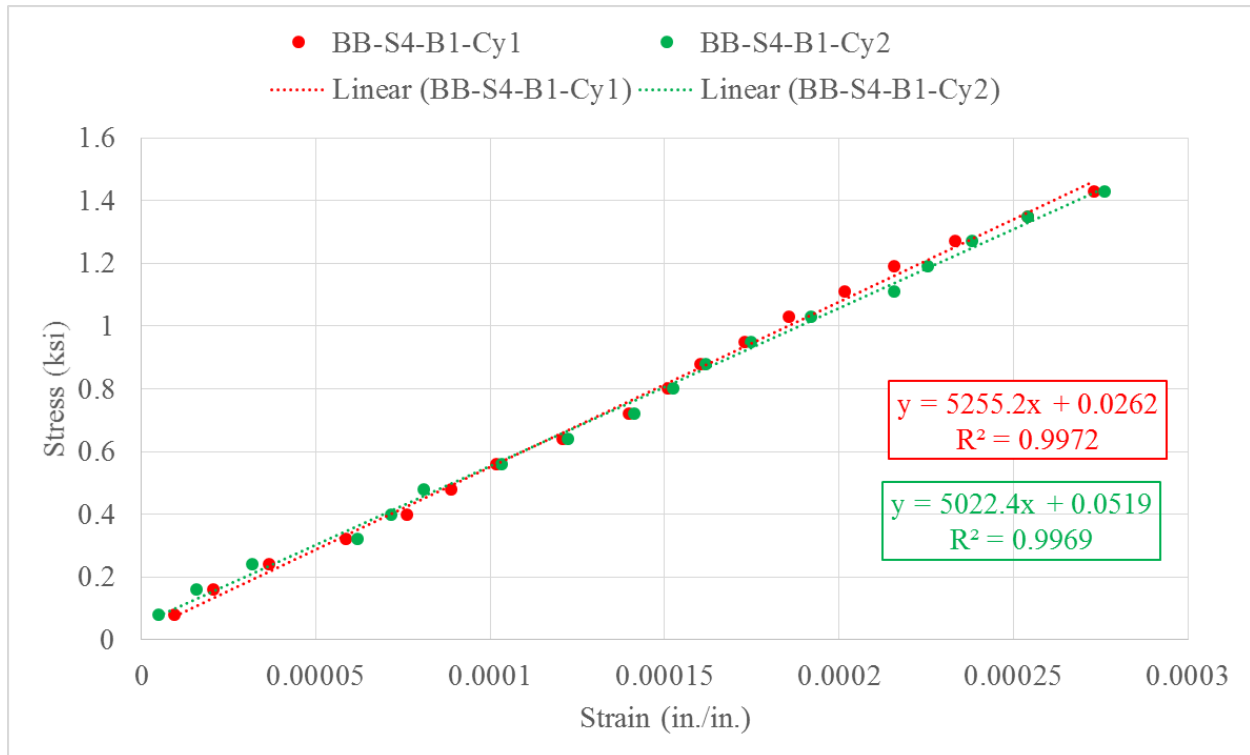
Figure 296: Modulus of elasticity of Batch I concrete used in Specimen 4.
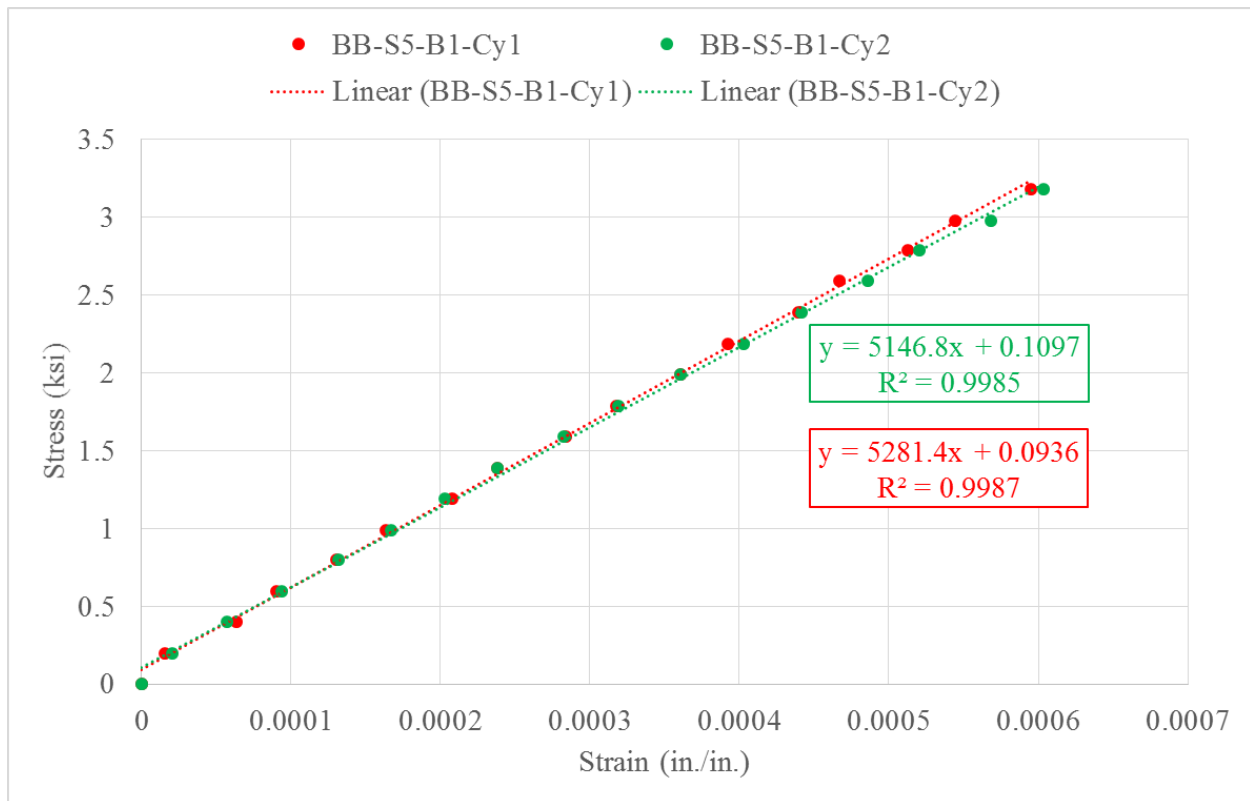
Figure 297: Modulus of elasticity of Batch I concrete used in Specimen 5.
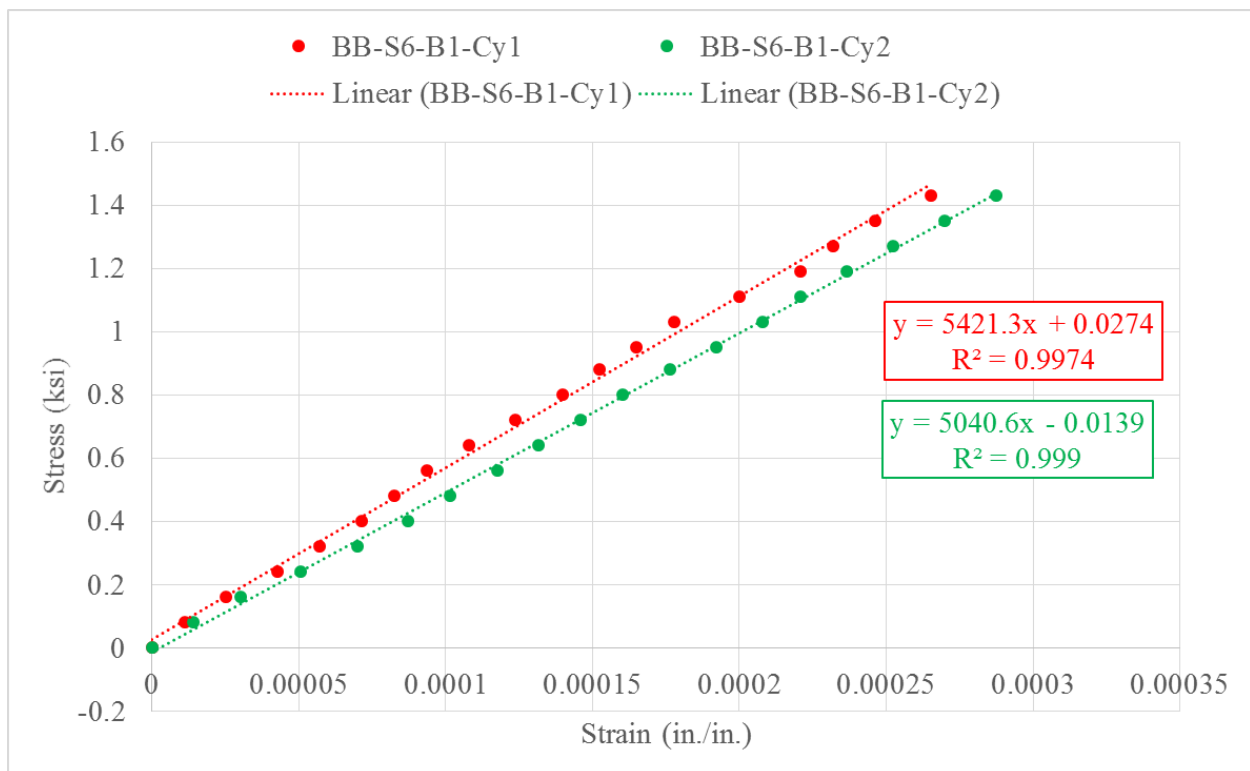
Figure 298: Modulus of elasticity of Batch I concrete used in Specimen 6.

Batch II Concrete:
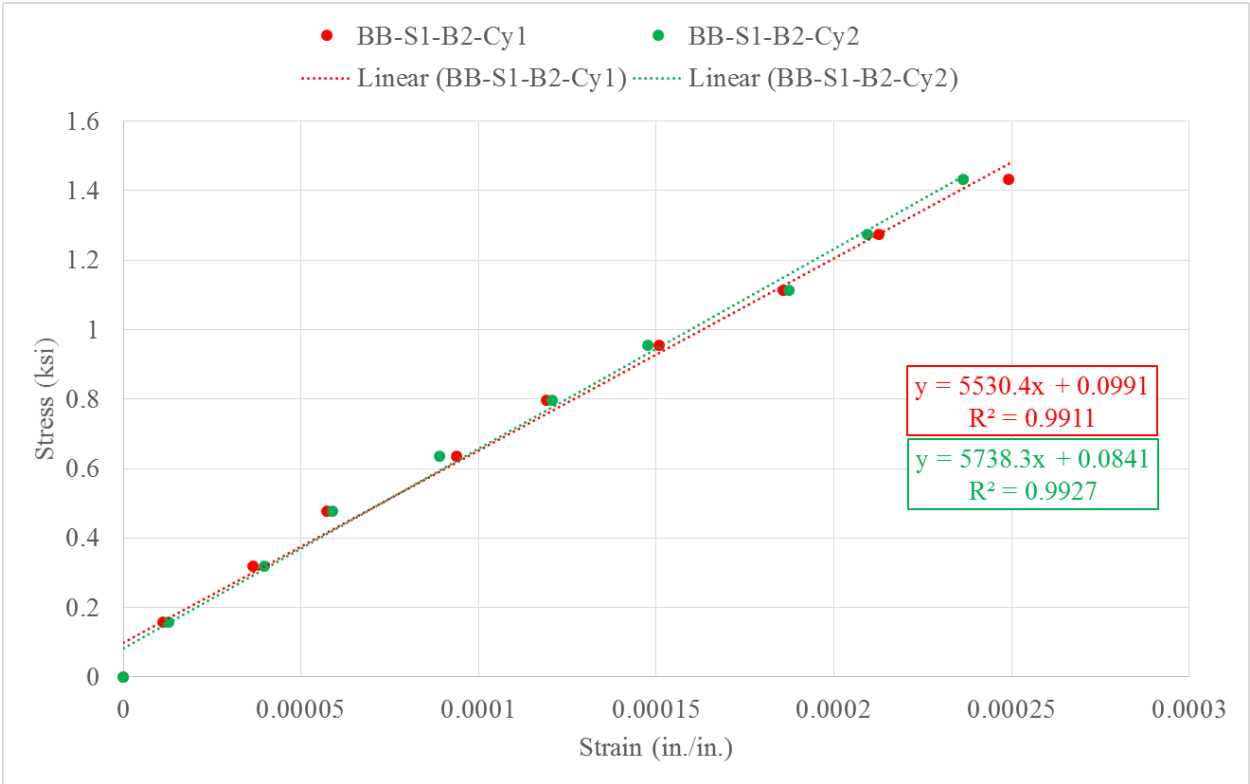
Figure 299: Modulus of elasticity of Batch II concrete used in Specimen 1.
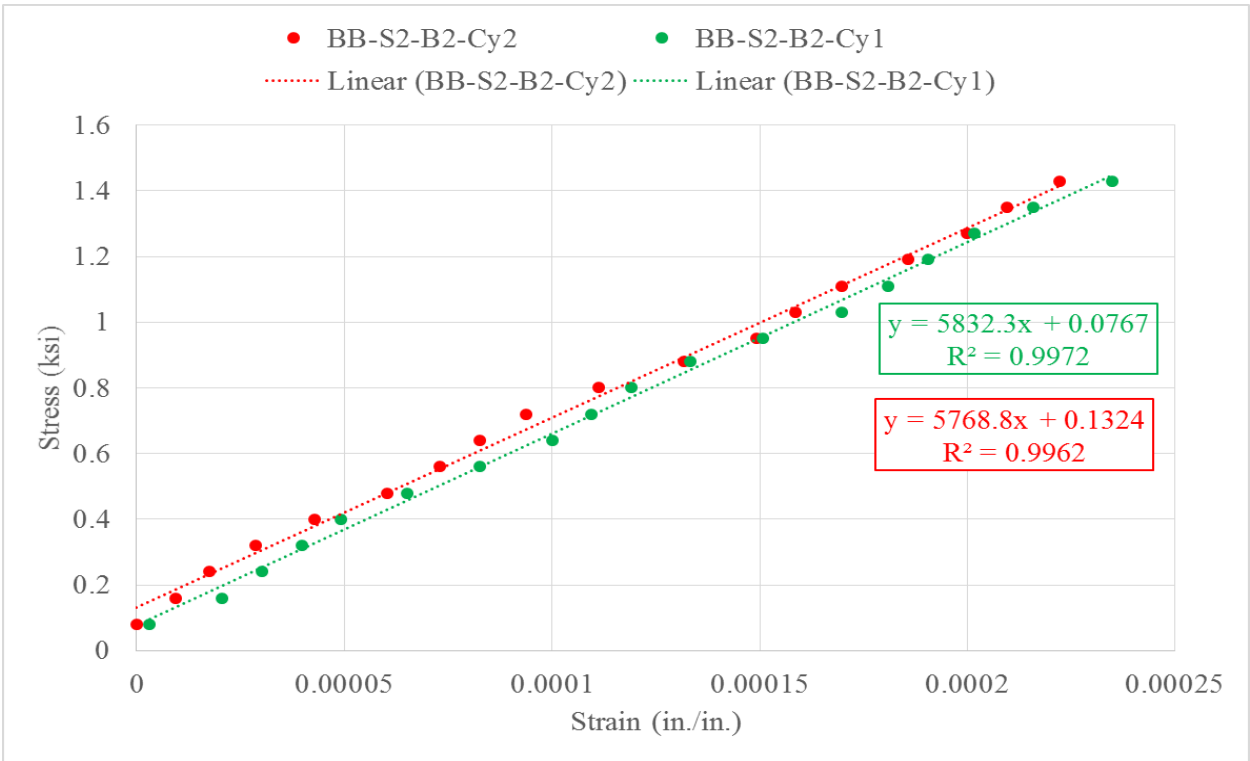
Figure 300: Modulus of elasticity of Batch II concrete used in Specimen 2.
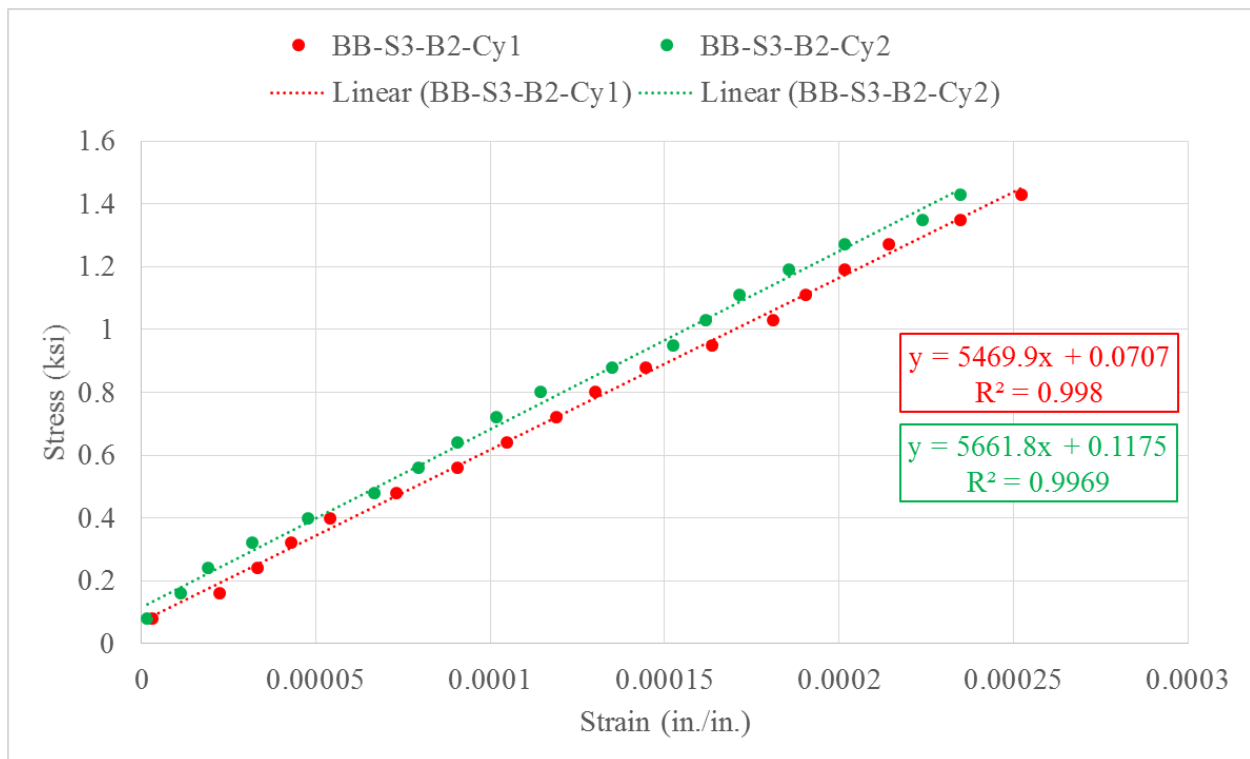
Figure 301: Modulus of elasticity of Batch II concrete used in Specimen 3.
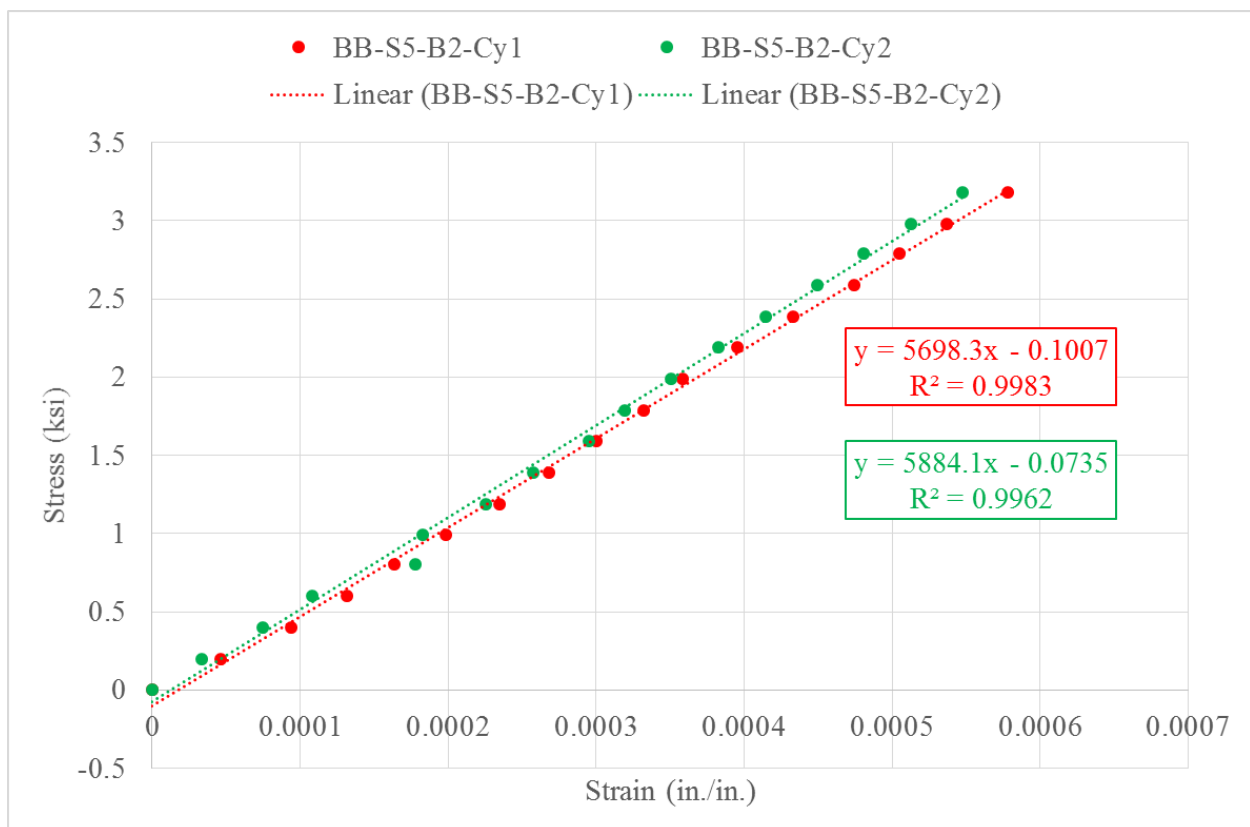
Figure 302: Modulus of elasticity of Batch II concrete used in Specimen 5.
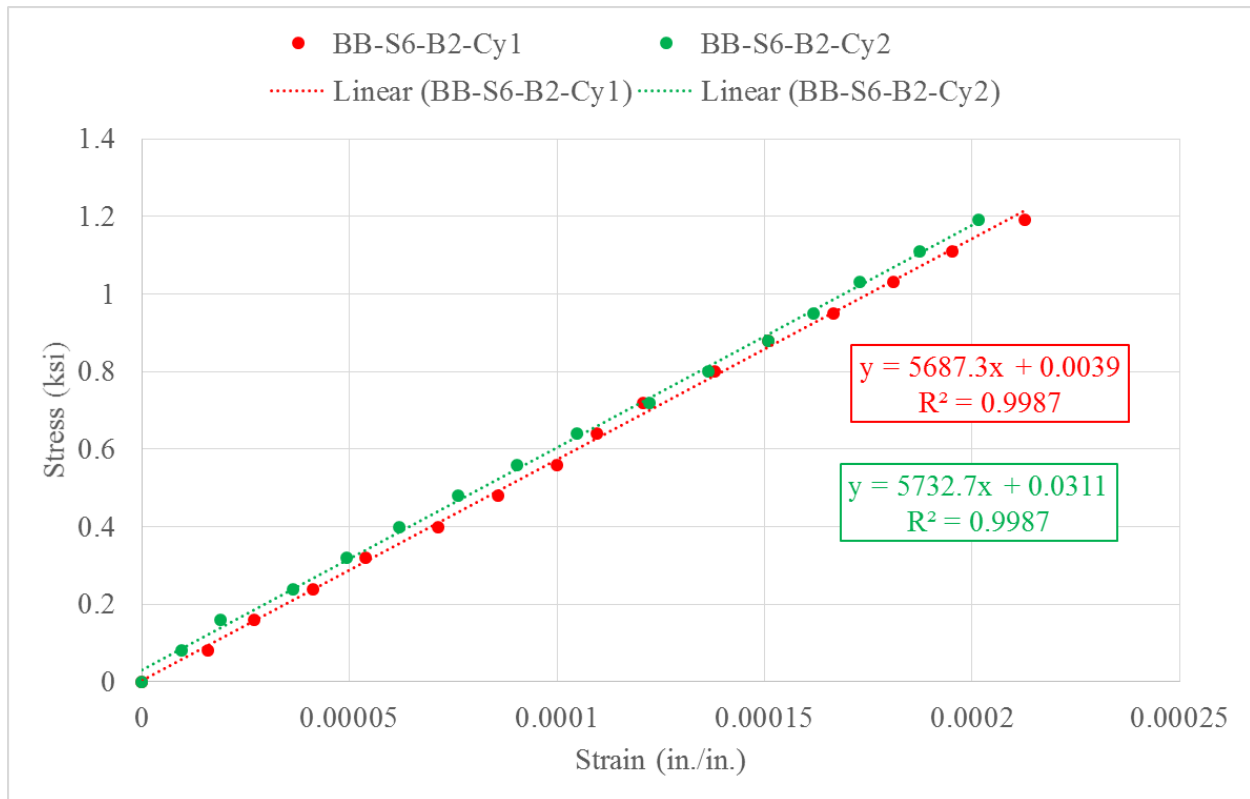
Figure 303: Modulus of elasticity of Batch II concrete used in Specimen 6.

Batch III:
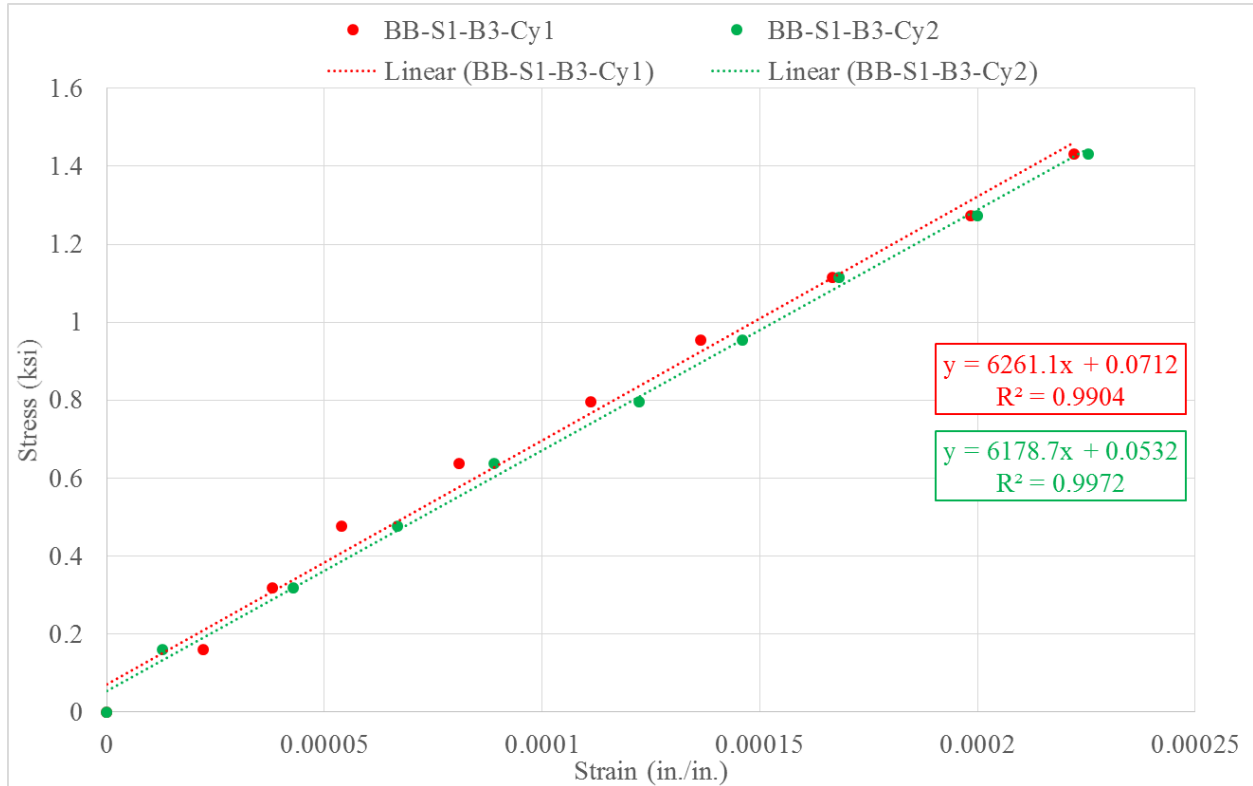
Figure 304: Modulus of elasticity of Batch III concrete used in Specimen 1.
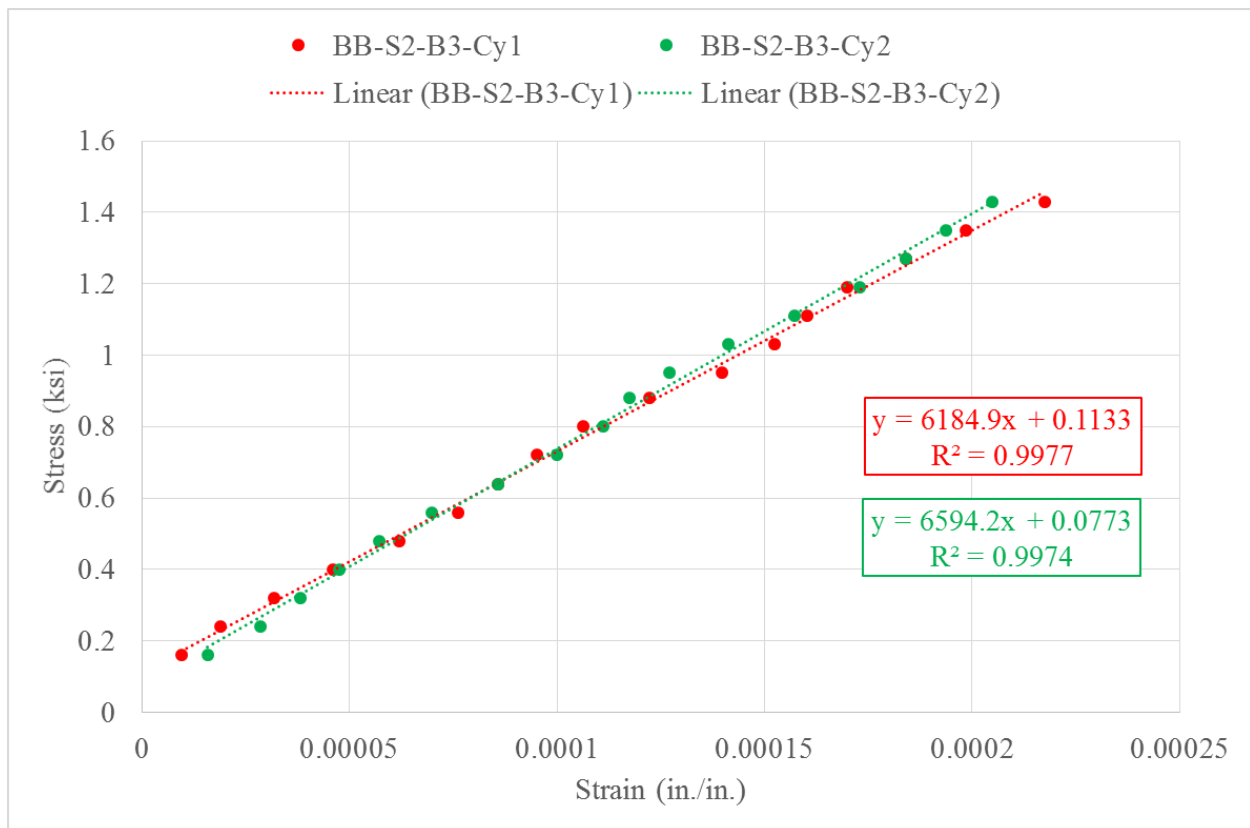
Figure 305: Modulus of elasticity of Batch III concrete used in Specimen 2.
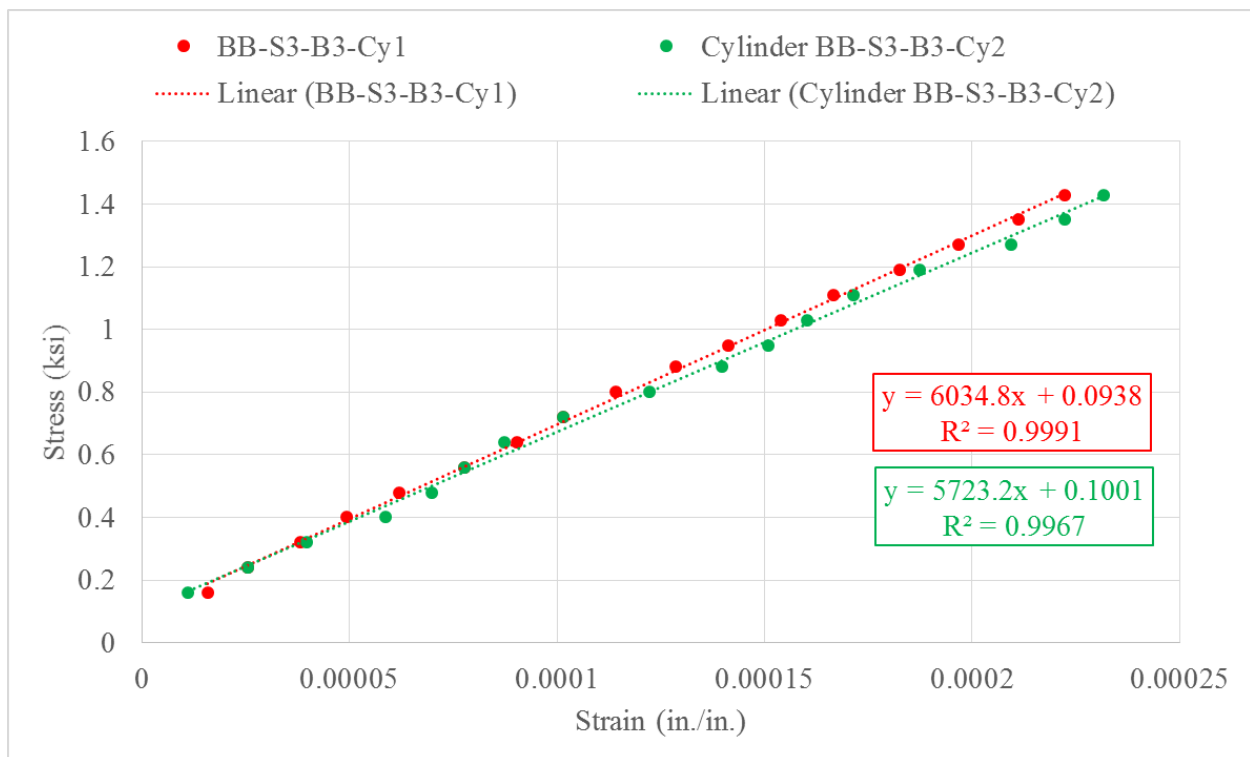
Figure 306: Modulus of elasticity of Batch III concrete used in Specimen 3.
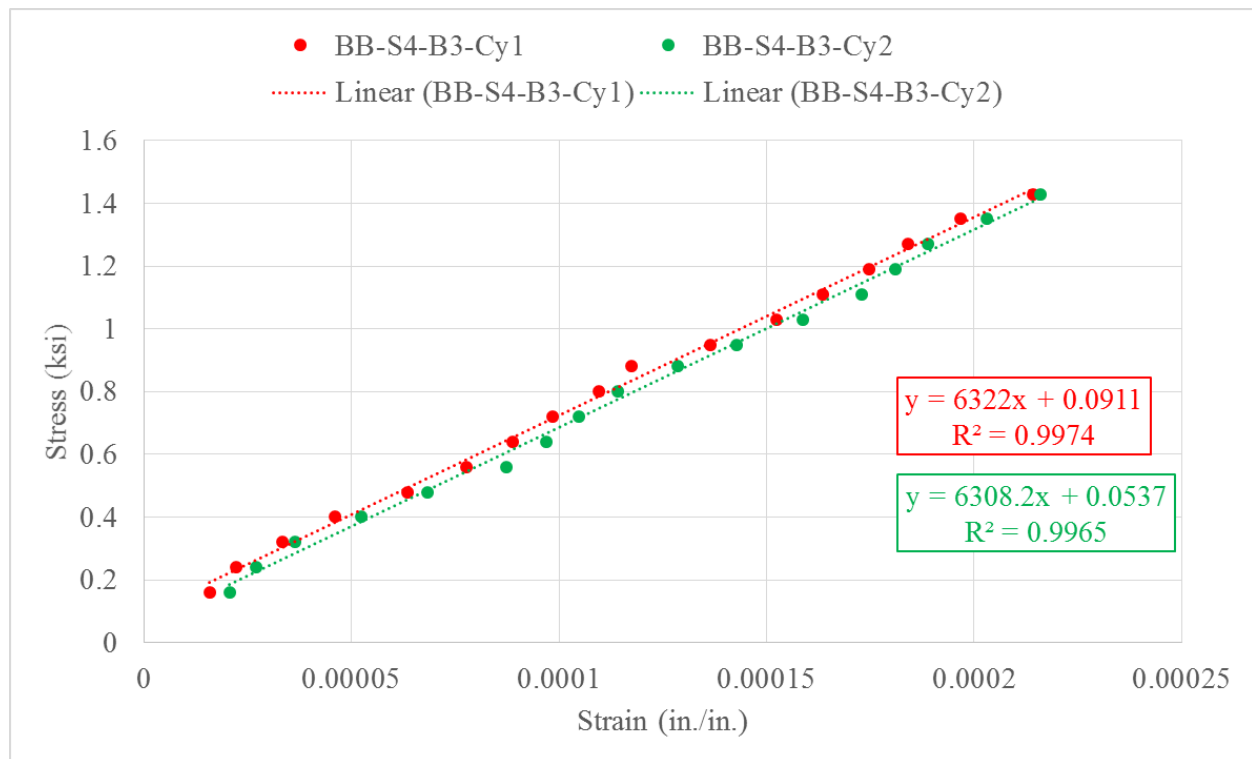
Figure 307: Modulus of elasticity of Batch III concrete used in Specimen 4.

Compressive strength of connection material

In

Table 43 and Table 44, the compressive strengths were measured using 2 in. x 2 in. cubes for specimens, S1, S2, S3 and S4. The compressive strengths for S5 and S6 were measured with 4 in. x 8 in. cylinders.

Table 43: Compressive strengths of connection materials at the start of fatigue test.

Specimen	Connection Material	Age (Days)	Cube or Cylinder*	Failure Load (lb)	Strength (psi)	Average Strength (psi)	Time (sec)	Average Load Rate (lb/sec)
S1	Grout	7	BB-S1-G-C7	29000	7250	7416.667	68	426.5
			BB-S1-G-C8	28500	7125		59	483.1
			BB-S1-G-C9	31500	7875		65	484.6
S2	UHPC	9	BB-S2-C2	64000	16000	15166.67	128.71	497.2
			BB-S2-C7	60000	15000		130.71	459
			BB-S2-C12	58000	14500		119.11	486.9
S3	UHPC	7	BB-S3-U-C1	61000	15250	14041.67	132.75	459.5
			BB-S3-U-C4	55500	13875		123.69	448.7
			BB-S3-U-C5	52000	13000		123.25	421.9
S4	Grout	7	BB-S4-G-C1	33000	8250	8208.333	69	478.3
			BB-S4-G-C2	31500	7875		65	484.6
			BB-S4-G-C3	34000	8500		72	472.2
S5	VHPC	7	BB-S5-V-Cy1	165000	13130.28	12838.5	339	486.7
			BB-S5-V-Cy2	159500	12692.61		321	496.9
			BB-S5-V-Cy3	159500	12692.61		333	479
S6	VHPC	7	BB-S6-V-Cy1	166000	13209.86	13063.97	345	481.2
			BB-S6-V-Cy2	165500	13170.07		322	514
			BB-S6-V-Cy3	161000	12811.97		331	486.4

Table 44: Compressive strengths of connection materials at the end of fatigue test

Specimen	Connection Material	Age (Days)	Cube or Cylinder*	Failure Load (lb)	Strength (psi)	Average Strength (psi)	Time (sec)	Average Load Rate (lb/sec)
S1	Grout	9	S1-G-C10	32500	8125	7833.333	63	515.9
			S1-G-C11	30500	7625		66	462.1
			S1-G-C12	31000	7750		72	430.6
S2	UHPC	15	BB-S2-C5	68500	17125	17583.33	138.9	493.2
			BB-S2-C9	70000	17500		144.1	485.8
			BB-S2-C11	72500	18125		147.7	490.9
S3	UHPC	14	BB-S3-U-C8	73000	18250	17166.67	152.09	480
			BB-S3-U-C3	67000	16750		143.78	466
			BB-S3-U-C7	66000	16500		143.77	459.1
S4	Grout	14	BB-S4-G-C4	36000	9000	8791.667	77	467.5
			BB-S4-G-C5	34500	8625		70	492.9
			BB-S4-G-C6	35000	8750		74	473
S5	VHPC	14	BB-S5-V-Cy4	167500	13329.23	13488.38	349	479.9
			BB-S5-V-Cy5	169000	13448.59		353	478.8
			BB-S5-V-Cy6	172000	13687.33		361	476.5
S6	VHPC	14	BB-S6-V-Cy4	183000	14562.68	13979.11	374	489.3
			BB-S6-V-Cy5	174000	13846.48		362	480.7
			BB-S6-V-Cy6	170000	13528.17		368	462

Splitting tensile strength of connection material

Table 45: Splitting tensile strength of connection materials at the end of fatigue test.

Specimen	Connection Material	Age (Days)	Cylinder	Length (in.)	Diameter (in.)	Failure Load (lb)	Strength (psi)	Average Strength (psi)
S2	UHPC	15	BB-S2-U-Cy1	8	4	92000	1830.282	2035.857
			BB-S2-U-Cy2	8	4	127000	2526.585	
			BB-S2-U-cy3	8	4	88000	1750.704	
S3	UHPC	14	BB-S3-U-Cy1	7.75	4	109500	2248.705	2195.01
			BB-S3-U-Cy2	7.8125	4	105500	2149.228	
			BB-S3-U-Cy3	7.75	4	106500	2187.097	
S5	VHPC	14	BB-S5-V-Cy7	8	4	87500	1740.757	1671.127
			BB-S5-V-Cy8	8	4	80500	1601.497	
S6	VHPC	14	BB-S6-V-Cy7	8	4	92000	1830.282	1899.912
			BB-S6-V-Cy8	8	4	99000	1969.542	

Modulus of elasticity of connection material
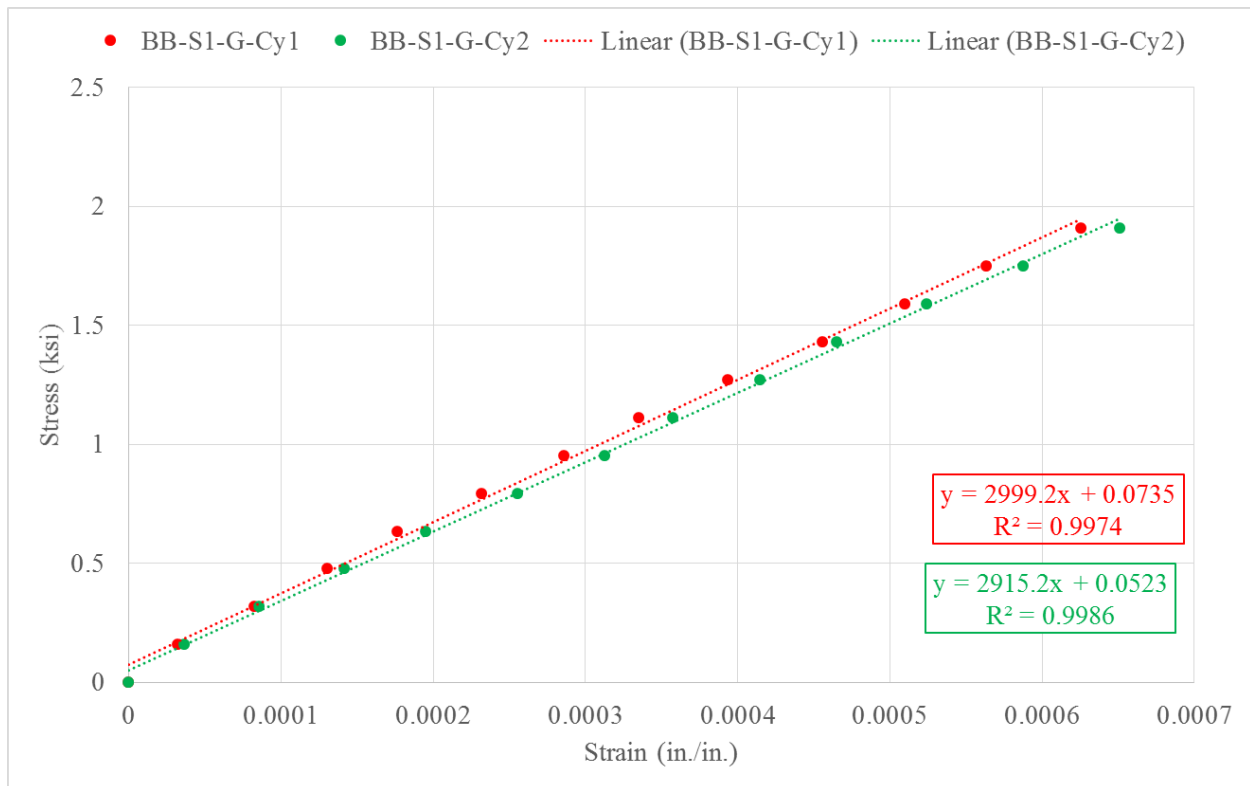
Figure 308: Modulus of elasticity of grout used in Specimen 1 at the start of fatigue test.
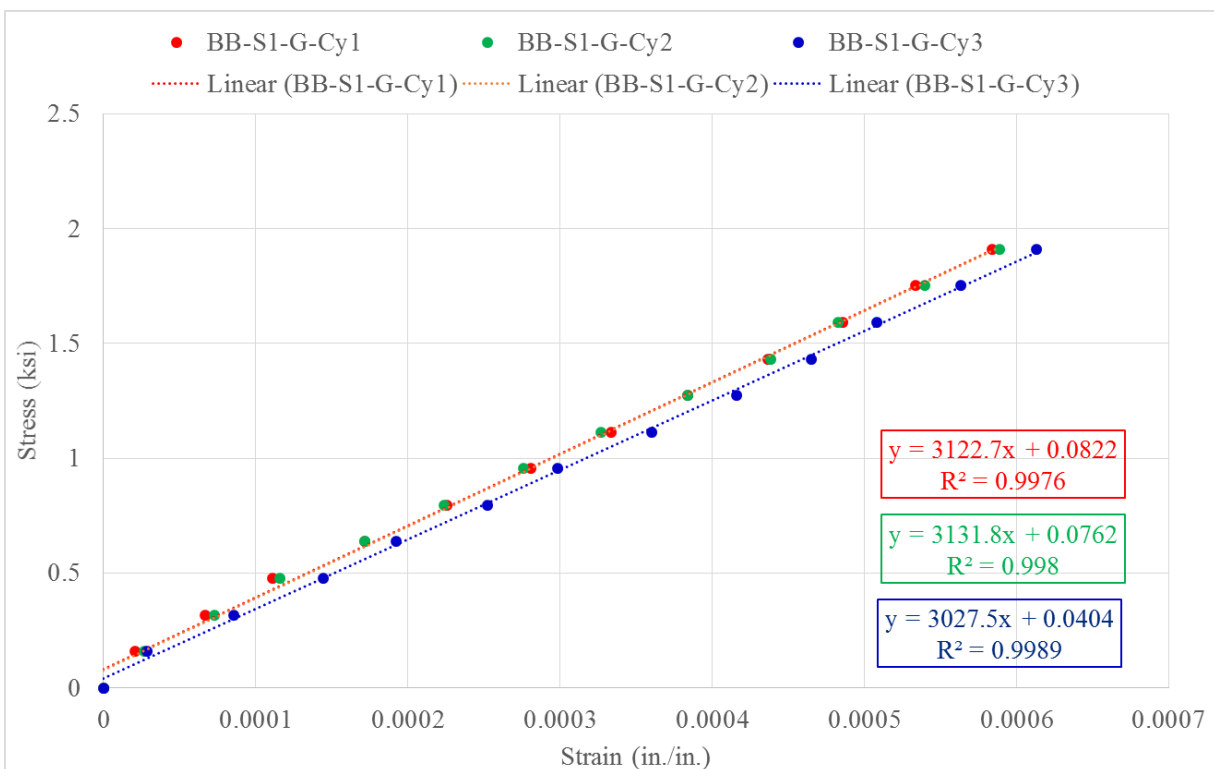
Figure 309: Modulus of elasticity of grout used in Specimen 1 at the end of fatigue test.
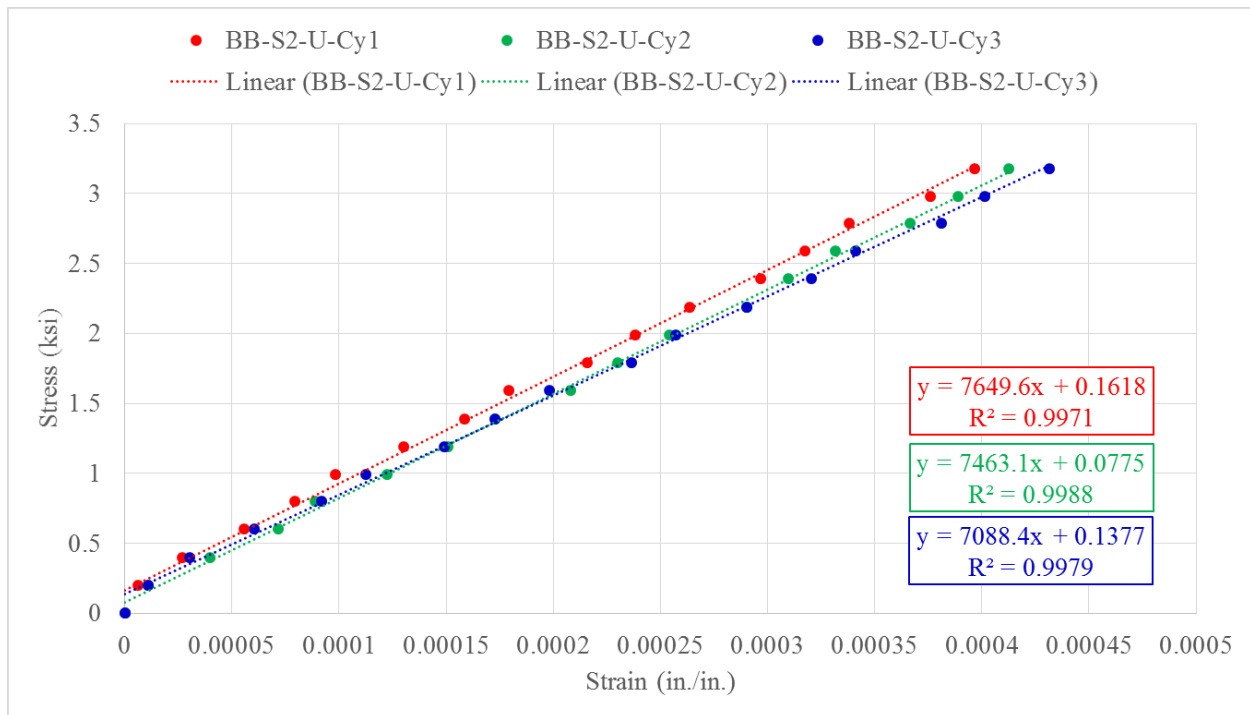
Figure 310: Modulus of elasticity of UHPC used in Specimen 2 at the start of fatigue test.
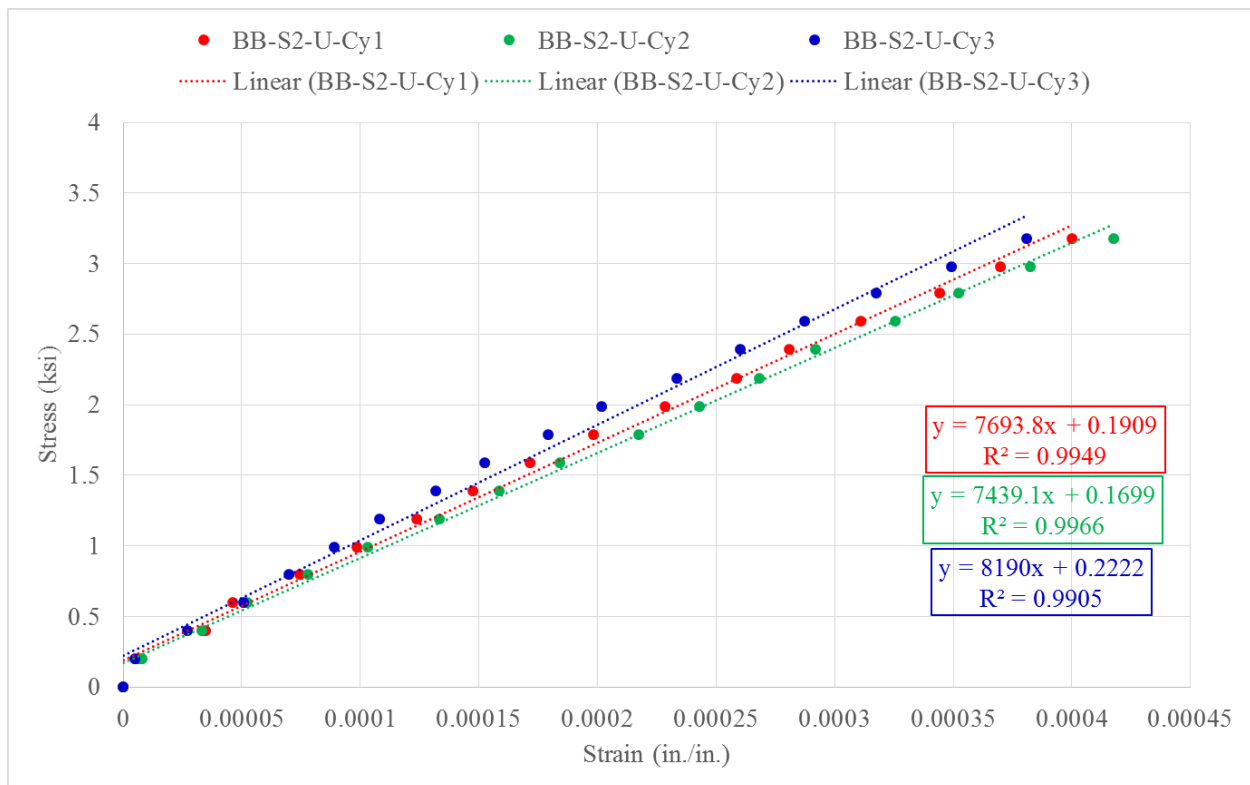
Figure 311: Modulus of elasticity of UHPC used in Specimen 2 at the end of fatigue test.
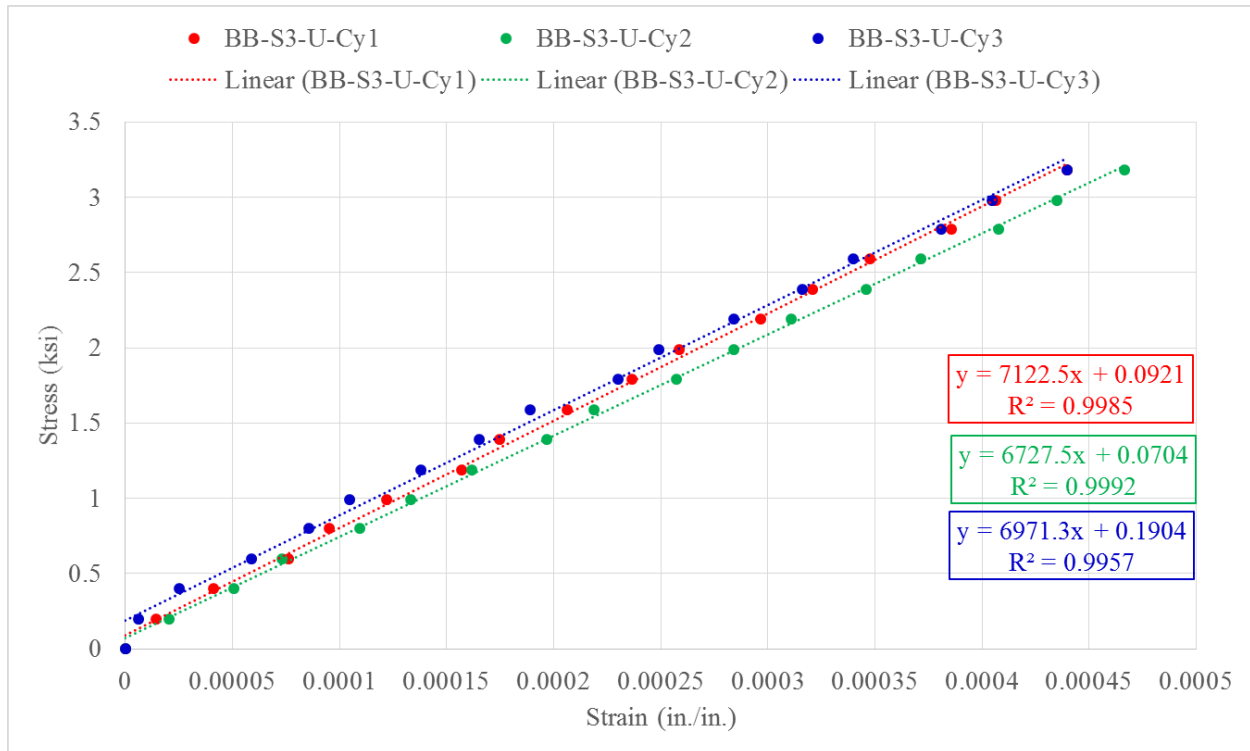
Figure 312: Modulus of elasticity of UHPC used in Specimen 3 at the start of fatigue test.
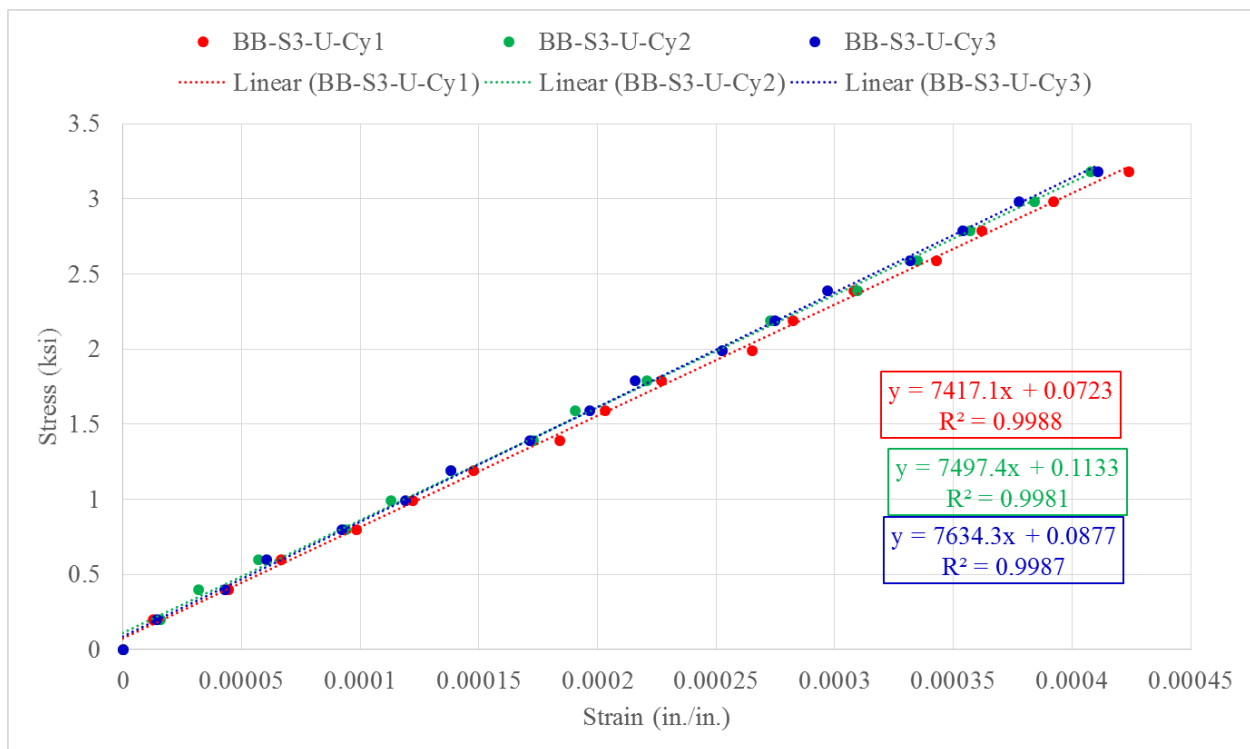
Figure 313: Modulus of elasticity of UHPC used in Specimen 3 at the end of fatigue test.
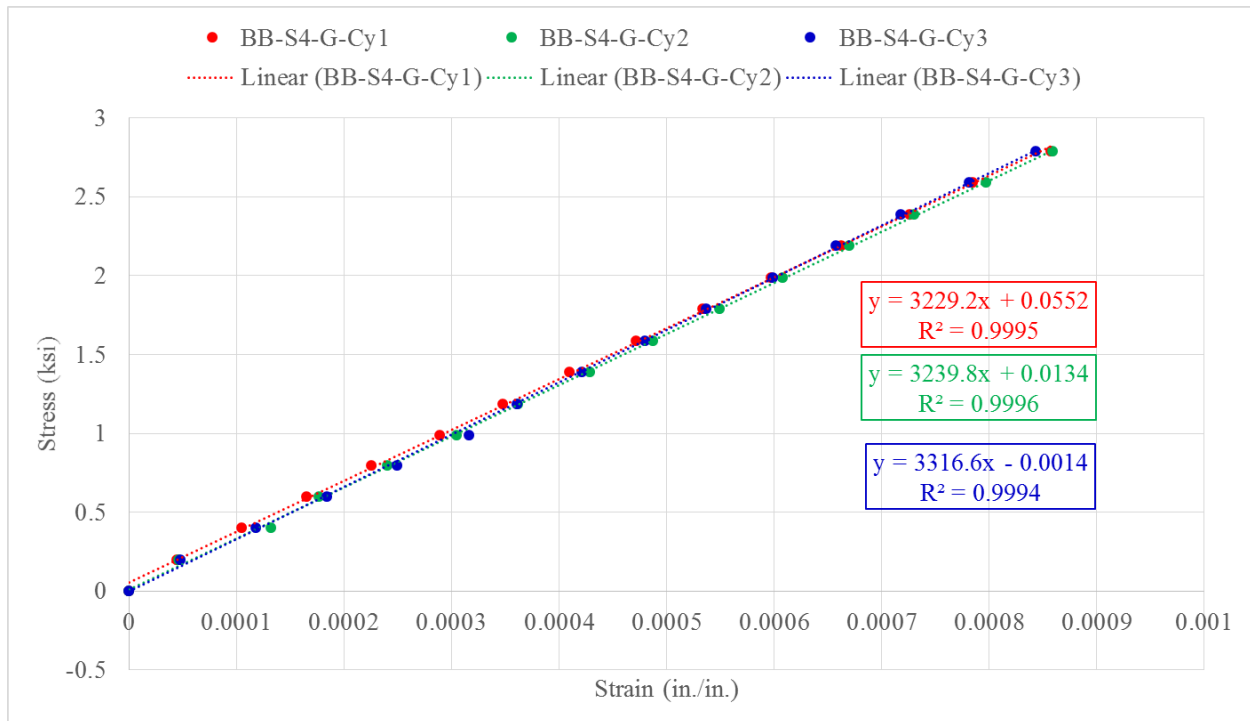
Figure 314: Modulus of elasticity of grout used in Specimen 4 at the start of fatigue test.
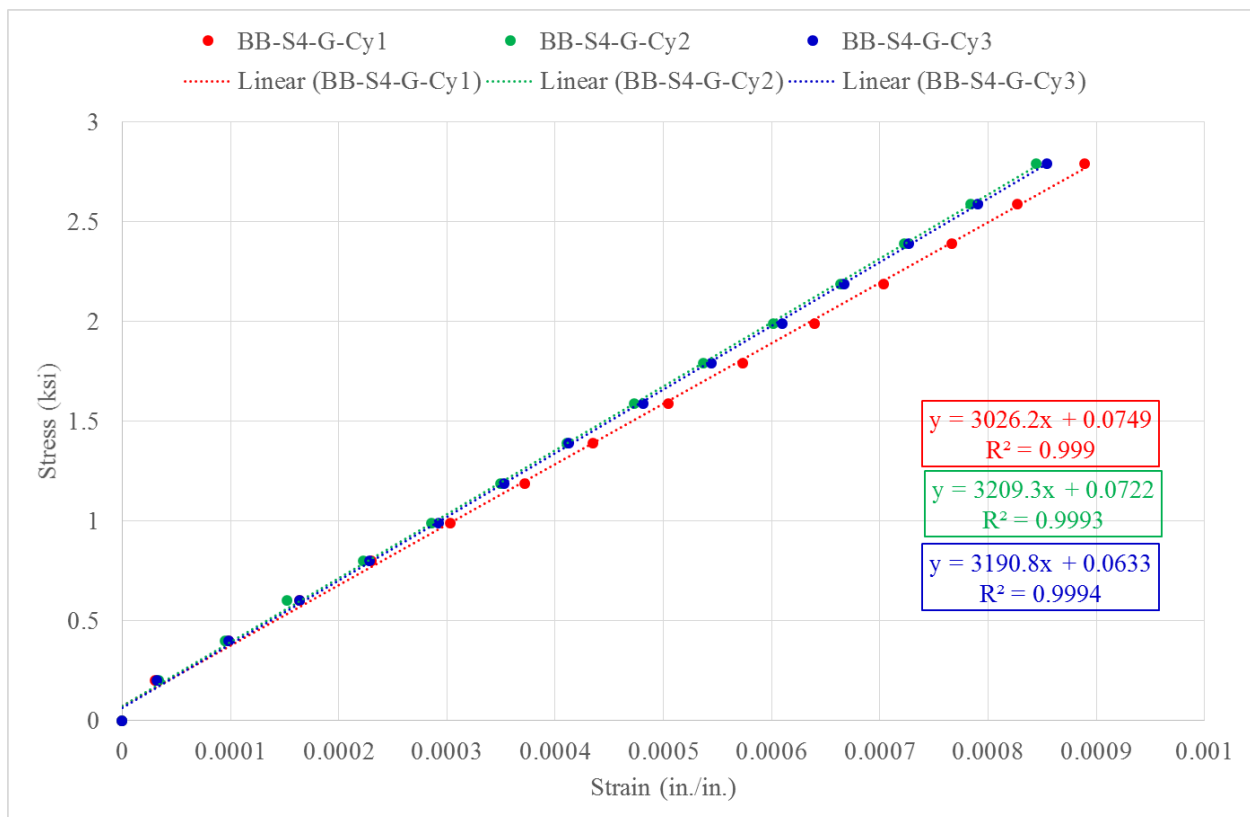
Figure 315: Modulus of elasticity of grout used in Specimen 4 at the end of fatigue test.

303
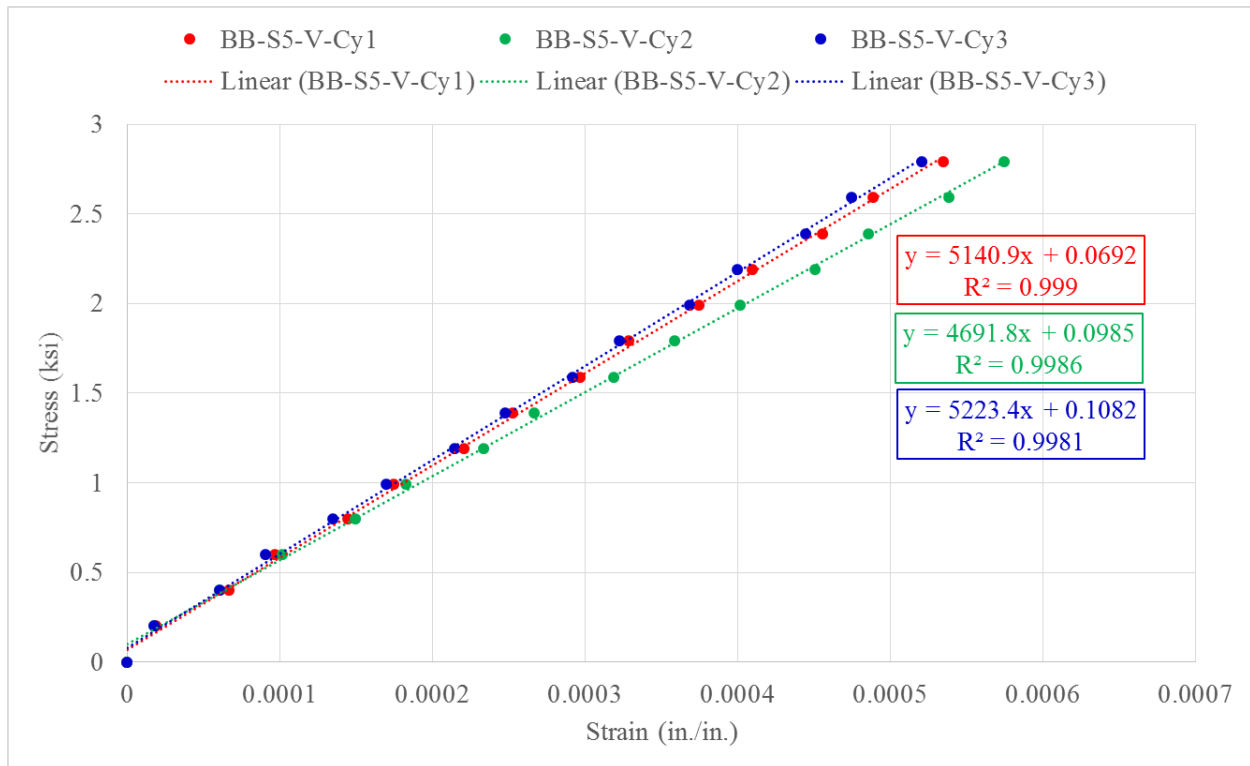
Figure 316: Modulus of elasticity of UHPC used in Specimen 5 at the start of fatigue test.
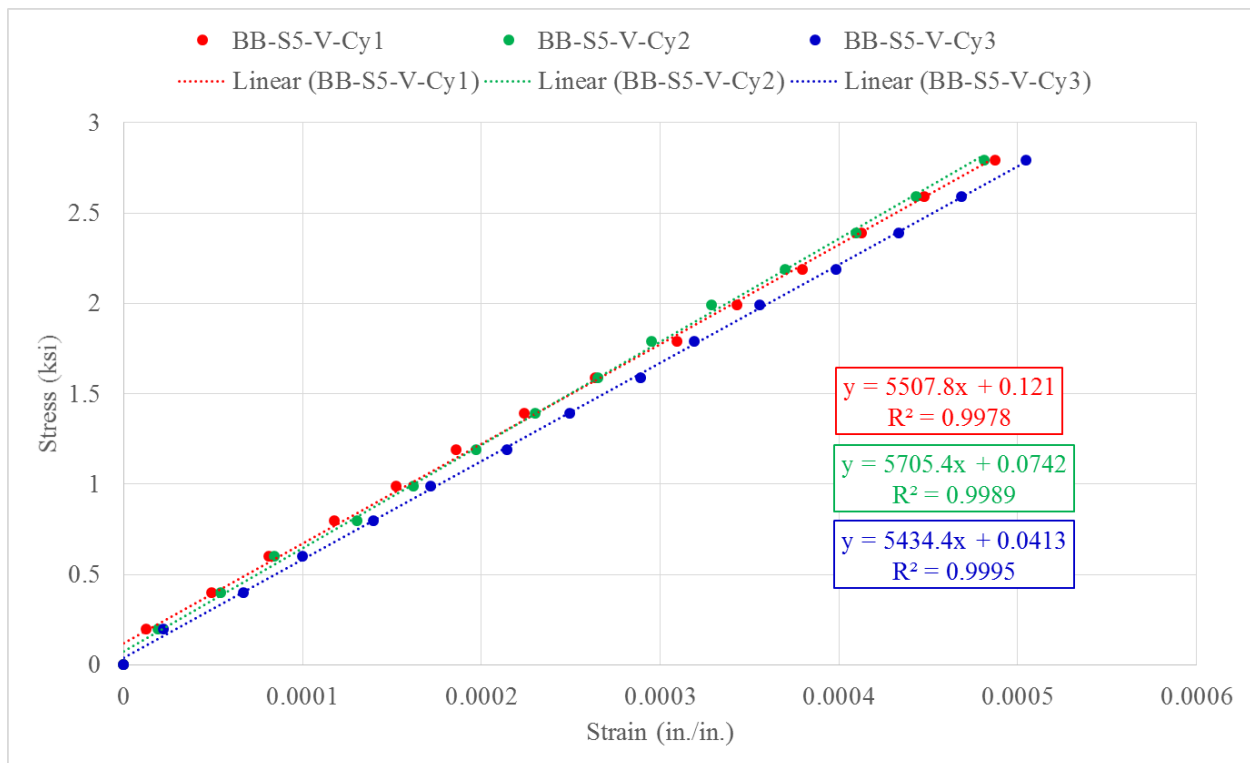
Figure 317: Modulus of elasticity of UHPC used in Specimen 5 at the end of fatigue test.
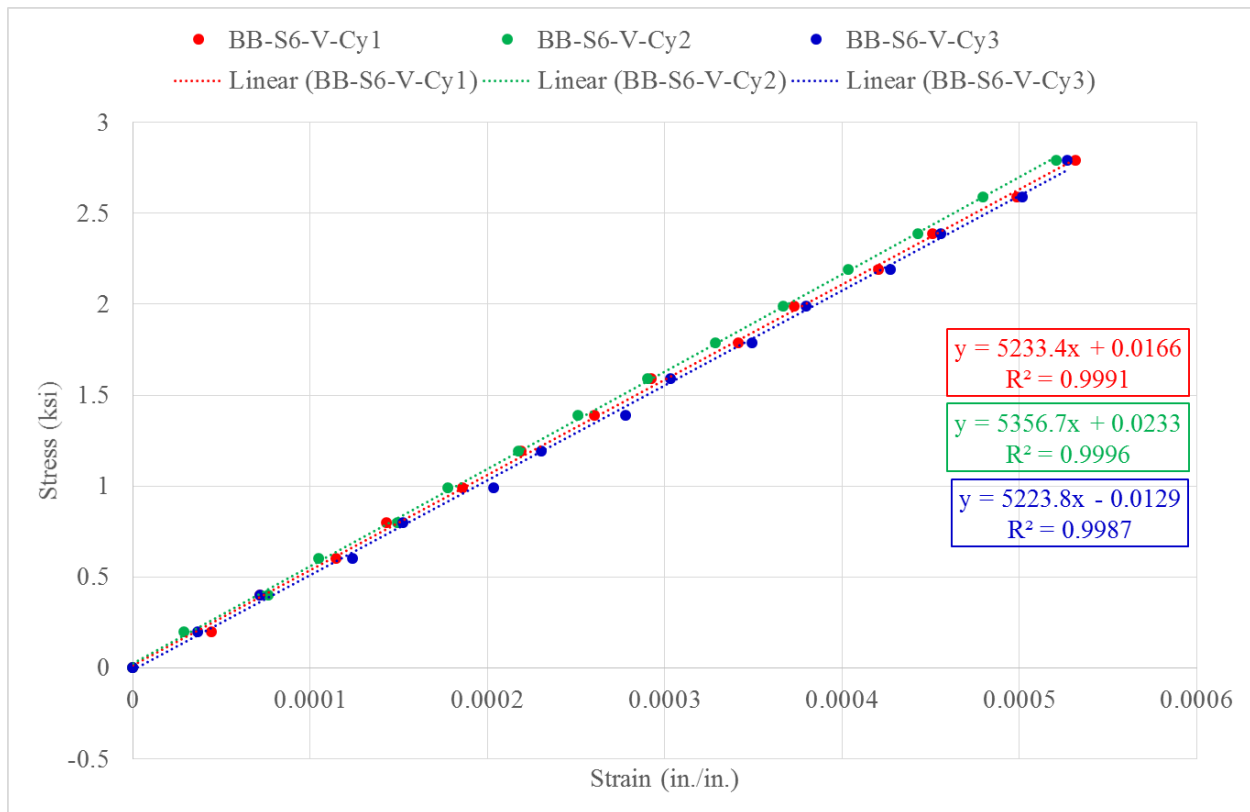
Figure 318: Modulus of elasticity of UHPC used in Specimen 6 at the start of fatigue test.
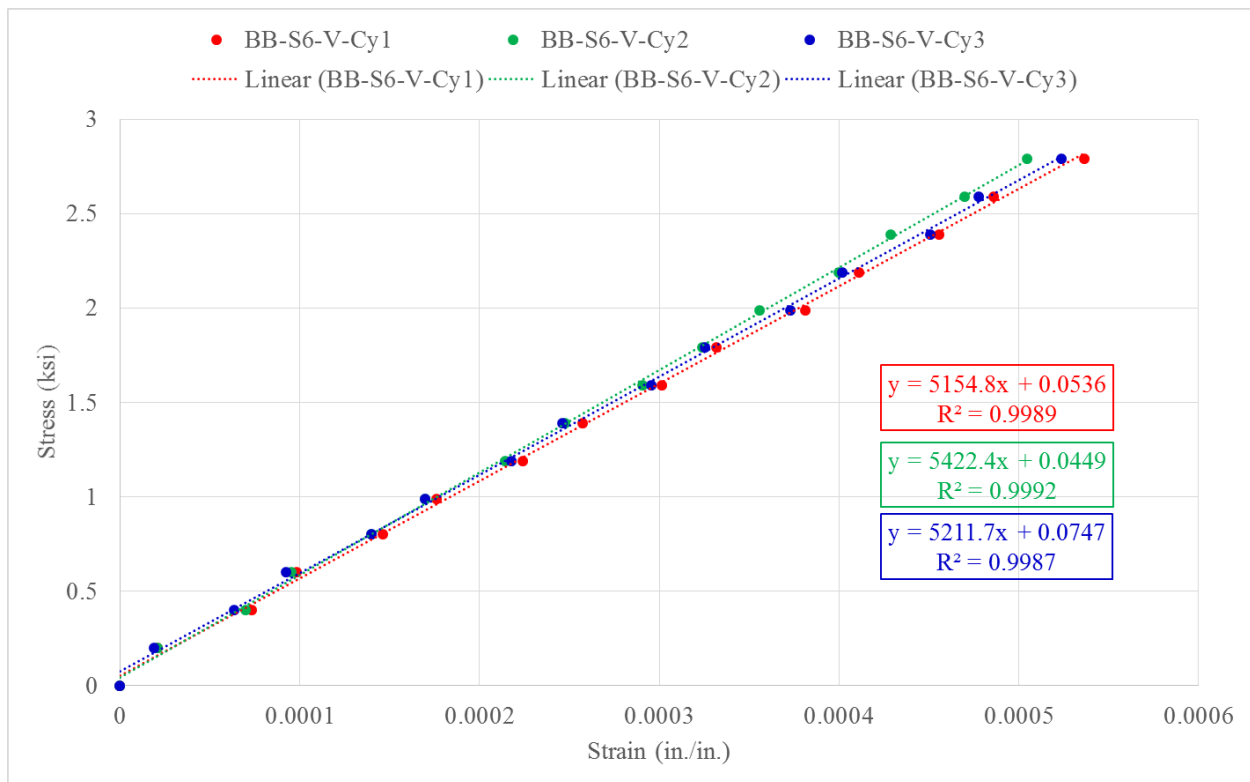
Figure 319: Modulus of elasticity of UHPC used in Specimen 6 at the end of fatigue test.

305

Connection material shrinkage
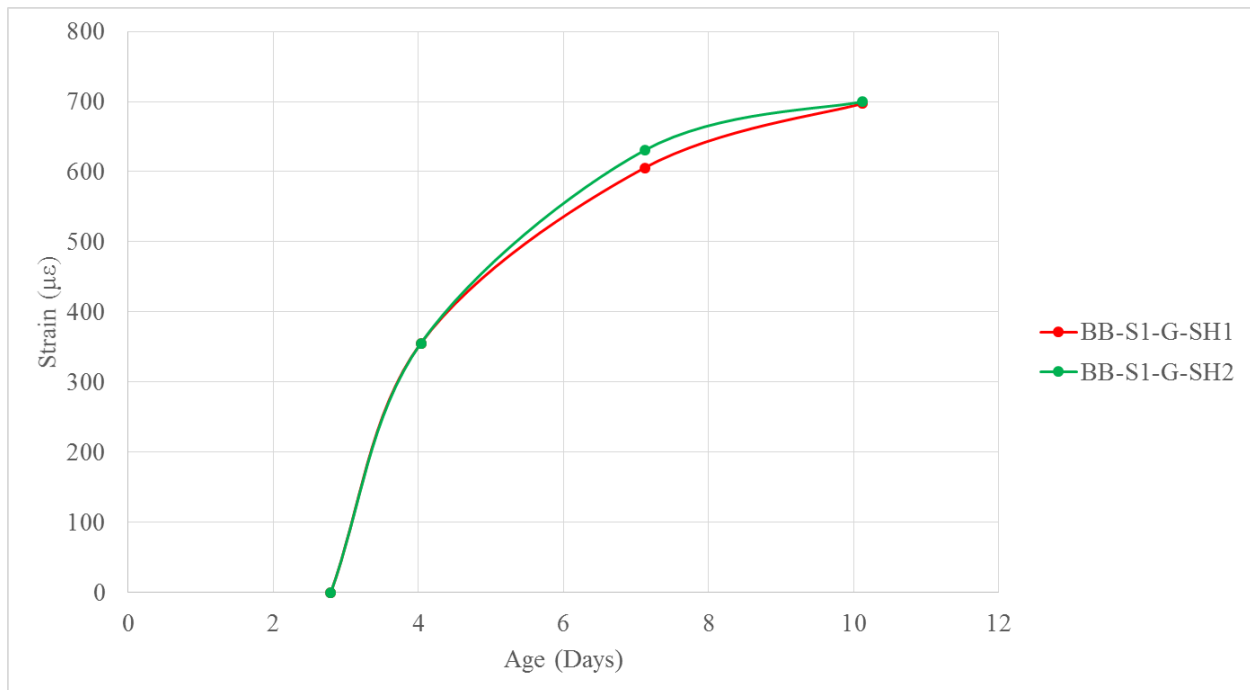
Figure 320: Shrinkage of grout used in Specimen 1.
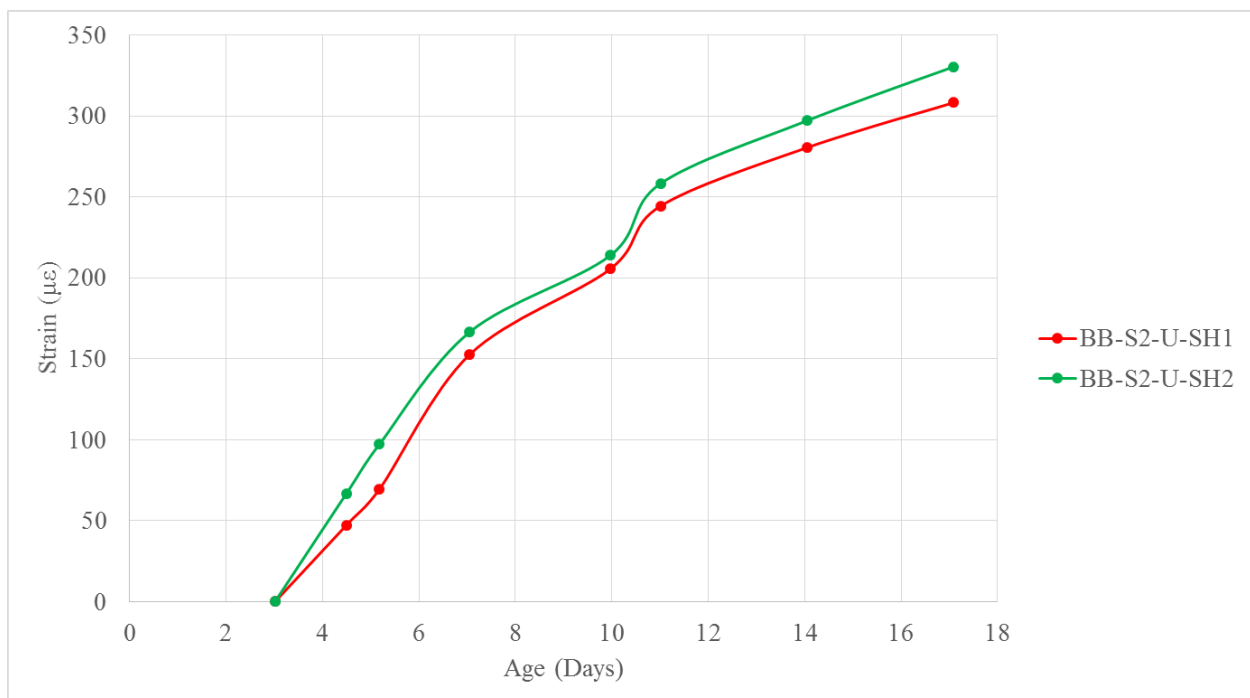
Figure 321: Shrinkage of UHPC used in Specimen 2.
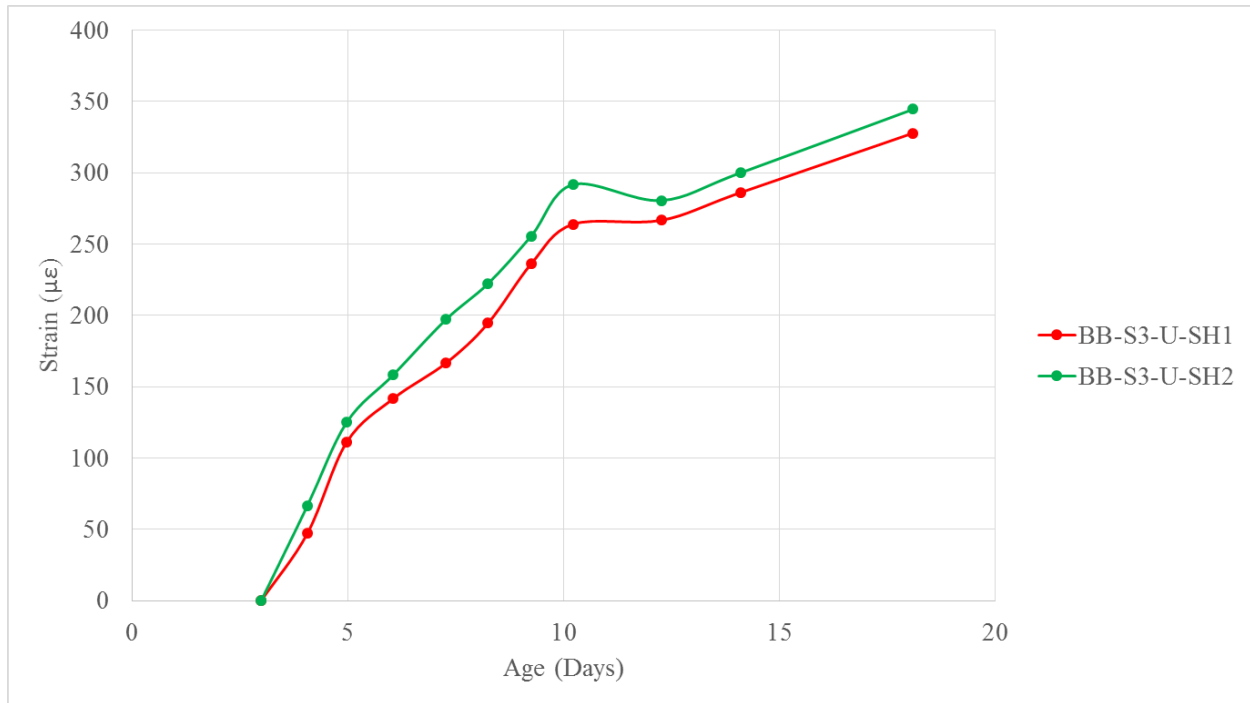
Figure 322: Shrinkage of UHPC used in Specimen 3.
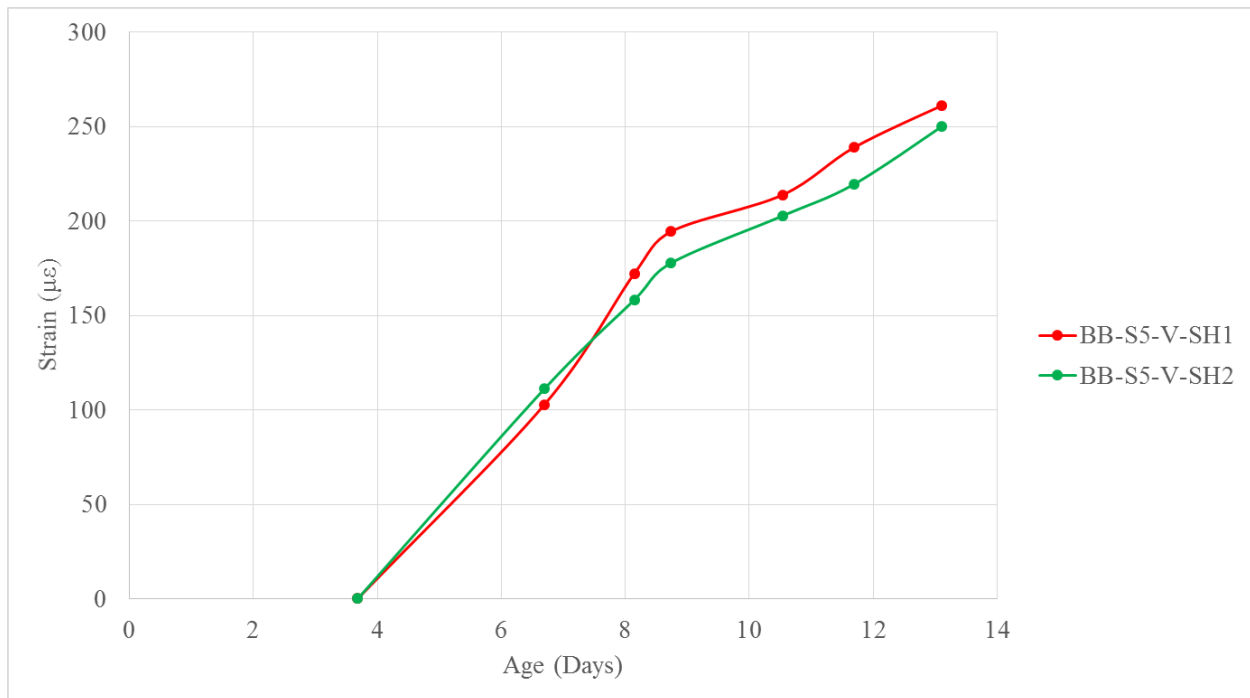
Figure 323: Shrinkage of VHPC used in Specimen 5.
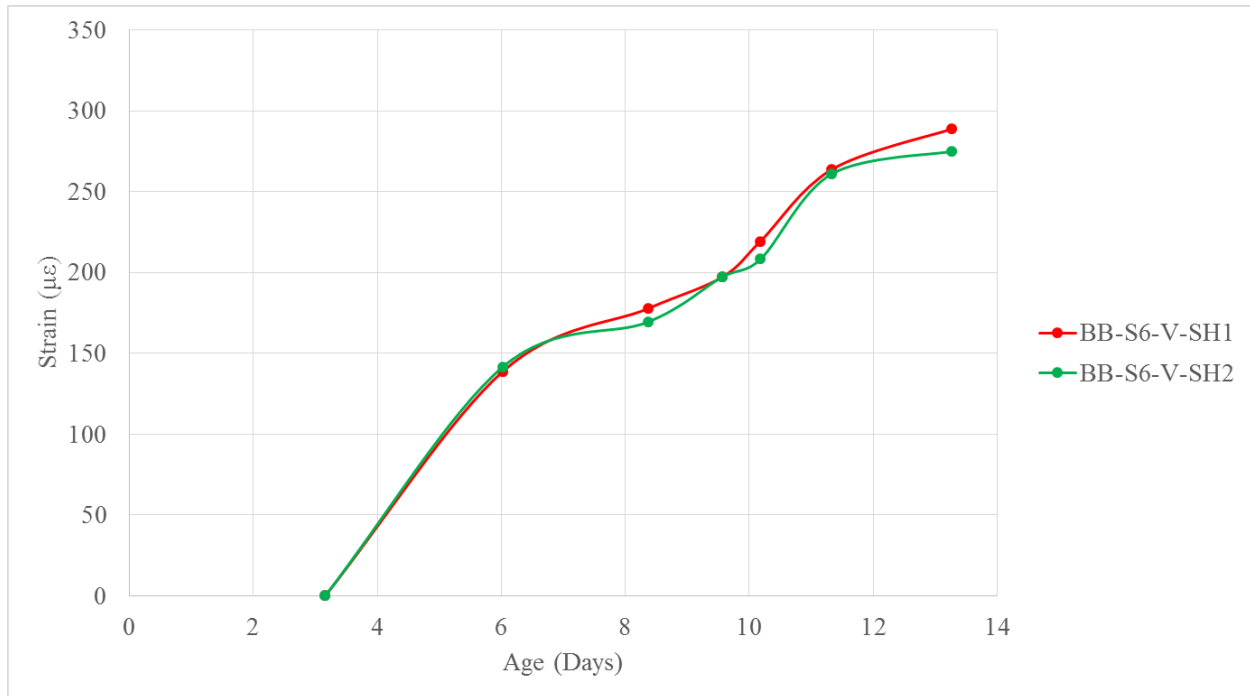
Figure 324: Shrinkage of VHPC used in Specimen 6.

Topping concrete compressive strength

Table 46: Compressive strengths of topping concrete at the start of fatigue test.

Specimen	Age (Days)	Cylinder	Failure Load (lb)	Strength (psi)	Average Strength (psi)	Time (sec)	Load Rate (lb/sec)
S3	4	BB-S3-T-Cy1	47500	3779.93	3832.982	104	456.7
		BB-S3-T-Cy2	48500	3859.507		122	397.5
		BB-S3-T-Cy3	48500	3859.507		110	440.9
S6	4	BB-S6-T-Cy1	26000	2069.014	2161.855	53	490.6
		BB-S6-T-Cy2	28500	2267.958		59	483.1
		BB-S6-T-Cy3	27000	2148.592		56	482.1

Table 47: Compressive strengths of topping concrete at the end of fatigue test.

Age (Days)	Cylinder	Failure Load (lb)	Strength (psi)	Average Strength (psi)	Time (sec)	Load Rate (lb/sec)
11	BB-S3-T-Cy4	55000	4376.761	4509.39	118	466.1
	BB-S3-T-Cy5	60000	4774.648		132	454.5
	BB-S3-T-Cy6	55000	4376.761		120	458.3
11	BB-S6-T-Cy4	42000	3342.254	3474.883	86	488.4
	BB-S6-T-Cy5	43000	3421.831		93	462.4
	BB-S6-T-Cy6	46000	3660.564		103	446.6

Appendix F

The sub-assemblage test data not presented in the results section is presented in this appendix. The data primarily focuses on the support reactions recorded by load cells and the vertical deflections recorded by the LVDTs under the specimens. The wire-potentiometer measurements for the first two specimens have not been presented because of the noise in the data as discussed in Chapter 6. The measurements for the surface strains and the bonded strain gauges on the steel beams are not presented since that data was not used in any of the prior discussions. Moreover, the magnitude of the surface strains was very small in the concrete beam sections owing to much higher stiffness as compared to the joints. The data is presented for each specimen independently.

Specimen 1 data
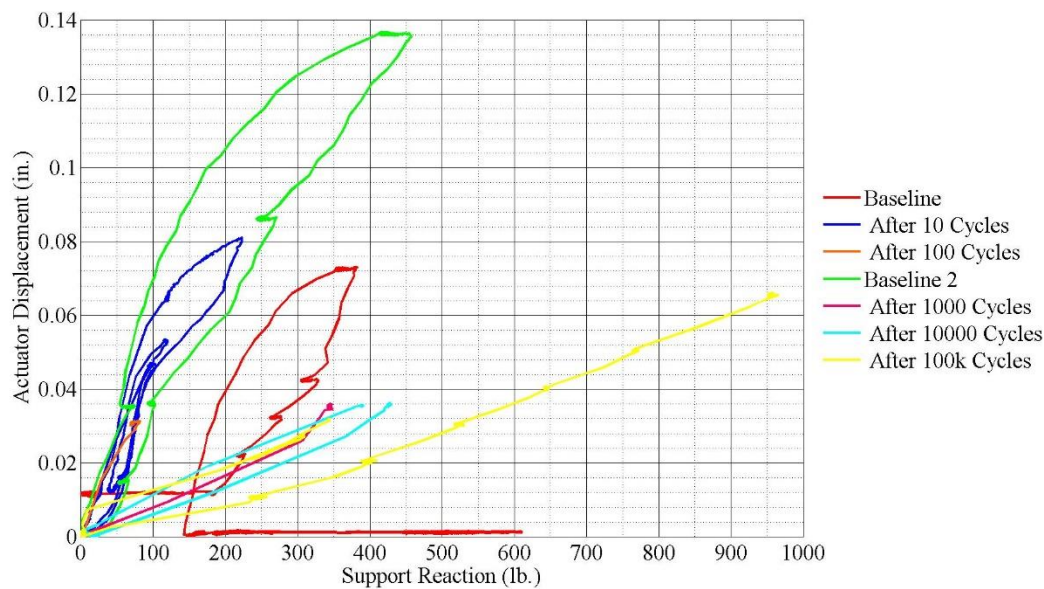
Figure 325: S1 – variation in east load cell values on exterior south beam.
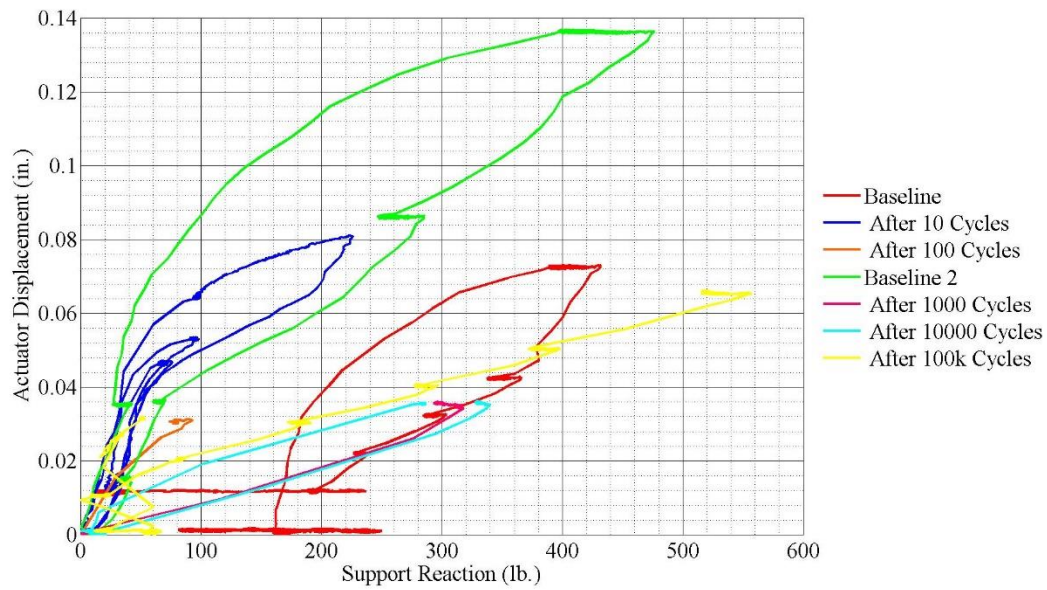
Figure 326: S1 – variation in west load cell values on exterior south beam.
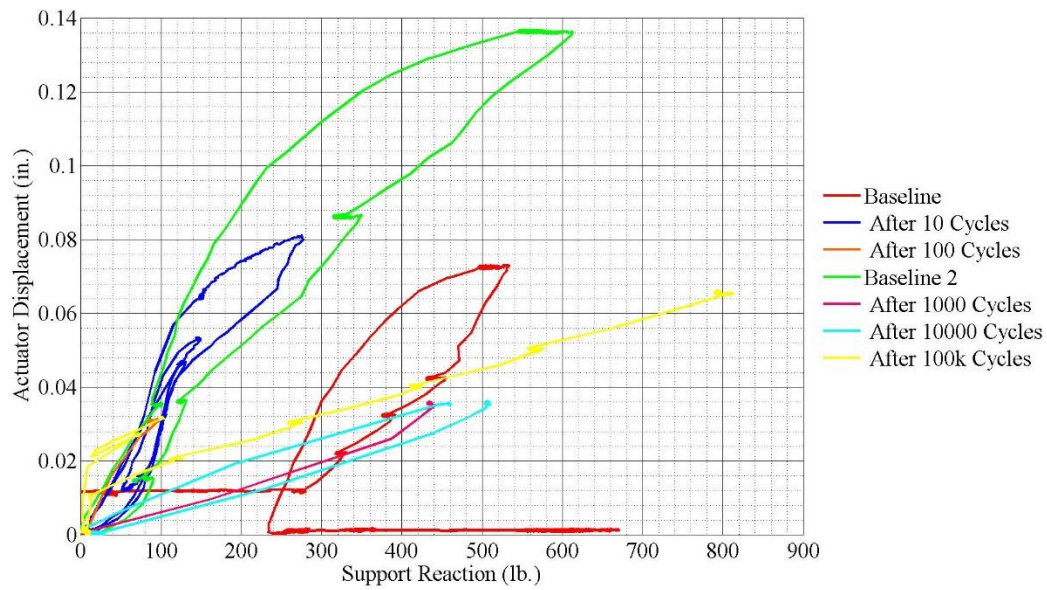
Figure 327: S1 – variation in east load cell values on interior south beam.
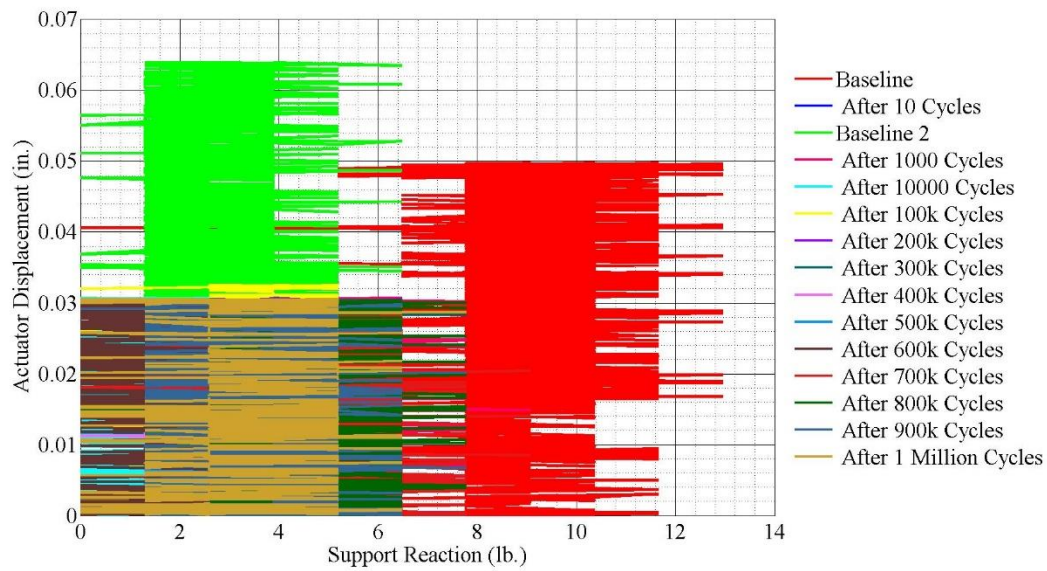
311
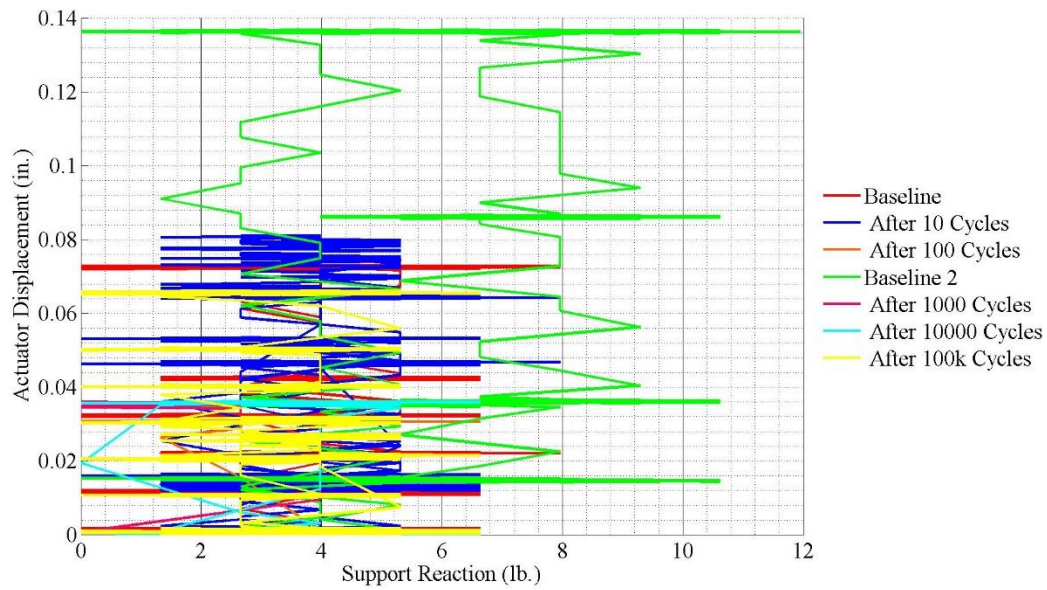
Figure 328: S1 – variation in west load cell values on interior south beam.

NOTE: The west load cell on the interior south beam in S1, shown in Figure 328, did not record any data on account that it did not work for the duration of testing and was replaced in the next test.
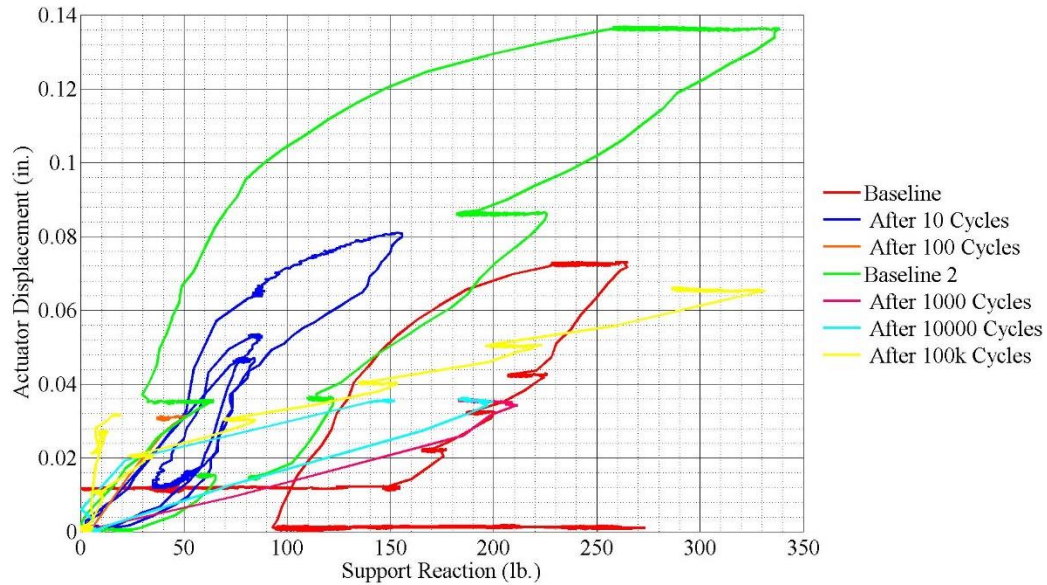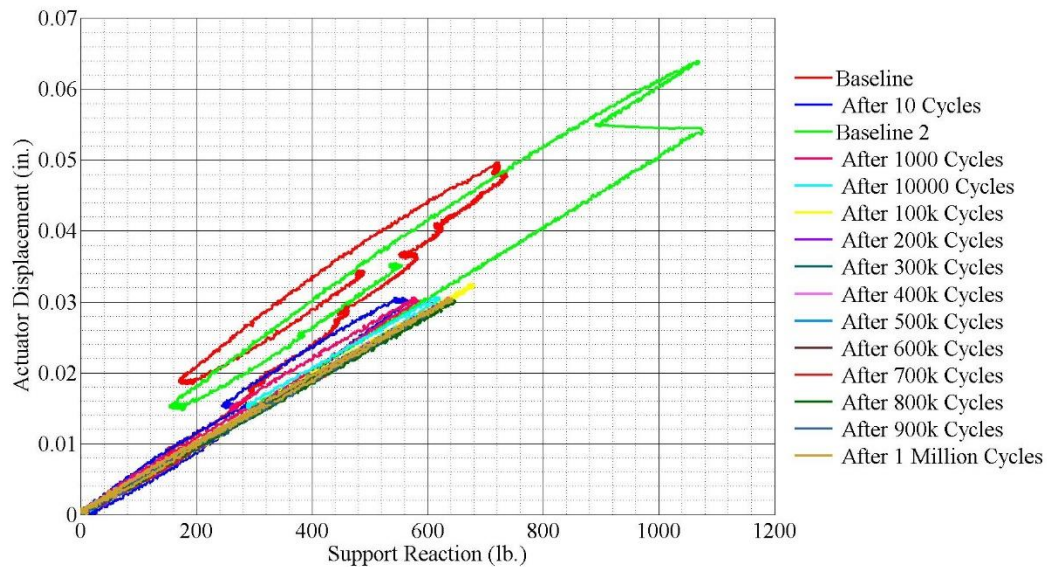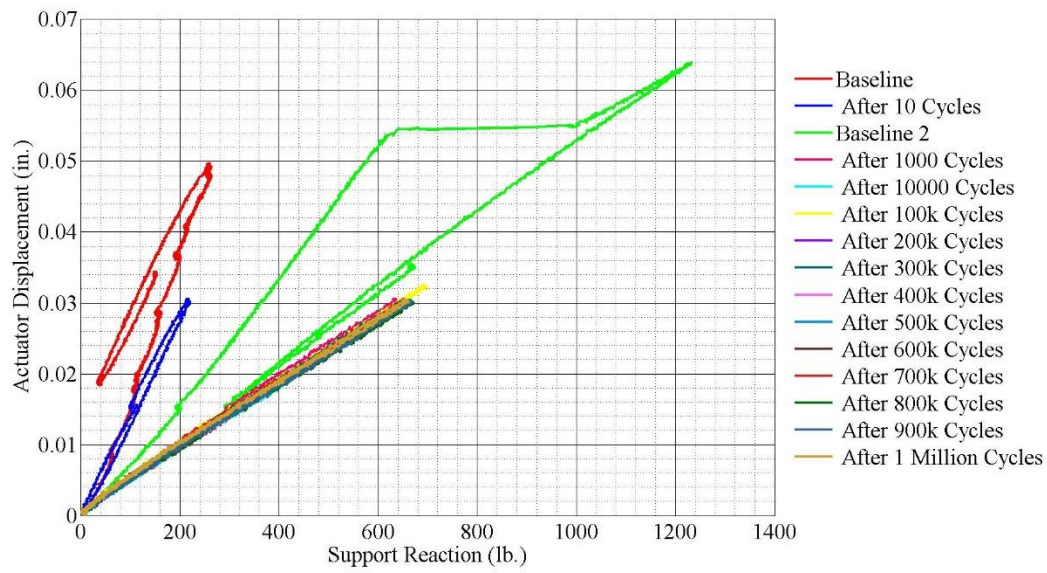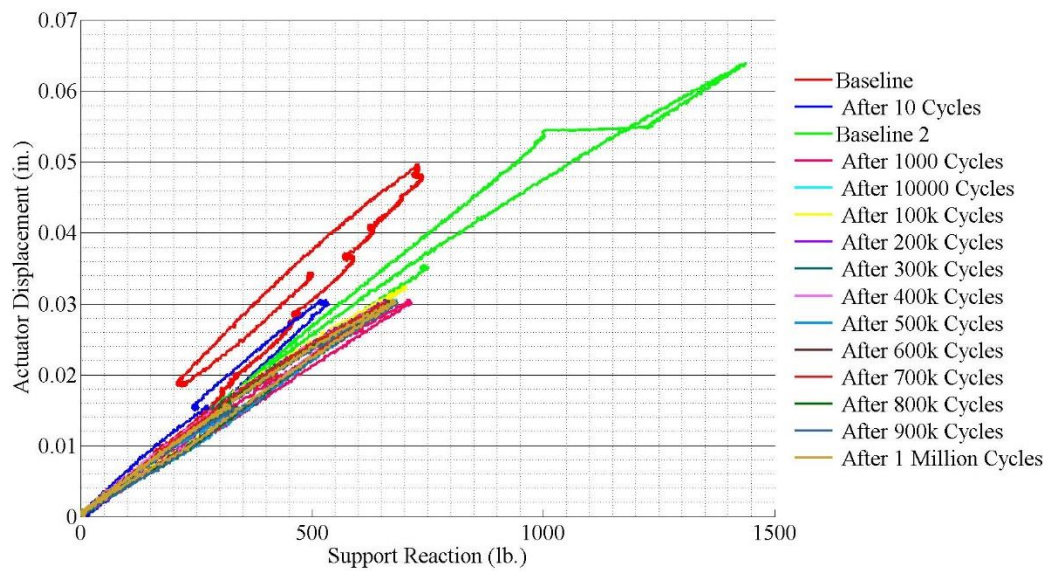

Figure 329: S1 – variation in east load cell values on interior north beam.
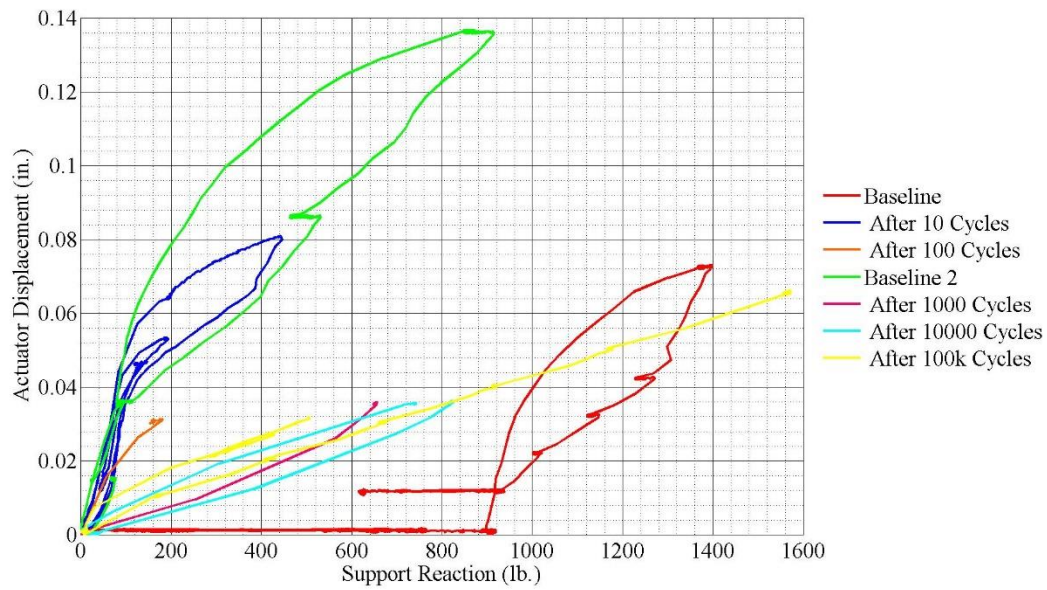
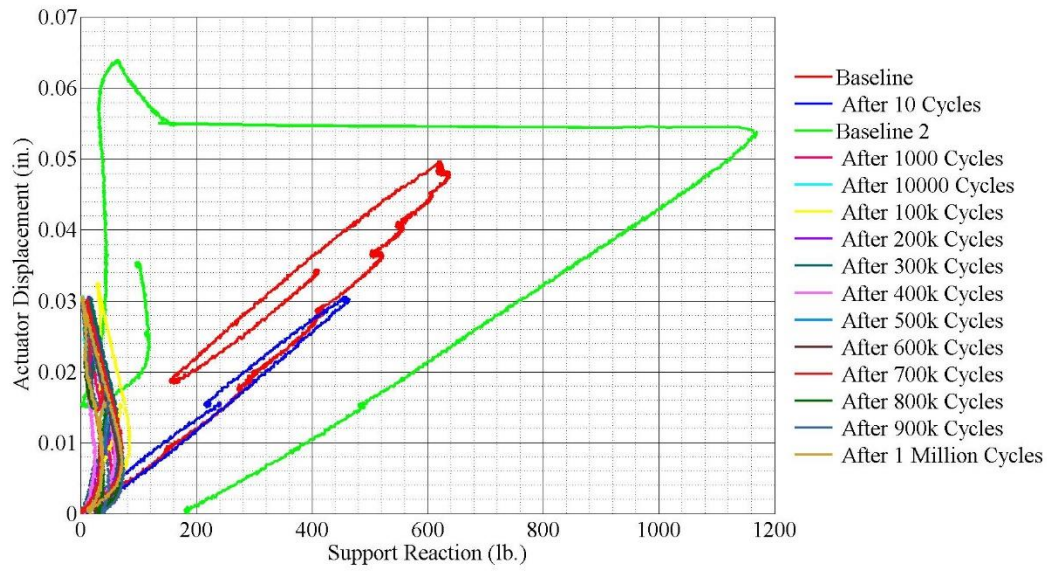*Figure 330: S1 – variation in west load cell values on interior north beam.*
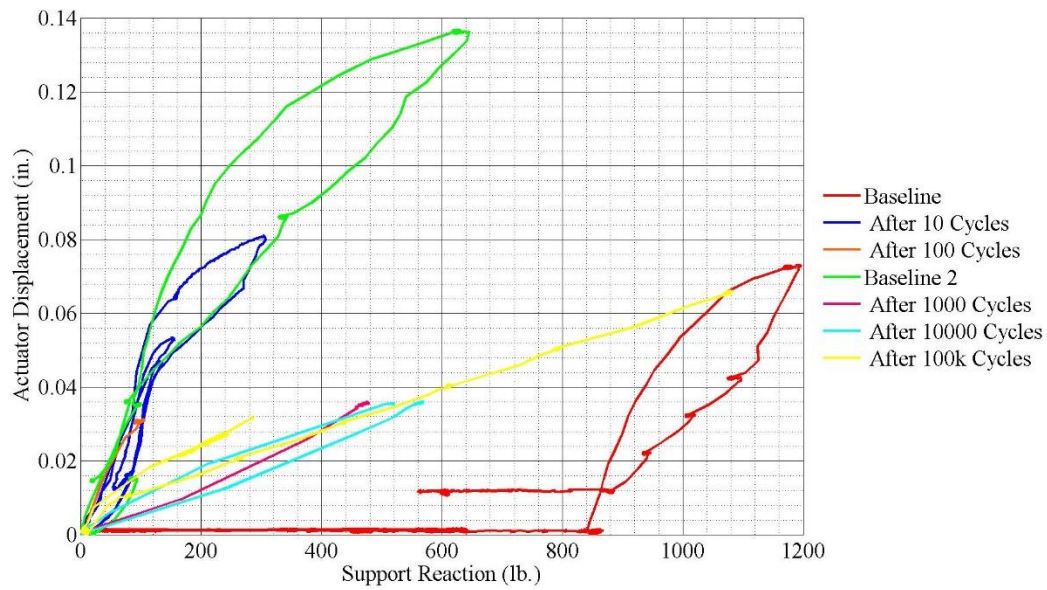
Figure 331: S1 – variation in east load cell values on exterior north beam.
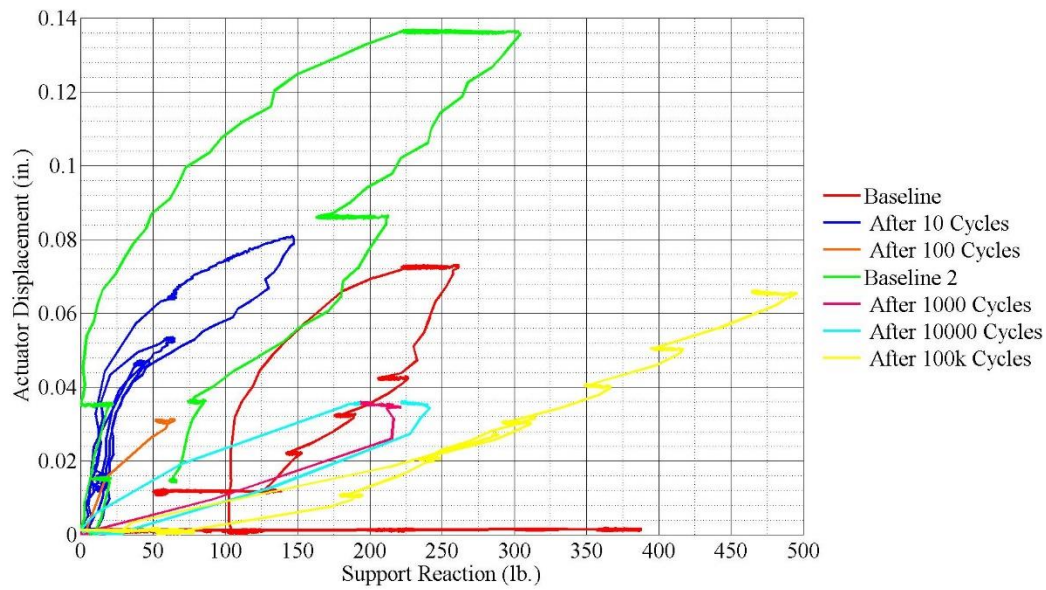
Figure 332: S1 – variation in west load cell values on exterior north beam.
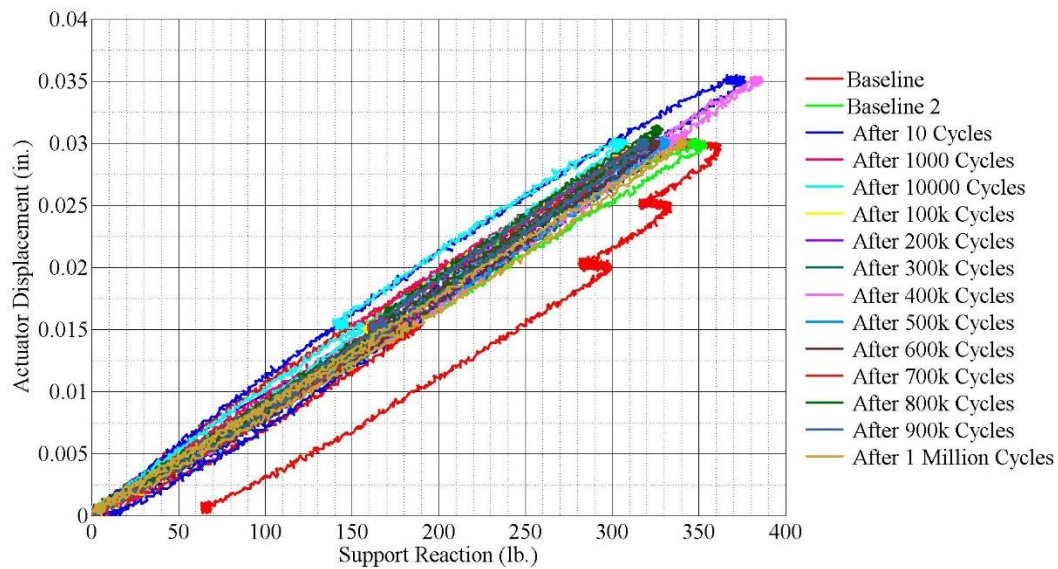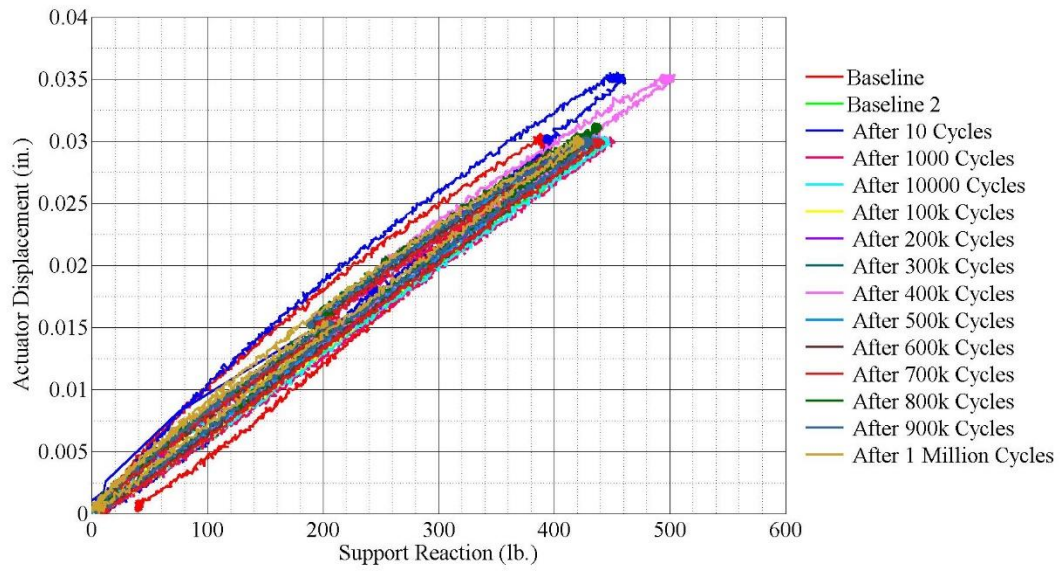
Specimen 2 data
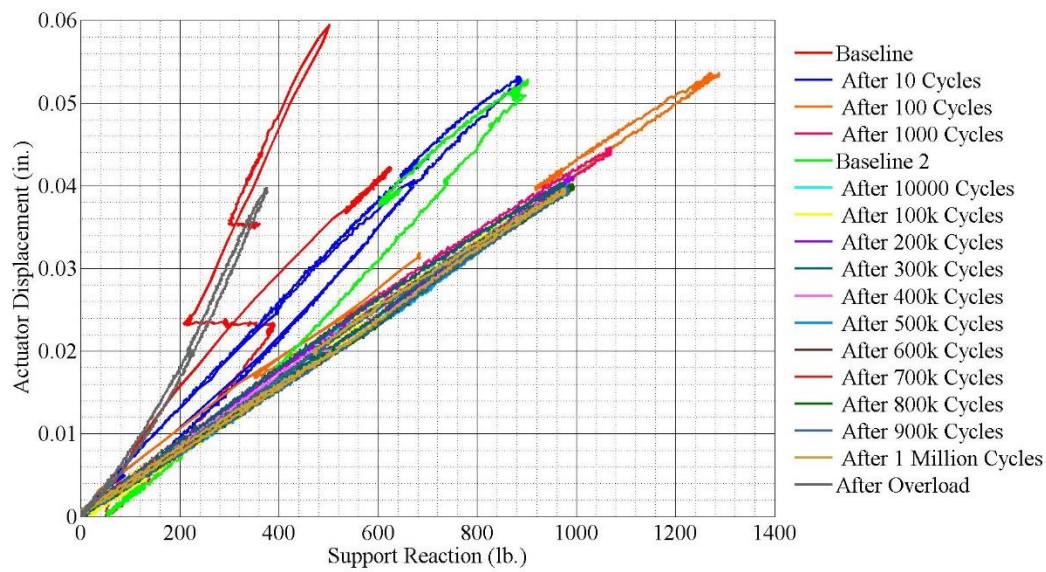
Figure 333: S2 – variation in load cell values on exterior south beam.
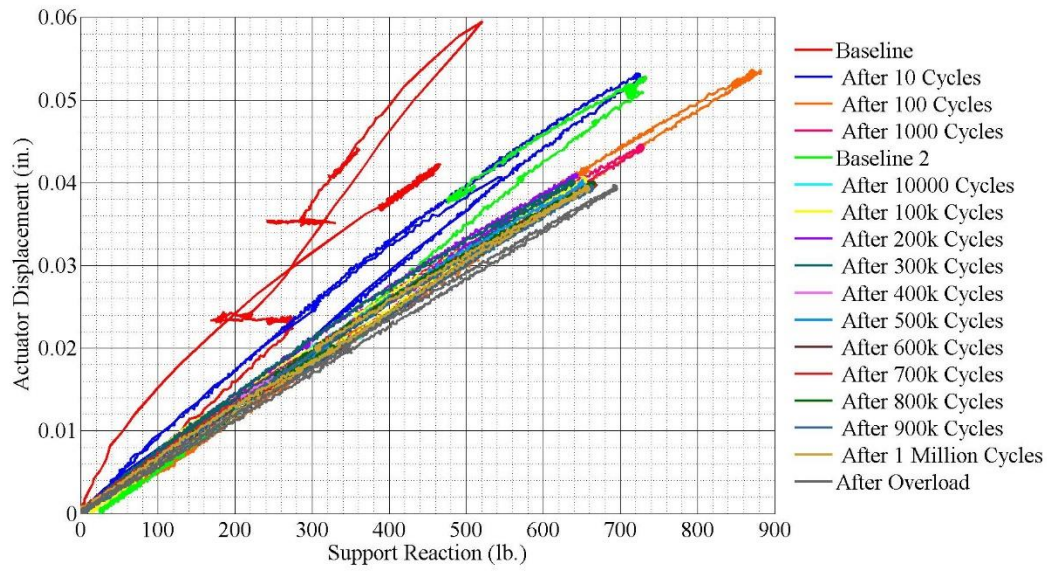
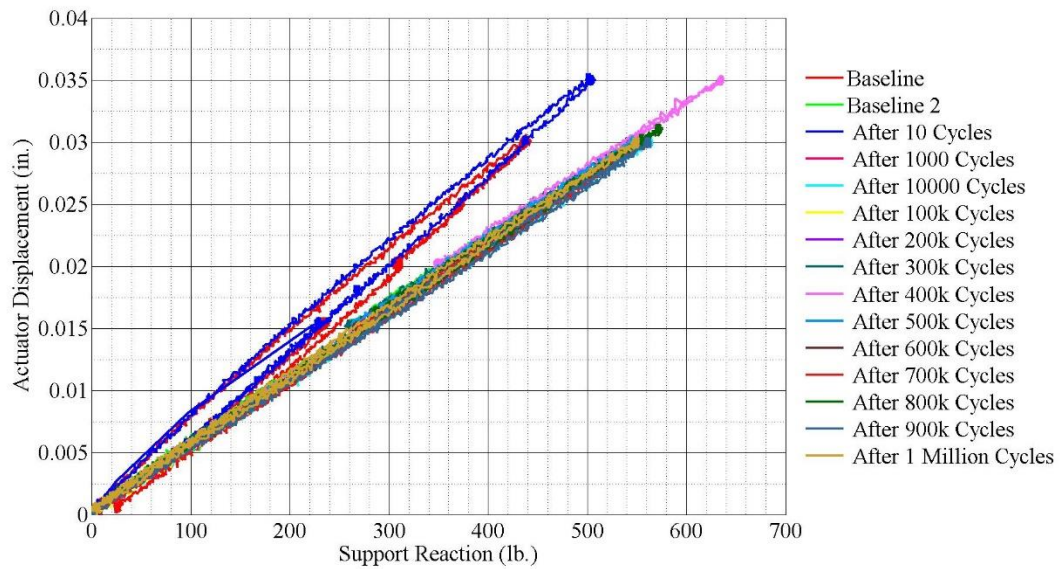*Figure 334: S2 – variation in east load cell values on interior south beam.*
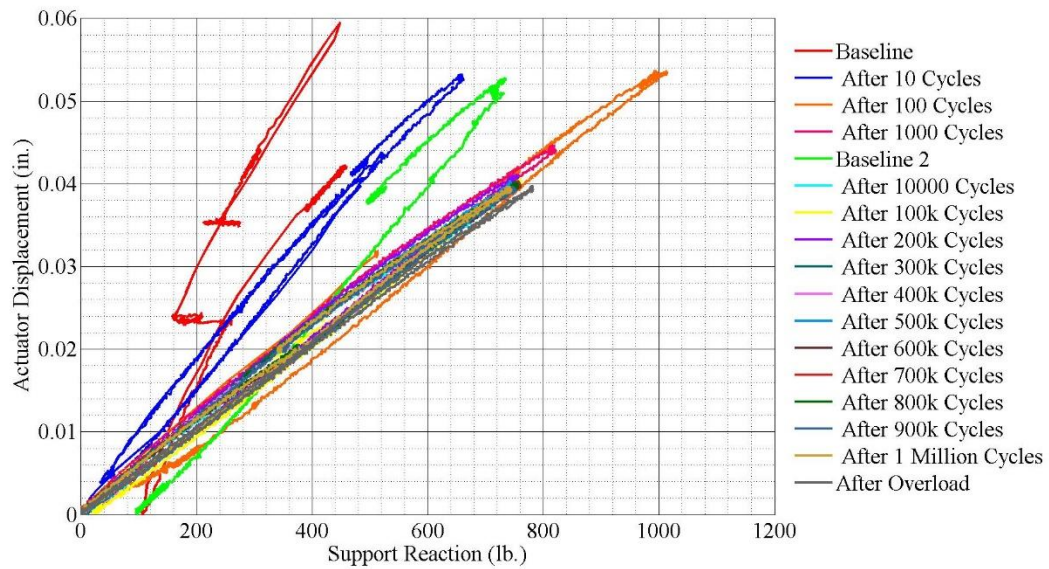
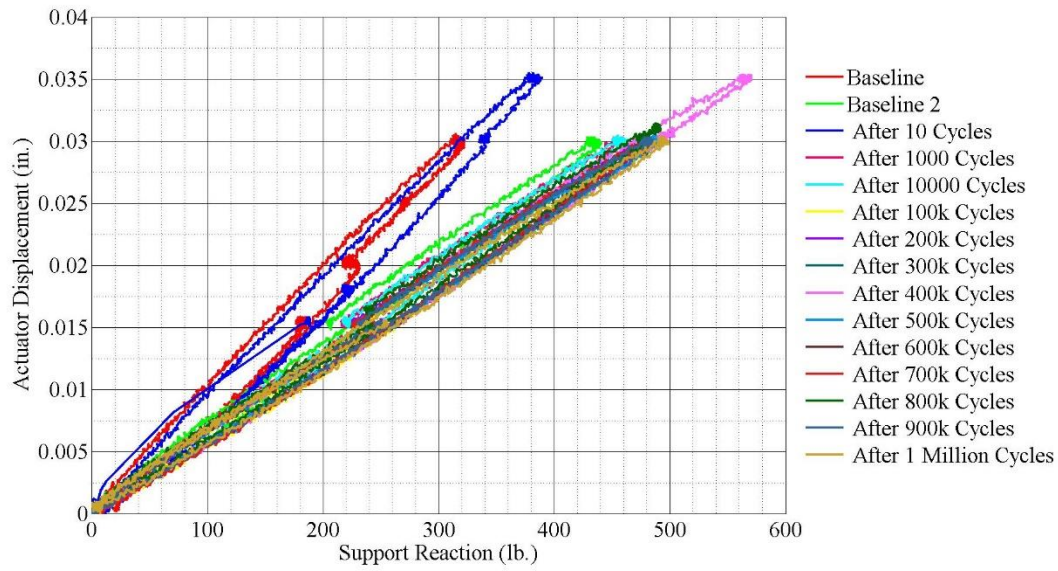*Figure 335: S2 – variation in west load cell values on interior south beam*

315
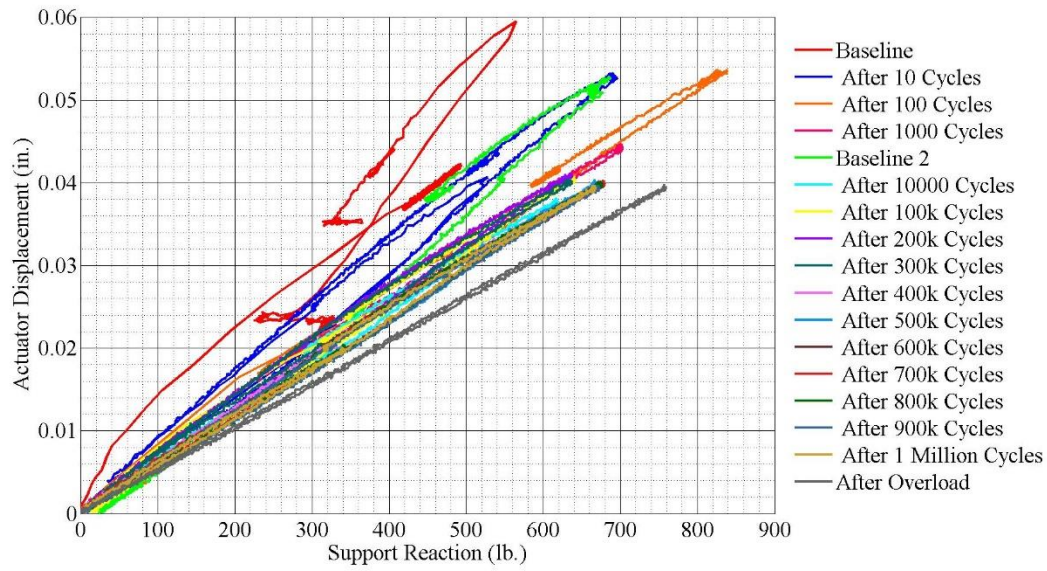
Figure 336: S2 – variation in east load cell values on interior north beam
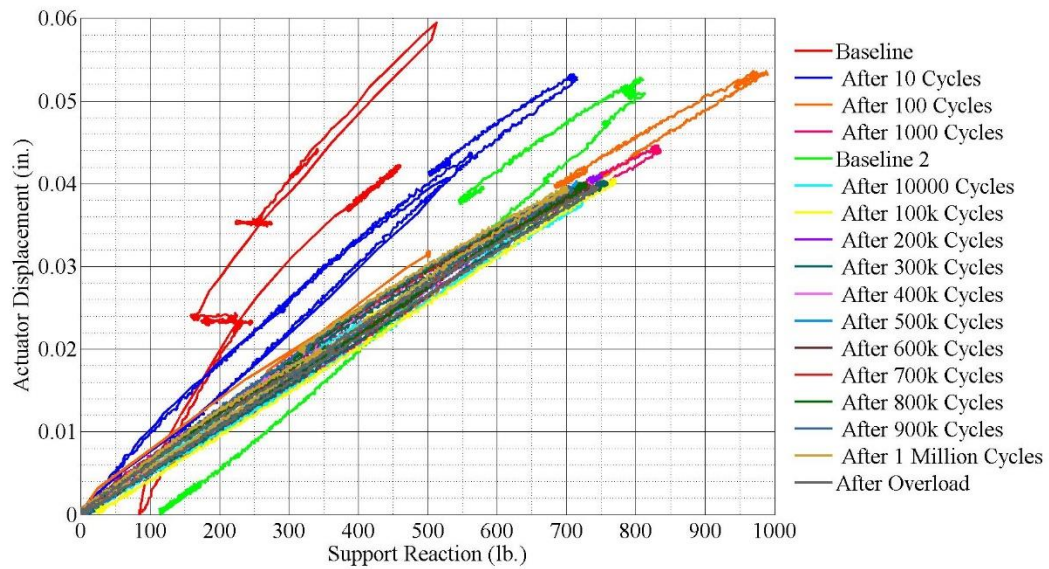
Figure 337: S2 – variation in west load cell values on interior north beam

316
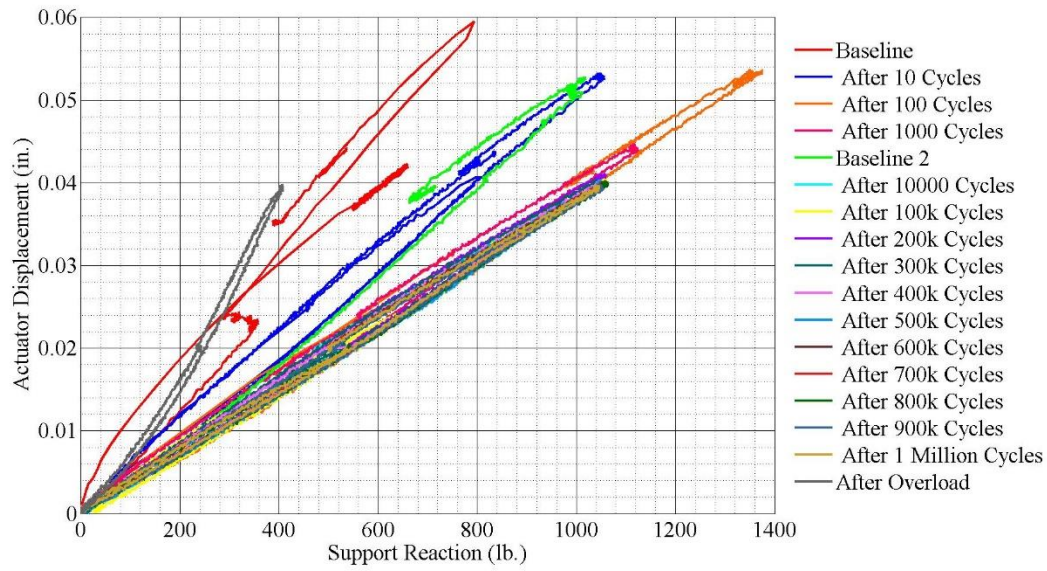
Figure 338: S2 – variation in load cell values on exterior north beam

Specimen 3 data
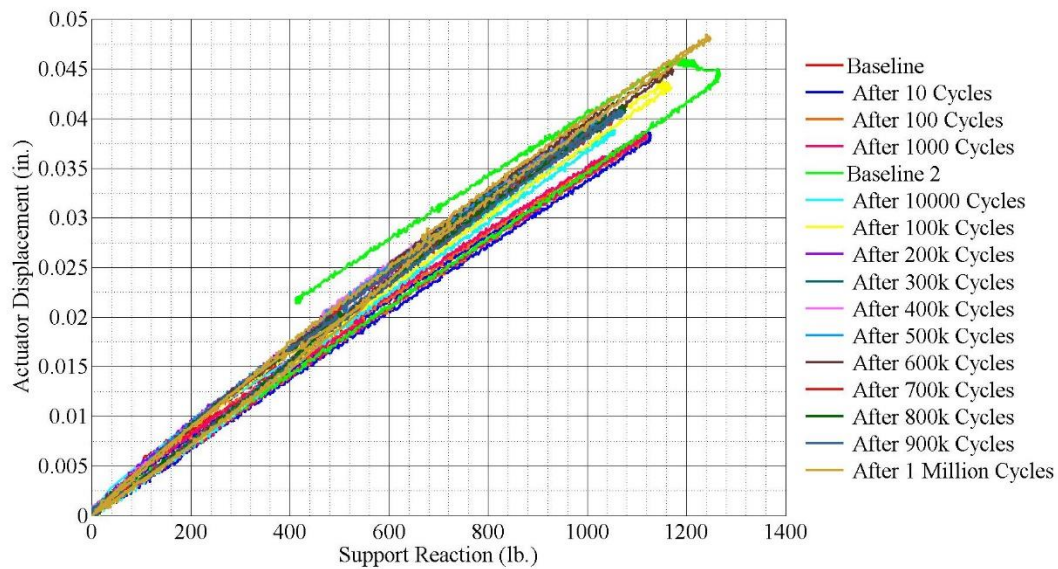
Figure 339: S3 – variation in load cell values on exterior south beam.
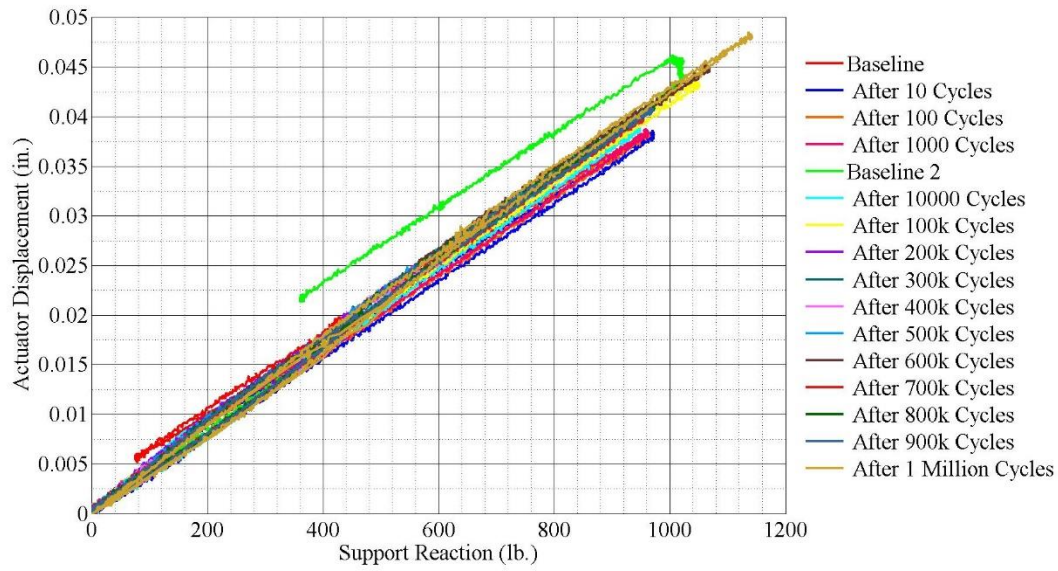
Figure 340: S3 – variation in east load cell values on interior south beam.
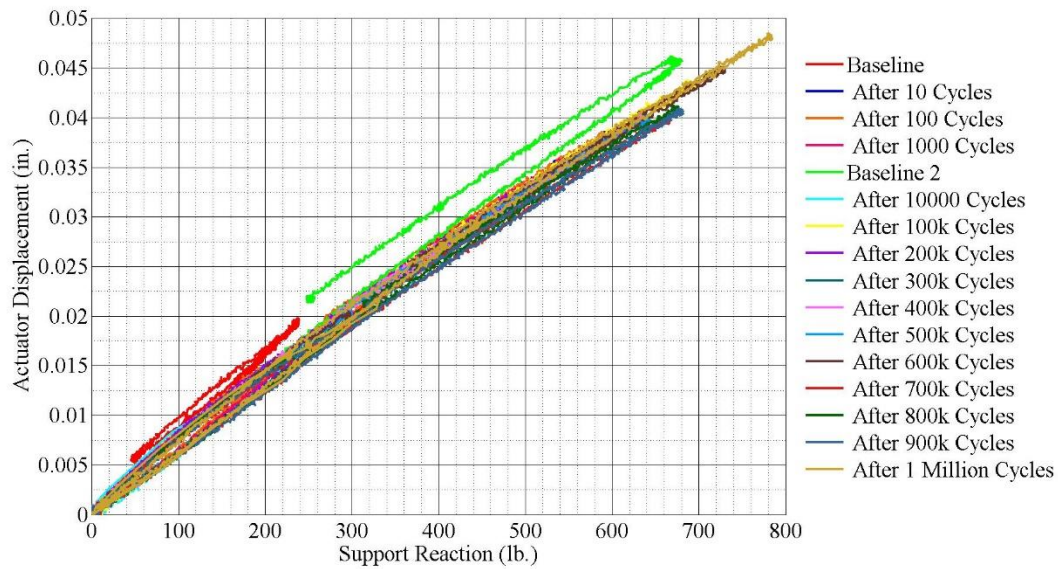
Figure 341: S3 – variation in west load cell values on interior south beam
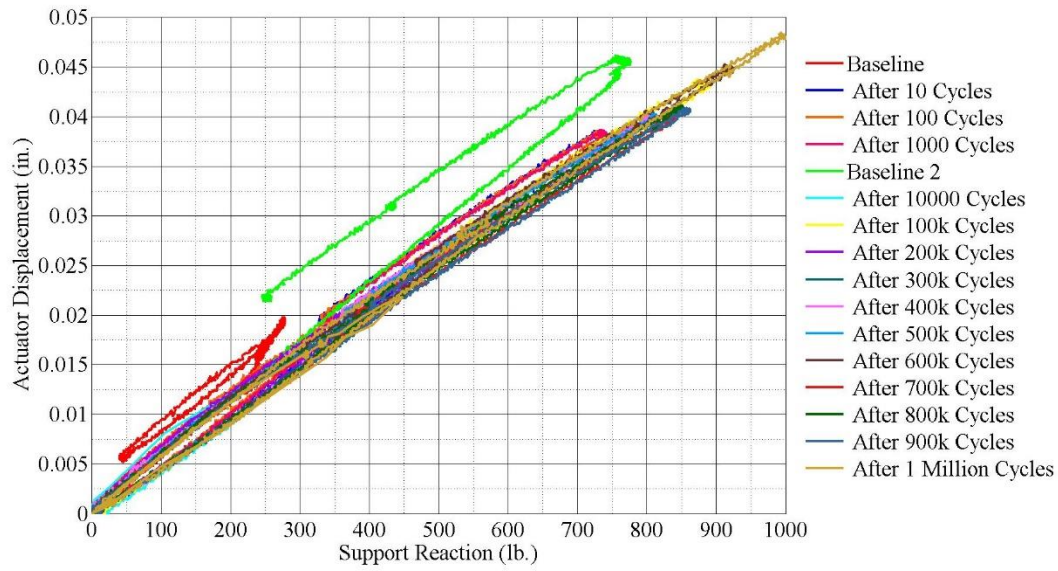
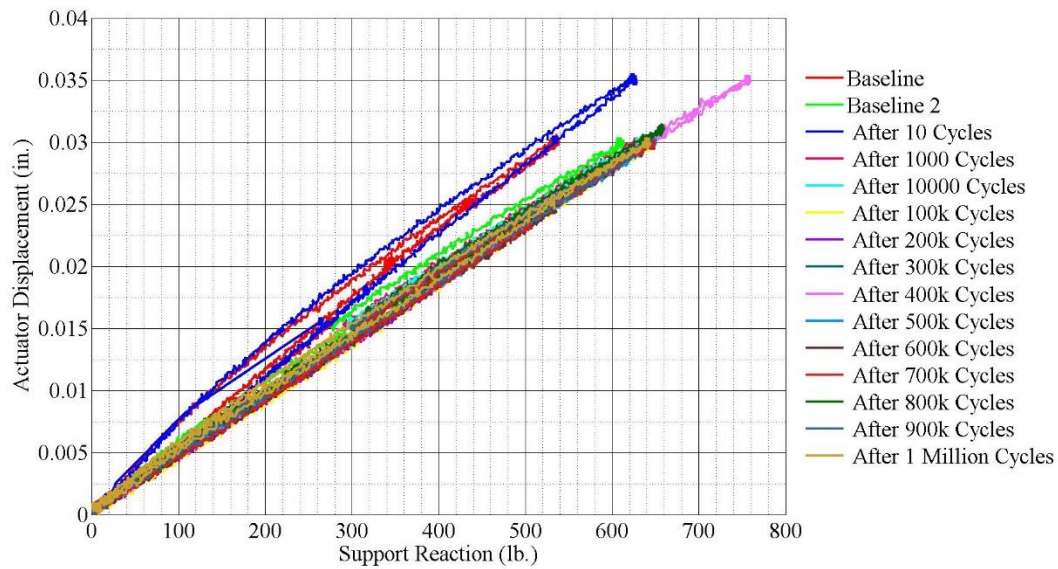*Figure 342: S3 – variation in east load cell values on interior north beam*
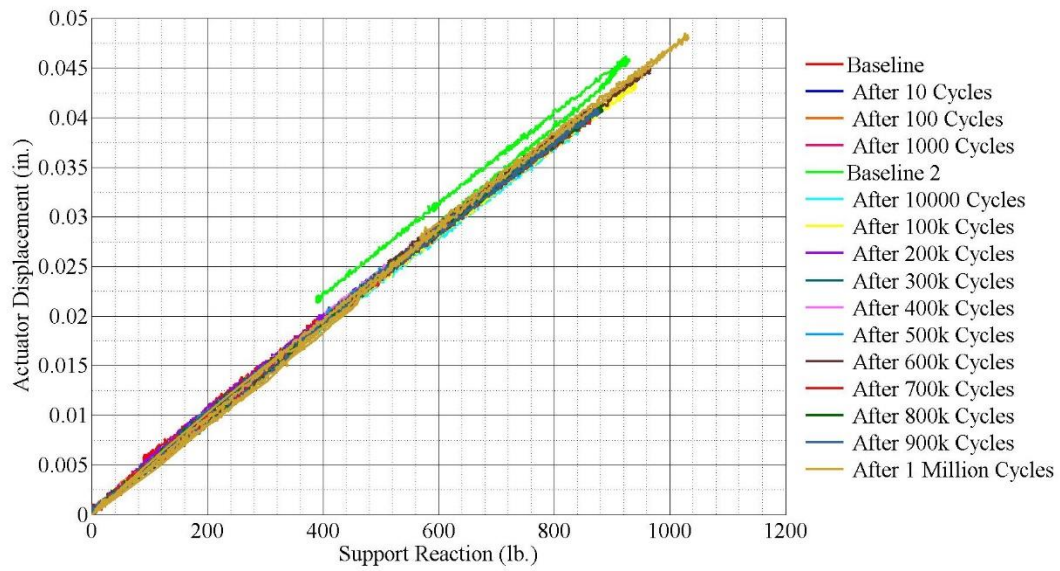
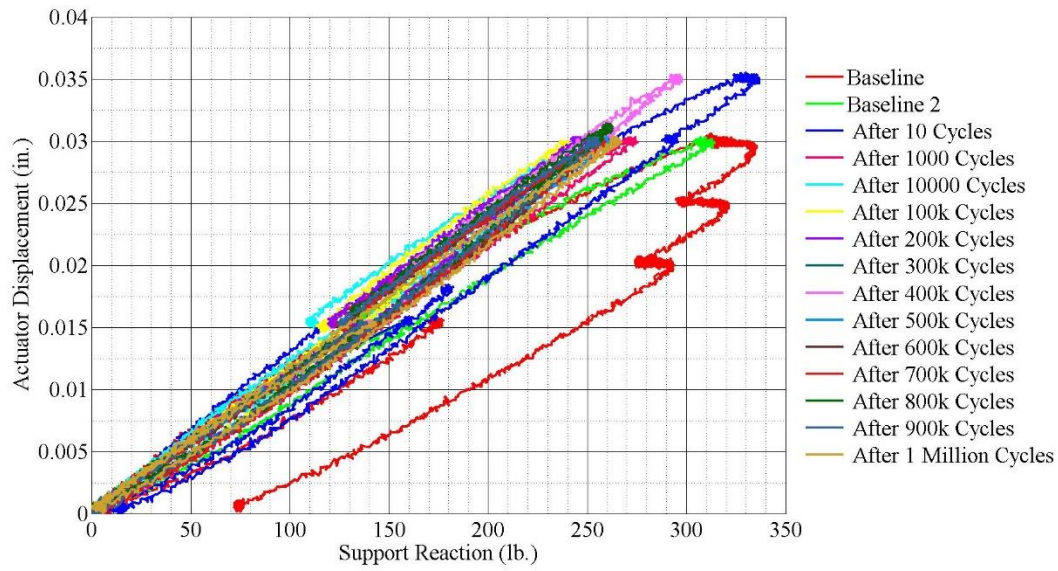*Figure 343: S3 – variation in west load cell values on interior north beam*

319
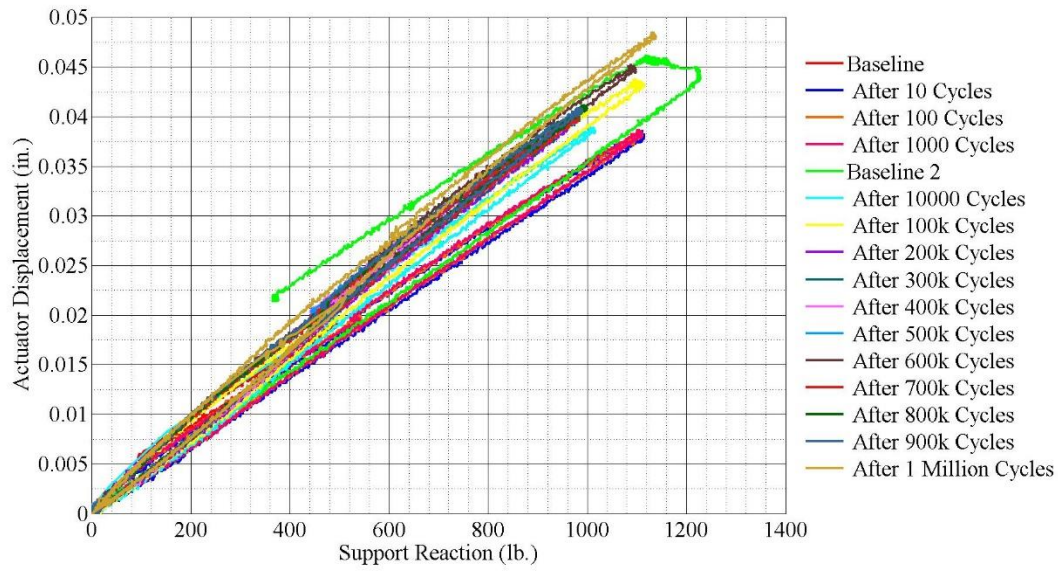
Figure 344: S3 – variation in load cell values on exterior north beam
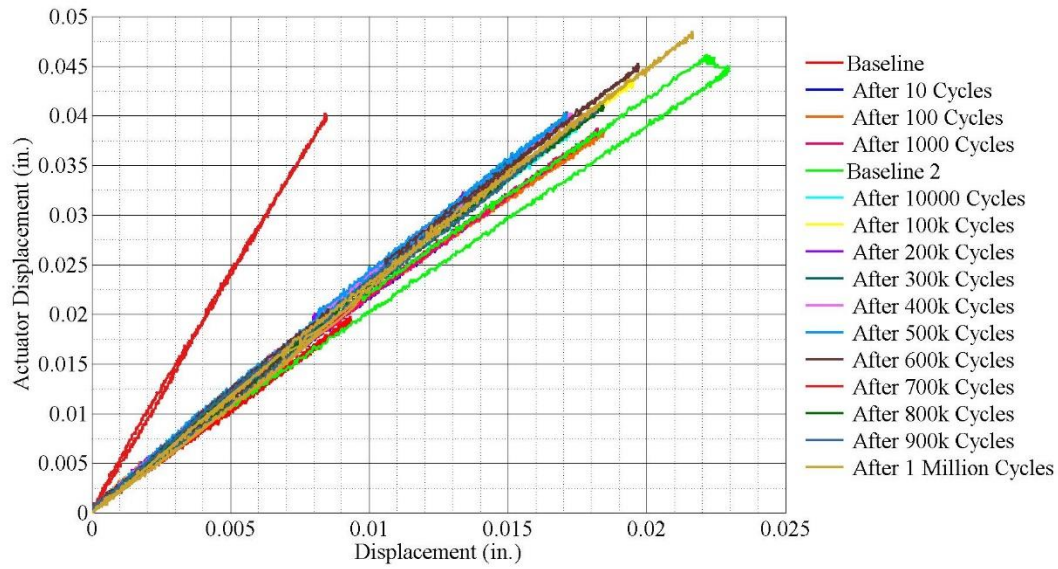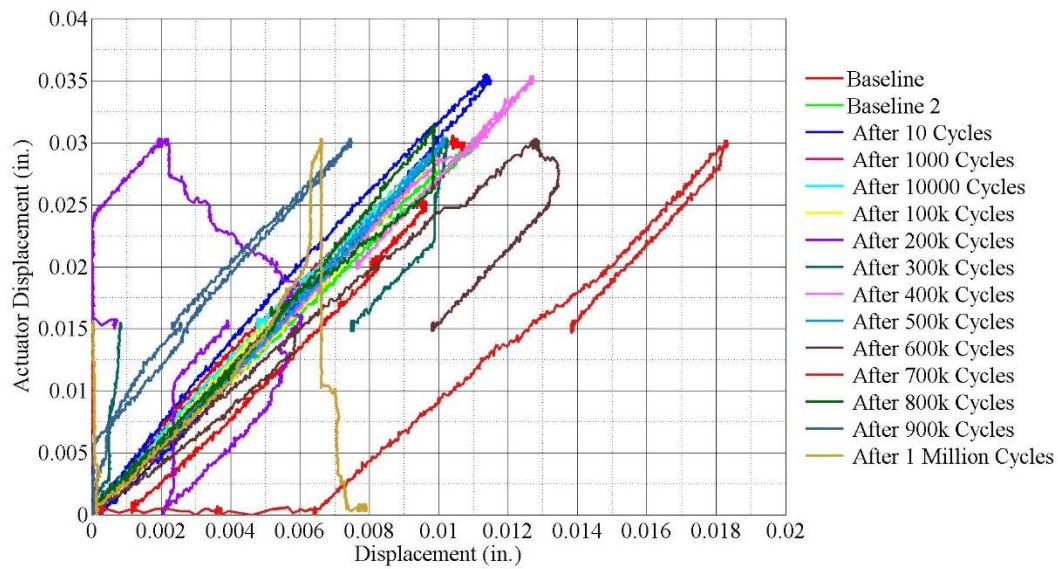

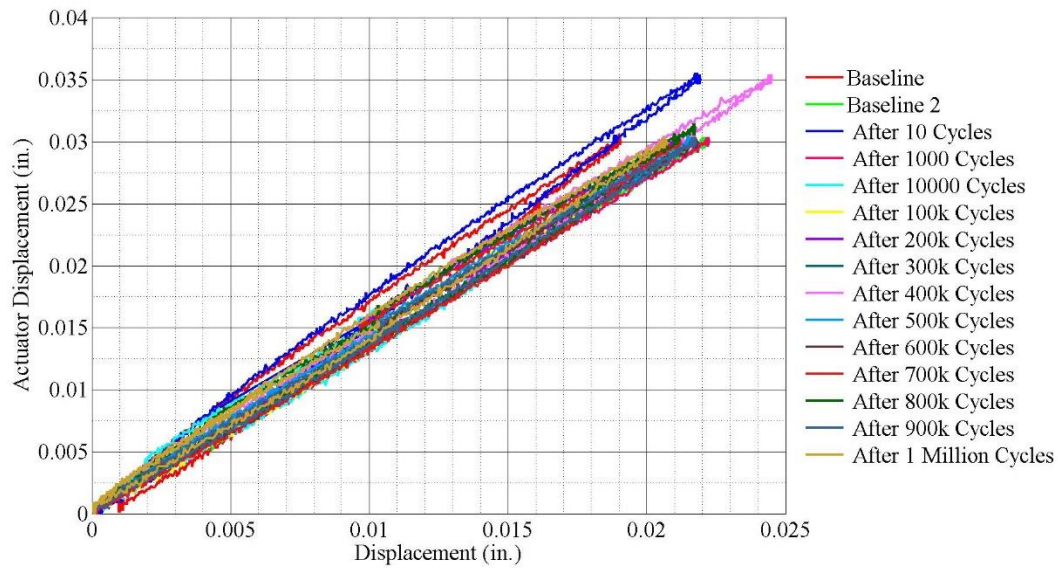*Figure 345: S3 – variation in vertical deflection near exterior south beam.*
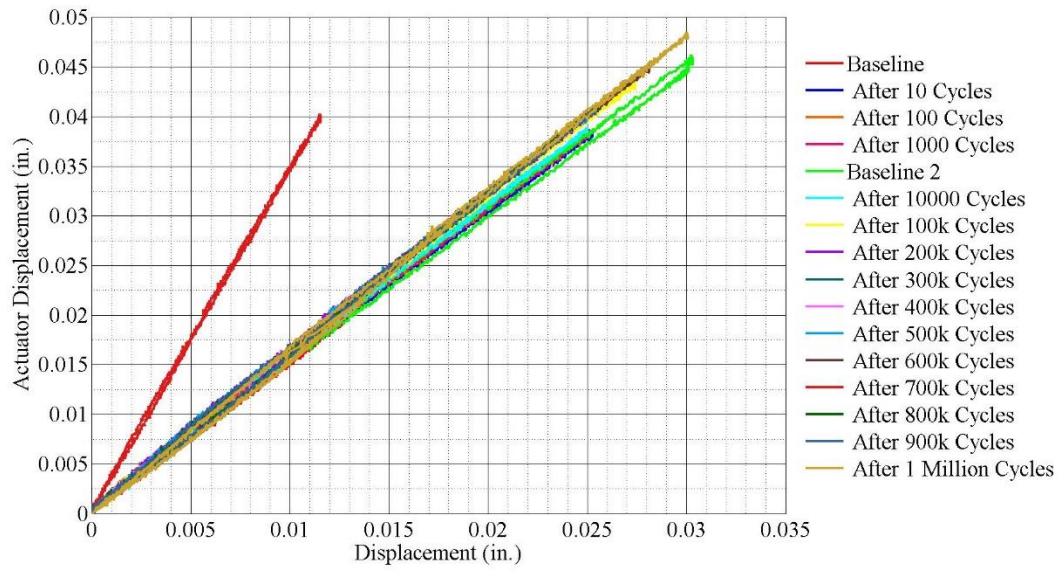
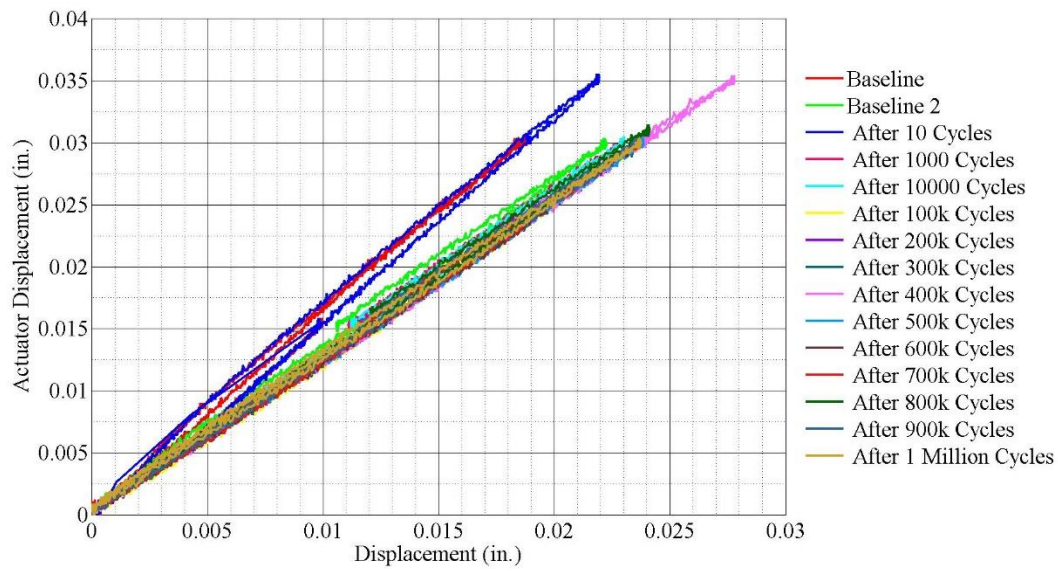*Figure 346: S3 – variation in vertical deflection near interior south beam.*
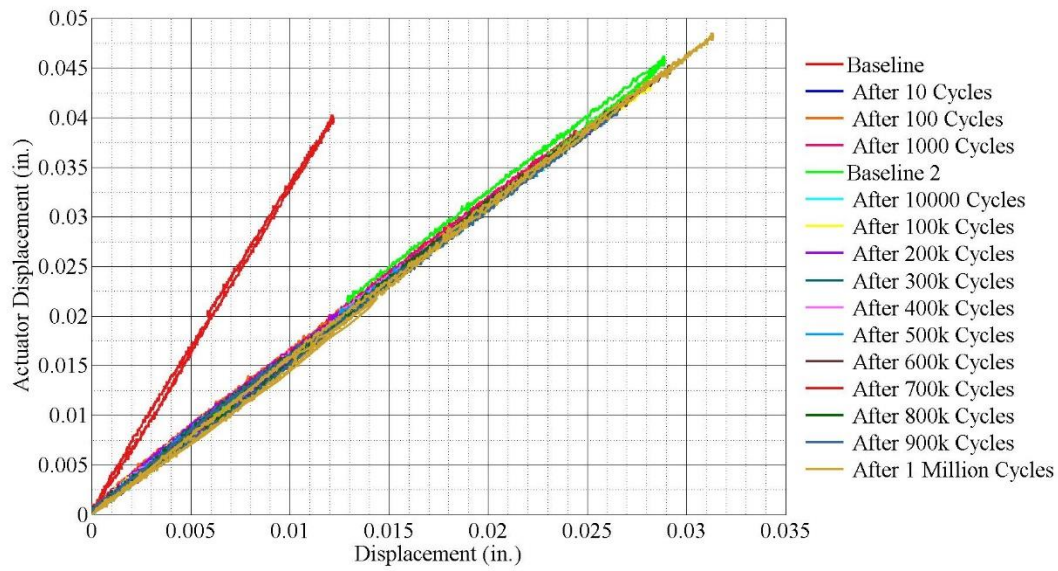
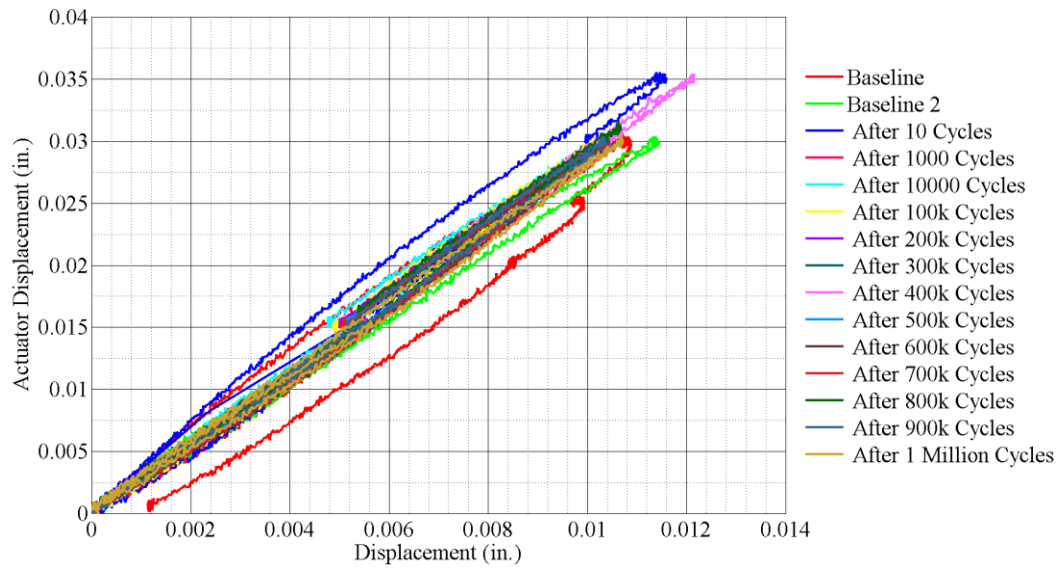*Figure 347: S3 – variation in vertical deflection near interior north beam.*
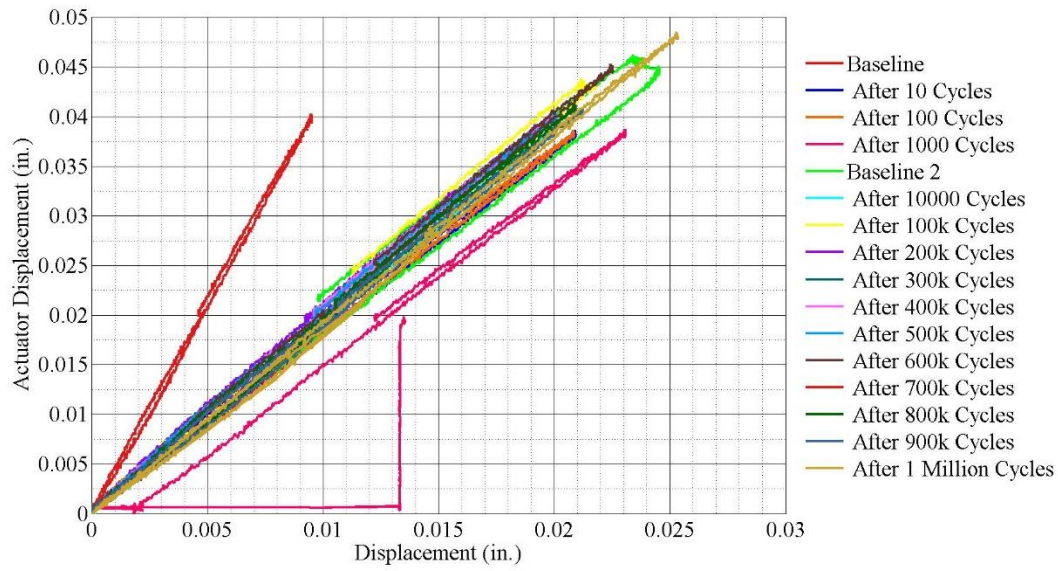
Figure 348: S3 – variation in vertical deflection near exterior north beam.
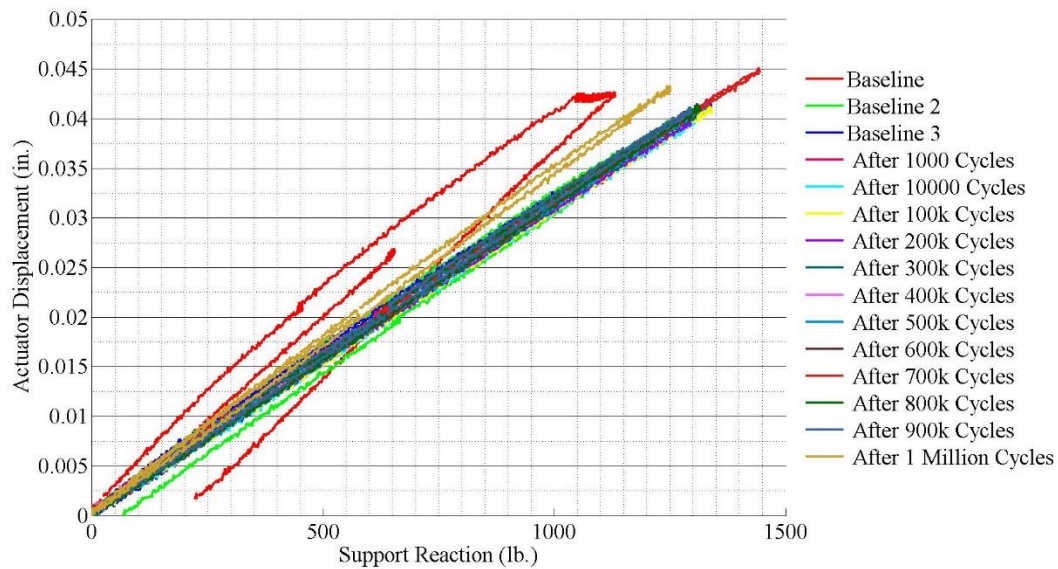
Specimen 4 data
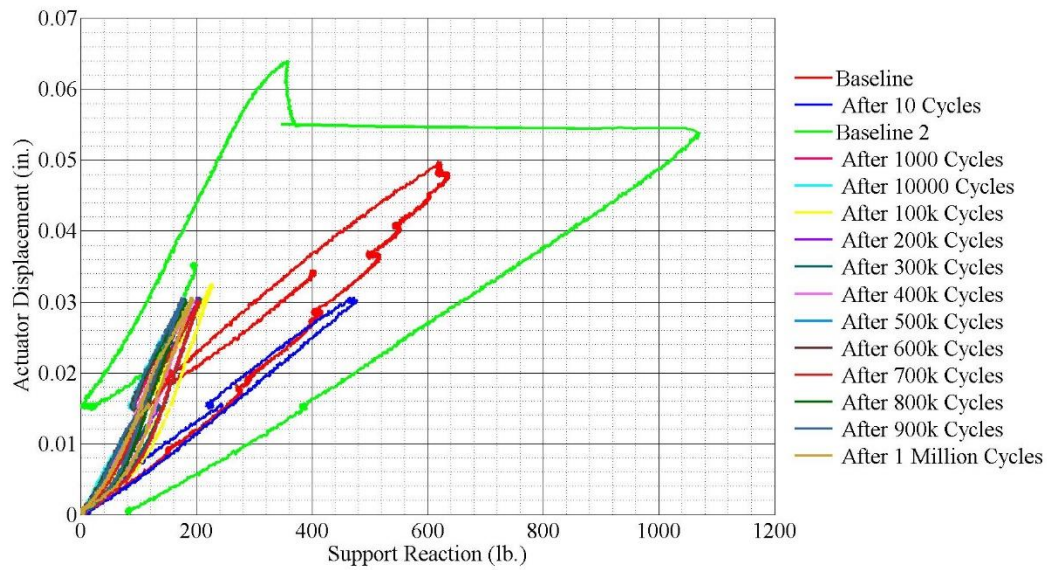
Figure 349: S4 – variation in load cell values on exterior south beam.

Figure 350: S4 – variation in east load cell values on interior south beam.

NOTE: The east load cell on interior south beam of S4, shown in Figure 350, did not record any data on account that it did not work for the duration of testing and was replaced in the next test.
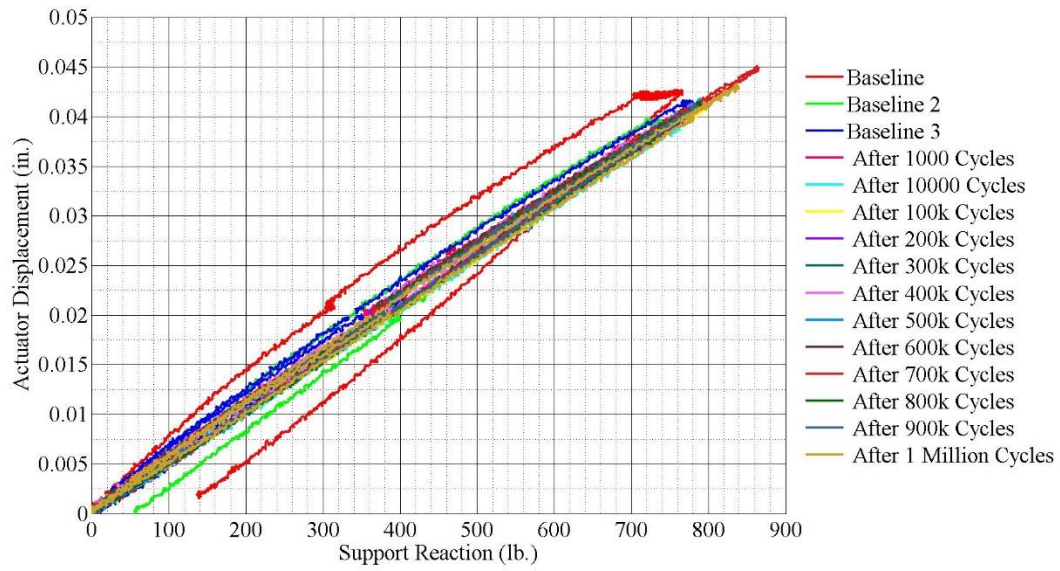

Figure 351: S4 – variation in west load cell values on interior south beam

Figure 352: S4 – variation in east load cell values on interior north beam

Figure 353: S4 – variation in west load cell values on interior north beam

324

Figure 354: S4 – variation in load cell values on exterior north beam

NOTE: The data for vertical deflection for S4 is presented in Section 6.2.4.1.

Specimen 5 data

Figure 355: S5 – variation in load cell values on exterior south beam.

Figure 356: S5 – variation in east load cell values on interior south beam.
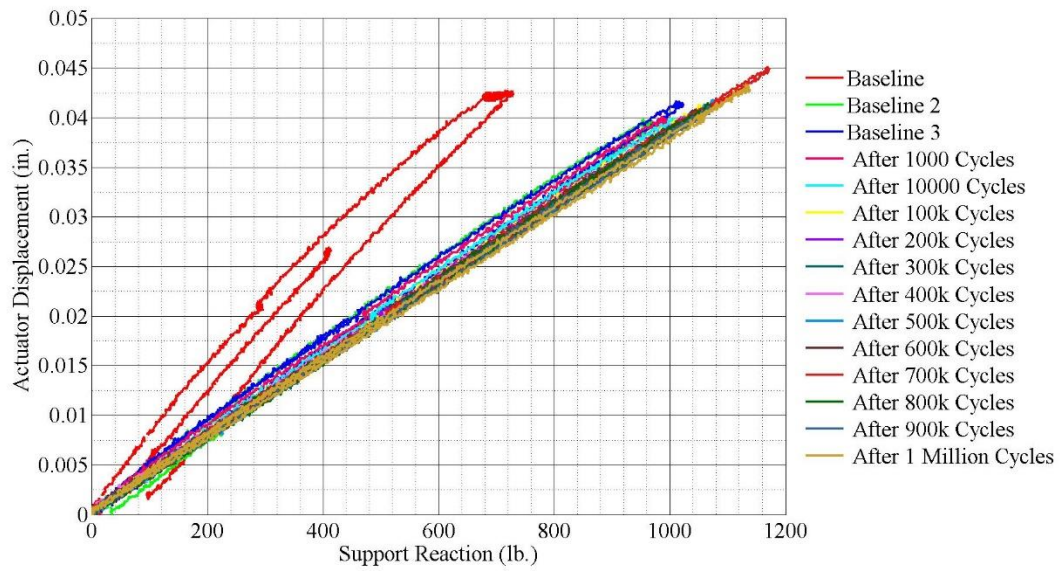

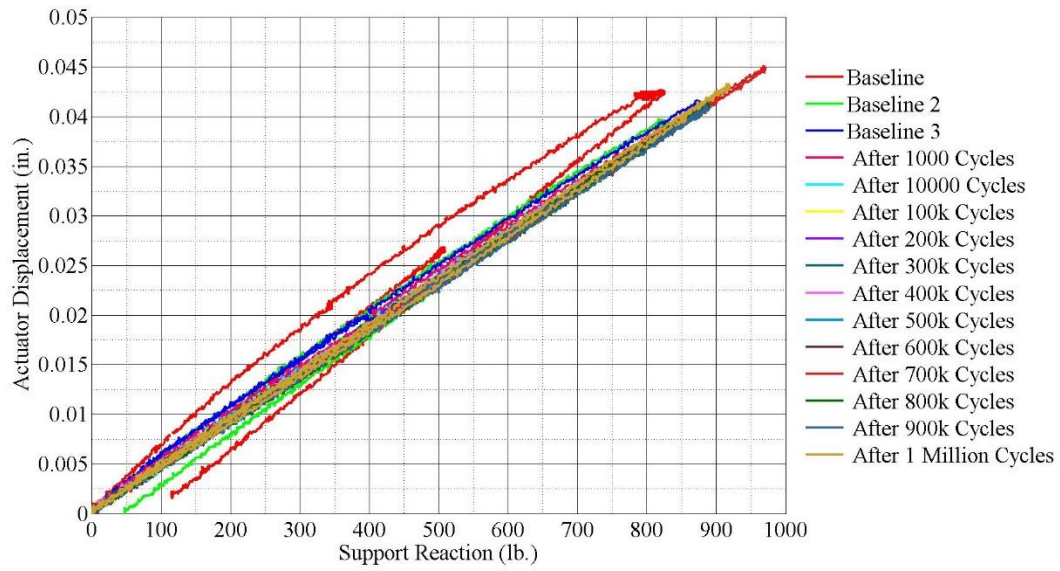*Figure 357: S5 – variation in west load cell values on interior south beam*

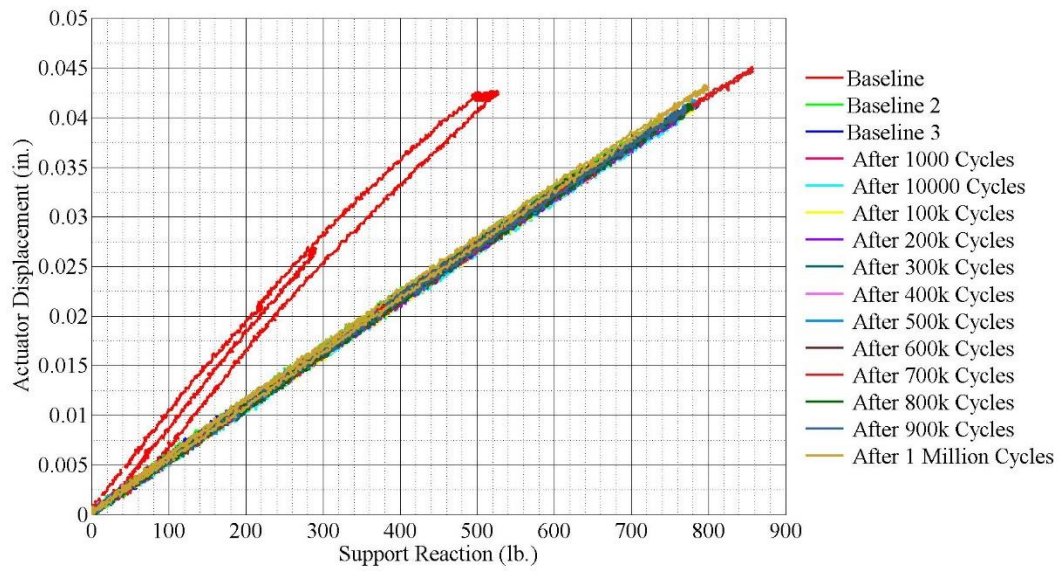*Figure 358: S5 – variation in east load cell values on interior north beam*

Figure 359: S5 – variation in west load cell values on interior north beam
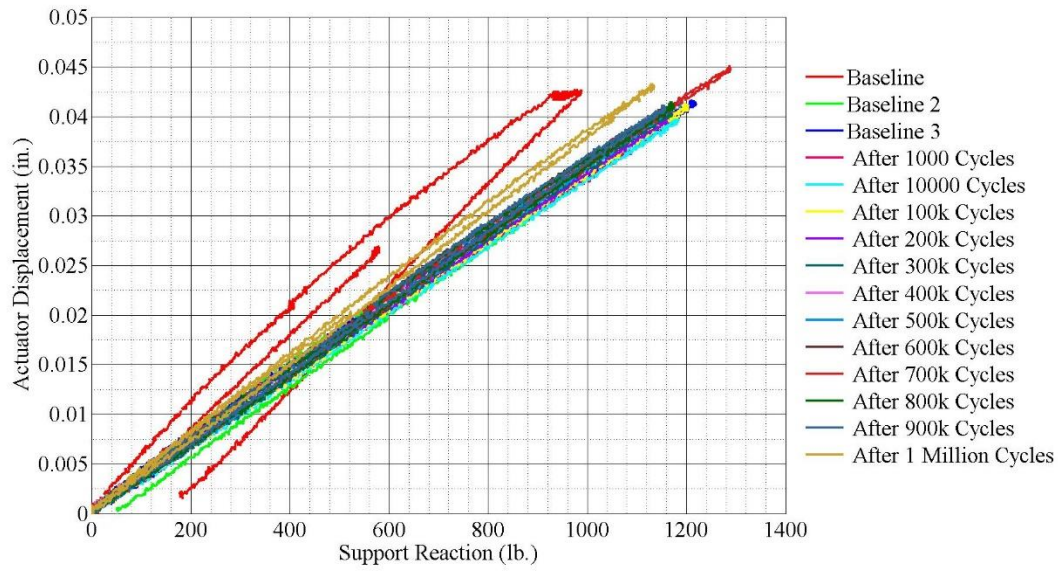
Figure 360: S5 – variation in load cell values on exterior north beam.

Figure 361: S5 – variation in vertical deflection near exterior south beam.

Figure 362: S5 – variation in vertical deflection near interior south beam.

Figure 363: S5 – variation in vertical deflection near interior north beam.

Figure 364: S5 – variation in vertical deflection near exterior north beam.

Specimen 6 data

Figure 365: S6 – variation in load cell values on exterior south beam.

Figure 366: S6 – variation in east load cell values on interior south beam.

Figure 367: S6 – variation in west load cell values on interior south beam

Figure 368: S6 – variation in east load cell values on interior north beam

Figure 369: S6 – variation in west load cell values on interior north beam

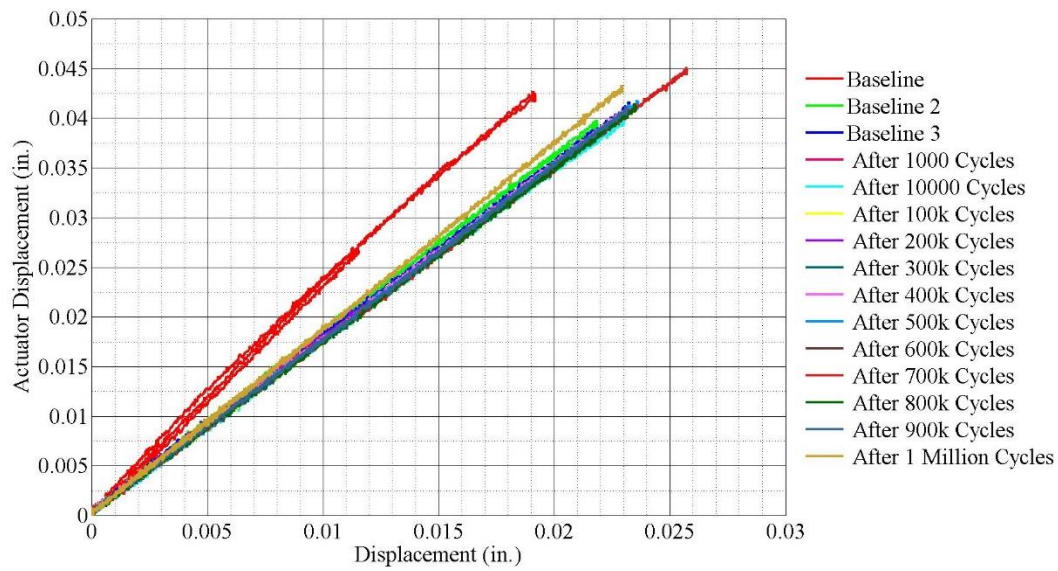*Figure 370: S6 – variation in load cell values on exterior north beam*

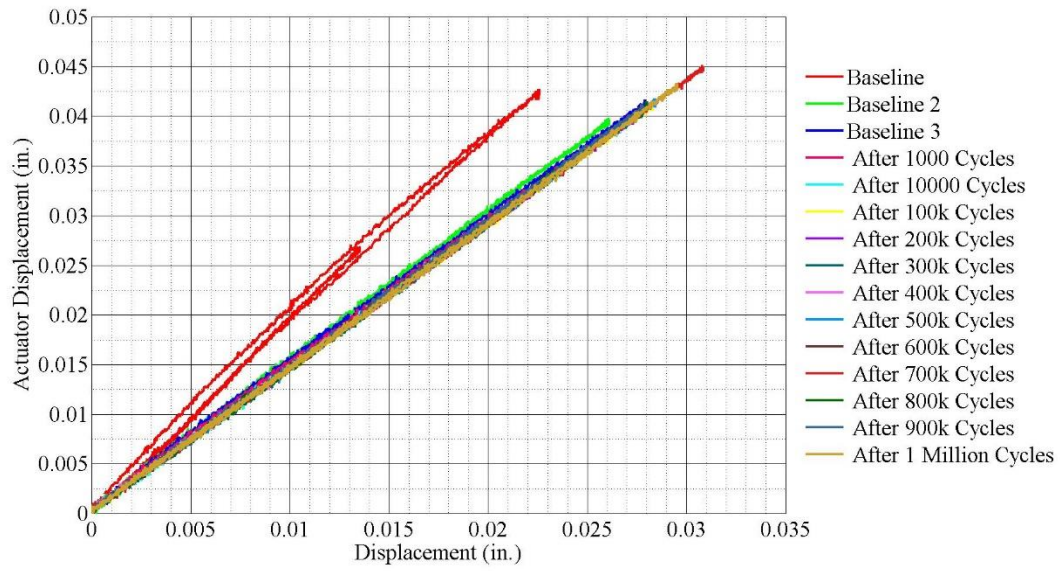*Figure 371: S6 – variation in vertical deflection near exterior south beam.*

Figure 372: S6 – variation in vertical deflection near interior south beam.
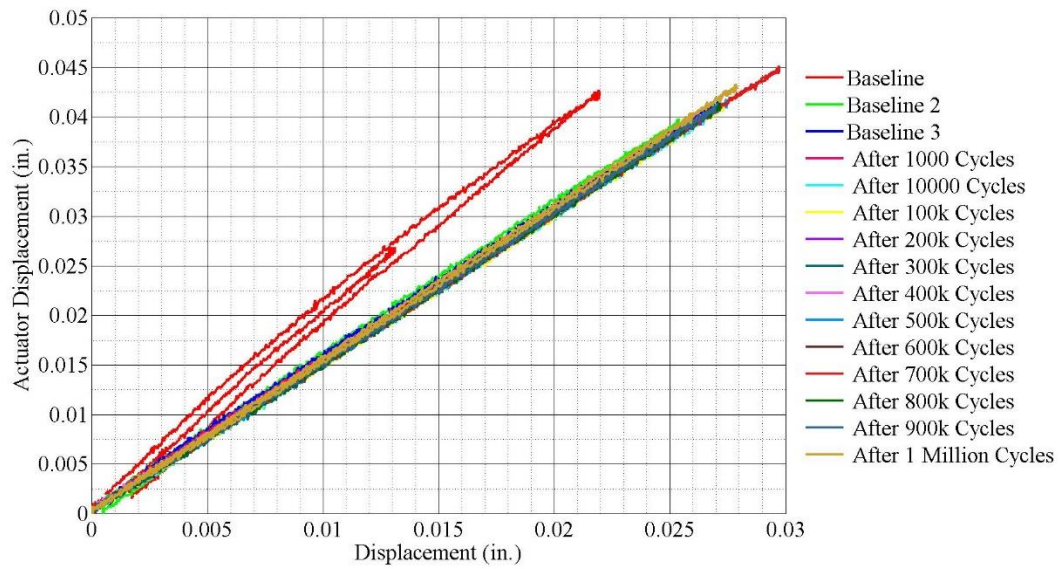

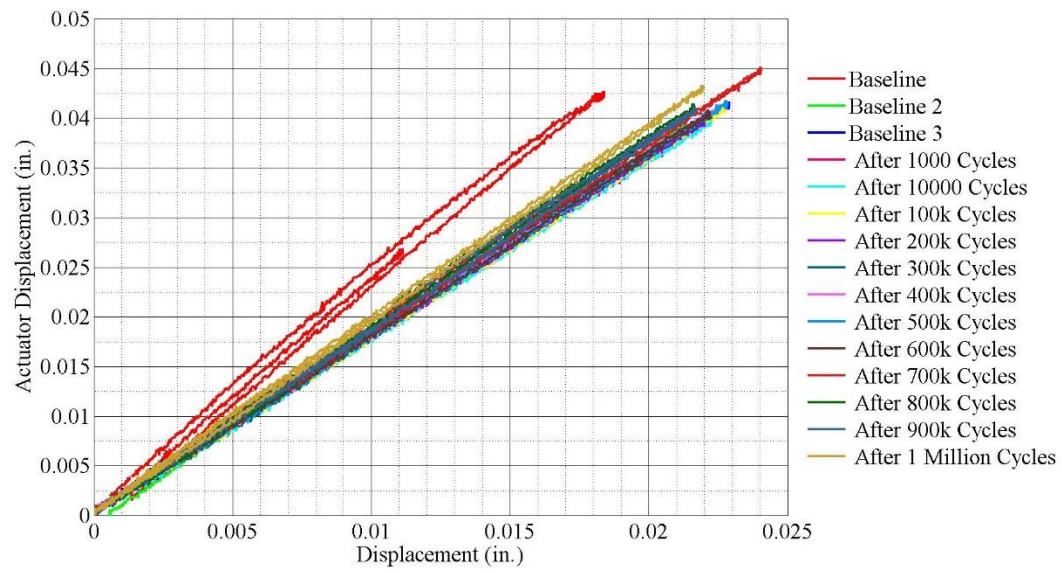*Figure 373: S6 – variation in vertical deflection near interior north beam.*

Figure 374: S6 – variation in vertical deflection near exterior north beam.